

WPP-170
ISSN 1022-6656
October 1999

International Workshop Proceedings

CLARE '98

Cloud Lidar & Radar Experiment

ESTEC, Noordwijk, The Netherlands
13-14 September 1999

**European Space Agency
Agence spatiale européenne**

Workshop Organiser: **P. Wursteisen**, ESA-ESTEC
Earth Sciences Division

Disclaimer:

This document is published in the ESA WPP (*Workshop Preliminary Proceedings*) series. This is an informal series and the documents do not necessarily carry the full authority of the formal ESA publication series. Such working documents are intended for issue to workshop participants only. Some papers in the WPP series may be selected for editing and inclusion in a formal ESA publication at a later date. There is no formal distribution of WPP publications; distribution is arranged by the workshop organiser.

Copyright © 1999 European Space Agency

CONTENTS

INTRODUCTION

- CLARE'98 CAMPAIGN SUMMARY 9
 P. Wursteisen, *ESA/ESTEC, Noordwijk, The Netherlands*;
 A. Illingworth, *University Reading, UK*

INSTRUMENT CALIBRATION AND PERFORMANCE

- OVERVIEW OF THE FLIGHTS AND DATASETS 17
 A. Illingworth, R. Hogan, *University Reading, UK*
- A SUMMARY OF THE CLOUD MICROPHYSICS DATA COLLECTED DURING CLARE '98 BY THE UKMO C-130 AIRCRAFT 25
 P. Francis, *UK Meteorological Office, Farnborough, UK*
- ARAT OBSERVATIONS OF WARM AND COLD CLOUDS DURING CLARE'98 FROM LIDAR, RADAR AND RADIOMETRY 33
 J. Pelon, V. Trouillet, C. Flamant, P. Genau, *IPSL, Service d'Aéronomie, Paris, France*; J. Testud, A. Guyot, *IPSL, CETP, Vélizy, France*; D. Leon, S. Aimov, G. Vali, *University Wyoming, USA*; C. Allet, F. Blouzon, *INSU/DT, St-Maur, France*
- THE 3 WAVELENGTHS LIDAR ALEX AND OTHER INSTRUMENTATION ONBOARD THE FALCON DURING CLARE'98 39
 H. Flentje, C. Kiemle, V. Weiss, M. Wirth, W. Renger, *DLR, Oberpfaffenhofen, Germany*
- AN OVERVIEW OF THE UKMO C-130 MEASUREMENTS FROM CLARE'98 43
 P. Francis, *UK Meteorological Office, Farnborough, UK*
- PROVISION OF CHILBOLTON INFRASTRUCTURE AND INSTRUMENTATION FOR CLARE '98 47
 J. Goddard, *RAL, Chilton, UK*
- THE GKSS 95 GHZ CLOUD RADAR DURING CLARE '98: SYSTEM PERFORMANCE AND DATA PRODUCTS 51
 O. Danne, M. Quante, *GKSS, Geesthacht, Germany*
- RADIATION MEASUREMENTS DURING CLARE'98: AN OVERVIEW 55
 A. v. Lammeren, E. Meijer, A. Feijt, *KNMI, De Bilt, The Netherlands*;
 S. Jongen, *University of Technology, Eindhoven, The Netherlands*;
 J. Erkelens, H. Russchenberg, *University of Technology, Delft, The Netherlands*
- CALIBRATION OF THE GROUND-BASED RADARS USED IN CLARE '98 63
 R. Hogan, *Univ. Reading, UK*; J. Goddard, *RAL, Chilton, UK*
- CALIBRATION OF THE UNIVERSITY OF WYOMING 95 GHZ AIRBORNE RADAR DURING CLARE '98 69
 A. Guyot, J. Testud, *IPSL, CETP, Vélizy, France*; O. Danne, M. Quante, *GKSS, Geesthacht, Germany*; P. Francis, *UK Meteorological Office, Farnborough, UK*

CLOUD BOUNDARY RETRIEVAL BY RADAR AND LIDAR

- ANALYSIS OF RADAR AND LIDAR RETURNS FROM CLOUDS:
IMPLICATIONS FOR THE PROPOSED EARTH RADIATION MISSION 75
R. Hogan, A. Illingworth, *University Reading, UK*

- CLOUD BOUNDARIES AND STRUCTURE IN MIXED PHASE, MID-LEVEL CLOUDS AS DEDUCED
FROM GROUND-BASED 95-GHZ RADAR AND AIRBORNE LIDAR MEASUREMENTS DURING
CLARE '98 81
M. Quante, O. Danne, *GKSS, Geesthacht, Germany*; A. Flentje,
W. Renger, *DLR, Oberpfaffenhofen, Germany*; P. Francis,
UK Meteorological Office, Farnborough, UK

- MEASUREMENTS FOR CLARE '98 CAMPAIGN USING THE CHILBOLTON UV RADAR 89
J. Agnew, A. Gibson, A. Marsh, *RAL, Chilton, UK*

LIQUID WATER RETRIEVAL

- OBSERVATIONS OF WARM AND COLD CLOUDS USING THE AIRBORNE BACKSCATTERING
LIDAR LEANDRE 1 DURING CLARE'98, PART 1: LIDAR DATA ANALYSIS 99
J. Pelon, V. Trouillet, C. Flamant, *IPSL, Service d'Aéronomie, Paris,
France*; H. Chepfer, L. Sauvage, V. Noel, P. Flamant, *Ecole Polytechnique,
Palaiseau, France*

- OBSERVATIONS OF WARM AND COLD CLOUDS USING THE AIRBORNE BACKSCATTERING
LIDAR LEANDRE 1 DURING CLARE'98, PART 2: SYNERGISM WITH RADAR 103
MEASUREMENTS
J. Pelon, V. Trouillet, *IPSL, Service d'Aéronomie, Paris, France*;
J. Testud, A. Guyot, *IPSL, CETP, Vélizy, France*; M. Quante, O. Danne,
GKSS, Geesthacht, Germany; P. Francis, *UK Meteorological Office,
Farnborough, UK*; H. Chepfer, V. Noel, P. Flamant, *Ecole Polytechnique,
Palaiseau, France*; D. Leon, S. Aimov, G. Vali, *University Wyoming, USA*

- STRATOCUMULUS LIQUID WATER CONTENT FROM DUAL WAVELENGTH RADAR 107
R. Hogan, A. Illingworth, *Univ. Reading, UK*; J. Goddard, *RAL, Chilton,
UK*; S. Jongen, *University of Technology, Eindhoven,
The Netherlands*; H. Sauvageot, *Université P. Sabatier, Toulouse, France*

- STUDY OF THE MICRO-PHYSICAL AND MACRO-PHYSICAL MEASUREMENTS OF WATER
CLOUDS DURING CLARE '98 111
R. Beadi, J. de Wit, H. Russchenberg, *University of Technology, Delft,
The Netherlands*; J. Póiares Baptista, *ESA-ESTEC, Noordwijk,
The Netherlands*

- DEVELOPMENT OF RETRIEVAL ALGORITHMS OF CLOUD PARAMETERS FROM RADAR AND
LIDAR BASED ON THE CLARE '98 DATA SET 117
J. de Wit, R. Beadi, J. Erkelens, *University of Technology, Delft,
The Netherlands*; J. Póiares Baptista, *ESA-ESTEC, Noordwijk,
The Netherlands*; H. Russchenberg, *University of Technology, Delft,
The Netherlands*

- ALTERNATIVE ALGORITHM FOR CORRECTING FSSP MEASUREMENTS 123
R. Beadi, J. de Wit, H. Russchenberg, *University of Technology, Delft,
The Netherlands*; J. Póiares Baptista, *ESA-ESTEC, Noordwijk,
The Netherlands*

ESTIMATION OF CLOUD MICROPHYSICAL PARAMETERS FROM RADAR, LIDAR AND MICROWAVE RADIOMETER DURING CLARE'98	129
J. Erkelens, H. Russchenberg, <i>University of Technology, Delft, The Netherlands</i> ; S. Jongen, M. Herben, <i>University of Technology, Eindhoven, The Netherlands</i> ; J. Goddard, C. Wrench, <i>RAL, Chilton, UK</i> ; H. Sauvageot, <i>Université P. Sabatier, Toulouse, France</i> ; R. Hogan, <i>University Reading, UK</i> ; P. Francis, <i>UK Meteorological Office, Farnborough, UK</i> ; M. Quante, <i>GKSS, Geesthacht, Germany</i>	
PHOTON PATHLENGTHS DISTRIBUTIONS AND CLOUD OPTICAL DEPTH DERIVED FROM HIGH RESOLUTION OXYGEN A-BAND ABSORPTION SPECTROSCOPY	137
O. Funk, C. Kurz, U. Platt, K. Pfeilsticker, <i>University Heidelberg, Germany</i>	
COMPARISON OF CLOUD LIQUID WATER PATH ESTIMATES DURING CLARE'98	141
C. L. Wrench, <i>RAL, Chilton, UK</i> ; S. C. H. M. Jongen, <i>University of Technology, Eindhoven, The Netherlands</i> ; O. T. Davies, <i>University of Bath, Avon, UK</i>	
ICE WATER RETRIEVAL BY RADAR / LIDAR SYNERGY	
CLOUD EFFECTIVE RADIUS AND WATER CONTENTS INFERRED FROM COMBINED LIDAR AND RADAR OBSERVATIONS DURING CLARE '98	147
D. Donovan, A. von Lammeren, <i>KNMI, De Bilt, The Netherlands</i> ; J. Goddard, <i>RAL, Chilton, UK</i> ; H. Sauvageot, <i>Université P. Sabatier, Toulouse, France</i> ; R. Hogan, <i>University Reading, UK</i>	
SYNERGY IN ICE CLOUDS BETWEEN AIRBORNE NADIR POINTING RADAR AND LIDAR DURING CLARE '98	153
A. Guyot, J. Testud, <i>IPSL, CETP, Vélizy, France</i> ; J. Pelon, V. Trouillet, <i>IPSL, Service d'Aéronomie, Paris, France</i> ; P. Francis, <i>UK Meteorological Office, Farnborough, UK</i>	
NON-RAYLEIGH SCATTERING EFFECTS IN MIXED-PHASE CLOUD OBSERVATIONS	157
N. Gaussiat, H. Sauvageot, <i>Observatoire Midi-Pyrénées, Toulouse, France</i>	
A CLIMATOLOGY OF SUPERCOOLED LAYER CLOUDS FROM LIDAR CEILOMETER DATA	161
R. Hogan, A. Illingworth, <i>University Reading, UK</i>	
POLARIMETRIC RADAR OBSERVATIONS OF THE GROWTH OF HIGHLY-ALIGNED ICE CRYSTALS IN THE PRESENCE OF SUPERCOOLED WATER	167
R. Hogan, A. Illingworth, <i>University Reading, UK</i> ; P. Field, <i>DERA, Farnborough, UK</i>	
COMPARISON OF LIDAR/RADAR ICE CLOUD PARAMETER RETRIEVALS WITH IN-SITU MEASUREMENTS	173
D. Donovan, A. van Lammeren, <i>KNMI, De Bilt, The Netherlands</i> ; R. Hogan, A. Illingworth, <i>University Reading, UK</i> ; P. Francis, <i>UK Meteorological Office, Farnborough, UK</i> ; J. Testud, <i>IPSL, CETP, Vélizy, France</i> ; J. Pelon, <i>IPSL, Service d'Aéronomie, Paris, France</i> ; M. Quante, <i>GKSS, Geesthacht, Germany</i> ; J. Goddard, <i>RAL, Chilton, UK</i>	

SATELLITE IMPLICATIONS AND COMPARISONS

- MULTIPLE SCATTERING IN CIRRUS AND MIXED PHASE MID-LEVEL ICE/WATER CLOUDS DURING CLARE '98 AND IMPLICATIONS FOR SPACE LIDAR 181
 H. Flentje, C. Kiemle, W. Renger, *DLR, Oberpfaffenhofen, Germany*
- CLOUD-FIELD VARIABILITY FROM GROUND-BASED LIDAR AND RADAR OBSERVATIONS 191
 D. Donovan, A. van Lammeren, *KNMI, De Bilt, The Netherlands*;
 H. Russchenberg, *Technical University, Delft, The Netherlands*;
 A. Apituley, *RIVM, Bilthoven, The Netherlands*
- IMPLICATIONS FOR THE SPLIT MISSION SCENARIO 215
 R. Hogan, A. Illingworth, *University Reading, UK*
- COMPARISON OF ECMWF CLOUD COVER WITH RADAR DERIVED VALUES 217
 R. Hogan, *University Reading, UK*; C. Jakob, *ECMWF, Reading, UK*;
 A. Illingworth, *University Reading, UK*

RADIATION CALCULATIONS

- AN ANALYSIS OF THE AIRBORNE BROAD-BAND RADIOMETER MEASUREMENTS COLLECTED DURING CLARE'98 225
 P. Francis, *UK Meteorological Office, Farnborough, UK*; H. Flentje, *DLR, Oberpfaffenhofen, Germany*; J. Pelon, *IPSL, Service d'Aéronomie, Paris, France*; J. Testud, *IPSL, CETP, Vélizy, France*
- ACTIVE-PASSIVE SENSOR SYNERGY FOR CLOUD OBSERVATION: IR CLOUD PROPERTIES AND CLOUD LIQUID WATER 233
 H. Bloemink, A. van Lammeren, A. Feijt, *KNMI, De Bilt, The Netherlands*; S. Jongen, *Technical University, Eindhoven, The Netherlands*

Introduction



CLARE'98 Campaign Summary

P. Wursteisen¹, A. Illingworth²

[1] ESA-ESTEC, Noordwijk, The Netherlands

[2] University Reading, UK

E-mail: [1] pwurstei@estec.esa.nl,

E-mail: [2] a.j.illingworth@reading.ac.uk

INTRODUCTION

The Cloud Lidar And Radar Experiment CLARE'98 campaign is part of the ESA 's Earth Observation Preparatory Programme (EOPP). The objectives of the CLARE'98 campaign are to collect and analyse radar and lidar as well as *in-situ* data to support the development of retrieval algorithms and to consolidate the scientific requirements of the future Earth Radiation Mission.

The campaign took place during the period 5-23 October 1998 at the Observatory of Chilbolton, Hampshire, UK, to take advantage of a number of supporting ground-based observations. The largest instrument located at Chilbolton, the 3 GHz radar CAMRa with its 25 metres antenna, is shown on figure 1.



Figure 1: The 25-metre antenna at Chilbolton, during an overflight of the UK Met. Office C-130 aircraft.

OVERVIEW OF THE INSTRUMENTS

A considerable number of instruments were available for the campaign, on ground and airborne. They are described in more details in the paper on page 17.

The C-130 and ARAT aircraft were present throughout the campaign. The German Falcon aircraft was present from

12-23 October. Seven missions were flown and sampled a wide variety of liquid water, mixed phase and ice clouds.

One of the aircraft, the C-130, operated by the UK Met. Office is shown on figure 2. The ARAT aircraft, owned by the French IPSL is shown on figure 3.



Figure 2: A front view of the UK Met. Office C-130 aircraft.



Figure 3: A view of the ARAT aircraft from the IPSL.

An overview of the meteorological conditions and the data obtained during these seven flight is given in the paper on page 17. A summary of the specifications and performance of the various airborne instruments, together with the ground based instruments which operated continuously

thin layer of enhanced lidar backscatter on 20 October (see the papers on page 17 for overview, page 51 for discussion, and page 33). Analysis of more extensive ground based radar and lidar observations (paper page 167) reveals that such layers of supercooled liquid water are quite common and can be easily identified by the combined returns of the two active instruments. Clearly, the presence of such layers has important implications for the radiative properties of clouds and also the glaciation and lifetime of cloud which must be correctly represented in global models. The projected spaceborne mission would be able to detect such layers and this is an exciting finding.

Further work is needed, requiring analysis and new observations, to perfect the algorithms for detecting such layers and to define and remove any remaining ambiguities.

◆ Ice clouds.

Our lack of quantitative global data of ice clouds is a major gap in the validation of current global circulation models. The Earth Radiation Mission aims to fill this gap.

The combined radar and lidar should be able to detect virtually all significant ice clouds and their boundaries as discussed earlier (papers on page 75 and 81). The combined use of radar and lidar is analysed in the paper on page 147 and a stable method of correcting for lidar attenuation using the radar reflectivity as a first guess is proposed which then iterates to a solution for ice particle size and water content.

The paper on page 153 suggests an alternative retrieval approach to derive ice particle size and water content which involves making an initial assumption that the normalised ice particle concentration does not vary with altitude. The paper on page 157 shows that the algorithm for retrieving liquid water content from the differential attenuation of the radar return at two frequencies will fail when ice particles are present which are large enough to Mie scatter at one of the frequencies.

The paper on page 181 demonstrates that the degree of multiple scattering from a spaceborne radar in ice clouds (as opposed to liquid clouds) should be small and should not have a major effect on the spaceborne retrievals. The papers on page 191 and 215 confirm that, because of the variability of ice cloud properties over short distances, the simultaneous radar/lidar retrievals will only operate efficiently if the two instruments are embarked upon the same platform. A glimpse of how such ice cloud data from a future satellite could be used in model validation is provided by the paper on page 217 which compares the vertical profile of fractional cloud cover derived from radar and lidar at the Chilbolton site with the values held in the ECMWF operational model and finds that small but definite biases are apparent.

It is concluded that the combined use of radar and lidar from space should provide unique data on the ice cloud properties such as ice water content and particle size provided they are embarked upon the same platform, but the retrieval techniques are not yet definitive and further work is needed to perfect and validate the retrieval techniques and quantify their errors.

◆ Radiation Calculations.

At this stage in the analysis only a start has been made on radiation calculations. The paper on page 233 demonstrates that the ground based IR emissivity for water clouds of known temperature can be related to their liquid water path but that for ice the relationship is less simple. The paper on page 225 shows that, for water clouds, the observed radiative fluxes in the visible from the aircraft are consistent with the values of optical depth and albedo inferred for the cloud; for ice cloud the situation is more difficult. The ice clouds have many variable parameters so that it is impossible to take the measured radiative fluxes and derive a unique cloud profile. Instead, the philosophy to be adapted is the one that is envisaged for the spaceborne mission. Once the profiles of ice cloud properties have been derived from the active sensors, then these values will be fed into a radiative transfer model which predicts the radiative fluxes and these fluxes can then be compared with the aircraft flux observations. It is important that this work be carried out as it parallels exactly the procedures that will be followed in the pro-posed space mission.

OVERALL SUMMARY AND RECOMMENDATIONS

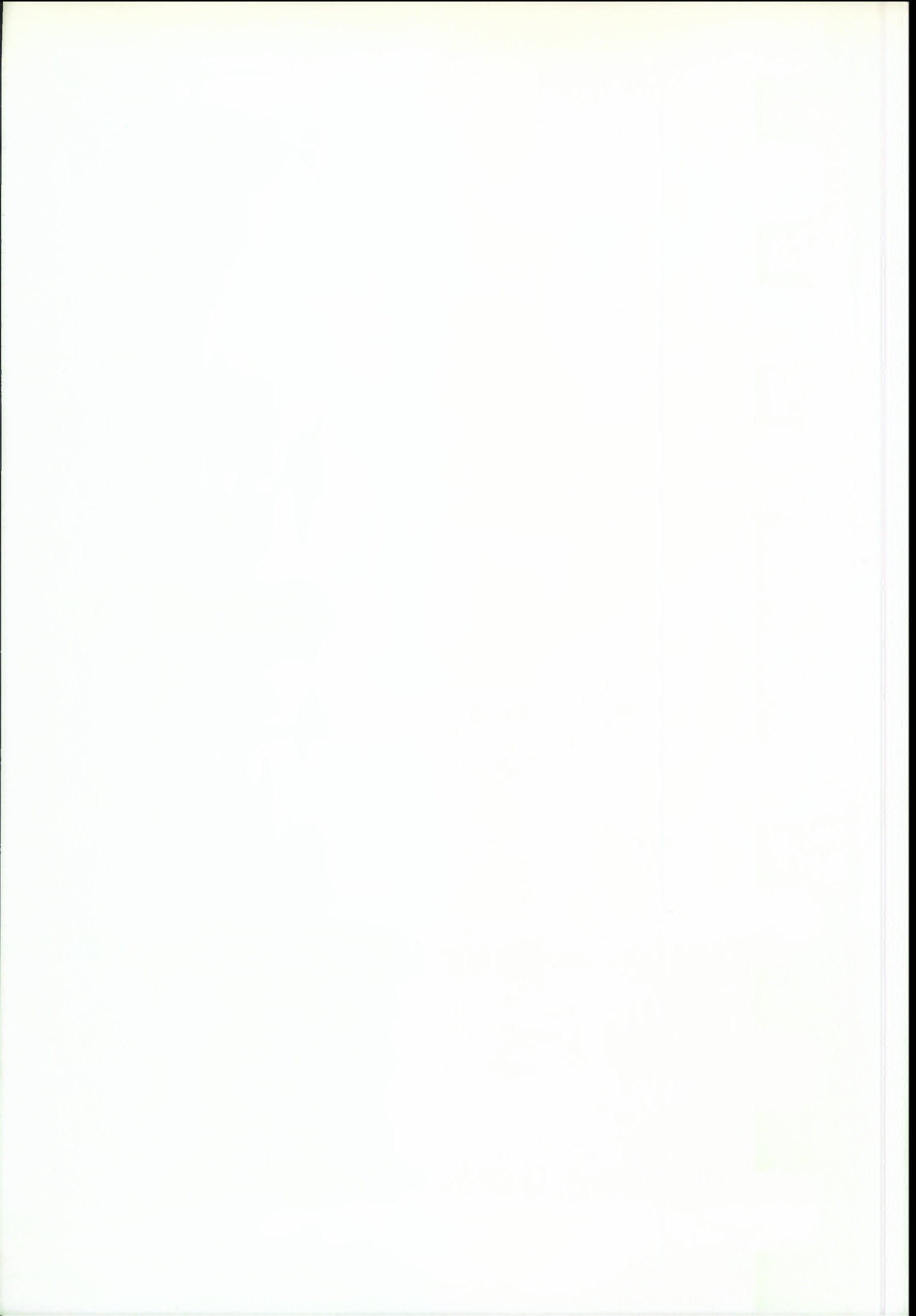
- i) There have been seven successful aircraft missions probing a variety of clouds.
- ii) The combination of radar and lidar spaceborne sensors should be able to detect virtually all radiatively significant ice clouds and the majority of water clouds together with their tops and bases and any multiple cloud layers.
- iii) Techniques have been developed and validated for deriving the vertical profiles of liquid water cloud characteristics but it will be difficult to adapt them for spaceborne use. From space it should be possible to define cloud top and cloud base of liquid water clouds and then, using passive information, infer cloud water content, but further work is needed to refine such retrievals.
- iv) The combination of spaceborne radar and lidar should prove a powerful tool to quantify the occurrence of layers of supercooled water. The representation of such layers is important in global models because of their effect on cloud radiation and cloud lifetime, but it is only with these new observations that the ubiquity of such clouds has been established. Further

work is needed to confirm the efficiency with which lidar and radar can identify such layers.

- v) The combination of radar and lidar is a uniquely powerful tool for quantifying the ice water content and effective radius of ice clouds providing the two instruments are embarked upon the same spaceborne platform. The global characteristics of such clouds are urgently needed for validating global circulation models. Further work is needed to refine and perfect the radar and lidar retrieval algorithms.
- vi) A start has been made on confirming that consistency of the radiative fluxes by the aircraft with the vertical profiles of cloud properties of the clouds inferred by remote sensing. Much more work is now needed on this aspect as it parallels exactly the retrievals envisaged for the future spaceborne mission.



Figure 5: The participants of the CLARE'98 campaign, posing in front of the 25-metre antenna at Chilbolton



**Instrument Calibration
and
Performance**



Overview of the flights and datasets

Anthony J. Illingworth* and all CLARE participants

*Department of Meteorology, University of Reading, RG6 6BB, UK.

Email: A.J.Illingworth@reading.ac.uk

INTRODUCTION

The CLARE98 Campaign was successfully executed during the period 5–23 October 1998. The C-130 and ARAT aircraft were present throughout the campaign. The DLR Falcon aircraft was present from 12–23 October. Seven missions were flown which used up the total flying hours available from the three aircraft. Ground based data were taken during the flights from radars at 3, 35 and 94/95 GHz, together with radiometers, interferometers, ceilometers, and flux meters. For most of these instruments data was also logged during the whole of the campaign; this data is described in subsequent summaries. In this document we concentrate on the seven aircraft flights.

The aircraft flew legs towards and away from the Chilbolton site on the 260° azimuth. The Falcon was flying at a high level of about 10 km with a downward looking lidar generally above the cloud; the ARAT was generally at its ceiling of 5 km with its radar and lidar looking downwards to cloud below where, ideally, the C-130 was making in-situ microphysical measurements. The co-ordination of the aircraft worked very well with a pair of synchronised inbound and outbound legs over Chilbolton typically every thirty minutes.

A summary of the number of single legs per mission is as follows:

Date	Mission	C-130 legs	ARAT legs	Falcon legs
7 Oct 98	1	8	8	-
13 Oct 98	2	16	10	10
14 Oct 98	3	14	8	8
16 Oct 98	4	14	-	-
20 Oct 98	5	28	18	18
21 Oct 98	6	8	6	6
22 Oct 98	7	12	-	-

Twelve single legs were identified for intensive analysis, which include data in liquid, ice and mixed-phase clouds:

Date	Mission	Time	Comments
20 Oct	5	1420	3.9 km 'Thick cirrus'
		1450	4.5 km '1.2 g kg ⁻¹ ice snow, -10.1°C
		1520	5.4 km 'thick ice cloud -14.5°C
13 Oct	2	1340	2.3 km '300m deep stratus 5°C
21 Oct	6	1020	5.7 km -20°C Ice cloud. ARAT lidar up, Falcon down.
7 Oct	1	1400	1.95 km, 'Supercooled Sc' (No Falcon).

The comments are those of the C-130 which was making in-situ penetrations. The times (UTC) are those for the nominal inbound overflight of Chilbolton. The data gathered thus cover a variety of clouds which are typical of those that a future spaceborne mission would sample.

OVERVIEW OF THE INSTRUMENTS

Ground based at Chilbolton:

RAL 3 GHz scanning and 94 GHz vertically-pointing radars. 22/28/78/94 GHz zenith pointing radiometers. UV lidar. Ceilometer. Standard Met instruments. Cloud camera.

CRA 35 GHz scanning radar. 35GHz radiometer.

GKSS 95 GHz vertically pointing radar.

KNMI IR radiometer. Video camera. Vis-IR radiative fluxes.

TU Delft/TU Eindhoven 21.3, 23.8, 31.65, 51.25, 53.85, 54.85 GHz ESTEC radiometers.

Scientists from Heidelberg operated a high resolution A-band radiometer from which it should be possible to derive the optical depth and photon path-length distribution through the clouds.

In addition, experimenters outside the main CLARE group were as follows: University of Bath, UK—GPS path integrated vapour, 95 GHz high performance radiometer; University of Portsmouth—40 GHz radiometer and satellite receiver.

During the flights the scanning radars performed slow RHIs (Range Height Indicator—that is, a scan in elevation at constant azimuth) following the aircraft as they flew along a radial to and from the site. On other occasions the radars performed more rapid RHIs to gain a greater knowledge of the total cloud environment. At other times the scanning radars joined the other instruments in recording vertical dwells during the period of the experiment.

Aircraft:

MRF Hercules aircraft: Temperature, wind, humidity, particle size spectra, bulk water measurements, radiation measurements—broad band, narrow band plus microwave.

IPSL ARAT aircraft: 94 GHz cloud radar (Kestrel from University of Wyoming) and lidar (LEANDRE) and an array of radiometers.

DLR Falcon with 'ALEX' lidar and FUBISS spectrometer together with short and long wave radiometers.

To avoid interference of ground based radars with those on the ARAT, the GKSS radar had its E-field vector at 45° to the aircraft azimuth, and the Galileo (RAL) scanning radar had its E-field in the vertical plane.



Fig. 1: Synoptic situation at noon on 7 October 1998 over the UK. Blue and red lines indicate objectively-analysed cold and warm fronts respectively.

Details of the performance of these instruments both on the aircraft and ground are given in subsequent papers. We now provide an overview of the seven missions illustrated with some typical data gathered.

FLIGHT/MISSION SUMMARIES FOR THE CLARE CAMPAIGN OCTOBER 1998

Times are those of nominal co-ordinated overpasses—precise times to the second (when available) are those when the aircraft were over Chilbolton. The comments and temperatures are from the C-130 when sampling cloud—usually when overhead Chilbolton. Unless otherwise stated the first time is for the inbound leg, the second for the outbound leg, and the aircraft are on a true azimuth of 260°. Flight heights are converted into km using 1000 ft = 304.8 m The runs in bold are those identified for priority analysis.

The synoptic analyses use the objective frontal identification of Hewson (1998, *Met. Apps.*, 5, 37–65: ‘Objective fronts’) in which the isobars are overlaid with the IR satellite data, warm fronts are red and cold front cold, with upper fronts marked hashed and the broad black lines represent upper level jets. The sondes ascents are from Larkhill which is 28 km to the west of Chilbolton.

Mission 1: 7 OCT 1998

Figure 1 shows the synoptic situation at noon. A slack north-easterly airstream was bringing low level stratocumulus in from the North sea. The sonde ascent shows a saturated profile up to about 770 mb with very dry air above. Stratocumulus cloud top was at about 2.2–2.4 km. Initially, the stratocumulus cover was continuous with thicker patches containing drizzle, but after 1410 some breaks were observed. The legs from the mission are listed in Table 1.

Figure 3 is a twenty minute section of the vertical profile of reflectivity taken with the 94GHz GKSS radar. Patches of reflectivity near -10 dBZ coincide with drizzle are clearly visible separated by thinner cloud (typically only 200 m) with reflectivities closer to -40 dBZ. The instrument only records reflectivities above 900 m.

The reflectivity viewed from the downward pointing KESTREL radar on the ARAT is displayed in Fig. 4. The regions of drizzle extending down to the ground with reflectiv-

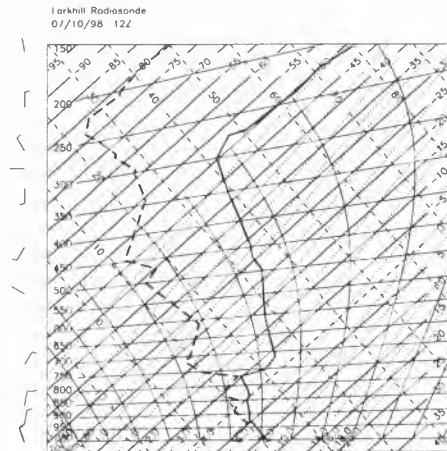


Fig. 2: Radiosonde ascent from Larkhill at 12Z on 7 October 1998.

ARAT and C-130 only. ARAT at 3 km.		
1130:02/1132:34	C-130 only	low level run
1200:16	C-130 only	2.74 km - clear air
1222:45/1226:12	C-130 only	2.74 km - clear air
1249:22/1252:35	C-130 only	2.29 km - ‘in/out cloud tops’
1330:46/1333:52	C-130+ARAT	1.5 km - mostly below cloud
1356:30/1359:49	C-130+ARAT	1.95 km - ‘mainly water droplets -3.7°C’
1426:17/1429:57	C-130+ARAT	1.8 km - -2.4°C ‘over Chilb very little cloud’
1456:26/1459:44	C-130+ARAT	2.1 km ‘no cloud over Chilbolton’

Table 1: Summary of legs in Mission 1.

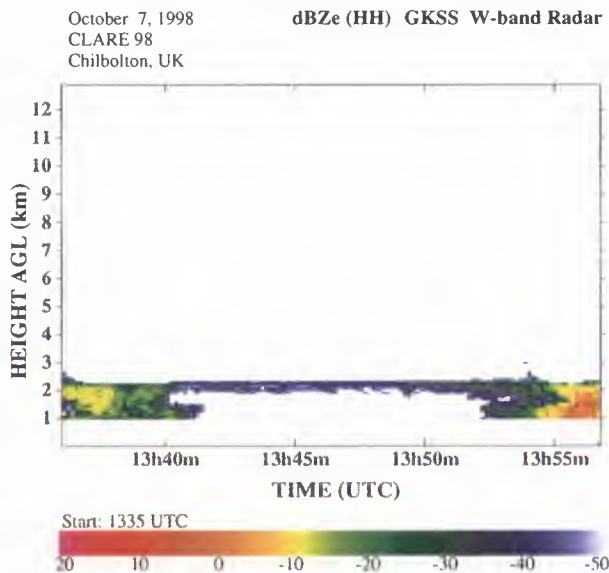


Fig. 3: Time-height section of radar reflectivity from the GKSS 95 GHz radar on 7 October 1998.

ities of about 0 dBZ are clearly visible embedded in lower regions of reflectivity. Figure 5 shows that the downward pointing LEANDRE lidar was severely attenuated by the water cloud and only able to penetrate a very few gates.

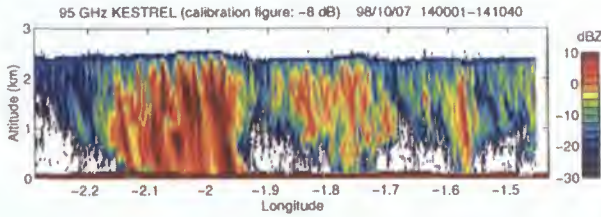


Fig. 4: Radar reflectivity from the airborne 95 GHz KESTREL radar.

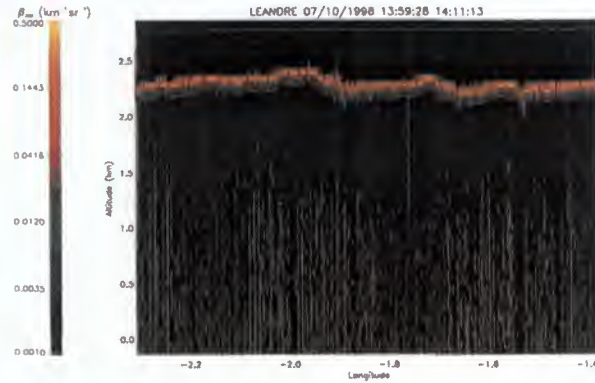


Fig. 5: Backscatter coefficient from the airborne LEANDRE lidar.



Fig. 6: Synoptic situation at noon on 13 October 1998.

Mission 2: 13 OCT 1998

Figure 6 shows that the Chilbolton area was in an open warm sector, and the noon day sonde ascent (Fig. 7) shows the air moist and saturated up to 680 mb, and then another moist layer from 500 mb to the tropopause. The ground based radars showed a thick layer of ice cloud extending from 5–10 km at 100h overlying low cloud, but by the time the aircraft took off this ice cloud had thinned and dispersed. The C-130 penetrated the ice cloud at 1204, but by the time the other two aircraft were on site the most interesting clouds were the thin (300 m) stratocumulus at a height of 2.3 km which were penetrated by the C-130 whilst the other two aircraft flew overhead. The ARAT and Falcon had to return after 1445, after which some higher cloud spread over and the C-130 made some penetration through very thin ice cloud between 5 and 7 km. Table 2 summarises the legs of the mission.

The stratocumulus cloud was thin and of low reflectivity during the 1345 penetration as confirmed by the ground based radar reflectivity displayed in Figure 8. The reflectivity was below the threshold for the KESTREL, although the LEANDRE

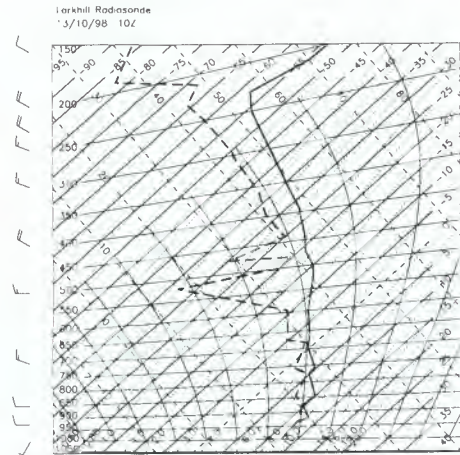


Fig. 7: Radiosonde ascent at 10Z on 13 October 1998.

ARAT at 4 km Falcon 10.5 km		
1108:32	C-130	low level run 1.0 km
1130:42	C-130	overhead climbing
1204:33/1210:06	C-130	7.29 km -28°C Crystals on 2D-C
<i>(Now co-ordinated with ARAT and Falcon)</i>		
1240/1244	C-130	3 km Ci 25k Ac/As 3 km St 1 km
1310:39/1314:42	C-130	3.2 km -1°C 'in thin cloud'
<i>(1316:33 Falcon ohd)</i>		
1340:35/1345:36	C-130	2.3 km '300 m deep Sc no drizzle +5°C'
1410:06/1414:25	C-130	2.1 km 'cloud breaks some blue sky, no cirrus above'
<i>(1409:55 Falcon)</i>		
1440:19/1445:05	C-130	1.2 km 'Entire run in Sc' (GKSS cloud up to 1.5 km)
<i>(ARAT/FALCON return)</i>		
1510:00/1514:34	C-130	4 km Apparently no cloud. GKSS no cloud at 4 km
1543:05/1547:38	C-130	6 km -20°C 'brushing cloud top'
1600	C-130	6 km

Table 2: Summary of legs in Mission 2.

lidar (not shown) received a strong signal from cloud top but again was attenuated after a very few gates by the liquid water cloud.

Mission 3: 14 OCT 1998

A weak cold front accompanied by some very light drizzle cleared through the Chilbolton area (Fig. 9) by 1200. The sonde ascent at 1200 (Fig. 10) shows that the air was saturated and stable up to 825 mb and then moist again above 400 mb. Behind the front until 1300 there was some low level stratocumulus and cumulus through which the C-130 flew. After 1340 the ARAT and Falcon had to return, just as a layer of cirrus between 7 and 8 km was spreading across; this layer was subsequently penetrated by the C-130. Table 3 summarises the legs in this mission.

A typical twenty minute vertical dwell through the cirrus from the ground based GKSS radar is displayed in Fig. 11. A well defined and persistent layer of cirrus between 7 and

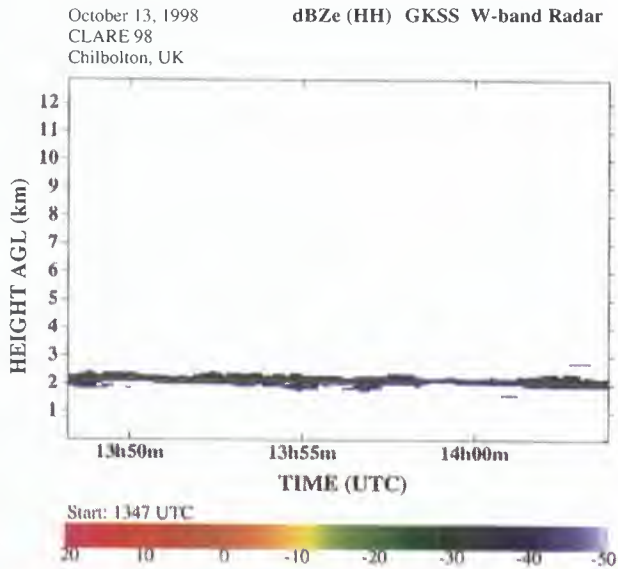


Fig. 8: Radar reflectivity from the GKSS 95 GHz radar.



Fig. 9: Synoptic situation at noon on 14 October 1998.



Fig. 10: Radiosonde ascent at 12Z on 14 October 1998.

9 km is evident with reflectivities generally in the range -30 to -10 dBZ. The final ARAT leg with the LEANDRE lidar looking up into the cirrus layer is shown in Fig. 12; in this case the lidar is able to penetrate the depth of the ice cloud. The track of the C-130 as it penetrates the cirrus deck just below 8 km is

ARAT at 3.7 km, Falcon 11.5 km	
1210:07/1215:00	1.8 km 6.2°C 'skimming Sc/Cu tops' but Z seems low (1209:35 Falcon)
1240:29/1245:02	1.5 km 'in stratus over Cu below', Z seems v. low (1239:54 Falcon in: 1240:14/1240:06 ARAT)
1310:00/1314:11	1.06 km 'only cirrus above' (1309:30 ARAT: 1310:18/1316:03 Falcon)
1339:30/1345:46	Falcon (1345:37 ARAT looking up) C-130 climbing (ARAT returns; Falcon returns - laser problem)
1424:40/1429:45	C-130 only 7.5 km -31°C 'thin cirrus' good echo 7.5 to 8 km
1458:42/1503:33	C-130 only 8.11 km 'tops of cirrus - aggregates and rosettes'

Table 3: Summary of the flight legs in Mission 3.

October 14, 1998
CLARE 98
Chilbolton, UK

dBZe (HH) GKSS W-band Radar

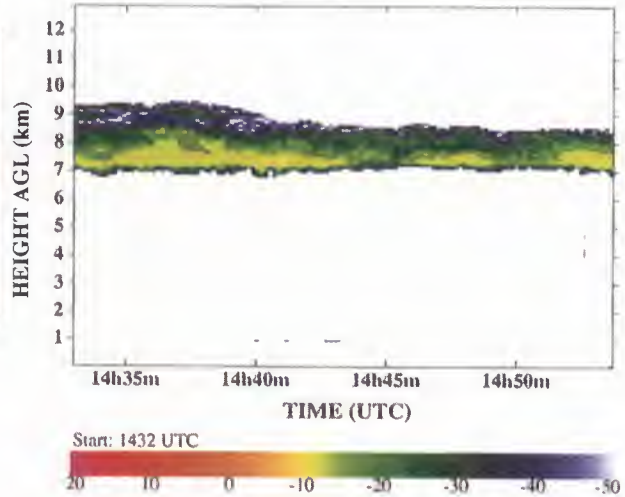


Fig. 11: Radar reflectivity from the GKSS 95 GHz radar.

shown in Fig. 13 superposed on the 3 GHz radar scan through the ice cloud. The lower panel of this figure compares the value of Z calculated from the 2-D probe on the aircraft compared with that measured by the radar.

Mission 4: 16 OCT 1998

On this day there were very strong SW winds in a warm sector ahead of an approaching cold front (Fig. 14). Because of the strength of the winds and the low visibility only the C-130 was able to take off. The midday ascent in Fig. 15 shows saturation up to 800 mb. There was persistent low cloud below 2 km, but although the C-130 remained airborne for four hours there was no cloud above this lower deck. About 30 minutes after the C-130 had landed a layer of cirrus spread across the area. The legs in this mission are summarised in Table 4.

Mission 5: 20 OCT 1998

Successful co-ordinated flights were made through ice and mixed-phase clouds ahead of advancing fronts in a strengthen-

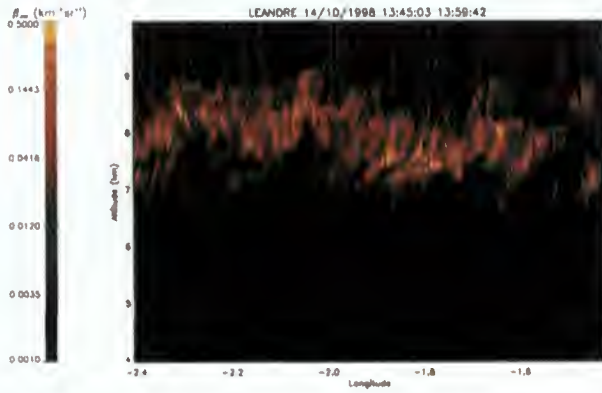


Fig. 12: Backscatter coefficient from the airborne LEANDRE lidar.

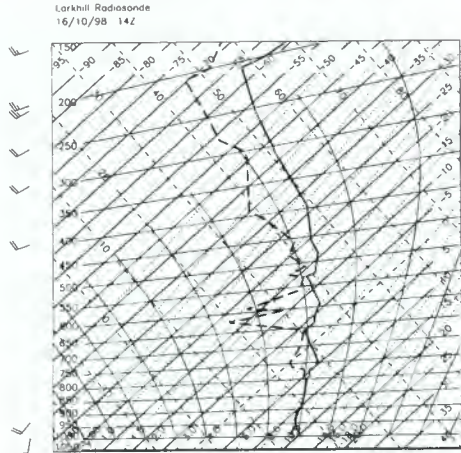


Fig. 15: Radiosonde ascent at 14Z on 16 October 1998.

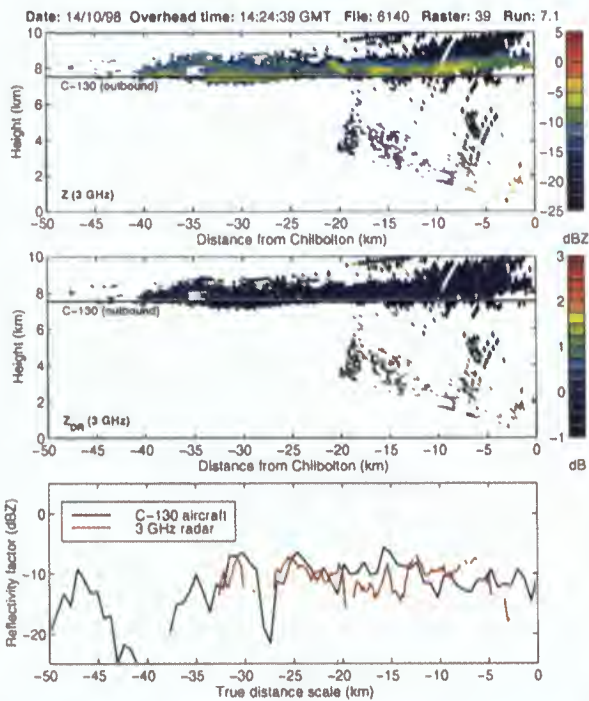


Fig. 13: Radar reflectivity and differential reflectivity measured by the CAMRa 3 GHz radar, and comparison with the C-130.

Cold front approaching—but no cirrus.	
Very windy so C-130 only. Warm sector.	
1103:53/1108:08	900 m climbing—in slight drizzle and cloud
1141:58/1147:38	7.31 km -31.7°C 'clear over Chilb'
1217:18/1222:38	6 km not in cloud
1250:37/1254:40	6.6 km -24°C 'no cloud'
1329:53/1335:47	'9 km' -46°C clear over Chilb
1420:41/1425:52	2.43 km 4°C
1454:41/1458	1.52 km 7.8°C 'not in cloud'

Table 4: Summary of the flight legs in Mission 4.

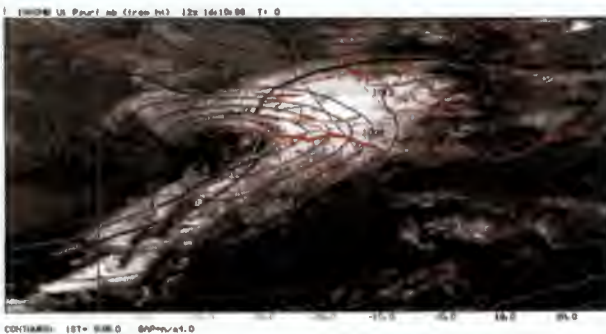


Fig. 14: Synoptic situation at noon on 16 October 1998.

ing SW windflow (Fig. 16). The ascent (Fig. 17) shows a saturated layer at 650–500 mb. The C-130 remained airborne for 8 hours but the other two aircraft had two sorties and returned at lunch time to refuel. The legs for this Mission are summarised

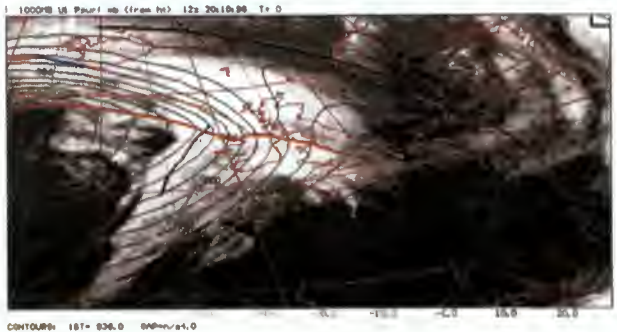


Fig. 16: Synoptic situation at noon on 20 October 1998.

in Table 5.

This flight has been the intensively analysed and is the subject of a number of subsequent papers. So, here we have chosen two examples of the data which are not reproduced later on. Figure 18 shows the ALEX lidar looking down from the Falcon for the 1400 leg. The upper cirrus layer between 10 and 12 km is clearly visible, and although the ice attenuates somewhat, some highly reflecting layers at a height of 4 to 6 km are evident. As these layers do not depolarise the laser signal, and the Johnson-Williams probe on the C-130 detects liquid water, it will be argued that they are supercooled liquid water cloud. By 1521, these layers have disappeared, and Fig. 19 shows a consistent comparison of the 3 GHz ground based radar with the Z values calculated from the C-130 probe data.

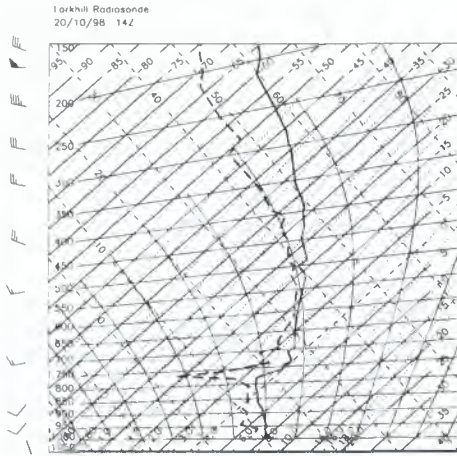


Fig. 17: Radiosonde ascent at 14Z on 20 October 1998.

0820:15	C-130	ohd climbing
0841:33/0845:10	C-130	3.04 km climbing
09:20:44/0924:50		3.64 km 'C-130 in tops for < 1 minute'
		(0918:26/0925:39 Falcon)
0950:22/0954:25		2.25 km 'skimming tops of clouds over Chilb'
		(0950:25/0955:11 ARAT)
		(0949:48/0956:00 Falcon)
1020:00/1024:10	C-130	'no cloud'
		(1019:30 ARAT in)
		(1020:21/1026:07 Falcon)
1050:06/1054:14	C-130	3.9 km just above thick cirrus over Chilb.
		(1049:50/50 ARAT in)
		(1050:00/1056:01 Falcon) ARAT & Falcon return to refuel
1120:12/1124:15	C-130 only	3.7 km in cloud thruout 'mixed phase -7.5°C
1152:01/1156:02		3.75 km, inborne 'in-cloud', outbound 'just above'
1223:33/1227:20		3.75 km -7°C 'thin cloud all around this level'
1300:18/1302:55		3.04 km 'drizzle o'head chilb'
1320:27/1327:03	ARAT	- No C-130.
		(1318:02/1327:03 Falcon)
1349:35	C-130	2.4 km 'above cloud'
		(13:50 Falcon, 1353:20 ARAT outbound)
1420:01/1423:30		3.9 km thick cirrus -6.3°C
		(1420:27 ARAT in, 1420:40 Falcon in)
1449:58/1454:24		4.5 km '1.2g/kg snow, ice bul rosettes -10.1°C'
		(1450:18/1454:48 ARAT: 1454:30 Falcon)
1521:00/1525:45		5.4 km 'thick ice cloud graupel, snow, needles -14.5°C
		(1519:58 ARAT - below C-130)

Table 5: Summary of the flight legs in Mission 5.

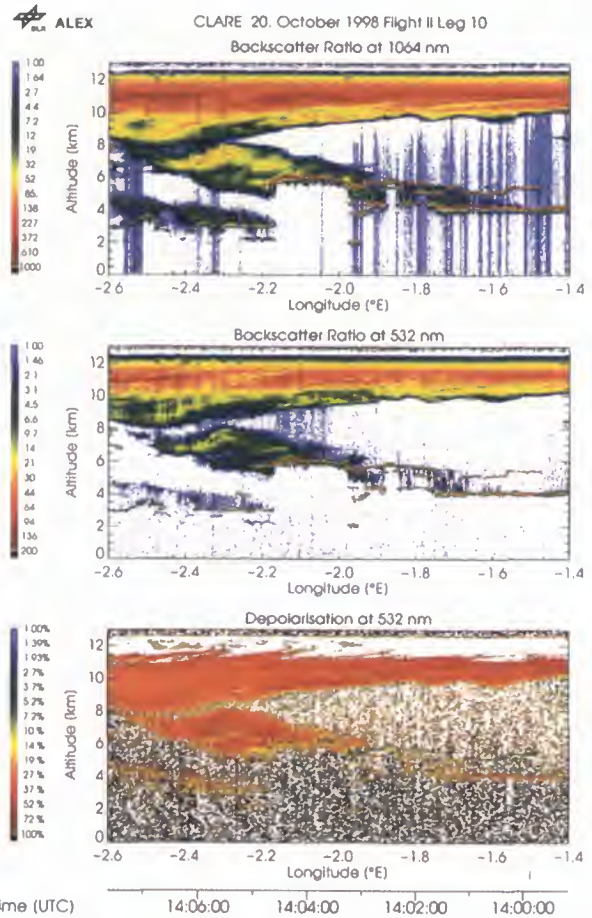


Fig. 18: Observations by the airborne ALEX lidar on 20 October 1998.

0923:53/0927:26	C130 at 0.380 km, 13°C, just clipping cloud base.
0948:22 (in)	3.04 km, -1°C ('go in cloud at 0957')
	(0950:23 Falcon inbound)
1019:51/1025:15	C-130 5.7 km -17°C 'in cloud base of cirrus- crystals'
	(1019:42 ARAT in looking up / 1019:03 Falcon in)
1050:15/1055:47	5.7 km -20°C 'not in cloud'
	(1049:33/1055:35 ARAT: 1049:51/1055:53 Falcon)

Table 6: Summary of the legs flown in Mission 6.

Mission 6: 21 OCT 1998

Figure 20 shows that a cold front which had cleared through Chilbolton by 0900 and was followed by a strong SW airflow with a moist layer from 500–350mb (Fig. 21). It was followed by low cloud which then broke somewhat, and subsequently a patch of cirrus above 5 km in height moved over the region at about 1100 followed by clear skies. The legs in this mission are summarised in Table 6.

The layer of ice cloud between 4.5 and 6.5 km is clearly visible in the ground-based radar return in Fig. 22. The lidar return from the LEANDRE lidar looking up is displayed in Figure 23 with the backscatter from the ice cloud clearly visible, and also a highly reflecting layer at cloud top which did not show up in the radar return. The highly reflecting layer at cloud top is

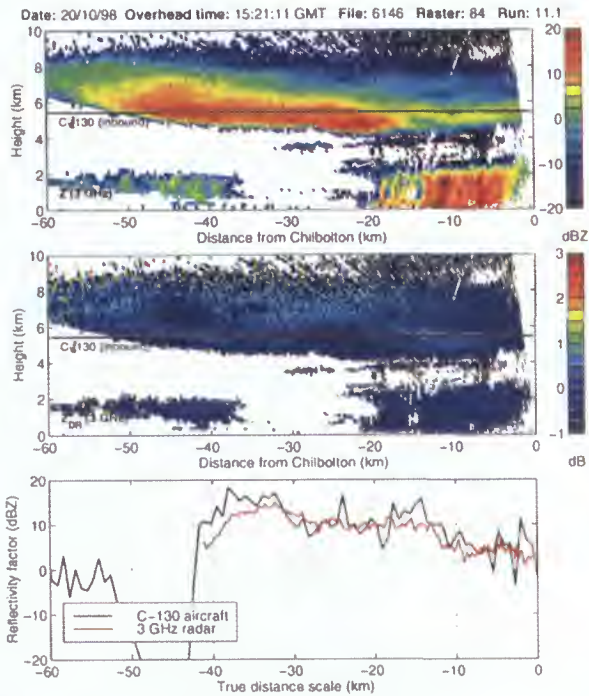


Fig. 19: Comparison of 3 GHz CAMRa reflectivity with values calculated from the concurrent C-130 in situ measurements.

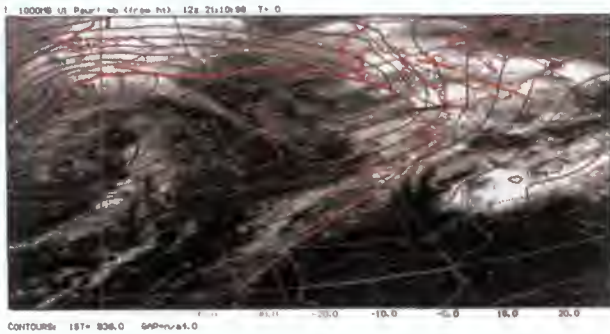


Fig. 20: Synoptic situation at noon on 21 October 1998.

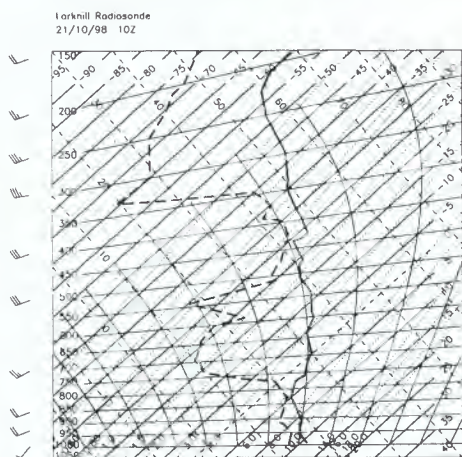


Fig. 21: Radiosonde ascent at 10Z on 21 October 1998.

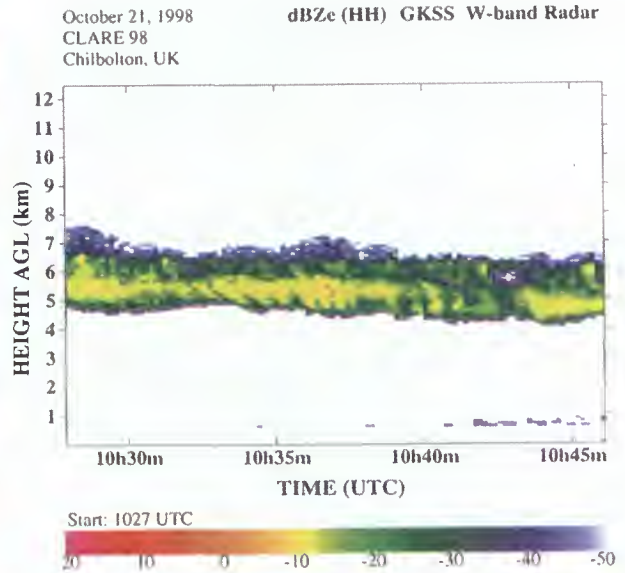


Fig. 22: Radar reflectivity from the GKSS 95 GHz radar.

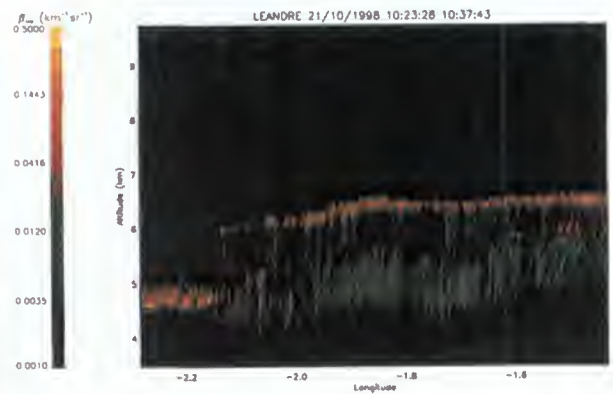


Fig. 23: Backscatter coefficient from the airborne LEANDRE lidar.

also clearly visible in the downward looking ALEX lidar data in Fig. 24; this layer saturated the ALEX lidar so the depolarisation data is unreliable, but the LEANDRE depolarisation data suggests liquid is present. The phase of this layer is debated further in subsequent papers.

Mission 7: 22 Oct 1998

The C-130 flew alone because of the strong SW cross winds. In the strong SW in the tropical maritime air (Figs. 25 and 26) there was persistent low cloud which was penetrated at the beginning and end of the flight. There was some cirrus to the north but none over Chilbolton. An approaching deep low with cirrus—arrived much later. This data has not yet been analysed in any depth. Table 7 summarises the legs flown in this mission.

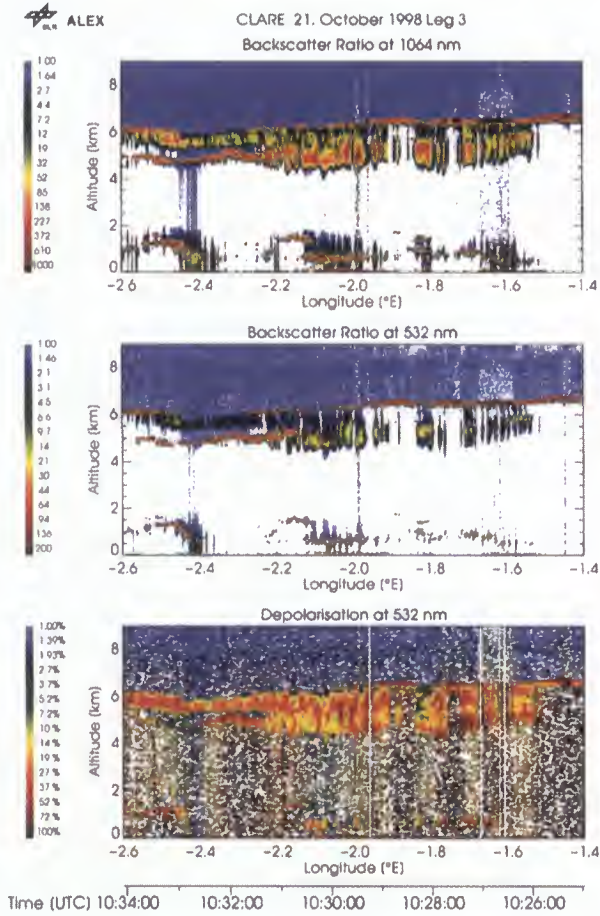


Fig. 24: Observations by the ALEX lidar on 21 October.

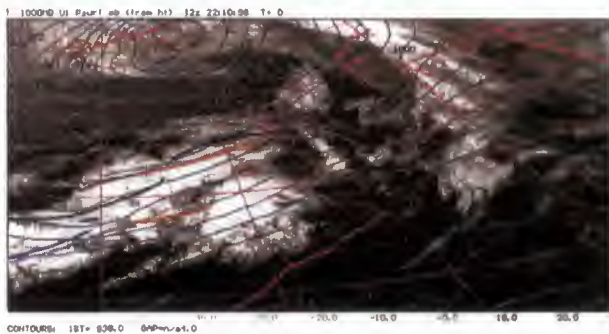


Fig. 25: Synoptic situation at noon on 22 October 1998.

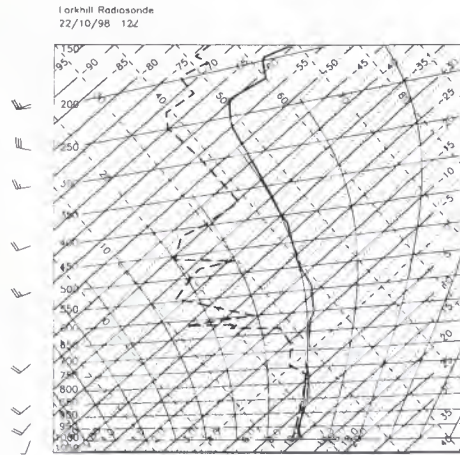


Fig. 26: Radiosonde ascent at 12Z on 22 October 1998.

1121:47/1125:50	900m +9°C 'thick cloud and drizzle'
1202:25/1207:30	7.5 km 'cirrus to the west'
1236:06/1240:57	7.5 km -35°C 'thickish cirrus' (7-10 km from radar)
	<i>(from satellite - we are southern edge of band of cirrus)</i>
1305:10	8.1 km - not in cloud
	<i>(Various clear air runs as cirrus moved away to the NW Then descend to run through low level stratus)</i>
1443	Expect overhead - 900m - break off - air traffic control
1507:20	Inbound 9.6°C 'in thick cloud' - THEN RETURN.

Table 7: Summary of the flight legs in Mission 7.

A Summary of the Cloud Microphysics Data Collected during CLARE'98 by the UKMO C-130 Aircraft

P.N. Francis

Meteorological Research Flight, UK Meteorological Office

Y46 Building, DERA Farnborough, Hampshire, GU14 0LX, United Kingdom

Phone : +44 (0)1252 395403 Fax : +44 (0)1252 376588 Email: pnfrancis@meto.gov.uk

INTRODUCTION

This paper provides a brief summary of the cloud microphysics data collected from the UK Meteorological Office C-130 aircraft during 5 sorties carried out as part of the CLARE'98 field campaign between 7 October and 23 October 1998. These include two flights which concentrated mainly on liquid water cloud (7 October and 13 October), two flights which sampled predominantly ice cloud (14 October and 21 October) and one flight in a complex mixed-phase cloud system (20 October).

7 OCTOBER 1998

Figure 1 shows temperature and humidity data from the 12 UTC and 15 UTC Larkhill radiosonde ascents. The right hand line is the temperature and the left hand line is the dew point in each case.

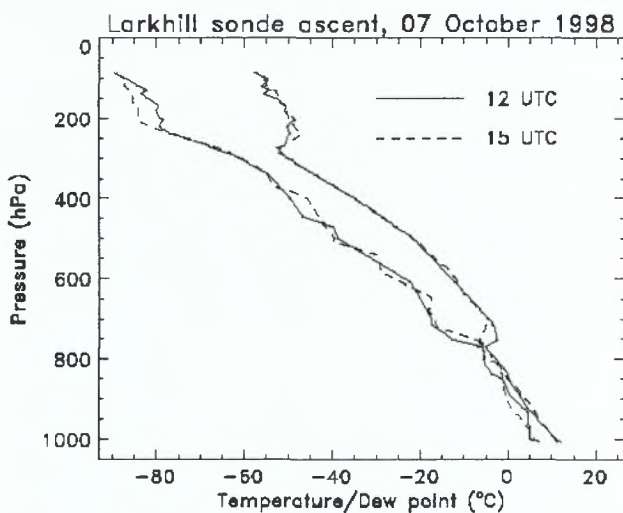


Figure 1. Larkhill radiosonde profiles from 7 October 1998.

The two profiles are very similar, in both cases showing a deep moist boundary layer up to around 750 hPa, with drier air above. These profiles would indicate the likelihood of cloud at all levels below around 2.5 km, which is consistent with all remote sensing measurements made during the day.

Two runs flown at a height of around 2.4 km were very close to the cloud top as reported by the C-130 aircraft scientist, consistent with simultaneous measurements from the

ground-based 94 GHz radar. A time series of liquid water content (LWC) from one of these runs is shown in figure 2, where one can see regions of high LWC interspersed with clear regions as the aircraft comes out of the cloud top. The air temperature within the cloud during this run was around -6°C , and some icing was reported on the airframe.

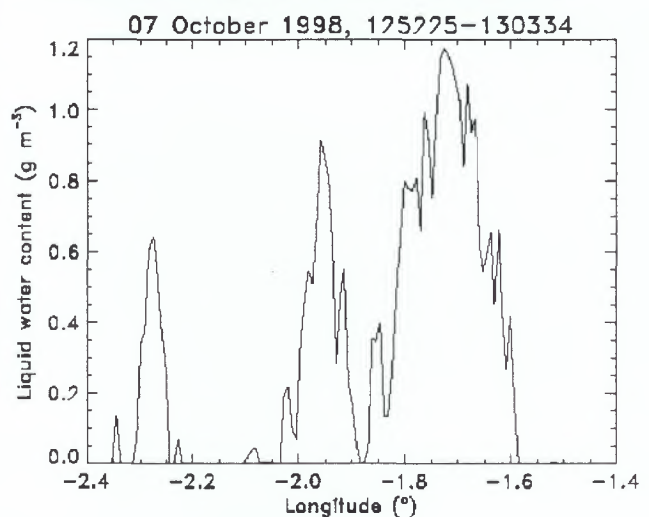


Figure 2. Liquid water content time series from a run flown at 2.4 km, near cloud top.

The next pair of runs, flown at around 1.6 km close to the freezing level, showed little in the way of cloud liquid water, and seemed to be mainly at or just below the cloud base. Figure 3 shows the LWC measured during one of these runs.

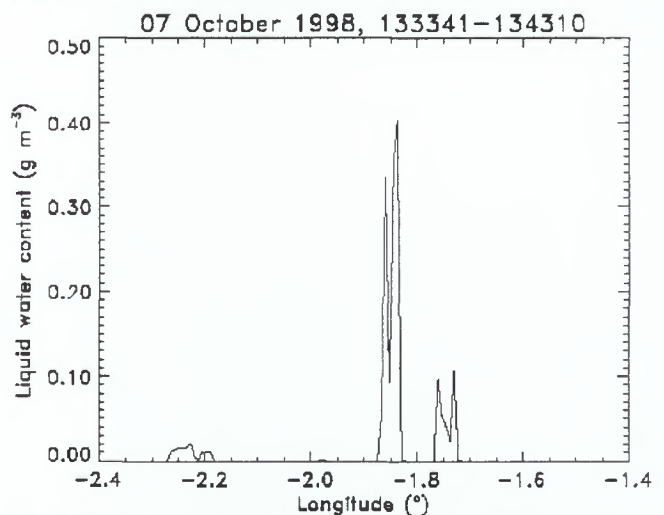


Figure 3. Liquid water content time series from a run flown at 1.6 km, near cloud base.

Following these runs, the aircraft ascended into the main cloud layer and performed two runs at around 2.1 km, where the air temperature was -4°C . Liquid water content and effective radius measurements from these runs are shown in figures 4 and 5 respectively.

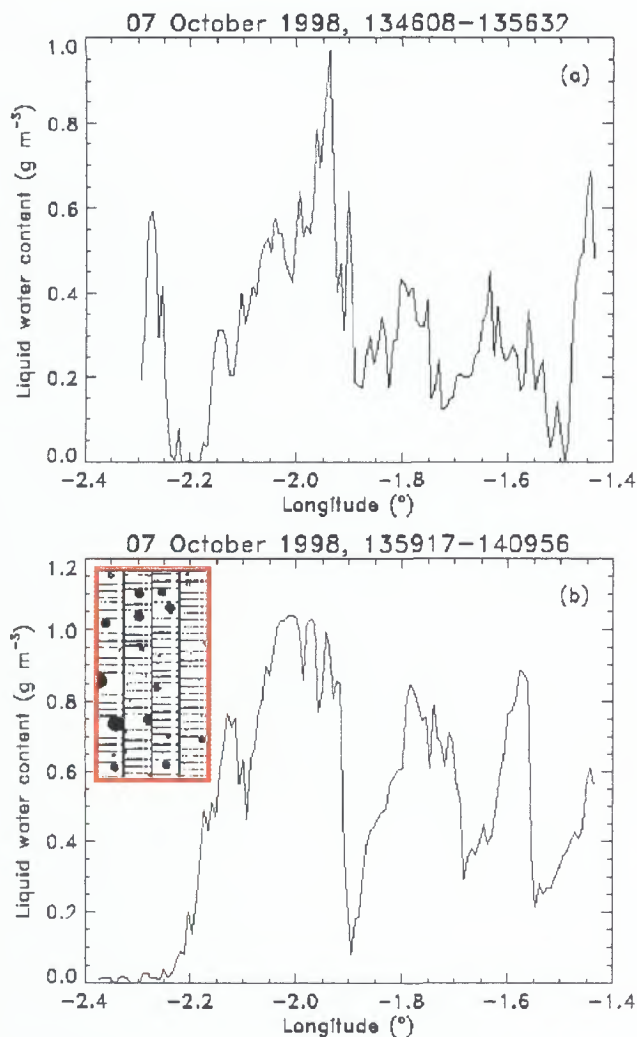


Figure 4. Liquid water content time series from runs flown at 2.1 km. Also shown in 4(b) are typical 2D-C images of the larger drops.

The high values of LWC shown in figure 4 reflect the deep nature of the boundary layer on this day, while the relatively small values of effective radius found in these runs (typically around $6 \mu\text{m}$) indicates the continental nature of the airmass on this day. Despite the temperature, no evidence was found of any ice crystals during these runs, the cloud in this region existing as supercooled liquid water at this stage. There were significant numbers of drizzle-sized drops encountered during these runs, and an example of the 2D-C images sampled is included in figure 4(b), in this case corresponding to a longitude of around -2.0° . Drops in the 2D-C range typically contributed around 5% of the total LWC during these runs.

On ascending to 1.9 km for the next pair of runs, significant numbers of columnar ice crystals were found. Figure 6 shows the liquid water content data collected from one of the runs, where the temperature was -2.5°C . Ice crystals were

detected between around -1.95° longitude and the Chilbolton end of the run. The 2D-C size distributions indicate that the ice mass associated with these crystals is small compared to the LWC.

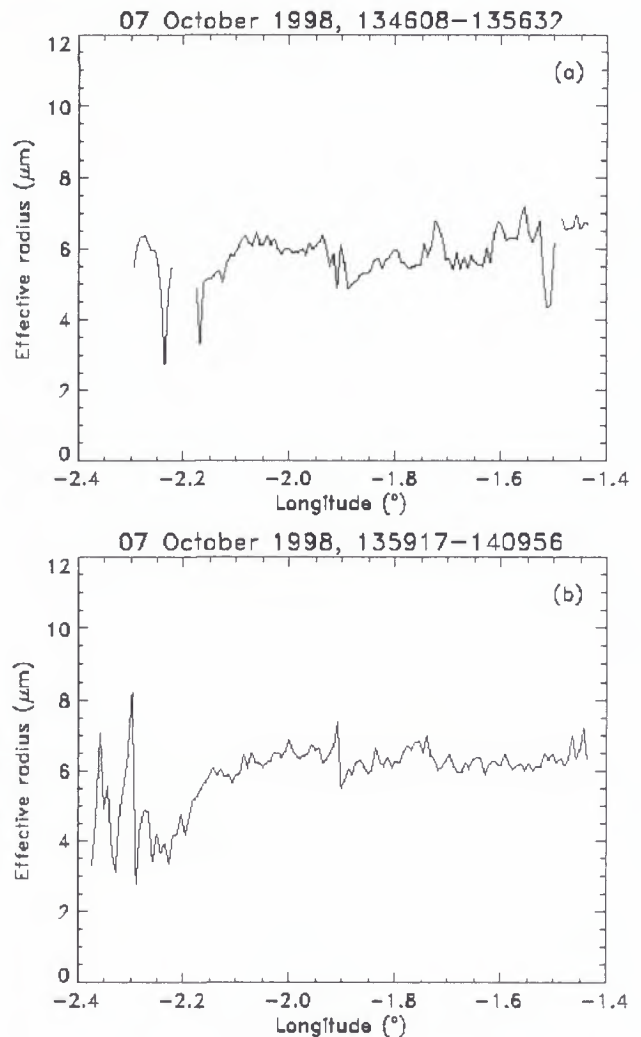


Figure 5. Effective radius time series from runs flown at 2.1 km.

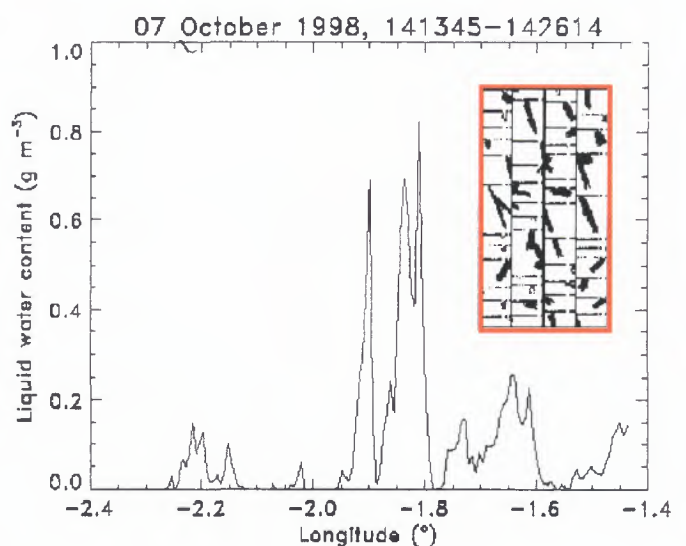


Figure 6. Liquid water content from a run flown at 1.9 km, together with a sample of 2D-C images from around -1.75° longitude.

Finally, a pair of runs was flown at around 2.2 km (temperature -4.7°C). The LWC from one of the runs is shown in figure 7. As with the previous pair of runs, column-like ice crystals were detected for part of the run, in this case between around -1.8° longitude and the Chilbolton end of the run.

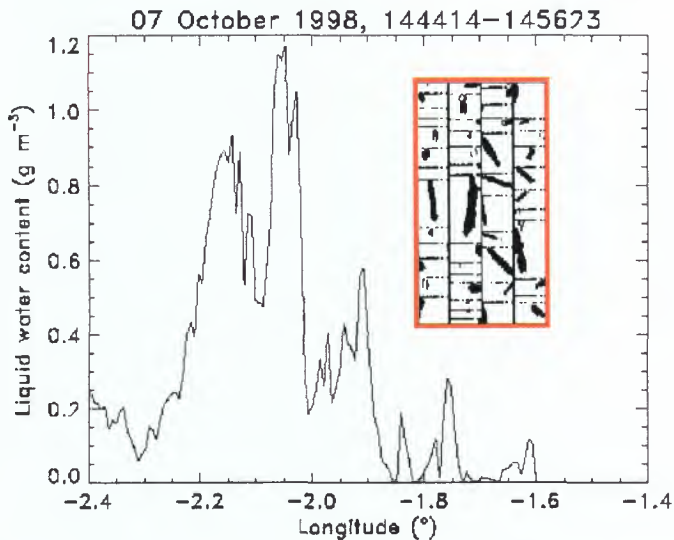


Figure 7. Liquid water content from a run flown at 2.2 km, together with a sample of 2D-C images from around -1.7° longitude.

13 OCTOBER 1998

Figure 8 shows temperature and humidity from the 14 UTC Larkhill radiosonde ascent. The profile is seen to be very moist up to around 620 hPa, with a drier slot between 620 and 500 hPa, followed by a further moist region centred around 470 hPa.

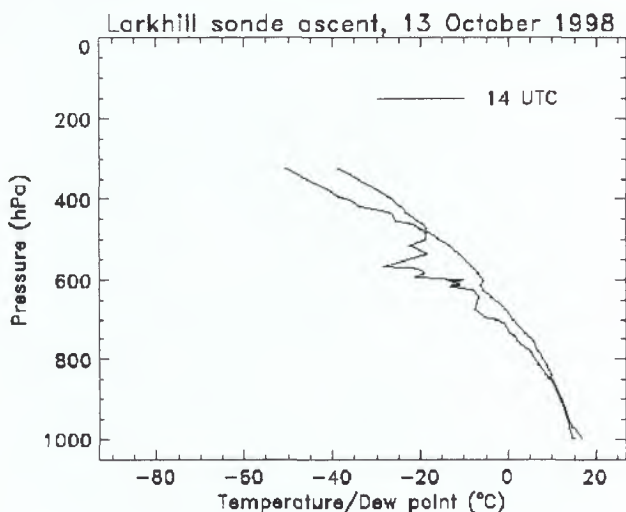


Figure 8. Larkhill radiosonde profile from 13 October 1998.

Four runs were carried out at heights around 3.1 to 3.2 km, where the temperature was in the range zero to -1°C . These runs seemed to be near the base of some fairly thick mid-level cloud, and significant drizzle events occurred during some of the runs. LWC data from two of these runs are

shown in figures 9 and 10, together with examples of 2D-C images. Drops in the 2D-C range typically contributed over 50% of the total LWC during the large LWC peaks in these runs.

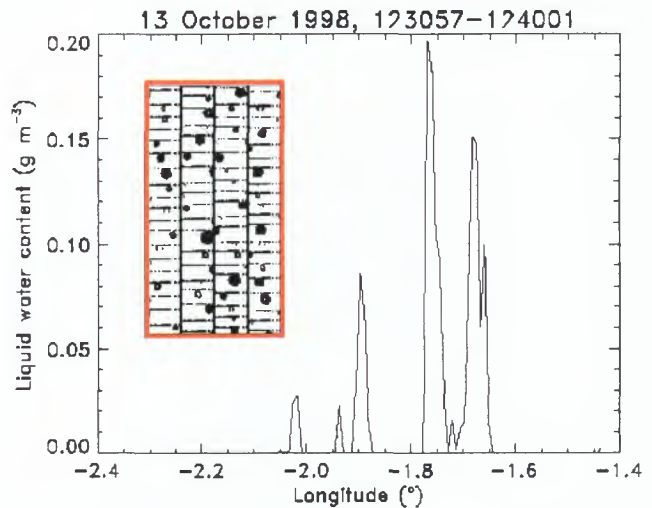


Figure 9. Liquid water content from a run flown at 3.1 km, together with typical 2D-C images of the larger drops.

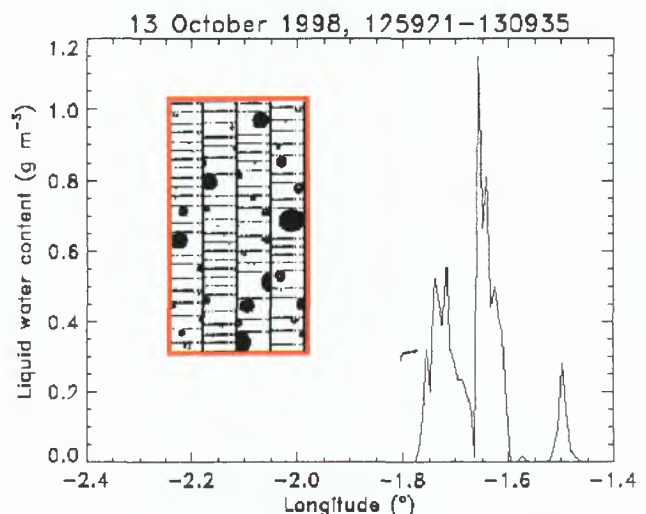


Figure 10. Liquid water content from a run flown at 3.2 km, together with typical 2D-C images of the larger drops.

The C-130 then descended to 2.4 km to perform a pair of runs. The ambient temperature during these runs was around 6°C . Liquid water content and effective radius data are shown for these runs in figures 11 and 12 respectively. Very little cloud was encountered during these runs, as can be seen in figure 11. The cloud was detected only by the FSSP in both runs, i.e. no drizzle-sized drops were present on the 2D-C. The effective radius is typically $6\ \mu\text{m}$, similar to that from the 7th October case. A second pair of runs was also performed at a similar altitude, but again little cloud was encountered.

Finally, the C-130 then descended to around 1.25 km for a pair of runs in a lower-level stratocumulus layer. Much larger values of LWC were encountered during these runs, as can be seen from figure 13, which shows the LWC data from the first of the two runs. Significant contributions to the total

LWC were made by drops in the 2D-C range during both of these runs, although it is apparent that the drizzle drops tend to be somewhat smaller than encountered during previous parts of the flight.

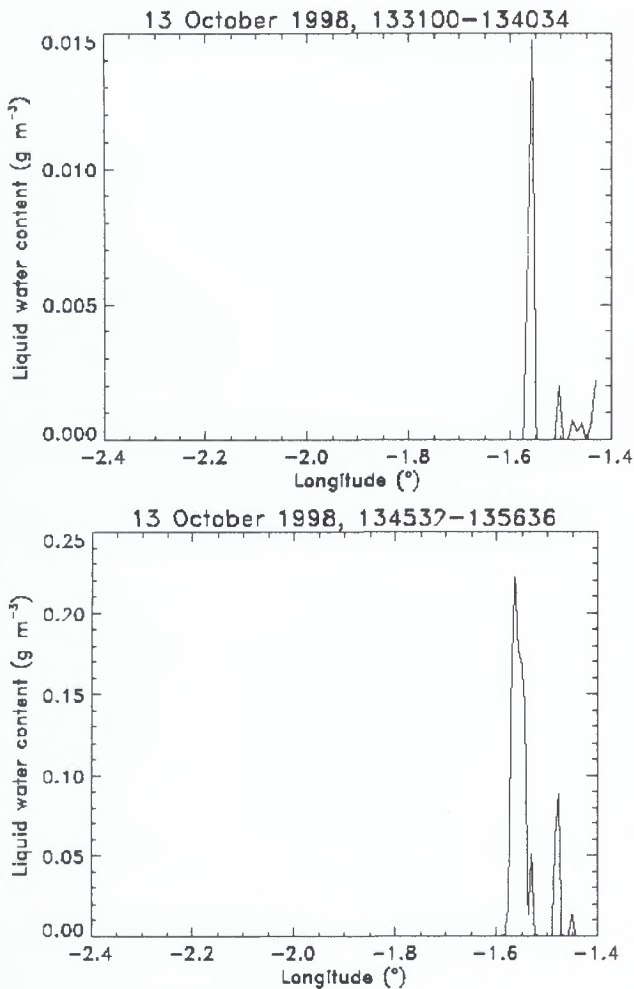


Figure 11. Liquid water content from runs flown at 2.4 km.

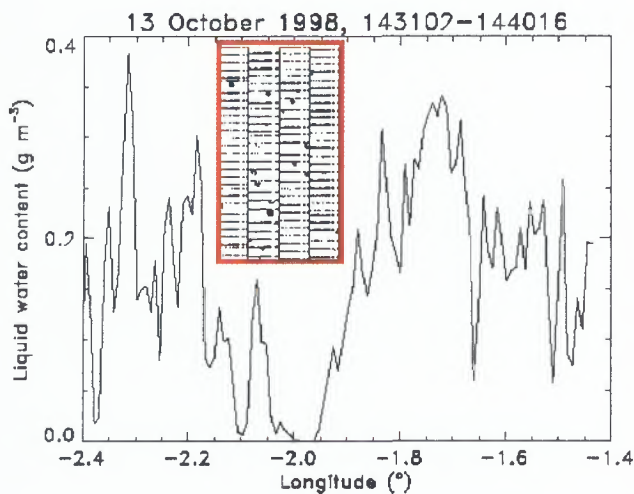


Figure 13. Liquid water content from a run flown at 1.25 km, together with typical 2D-C images of the larger drops.

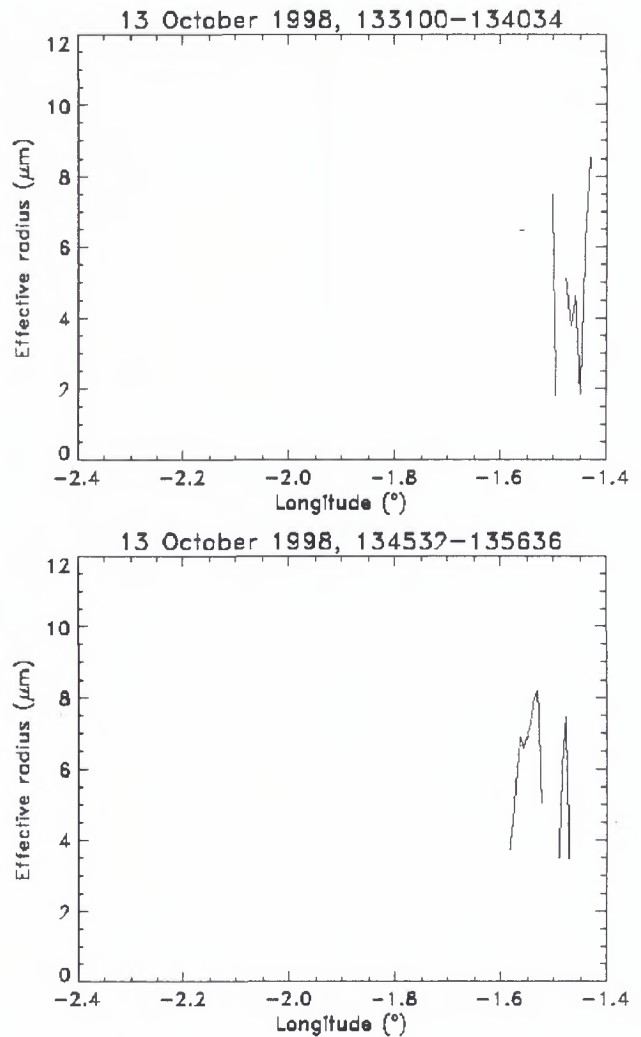


Figure 12. Effective radius from runs flown at 2.4 km.

14 OCTOBER 1998

Figure 14 shows temperature and humidity from the 14 and 15 UTC Larkhill ascents.

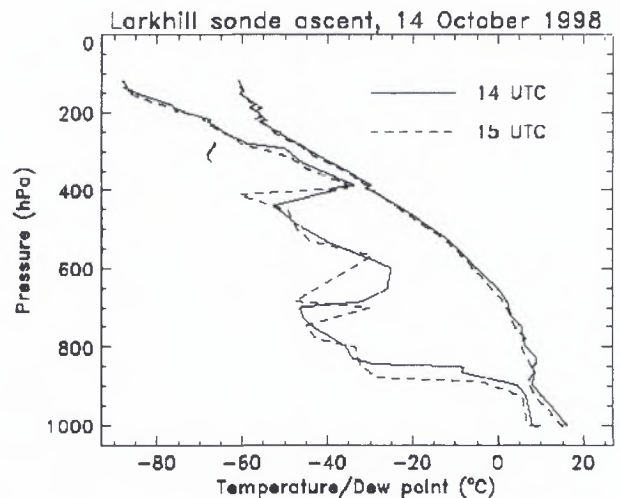


Figure 14. Larkhill radiosonde profiles from 14 October 1998.

In both cases a shallow moist layer is apparent around 900 hPa, followed by a large dry region up to around 400 hPa, with a further moist region above this, which would indicate a high probability of cirrus clouds forming at altitudes above 7 km.

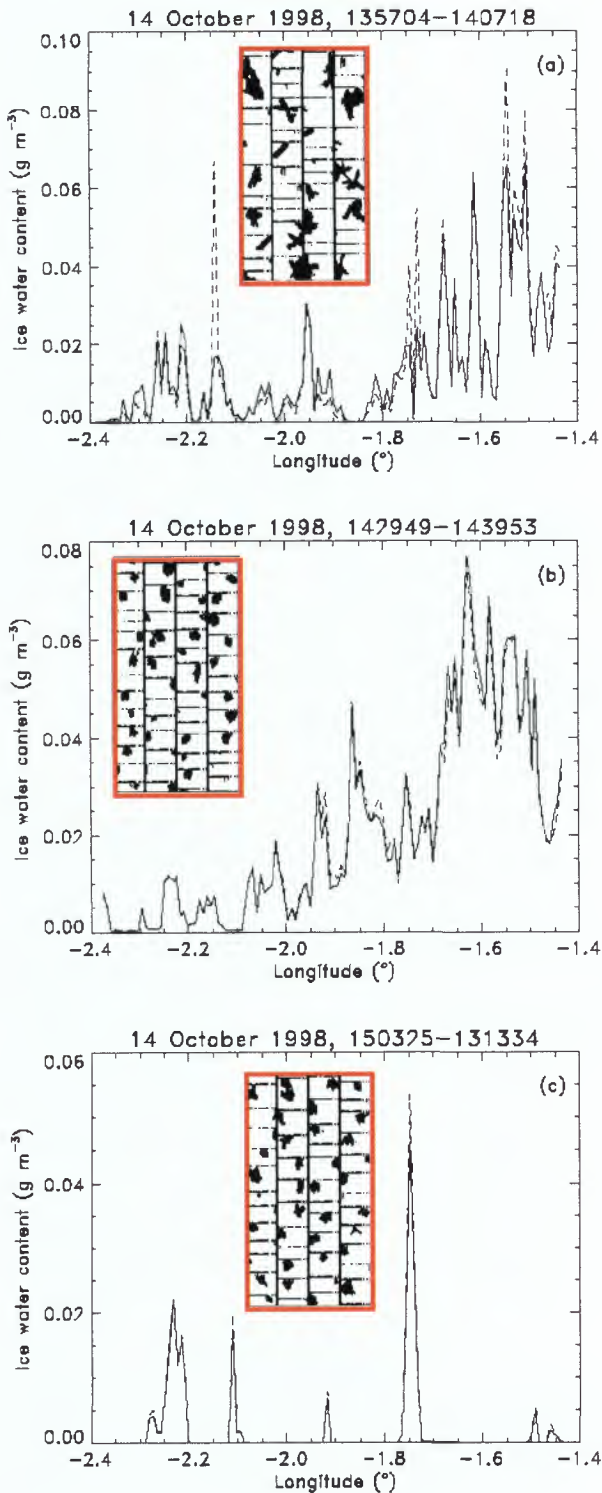


Figure 15. Ice water content from runs flown at (a), (b) 7.6 km and (c) 8.2 km. In each case, the solid line represents IWC calculated from the method of Francis *et al.* (1998), the dashed line from the method of Brown and Francis (1995). Typical 2D-C images from all three legs are also shown.

The runs of interest were flown at 7.6 km and 8.2 km, where the ambient temperature was -32°C and -37°C respectively. Ice water contents from three of the runs are shown in figure 15, together with typical 2D-C images. Two different ways of calculating IWC from the 2D probes have been used, those described by Francis *et al.* (1998), based on the particles' shadow areas, and by Brown and Francis (1995), based on the particles' mean diameters. Good agreement is noted between the two methods.

It is also possible to process the 2D probe data so as to classify the ice particles into specific crystal habits. An example of the output from this is shown in figure 16, which shows IWC associated with columns, aggregates, graupel and uncharacterized from one of the runs at 7.6 km. In this case, the majority of the IWC is associated with ice particles that have been characterized as graupel (dashed line).

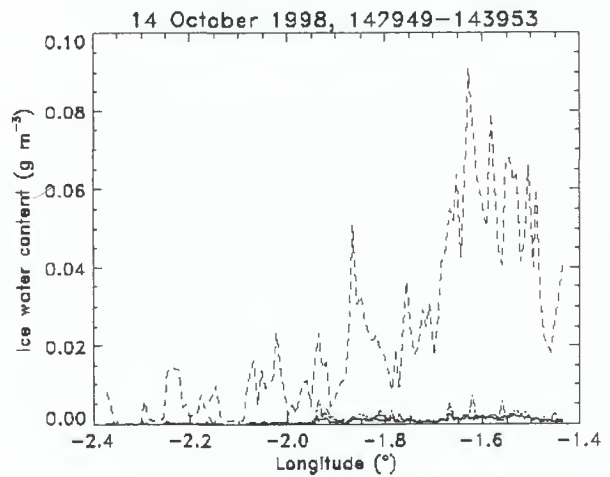


Figure 16. Ice water content from a run at 7.6 km sorted by particle habit. Solid line represents columns, dotted line aggregates, dashed line graupel, and dash-dotted line unclassified particles.

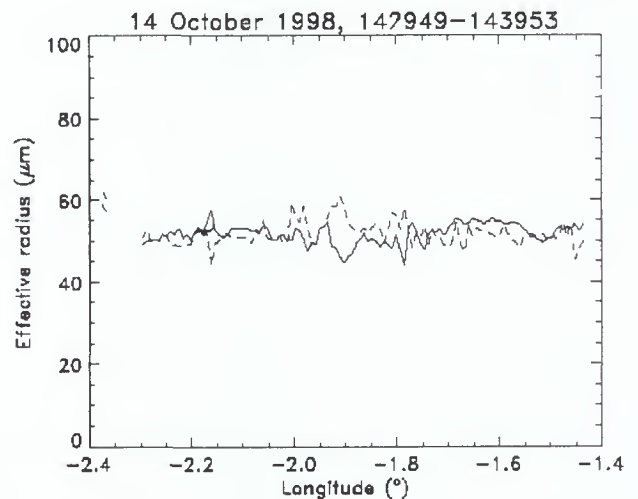


Figure 17. Effective radius from a run flown at 7.6 km. The solid line represents the method of Francis *et al.* (1998), the dashed line the method of Brown and Francis (1995).

The effective radius of the ice crystal size distribution may also be calculated from the 2D probe data. An example of this is shown in figure 17, using data again from 7.6 km. The definition of effective radius used is that given in Francis *et al.* (1998), and thus requires a knowledge of the IWC. As above, two methods of calculating the IWC are used, those of Francis *et al.* (1998) (solid line) and Brown and Francis (1995) (dashed line).

20 OCTOBER 1998

Figure 18 shows temperature and humidity from the 14 UTC Larkhill ascent. The profile is very moist for most of the troposphere, with only a slight dry layer between 750 and 800 hPa.

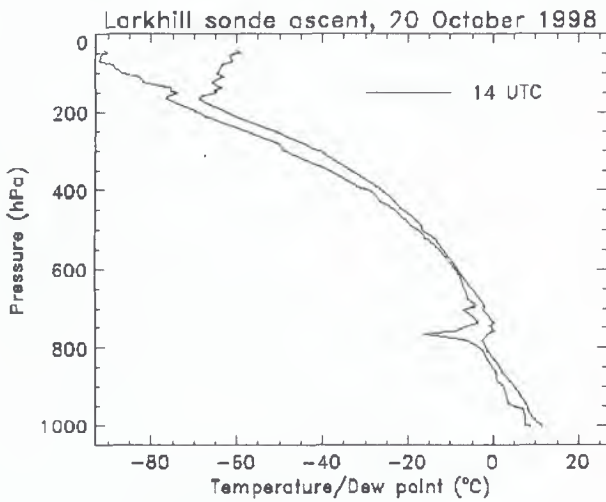


Figure 18. Larkhill radiosonde profile from 20 October 1998.

The legs of interest for this flight were three pairs flown at 4.0 km, 4.6 km and 5.5 km. IWC and LWC data for these runs are shown in figures 19, 20 and 21 respectively. During the legs at 4.0 km and 4.6 km the ARAT was flying above the C-130, whilst for the leg at 5.5 km, the ARAT was flying below the C-130.

Typical images from the 2D-C probe for these three pairs of legs are shown in figure 22. The particles from the legs at 4.0 km show a pronounced sector plate-like structure, as pointed out by Hogan *et al.* (1999). Crystals from the runs flown at the higher levels are generally less regular, although there is some evidence for small numbers of bullet-rosettes and columns.

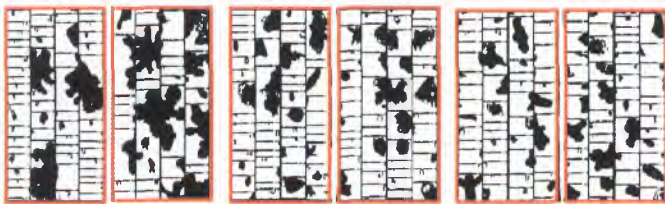


Figure 22. Sample 2D-C images from 20 October. Runs are at 4.0 km (left hand two panels), 4.6 km (middle two panels) and 5.5 km (right hand two panels).

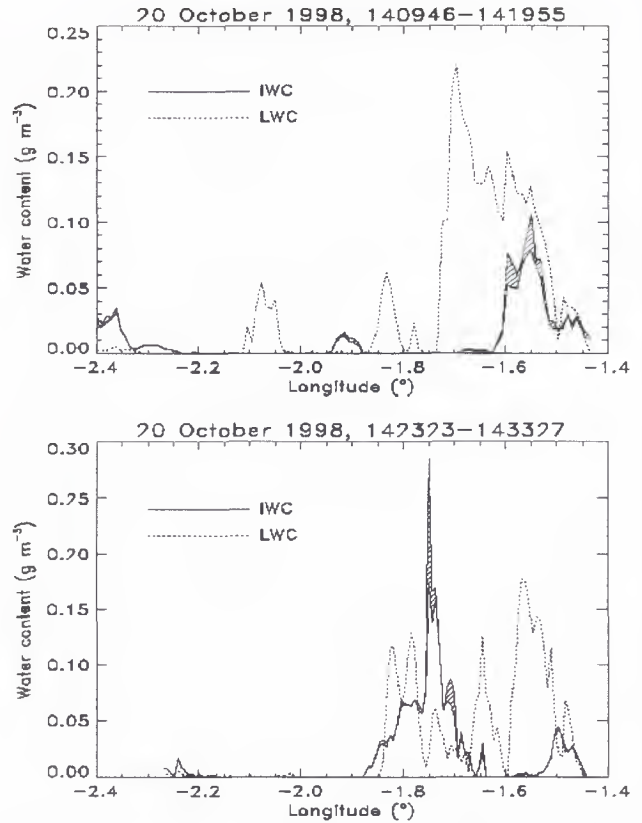


Figure 19. IWC (solid lines) and LWC (dotted line) from the pair of runs flown at 4.0 km. The hatched area between the solid lines indicates our estimate of the uncertainty in the determination of IWC from the 2D probes.

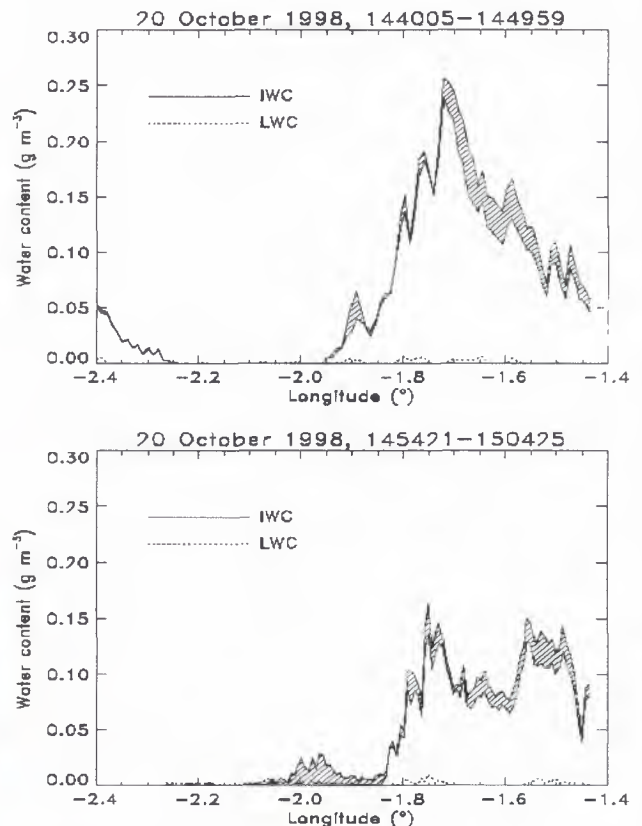


Figure 20. As for figure 19, but for runs at 4.6 km.

Significant quantities of liquid water are present on both of the runs at 4.0 km, and strongly support the belief that several layers of supercooled liquid water are embedded within the ice cloud (e.g. Hogan *et al.*, 1999). Very little evidence of liquid water is present for the runs at 4.6 km, given the detection threshold of around 0.01 gm^{-3} for the Johnson-Williams instrument used. There is possibly some evidence for LWC during the first of the legs flown at 5.5 km, although again the values are low and close to the detection limit of the instrument.

on any of the four runs was at the very start of the first run, around 80 km away from Chilbolton, as seen in figure 26.

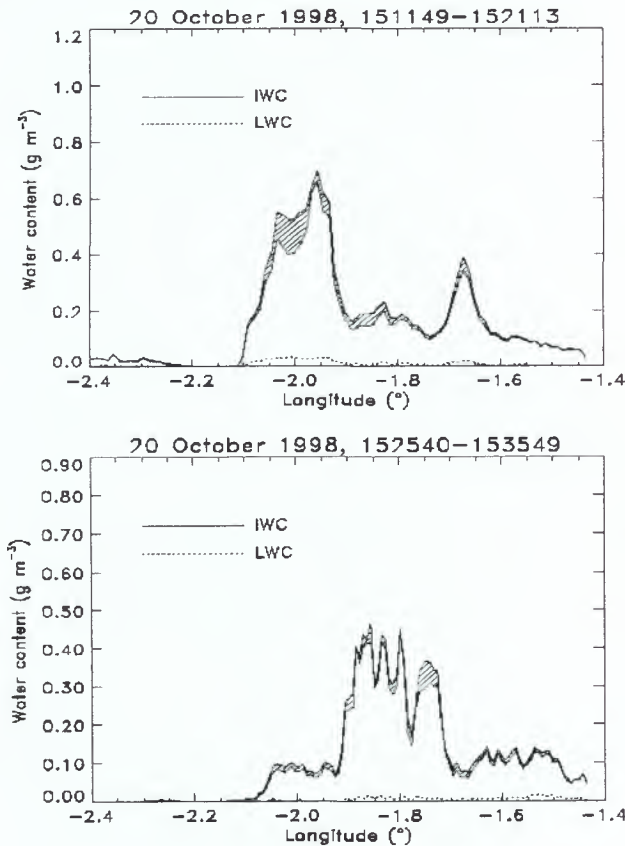


Figure 21. As for figure 19, but for runs at 5.5 km.

21 OCTOBER 1998

Figure 23 shows temperature and humidity from the 10 UTC Larkhill ascent. The profile is seen to be moist up to around 800 hPa, followed by a drier region between this and 500 hPa, with a further moist layer centred around 450 hPa. The legs of interest for this flight were flown around 5.8 km, and were carried out as two pairs of runs. Ice water content data from the four legs are shown in figures 24 and 25. Observed ice crystals are generally irregular in shape, and cannot be classified particularly well by the auto-classification software. There is seen to be some discrepancy between the two algorithms for calculating IWC from the 2D probes, but it is not possible at this stage to determine which of the two is the more accurate. The only evidence of any liquid water

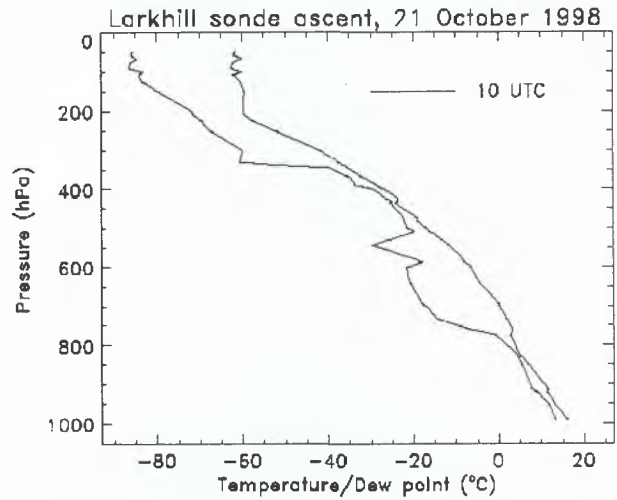


Figure 23. Larkhill radiosonde profile from 21 October 1998.

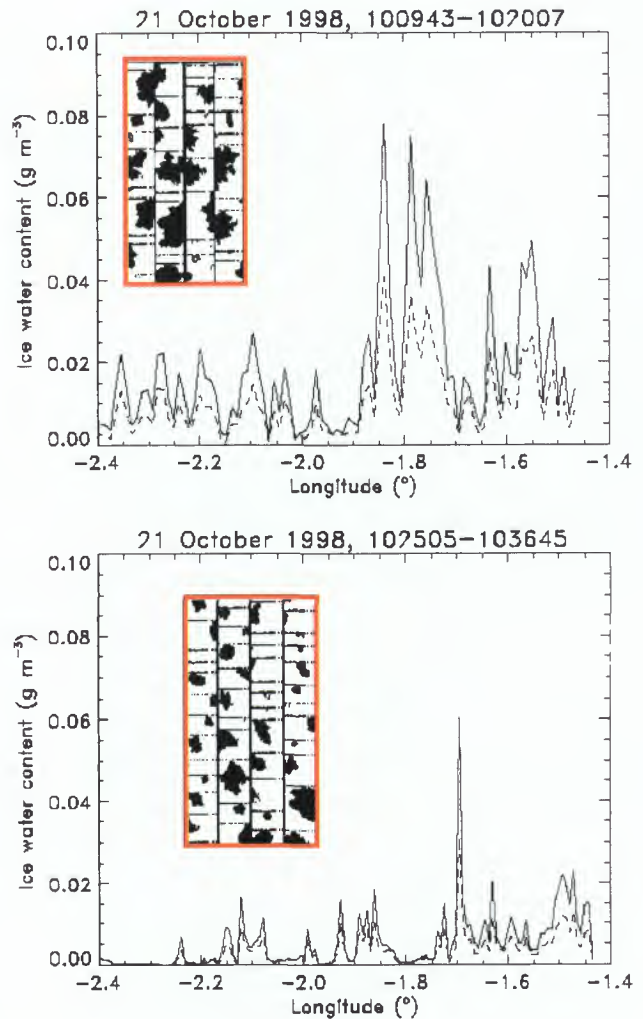


Figure 24. Ice water content from the first pair of runs flown at 5.8 km. In each case, the solid line represents IWC calculated from the method of Francis *et al.* (1998), the dashed line from the method of Brown and Francis (1995). Typical 2D-C images from both legs are also shown.

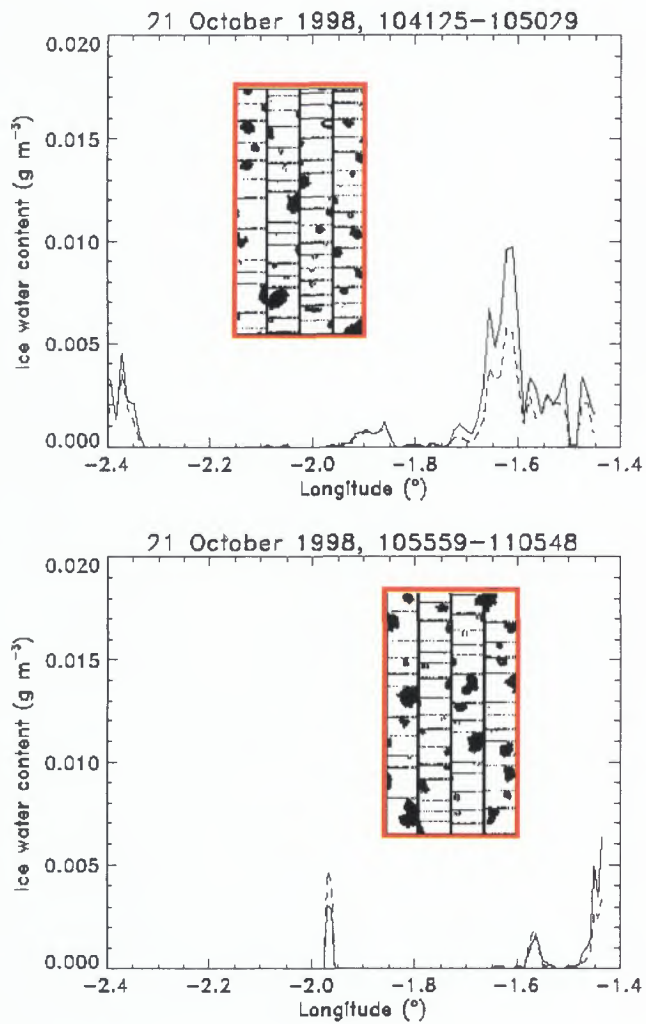


Figure 25. As for figure 24, but for the second pair of runs flown at 5.8 km.

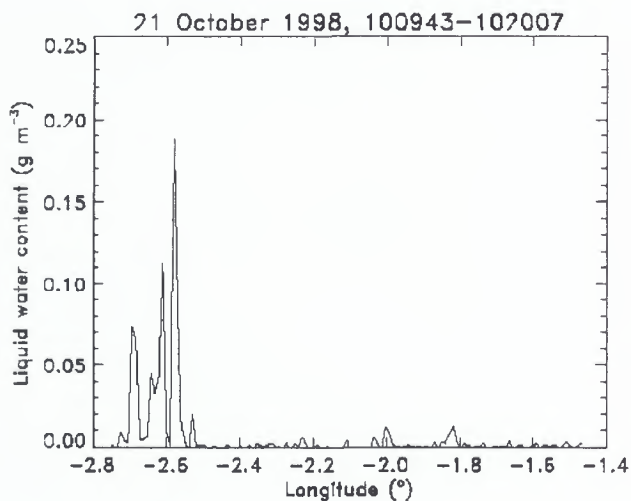


Figure 26. Liquid water content from the first run at 5.8 km.

REFERENCES

- Brown, P.R.A. and Francis, P.N., 1995: Improved measurements of the ice water content in cirrus using a total-water probe. *J. Atmos. Sci.*, **27**, 919-926.
- Francis, P.N., *et al.*, 1998: The retrieval of cirrus cloud properties from aircraft multi-spectral reflectance measurements during EUCREX'93. *Quart. J. Roy. Meteorol. Soc.*, **124**, 1273-1291.
- Hogan, R.J., *et al.*, 1999: Polarimetric radar observations of the growth of highly-aligned ice crystals in the presence of supercooled water. *This volume*.

ARAT Observations of warm and cold clouds during CLARE from lidar, radar and radiometry

J. Pelon¹, J. Testud², D. Leon³, C. Allet⁴, A. Guyot², V. Trouillet¹, S. Haimov³, F. Blouzon⁴,
C. Flamant¹, P. Genau¹, G. Vali³

1 IPSL, Service d'Aéronomie du CNRS, 4 Place Jussieu, B 104, F-75252 Paris, France

2 IPSL, CETP, 10-12 av. de l'Europe, 78140 Velizy, France

3 U. Wyoming, Wisconsin, USA

4 INSU/DT, 4 av. de Neptune, 94107 St-Maur, France

Phone : 33.1.44.27.37.79, Fax : 33.1.44.27.37.76, Email : Jacques.Pelon@aero.jussieu.fr

INTRODUCTION

A large variety of crystal size and shape is very often found from in situ measurements in cold clouds. If cloud temperature is warmer than -40°C , supercooled water droplets can also be found in a variable quantity. As radiative properties of water and ice particles are significantly different, and for ice depend on crystal shape, cloud radiation budget may be strongly affected by the spatial variability of cloud properties. The retrieval of optical and microphysical properties of cloud layers in cloud systems is thus of importance to better assess the radiation budget of the earth-atmosphere system.

During the CLARE'98 campaign, the dual polarization backscattering lidar LEANDRE 1 has been coupled with the KESTREL 95 GHz radar of U. Wyoming and radiometry onboard the Avion de Recherche Atmosphérique et de Télédétection (ARAT/F27) to document cloud properties.

The lidar has the potential to provide information on cloud structure, cloud extinction and phase, especially in semi-transparent layers. The radar has the capability to analyze more deeply denser clouds. Radiometry allows to derive integrated parameters. Radar data were taken in nadir viewing. Lidar measurements were taken in both nadir and zenith viewing to analyze low and mid-level clouds as well as upper level clouds. Radiometers measured the upward and downward visible and infrared fluxes. Observations performed during the CLARE'98 campaign with the ARAT are introduced in this first paper. Lidar and radar analysis methods are discussed in companion papers, where examples of the retrieved cloud properties are given. First results from a direct combined analysis will be presented in other papers, including ground-based radar measurements for cold clouds observed in zenith viewing.

LIDAR SYSTEM

LEANDRE 1 is a backscattering lidar based on the use of a Nd-Yag laser source operating in the visible (532 nm) and near infrared (1064 nm) (Pelon et al., 1990). The light emitted at 532 nm is linearly polarized and the backscattered signal is analyzed at both vertical and horizontal polarizations.

RADAR SYSTEM

The Kestrel radar is a Doppler radar operating at 94.92 GHz in dual polarization mode. It emits a peak power of 1.2 kW. Pulse duration can be varied between 50 ns and 2 μs , and the pulse repetition frequency can be increased up to 80 kHz. Dual beam 12" antenna allow to make slant (40°) and exact nadir measurements and ensure a gain of 49 dB. They are alternatively fed by the emitter.

OBSERVATIONS

In most cases lidar data were taken in nadir viewing simultaneously with the Kestrel radar.

Date	Mission	LEANDRE 1 pointing	Nr of legs	Cloud Type
07 Oct 98	M1	Nadir	9	Sc (single layer)
13 Oct 98	M2	Nadir	5	Cu-Sc-As/Ac (multilayer)
14 Oct 98	M3	Nadir + Zenith	6 + 2	Cu+Sc-clearing, then Ci
15 Oct.98	MC	-		Inter-Comparison
20 Oct 98	M4	Nadir	5	Sc+As/Ac
20 Oct 98	M4	Nadir	7	Sc +As/Ac
21 Oct 98	M5	Nadir + Zenith	4 + 1	Cu+Sc+As+ Ci

Table 1 : ARAT flights over Chilbolton

In some other cases, zenith measurements have been taken in the most interesting situations when cold clouds were observed above the aircraft. Table 1 summarizes the ARAT flights performed during CLARE'98.

LIDAR AND RADAR CALIBRATION

Lidar signal is due to scattering by atmospheric molecules and particles. Scattering by molecules and droplets (or crystals) correspond to different regimes. Rayleigh scattering by molecules can be used as a reference in the visible as the corresponding signal can be easily measured.

Only signals obtained in the two channels operated at 532 nm are used. In the parallel polarization channel (polarization identical as the emitted one) the lidar signal is normalized to atmospheric scattering at an altitude close to the aircraft, using onboard nephelometer measurements (Flamant et al., 1998). This method cannot be used if the aircraft is flying in cloud, and the existence of an aerosol free area must be assumed to reference signal to molecular scattering.

Depolarization signal is also referenced to molecular depolarization taken as equal to 2.8 % (Young, 1980). In dense clouds depolarization is mainly due to multiple scattering. In semi-transparent cold clouds, the occurrence of ice can be better identified if their optical thickness remains small (say below 1).

Radar calibration will be further discussed in the companion papers (see Guyot et al., this report). It is to be noticed that during the campaign, the calibration of the Kestrel radar was in error by about 10 dBZ and a new calibration has been made after the campaign based on several comparisons.

SIGNAL ANALYSIS

For an ideal detection system, the normalization procedure allows to derive the so-called attenuated backscattering coefficient β_a , defined as the real atmospheric backscattering coefficient β not corrected from transmission

$$\beta_a(\lambda, z) = \beta(\lambda, z) T^2(\lambda, z, z_a) \quad (1)$$

where z_a is the altitude of the airborne lidar. $T(\lambda, z, z_a)$ is the atmospheric transmission between z and z_a . This equation applies to both lidar and radar measurements. However, transmission of the atmosphere is quite different at visible and microwave wavelengths.

Water clouds (such as stratocumulus) are usually dense media. Extinction becomes very large (wavelength and droplet size are comparable) for lidar observations and signal can only be obtained from the first layers the laser beam penetrates. In this case, the apparent backscattering coefficient is altered by the detection time response and can be strongly reduced as compared to its true value (Pelon et al., 1999). This point will be further discussed in part 2. Furthermore, due to the large optical thickness of water clouds, multiple scattering contributes very significantly to the signal amplitude in both polarizations.

In cold clouds, optical thickness is smaller so that signal analysis can be usually performed using a second order scattering approximation (Ruppersberg et al., 1997). In such clouds, crystals are much larger than the wavelength, and diffraction must be accounted for in the analysis of the cloud optical properties. As this does not modify polarization, the depolarization ratio (defined as the ratio of the signals measured in the two polarizations) can be measured directly from the signals in the two visible channels to better characterize crystal shape (Chepfer et al., 1999).

Multiple scattering and diffraction are accounted for using a simple formalism proposed by Platt (1979), who introduced a parameter η ($\eta < 1$) in the transmission term

$$T(\lambda, z, z_a) = \exp \left[-2 \int_{z_a}^z \eta \alpha(\lambda, z') dz' \right] \quad (2)$$

The same formalism can be used for all cloud types.

A 95 GHz radar is sensitive to clouds, and most particularly to large droplets or crystals as sensitivity increases with D^6 in the Rayleigh scattering regime where it is mostly operating (droplet and most crystals have sizes must smaller than the wavelength). Transmission loss is small and mainly due to absorption by liquid water and water vapor (Lhermitte, 1988).

RADIOMETRY

Simultaneous radiation flux measurements were made onboard the ARAT with broadband visible Eppley pyranometers. Calibration flights performed with the C130 and the Falcon 20 of DLR allowed to compare flux measurements made by the three aircraft (see Francis et al., this report). The plane albedo A_A of the surface-cloud-atmosphere system was deduced from the ratio of the upward and downward shortwave flux F_{sw} measured by the upward and downward looking pyranometers as the ARAT flew over the stratocumulus layer

$$A_A = \frac{F_{sw} \uparrow}{F_{sw} \downarrow} \quad (3)$$

As a first approximation, a plane-parallel cloud model assuming no absorption and relying on two-stream radiative transfer calculations show that the cloud optical thickness τ can be deduced from the total plane albedo A_A as (Meador and Weaver, 1980)

$$\tau = \frac{A_A}{\gamma(1 - A_A)} \quad (4)$$

where γ is a parameter depending on the radiation model used. In the case of the Eddington scheme the value of γ is $\frac{3}{4}(1-g)$, where g is the asymmetry factor of the cloud

droplet distribution. As $g = 0.85$ for water spheres, we obtain $\gamma = 8.8$.

RESULTS

Examples of lidar cross-sections are shown on Figure 1 for the stratocumulus case of 7 October. Attenuated backscatter profiles obtained in nadir pointing show that the lidar signal is rapidly attenuated in such dense clouds.

One can notice that the maximum attenuated backscatter coefficient value in the stratocumulus is about 0.5 km^{-1} , which is much smaller than the expected value, as can be obtained from radiometry measurements.

In fact, the optical thickness of the cloud estimated from radiometric measurements using Eq. (4) and (3) is larger than 30 as shown in Figure 2

Given the cloud depth of 300 m deduced from the temperature measurements during ascent and assuming a linear increase of the extinction coefficient with height as a first approximation, one can estimate the extinction at cloud top to be of the order of 0.2 m^{-1} . The true backscatter coefficient at cloud top is thus about $0.01 \text{ m}^{-1} \cdot \text{sr}^{-1}$ (10 km^{-1}), which is about 20 times larger than the observed value. This point will be further discussed in part 2.

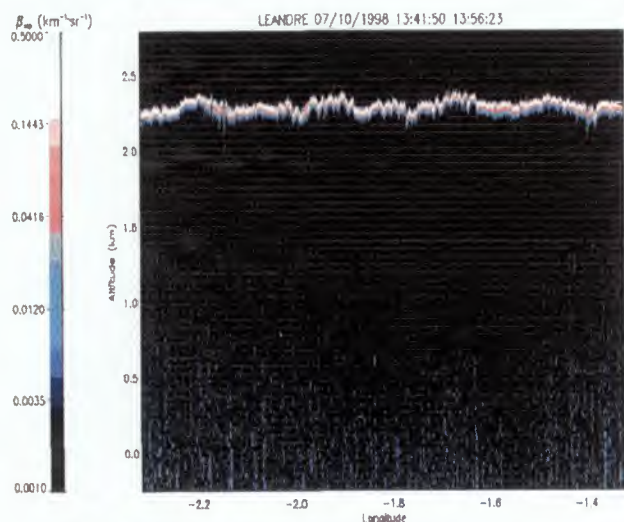


Figure 1 : Attenuated backscatter cross-section obtained during leg 2 over the stratocumulus deck overflow during mission 1.

It is however to be noted that the cloud base cannot be retrieved during this leg. In following measurements, as the cloud deck was breaking, the optical thickness was strongly decreasing in downdrafts, allowing to detect the surface.

A fairly good estimate of the cloud base height can be obtained in this latter case, as multiple scattering contribution apparently coming from below cloud base is small. Cloud depth was confirmed to be 300 m.

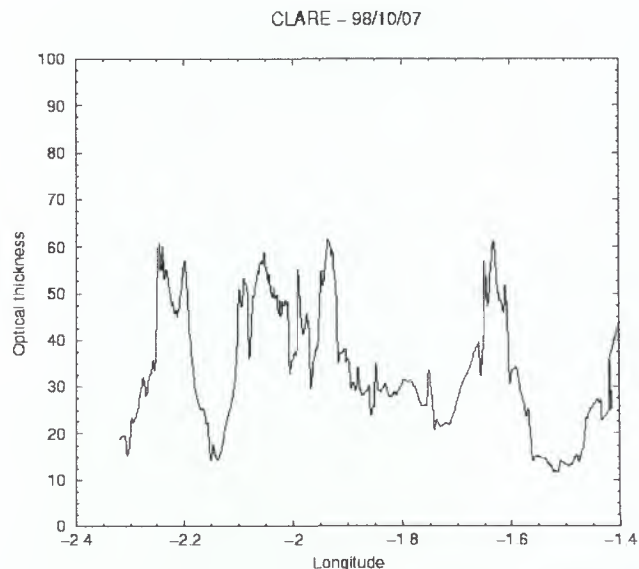


Figure 2 : Cloud optical thickness estimated from radiometry for the same stratocumulus case as in Fig. 1.

Radar measurements performed at the same time show that the cloud top height variation observed by lidar is corresponding to the existence of precipitating cells. This is confirmed by downward vertical speed of -1 to -3 m/s in the cells (not shown). Figure 3 shows that precipitations are detected down to the surface by the Kestrel radar, and that no specific transition is due to the transition at cloud base, as rain signal dominates. These cells are observed to correspond to areas of larger optical thickness in Figure 2.

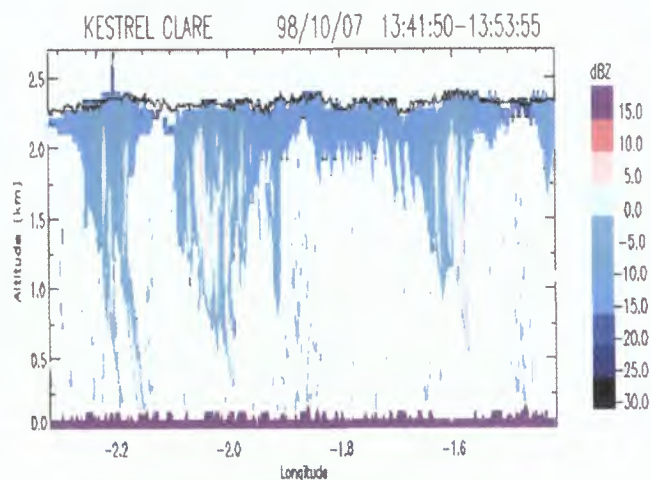


Figure 3 : Radar reflectivity measured simultaneously to lidar and radiometry shown in Figs 1 and 2.

The altitude of cloud top measured by lidar reported in the same figure, is in good agreement with the radar cloud top altitude. It is to be noticed that values of radar reflectivity reported in Figure 3 correspond to the old calibration.

Figures 3 and 4 show the derived attenuated lidar backscattering coefficient for the two cold cloud cases of 14 and 21 October, respectively. The meteorological situation is described in Illingworth et al. (this report).

Cross-sections have been obtained with a vertical resolution of 15 m and an horizontal resolution of 100 m, corresponding to an acquisition time of 1s (12 laser shots). It is seen that maximum values of the attenuated backscattering coefficient comparable with the Sc case are obtained.

The vertical structure is however very different as such clouds are not so opaque. Average depolarization values obtained are comparable for the Sc and cold cloud cases. They are in all cases about 10 to 25 %. However, depolarization in Sc is mainly due to multiple scattering.

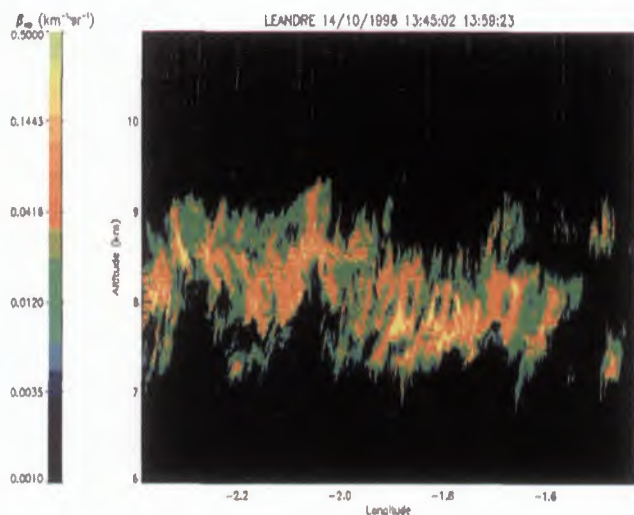


Figure 3 : Attenuated backscatter cross-section obtained during leg 5 of mission 3.

Depolarization values for the 14 October are within 20 to 25%, those for the 21 October are within 10%. Such low values for elevated clouds are comparable to the ones obtained at warm temperatures in previous measurements (Platt et al., 1987). Here we observed about -35°C for the

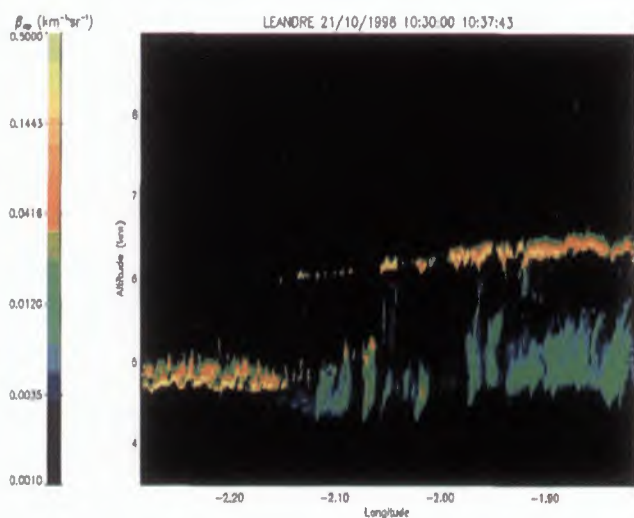


Figure 4 : Attenuated backscatter cross-section obtained during leg 5 of mission 5.

14 October and -15°C for the 21 October as observed with the C130 -see Francis et al., this report-).

The cold cloud case of 14 October (Figure 3) shows the occurrence of structures possibly associated to falling crystals (fallstreaks). On the 21 October a particular vertical structure is observed with a thin layer embedded in similar fallstreaks. Larger values of the attenuated backscatter coefficient associated to low depolarization coefficient are measured in the upper layer. Such a result may be representative of an upper cloud layer with supercooled water droplets (small droplets strongly scattering and weakly depolarizing light) and large simple shaped ice crystals below. Note the difference in scattering in the lower level layer when the upper layer is not present. This may be indicative of precipitating large crystals as observed during the glaciation of altocumulus clouds (Hobbs and Rangno, 1985). Similar observations of enhanced backscattering in a thin cloud layer (attributed to a supercooled water layer) embedded in a larger one were made on the 20 October. Radar measurements did not give evidence of such regions, which reinforce the hypothesis of small water droplets.

CONCLUSION

ARAT flights performed during CLARE'98 have allowed to perform lidar and radar observations on different types of clouds. Multi-layered cloud structure was frequently observed. Thin layers of enhanced backscattering observed in cold clouds by lidar and not by radar were attributed to the presence of a super-cooled water layer with small droplets. Measurements cannot be interpreted directly in terms of cloud parameters and require specific analysis methods. This topic will be discussed in the companion papers.

ACKNOWLEDGMENTS

The ARAT/F27 flights were funded by the European Space Agency which is acknowledged. The ARAT/F27 is a research aircraft of CNRS, CNES, Météo-France and IGN.

REFERENCES

- Chepfer H., G. Brogniez, L. Sauvage, P. H. Flamant, V. Trouillet, J. Pelon, 1999 : Remote sensing of cirrus radiative properties during EUCREX'94. Case study of 17 april 1994. Part 2 : Microphysical modelling, Mon. Wea. Rev., 127, 504-518.
- Flamant C., Trouillet, P. Chazette, J. Pelon, 1998 : Wind speed dependence of atmospheric boundary layer optical properties and ocean surface reflectance as observed by airborne backscatter lidar, J. Geophys. Res., 103, C11, 25 137-25 158.
- Hobbs P. V. and A. L. Rangno, 1985 : Ice particle concentrations in clouds, J. Atmos. Sci., 42, 2523-2549.

Meador W. E. and W. R. Weaver, 1980 : Two-stream approximations to radiative transfer in planetary atmospheres : a unified description of existing methods and a new improvement, *J. Atmos. Sci.*, 37, 630-643.

Pelon J., P. H. Flamant, M. Meissonnier, The French airborne backscatter lidar LEANDRE 1 : conception and operation, Proc. of the 15th. International Laser Radar Conference, 36, TOMSK, 1990.

Pelon J., C. Flamant, V. Trouillet, and P. H. Flamant, Optical and microphysical parameters of dense stratocumulus clouds during mission 206 of EUCREX'94 as retrieved from measurements made with the airborne lidar LEANDRE 1, submitted to *Atm. Res.*.

Platt C. M. R., 1979 : Remote sensing of high clouds : I. Calculations of visible and infrared optical properties from lidar and radiometer measurements, *J. Appl. Meteor*, 18, 1130-1143.

Platt C. M. R., J. C. Scott and A.C. Dilley, 1987 : Remote sensing of high clouds. Part VI : Optical properties of midlatitude and tropical cirrus, *J. Atm. Meteor.*, 18, 1130-1143.

Ruppertsberg G. H., M. Kerscher, M. Noormohammadian, U. G. Oppel, and W. Renger, 1997 : The influence of multiple scattering on lidar returns by cirrus clouds and an effective inversion algorithm for the extinction coefficient, *Beitr. Phys. Atmos.*, 70, 2, 91-107.

Sauvage L., H. Chepfer, V. Trouillet, P. H. Flamant, G. Brogniez, J. Pelon, F. Albers, 1999 : Remote sensing of cirrus radiative properties during EUCREX'94. Case study of 17 April 1994. Part 1 : Observations, *Mon. Wea. Rev.*, 127, 486-503.

Young, A. T., 1980 : Revised depolarization corrections for atmospheric extinction, *Appl. Opt.*, 34, 7019-7031.



The 3 wavelengths lidar ALEX and other instrumentation onboard the FALCON during CLARE'98

H. Flentje, C. Kiemle, V. Weiss, M. Wirth and W. Renger
 Arbeitsgruppe Lidar, DLR-Oberpfaffenhofen, D-82234 Wessling, Germany
 Phone : +49 8153 282525 Fax : +49 8153 281271
 Email: harald.flentje@dlr.de

INTRODUCTION

During the CLARE'98 campaign from 5 to 23 October 1998 near Chilbolton, southern UK, the 3-wavelengths lidar ALEX and a set of in-situ sensors to measure standard meteorological, radiometric and aviation parameters were installed onboard the DLR FALCON aircraft (Figure 1). The sensors onboard the FALCON aircraft as well as their respective accuracy are given in Tables 1 and 2.



Figure 1: FALCON 20-E5 jet aircraft with lidar beam in downward-looking mode

Table 1: FALCON 20-E5 basic sensor-systems

Temperature	<ul style="list-style-type: none"> fast / slow Rosemount PT500 / PT100-sondes OAT / TAT via Air-Data-Computer
Radiation	<ul style="list-style-type: none"> Radiometer Barnes PRT-6 (down) Pyrgometer Eppley PSP (up/down) Pyranometer Eppley PIR (up/down)
Humidity	<ul style="list-style-type: none"> Thermoelectrically cooled dewpoint mirror Dielectric sensor (relative humidity) Lyman-alpha (absolute humidity) Cryogenically cooled dew-point mirror (optional)
Pressure and wind	<ul style="list-style-type: none"> Pitch sensor (nose-mast) for 3D-turbulence and wind-measurements Absolute & differential pressure sensors Barometric height (Air-Data-Computer)

Table 2: Accuracy of quantities recorded by the avionic data acquisition system onboard the FALCON aircraft

Static pressure	± 0.5 hPa
Temperature	± 0.5 K
Humidity	1 % to 5 %
Total Water Content	0.1 g/m^3
Solar Flux Eppley	± 2 %
Longwave Flux	± 5 %
Horizontal position GPS/INS	± 50 m
Pitch (Gyro)	± 0.1 deg
Roll (Gyro)	± 0.1 deg
Heading	± 0.5 deg

The standard meteorological and aviation data listed in Tables 1 and 2 (also available at the web-site of the DLR flight facility: <http://www.dlr.de/FB>) are recorded by the data acquisition system onboard the FALCON aircraft with a temporal resolution of 10 Hz. From these quantities the present position, i.e. latitude, longitude and pressure altitude as well as the true air speed are calculated with an effective resolution of one second. These parameters are online available and stored together with the lidar data which allows to process automatically updated quicklooks of the back-scattered signals during the flight. This is very useful for in-flight mission co-ordination.

THE BACKSCATTER LIDAR

The 3 wavelength lidar of the DLR (ALEX - see Figure 2) was operated in downward-looking mode. It makes use of a flashlamp-pumped Nd:YAG laser with a fundamental wavelength of 1064 nm. Frequency doubling and tripling provides simultaneous output at 532 nm and 355 nm. The instrument emits the laser beam in an off-axis mode via an extra window in the aircraft fuselage (Figure 2). Complete overlap of the laser beam and the receiver field-of-view is achieved after a distance of 1 – 1.5 km.

The receiver is a Cassegrain telescope ($r = 17.5$ cm) with 1 mrad field of view. Narrow band filters are positioned in front

of the detectors to minimise the contributions of the background illumination from the atmosphere and the surface. The received 532 nm signal is split into two perpendicularly polarised portions which allows to calculate the depolarisation of the light. The depolarisation contains information about the asphericity of the back-scattering particles which allows to characterise different aerosol or cloud particle types. The performance of the lidar system has been described on principle by [1].

ALEX Principle

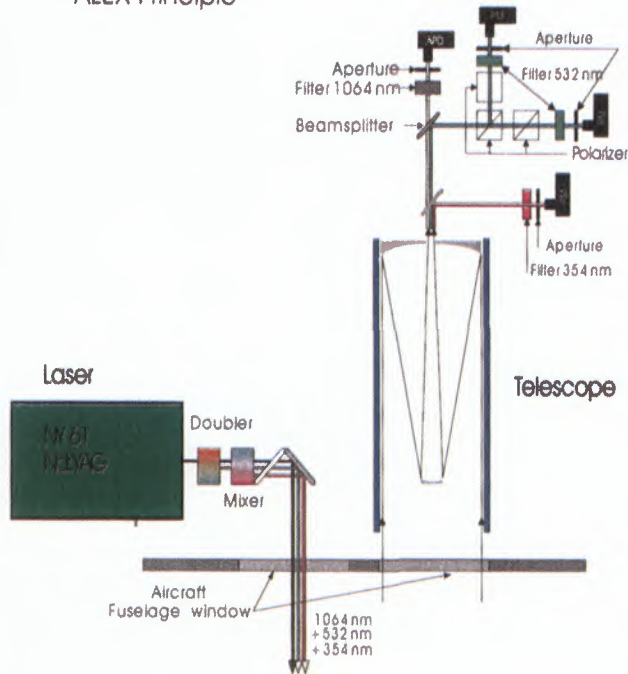


Figure 2: Biaxial optical system and beam path of the ALEX lidar. Left side: transmitter and crystals for frequency conversion, right side: receiver and data acquisition system. The system parameters are listed in Table 3. Full overlap of the laser beam and the receiver field-of-view is achieved after a distance of about 1 - 1.5 km.

With a repetition rate of 10 Hz and a typical aircraft speed of 150 m/s the raw data resolution is 15 m horizontally. Vertically the 10 MHz ADC sampling rate results in a resolution of 15 m. However, depending on the specific demand a trade-off between signal noise and spatial resolution is performed. In order to qualitatively investigate small scale structures in an inhomogeneous environment (e.g. for comparison of cloud boundaries obtained from ground based radar and airborne lidar) only few shots (< 1 s) are averaged degrading the horizontal resolution to about 100 m. For the derivation of quantitative optical parameters like optical depth or the multiple scattering contribution the signal is typically averaged over 10 - 20 s and slightly smoothed vertically which leads to a resolution of 1 - 3 km horizontally and 30 m vertically.

Table 3: Aerosol Lidar EXperiment (ALEX) system parameters

Transmitter	Continuum Nd:YAG-laser NY61
Pulse energy at λ	150 mJ @ 1064 nm 120 mJ @ 532 nm 150 mJ @ 355 nm
Pulse length	6 ns
Beam divergence	0.7 mrad
Pulse repetition rate	10 Hz
Telescope	B. Halle Nachf.
Type	Cassegrain
Diameter	35 cm
Field of view (full angle)	1 mrad
Focal length	5 m
Filter (Comp., Half width, max. Transmission)	1064 nm: LOT, 1.0 nm, 40% 532 nm: LOT, 0.5 nm, 60% 355 nm: FHE-Jena, 1.5 nm, 45%
Detector	Hamamatsu R5600U
PMT (355 nm, 532nm)	Advanced Photonics 197-70-7X-520
APD (1064 nm)	520
Transient-recorder	DLR, 12 bit / 20 MHz DLR, 14 bit / 10 MHz
Data handling	VME-BUS: (FORCE-Computer) CPU: SUN SPARC 10 Data storage medium: Magneto-optical disks (2 GB) and DAT (3 GB)

The attenuated atmospheric backscatter directly measured by the lidar is either given absolutely as backscatter coefficient [$\text{m}^{-1}\text{sr}^{-1}$] or relative to Rayleigh scattering (calculated from air density) as backscatter ratio $\gamma = (\beta_{\text{particle}} + \beta_{\text{molecule}}) / \beta_{\text{molecule}}$, the relative contribution of total to pure molecular scattering (cf. [2] this issue). The attenuation of the laser beam in the atmosphere is considered employing a numerical Klett-type [3] inversion of the lidar equation whereby an extinction/backscatter coefficient ratio (lidar ratio) and a starting value at some distance from the receiver have to be assumed to iteratively derive the profiles. With the inferred lidar ratio the extinction coefficient and its integral, the optical depth, can be estimated from the backscatter signal. The ratio of the orthogonal and parallel (to the incident beam) polarised 532nm signals $\beta_{\perp} / \beta_{\parallel}$ i.e. the depolarisation of the light by the scattering particles contains information about their sphericity. A volume depolarisation of 0.014 (or 1.4%) occurs if only the unsymmetrical air molecules contribute to the depolarisation. If the sampled volume contains depolarising (non-spherical, solid) particles, the volume depolarisation is between 0.014 and 1 depending on the concentration and shape of the scattering particles. Clouds with *only* spherical (liquid) particles may cause volume

depolarisation below 1.4% since they increase only the intensity in the parallel channel.

LIMITATIONS

Lidar measurements under optically dense conditions typically suffer from several constraints. Strong atmospheric attenuation of the beam along its path increases the signal/noise (S/N) ratio and reduces the penetration depth of the laser beam. In clouds the signal may be blocked after a short distance. The S/N ratio therefore depends on the optical depth of the atmosphere between the lidar and the scattering target. If the optical depth along this path is low, the detection limit (defined as the equivalent noise superposed to the offset) is $\Delta\beta \approx 2 \dots 5 \cdot 10^{-10} \text{ m}^{-1} \text{ sr}^{-1}$ or below $\Delta\gamma \approx 1\%$ in terms of the backscatter coefficient β or the backscatter ratio γ at 1064 nm, respectively. At the lower wavelength channels the offset is somewhat higher, and the equivalent noise is of the order of $\Delta\beta \approx 10^{-9} \text{ m}^{-1} \text{ sr}^{-1}$ to $10^{-8} \text{ m}^{-1} \text{ sr}^{-1}$ in terms of the backscatter coefficient. Due to the increase of the Rayleigh scattering efficiency with decreasing wavelength the detection limit expressed as a backscatter ratio is also $\gamma < 1\%$ at 355 nm and 532 nm. These values all refer to integration times of at least 30 s (i.e. 300 pulses).

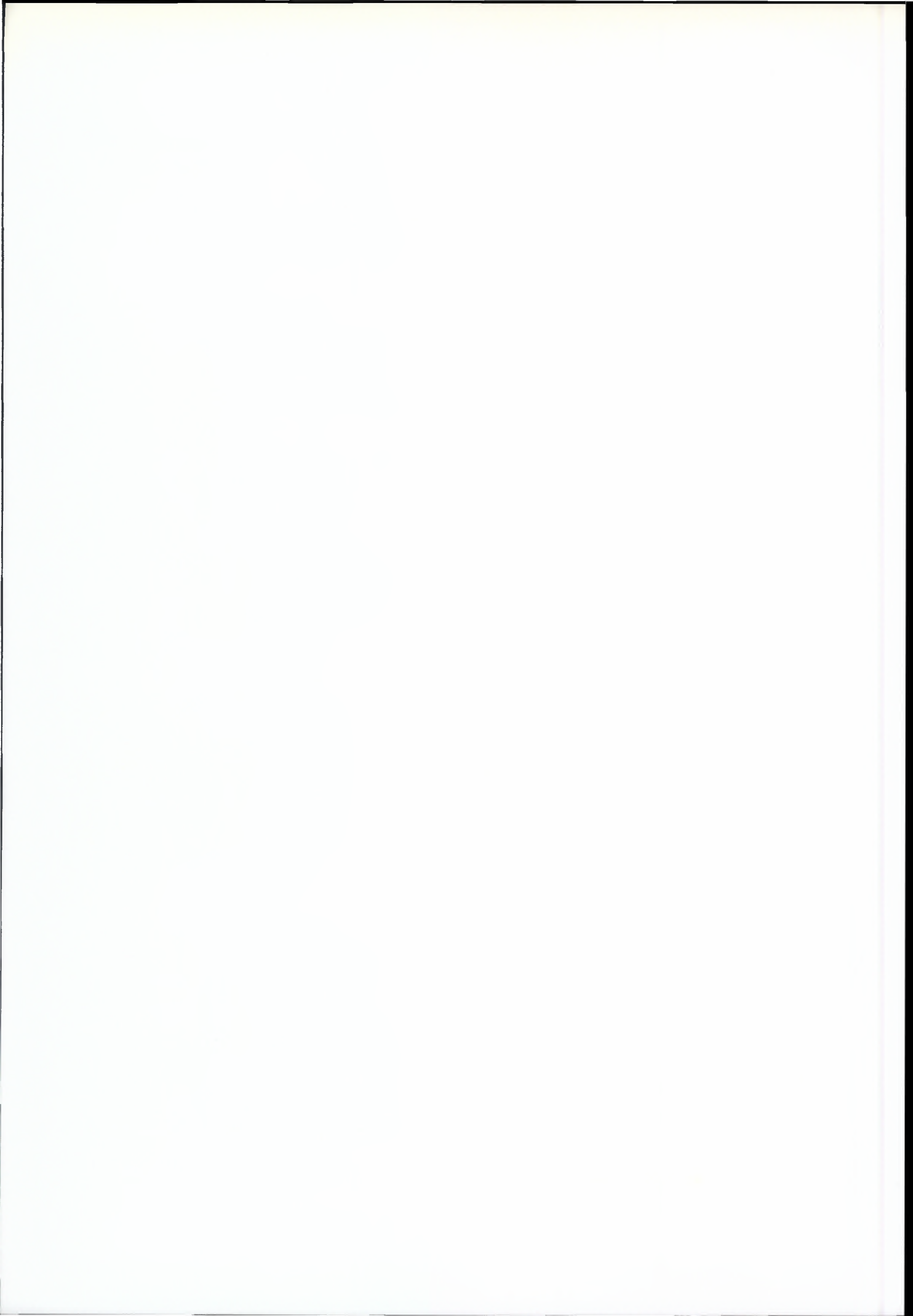
Another problem occasionally arises when the signal is saturated in one or more channels due to transient very strong back-scattering by nearby clouds which destroys all quantitative information about the scatterers in the corresponding channels. Especially the relation between the co- and cross polarised 532 nm signals is affected if one (or both) of them is saturated. Since the parallel signal generally is higher (or equal) than the cross-polarised signal, this means always a relative enhancement of the cross-polarised signal and thus leads to an erroneously high depolarisation ratio. Not taking into account the multiple scattering effect also feigns a stronger depolarisation [2].

Third, an uncertainty of the absolute value of the backscatter coefficient is caused by possible errors in the atmospheric calibration at the starting point of the inversion. Presently applied lidar inversion algorithms based on the Klett-method [3] need to assume two independent parameters for the retrieval of each profile. These are the reference backscatter ratio $\gamma_0(r_0)$ at a selected distance r_0 in the column and the backscatter/extinction coefficients ratio $\beta(r)/\alpha(r)$ (lidar ratio) which mostly (but not properly) is assumed to be range independent, although it actually is a function of the particle ensemble scattering function and the particle number density in the sampled air volume. The reference backscatter ratio $\gamma_0(r_0)$ may be estimated from suitable simultaneous measurements, from standard atmospheric extinction profiles respecting the air-mass type of the sampled volume or by (however vague and subjective) visibility observations. An erroneous value results in an offset of the profile, which depends on the quality of the reference estimate, and thus stronger affects the low backscatter-coefficients. Larger

uncertainties arise from the lidar ratio, which tends to be too large if multiple scattering is not taken into account and may be only vaguely inferable in a clean atmosphere with low optical depth. This uncertainty propagates especially to quantities which are calculated from the inferred lidar ratio like the optical depth. Though the discussed errors are mostly of the order of a few percent, they may occasionally become a factor of two or more.

REFERENCES

- [1] Mörl, P., M.E. Reinhardt, W. Renger and R. Schellhase, The use of the airborne LIDAR system "ALEX F1" for aerosol tracing in the lower troposphere, *Beitr. Phys. Atmos.*, 54, 401-410, 1981.
- [2] Flentje, H., C. Kiemle and W. Renger, Multiple scattering in mixed phase mid-level ice/water clouds during CLARE'98 and implications for space lidar, *this issue*.
- [3] Klett, J.D., Lidar inversion with variable backscatter/extinction ratios, *Appl. Optics*, 24, 1638-1643, 1985.



An Overview of the UKMO C-130 Measurements from CLARE'98

P.N. Francis

Meteorological Research Flight, UK Meteorological Office

Y46 Building, DERA Farnborough, Hampshire, GU14 0LX, United Kingdom

Phone : +44 (0)1252 395403 Fax : +44 (0)1252 376588 Email: pnfrancis@meto.gov.uk

INTRODUCTION

This paper provides an overview of the C-130 measurements taken during the CLARE'98 field campaign. Particular emphasis is given to the cloud microphysics measurements, highlighting certain strengths and weaknesses. The broadband radiometer data are also discussed, with reference to the inter-comparison flight carried out on 15 October 1998.

CLOUD PHYSICS DATA IN WATER CLOUDS

The instruments used to measure cloud microphysics data in water clouds were the Forward Scattering Spectrometer Probe (FSSP), and PMS two-dimensional cloud probe (2D-C) and the Johnson-Williams (J/W) liquid water content meter. The former two instruments provide droplet-size dependent information, whereas the latter provides a bulk measurement of the liquid water content. An example of a 5 second averaged spectrum from the FSSP and 2D-C probes is shown in figure 1.

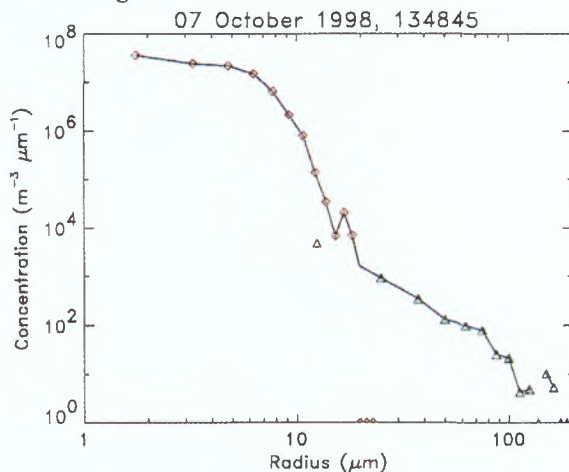


Figure 1. A typical 5-second average spectrum from the FSSP (red diamond) and 2D-C (green triangle) measurements, taken from the 7 October 1998 case. The blue line represents the merged spectrum used from these measurements to calculate bulk quantities such as liquid water content and effective radius.

The blue line represents an attempt to merge the measurements from the two probes so as to produce a continuous spectrum. This has been done by using data from as many of the FSSP bins as possible (i.e. disregarding bins having no counts, the largest three bins in this example),

ignoring the smallest 2D-C bin, and interpolating 2D-C data onto the FSSP bins in the overlapping region. An alternative method of merging the spectra from these two instruments has been considered by Baedi *et al.* (1999a).

When the integrated liquid water contents from these probes were compared with the bulk measurements from the J/W probe, they were found to systematically underestimate the J/W readings by typically a factor of 4 for much of the CLARE'98 experiment. An example of this is presented in figure 2, which shows a run in stratocumulus cloud from 7 October.

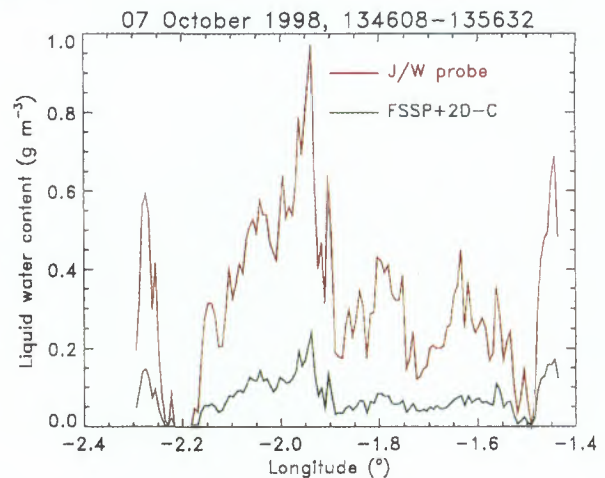


Figure 2. Liquid water content time series from a run in stratocumulus on 7 October 1998. The red line shows the bulk measurement from the J/W probe, the green line shows the result of integrating the combined spectra from the FSSP and 2D-C instruments.

This discrepancy has been noted on many previous C-130 datasets, and the magnitude of the FSSP under-reading can be shown to be correlated to various size distribution size parameters such as the effective radius. Thus, the liquid water contents are in very good agreement with each other when the effective radius exceeds around 9-10 μm , but when the effective radius drops to around 5-6 μm , as in the CLARE'98 dataset, the FSSP underestimates the liquid water content relative to the J/W by a factor of around 4. It is not clear at the present time exactly what the cause of the under-reading is, nor what form a suitable size-dependent correction could be added to the FSSP data to bring them into line with the J/W probe. For these measurements, therefore, we have taken the most straightforward option and increased the FSSP concentrations by a constant factor, independent of size, so as to bring the two liquid water

content measurements into agreement. Attempts to introduce a size-dependent correction have been made by Baedi *et al.* (1999b).

CLOUD PHYSICS DATA IN ICE CLOUDS

The instruments used to look at cloud microphysics data in ice clouds were primarily the PMS two-dimensional cloud (2D-C) and precipitation (2D-P) probes. Two different ways of calculating IWC from the 2D probes have been used, those described by Francis *et al.* (1998), based on the particles' shadow areas, and by Brown and Francis (1995), based on the particles' mean diameters. An example of the ice water contents derived from the 14 October cirrus flight is shown in figure 3, with very good agreement being found between the two algorithms.

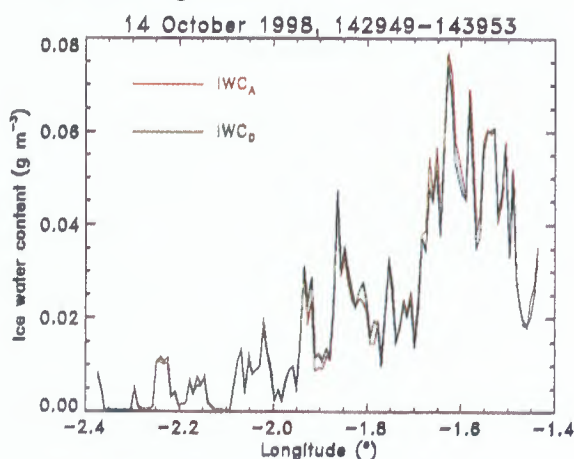


Figure 3. Ice water content time series taken from 14 October 1998, when the C-130 was flying in a cirrus layer at 7.6 km. The algorithm based on the particle shadow area (IWC_A) is plotted as the red line, and that based on the particle mean diameter (IWC_D) as the green line.

Another example where the agreement is not so good is shown in figure 4, which shows data from a run flown at 5.5 km on 20 October 1998, in a region of the cloud where there were no indications of significant liquid water.

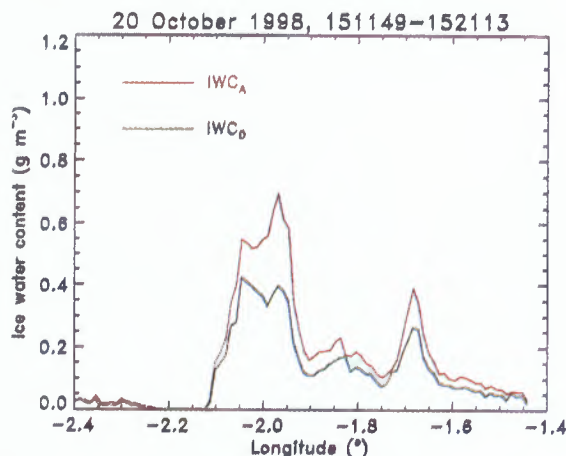


Figure 4. As figure 3, but for a run flown at 5.5 km in ice cloud on 20 October 1998.

In an attempt to validate these ice water contents against independent measurements, we have also compared them with bulk measurements based on taking the residual of measurements of total water content (from the TWC meter on the C-130) and water vapour content (taken from a General Eastern hygrometer). Because the hygrometer has very slow response times at cirrus altitudes, we have had to take 30 second averages in order to perform meaningful comparisons. Examples from the 14 October and 20 October flights are shown in figures 5 and 6 respectively, and correspond to the same data shown in figures 3 and 4.

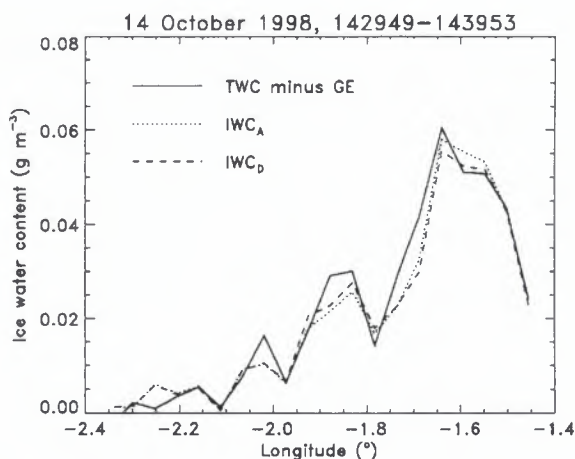


Figure 5. Bulk measurement of ice water content (solid line) compared with values derived from the 2D probes. The data correspond to those shown in figure 3.

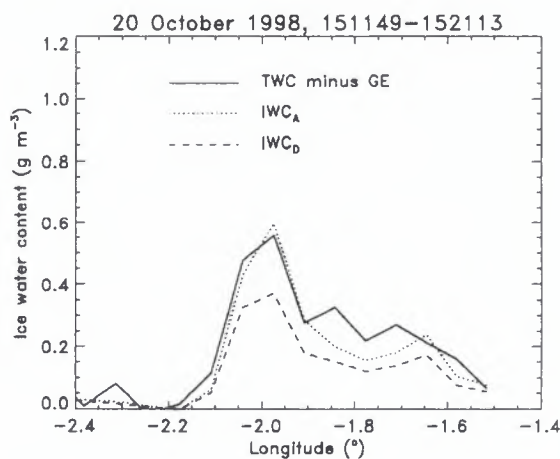


Figure 6. Bulk measurement of ice water content (solid line) compared with values derived from the 2D probes. The data correspond to those shown in figure 4.

The generally good agreement between the 2D probe derived values and the bulk values shown in figure 5 gives us some confidence that the ice water contents from the 14 October case are accurate to at least 25%, as quoted by Francis *et al.* (1998). Turning to figure 6, the agreement is not quite as good for either of the 2D algorithms, although there is a suggestion that, in the region of high ice water content centred around -2.0° longitude, the IWC_A method produces slightly better values.

MEASUREMENTS IN MIXED-PHASE CLOUDS

On 20th October, a complex mixed-phase cloud system was sampled in the observing area, and during some of its runs the C-130 sampled liquid water and ice simultaneously. The liquid water content was measured with the J/W meter and the ice water content with the 2D-C and 2D-P probes. An example of one of these penetrations is shown in figure 7.

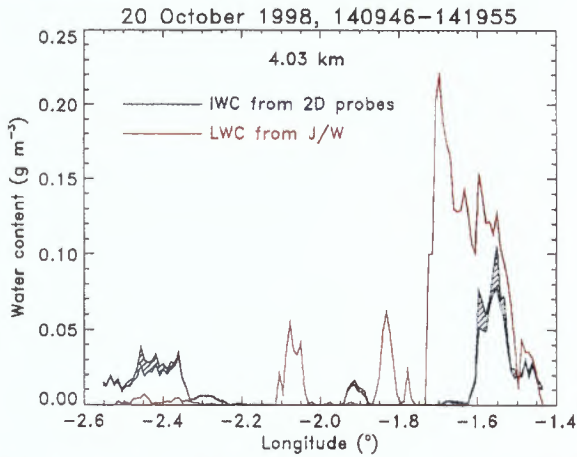


Figure 7. Liquid and ice water contents from a run at 4.03 km on 20 October 1998. The red line is the J/W liquid water content, the blue hatched area represents the ice water content.

The blue hatched area represents the uncertainty introduced into the inferred ice water content due to the fact that a certain proportion of the 2D-C particle images are too small to be classified, and could therefore be either ice crystals or water droplets.

RADIOMETER INTERCOMPARISON FLIGHT

This section deals with broad-band radiometer comparisons from the sortie flown on 15 October 1998, when the C-130 and ARAT flew a side-by-side flight pattern, followed by a similar pattern flown by the C-130 and the Falcon. Figures 8 and 9 show comparisons between the shortwave and longwave irradiances measured from one of the legs of the C-130/ARAT flight pattern, and figures 10 and 11 show the corresponding data from one of the legs from the C-130/Falcon inter-comparison.

The agreement is seen to be satisfactory, with the relative differences generally lying well within 5%, although slightly larger differences are apparent when the downwelling longwave irradiances from the C-130 and Falcon are compared in figure 11. Figure 11 also demonstrates the importance of temperature stabilization on the quality of pyrometer data, the Falcon upwelling longwave measurements taking several minutes to come into equilibrium after transit, and into agreement with the C-130 data.

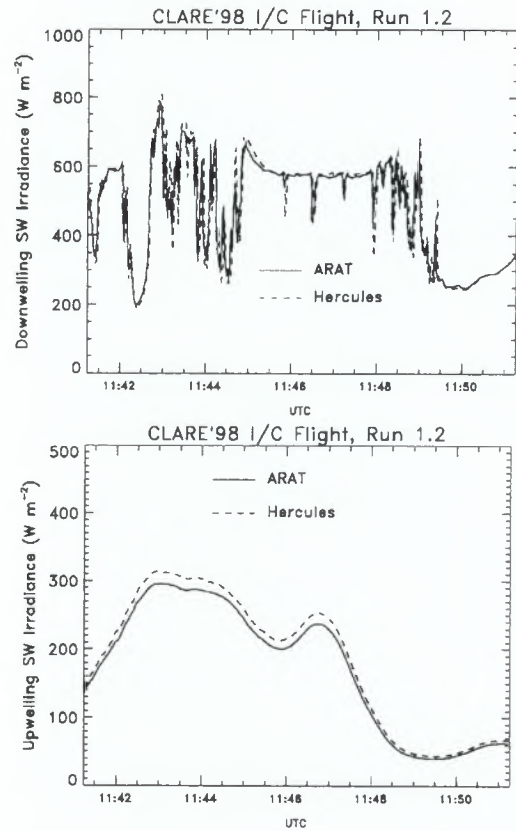


Figure 8. Comparison of downwelling and upwelling irradiances measured by the C-130 and ARAT aircraft.

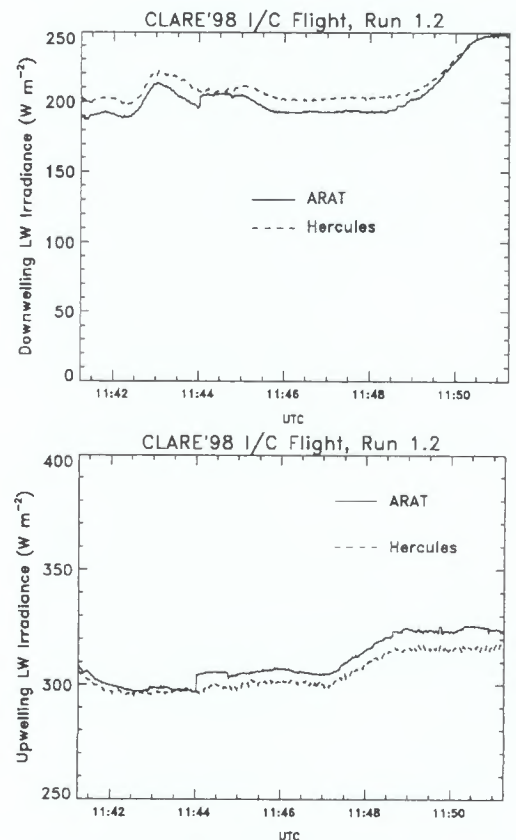


Figure 9. Comparison of downwelling and upwelling longwave irradiances measured by the C-130 and ARAT aircraft.

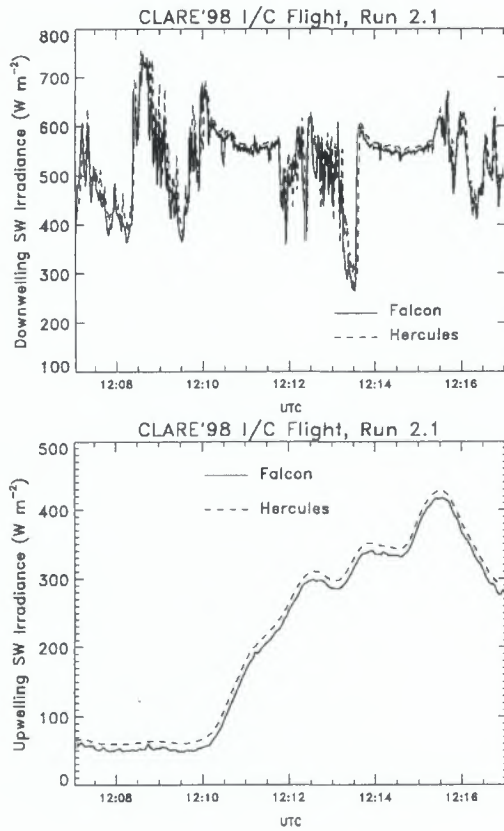


Figure 10. Comparison of downwelling and upwelling shortwave irradiances measured by the C-130 and Falcon aircraft.

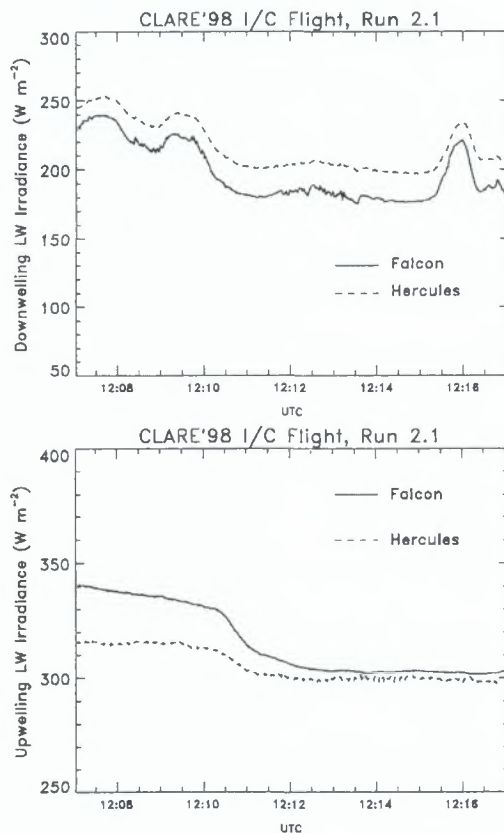


Figure 11. Comparison of downwelling and upwelling longwave irradiances measured by the C-130 and Falcon aircraft.

REFERENCES

- Baedi, R.J.P., *et al.*, 1999a: Study of micro-physical and macro-physical measurements of water clouds during CLARE'98. *This volume*.
- Baedi, R.J.P., *et al.*, 1999b: Alternative algorithm for correcting FSSP measurements. *This volume*.
- Brown, P.R.A. and Francis, P.N., 1995: Improved measurements of the ice water content in cirrus using a total-water probe. *J. Atmos. Sci.*, **27**, 919-926.
- Francis, P.N., *et al.*, 1998: The retrieval of cirrus cloud properties from aircraft multi-spectral reflectance measurements during EUCREX'93. *Quart. J. Roy. Meteorol. Soc.*, **124**, 1273-1291.

Provision of Chilbolton Infrastructure and Instrumentation for CLARE 98.

J W F Goddard

Radio Communications Research Unit

Rutherford Appleton Laboratory, Chilton, Didcot, Oxon OX11 0QX, UK

Phone : +441235446127 Fax : +441235446140 Email: j.w.f.goddard@rl.ac.uk

INTRODUCTION

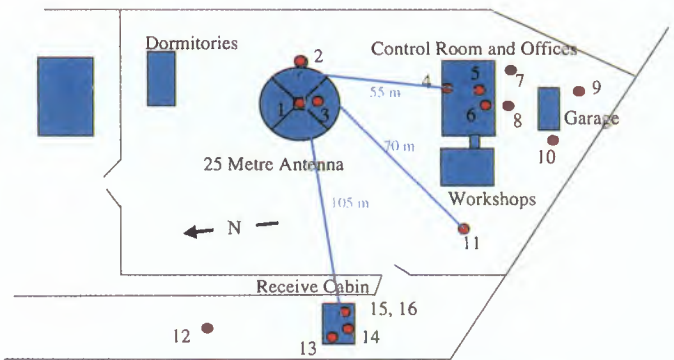
The CLARE 98 campaign was centred on the Chilbolton Observatory in Hampshire, UK, which is operated by the Radio Communications Research Unit of the Rutherford Appleton Laboratory. Chilbolton not only provided several instruments, but also acted as a communications centre for controlling the entire operation and provided facilities for initial analysis of data from each day. This document summarises the performance of the ground-based instruments operated by the Radio Communications Research Unit at Chilbolton during the CLARE campaign.

OVERVIEW OF CHILBOLTON FACILITIES

Chilbolton is a secure rural site ideally suited for mounting atmospheric science campaigns. Figure 1 shows the 25 metre antenna with the main buildings in the background. The fully steerable 25 metre antenna is capable of supporting bolt-on experiments, and there is ample space for stand-alone equipment, either on the ground, on the flat roofs of the main buildings or in portacabins. The Chilbolton intranet is connected to the main UK Janet network via a high speed telephone line, allowing fast internet access. Figure 2 shows how the various instruments were distributed around the site.



Fig. 1 The Chilbolton site, looking South East



- | | |
|------------------------------------|-------------------------------------------|
| 1 - CAMRa 3GHz Radar (RCRU) | 9 - 93 GHz Radiometer (U. Bath) |
| 2 - Rabelais 35 GHz Radar (UPS) | 10 - Interferometer (MPI) |
| 3 - IR Radiometer (KNMI) | 11 - Miracle 95 GHz Radar (GKSS) |
| 4 - UV Raman Lidar (RCRU) | 12 - IR Radiometer (KNMI) |
| 5 - IR Ceilometer (ESTEC) | 13 - Met Instruments, Cloud Camera (RCRU) |
| 6 - 20/30/50 GHz Radiometers (TUE) | 14 - Galileo 94 GHz Radar (ESTEC) |
| 7 - 35 GHz Radiometer (UPS) | 15 - GPS Receiver (U. Bath) |
| 8 - Interferometer (U. Heidelberg) | 16 - 40 GHz Rx, radiometer (U. P'smouth) |

Fig 2. Site plan of instrumentation at Chilbolton during the CLARE campaign (not to scale)

RADARS

3 GHz CAMRa Radar

This radar uses the fully-steerable 25 m antenna (see Table 1 for details). Parameters measured and recorded during the campaign were reflectivity, differential reflectivity, linear depolarisation ratio, Doppler velocity and differential phase.

Frequency	3.075 GHz
Peak Power	600 kW
Pulse Rep Frequency	610 Hz
Pulse Width	0.5 μ s
Antenna Diameter	25 m
Beam Width	0.26°
Polarisation	H/V
Scan Rate	1° /sec
Unambiguous velocity	± 15 m/sec

Table 1: Details of the CAMRa radar

The radar was used to characterise the horizontal and vertical cloud and precipitation structure through regular RHI scans along the aircraft bearing, and, in addition, a special macro incorporating variable scan rates was used to allow the radar to track the aircraft flight. Vertical pointing data were not obtained, because the near-field distance of this radar is over

6 km, and also because ground clutter in the side/backlobes contaminates meteorological targets. Table 2 summarises the periods of data acquisition with the radar during CLARE. The CAMRa radar played an important role in calibration of the other radar systems used during CLARE. For details, see Hogan and Goddard (1999).

Day (Oct)	Scanning Reflectivity Data (UTC)
7	0716 – 1500
8	
9	1610 – 1812
10	
11	
12	1013 – 1045 1421 – 1526
13	0814 – 0937 1047 – 1615
14	1059 – 1503
15	1458 – 1548
16	1055 – 1335
17	
18	
19	0926 – 0940 1447 – 1708
20	0815 – 1601
21	0907 – 1104
22	0951 – 2044
23	

Table 2: Summary of data from the 3 GHz CAMRa radar

35 GHz Rabelais Radar

This radar, on loan from the University of Toulouse, was mounted on the rim of the 25 m antenna, and so scanned in tandem with the CAMRa radar.

Frequency	34.94 GHz
Peak Power	50 kW
Pulse Rep Frequency	2688/3125 Hz
Pulse Width	0.3 μ s
Antenna Diameter	1.4 m
Beam Width	0.43°
Polarisation	H/V
Scan Rate	1°/sec
Unambiguous velocity	± 6 m/sec

Table 3: Details of the Rabelais radar

However, when scanning was not required, the radar was generally operated in a vertical pointing mode. Details of the radar are given in Table 3. Parameters measured and recorded were reflectivity and differential reflectivity. Pulse-to-pulse data were also collected whenever aircraft flights were in progress. Table 4 summarises the periods of data collection with Rabelais. For details of the radar calibration see Hogan and Goddard (1999).

Day (Oct)	Zenith Pointing Reflectivity Data (UTC)	Scanning Reflectivity Data (UTC)	Pulse-to-pulse IQ Data (UTC)
7		0840 – 0910 1020 – 1030 1117 – 1500	1129 – 1501
8			
9	1111 – 2320	1611 – 1820	
10	0030 – 1630		
11			
12	1002 – 2319		
13	0016 – 2302	1013 – 1547	1154 – 1548
14	0002 – 2350	1059 – 1503	1209 – 1503
15	0050 – 2325		
16	1115 – 1545	0940 – 1507	1107 – 1458
17	0048 – 2349		
18	0049 – 2350		
19	0050 – 2318		
20	0019 – 2306	0816 – 1539	0811 – 1528
21	0006 – 2358	0908 – 1104	0921 – 1123
22	0058 – 2306	0953 – 1047 1127 – 1436	1119 – 1510
23	0038 – 2351		

Table 4: Summary of data from the 35 GHz Rabelais radar

95 GHz Galileo Radar

The hardware and software for this radar were still under development as the CLARE campaign got underway. It was located in the Receive Cabin, operating through a window (reasonably transparent at 95 GHz) with an externally mounted flat reflecting plate at 45° to produce a vertically-pointing beam. Details of the radar are given in Table 5.

Frequency	94.8 GHz
Peak Power	2 kW
Pulse Rep Frequency	6250 Hz
Pulse Width	0.5 μ s
Antenna Diameter	0.5 m
Beam Width	0.5°
Unambiguous velocity	± 5 m/sec

Table 5: Details of the Galileo radar

Averaged reflectivity data were recorded towards the end of the campaign, using newly developed data acquisition software. Throughout the campaign, however, pulse-to-pulse data were collected whenever aircraft flights were in progress. Table 6 summarises the periods of data collection with the Galileo radar. For details of the radar calibration see Hogan and Goddard (1999).

Day (Oct)	Reflectivity Data (UTC)	Pulse-to-pulse IQ Data (UTC)
7		1127 - 1454
8		
9		
10		
11		
12		
13		1322-1616
14		1205-1508
15		
16	1115 - 1545	1058-1525
17		
18		
19		
20	1350 - 1500	0844-1525
21	1005 - 1650	1026-1636
22	0925 - 1715	1119-1313
23		

Table 6: Summary of data from the 94 GHz Galileo radar

LIDARS

IR Ceilometer CT75K

This instrument, manufactured by Vaisala and on long term loan from ESTEC, was located on the roof of the Control Room. Pointing at zenith, it recorded data continuously throughout the CLARE campaign. Details are shown in Table 7.

Centre Wavelength	905 nm
Peak Power	16 W
Pulse Rep Frequency	3670 Hz
Pulse Width	100 ns
Resolution	30 m

Table 7: Details of the CT75K ceilometer

UV Raman Lidar

This lidar, although designed primarily for temperature and water vapour profiling, was operated throughout the campaign in a simple Rayleigh backscatter mode. Details are given in Table 8.

Centre Wavelength	354.7 nm
Peak Power	1 MW
Pulse Rep Frequency	50 Hz
Pulse Width	7 ns
Resolution	1 m

Table 8: Details of the UV Raman Lidar

A full description of the lidar, together with analysis and comparisons with the IR ceilometer and the Galileo radar is given in *Agnew et al, 1999*.

Day (Oct)	Zenith Pointing Data (UTC)
7	1054 - 1630
8	1437 - 1600
9	0939 - 1000 1211 - 1310 1339 - 1400
10	
11	
12	0932 - 1237
13	1040 - 1555
14	1015 - 1515
15	1236 - 1315 1439 - 1458
16	1000 - 1525
17	
18	
19	1110 - 1209 1341 - 1543
20	0822 - 0913 1044 - 1540
21	
22	1243 - 1514
23	

Table 9: Summary of data from the UV Raman Lidar

RADIOMETERS AND METEOROLOGICAL INSTRUMENTATION

93 GHz Radiometer

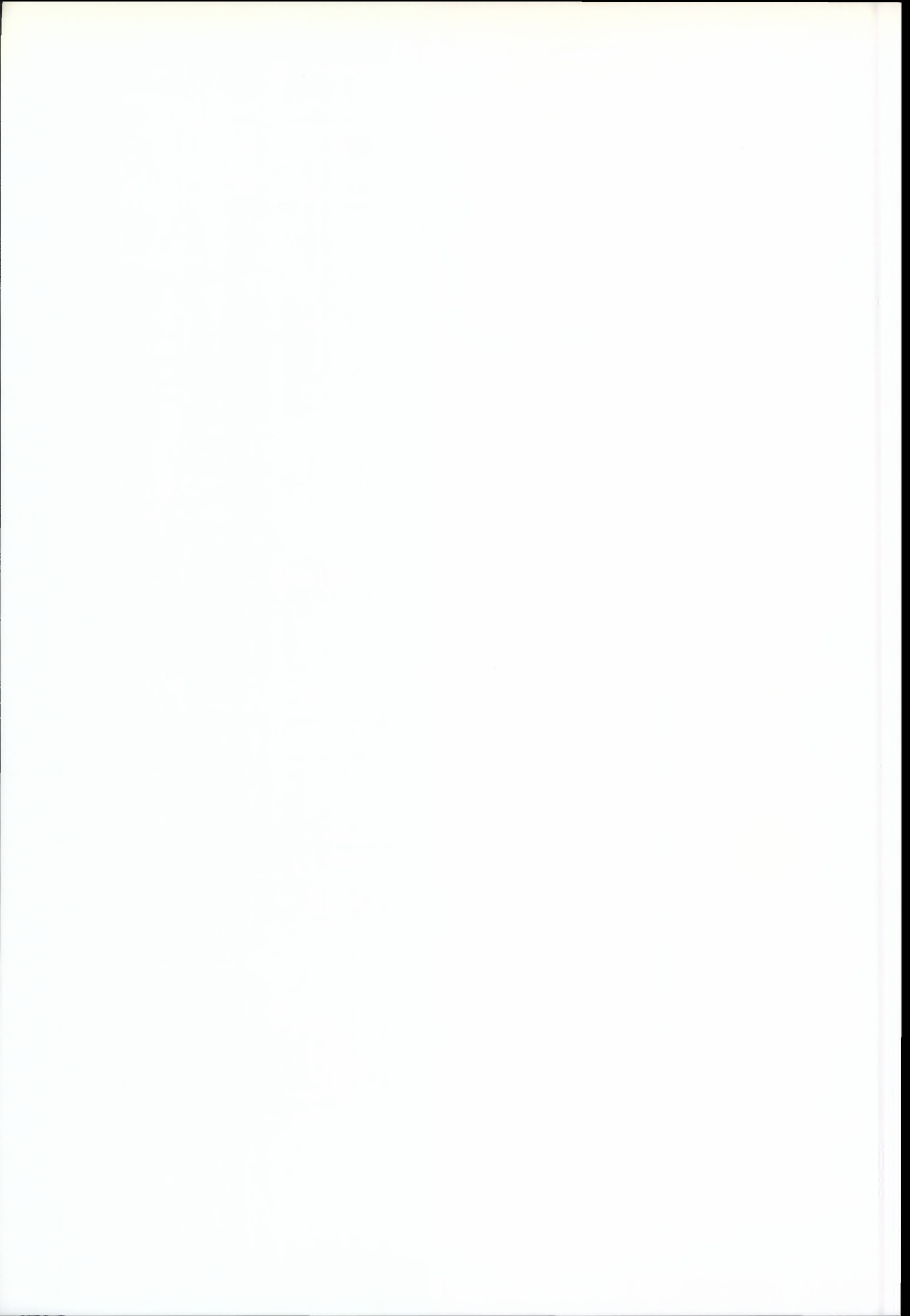
This instrument is operated at Chilbolton on behalf of the University of Bath. A failed pin switch on 13 October prevented further operation of the radiometer. Total liquid water estimates were made on three days, 7th, 12th and 13th October.

Meteorological Measurements

Routine meteorological measurements were made throughout the campaign, including rainfall, pressure, temperature and dew point. Finally, a cloud camera was installed at Chilbolton for the duration of CLARE. This recorded cloud images once every 15 seconds, along a typical aircraft bearing, covering a range of elevations from 45° to 90°.

REFERENCES

- [1] Hogan R. J. and Goddard J.W.F., "Calibration of the ground-based radars during CLARE 98", This issue, 1999.
- [2] Agnew J.L., Gibson A.J. and Marsh A.K.P., "Measurements for the CLARE 98 campaign using the Chilbolton UV lidar", This issue, 1999.



The GKSS 95 GHz cloud radar during CLARE 98: System performance and data products

Olaf Danne, Markus Quante

GKSS Research Centre, Institute for Atmospheric Physics, D-21502 Geesthacht, Germany
Phone: +49 4152 87 1520 Fax: +49 4152 87 2020 Email: danne@gkss.de

INTRODUCTION

For its participation in the CLARE 98 campaign, the transportable 95 GHz cloud radar MIRACLE was moved to England. It was set up on the field site of the Radio-communication Research Unit of the Rutherford Appleton Laboratory at Chilbolton, where the RAL radars are installed. The position was just outside the workshop, the distance from the main dish of the 3 GHz radar CAMRa was about 40 m, and from the 94 GHz radar GALILEO it was about 50 m. Figure 1 shows MIRACLE in front of the CAMRa during the campaign.



Fig. 1: The GKSS 95 GHz radar MIRACLE in front of the 3 GHz radar CAMRa during the campaign.

SYSTEM DESCRIPTION

The GKSS cloud radar was built by Quadrant Engineering Inc., Amherst, Mass. The system was taken into operation in summer 1996. The radar control and data handling is based on an HP-VXI data acquisition and processing system. The radar is designed for ground-based use

and is installed in a transportable container. The RF-component and antenna are integrated in an azimuth-elevation scanning device.

The pulsed Doppler radar is fully polarimetric and has a peak power of 1.7 kW. Pulse repetition frequency, number and location of range gates, pulse width and pulse polarization are software selectable and allow for a range resolution between 7.5 m and 82.5 m up to a range of 15 km. The beamwidth of the center-fed Cassegrain antenna of 0.17° leads to a range cell diameter of 30 m at a distance of 10 km. The far-field of the antenna starts at a range of about 900 m.

Further specifications are listed in Table 1.

Table 1: Parameters of the GKSS cloud radar.

Frequency (Wavelength)	95 GHz (3 mm)
Peak Power (EIA)	1.7 kW
Duty cycle	1.2 % max.
Pulse repetition freq.	50 Hz - 80 kHz
Pulse width	50 - 2000 ns
Beam width $\vartheta_{3\text{dB}}$	0.17°
Antenna diameter	1.2 m (Cassegrain)
Antenna gain	60 dB
Polarization	linear (H, V)
Cross-polarization isolation	26 dB
Dynamic range	> 70 dB

DATA PRODUCTS AND DATA PROCESSING

The real-time data products include the three Doppler moments (total power, mean velocity, velocity variance) obtained from a pulse-pair algorithm. Alternatively, the radar can be operated in an up to 1024 point FFT mode to obtain full Doppler spectra. In the pulse-pair mode, polarimetric quantities such as ZDR and LDR are also obtained. ZDR provides useful information about particle shape by comparing copolarized backscatter at linear vertical and horizontal polarizations. LDR is a measure of the amount of depolarization detected and indicator of both particle asymmetry and orientation.

During CLARE, the radar was operated in a vertical pointing mode. Typical height-time sections of radar reflectivities as available in the CLARE dataset are produced in several steps. At first, profiles of received power are

calculated by averaging over a large number of samples (in general several thousand pulses). To obtain an estimate for the receiver noise, the 10 contiguous range gates with the lowest average power value in cloud free regions are determined for each profile. This value is defined as noise power P_n . Initially, a range gate is then set as "cloudy" if

$$P \geq P_n + \alpha \frac{1.28 \cdot P_n}{\sqrt{M}}, \quad (1)$$

where P is the signal plus noise power and M is the number of samples [1]. The factor 1.28 appears from the logarithmic form of the receiver transfer function. However, the value of α can be adjusted and is somewhat arbitrary [2]. For the final CLARE dataset, a value of $\alpha = 2$ was used. In the next step, a binary cloud mask is applied to remove the remaining speckle noise in cloud-free regions. This procedure, applied for both H and V received powers, is described in detail in [2]. For the remaining "cloudy" range gates, the corresponding H and V radar reflectivities are calculated from the radar equation. The pulse-pair estimates of mean Doppler velocity and spectral width are also determined for these gates. For each gate, the noise power P_n as calculated above is subtracted from the zero lag autocovariance term, following [3]. It must be mentioned that this method only removes the white noise contribution from the receiver, therefore, radar phase noise may still be present and can bias the spectral widths in very low signal to noise conditions [4].

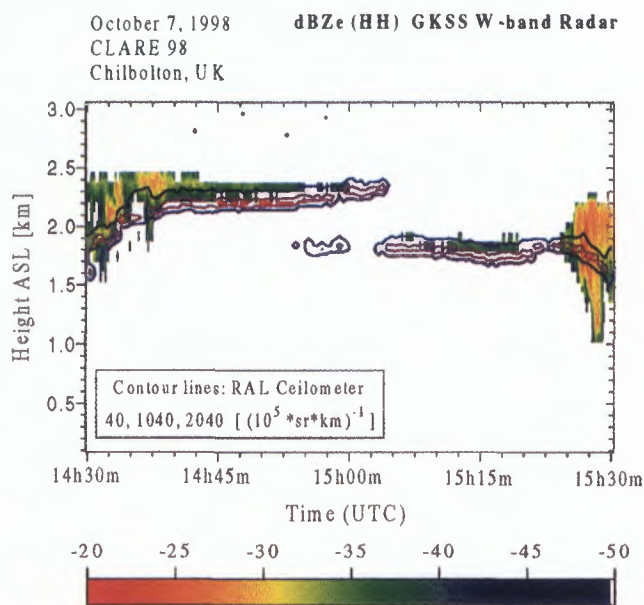


Fig. 2: Height-time section of MIRACLE radar reflectivity and RAL Vaisala ceilometer returns, observed during CLARE on October 7, 1998. (Ceilometer data provided by J. Goddard, RAL.)

The minimum sensitivity at an altitude of 1 km and 10 s integration is about -45 dBZ. As an illustration, Fig. 2 shows a section of low- and mid-level clouds simultaneously observed by the MIRACLE radar and the RAL Vaisala CT 75K ceilometer. It can be seen that in the cloud layer starting at about 1500 UTC in 1.8 km, the lowest reflectivity values are between -40 and -45 dBZ. Especially the lower part of this cloud layer, probably with lower reflectivities in non-drizzle conditions, is detected by the ceilometer, but not by the radar.

The final CLARE dataset contains reflectivity and Doppler velocity data with a temporal resolution of about 10 seconds and a vertical resolution of 82.5 meters. After an internal calibration procedure, the reflectivities are cross-calibrated following a "chain-calibration" procedure using data of the 3 GHz radar CAMRa, the 35 GHz radar RABELAIS, the 94 GHz radar GALILEO, and the 95 GHz radar MIRACLE [5]. I.e., a final result of this procedure is that **2 dB need to be added** to the MIRACLE reflectivities archived on the CLARE ftp site.

Table 2: Operation of the GKSS radar during CLARE.

Day (October)	Pulse-Pair data	FFT data	Operation time (UTC)
2	X		1040-1200
3			
4	X		0830-1020
5	X		0820-1325
6	X		0830-1020
7	X		0820-1550
8	X		0850-1445
9	X		0845-1825
10			
11			
12			
13	X	X	0955-1810
14	X	X	1010-1550
15	X		1000-1410
16	X		0810-1735
17			
18			
19	X		0825-1735
20	X	X	0750-1715
21	X	X	0930-1140
22	X		0835-1630
23	X		0945-1450

During relevant aircraft overpass periods (several minutes each), full Doppler spectra were recorded with a 256 point FFT mode instead of pulse-pair data. This FFT data did not go through a cloud mask scheme. The spectral amplitudes (powers) are given in dB, and they are normalized in a way that the integral over the whole spectrum gives

the corresponding reflectivity in dBZ. The FFT data is supplied with a temporal resolution of about 30 seconds and a vertical resolution of 37.5 meters. Due to the large amount of necessary real-time computing operations in the FFT mode, the number of range gates is limited so that the observed height bands did not exceed 3 km in thickness.

It must be noted that in the full Doppler spectra different noise features, affecting either defined height bands or certain spectral bins, were detected from time to time. Algorithms to remove these artifacts would require changes in the original FFT signal processing software of the manufacturer (which we do not have access to at present). However, the noise features can be easily identified by eye and removed manually from the Doppler spectra. The pulse-pair data are not affected by these problems.

Table 2 summarizes the MIRACLE operation days and periods and the availability of pulse-pair or FFT data.

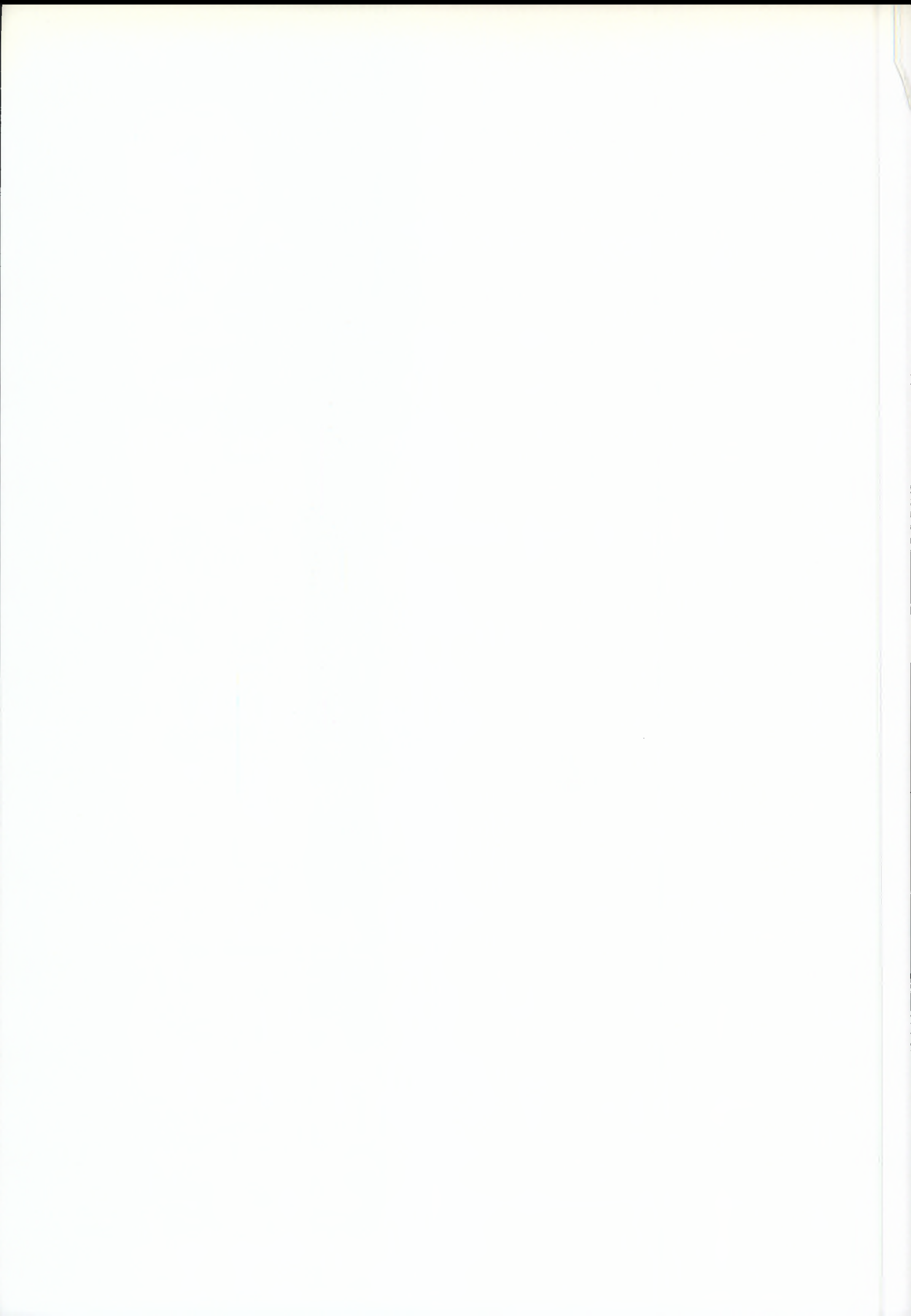
More information can be found on the Web:

<http://w3.gkss.de/english/Radar/clarearchive.html> .

This site is also reachable via the CLARE 98 ftp site.

REFERENCES

- [1] J.S. Marshall and W. Hitschfeld, "Interpretation of the fluctuating echo from randomly distributed scatterers." *Can. J. Phys.*, Vol. 31 No. 1, pp. 962-995, 1953.
- [2] E.E. Clothiaux, E.E., M.A. Miller, B.A. Albrecht, T.P. Ackerman, J. Verlinde, D.M. Babb, R.M. Peters, and W.J. Syrett "An Evaluation of a 94-GHz Radar for Remote Sensing of Cloud Properties." *J. Atmos. Oceanic Technol.*, Vol. 12, pp. 201-229, 1995.
- [3] R.J. Doviak and D.S. Zrnić, "Doppler Radar and Weather observations." Second Edition, Academic Press, 1993.
- [4] R. Lhermitte, "A 94-GHz Doppler Radar for Cloud Observations." *J. Atmos. Oceanic Technol.*, Vol. 4, pp. 36-48, 1987.
- [5] R.J. Hogan and J.W.F. Goddard, "Calibration of the ground-based radars during CLARE 98." This issue, 1999.



Radiation measurements during CLARE'98: an overview

André van Lammeren, Eric Meijer and Arnout Feijt, Royal Netherlands Meteorological Institute (KNMI), P.O. Box 201, 3730 AE De Bilt, The Netherlands

Suzanne Jongen, University of Technology Eindhoven (TUE)

Jan Erkelens and Herman Russchenberg, University of Technology Delft, International Research Centre on Telecommunications-transmission and Radar (TUD/IRCTR)

Abstract

During CLARE'98 several radiometers were operated. In this paper an overview of the instruments operated by KNMI, TUE and TUD/IRCTR is given. This includes the net- and shortwave radiometers operated by KNMI and the sky temperature observations as measured by two IR-radiometers. One IR-radiometer was pointing vertically upwards, the second instrument was mounted in the 25m antenna dish of the Chilbolton radar. A 20/30/50 GHz microwave radiometer (the 20/30 GHz system is on loan from ESTEC) was used to derive the column integrated liquid water and water vapour. Satellite data from the AVHRR instrument were collected and analysed. A time-lapse S-VHS video system was used to monitor the clouds at day-time.

All systems were continuously operational during the CLARE'98 campaign. Except for the upward pointing IR-radiometer, no technical problems were encountered. Data has been collected, calibrated and submitted to the CLARE'98 database.

1. Introduction

The CLARE'98 campaign which took place in Chilbolton, aimed at the study of mixed phase clouds with advanced remote sensing instruments. At the experimental site in Chilbolton, a large set of instrumentation was installed and operated. Together with the observations taken from three aircraft, this resulted in a data-set which can be used for extensive further research.

In this paper the contributions to CLARE'98 from different Dutch research groups (KNMI, TUE and TUD/IRCTR) are described. In section 2 the IR-radiometers are described and in section 3 the shortwave and longwave observations. The microwave radiometer is described in the next section. An overview of the satellite data follows and a description of the time-lapse S-VHS video system is given in section 6. Section 7 summarizes the paper.

2. IR-radiometers

Two narrow band infrared radiometers (type Heimann KT15.85A) were operated. The wavelength range of the used radiometer is 9.6-11.5 μm . The opening angle of the lens is 50 mrad. The measurement range of the sensor is between +50 and -53°C with a typical accuracy of 1-2°C. To obtain this accuracy, the temperature of the IR-radiometers housing is stabilized at 35°C. A precipitation detector controls the cover to shield the sensor. If precipitation is detected, the cover is closed. In this way the instrument is protected against rain. The data-acquisition is incorporated in the housing. Data is stored on memory cards. So, the instrument is completely

stand-alone. Only 220V power has to be supplied. In order to limit the amount of stored data the histogram of observed temperatures within a 10-minute period is characterized by only a few

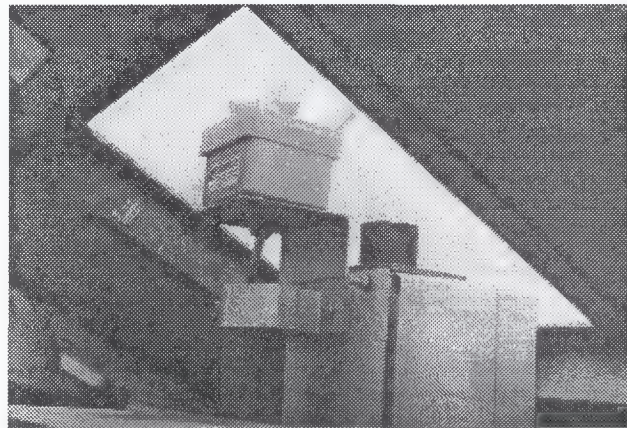


Figure 1. IR-radiometer mounted on the roof of the laboratory (left). Also visible is the video camera housing. At the background the 3 GHz radar is seen. In the 25 m antenna of this radar the second IR-radiometer was mounted (right). The precipitation detector, which steers the cover, is clearly visible.

numbers. Every 10 minutes the following characteristics of the measured sky temperature, T_{sky} , are collected:

- T_{ave} , average sky temperature of the 10-minute period,
- T_{max} , maximum sky temperature in the 10-minute period,
- τ_{max} , fraction of time that: $T_{\text{max}} - 5^{\circ}\text{C} \leq T_{\text{sky}} \leq T_{\text{max}}$,
- T_{min} , minimum sky temperature in the 10-minute period,
- τ_{min} , fraction of time that: $T_{\text{min}} \leq T_{\text{sky}} \leq T_{\text{min}} + 5^{\circ}\text{C}$.

The sensitivity of -50°C limits the maximum height for the detection of optically thick clouds to a range of 8-10 km. In the case of thin clouds this maximum height is decreased significantly. So, it is important to realize that high thin Cirrus clouds could remain undetected.

During CLARE'98 the two IR-radiometers were installed in separate places. One instrument was located on the roof of the workshop and was pointing in the vertical direction (Figure 1). The data was written to the memory card every 10 minutes. In the period from 7-15 October, the instrument was operated continuously. After that an error in the data acquisition occurred and all data was lost.

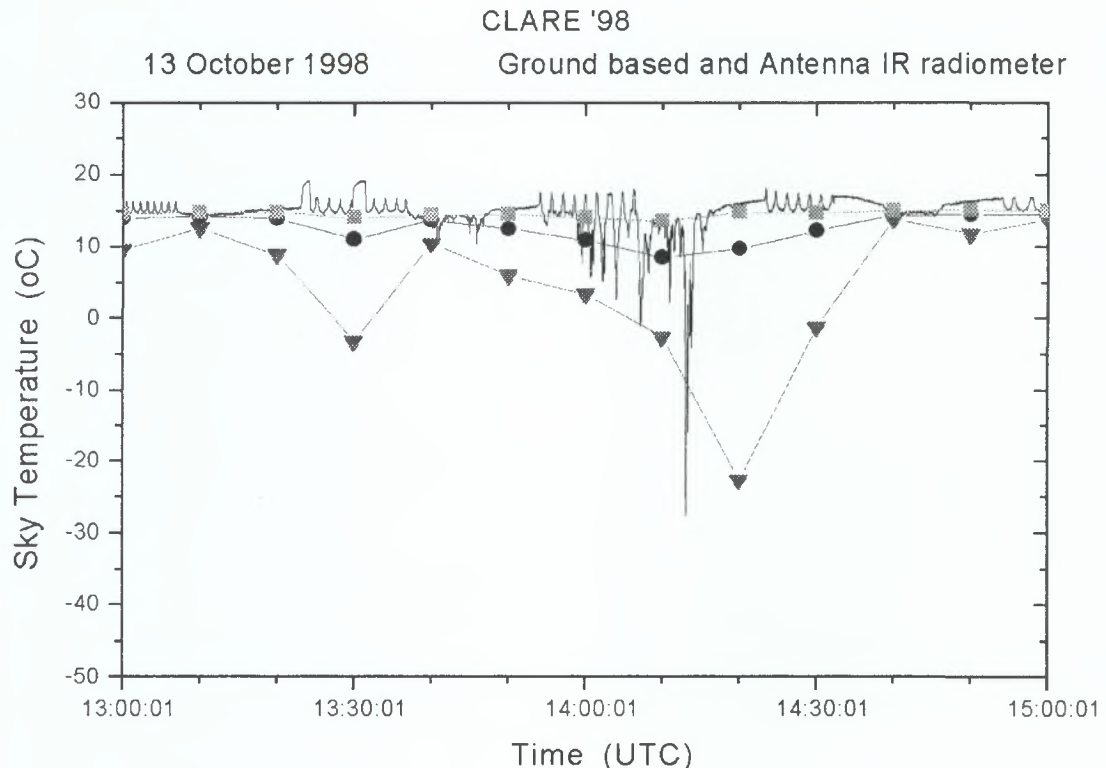


Figure 2. Sky temperatures as observed by the two IR-radiometers. The drawn line without symbols is the data from the IR-radiometer mounted on the antenna. The lines with the symbols are the observations from the vertically pointing IR radiometer: minimum (triangle), average (circles) and maximum (square) values.

The second IR-radiometer was mounted in the 25m antenna of the 3 GHz radar (see Figure 1). Every 2 seconds data was stored on the data disk. Due to the limited storage capacity of the data disks approx. 9 hours of data could be stored on one disk. During flights of the aircrafts the system was switched on. Data was taken for the flights on October 7, 13, 14, 16 and 22.

In Figure 2 results from October 13 are shown. In the data from the IR-radiometer mounted on the antenna the detailed structure is visible. This is the effect of the scanning of the antenna on the IR-radiometer. When the antenna is looking upward the contribution of the relatively "warm" atmosphere is minimal. When the antenna is oriented in any other direction the path through the atmosphere increases. This results in a higher observed sky temperature. For comparison the 10-minute average, minimum and maximum sky temperatures of the second IR-radiometer on the roof of the workshop is plotted in the same figure. There is a good agreement between the absolute values of the two IR-radiometers.

3. Shortwave and Net-radiometer

Both short-wave (SW) and long-wave (LW) radiation intensities were recorded for the duration of the campaign. SW radiation was measured with two Kipp CM-11 pyranometers; one looking upward and one looking downward.

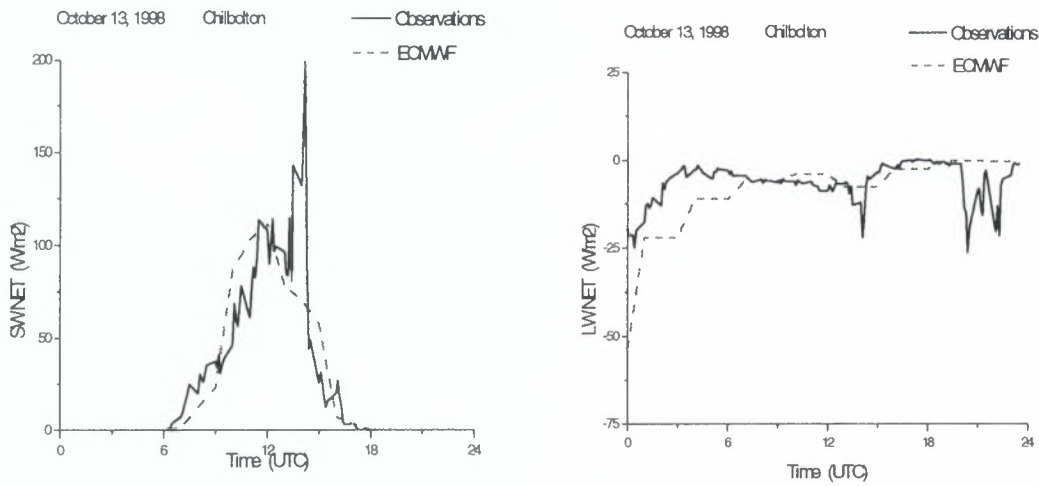


Figure 3. Observed (drawn line) net SW and net LW fluxes at the surface for October 13, 1998. The dashed lines are the results from the ECMWF model.

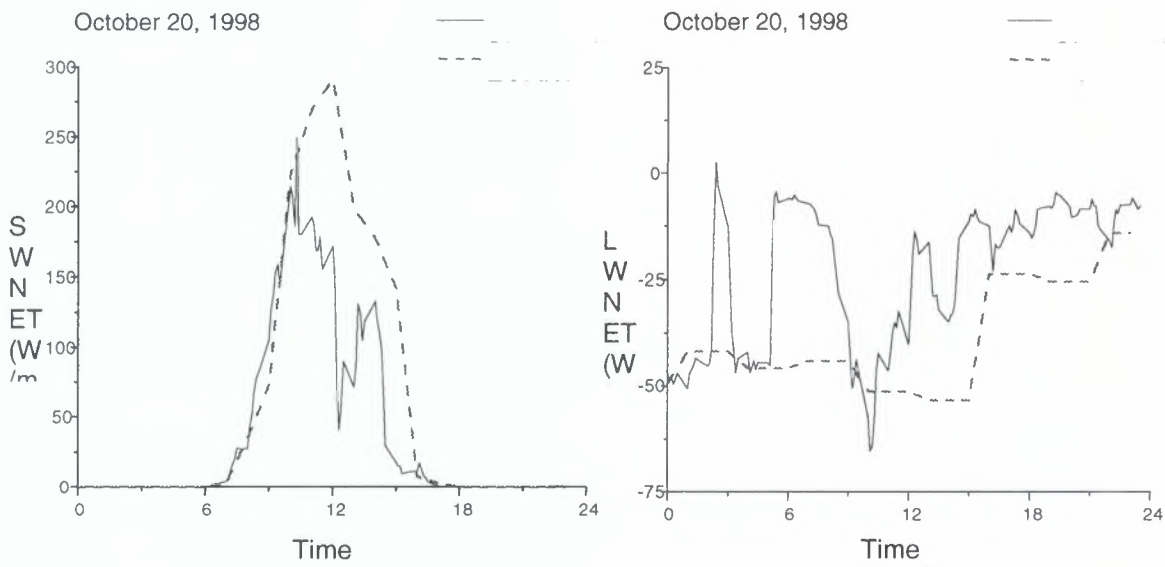


Figure 4. Observed (drawn line) net SW and net LW fluxes at the surface for October 20, 1998. The dashed lines are the results from the ECMWF model.

The NET LW radiation was calculated from the net radiation measurements of a Schulze dual-dome radiometer and the SW observations. Data was recorded with a Campbell 21X datalogger. 10 Minute averages are available.

In Figure 3 the observed net SW and net LW fluxes at the surface are presented for October 13. Also the ECMWF forecasted fluxes are shown for the grid point closest to Chilbolton. In general there is a good agreement between the observations and the ECMWF model results.

The same quantities are shown for October 20, in Figure 4. In this case the agreement is much worse. Differences of 50 W/m^2 or more occur between the measured and modelled net SW and LW fluxes. Apparently the ECMWF model had problems with forecasting the correct cloud situation.

4. Microwave radiometer

The microwave radiometer is composed of an antenna, a receiver, a positioner and a PC computer. Brightness temperature measurements are taken at the following frequencies 21.3/31.7/51.25/53.85/54.85 GHz. The instrument is shown in figure 5. Regular tip curve calibrations were taken during the campaign. From the observations column integrated water vapour (V), liquid water path (L) and temperature information for the lower part of the atmosphere can be derived.

For V- and L- retrieval, two kind of algorithms have been used: linear models and a non linear model called the Matched Atmosphere Algorithm (MAA). Linear algorithms assume a linear relation between the attenuation or an L invariant parameter and V and L. A disadvantage of these algorithms is that they are time- and site dependent. Constants for one site can be determined by calculating brightness temperatures (T_b), and V- and L values from a large set of radiosonde profiles and use these to derive the retrieval constants. For CLARE'98 the linear algorithm has been used to process the data with typical "mid-latitude" constants. This approach may cause the L to become negative in certain cases.

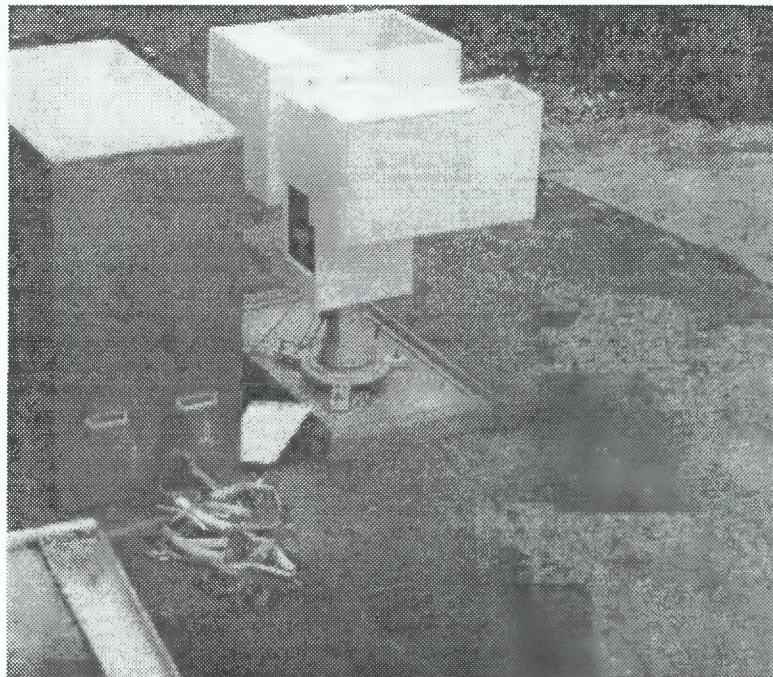


Figure 5. The microwave radiometer at the Chilbolton site

5. Satellite observations

It was planned to archive the NOAA/AVHRR images, which included Chilbolton. However, due to technical problems at the receiving station at De Bilt, data was lost. To account for this loss, data was retrieved from the data centre in Dundee. The satellite data from the overpasses which

(more or less) coincide with the "high priority cases", are now available for analysis. The data for all spectral channels was collected.

A derivative of the AVHRR Processing scheme Over cLOUDs, Land and Ocean (APOLLO) is used for detection of cloud contamination and fully cloudy pixels from AVHRR measurements [Saunders, 1986; Saunders and Kriebel, 1988]. Cloud properties that are retrieved using modified APOLLO extensions are: cloud cover, cloud top temperature, reflectivity, optical thickness, IR-emissivity and ice-detection.

As an example part of the satellite image for October 20 is shown in Figure 6. Chilbolton is within the encircled area. For the pixels inside this area an analysis based on the APOLLO scheme was performed. In Figure 6b the channel 4 cloud top temperature is plotted against the derived optical depth. The correlation between the two is clear, indicating the presence of a semi-transparent Cirrus cloud with a cloud top temperature of approx. 207 K.

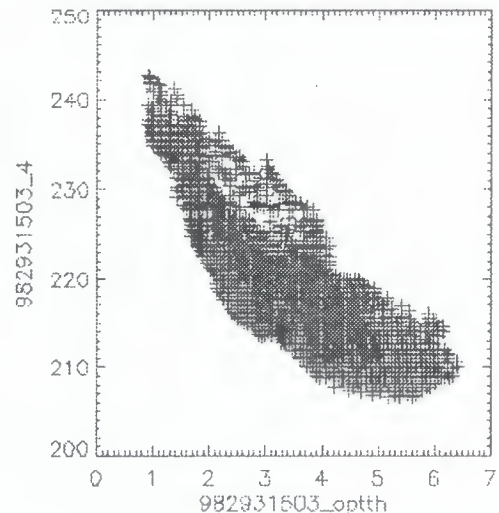


Figure 6. AVHRR image of the area around Chilbolton for October 20 (14:20 UTC). Chilbolton is located in the encircled area. The pixels within the circle are used to generate the right hand figure: channel 4 cloud top temperature versus the derived optical depth.

6. The Timelapse S-VHS Video system

During the campaign, a cloud videotape is made with a S-VHS time lapse recorder. The view reaches from the western horizon to near zenith. (Opening angle of the lens: Vert. 88 degrees, Hor. 107 degrees). Every 3.2 seconds an image was stored on the tape. The tapes are mainly used as a visual archive of the actual sky situation.

For the CLARE data-base six MPEG video movies were made from this tape for the chosen priority legs. Each 1.5 minute MPEG-movie shows 4 hours of time lapsed video recording; approximately 2 hours before and 2 hours after aircraft passed overhead.

André van Lammeren, et. al: "Radiation measurements during CLARE'98: an overview"



Figure 7. Snapshot of the VHS cloud video system for October 13, 14:08 UTC.

7. Concluding remarks

During the CLARE'98 campaign an extensive set of instrumentation was employed. In this paper we have described the instruments operated by several Dutch research institutes/universities. Most of the instrumentation operated without any technical problems during the campaign. The data has been calibrated and submitted to the CLARE'98 ftp site.

At present the data is intensively used for further research on sensor synergy algorithms and validation of satellite retrieval algorithms.

References

Saunders, R.W., 1986: An automated scheme for the removal of cloud contamination from AVHRR radiances over western Europe. *Int. J. Remote Sens.*, **7**, 867 - 886.

Saunders, R.W. and K.T. Kriebel, 1988: An improved method for detecting clear sky and cloudy radiances from AVHRR data. *Int. J. Remote Sens.*, **9**, 123 - 150.



Calibration of the ground-based radars during CLARE'98

Robin J. Hogan

Department of Meteorology, University of Reading, UK. Email: R.J.Hogan@reading.ac.uk

John W. F. Goddard

Radiocommunications Research Unit, Rutherford Appleton Laboratory, Chilton, UK.

Email: J.W.F.Goddard@rl.ac.uk

INTRODUCTION

During the CLARE'98 campaign between 5 and 23 October 1998 at Chilbolton, England, four ground-based radars were in operation. These were the 3 GHz Chilbolton Advanced Meteorological Radar (CAMRa), the 35 GHz 'Rabelais', the 94 GHz 'Galileo' and the 95 GHz 'Miracle'. Throughout the duration of the experiment the Rabelais was mounted on the side of the steerable 25 m antenna of CAMRa. The Galileo radar was operated in a zenith-pointing configuration from the receive cabin at Chilbolton, 100 m from the main 25 m dish. The Miracle radar was also vertically pointing, and was situated just outside the workshop at Chilbolton, around 40 m from the main dish.

The approach used to calibrate the radars is to start with the absolute calibration provided by the polarisation variables of the 3 GHz radar in heavy rain, then to match up with the reflectivity measured by the Rabelais radar in Rayleigh-scattering light rain or cloud. Finally the W-band radars are calibrated by comparing them with the calibrated Rabelais at vertical incidence in Rayleigh-scattering liquid-water cloud. At each stage the comparison must be performed at a close enough range that the atmospheric attenuation at the higher frequency is minimised, yet at a far enough range that the far-field approximation is reasonably good at both frequencies. These uncertainties mean that a certain amount of error is introduced at each stage of the process.

Table 1 summarises the calibration figures that need to be applied to the raw reflectivity data from the four radars. All the **vertically-pointing** data on the CLARE'98 FTP site has been calibrated using the old calibration values, which are **2 dB less** than the new values; i.e. 2 dB should be added to these data. The reflectivity in the scanning 3 GHz HDF files on the site has **not** been calibrated; **5 dB** needs to be added to these data. The last column gives an estimate of the likely accuracy of the calibration for each system.

CALIBRATION CONVENTION

It is very important to understand the convention used in the intercalibration of radars of different frequencies because of the temperature dependence of the $|K|^2$ parameter of liquid water at millimetre wavelengths. In this paper the radars have been calibrated such that Rayleigh-scattering liquid water droplets at 0°C produce the same reflectivity factor Z at all frequencies. For example, a population of 100 μm droplets with a concentration of 10^6 m^{-3} at 0°C would have a Z of 0 dBZ at all frequen-

cies. Hence a radar at frequency f after calibration will report an effective reflectivity given by

$$Z_f = \int_0^\infty \frac{|K_f|^2}{|K_{f,0}|^2} n(D) D^6 \gamma_f(D) dD,$$

where γ_f is the Mie/Rayleigh backscatter ratio. $|K_{f,0}|^2$ is the dielectric parameter of liquid water at 0°C, and is 0.93 at 3 GHz, 0.877 at 35 GHz and 0.668 at 94 GHz. Because the $|K|^2$ of liquid water varies with temperature at 94 GHz, if the example above were repeated at 20°C, a 94 GHz radar using this calibration convention would report a Z of +0.82 dBZ while a 3 GHz radar would still report 0 dBZ. Formulae for the dielectric constants of ice and liquid water at these frequencies can be found in Liebe et al. (1989).

3 GHz CAMRA

The shape of raindrops is a unique function of size, and it turns out that at centimetre wavelengths the three radar variables Z , Z_{DR} and ϕ_{DP} are not independent in rain. Goddard et al. (1994a) showed that this property could be exploited to calibrate a polarimetric radar since only the correct calibration of Z will permit the three variables to be self-consistent. The procedure is to examine rays through heavy rain in which there is at least 10° of differential phase shift (ϕ_{DP}), and to use the values of Z and Z_{DR} along this path to calculate the ϕ_{DP} that should be observed. Z is then adjusted until the calculated and measured values of ϕ_{DP} match up. Z_{DR} can be calibrated fairly easily by setting it to zero in light drizzle in which Z is around 0 dBZ, since here the drops will be spherical. It is important to ensure that the beam is well below the melting layer, that the rain is not so intense that differential or total attenuation becomes important (indicated by regions of negative Z_{DR} at the back of the rain), and also that there is no contamination by hail. The technique is reported by Goddard et al. (1994a) to be accurate to 0.5 dB, provided the correct drop shapes are used. This small error is due to residual uncertainties in the drop shapes, and the fact that the shape of the distribution can vary somewhat from event to event.

Comparisons with raingauges have been carried out since the technique was first employed at Chilbolton, and they confirm its accuracy. Figure 1 is an example of comparisons between CAMRa and a drop-counting raingauge obtained during the HYREX project, on 13 September 1994. The time series plot on the left shows raingauge data integrated over 30 seconds and 90 seconds, and two radar estimates of rainfall rate, one using a standard Z - R relationship and the second using Z and Z_{DR}

System	Freq. GHz	Recording mode	5/10/98–28/10/98 (CLARE'98)	29/10/98–6/11/98	from 6/11/98	FTP site data	Error dB
CAMRa	3	scanning		add 5 dB		uncalibrated	± 0.5
Rabelais	35	scanning	see text	?	subtract 5 dB	not on site	± 1
		vertical	subtract 15.5 dB		subtract 25 dB	old	± 1
Galileo	94	vertical		add 16 dB		calibration:	± 1.5
Miracle	95	vertical		add 2 dB		add 2 dB	± 1.5

Table 1: Summary of the calibration figures that need to be applied to the raw data from each of the radars used in CLARE'98. The second-to-last column indicates whether the data on the CLARE'98 FTP site have been calibrated or not.

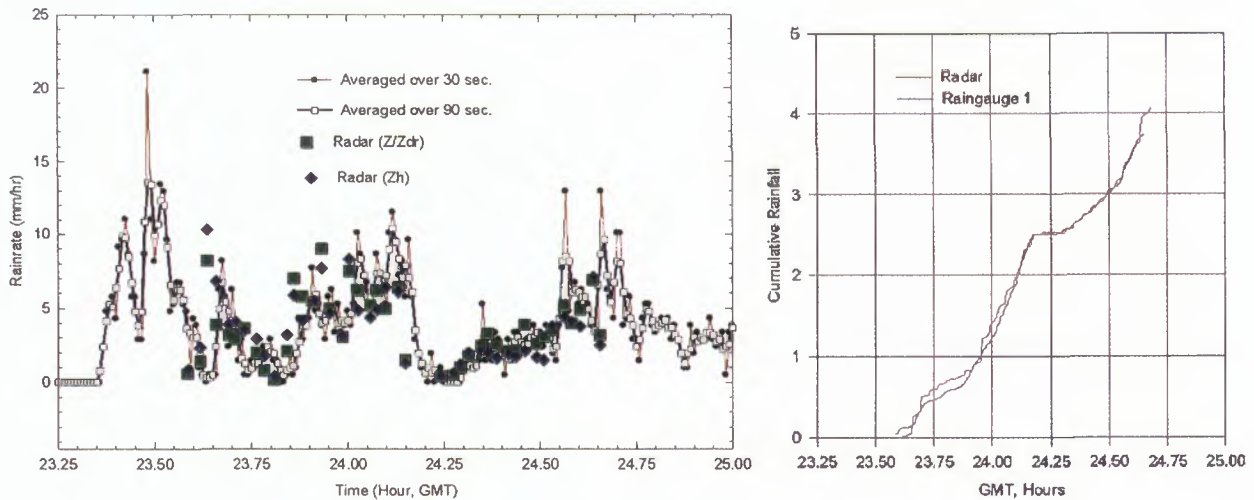


Fig. 1: Comparison of radar retrievals of rain rate with values measured by a raingauge on 13 September 1994.

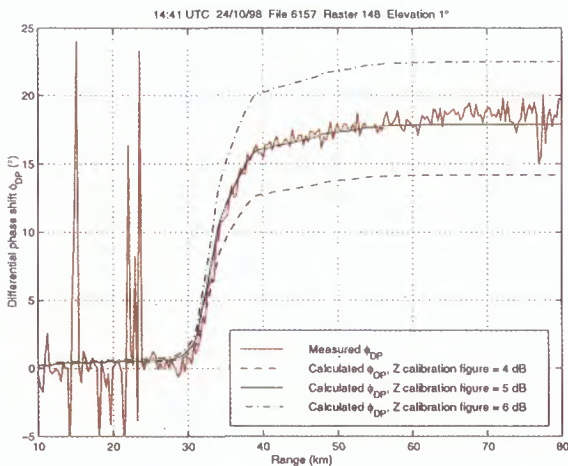


Fig. 2: The result of the $Z-Z_{DR}-\phi_{DP}$ calibration technique on 24 October 1998, just after the end of CLARE'98. Measured ϕ_{DP} is shown, together with that calculated from Z and Z_{DR} after 4, 5 and 6 dB has been added to raw Z . Clearly the correct calibration figure is 5 dB. The fluctuations at 15 and 22 km are due to ground clutter.

with an exponential drop-size distribution. The radar calibration was performed with what was then the new $Z-Z_{DR}-\phi_{DP}$ technique. (See also Goddard et al. 1994b). The right panel of Fig. 1 shows the accumulated rainfall rates from the raingauge and from the radar $Z-Z_{DR}$ estimate of rainfall. The final difference in totals is around 10%.

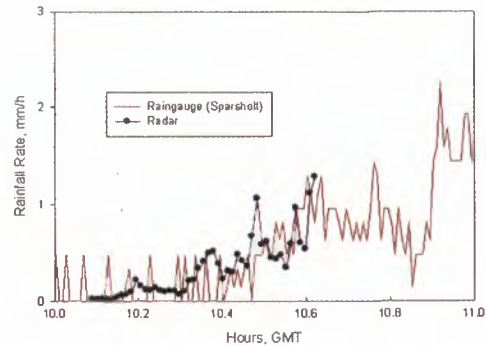


Fig. 3: A comparison of radar and gauge rain rates from 19 January 1999 using the same radar calibration as during CLARE'98.

The calibration method has been performed using events in October and November 1998. Figure 2 shows measured and calculated ϕ_{DP} for an event on 24 October 1998, just after the end of the campaign. We conclude that **5 dB should be added to all CAMRa reflectivity data taken since 5 October 1998, including those in the HDF files on the CLARE'98 FTP site.** After this calibration figure has been added the 3 GHz radar has a noise-equivalent reflectivity at 1 km of -36.7 dBZ. This value is fairly stable and is a useful reference to verify whether data has been calibrated or not. It can also be regarded as a crude indicator of the absolute sensitivity of the radar. Figure 3 shows a recent comparison (19 January 1999) between the CAMRa

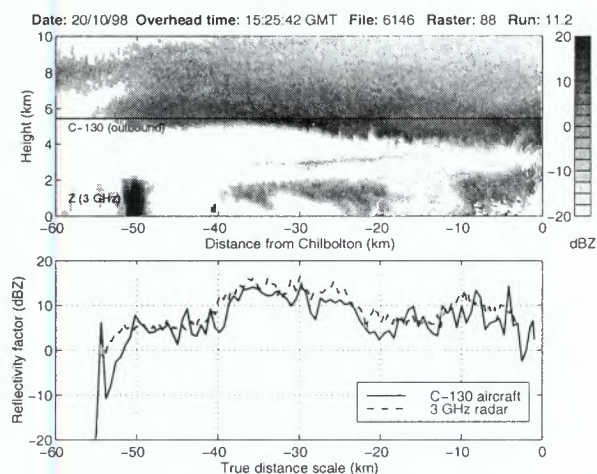


Fig. 4: A comparison of CAMRa reflectivity and that calculated from C-130 size spectra in ice cloud during a CLARE'98 flight.

radar and a raingauge situated at Sparsholt, 7.8 km away from Chilbolton. These data are not ideal because they were obtained from routine scans along the Earth-Space path to the ITALSAT satellite. Radar gates close to the Sparsholt gauge at a height of around 500 m were used to estimate the rainfall rate. The same radar calibration was used here and during the CLARE'98 campaign. Figure 4 shows a comparison of radar reflectivity in ice cloud during one of the CLARE'98 flights, with that calculated from simultaneous C-130 aircraft measurements of size spectra. The established mass-diameter relationship for ice crystals of Brown and Francis (1995) was used, and the agreement is good to within a few dBs. It is clear from these comparisons that the calibration of the 3 GHz radar is reliable.

35 GHz RABELAIS

The Rabelais radar can reasonably be regarded as the weak link in the chain of calibration. The main problem has been that until the beginning of the CLARE'98 campaign it had been understood that the configuration of the logarithmic amplifier and the voltage range of the 8-bit A-to-D converter was such that a 1-bit change in the output of the A-to-D converter corresponded to a 0.25 dB change in signal power. On examination of the instrument near the beginning of the campaign, Gilbert Despaux reported that the correct value should in fact be 0.2 dB per bit. An accurate calibration of this part of the data acquisition system by Jon Eastment after the campaign had finished confirmed that the correct value should be somewhere between 0.2 and 0.21 dB per bit (the response of the logarithmic amplifier not being exactly constant throughout its dynamic range). The data acquisition software for the instrument in vertically-pointing configuration was changed to 0.2 dB per bit before any such data was taken in CLARE'98, but the software for recording the data in scanning mode continued to use a value of 0.25 until 6 November. The data can be corrected in retrospect, but this does introduce some uncertainty with regard to calibration.

The receiver circuitry of the Rabelais radar has an attenuator such that the level of the received signal can be adjusted manually in order that the normal dynamic range of the signal is matched well with the range of the logarithmic amplifier. A

further possible problem was revealed on 28 October when it was discovered that this attenuation was set too high, and at low signal-to-noise ratios the received power was into the region at the bottom end of the range of the logarithmic amplifier where the correspondence between its output voltage and the logarithm of its input voltage is not linear.

The effect of this on CLARE'98 data is that the range of measured powers is 'compressed' in the vicinity of the noise floor. It turns out that when the thermal/receiver noise is subtracted from the measured power (standard practice in the analysis of cloud radar data), this compression effect is removed and the *relative* values of reflectivity can be trusted right down to the minimum measurable signal, although it makes absolute calibration a little more difficult. All 35 GHz data on the CLARE'98 FTP site has had noise subtracted. At 18:00 UTC on 28 October the attenuator setting was changed by a nominal 10 dB to bring the input power up into the main part of the dynamic range of the logarithmic amplifier. The exact value of this attenuation was later measured by Jon Eastment to be 9.5 dB.

With all this information it is possible to work out the calibration figure of the Rabelais in vertically-pointing configuration. The first approach is to use comparison events on dates after these two problems had been rectified. A number of events from 12 November (Chilbolton file 6180) have been examined. Figure 6 shows a comparison of the 35 GHz and calibrated 3 GHz radars on this date. A correction for two-way gaseous absorption at 35 GHz has been performed using the thermodynamic variables of the ECMWF model. The two radars agree well to a range of 15 km (where the melting layer was encountered) provided 5 dB is subtracted from the raw 35 GHz reflectivity. This calibration figure is valid for data recorded in scanning mode from 7 November onwards. For data storage reasons the vertically-pointing data acquisition system adds an arbitrary 20 dB to the reflectivity, so for vertically-pointing 35 GHz data recorded from 29 October onwards, 25 dB should be subtracted from the raw reflectivity to obtain the correct value. Comparison of the noise floor from 35 GHz scanning file 6180 and all the 35 GHz vertically-pointing files from this period confirm that after applying this calibration they have the same noise-equivalent reflectivity at 1 km, of around -29.7 dBZ.

For the vertically-pointing data taken on 28 October and before (i.e. during CLARE'98), we need to include the effect of the 9.5 dB change in the attenuator, with the result that **15.5 dB should be subtracted from the raw reflectivity**. The data on the CLARE'98 FTP site was calibrated using the old figure of 17.5 dB, so **2 dB should be added to this and all the other vertically-pointing data on the CLARE'98 FTP site**. The noise-equivalent reflectivity at 1 km of this data after calibration should be around -25.2 dBZ. The 4.5 dB difference between this and the figure for the data taken after 28 October is presumably due to the 'compression' problem at low signal-to-noise ratios that was described earlier.

The scanning data taken during CLARE'98 still suffers from being recorded using 0.25 dB per bit, so needs to be rescaled as well as calibrated before it can be used quantitatively. This is done by removing the range correction, multiplying by

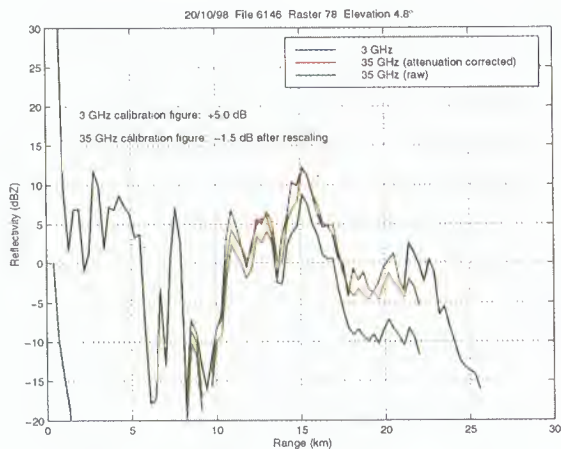


Fig. 5: A comparison of CAMRa and Rabelais reflectivity in scanning mode through drizzle on 20 October 1998, after rescaling the Rabelais. The signal at 3 GHz in the first 8 km is entirely due to ground clutter.

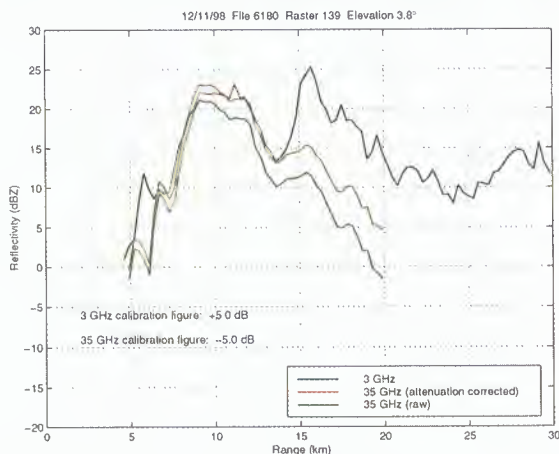


Fig. 6: A comparison of CAMRa and Rabelais reflectivity in scanning mode through a weak rain cell on 12 November 1998. On this occasion the melting layer was at an altitude of 1.1 km which explains why the two rays suddenly diverge at 15 km.

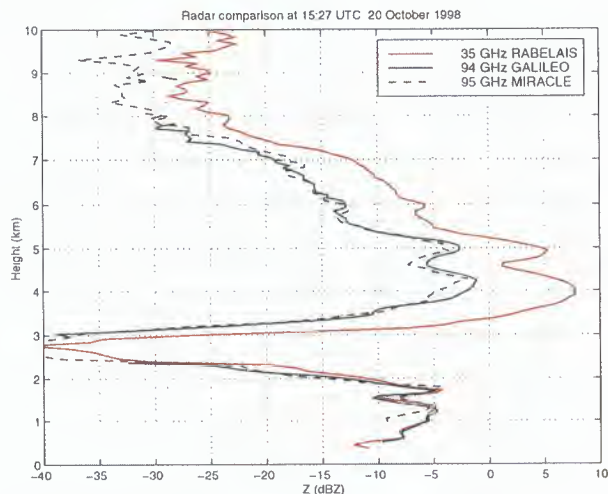


Fig. 7: A comparison of vertical profiles of reflectivity from the Rabelais, Galileo and Miracle radars during CLARE'98.

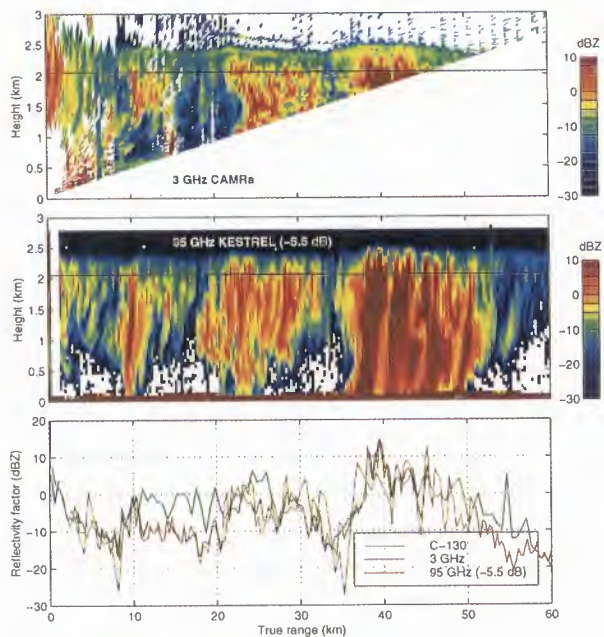


Fig. 8: Comparison between Kestrel and CAMRa reflectivities at an altitude of 2.05 km on 7 October 1998, for the outbound leg of the aircraft starting at 14:00 UTC. The CAMRa has been calibrated using the standard calibration figure of +5 dB, and 5.5 dB has been subtracted from the Kestrel reflectivity to maximise the agreement between the two instruments. Also show is the reflectivity calculated from the microphysical probes on the C-130 aircraft.

0.8 (in logarithmic units), reintroducing the range correction, and adding a calibration figure:

$$Z_{\text{true}} = 0.8 [Z_{\text{raw}} - 20 \log_{10}(r)] + 20 \log_{10}(r) + C$$

where Z is in dBZ, r is the range is in km, and C is the calibration figure in dB. By recovering the data in this way we can also calibrate the 35 GHz radar against the 3 GHz using events during CLARE'98. Figure 5 shows a ray through drizzle taken on 20 October 1998, from which a value for C of -1.5 dB is obtained. After this calibration figure is applied, the noise-equivalent reflectivity at 1 km (as derived from the cloud-free gates at the end of the ray) is -25.2 dBZ, the same as that for the vertically-pointing data after calibration. This confirms nicely that the problems with the instrument can be overcome and a consistent calibration can be derived.

Because of the rescaling that is necessary for the scanning 35 GHz data during CLARE'98, it has not been put on the FTP site. In any case the fact that the 3 GHz radar is over 10 dB more sensitive than the 35 GHz radar means that for most scanning applications the 3 GHz radar is more useful.

94 GHz GALILEO AND 95 GHz MIRACLE

The two W-band radars have been calibrated by comparison with the Rabelais from a number of vertically-pointing observations of low stratiform clouds during CLARE'98. The comparison must be performed at short range to minimise atmospheric attenuation at the higher frequency, but far enough away that the far-field approximation is reasonably good. Calibration cannot be performed using ice clouds because the two-way atmo-

spheric attenuation at W-band can easily exceed 5 dB at cirrus altitudes, and Mie scattering by large ice crystals can introduce a further 5 dB difference. Because the scattering behaviour at 94 and 95 GHz is virtually the same, it was found that reflectivity profiles from the Galileo and Miracle matched up very well in cirrus.

The agreement in low clouds was less good because such clouds are intrinsically less homogeneous in the horizontal, and the Galileo was around 100 m from the other two radars. The fact that the near-field zone of the Miracle extends to 900 m meant that better calibration from the Rabelais could be achieved with the Galileo. An example profile through low cloud and cirrus from 20 October 1998 for the three cloud radars after calibration is shown in Fig. 7. The Rabelais and Galileo data has been averaged over 10 seconds and the Miracle data over 6.6 seconds. The agreement between the two W-band radars in cirrus is very good given their separation. The Rabelais signal is between 7 and 10 dB higher in the cirrus due to the combined effects of differential attenuation at low levels and Mie scattering at the higher frequencies by large ice crystals, although it matches up well with the Galileo in the low cloud.

The result of these comparisons is that **16 dB** should be added to raw Galileo reflectivities during CLARE'98 and **2 dB** should be added to Miracle reflectivities in order for them both to be calibrated in agreement with the Rabelais and therefore CAMRa. **The Galileo and Miracle data on the CLARE'98 FTP site are currently calibrated using the old calibration values. Therefore 2 dB needs to be added to them.** The corresponding noise-equivalent reflectivity at 1 km after calibration is **-36 dBZ for both radars**. This figure tends to vary in time more than the equivalent figures at lower frequencies because of the stronger contribution from atmospheric thermal noise, which varies as low clouds pass overhead.

95 GHZ KESTREL

Comparisons of the airborne 95 GHz 'Kestrel' radar with the ground-based Miracle radar by Anne Guyot seem to indicate that the Kestrel consistently reports reflectivities between 8 and 10 dB higher than the Miracle. Recent work to investigate the cause of this discrepancy has identified a non-linear response in the Kestrel's receiver amplifier. The radar was calibrated with a corner reflector, which has a very large backscatter cross-section and therefore the echo from it tends to lie near the top of the dynamic range of the receiver. Clouds on the other hand give a relatively low return, so given that the dynamic range of a radar receiver is typically around 80 dB, it is easy to see how a receiver non-linearity could cause the calibration of meteorological signals to be in error by this magnitude. Unfortunately it means that a simple calibration figure is probably not sufficient to correct the reflectivity values and that at the very least a look-up table is required. One should bear in mind that such a table would correct the raw echo power (i.e. before range correction) rather than the reflectivity, in the same way as the formula given earlier to correct the scanning Rabelais data.

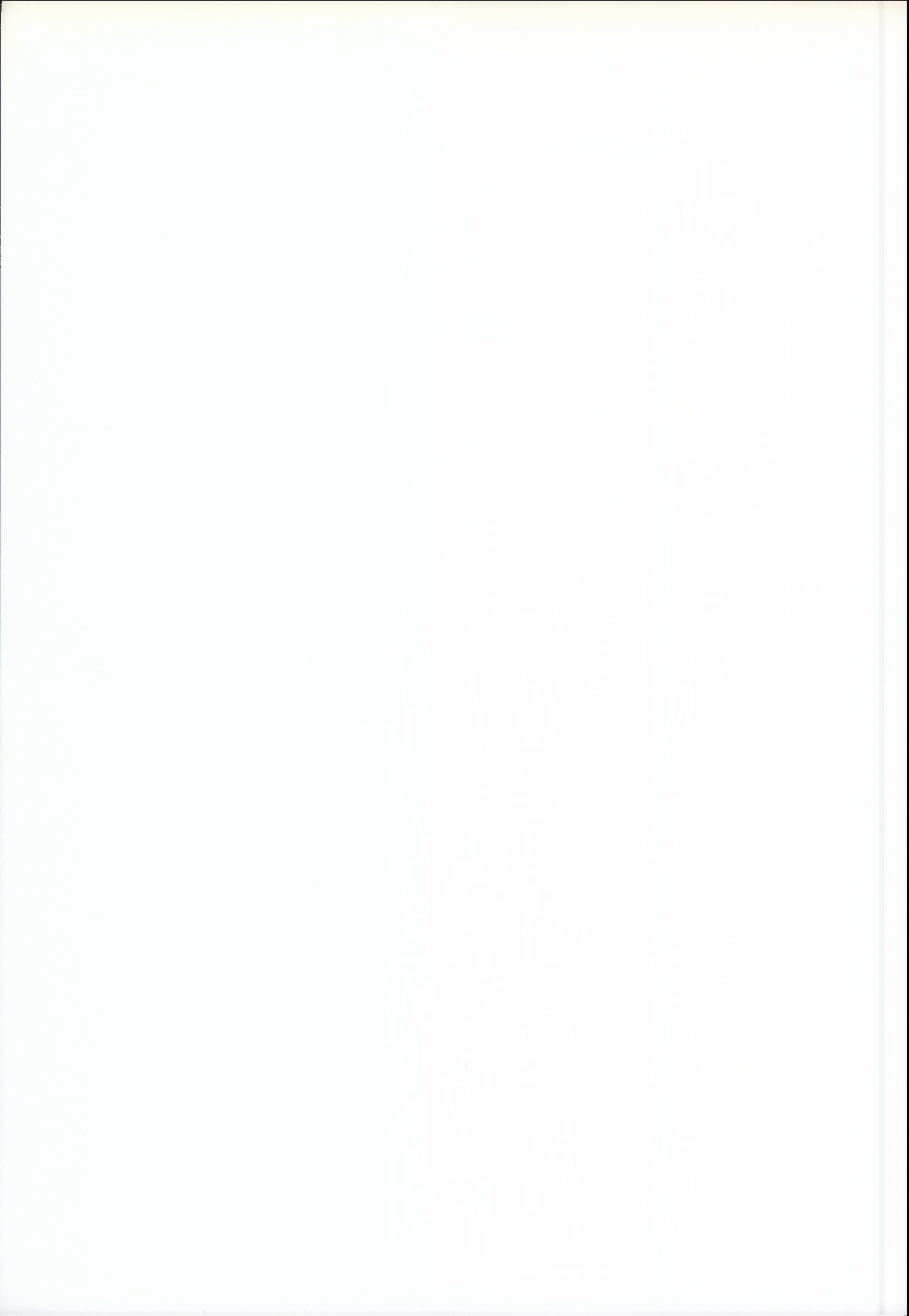
To illustrate that there is a real difference between the CAMRa and the Kestrel, and to circumvent any errors introduced in calibrating the Miracle from the CAMRa, it

seems sensible to go directly from CAMRa to Kestrel during CLARE'98 flights in Rayleigh-scattering stratocumulus. The only day for which this is suitable is 7 October 1998, because the stratocumulus contained drizzle and was therefore visible by the two radars at a reasonable range. A crucial additional point is that the CAMRa employed a variable scan-rate so that it could track the C-130 at an altitude of 2 km. This meant that the beams of the two radars were well matched in time and space at the altitude of the C-130 aircraft. Precise matching is necessary because of the extreme inhomogeneity of drizzle.

The outbound leg following the 14:00 UTC overhead has been used, and the comparison is performed at a height of 2.05 km since the variable scan-rate was configured to follow the C-130 at this altitude. It is found that for this leg, the Kestrel measured a 5.5 dB higher reflectivity on average than the CAMRa. Figure 8 shows the excellent agreement between the two radars after this value has been subtracted from the Kestrel reflectivity. However, the Johnson-Williams probe aboard the C-130 aircraft measured liquid water contents of between 0.4 and 0.9 g m⁻³, corresponding to a two-way liquid water attenuation at 95 GHz in the 300 m between the sampling altitude and the top of the cloud of between 1.1 and 2.5 dB. Using the thermodynamic variables of the ECMWF model, the two-way attenuation by atmospheric gases between the sampling altitude and the altitude of the aircraft (3.1 km) was around 0.25 dB. Hence the true Kestrel calibration figure is closer to -7.5 dB, in agreement with the difference found between the Miracle and the Kestrel. Because liquid water content tends to increase with height in stratocumulus, this estimate of liquid water attenuation could be an underestimate and the Kestrel calibration figure could be as much as -8.5 dB. Note that this value may only be valid to correct signals of this strength and at this distance from the antenna. Unfortunately the comparison could not be performed closer to the top of the cloud to reduce the uncertainty in liquid water attenuation, because the features of the reflectivity time series matched up much less well due to the poorer temporal coincidence of the samples.

REFERENCES

- Brown, P. R. A., and P. N. Francis, 1995: Improved measurements of the ice water content in cirrus using a total-water probe. *J. Atmos. Oceanic Tech.*, **12**(2), 410-414.
- Goddard, J. W. F., J. Tan and M. Thurai, 1994a: Technique for calibration of meteorological radars using differential phase. *Electronics Letters*, **30**(2), 166-167.
- Goddard, J. W. F., J. D. Eastment and J. Tan, 1994b: Self-consistent measurements of differential phase and differential reflectivity in rain. *Invited Paper, Proc. International Geoscience and Remote Sensing Symposium, Pasadena, August 1994*, 369-371.
- Liebe, H. J., T. Manabe and G. A. Hufford, 1989: Millimeter-wave attenuation and delay rates due to fog/cloud conditions. *IEEE AP*, **37**, 1617-1623.



Calibration of the University of Wyoming 95 GHz airborne radar during CLARE'98

Anne Guyot, Jacques Testud

IPSL - Centre d'étude des Environnements Terrestre et Planétaires, Vélizy, France

Olaf Danne and Markus Quante

GKSS Research Center, Institute for Atmospheric Physics, Geestacht, Germany

Peter Francis

UK Meteorological Office, Met. Research flights, Farnborough, U.K.

INTRODUCTION

The University of Wyoming 95 GHz radar (Kestrel) during the CLARE'98 campaign was mounted on board the ARAT (Avion de Recherches Atmosphériques et de Télédétection) : a Fokker 27 operated by INSU (Institut National des Sciences de l'Univers). The radar had two beams, one at nadir and the other one about 40° fore. During the campaign Kestrel was calibrated using a corner reflector. Our main objective in this paper is to check the validity of the calibration.

Another instrument operating during this campaign is the GKSS Institute for Atmospheric Physics 95 GHz ground based radar : Miracle. The radar was at Chilbolton pointing to zenith during the whole campaign. This allows us to compare the measurements of the two radars when the ARAT flew over Miracle (only with Kestrel nadir beam). These comparisons will provide us an intercalibration of the two radars that we perform using a method very similar to the one developed by Testud et al. (1999).

The U.K. Meteorological Office C-130 made combined flights with the ARAT in order to make in situ measurements. These data will be useful for us to make an absolute calibration of the radars after the determination of relative calibration between the two radars.

METHOD

Reflectivities from both radars will first be corrected for attenuation by water vapor, using the calculations performed by Robin Hogan, from the U.K. Meteorological Office unified model over Chilbolton.

At an attenuated frequency as 95 GHz, a radar does not measure the true reflectivities Z , but apparent reflectivities Z_a subject to the two-way path attenuation: $Z_a = Z - 2\int K dr$ (1) K is the specific attenuation in dB/km.

The method we developed to correct the two reflectivity profiles for along path attenuation is based on a rain profiling algorithm (Testud et al., 1999) for dual polarization measurements. In this paper we show how we adapted it to our configuration of measurements where a cloud is sampled at the same time in the two vertical opposite directions.

This method can be applied only if there is a single type of particles, which implies that there is no drizzle. Under the assumption of a powerlaw between the true reflectivity and

the specific attenuation: $K = aZ^b$, the Hitschfeld and Bordan (1954) solution of equation (1) is:

$$Z(h) = \frac{Z_a(h)}{(1 - aI(0,h))^{1/b}} \quad (2)$$

Where $I(0,h) = 0.46b \int_0^h Z_a^b ds$

The subscripts M and K will respectively be used for Miracle and Kestrel radars. The common zone of measurements is characterized by its bottom height h_1 and top height h_2 and the equations are written at the altitude h of measurement. We choose a reference altitude h_0 (in the middle of the layer, see Fig.1).

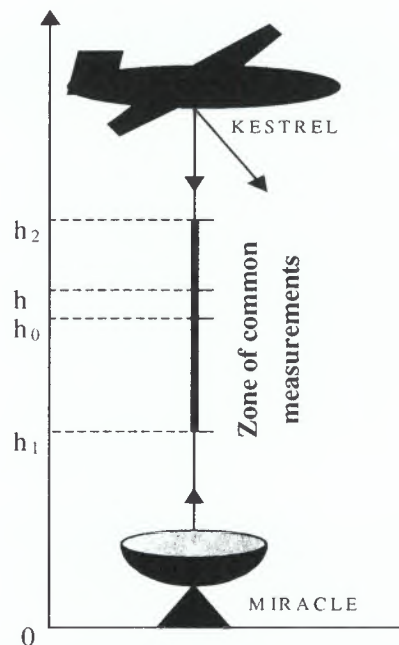


Fig.1: Principle of the sampling of a cloud simultaneously by Kestrel and Miracle during CLARE'98.

Using equation (2), the specific attenuations can be expressed for each radar measurement, as functions of a reference attenuation at the altitude h_0 . The determination of K is totally independent of calibration since reflectivity appears at numerator and denominator.

$$K_M(h) = K(h_0) \frac{Z_{Ma}^b(h)}{Z_{Ma}^b(h_0) + K(h_0)I_M(h, h_0)} \quad (3)$$

$$K_K(h) = K(h_0) \frac{Z_{Ka}^b(h)}{Z_{Ka}^b(h_0) - K(h_0)I_K(h, h_0)} \quad (4)$$

A constraint on the whole common zone will be used, instead of a point by point constraint which would be too strong:

$$\int_{h_1}^{h_2} K_M(h) dh = \int_{h_1}^{h_2} K_K(h) dh \quad (5)$$

There is an analytical solution of the integration of both equations (3) and (4), so equation (5) can be solved by determining $K(h_0)$:

$$K(h_0) = \frac{I_M(h_1, h_0)Z_{Ka}^b(h_0) - I_K(h_1, h_0)Z_{Ma}^b(h_0)}{I_M(h_1, h_0) \cdot I_K(h_1, h_0)} \quad (6)$$

Replacing $K(h_0)$ in equations (3) and (4), the attenuations $K_K(h)$ and $K_M(h)$ are determined along the profiles.

The last step consists in correcting reflectivities for attenuation which then allows us to find the difference between the 2 profiles.

APPLICATION TO THE DATA

Only a few profiles were selected for the whole campaign since both radars had to be operating during the overpasses, and that measured profiles had to be close enough to have a real significance. The maximal horizontal distance accepted between ARAT and Miracle is less than a 150 m.

Three cases are left: October the 7th at 13:52:53 (a) and 14:24:42 (b), and October the 20th at 13:20:25 (c) (the thin layer at about 2 km). First we correct the profiles for attenuation by water vapor.

Figure 2 (a), (b) and (c) display the profiles measured by Kestrel and Miracle before the correction for along-path attenuation. For each case the profile shapes are quite close, but there is a big difference between the values measured by the two radars. It clearly appears that it is necessary to correct the radar measurements with a calibration constant.

It can also be seen that the effect of along-path attenuation is not negligible since Kestrel reflectivities really seem attenuated at the bottom of the cloud and Miracle at the top. It is important to correct for this effect before comparing the reflectivities point by point.

From these figures, one can determine the common zone of measurements for each case, and reposition each point of the profiles for a systematic comparison between the two radars. For the case (a): 7th of October at 13:52:53, the measurements between 1 and 1.5 km will not be taken into account for our algorithm.

The 3 selected cases are stratiform cases, so we use the assumption of a constant total droplet distribution N_T in the cloud, such as the b coefficient is 0.5.

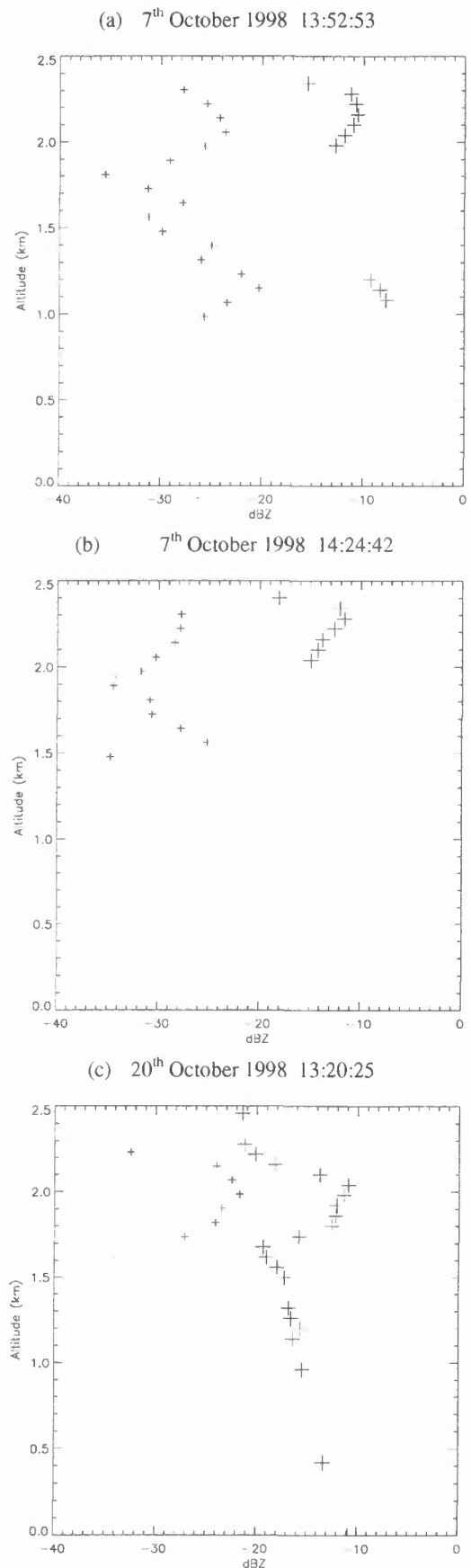


Fig. 2: Reflectivity profiles corrected for water vapor attenuation of + Kestrel and + Miracle radars, for the 3 selected cases

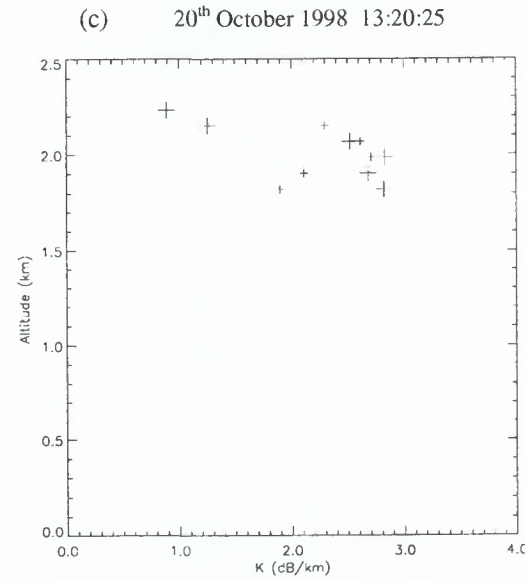
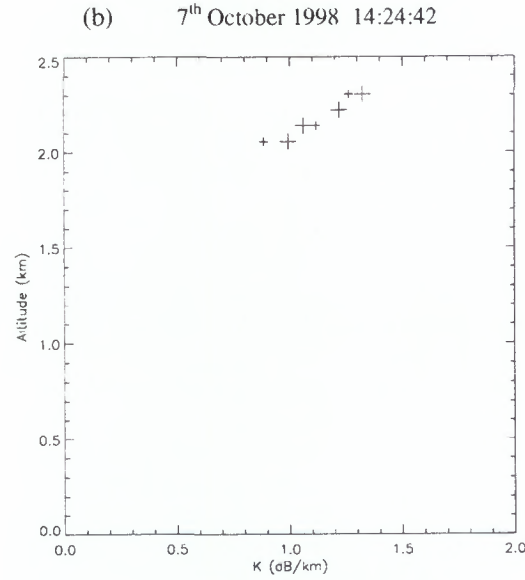
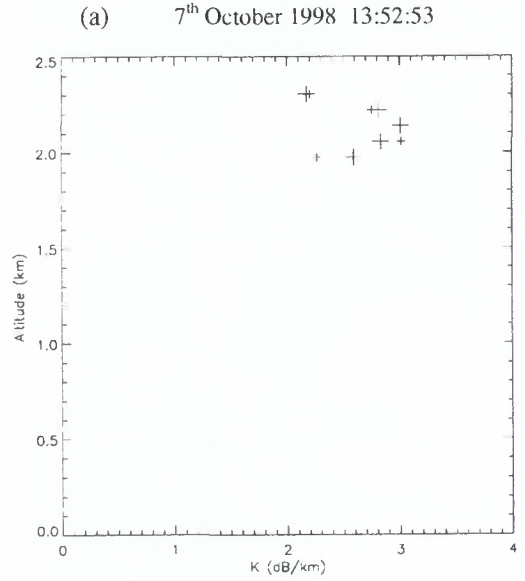
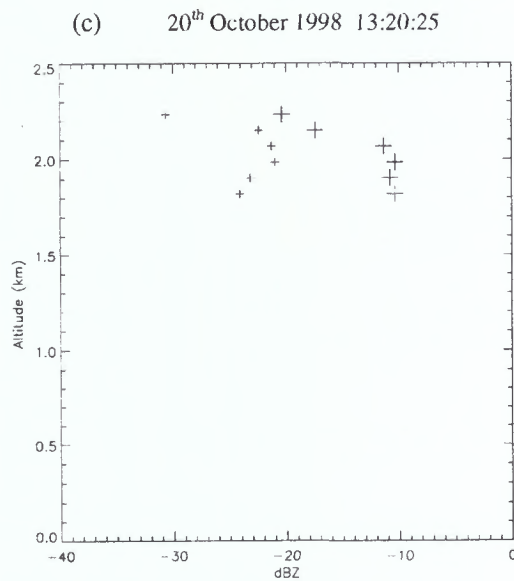
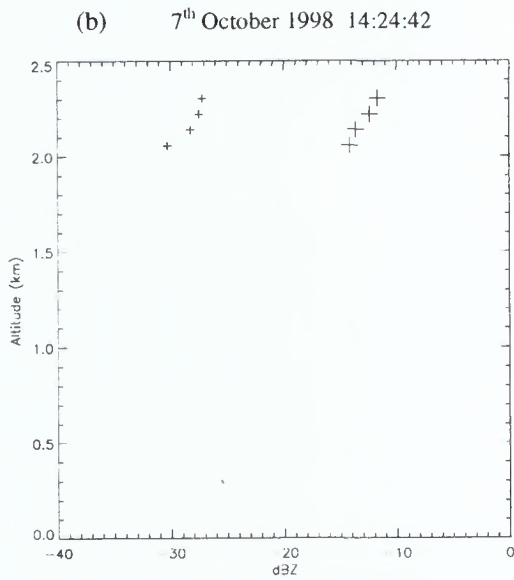
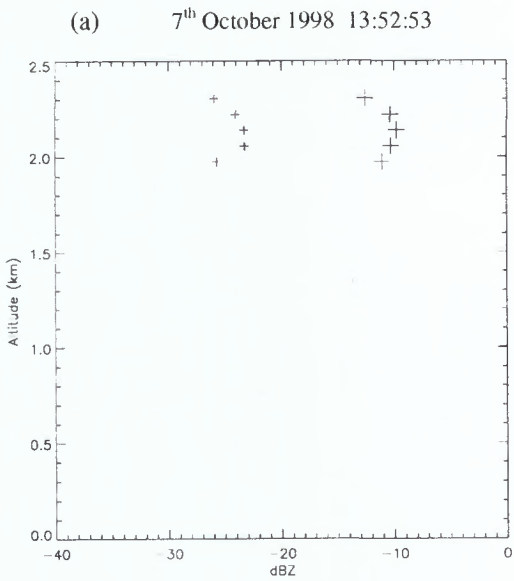


Fig. 3: True reflectivity profiles for + Kestrel and + Miracle determined from our method.

Fig. 4: Specific attenuation profiles from + Kestrel and + Miracle determined from our method.

Figure 3 (a), (b) and (c) display the reflectivity profiles corrected for attenuation from our method. For each case the two profiles follow quite well the same curve after this correction, except for the (c) case, where the profiles are not very similar.

Attenuation profiles are displayed in Fig.4 (a), (b) and (c). For the 7th of October the specific attenuation profiles are quite close for the two radars. On the other hand, for the 20th, the profiles show some big discrepancies.

From these profiles, liquid water content profiles can be determined. Since this is not the main objective in this paper we will only give mean values for each case. For cases (a) and (c), $LWC \approx 0.57 \text{ g/m}^3$, and for the (b) case $LWC \approx 0.27 \text{ g/m}^3$. For the three cases the radars are sampling very thin stratiform clouds, so these low values seem correct.

In order to determine a value for the difference of calibration between the two radars the results for the case of the 20th will not be taken into account, since they show too large differences between the retrieved K profiles. So the difference between reflectivity profiles determined using our method is not reliable for this case.

The average for the cases (a) and (b) gives a difference between Kestrel and Miracle of **14.4 dB +/- 1 dB**. With Kestrel values overestimating reflectivity.

ABSOLUTE CALIBRATION

From our algorithm, using the assumption that N_T is constant, we can determine the value of N_T from $K(h_0)$ and $Z(h_0)$ retrieved for each radar. So for each case we will have two values of N_T : one for Kestrel and the other for Miracle. The relation for stratiform clouds is $K \propto (N_T Z)^{0.5}$ (7) So it is very straightforward to obtain the values of total droplet concentration for each case (see Table 1)

$N_T \text{ (cm}^{-3}\text{)}$	Kestrel N_{TK}	Miracle N_{TM}
(a) 7 th Oct. 13:52:53	93	2105
(b) 7 th Oct. 14:24:42	24	810

Table 1: N_T determined from the results of our method, in the K-Z relation.

For the 7th UKMO C-130 in-situ measurements are available at about 2 km, which is the altitude of the common zone of sampling for the two radars. The data from 2 probes: FSSP and 2-DC were analyzed in order to get the value of N_T over Chilbolton at a time very close to the one of the common radar measurements (less than 3 minutes). Again we have to take mean values since there are strong fluctuations in the value of N_T from the microphysical data: $N_T(a) = 1000 \text{ cm}^{-3}$ and $N_T(b) = 450 \text{ cm}^{-3}$. To determine the constants of calibration C_K for Kestrel and C_M for Miracle: $Z_M = C_M Z$ and $Z_K = C_K Z$ (where Z is the true reflectivity). Using equation (7), we will determine $C_K = N_T/N_{TK}$ and $C_M = N_T/N_{TM}$. Table 2 gives the results for the 2 cases.

These results show again that from one case to another there is a strong fluctuation of the values determined. The Kestrel calibration constant is about **11.5 dB** from table 2.

C (dB)	Kestrel C_K	Miracle C_M
(a) 7 th Oct. 13:52:53	12.7	-2.5
(b) 7 th Oct. 14:24:42	10.3	-3.2

Table 2: Calibration constants determined from the C-130 microphysical data.

There are a lot of fluctuations in the value of N_T computed from the microphysical data. But we need to fix a value for the calibration constant. Robin Hogan (1999) calibrated all radars from the absolute calibration of the 3 GHz ground-based radar using its polarization variables. He found an estimation of the calibration constant of 8 dB with an error bar of about 2 dB. Considering the reliability of our method compared to this method (where whole legs were compared), we assume that the value of Kestrel's calibration constant of **9 dB** is a reasonable choice.

SUMMARY

In the inter-comparison between two reflectivity profiles measured simultaneously we met several problems:

- the profiles are not perfectly along the same vertical axis due to the position of the aircraft, and its roll.
- in the 3 cases we compared, clouds were very thin, so there are only a few points along the profiles to compare the measurements.

There is a significant variability in the results, depending on the case that is studied. The case of the 20th which was not reliable was withdrawn. The estimate of the difference between the reflectivities measured by Kestrel and Miracle is quite close to the difference found by R. Hogan (1999). For the absolute calibration, we use the C-130 microphysical data that we had to average over Chilbolton, since the aircraft was not perfectly synchronized with the ARAT.

Nevertheless, the calibration constants we find with our method are quite consistent with the values found by Robin Hogan. The compromise between these two methods is to take an absolute calibration constant of **9 dB** for Kestrel.

REFERENCES

- Hitschfeld, W., and J. Bordan, 1954: Errors inherent in the radar measurement of rainfall at attenuating wavelengths. *J. Meteor.*, **11**, 58-67.
- Hogan, R. J., and J. W. F. Goddard, 1999: Calibration of the ground-based radars during CLARE'98. *This issue*.
- Testud, J., E. LeBouar, E. Obligis, and M. Ali-Mehenni, 1999: The rain profiling algorithm applied to polarimetric weather radar. Accepted at *Journal of Atmos. and Oceanic Technol.*

**Cloud Boundary Retrieval
by Radar and Lidar**



Analysis of radar and lidar returns from clouds: Implications for the proposed Earth Radiation Mission

Robin J. Hogan*

Anthony J. Illingworth

Department of Meteorology, University of Reading, UK

*Email: R.J.Hogan@reading.ac.uk

INTRODUCTION

In the three months between 24 October 1998 and 23 January 1999, a near-continuous dataset of observations by cloud radar, lidar ceilometer and drop-counting rain gauge was obtained at Chilbolton, England. There are many uses for it that are relevant to the proposed ESA Earth Radiation Mission, and in this study we examine the frequency distribution of radar reflectivity, the difference in radar and lidar measured cloud base, and the frequency of occurrence of radiatively significant clouds that are seen by the lidar but not the radar.

DISTRIBUTION OF RADAR REFLECTIVITY

The first simple way to characterise the clouds in the dataset is to calculate the probability distribution of radar reflectivity (Z) of all clouds at all heights. This is shown in Fig. 1, and includes data from both the 35 GHz 'Rabelais' radar and the 94 GHz 'Galileo' radars, although not for the same days. It was calculated from data averaged over 2 minutes and 2 range gates, so for the 35 GHz radar the range resolution after averaging is 150 m and for the 94 GHz radar is 120 m. We see that in the lowest 4 km of the atmosphere the most probable value of Z is around 2 dBZ. Above this height the most probable value of Z drops steadily, from around -5 dBZ at 5 km to around -27 dBZ at 9 km. The lack of observations below -35 dBZ at high levels reflects the sensitivity limit of the radars; the dashed line shows the approximate minimum-detectable reflectivity for the 94 GHz radar with 2 minute/120 m averaging. At a range of 1 km this radar can see down to around -52.5 dBZ. It should be noted that the radiative significance of the clouds that are missed because of the sensitivity limit is likely to be very small (Brown et al. 1995).

The next step is to perform the analysis on stratocumulus only; globally stratocumulus is the most common cloud type and also the most important for the earth's radiation budget. It has been suggested that radar reflectivity is related to liquid water content (LWC) in stratocumulus and therefore that a spaceborne radar could retrieve LWC using a simple empirical relationship. However it was shown by Fox and Illingworth (1997) using aircraft-measured size spectra from the Atlantic Stratocumulus Transition Experiment (ASTEX) that these clouds nearly always contain drizzle drops several hundred microns in diameter, which contribute negligibly to LWC while dominating Z . This is shown clearly in the scatterplot of Fig. 2. Drizzle-free stratocumulus typically has a reflectivity less than -30 dBZ, so

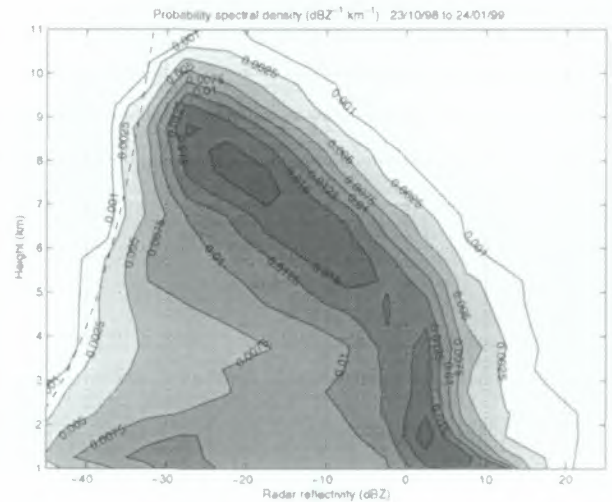


Fig. 1: The probability spectral density of Z for all the cloud radar data taken at Chilbolton in the three months between 23 October 1998 and 24 January 1999. The dashed line indicates the approximate sensitivity limit of the 94 GHz radar.

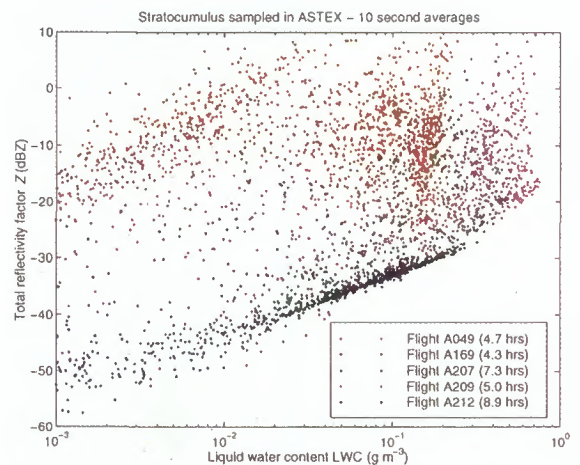


Fig. 2: Scatterplot of radar reflectivity versus liquid water content in stratocumulus, calculated from the FSSP and 2DC size spectra measured by the UK Meteorological Office C-130 aircraft during 5 flights of ASTEX. Only flight A169 is entirely free from drizzle.

the beneficial effect of these drops is to raise the reflectivity so that the cloud is well above the sensitivity limit of a spaceborne radar, but conversely this has the effect that LWC is essentially unrelated to Z .

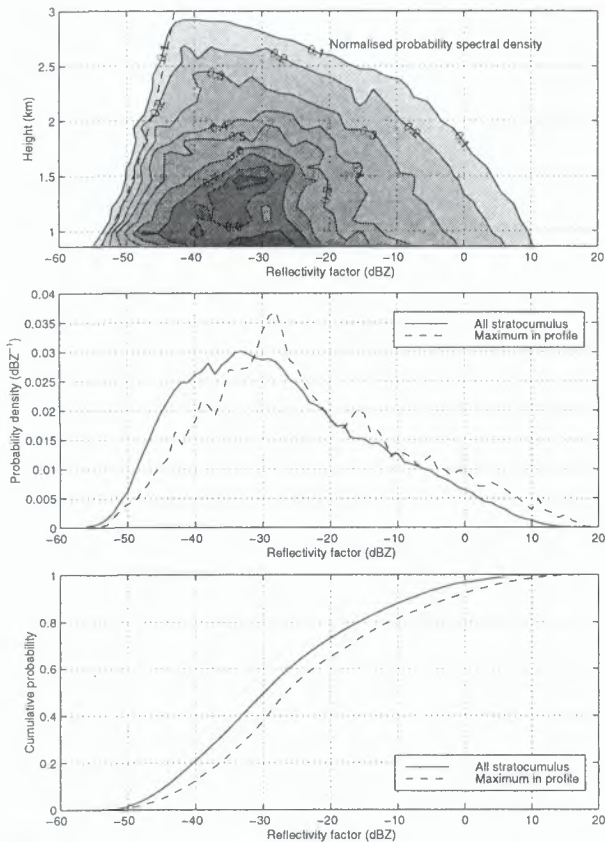


Fig. 3: Statistics of the distribution of Z within stratocumulus only, taken from all the 94 GHz radar observations in the dataset. The top panel depicts the probability density in arbitrary units as a function of height and Z . Again the dashed line indicates the approximate minimum-detectable reflectivity of the radar. The second panel shows the probability distribution of both the Z of all stratocumulus, and of the maximum Z in each profile. The last panel shows the cumulative probability.

Naturally conclusions drawn from aircraft measurements need to be confirmed using real radar observations. To isolate stratocumulus from the other cloud types in the dataset we impose the following conditions on each ray in turn:

- Only clouds lower than 3 km are considered.
- Any cloud extending below 3 km that has a cloud top higher than 3 km is rejected. However, if there is a lower layer with cloud top lower than 3 km then it is not rejected.
- The rain rate at the ground should be less than 0.1 mm hr^{-1} (although it is found that the results are virtually unchanged if the more-stringent requirement that there should be absolutely no rain at the ground is imposed).

Only the 94 GHz radar is used for this analysis because it is more sensitive than the 35 GHz radar at short range. The results for the 76 days of 94 GHz data are shown in Fig. 3. The first panel shows the probability density as a function of height and reflectivity. Around 61% of all cloud between 0.9 and 3 km have been rejected by the imposition of the conditions listed above, most because their cloud top was above 3 km. For

this reason the probability density is in arbitrary units (unlike Fig. 1). Again the effect of the sensitivity limit of the radars is very apparent in the sharp cut-off in probability density at low reflectivities.

The probability distribution of Z is indicated by the solid line in the second panel. Below 900 m the sensitivity of the radar was much less because of the leakage of the transmit pulse into the receiver, so to avoid biasing the distribution, data below 900 m has not been included in this analysis. The distribution peaks at around -33 dBZ , corresponding to the secondary peak apparent at 1 km in Fig. 1. The primary peak in Fig. 1 at around 2 dBZ and 1 km has been entirely removed by the rejection of non-stratocumulus clouds.

The last panel shows the cumulative distribution of Z , from which we see that 50% of the data has Z greater than -30 dBZ . Aircraft observations suggest that value this can be approximately regarded as the threshold above which stratocumulus contains drizzle drops, and hence we conclude that around half of the stratocumulus observed over Chilbolton during the period contained drizzle.

The dashed line in the last two panels of Fig. 3 corresponds to the probability distribution of the *maximum* reflectivity in each profile (or ray). Using the same -30 dBZ criterion for cloud containing drizzle, it can be seen that approximately 60% of profiles through stratocumulus contain drizzle somewhere through their depth.

The geographical location of Chilbolton is such that most of the time the stratocumulus can be considered to be continental, that is, containing relatively large numbers of cloud condensation nuclei. The results of Fox and Illingworth (1997) were derived from stratocumulus with much more maritime characteristics, which explains why drizzle was somewhat more prevalent in their dataset. However drizzle is still clearly significant in more than half the stratocumulus sampled at Chilbolton, and hence this analysis supports their claim that in most stratocumulus, radar reflectivity alone cannot be used to infer liquid water content.

COMPARISON OF RADAR AND LIDAR CLOUD BASE

The apparently very different scattering behaviour of radar and lidar implies that the sizes of cloud particles they are sensitive to are very different, and hence that there will be some clouds that one can see that the other cannot, or at the very least cloud base height will be different. This is certainly true for non-meteorological targets in the boundary layer; here the lidar can detect aerosols invisible to the radar, but conversely the radar can see insects that the lidar cannot. The question is whether it is a problem in the case of fall streaks beneath ice clouds and drizzle beneath liquid-water clouds.

The location of a cloud is obviously of primary importance in determining its radiative properties in the infra red so there is a need to investigate whether radar and lidar see the same cloud boundaries. Short periods of simultaneous ground-based radar/lidar observations have been presented previously by Uttal et al. (1995), who found good agreement in cloud base height, and by Weitkamp et al. (1997) who found apparent disagreement. It should be noted that the data presented in the lat-

ter study were not accompanied by absolute units, so it was impossible to judge what part the sensitivity of the instruments could have played. Some comparisons in the past have also been biased by inappropriate definitions of cloud base, such as the height at which the signal falls to 10% of its peak value (Russchenberg et al. 1998). Clearly the rejection of a good cloud signal near cloud base merely because the peak value several kilometres higher up has increased can severely distort the results of such comparisons. With the long dataset obtained at Chilbolton it is now possible to investigate the issue more systematically.

In this study, 45 hours of data from 6 different days have been identified in which the lidar had an unobstructed view of the base of an ice cloud. Only the 94 GHz radar was used since this is the proposed frequency of the spaceborne radar. The data in the lowest 900 m are unreliable because of leakage of the transmit pulse into the receiver, so such a comparison is much more difficult to perform on low-level liquid water clouds. Aerosols are also apparent in the lidar data below 2 km, so the cloud bases in the study have been selected to range between 2 km and 9 km. We consider two different instrument sensitivity scenarios. In the 'ground-based' scenario the maximum achievable sensitivity of each instrument is used; for the lidar this is $2 \times 10^{-7} (\text{srad m})^{-1}$ and for the radar it varies with altitude, although at the base of ice clouds is typically between -40 dBZ and -35 dBZ . In the 'spaceborne' scenario we calculate cloud base after first reducing the sensitivity of the instruments to approximately match that of the instruments on the proposed Earth Radiation Mission; $8 \times 10^{-7} (\text{srad m})^{-1}$ for the lidar (in the daytime) and -35 dBZ for the radar. Note that sometimes the minimum-detectable reflectivity of the ground-based radar is greater than -35 dBZ , in which case its sensitivity is left unchanged. Cloud base is defined simply as the height corresponding to the boundary between the first cloudy pixel and the empty pixel immediately beneath it. The cloud must however be at least three pixels deep to reject the occasional anomalous echo. The maximum vertical resolution of each instrument is used; this is 30 m for the lidar and 60 m for the 94 GHz radar. The temporal resolution of both instruments is 2 minutes and where there is a time offset between the two we interpolate the cloud base height on to a common time axis before computing the difference.

Two examples of the comparison, from 19 and 28 December 1998, are shown in Fig. 4. The difference in cloud base is shown in the bottom panels for the two different instrument sensitivities, and the features appear to match up very well. On 19 December cloud base is relatively low, and radar cloud base is mostly between 0 and 200 m below that of the lidar for both sensitivity scenarios, because of the presence of large snowflakes at the base of the cloud. In the second case cloud base is higher and there is a tendency for the lidar cloud base to be lower than that of the radar, because the particles are smaller and therefore give a relatively larger return at lidar wavelengths. In addition, the decrease in radar sensitivity with height probably contributes to the radar base rising above that measured by the lidar when above 6 km. In both cases the lidar signal is strongly attenuated, and is completely extinguished after penet-

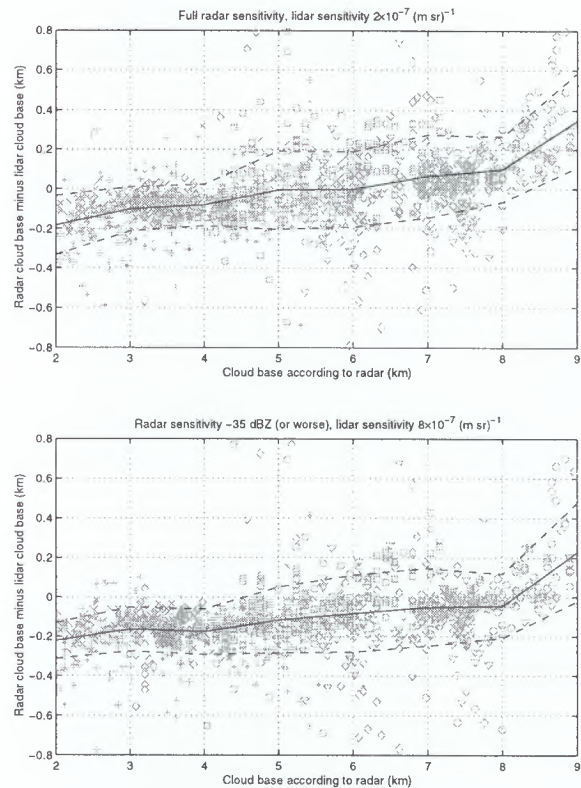


Fig. 5: The distribution of the difference in cloud base height between the radar and the lidar, versus the radar base height, for ground-based (upper panel) and spaceborne (lower panel) sensitivities. Negative values correspond to a lower radar cloud base (indicating that the radar is more sensitive). The 1362 grey symbols correspond to individual cloud-base comparisons from 2-minute averaged data from 11 November (\circ), 19 December (\times), 27 December ($+$), 28 December (\square), 7 January (\diamond) and 16 January (∇). Overlaid on each is the mean cloud-base difference (solid line) and one standard deviation to either side (dashed lines).

rating 2 km through the cloud.

Figure 5 shows the difference in cloud base as a function of cloud base height, from these and four other days in which the lidar had an unobstructed view of the base of an ice cloud. As one might expect, the radar is more sensitive for the lower clouds and the lidar more sensitive for high clouds, because of the intrinsic sensitivity of the radar to large particles and the lidar to small particles. Using the full ('ground-based') instrument sensitivity it is found that 80% of the time cloud base agrees to within 200 m and 96% of the time it agrees to within 400 m. Using the spaceborne instrument sensitivities, we find that these values become 73% and 95% respectively. The reason that these values are lower is that the sensitivity of the spaceborne radar is not very different to that of the ground-based radars at Chilbolton, whereas the spaceborne lidar is around four times less sensitive than the Chilbolton lidar ceilometer. Hence when the Chilbolton data are degraded to simulate spaceborne instrument sensitivities, the effect on the lidar is much greater. This illustrates the need to always consider instrument sensitivity when comparing cloud base.

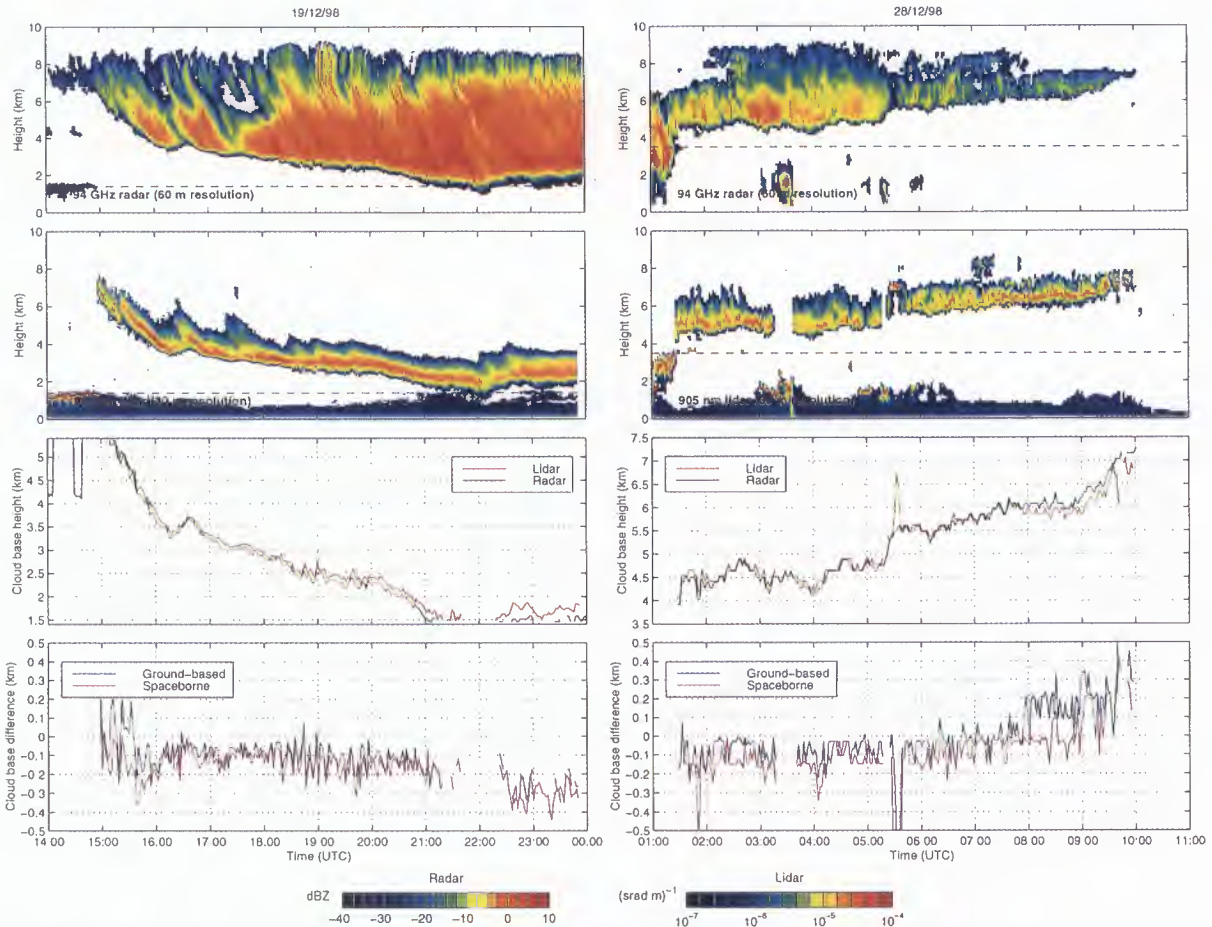


Fig. 4: Two examples of the comparison of radar and lidar cloud base, from 19 and 28 December 1998. The top panels show 94 GHz radar reflectivity (resolution 2 minutes/60 metres) and the second show 905 nm backscatter coefficient (resolution 2 minutes/30 metres). The dashed horizontal lines in each show the minimum cloud base height permitted for this particular day (to ensure that the two instruments are observing the same cloud, and that the lidar is not detecting aerosol layers). The third panel in each example shows cloud base height from the two instruments using the full 'ground-based' sensitivities, and the last depicts the difference in cloud base height calculated assuming both ground-based and spaceborne instrument sensitivities (see text for details).

In conclusion, there is a difference in the cloud base measured by radar and lidar but it is usually less than 200 m, which is not really of great importance. This is particularly true for the Earth Radiation Mission since the vertical resolution of the radar will be 500 m. It should be noted that given typical lapse rates in the troposphere, a change in cloud base of 500 m corresponds to a change in long-wave emission of approximately 10 W m^{-2} . This is commonly considered to be the accuracy required for both observations and model radiation schemes, so the differences in cloud base found in this study are not large enough to be a serious concern.

COINCIDENCE OF ECHOS FROM RADAR AND LIDAR

It is very common for the lidar signal to be extinguished completely, even in ice clouds as seen in Fig. 4, but it is of interest to determine how often there are clouds detected by the lidar that are not seen at all by the radar, and to characterise them by height and optical depth.

We use all the 94 GHz radar data taken in the three-month

period. The lidar and radar data are both averaged by 2 minutes and 120 m, and are interpolated on to a common grid. Because the lidar sees aerosols in the boundary layer, only data above 2 km are considered. For each day a 'hit/miss' field is calculated, which for each point on the grid contains a value that states whether

1. One (or both) of the instruments was not operational at the time.
2. No cloud was seen by either instrument.
3. Cloud was seen by both instruments.
4. The radar saw cloud and the lidar did not.
5. The lidar saw cloud and the radar did not.

Each ray is examined in turn, and clouds are identified that are more than three pixels thick (to reject anomalous echos), consist entirely of cloud seen by the lidar and not the radar, and

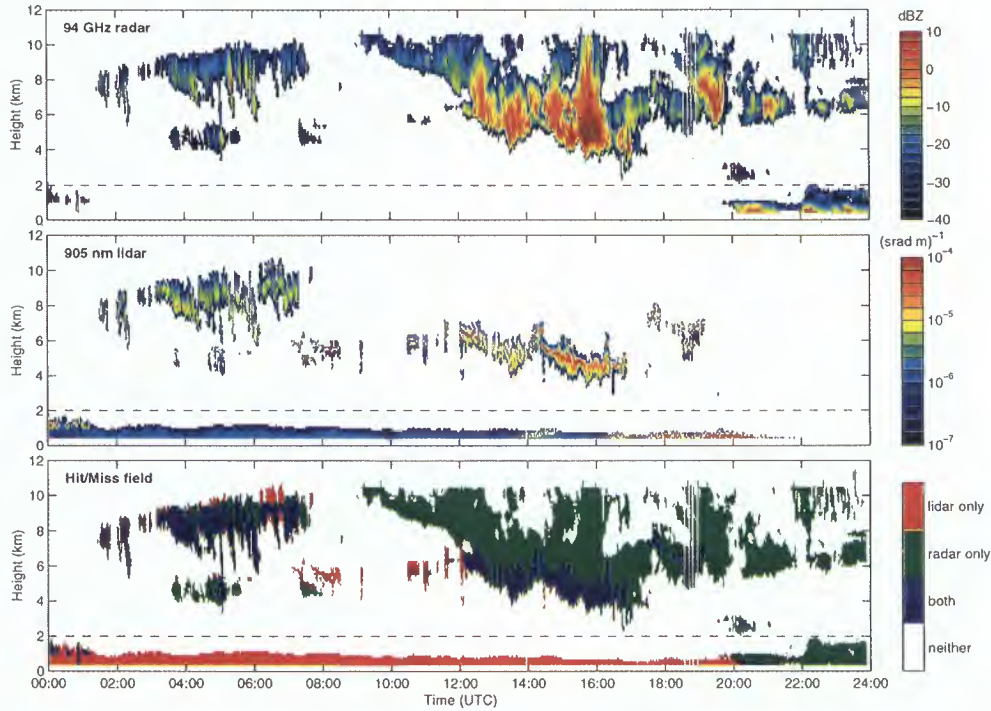


Fig. 6: Comparison of radar and lidar observations of cloud occurrence on 13 December 1998. The top panel shows 94 GHz radar reflectivity, the second shows lidar backscatter coefficient, and the third shows the 'Hit/Miss' field, described in the text, for the full 'ground-based' sensitivity scenario. The dashed line at 2 km indicates the minimum height at which one can be sure the lidar is observing cloud and not aerosol.

are bounded at the top and the bottom by pixels for which no cloud was seen by either instrument. The same two sensitivity scenarios that were used in the previous section are again considered here. An example is shown in Fig. 6 for a whole day of data. In this case there are some supercooled water clouds at around 6 km that are seen by the lidar but only intermittently by the radar. It was found from the CLARE'98 campaign that supercooled water tends to occur in the form of thin layers that, because of the small droplet size, give a much larger echo for the lidar than the radar.

For the full or 'ground-based' instrument sensitivities, 3.9% of clouds detected by the lidar in the entire three-month period were not seen by the radar. For the 'spaceborne' sensitivity scenario (-35 dBZ for the radar, 8×10^{-7} (srad m) $^{-1}$ for the lidar), this value drops to 2.1%. Again, the difference is because in degrading the data to spaceborne sensitivities the lidar loses relatively more signal than the radar.

These are very small fractions, but it is important to know how radiatively significant the clouds missed by the radar are. Figure 7 shows the distribution of the base height and optical depth of the clouds seen by the lidar and not the radar. Optical depth is estimated by simply converting the observed backscatter coefficient to an extinction coefficient using an assumed extinction-to-backscatter ratio of 14 srad (the value used by the ARMAR ESTEC cirrus model), and integrating up through the cloud. We find that the mean optical depth of these clouds is around 0.05 which is fairly low, although the maximum is 0.27. These low values justify the fact that no attempt was made to

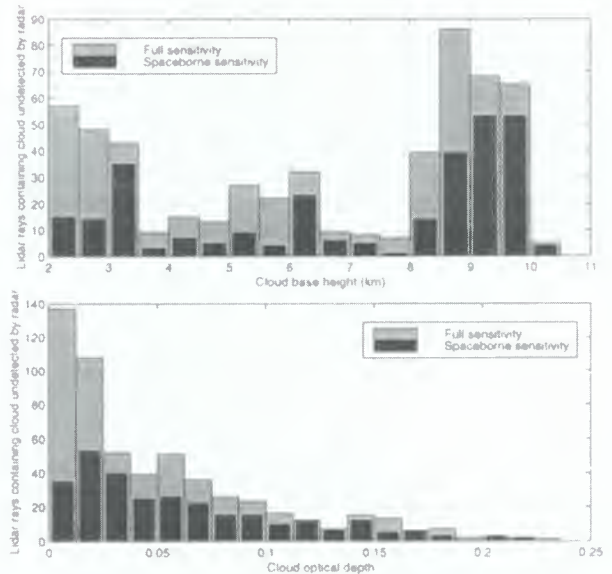


Fig. 7: Distribution of cloud base height and optical depth for all clouds in the dataset that were detected by the lidar but not the radar. The same two sensitivity scenarios have been considered.

correct for attenuation. For a cloud to be undetected by the radar means that the particles must be very small; it is likely that they are either tenuous supercooled water clouds before the onset of glaciation, or aircraft contrails consisting of very small ice crystals. It was estimated by Brown et al. (1995) that the radiative

significance threshold for mid-latitude cirrus is an optical depth of around 0.05. Hence we can calculate the fraction of *radiatively significant* clouds seen by the lidar but not the radar; it is found that for ground-based instrument sensitivities the value is 1.5%, and for spaceborne sensitivities it is only 1.0%.

In summary, it seems that there will not be large expanses of radiatively significant cloud not seen by the proposed spaceborne radar. The same conclusion was reached by Brown et al. (1995) using aircraft data. It is clear that much more radiatively significant clouds will be missed by the lidar because of the problem of attenuation.

CONCLUSIONS

The proposed ESA Earth Radiation Mission is likely to involve both a radar and lidar on a spaceborne platform. A number of misconceptions about the ability of these instruments to measure clouds are frequently stated, and analysis of this dataset has enabled them to be examined more closely:

"Radar reflectivity can be used in stratocumulus clouds to retrieve liquid water content"

We have found that even over Chilbolton where the air is predominantly continental, 60% of the stratocumulus clouds have a radar reflectivity of in excess of -30 dBZ at least somewhere in the profile; this can be regarded as a crude indication that there is drizzle present, and therefore that reflectivity is essentially unrelated to liquid water content. For a spaceborne radar that is to observe clouds on a global scale, it should be noted that 90% of the earth's stratocumulus occurs over the oceans, and drizzle is ubiquitous in maritime stratocumulus (Fox and Illingworth 1997).

"Cloud boundaries measured by radar and lidar are very different"

Differences in cloud boundaries are very much a function of the sensitivity of the two instruments. Because the data in this study were taken from the ground during winter, it has only been possible to examine the differences in the height of the base of ice clouds. We have found that with the proposed sensitivity of the spaceborne radar and lidar, 73% of the time cloud base should agree to within 200 m and 95% of the time to within 400 m. Given that the range-gate spacing of the spaceborne radar will be 500 m, this is acceptable. The next step is to perform the analysis on the bases of liquid water clouds (using data taken in summer when the 0°C isotherm is much higher). Because of the strong attenuation of the lidar signal, the coincidence of radar and lidar cloud top cannot be meaningfully compared from the ground.

"There are many radiatively significant clouds that the radar will not detect"

We have found that using the full sensitivity of the instruments, 3.9% of the clouds detected by the lidar above 2 km were not seen by the radar. When the data are degraded to the sensitivity of the spaceborne instruments this figure drops to 2.1%. If we further only consider 'radiatively significant' clouds, defined as

those with an optical depth greater than 0.05, this value becomes only 1%. Hence it would appear that there are *not* large expanses of radiatively significant cloud that will not be detected by the radar. This is certainly true for ice clouds, but the restriction that only observations above 2 km could be used (because of boundary-layer aerosols) meant that the amount of low-level liquid water cloud considered in the analysis was relatively low.

ACKNOWLEDGEMENTS

We wish to thank the Radiocommunications Research Unit at the Rutherford Appleton Laboratory for the use of the Chilbolton radars and lidar ceilometer. The Galileo radar was developed for the European Space Agency by Officine Galileo, the Rutherford Appleton Laboratory and the University of Reading under ESTEC Contract No. 10568/NL/NB. The ASTEX data were supplied by Philip Brown. This research received funding from NERC grant GR3/8765.

REFERENCES

- Brown, P. R. A., A. J. Illingworth, A. J. Heymsfield, G. M. McFarquhar, K. A. Browning and M. Gosset, 1995: The role of spaceborne millimeter-wave radar in the global monitoring of ice-cloud. *J. Appl. Met.*, **34**(11), 2346–2366.
- Fox, N. I., and A. J. Illingworth, 1997: The potential of a spaceborne radar for the detection of stratocumulus clouds. *J. Appl. Met.*, **36**(6), 676–687.
- Russchenberg, H. W. J., V. K. C. Venema, A. C. A. P. van Lammeren, A. Feijt and A. Apituley, 1998: *Cloud measurements with lidar and a 3 GHz radar*. Final report, ESTEC Contract 151912.
- Uttal, T., E. E. Clothiaux, T. P. Ackerman, J. M. Intrieri and W. L. Eberhard, 1995: Cloud boundary statistics during Fire II. *J. Atmos. Sci.*, **52**(23), 4276–4284.
- Weitkamp, C., O. Danne, H. Flint, W. Lahmann, M. Quante, E. Raschke and F. E. Theopold, 1997: Lidars for cloud measurements at GKSS and first radar-lidar comparisons. *Workshop on 'Synergy of active instruments in the Earth Radiation Mission', 12-14 November 1997*, GKSS, Geestacht, Germany.

Cloud boundaries and structure in mixed phase, mid-level clouds as deduced from ground-based 95-GHz radar and airborne lidar measurements during CLARE'98.

Markus Quante, Olaf Danne

GKSS Research Centre, Institute for Atmospheric Physics, D-21502 Geesthacht, Germany
Phone: +49 4152 87 1501 Fax: +49 4152 87 2020 Email: markus.

Harald Flentje, Wolfgang Renger

Lidar Group, DLR, PO Box 1116, D-82234 Wessling, Germany
Phone: +49 8153 28 2525 Fax: +49 8153 28 1271 Email: harald.flentje@dlr.de

Peter Francis

UK Meteorological Office, Met. Research Flight, Farnborough, Hampshire, GU14 6TD, UK
Tel.: +44 1252 39 5403, Fax: +44 1252 37 6588, Email: pnfrancis@meto.gov.uk

INTRODUCTION

For the assessment of the influence of clouds on global climate and related feedback mechanisms an accurate knowledge of macroscopic parameters of clouds like altitudes of their boundaries, number of layers, their internal structure and dominant phase is essential. Present observational methods only deliver crude estimates of these quantities. The combined use of cloud radar and lidar measurements is in the focus of current research in order to improve the retrieval of cloud parameters.

The combination of cloud radar and lidar has previously been used to obtain information on cloud boundaries, e.g. [1, 2, 3, 4], or cloud microphysical structure [5]. The studies concentrated mainly on the derivation of location and boundaries of either ice or water clouds. No systematic investigations on mixed phase clouds are available, essentially because the lidar beam often is attenuated by liquid water in the clouds. However, the examples of this study show that the complimentary information in radar and lidar data is potentially useful for research on mixed phase clouds.

The CLARE'98 campaign between 5 and 23 October 1998 at Chilbolton, UK, concentrated on the combined use of cloud radar and lidar for the detection of cloud properties of mid-level clouds. During conducted flight missions, additionally *in situ* microphysical data was obtained by instrumented aircraft for validation purposes. Here, results from the ground-based GKSS cloud radar 'Miracle' and the airborne DLR lidar 'Alex' for two case studies targeting on mixed phase clouds are presented.

INSTRUMENTATION

In this section we briefly describe the measurement systems used for the study. A more detailed description of the instruments along with a discussion of their performance during Clare'98 is provided in respective chapters at the beginning of this report.

Cloud radar MIRACLE

For the Clare'98 campaign the transportable 95-GHz cloud radar operated by GKSS, Institute for Atmospheric Physics, was set up at Chilbolton, UK.

The pulsed-Doppler radar is fully polarimetric and has a peak power of 1.7 kW. The system has been taken into operation in summer 1996. Since its capabilities cover those of a planned spaceborne system, the radar is well suited for preparatory studies for such a mission. Pulse repetition frequency (up to 80 kHz), number and location of range gates, pulse width and pulse polarisation are software selectable and allow for a range resolution between 7.5 m and 82.5 m up to a range of 15 km. The beamwidth of the center-fed Cassegrain antenna of 0.17° leads to a range cell diameter of 30 m at a distance of 10 km. Tab. 1 provides the main specifications of the radar.

Tab. 1 Main characteristics of the MIRACLE cloud radar.

Transmitter	EIA (klystron)
Frequency	95 GHz (3.2 mm)
Peak power (EIA)	1.7 kW
Pulse repetition frequency	50 Hz – 80 kHz
Pulse width	50 – 550 ns
Antenna diameter	1.2 m
Beamwidth (3dB)	0.17°
Antenna gain	60 dB
Transmit polarization	lin. horizontal and vertical
Dynamic range	70 dB

The real-time data products include, beside reflectivities, polarimetric quantities (ZDR, LDR, ρ) and the first three moments of the Doppler spectrum (total power, mean velocity, velocity variance) derived by the pulse pair algorithm or an up to 1024 point FFT full spectrum analysis. The minimum sensitivity at an altitude of 1 km and 1 s integration is about -40 dBZ. The GKSS radar is currently used for a variety of studies related to the structure and properties of layer clouds, e.g. [6, 7, 8].

The system has been internally calibrated and operated simultaneously with the externally calibrated Cloud Profiling Radar Sytem (CPRS) [9]. The absolute error of the derived reflectivities was found to be less than 3 dB. This value was confirmed by recent comparisons with in situ forward scattering spectrometer data obtained over Geesthacht from simultaneous measurements in pure water clouds. Cross-calibration with the calibrated CAMRa (3 GHz), 'Rabelais' (35 GHz), and 'Galileo' (94 GHz) radars at Chilbolton suggested a difference of 2 dB to 'Miracle' [10], which has been corrected for in this study.

For the determination of cloud boundaries a cloud mask scheme based on probability decisions for running 5x5 pixel matrices was used in order to separate cloud signals from those produced most probable by noise. A comprehensive description of the radar is provided in [11], the system performance and data products with respect to Clare'98 measurements are summarised in [12].

Backscatter lidar ALEX

During Clare'98 the lidar system ALEX was installed onboard the FALCON 20 of the DLR, Oberpfaffenhofen. It was operating in a downward looking mode.

The 3 wavelengths lidar makes use of a Nd:YAG laser emitting at 1064nm. Frequency doubling and tripling provides 532nm and 354nm channels. The received 532nm signal is split into the two perpendicularly polarised portions which allows to calculate the depolarisation of the light. With a repetition rate of 10Hz for typical aircraft speed of 150m/s the raw data resolution is about 15m horizontally and 12m vertically. However, to improve the S/N ratio the compromise between signal noise and resolution leads to a respective processed data resolution of some 100m/some 10m horizontally/vertically. The receiver is a Cassegrain telescope ($r = 17.5\text{cm}$) with 1mrad field of view. Technical aspects concerning ALEX are given in [13], the performance of the lidar system and the other FALCON instruments during the Clare'98 campaign is described in more detail in [14]. Main characteristics of ALEX are provided by Tab. 2.

Tab. 2: Main characteristics of the ALEX lidar.

Transmitter	Nd:Yag-laser
Wavelengths	1064, 532, and 354 nm
Pulse energy	150 mJ at 1064 and 354 nm 120 mJ at 532 nm
Pulse repetition rate	10 HZ
Pulse length	6 ns
Beam divergence	0.7 mrad
Telescope diameter	35 cm
Field of view	1 mrad
Receive polarisation	horizontal and vertical

The lidar directly measures atmospheric backscatter which is either given absolutely as backscatter coefficient [$\text{m}^{-1}\text{sr}^{-1}$] or relative to Rayleigh scattering (calculated from air density) as backscatter ratio $(\beta_{\text{particle}} + \beta_{\text{molecule}})/\beta_{\text{molecule}}$, the relative

contribution of particle scattering to the total signal. The attenuation of the laser beam in the atmosphere is considered employing a numerical inversion whereby an extinction/backscatter ratio (lidar ratio) and a starting value at some distance from the receiver has to be assumed to iteratively derive the profiles. With the inferred lidar ratio the extinction coefficient and its integral, the optical depth, can be estimated from the backscatter signal [15]. The ratio of the orthogonal and parallel (to the incident beam) polarised 532nm signals $\beta_{\perp}/\beta_{\parallel}$ i.e. the depolarisation of the light by the scattering particles can be used directly to obtain information about their sphericity. A volume depolarisation of 1.4% occurs if only the unsymmetrical air-molecules contribute to the depolarisation. If depolarising (non-spherical, solid) particles are within the measured volume the volume-depolarisation is between 0.014 and 1 depending on the concentration and shape of the scattering particles. Clouds with *only* spherical (liquid) particles may cause volume-depolarisation ratios below 1.4% since they increase only the intensity in the parallel channel.

MEASUREMENTS AND RESULTS

The measurements presented here were obtained on two days, 20 October and 21 October, 1998, during the Clare'98 campaign. These days were chosen because simultaneous radar, lidar and in situ observations are available for mixed phase mid-level clouds. The four overpasses of the Falcon over the radar site (co-ordinates: 1.4367E, 51.1444N) selected for analysis are listed in table 3, which in addition provides the lidar ratio used for the data inversion.

Table 3: Date, time, position, and applied lidar ratio for selected passings of the Falcon over the radar site. The position difference is given in meters as indicated by the navigation system of the Falcon relative to the ground site co-ordinates.

Date	Time UTC hh:mm:ss	relative position of Falcon	applied lidar ratio
20 Oct. 1998	14:20:29	170 m south	15
20 Oct. 1998	14:32:53	40 m south	11
21 Oct. 1998	10:19:03	220 m south	(170)*
21 Oct. 1998	10:49:54	50 m south	25

* qualitative lidar-inversion due to strong attenuation

Lidar backscatter coefficients (β) presented here are corrected for extinction. Shown radar reflectivities are not corrected for atmospheric attenuation, but estimates of the respective values are provided.

Case 20 October 1998:

On October 20 fronts were approaching from south west with strengthening south westerly winds. Fig. 1 shows a NOAA-AVHRR composite image for 14:55 UTC. At this time the experimental area (Chilbolton is marked by a cross) is fully

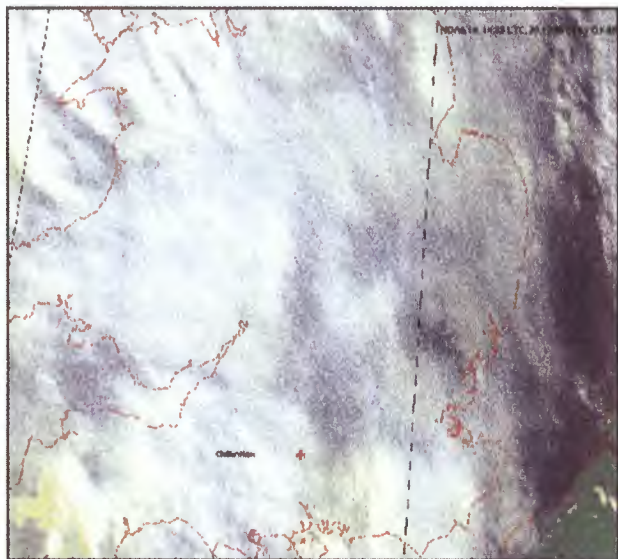


Fig. 1: 14:55 UTC 20 October 1998 satellite image from NOAA-14. Composite of channels 1, 2, and 4, red cross marks Chilbolton.

covered by clouds. The passive instrument onboard the satellite indicates the presence of thin high level cirrus above lower level clouds.

MIRACLE radar measurements on this day started at 7:53 UTC and ended at 17:16 UTC. Backscatter coefficients from ALEX are available for 9:25 to 10:50 UTC and 12:43 to 14:55 UTC (2 flights).

The inspection of the radar data revealed the changing appearance of the clouds during the day. In the morning low-level clouds dominated with occasionally thin cirrus above. At about 13:00 UTC the upper level clouds thickened followed by a layer of mid-level cloud which developed into an extended altostratus during the course of the day (from about 4 to 11 km in the later afternoon). The mid-day change in cloudiness can also be seen in Fig. 1, it is marked by a band of lower clouds east of Chilbolton.

Fig. 2 a) and b) shows radar reflectivities from 14:01 to 14:45 UTC covering the time period of the selected overpasses of the lidar. The mid-level clouds appear in the radar data at altitudes between about 2.5 and 5.5 km and have typical reflectivities ranging from 0 dBZ_e to -20 dBZ_e. The two-way attenuation by gases at 95 GHz calculated (by R. Hogan) from data diagnosed by the UK Met. Office Unified Model added up to about 2 dB at an altitude of 5 km. The given reflectivities are not corrected for this effect.

As can be seen in figure 2 a), the mid-level clouds first appeared in two well separated layers which later merged into more or less one layer by keeping the layer signature up to about 14:35 UTC. Doppler data for the time period (not shown here) reveals downward velocities of about -0.5 ms^{-1} in the upper layer and values around -1 ms^{-1} and slightly higher for the lower layer.

An upper level ice cloud with maximum reflectivities below -20 dBZ_e is also visible in the radar data between altitudes of 10 and 12 km.

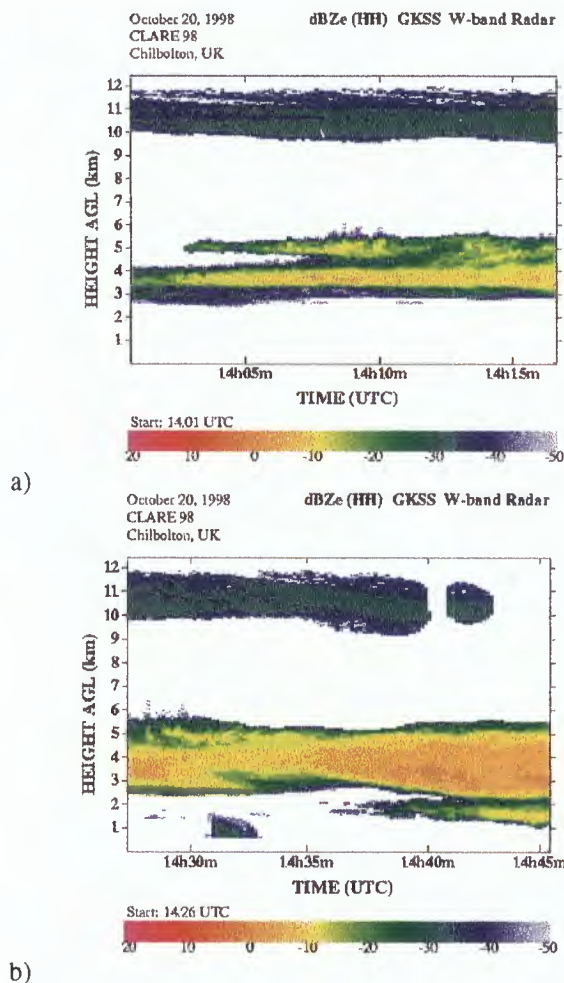


Fig. 2: Height-time cross-section of equivalent radar reflectivities in dBZ_e for time segments a) 14:01 to 14:17 UTC and b) 14:26 to 14:45 UTC on 20 October 1998.

The corresponding lidar data is shown in Fig. 3, which displays the backscatter ratio at 532nm and 1064 nm as well as the depolarisation at 532 nm along flight leg 11 of the Falcon (second flight). Around the time when the Falcon overflow the radar site (at 14:20:29 UTC) the lidar detected a cirrus layer between about 9.5 km and 12.5 km. Below the cirrus 3 thin layers appear in the lidar data between 4 and 5.5 km, where the radar measurements suggest a continuous, (although structured) cloud layer. Radar reflectivity and lidar backscatter coefficient profiles for the overpass are directly intercompared in Fig. 4. The altitudes are given with respect to sea level, their accuracy is estimated to be about $\pm 30 \text{ m}$. The lidar profile is averaged for 1 s which can be converted to a horizontal cloud scale of 218 m using the true airspeed of the aircraft. The radar data has been averaged over 9 s in order to match the spatial scale of the lidar data at an altitude of 4 km. Here, the time-space conversion used the horizontal wind measurements obtained by the UK Met. Office Hercules aircraft. For the displayed time segment the radar was operated in FFT-mode, with a resulting limited range window [12] which was set between 2.8 and 5.2 km (resolution: 37.5m). Comparison of the profiles in the overlapping height

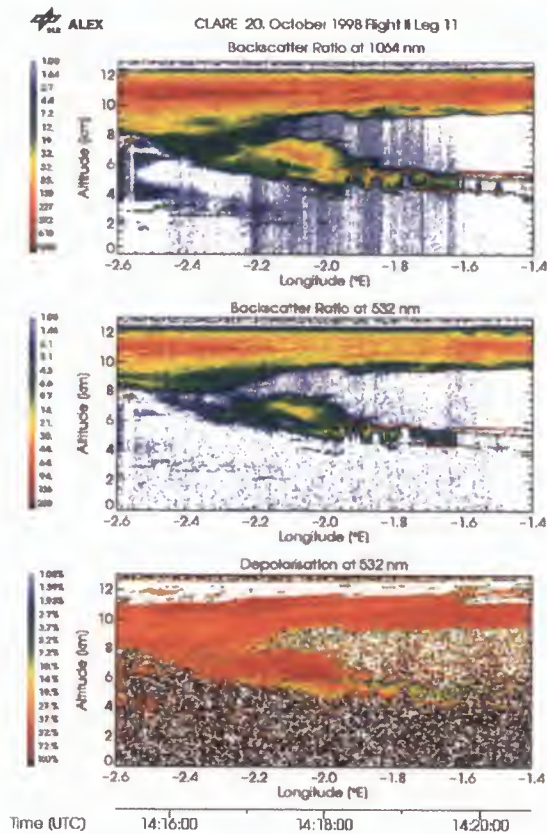


Fig. 3: Lidar backscatter ratio at 1064 nm, 532 nm and the depolarisation ratio at 532 nm as measured by ALEX along flight leg 11 of the Falcon.

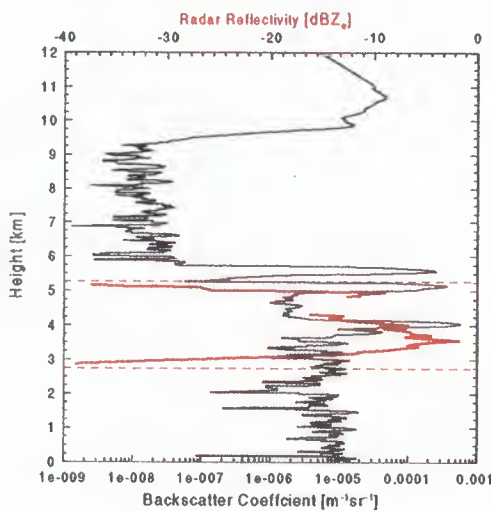


Fig. 4: Vertical profiles of radar reflectivity (red) and lidar backscatter coefficient for 1064 nm (black) at 14:20:29 on 20 October 1998. The lidar data has been averaged over 1 s (about 218 m), the radar data was averaged over 9 s to represent the same spatial scale.

band reveals the different cloud signature for the sensors. The lidar detected two narrow, well separated peaks. The radar profile shows also two peaks, of which the lower peak is

much broader and maximum values occur well below the corresponding lidar peak. The gap in the radar data between 4.3 and 4.8 km is due to noise effects [12]. The lidar signal probably experienced strong attenuation along the path through the thin layers, as an inspection of neighbouring time segments in Fig. 3 suggests, and therefore could not detect the weaker signals from in between and below them. The thin layers did not appear as a clearly distinguishable feature in the radar data.

The differences between the profiles are due to the different microphysical characteristics of individual parts in the cloud region affecting the scattering properties and attenuation. In Rayleigh approximation the radar signal is proportional to D^6 , while the lidar signal is proportional to about D^2 , with D denoting the diameter of the scattering particles. The phase of the particles plays a role for signal attenuation. It is assumed that the extended thin layers detected by the lidar consisted of liquid water droplets while the rest of the cloud consisted of larger ice crystals dominating the radar backscatter. As can be seen in Fig. 3, the depolarisation of the lidar signal around 14:20 UTC was very low in the 3 layers suggesting that the relevant scatterers for the lidar tended to be mainly spherical particles. Depolarisation ratios of less than 10 % were found. Due to sensitivity limitations, linear depolarisation ratios measured by the radar only indicate the presence of crystals in the lower part of the cloudy region (cross-pol. isolation is 26 dB). There is no evidence for a decreased LDR around the height of the lowest lidar peak at 4 km. This might be an indication for the coexistence of liquid water and ice at this

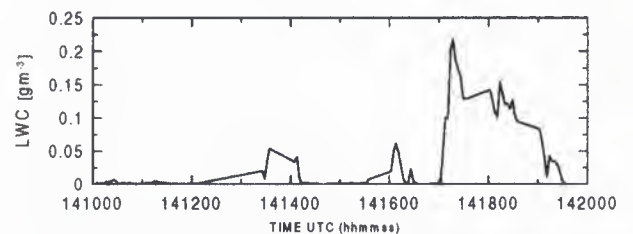


Fig. 5: Liquid water content (LWC) as measured with the Johnson-Williams Liquid Water probe of the Hercules along flight leg 9.1. on 20 October 1998.

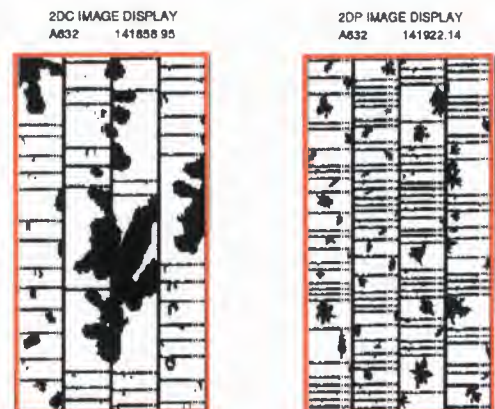


Fig. 6: Examples of particle images from the OAP-2-DC (left) and OAP 2-DP probe (right) onboard the Hercules during the overpass at about 14:20 UTC on 20 October 1998.

height level. This aspect is confirmed by *in situ* microphysical measurements made with probes installed on the Hercules C-130, which passed Chilbolton at 14:19:53 UTC at an altitude of 4 km and detected ice as well as liquid water. The liquid water content measured with the Johnson-Williams liquid water probe along flight leg 9.1 of the Hercules is given in Fig. 5. In parts of the cloud the liquid water content exceeded 0.1 gm^{-3} .

The super-cooled liquid layers do not appear as discernible peaks in the radar signals because the droplets were probably very small (an indication for small droplets is the large difference between Johnson-Williams derived LWC and PMS 2D-probe habit derived LWC, not shown here). The radar signal is mainly produced by the ice component of the cloud, which contained fairly large particles. The radar beam might have been slightly attenuated by the liquid water droplets. Typical two-way attenuation is $10 \text{ dB/km per gm}^{-3}$.

Fig. 6 shows examples of particle images from the PMS OAP-2-DC (nominal size range: 25 to $800 \mu\text{m}$) and OAP 2-DP (nominal size range: 0.2 to 6.4 mm) probes onboard the Hercules. It can be seen that quite large particles were present in the lower cloud layer, some of the ice crystal had sizes up to a few millimetres. The effective radius derived from these measurements varies between about 60 and $80 \mu\text{m}$ around this overpass.

The direct comparison of radar reflectivity and lidar backscatter coefficient profiles for the overpass at 14:32:59 UTC is shown in Fig. 7. At this instance the radar was profiling the entire troposphere and a signal from the upper level cirrus layer with reflectivities around -30 dBZ_e was also received. At mid-level again the two dominant narrow peaks in the lidar data between 4 and 4.5 km are not an obvious feature in the radar profile, which received signals from a much thicker layer. The lidar obtained also signals from the probably ice dominated part of the cloud between 4.5 and 5.3 km . For the mid-level layer the cloud top detected by the lidar

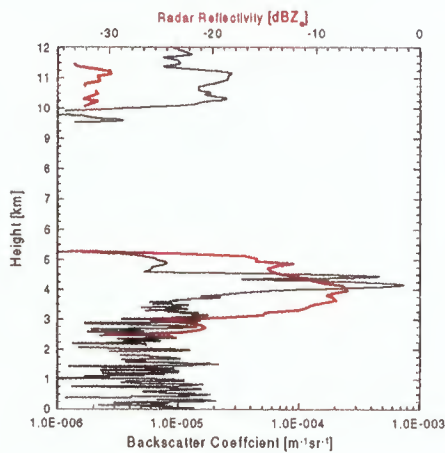


Fig. 7: Vertical profiles of radar reflectivity and lidar backscatter coefficient (1064 nm) at 14:32:53 on 20 October 1998. The lidar data was averaged over 1 s (about 212 m), the radar data was averaged over 8 s in order to match the spatial scale.

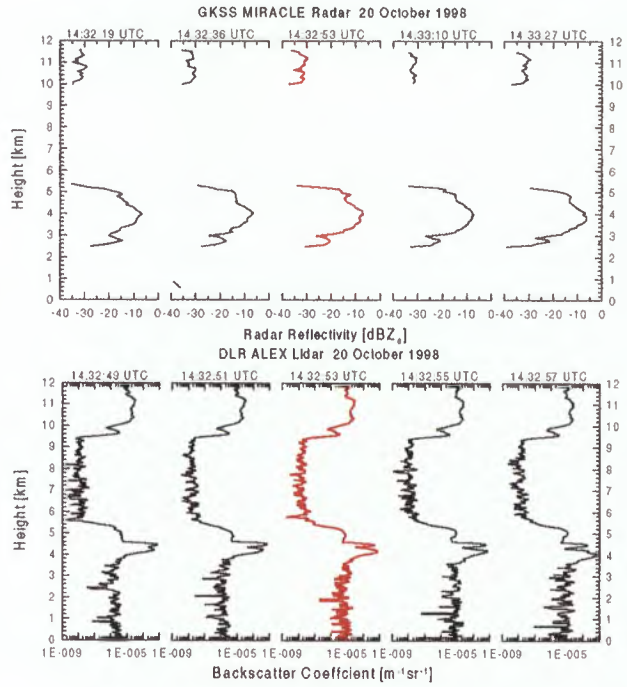


Fig. 8: Five consecutive profiles of equivalent radar reflectivity and lidar backscatter coefficient (1064 nm) for the overpass at 14:32:53 UTC on 20 October 1998. Different times are selected for corresponding radar and lidar profiles to partly account for the relative movement of aircraft and clouds.

is placed about 100 to 200 m above that of the radar when lidar signals down to $10^{-8} \text{ m}^{-1} \text{ sr}^{-1}$ are considered. Exact matching is not expected due to sampling of slightly different locations. Due to attenuation the base region, which extended down to about 2.5 km , and its structure is not resolved by the lidar. Fig. 8 compares 5 consecutive profiles (averaged horizontally over 212 m) of radar reflectivities and lidar backscatter coefficients around the overpass time. It can be seen that the lowest lidar peaks, which are again associated with a thin, presumably liquid layer, decrease in altitude, while the radar peaks stay almost at a constant height. This

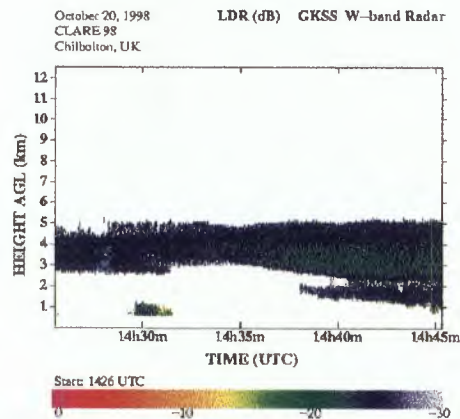


Fig. 9: Linear depolarisation ratio (LDR) as measured by MIRACLE from 14:26 to 14:45 UTC on 20 October 1998.

could be an indication that the liquid layers might have been detached from the rest of the cloud.

Inspection of the lidar derived depolarisation again provides the tendency of low values for the thin layers pointing toward a dominance of the liquid phase. LDR values measured by the radar around the overpass at 14:32:53 UTC shown in Fig. 9 are quite small but indicate the presence of non-spherical particles up to an altitude of about 5 km. Above this height the sensitivity limit of the cross-pol channel was reached. There is no structure in LDR data which would support the dominance of spherical particles, where the lidar detected the thin layers.

Doppler velocities from the radar for this time segment show an increase by about 0.5 ms^{-1} for the layer between about 3.5 and 4 km (just below the lowest lidar peak) pointing to the presence of larger particles. Whether the lowest radar signals mark the cloud base or are caused by some falling larger particles stays open.

In conclusion it can be stated that without the lidar there would have been almost no indication for the liquid layers. On the other hand in case of strong attenuation the lidar could not penetrate to the cloud base area, on which information can be obtained from radar data.

Case 21 October 1998

Behind a cold front passing by on 21 October at about 9:00 UTC low clouds broke up, they were followed by midlevel clouds approaching in a strong south westerly flow. According to the radar measurements these midlevel clouds disappeared after 11:15 UTC. The NOAA-15 image from 8:19 UTC (Fig. 10) shows the less cloudy air mass approaching behind the cloud band associated with the passing cold front.

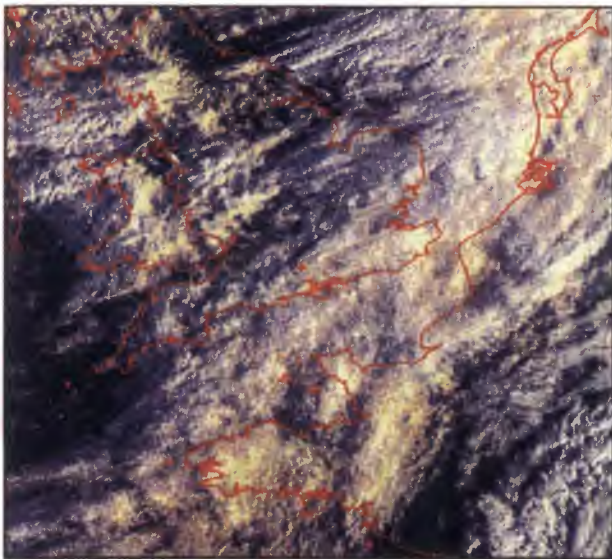
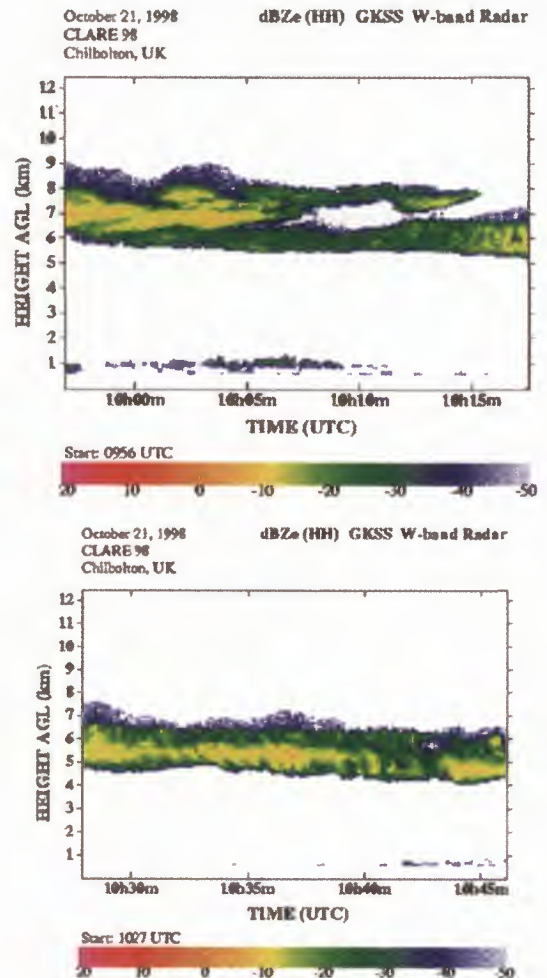


Fig. 10: 8:19 UTC 21 October 1998 satellite imagery from NOAA-15. Composite of channels 1,2, and 4, red cross marks Chilbolton.



a)

b)

Fig.11: Height-time cross-section of equivalent radar reflectivities in dBZ_e for time segments a) 9:56 to 10:17 UTC and b) 10:27 to 10:46 UTC on 21 October 1998.

The radar was operating from 9:34 UTC to 11:37 UTC, the lidar gathered data between 9:57 and 10:50 UTC.

As can be seen in figure 11 a) and b), in which the radar reflectivities for the time periods around and respectively just before the discussed overpasses are displayed, the cloud altitude as well as the thickness of the upper cloud layer decreased with increasing time. Cloud top sank from 9 km to about 6 km. Typical radar reflectivities ranged between -10 dBZ_e and -25 dBZ_e . Also some thin low level clouds are visible in Fig. 11.

Fig. 12 provides lidar profiles along leg 4 of the Falcon on this day. The backscatter returns show the elevated mid-level cloud layer as well as the lower level clouds. Again thin band-like structures can be seen in the midlevel clouds.

The direct comparisons between the radar and lidar profiles for the overpasses at 10:19:03 UTC and 10:49:54 UTC are plotted in figures 13 and 14 respectively. At 10:19 UTC the 500 m thick cloud layer around 6.7 km seen by the lidar, which attenuates its beam totally, is only barely detected by the radar. The maximum radar reflectivities occur about 1 km lower at 5.5 km. Either the lidar data or the radar data alone would lead to totally different statements on the cloud layer

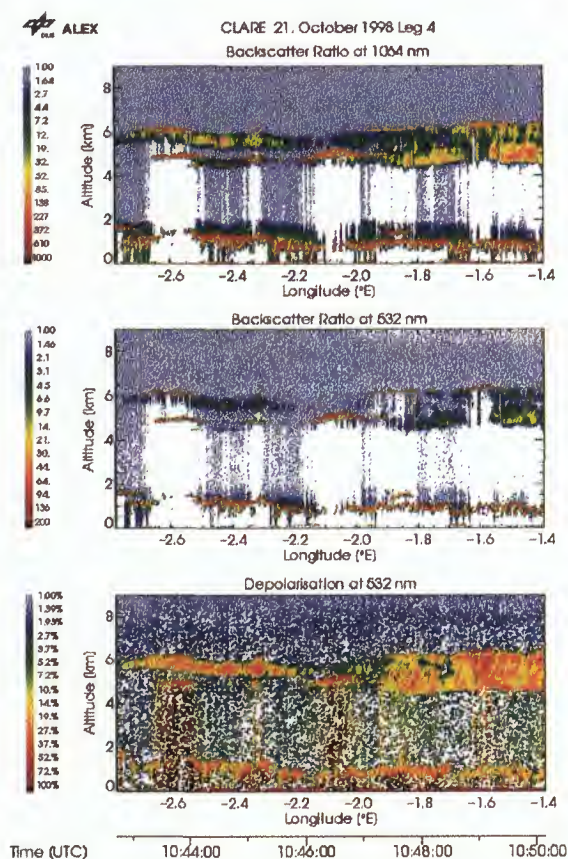


Fig. 12: Lidar backscatter ratio at 1064 nm, 532 nm and the depolarisation ratio at 532 nm as measured by ALEX along flight leg 4 of the Falcon on 21 October 1998.

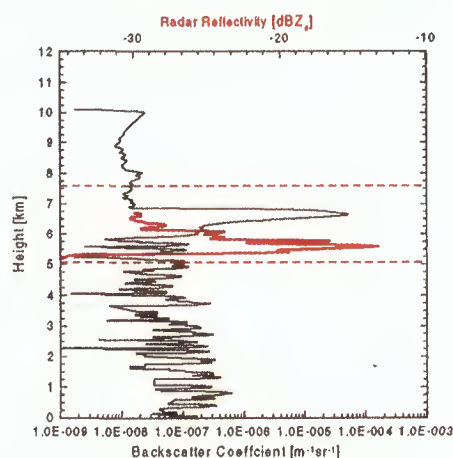


Fig. 13: Vertical profiles of radar reflectivity and lidar backscatter coefficient (1064 nm) at 10:19:04 on 21 October 1998. The lidar data has been averaged over 1 s (about 175 m), the radar data has been averaged over 6 s in order to match the same spatial scale. Red dashed lines mark the range window for the radar.

and its boundaries. The situation altered at 10:49:54 UTC (Fig. 14), here the radar and lidar detected almost the same macroscopic structure and estimates of cloud boundaries would agree better. An indication for layer separation is shown in both data sets at an altitude of 5.6 km. Small scale

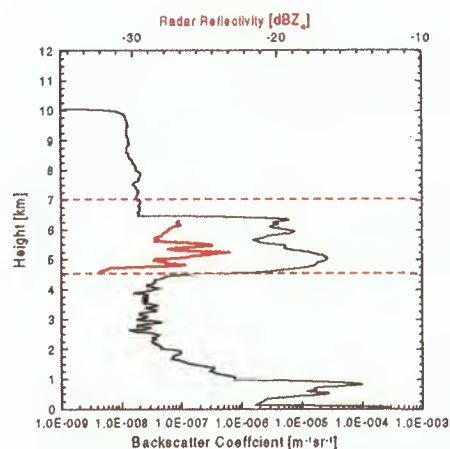


Fig. 14: Vertical profiles of radar reflectivity and lidar backscatter coefficient (1064 nm) at 10:49:54 on 21 October 1998. The lidar data has been averaged over 1 s (about 185 m), the radar data was averages over 6 s in order to match the spatial scale. Red dashed lines mark the range window for the radar.

features (about 100 m) in the profiles show a different behaviour. Again, a close matching is not expected, because of spatial differences as well as the distinct scattering properties for the different wavelengths used. By this time the cloud has become weaker, maximum radar reflectivities were less than -23 dBZ, (no correction applied for attenuation by liquid water in the low level cloud and by water vapour; two-way about 2.6 dB at 5 km). And the signature of a thin super-cooled liquid layer in the lidar data was not that evident any more (less pronounced and broken; see Fig. 12). The Hercules sampled microphysical data at an altitude of about 5.7 km and detected little liquid water at that height level (LWCs below 0.005 gm^{-3}), where it obviously did not penetrate a liquid layer. Ice crystal sizes were smaller at this level, compared to those found around the 14:20 UTC overpass in the 20 October case. Largest particles had sizes of about 1 millimetre, the effective radius varied between 40 and

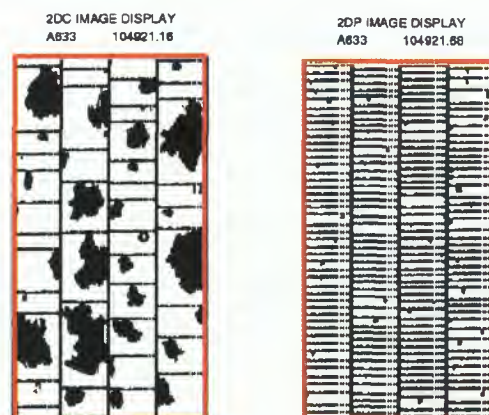


Fig. 15: Examples of particle images from the OAP-2-DC and OAP 2-DP probe onboard the Hercules during the overpass at about 10:49 UTC on 21 October 1998.

60 μm . Typical examples of optical array probe images for the Hercules overpass at about 10:49 UTC are provided in Fig. 15. The fewer big particles along with a lower IWC (not shown here) at this overpass time explain the lower radar reflectivities. Here, due to the absence of a strong attenuating liquid layer the lidar could penetrate to the cloud base. Since radar and lidar derived almost the same base heights, it can be assumed that the base region was not dominated by a few big falling particles.

SUMMARY AND CONCLUDING REMARKS

Ground based cloud radar measurements and co-located airborne lidar measurements of mid-level, mixed phase clouds sampled during Clare'98 were analyzed and compared. In general, the two instruments highlighted different features of the clouds, which can be explained by their different sensitivities to particle size distributions and signal attenuation.

The complimentary information on cloud boundaries and cloud structure, revealed the usefulness of co-located cloud radar and lidar measurements. Only the combined use of the instruments could uncover the complete appearance of the mixed phase clouds with embedded thin layers of super-cooled liquid water and fall streak areas below cloud base. In the absence of the mentioned features the radar and lidar profiles led to almost the same conclusions concerning cloud boundaries.

The detected phenomena are of great interest for the parameterization of mixed phase clouds in numerical models. A major question is, how often this kind of super-cooled layers occur, since they will strongly influence the radiative transfer through the clouds. Systematic information on the extension of fall streak areas and their frequency of occurrence in conjunction with mid-level clouds would support research on the life-cycle of this cloud type.

A cloud radar and a backscatter lidar on a spaceborne platform would allow to derive such information for larger areas and different geographical regions.

REFERENCES

- [1] Uttal, T., E.E. Clothiaux, T.P. Ackerman, J.M. Intrieri, and W.L. Eberhard, "Cloud boundary statistics during FIRE II." *J. Atmos. Sci.*, **52**, 4276-4284, 1995.
- [2] C. Weitkamp, H. Flint, W. Lahmann, F.A. Theopold, O. Danne, M. Quante, and E. Raschke, "Simultaneous radar and lidar cloud measurements at Geesthacht (53.5° N, 10.5° E)." *Phys. Chem. Earth (B)*, **24**, 163-166, 1999.
- [3] E.E. Clothiaux, T.P. Ackerman, G.G. Mace, K.P. Moran, R.T. Marchand, M.A. Miller, and B.E. Martner, "Objective Determination of Cloud Heights and Radar Reflectivities Using a Combination of Active Remote Sensors at the ARM CART Site." Accepted for publication, *J. Appl. Meteor.*, 1999.
- [4] V. Venema, H. Russchenberg, A. Apituley, A. v. Lammeren, L. Ligthart, "Cloud boundary height measurements using lidar and radar." *submitted to Phys. Chem. Earth (B)*
- [5] J.M. Intrieri, G.L. Stephens, W.L. Eberhard, and T. Uttal, "A method for determining cirrus cloud particle sizes using a lidar/radar backscatter technique". *J. Appl. Meteor.*, **32**, 1074-1082, 1993.
- [6] M. Quante, O. Danne, E. Raschke, I. PopStefania, and A. Pazmany, "Observations of cloud structure with a 3.2 mm-wave radar. Proceedings 12th International Conference on Clouds and Precipitation, Zürich, Schweiz, Vol. 1, 424-427, 1996.
- [7] O. Danne, M. Quante, D. Milferstädt, H. Lemke, and E. Raschke, "Relationships between Doppler spectral moments within large-scale cirro- and altostratus cloud fields observed by a ground-based 95 GHz cloud radar." *J. Appl. Meteor.*, **38**, 175-189, 1999.
- [8] Y. Fujiyoshi, M. Quante, O. Danne, and E. Raschke, "Properties of Deep Stratiform Ice Cloud Revealed by 95 GHz Cloud Radar - A Case Study." *Contr. Atmos. Phys.*, **72**, 113-125, 1999.
- [9] S.M. Sekelsky, S.M., and R.E. McIntosh, "Cloud observations with a polarimetric 33-GHz and 95-GHz radar." *Meteor. Atmos. Phys.*, **59**, 123-140, 1996.
- [10] R.J. Hogan, and J.W.F. Goddard, "Calibration of the ground-based radars during CLARE'98". *This report*.
- [11] M. Quante, O. Danne, H. Lemke, D. Milferstädt, and E. Raschke, "The GKSS 95-GHz cloud radar: system description and potential contributions in support of the Earth Radiation Mission." In Quante, M., J.P.V. Póiares Baptista, and E. Raschke, (eds.): Synergy of Active Instruments in the Earth Radiation Mission. Proceedings of ESA/GKSS Workshop, 12.-14. November 1997, ESA EWP-1968, GKSS 98/E/10, 205pp, (ISSN 0344-9629), 1998.
- [12] O. Danne, and M. Quante, "The GKSS 95-GHz Cloud Radar during CLARE'98: System Performance and Data Products." *This report*.
- [13] P. Moerl, M.E. Reinhardt, W. Renger, and R. Schellhase, "The use of the airborne lidar ALEX-F for aerosol tracing in the lower troposphere." *Contr. Atmos. Phys.*, **45**, 403-410, 1981.
- [14] contribution by H. Flentje and W. Renger to this report.
- [15] M. Kästner, K.T. Kriebel, R. Meerkötter, W. Renger, G.H. Ruppertsberg, and P. Wendling, "Comparison of Cirrus Height and Optical Depth Derived from Satellite and Aircraft Measurements." *Mon. Wea. Rev.*, **121**, 2708-2717, 1993.

Measurements for the CLARE 1998 campaign using the Chilbolton UV lidar

J. L. Agnew, A. J. Gibson and A. K. P. Marsh
 Radio Communications Research Unit, CLRC Rutherford Appleton Laboratory
 Chilton, Didcot, OX11 0QX, UK
 Phone : +441235445770 Fax : +441235446140 Email: J.L.Agnew@rl.ac.uk

INTRODUCTION

The Chilbolton UV lidar was used during the CLARE campaign to make sensitive measurements of vertical cloud profiles above the Chilbolton site. Lidar and radar systems provide a remote sensing method for measuring a variety of atmospheric properties. The Chilbolton UV lidar system is designed to profile the temperature and humidity of the atmosphere and also detect the presence of clouds [1]. Cloud measurements represent a relatively straightforward operation for a lidar system such as this, as their presence is easily detected by elastic scattering of the laser radiation. These signals are several orders of magnitude stronger than the inelastically Raman scattered signals used to quantify other parameters such as temperature and humidity. The laser power used to achieve adequate returns for temperature and humidity measurements is high enough that cloud measurements can be made without the need for long signal integration times. At UV wavelengths the cross section for Rayleigh scattering is such that the elastically scattered returns from molecular species are comparable to those from larger atmospheric species such as aerosols and water droplets.

UV lidar data from 3 days during the campaign are presented and compared with results from an infrared ceilometer and (for one of these days) with a 94 GHz radar system. The strengths and weaknesses of the systems for detecting the presence of different cloud types are assessed.

THEORY

The lidar equation relates the measured signal from a given height to atmospheric and equipment parameters and can be written as

$$C(h) = \frac{KO(h)}{h^2} T^2(h)B(h) , \quad (1)$$

where $C(h)$ is the detected signal from height h , K is a constant of the lidar system dependent on the transmitted laser power and the efficiency of the detection system, $O(h)$ is the fractional overlap between the transmitted and received beams at height h , $B(h)$ is the backscatter coefficient at height h and $T(h)$ is the fraction of radiation

transmitted to height h . $B(h)$ and $T(h)$ are dependent on the wavelength of the radiation.

$T(h)$ is related to the attenuation coefficient of the atmosphere, $\alpha(h)$, by

$$T(h) = \exp\left(-\int_0^h \alpha(h)dh\right) . \quad (2)$$

In general, there are contributions to $B(h)$ from both molecular scattering and scattering from larger particles, such as aerosols. The cross section for molecular scattering is well approximated by Rayleigh scattering which has an approximately λ^{-4} wavelength dependence. Hence for UV wavelengths there is appreciable Rayleigh scattering from atmospheric molecules. Scattering from larger spherical particles such as water droplets can be treated using Mie scattering theory and can be approximated as having a λ^{-1} wavelength dependence. When the sky is clear, molecular Rayleigh scattering dominates and analytical expressions for $B(h)$ and $\alpha(h)$ can be applied so that a value for $KO(h)$ can be calculated.

$B(h)$ for a species in the atmosphere is given by

$$B(h) = n(h) \frac{d\sigma(\pi)}{d\Omega} , \quad (3)$$

where $n(h)$ is the number density of the species at height h and $\frac{d\sigma(\pi)}{d\Omega}$ is its cross-section for scattering through π radians (i.e. backscattering).

For Rayleigh scattering, $\frac{d\sigma(\pi)}{d\Omega}$ is given by

$$\frac{d\sigma(\pi)}{d\Omega} = 5.45 \times 10^{-24} \left[\frac{\lambda}{550} \right]^{-4.09} \text{ m}^2 \text{ sr}^{-1} , \quad (4)$$

and $B_R(h)$ (for Rayleigh scattering) is related to $\alpha_R(h)$ by

$$\alpha_R(h) = \frac{4\pi B_R(h)}{1.5} . \quad (5)$$

Hence it was possible to take a profile where scattering was predominantly molecular up to height h and substitute analytical values for $B_R(h)$ and $T(h)$ to calculate K . The value of K was then applied to all other profiles from the day. In the data analysis contained in this report, $O(h)$ has been assumed to be equal to one for all heights as there was not sufficient clear sky data available to make a more accurate evaluation of $O(h)$. In practice, $O(h)$ was zero at low heights (less than around 1 km), then increased to a maximum value of 1 at around 4 km. The use of this assumption means that the returns from low altitudes are underestimated in the UV lidar plots. If scattering is not purely molecular Rayleigh, equations (3) to (5) do not apply and there is no analytical expression for $T(h)$. It must then be deduced from the difference between the measured signal and that expected if only molecular Rayleigh scattering occurred. In the current work this has not been attempted and the UV lidar data are displayed using the product $B(h)T^2(h)$.

EXPERIMENTAL DETAILS

The parameters of the lidar system are shown in Table 1 and a diagram of the experimental layout is shown in Figure 1. The transmitter and receiver optics are arranged in a biaxial orientation. The beam is transmitted vertically and the orientation of the receiver mirror axis is inclined by a small angle from vertical so that its field of view overlaps the transmitted beam at the required height. Fine adjustments to this inclination are made by observing the returned signals.

Laser type	Pulsed Nd:YAG
Laser wavelength (nm)	354.7
Energy per pulse (mJ)	350
Pulse repetition frequency (Hz)	50
Pulse duration (ns)	7
Transmitted beam diameter (mm)	120
Transmitted beam divergence (mr)	<0.5
Diameter of receiving mirror (m)	0.45
Receiver field of view (mr)	0.3
Detectors	Photomultiplier (bialkali cathode)

Table 1: Parameters of the UV lidar system

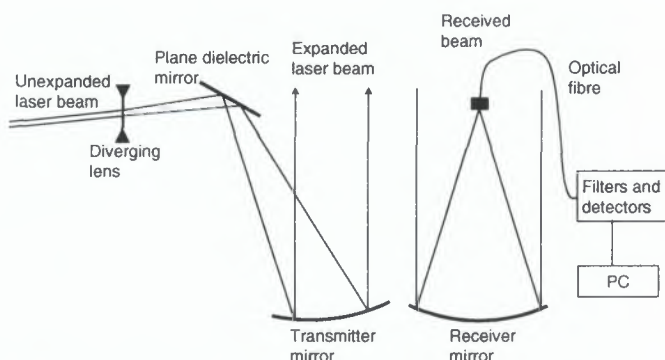


Figure 1: Layout of the lidar system

Since the elastically scattered signals obtained by the lidar are of relatively high intensity, the photomultiplier signal was measured in analog mode. After each laser pulse data were acquired over 4096 time bins at a frequency of 50 MHz, giving a profile with a vertical range of 12.3 km in steps of 3 m. The data from 1000 laser pulses (20 seconds) were averaged and stored, so that profiles were acquired at approximately 30 second intervals. The background signal resulting from the data acquisition electronics was calculated as the mean signal from the last 50 time bins and removed from each profile. The signals were range normalised and calibrated as described in the previous section.

During much of the campaign low cloud was present and under such conditions the UV lidar does not yield particularly useful data. The beam is highly attenuated by the cloud and only a large return from the lower levels of the cloud layer is seen. Also, several improvements were made to the sensitivity of the UV lidar system during the campaign. For these reasons, UV lidar data from 14/10/98, 19/10/98 and 20/10/98 are presented and compared with IR ceilometer data (available for all three days) and 94 GHz radar data (available for 20/10/98 only).

The IR ceilometer is a Vaisala CT75K system which uses an indium gallium arsenide diode laser operating at 905 nm as its source. It operates at a typical peak power of 16 W and a pulse rate of 5 kHz. Its transmitted beam divergence and receiver field of view are both approximately 0.7 mrad. The 94 GHz radar (Galileo) has a peak power of 2 kW and a pulse rate of 6250 Hz. It has an antenna diameter of 0.5 m and a beam divergence of 0.5°. Both the IR ceilometer and the 94 GHz radar system are on loan from ESTEC.

RESULTS AND DISCUSSION

Colour plots showing the results for each day from the available systems are shown in figure 2. The UV lidar data are shown as colour plots of the product $B(h)T^2(h)$ as a function of altitude and time. The IR ceilometer data are plotted using the backscattering coefficient $B(h)$, a correction having been applied for the atmospheric transmittance $T(h)$. The 94 GHz radar data are plotted using the reflectivity Z , converted to decibels. Z is equal to nD^6 , where n is the number density of the scattering particles and D is their diameter. Hence the 94 GHz radar data are effectively plotted on a logarithmic scale, whereas linear scales are used for the UV and IR data.

14/10/98 began with low cloud, typically at around 0 - 1 km. This was seen rather more clearly with the IR ceilometer, because the overlap function of the UV lidar is low at these altitudes. At some times, for example around 12:00, 2 distinct cloud layers at around 0.5 km and 1 km are visible with both systems. The low cloud cleared at around 13:00 and cirrus clouds at around 7 - 8 km became visible, with only occasional low cloud. The cirrus cloud is seen more clearly with the UV lidar, but altitude agreement between the 2

systems is good. In the IR system the return from cirrus is not present in every profile, even though there is no indication of low cloud. These differences are discussed further below. The ice crystals in cirrus clouds can be oriented so as to produce high specular reflectance for wavelengths smaller than the crystal size (as is the case for the UV and IR systems). Specular reflection and other effects due to non-spherical particles enhance the received signal over that expected for Mie scattering alone. Examples can be seen at 14:10 – 14:15 and 14:45 in the UV lidar plot of how the presence of low cloud causes attenuation of the beam and a subsequent reduction in the signal from the higher cirrus cloud. The backscattering coefficient of the low clouds causing the attenuation is underestimated by the UV lidar due to the low overlap function at altitudes of around 1 km, but they can be seen more clearly in the IR ceilometer data. A 95 GHz radar system operated by GKSS [2] which was present at Chilbolton during the campaign had the ability to detect higher level cirrus through low cloud. It indicated that cirrus cloud was also present during the period 10:00 to 11:00, then intermittently until 13:40. After this time the returns from the cirrus layer became much stronger. The clouds were in the altitude range 7 – 10 km. The intermittent signals seen in the UV data centred around 4 km between 13:00 and 14:00 are noise, related to changes in the gain of the detection system.

19/10/98 had intermittent cloud in the range 1-2 km between 10:30 and 15:00, which was seen more clearly by the IR ceilometer. Cirrus cloud became visible at around 15:00 at an altitude of 6.5 – 8 km and was seen more clearly with the UV system. The GKSS 95 GHz radar also began to detect the cirrus layer at around 15:00. The UV lidar returns from the cirrus show some descending band structure to the cirrus clouds and evidence of wind shear at around 15:30 which was also seen by the GKSS system.

Of the 3 days studied, 20/10/98 showed the most cloud, together with precipitation over the periods 12:30 to 13:00 and 15:00 to 15:40. For this day Chilbolton 94 GHz radar data are available over the period 13:55 to 15:35. The height agreement between the UV and IR systems is good, but again the IR system shows stronger signals from low cloud. In particular the precipitation is not detected by the UV lidar system. Examples of higher level cloud returns being obscured when lower level cloud is present are seen, particularly in the period 11:00 to 12:00. The 94 GHz data show similar trends to the two laser systems, but some differences can be seen. The layer at around 1.5 km which appears at around 14:30 in both laser systems is not seen so clearly by the radar system. This would occur if the droplets had a relatively small diameter (of the order of a few microns), as the ratio of radar reflectivity to lidar extinction increases rapidly with droplet size. Throughout its period of measurement the 94 GHz radar shows the layer centred around 4 km as being broader than that seen by the laser systems. This is probably due to the ability of the 94 GHz system to make measurements through thicker cloud layers

and also a consequence of displaying the 94 GHz data using logarithmic units. It clearly shows the precipitation which began at around 15:00, together with a weaker signal from a melting layer at around 2 km. Due to the lower absorption of the 94 GHz signal by the rain cloud it continues to see the upper layer during the precipitation, whereas it is obscured in both laser systems. The ability of systems operating at around 94 GHz to see clouds to greater heights than shorter wavelength systems during periods of relatively high attenuation has been seen by other observers [3].

Figure 3 shows a sample of vertical profiles. The three profiles in each plot indicate changes in the returns over a 10 minute period. Figure 3a shows the UV lidar returns from the cirrus layer seen on 14/10/98. The measured values of $B(h)T^2(h)$ for this cirrus layer are typically ~ 50 times higher than the intermittent values of $B(h)$ measured using the IR ceilometer. In contrast, figures 3b – 3d show vertical profiles recorded on 20/10/98 through a lower cloud layer. The IR ceilometer now shows a slightly stronger return than the UV lidar. The UV beam will be more strongly attenuated in reaching this layer in addition to having a different backscattering coefficient from it, so some differences are to be expected. The cause of the large difference in the relative responses of the UV and IR systems to the two cloud layers is not known. Specular reflection is known to enhance returns from cirrus layers, and this may be different at the two wavelengths. The strength of the specular return will depend on the shape of the crystals, their degree of alignment and the angle of the incident beam to the vertical. Different sizes of the crystals in the two cloud layers may also have an effect. Theoretical studies, both by geometric optics and the T-matrix approach, of lidar backscatter from cirrus are in progress to explain the enhanced UV response to cirrus [4,5]. All the UV lidar plots show a continuous background due to Rayleigh scattering. No such background is detectable in the IR ceilometer data as the IR radiation has a much smaller cross section for Rayleigh scattering (equation 4).

The 94 GHz radar has lower height resolution than the lidar systems. It shows the cloud layer at 4 km as being much broader and extending to higher altitudes. It also shows the peak signal from this layer as occurring at a slightly lower altitude than measured by the lidar systems. This effect has been observed previously and has been attributed to differing microphysical states within the cloud which produce a different response in the two wavelength ranges [3]. The signal at 0.5 km is noise resulting from the end of the transmitted pulse.

CONCLUSIONS

The UV lidar system at Chilbolton was successfully operated during the CLARE campaign to obtain cloud profiles using elastic scattering. The data obtained showed good overall agreement with that from other systems operating at lower frequencies. Due to its high sensitivity it was more useful on days with lesser amounts of cloud, as dense cloud causes

large amounts of scattering of the transmitted beam. It showed high sensitivity to cirrus clouds, with much stronger returns than those from the IR ceilometer. The 94 GHz radar was capable of providing useful information through thicker cloud layers but without the sensitivity to finer structures which is available using lidar. The experiment also highlighted areas needing improvement in the UV lidar system and work is in progress to reduce the divergence of the transmitted beam, to increase the overlap function at low altitudes and to enable simultaneous measurements of Raman and elastic scattering.

REFERENCES

- [1] A. J. Gibson, K. H. Craig and U. M. Yilmaz, "Remote Sensing of Radio Refractivity by Lidar", Proceedings 10th International Conference on Antennas and Propagation, IEE Conference Publication No. 436, pp. 2.325 – 2.328, 1997
- [2] M. Quante, O. Danne, H. Lemke, D. Milferstädt and E. Raschke, "The GKSS 95 GHz Cloud Radar: System Description and Potential Contributions in Support of the Earth Radiation Mission", Proceedings Workshop on Synergy of Active Instruments in the Earth Radiation Mission, ESA EWP-1968, GKSS 98/E/10, pp. 75 – 80, 1997
- [3] C. Weitkamp, O. Danne, H. Flint, W. Lahmann, M. Quante, E. Raschke and F. E. Theopold, "Lidars for Cloud Measurements at GKSS and first Radar – Lidar Comparisons", Proceedings Workshop on Synergy of Active Instruments in the Earth Radiation Mission, ESA EWP-1968, GKSS 98/E/10, pp. 87 – 90, 1997
- [4] A. Macke, "Scattering of Light by Polyhedral Ice Crystals", *Appl. Opt.* Vol. 32, pp. 2780 – 2788, 1993
- [5] M. I. Mishchenko, D. J. Wielaard and B. E. Carlson, "T-matrix Computations of Zenith-Enhanced Lidar Backscatter from Horizontally Oriented Ice Plates", *Geophys. Res. Lett.* Vol. 24, No. 7, pp. 771 – 774, 1997

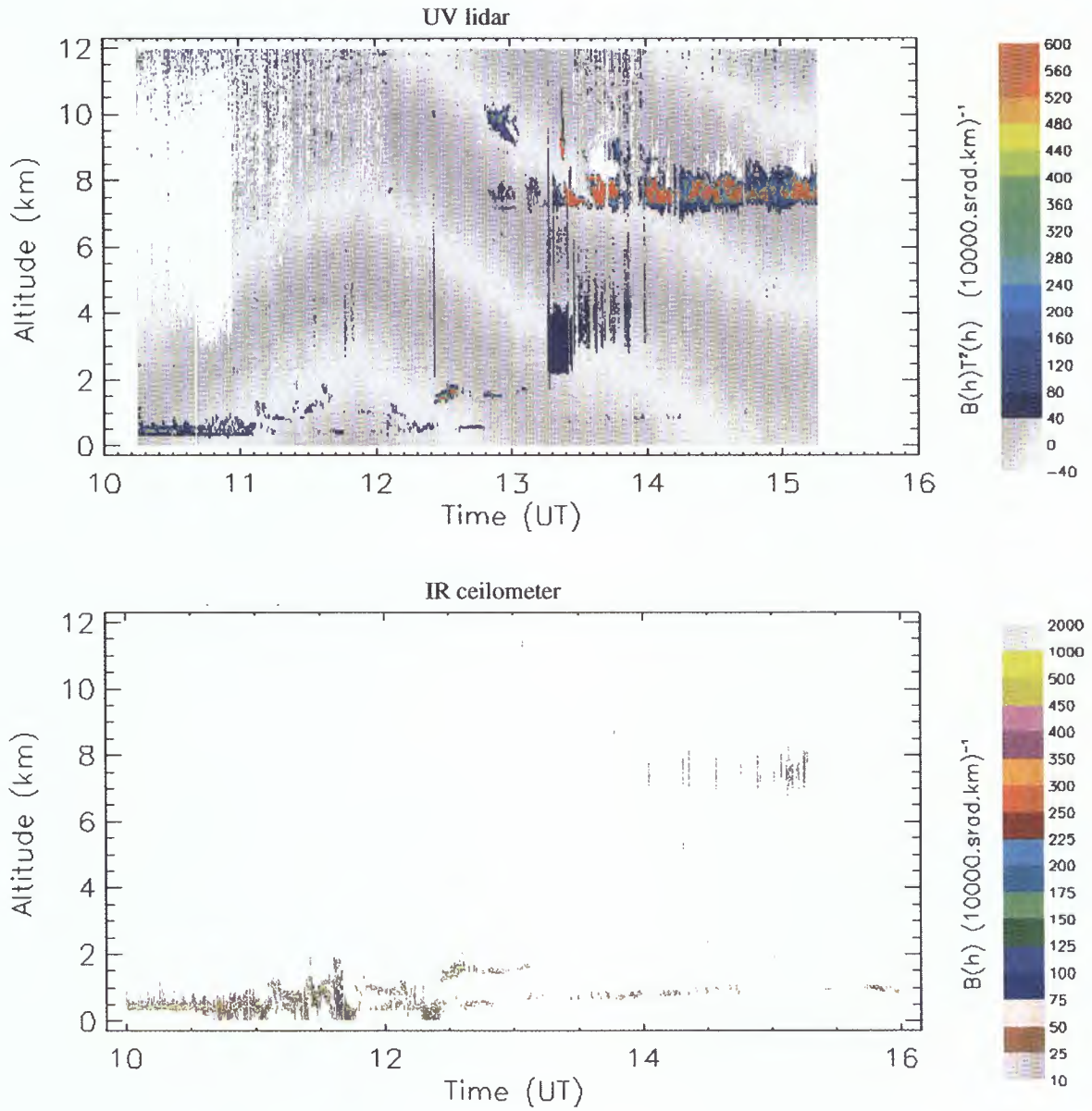


FIGURE 2a: UV lidar and IR ceilometer data from 14/10/98

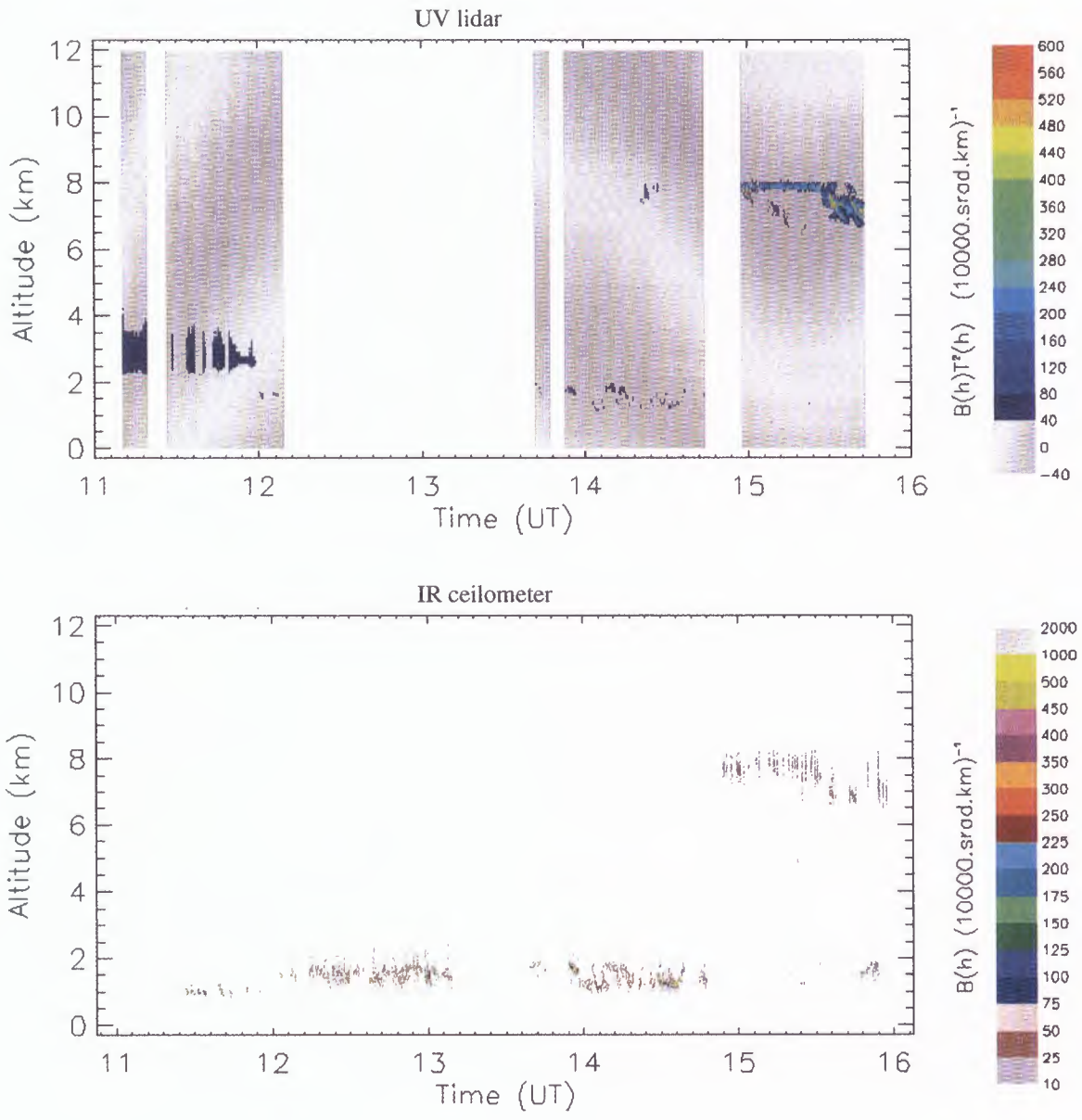


FIGURE 2b: UV lidar and ceilometer data from 19/10/98

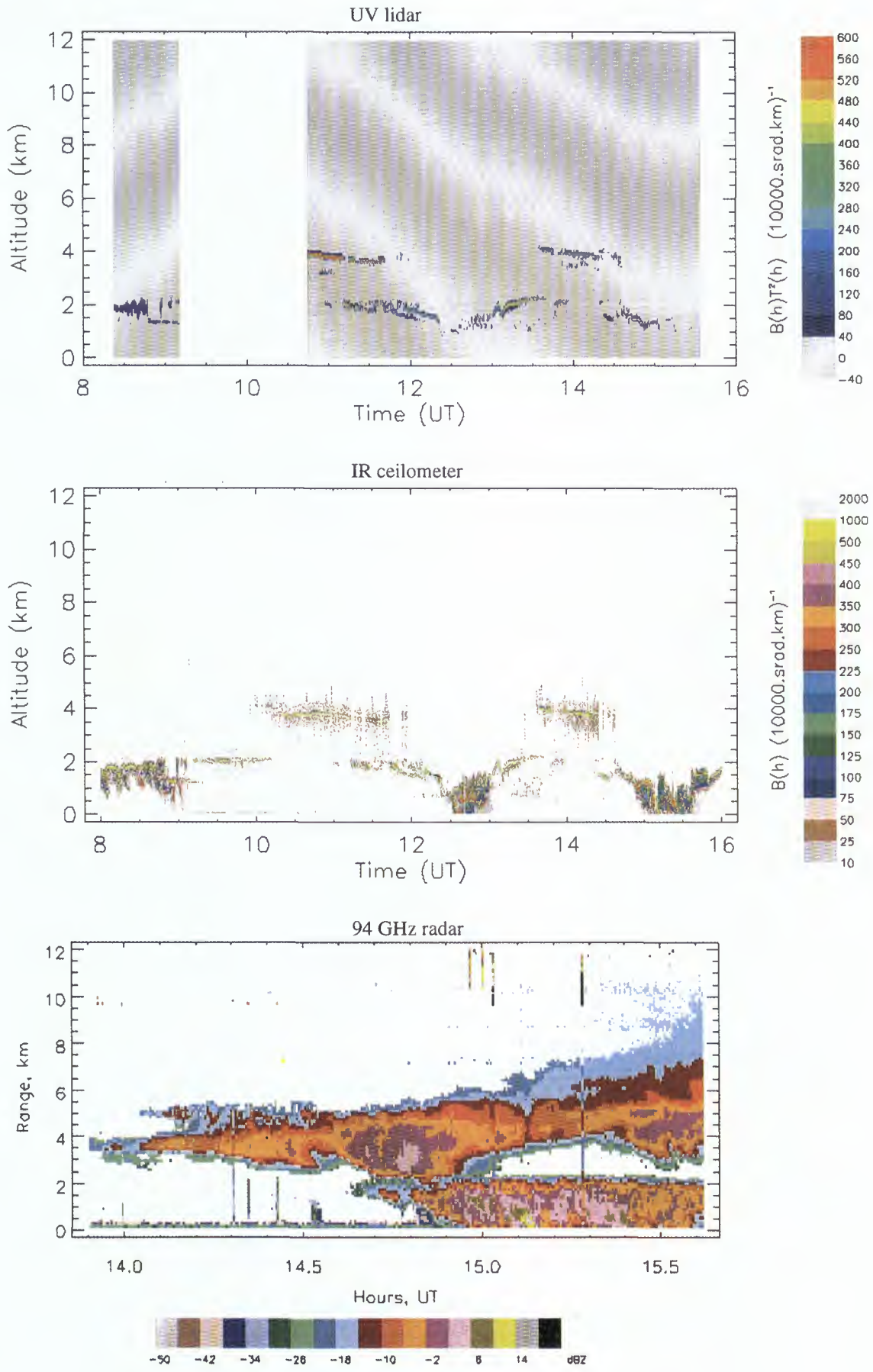


FIGURE 2c: UV lidar, ceilometer and 94 GHz radar data from 20/10/98

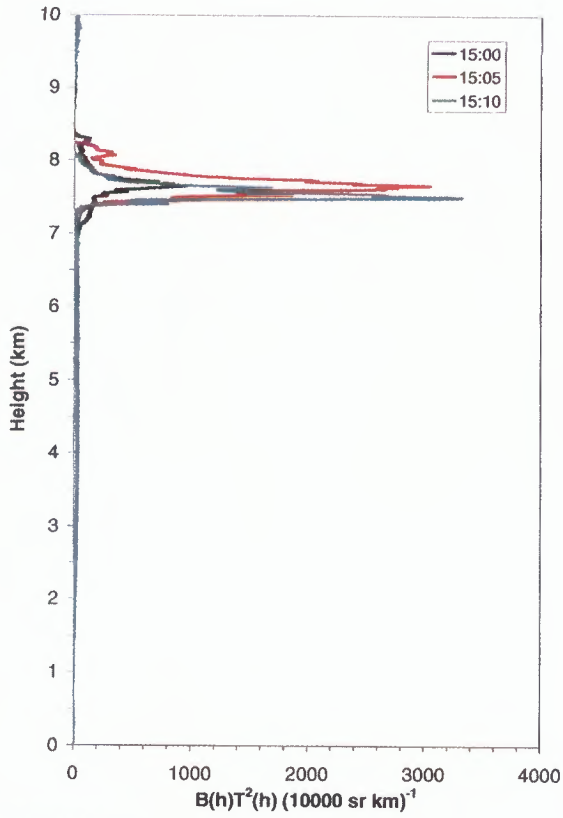


FIGURE 3a UV lidar 14/10/98

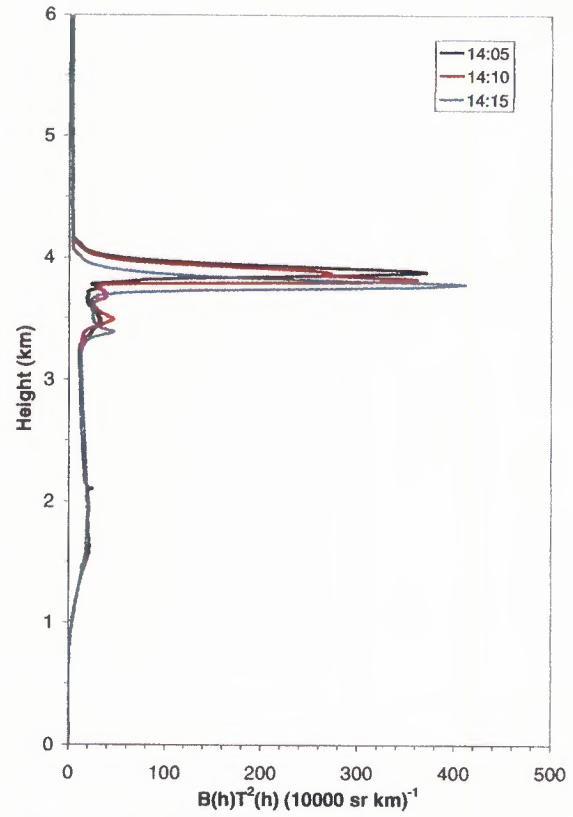


FIGURE 3b UV lidar 20/10/98

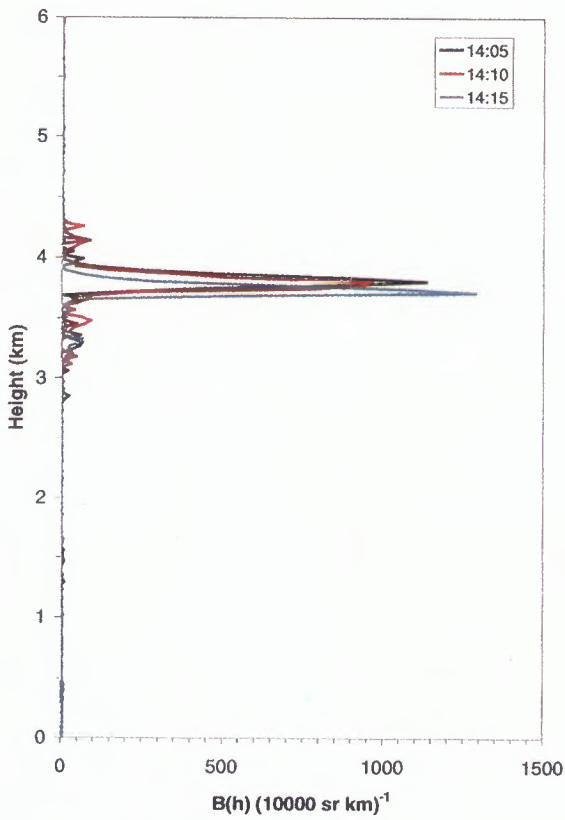


FIGURE 3c IR ceilometer 20/10/98

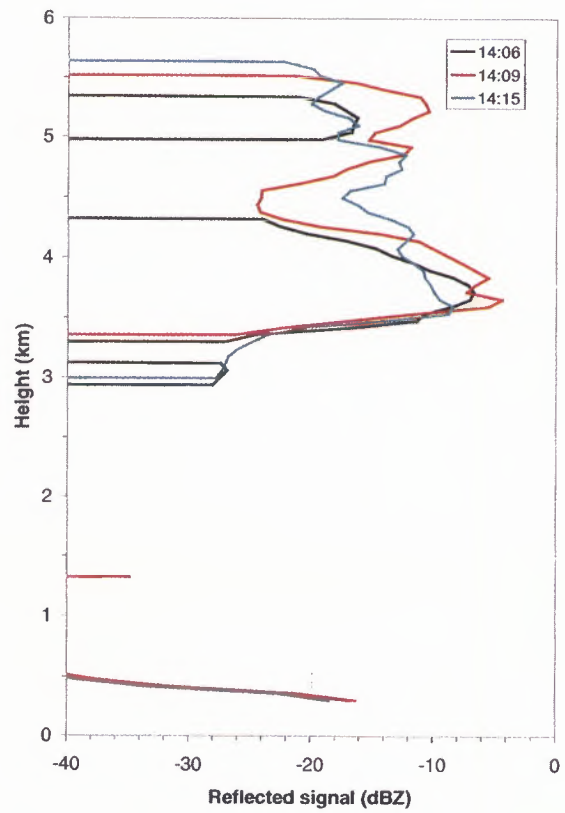


FIGURE 3d 94 GHz radar 20/10/98

FIGURE 3 Vertical profiles from 14/10/98 and 20/10/98 from the different measurement systems

Liquid Water Retrieval



Observations of warm and cold clouds using the airborne backscattering lidar LEANDRE 1 during CLARE, part 1 : Lidar data analysis

J. Pelon , V. Trouillet , C. Flamant,
IPSL, Service d'Aéronomie du CNRS, 4 Place Jussieu, B 104, F-75252 Paris, France

H. Chepfer, L. Sauvage, V. Noel, P. Flamant
IPSL, Laboratoire de Météorologie Dynamique, Ecole Polytechnique, 91128 Palaiseau, France

Phone : 33.1.44.27.37.79, Fax : 33.1.44.27.37.76, Email : Jacques.Pelon@aero.jussieu.fr

INTRODUCTION

The analysis of cloud properties from lidar measurements requires to account for multiple scattering and detection limitations which alter the signal as compared to the ideal response.

The retrieval of optical and microphysical parameters of dense clouds from lidar measurements is usually limited to values smaller than 4 (Spinhirne et al., 1989). However, in denser clouds, the extinction coefficient at cloud top can be retrieved after correction. For semi-transparent ice clouds, the multiple scattering contribution is mainly controlled by diffraction and strongly depends on crystal size. The analysis method is thus dependent on the characteristics of the cloud particles.

In this paper we describe methods used to derive cloud optical parameters from CLARE lidar data as presented in the introduction paper. The importance of critical parameters such as the multiple scattering factor is emphasised.

LIDAR SIGNAL ANALYSIS

In direct detection, the detected lidar signal is proportional to the optical intensity backscattered by the atmosphere. It can be written as the double convolution of the emitted laser pulse power $P_e(t)$ as a function of time t , with the impulse response of the atmosphere $\frac{\beta_a(z)}{z^2}$ as a function of altitude z , and the detection response $D(t)$

$$S(z, t) = K_s \left[\frac{\beta_a(z)}{z^2} \otimes P_e(t) + P_b(t) \right] \otimes D(t) + S_b(t) \quad (1)$$

where P_b and S_b are additive optical and electrical noises, respectively. K_s is the overall detection efficiency of the lidar system. In the LEANDRE 1 data analysis, the value of this efficiency factor is determined during upper level flights with reference to molecular or particular extinction so that S corresponds to the attenuated backscattering coefficient ($\text{km}^{-1} \cdot \text{sr}^{-1}$).

As the light pulse duration of the LEANDRE 1 laser source is very short as compared to the signal sampling time constant of the detection electronics, only the second convolution in Eq. (1) is considered. Following the analysis previously developed for EUCREX data analysis (Pelon et al., 1999), this convolution product can be

estimated from the knowledge of the detection bandwidth and of the multiple scattering contribution parametrized as proposed by Platt (1973). In this formalism, the multiple scattering factor η defines the reduction of the real cloud extinction coefficient α ($\eta < 1$). It can be estimated from the attenuated backscatter coefficient $\beta_a(z)$ integrated over the geometrical cloud depth (Platt, 1973) and accounting for the detection filtering. Assuming a first order frequency response of the detection system and a constant backscatter to extinction ratio k , the in-cloud attenuated backscatter coefficient is given as a function of altitude z^* above cloud base ($z^* = z - z_b$) as

$$\beta_a(z^*) = \frac{\beta}{(1 - 2\eta\alpha z_s)} \left[\exp(-2\eta\alpha z^*) - \exp\left(-\frac{z^*}{z_s}\right) \right] \quad (2)$$

where z_s is the equivalent height scale of the detection system corresponding to the electronic bandwidth. The first term in Eq. (2) corresponds to the two-way atmospheric transmission, the second term to the system response.

In the case of weak cloud extinction as in semi-transparent clouds, this equation reduces to the standard lidar equation

$$\beta_a = \beta \exp\left(-2 \int_{z_0}^z \eta \alpha z' dz'\right) \quad (3)$$

Critical cloud parameters to be retrieved are multiple scattering parameter η , the backscatter-to-extinction ratio k and α or β . We will discuss methods to derive such quantities for dense and semi-transparent clouds using lidar measurements only.

CLOUD BOUNDARIES

Values of β_a much larger than molecular scattering correspond to cloud scattering. To compare cloud boundaries measured by lidar and radar, a standard threshold algorithm based on the value of the attenuated backscatter gradient can be used to derive cloud base and top heights (Trouillet, 1997) from nadir and zenith measurements. For nadir measurements over dense clouds, top altitude can be precisely derived due to the large signal gradient observed near cloud top and the lack of attenuation above (see Figure 1 of the introduction paper). Only in semi-transparent clouds can the cloud base (top)

be observed from nadir (zenith) measurements due to the high extinction of the lidar beam caused by cloud scattering (transmission rapidly decreases to zero).

STRATOCUMULUS CLOUD PARAMETERS

In dense cloud, the detection bandwidth may significantly contribute to the signal amplitude limitation, and this effect needs to be corrected. This can be done using the formalism presented in the previous section.

Integrating the apparent backscattering coefficient given by Equation (2) allows to derive the apparent backscatter to extinction ratio $k_a = k/\eta$ from the asymptotic value of the integrated attenuated backscatter $\Gamma(z)$ which at large optical thickness is

$$\Gamma_\infty = k/2\eta \quad (4)$$

In the case of water droplets, a constant backscatter to extinction ratio $k = 0.057 \text{ sr}^{-1}$ is measured in clouds, independently of the cloud droplet distribution (Pinnick et al., 1983). The asymptotic value of $\Gamma(z)$ thus allows to derive the average multiple scattering factor with a good accuracy (about 20 %).

The true extinction coefficient α at cloud top is then retrieved from the value of the maximum apparent backscattering coefficient after solving Equation (2). A linear relationship between backscattering and extinction coefficients, $\beta = k\alpha$, is assumed as for lidar measurements they both are related to the second order moment of the size distribution (see part 2). However, in case of large amplitude limitation caused by the finite detection bandwidth, the use of the inverse relationship may lead to large errors in the extinction values.

In stratocumulus clouds, updrafts and downdrafts are observed as a result of internal instability. In updrafts, adiabatic motions take place so that the liquid water content W increases linearly with height above cloud base altitude z_b

$$W = C_w z_t^* = C_w (z_t - z_b) \quad (5)$$

Once updraft is identified from cloud top boundaries, the effective radius at cloud top can be directly retrieved from lidar measurements alone as (Pelon et al., 1999)

$$r_{e(z_t^*)} = \frac{3}{4\rho} Q_e \frac{C_w z_t^*}{\alpha(z_t^*)} \quad (6)$$

Q_e is the scattering efficiency. It is close to 2 if the average radius of droplets is assumed to be much larger than the wavelength (Pinnick et al., 1983). From the value of C_w at cloud temperature ($C_w = 0.015 \text{ g/m}^4$), a value of the effective radius equal to $6 \mu\text{m}$ can be estimated for mission M2 (13 October). Assuming the effective radius weekly varies at cloud top, the liquid water variation at cloud top can be estimated from the retrieved extinction

coefficient using Eq. (5) and (6). Figure 1 shows the variation of the cloud top extinction coefficient obtained as a function of cloud top altitude for the stratocumulus observed during mission M2. It is proportional to the liquid water content ($W(z) = 4 \cdot 10^{-3} \alpha(z)$). The straight line represents the adiabatic increase in W with height. Data processed over 1s (100 m) have been filtered over 5 points using a median filter.

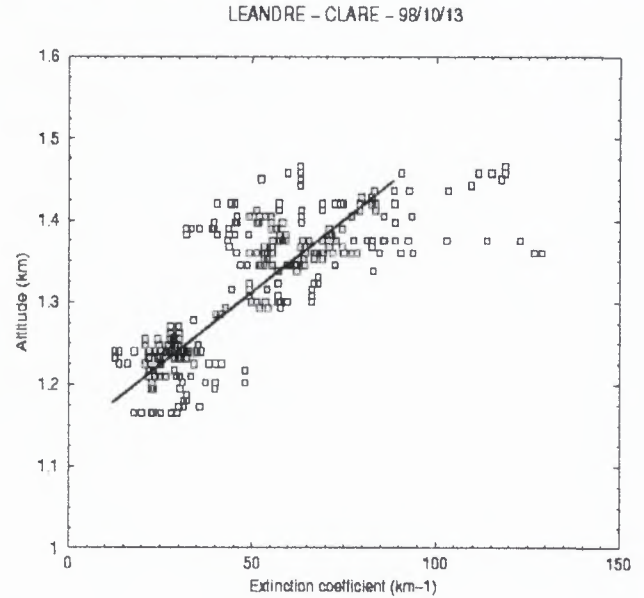


Figure 1 : Liquid water content variation at cloud top estimated from lidar measurements during mission 2 (13 October) using a constant value $r_e = 6 \mu\text{m}$.

It is seen from Figure 1, that in this case the cloud base can be estimated from cloud top observations, as large variations in the top height are observed due to entrainment.

CIRRUS CLOUDS

In the case of cirrus clouds the attenuated backscattering β_a coefficient is given by the simplified lidar equation (3).

The determination of the extinction coefficient by lidar requires to derive the backscatter-to-extinction ratio k and to account for the diffraction and scattering contribution in the lidar signal to estimate η . k and η depend on crystal shape and size.

A first step is to determine the apparent optical thickness. In semi-transparent clouds, the apparent optical thickness $\tau_a = \eta\tau$ can be directly determined from the measurements, identifying reference zones where the backscattering coefficient is known above and below the cloud (Pelon et al., 1996).

The vertically averaged apparent extinction to backscatter ratio $k_a = k/\eta$, can then be directly retrieved from the

backscattering coefficient integrated over the cloud depth Γ_c , which from Eq. (3) writes

$$\Gamma_c = \frac{k}{2\eta} [1 - \exp(-2\eta\tau)] \quad (7)$$

The value $\Gamma_\infty = k/2\eta$ is deduced from the retrieval of several estimates of the apparent optical thickness (Pelon et al., 1996, Sauvage et al., 1999).

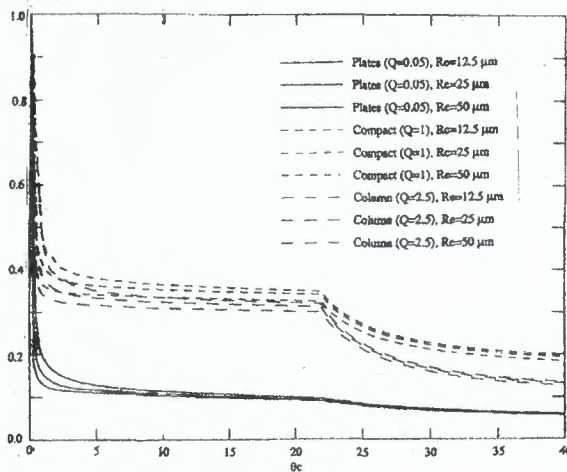


Figure 2 : Estimated multiple scattering parameter η as a function of field of view for different crystal types.

In order to derive k , representative of the crystal shape, the value of the parameter η must be known. Ray tracing and diffraction calculations made to estimate η (Chepfer et al., 1999) show that for small field of views allowing only small scattering angles, η is highly dependent on the size but also on the shape of the crystal. This is shown on Figure 2, where η is estimated under the hypothesis of double scattering approximation.

The value of η is observed to be somewhat different for plates and the error is about 20 to 40 % depending on the crystal characteristics and lidar geometry. In figure 2, one can see that for the crystals studied most the energy scattered is in the diffraction peak, so that at angles larger than the diffraction peak, the variation of η is small. This means that for space observations, the value of η may be similar to the one of ground-based or airborne ones in specific conditions.

The total backscatter coefficient is the sum of both molecular and particular scattering. It can be retrieved inverting Eq. (3) with a forward inversion procedure (Klett, 1985)

$$\beta(\lambda, z) = \frac{\beta_a(\lambda, z)Q(\lambda, z)}{1 - 2 \int_z^{z_a} \frac{1}{\varphi_p(\lambda, z')} \beta_a(\lambda, z') Q(\lambda, z') dz'} \quad (8)$$

Where z_a is the altitude of the emission. $Q(\lambda, z)$ is the correction related to the differential molecular optical thickness calculated from the vertical profile of the molecular backscatter coefficient. The extinction coefficient can then be obtained using (8) and $k=\phi(\lambda, z)$. The optical thickness is calculated as the integral of the extinction coefficient from the emitter up to the studied altitude. Figure 3 gives the average value of the extinction coefficient resulting from the inversion of lidar measurements made over Chilbolton during M3 (14 October).

The value of the apparent backscatter to extinction ratio retrieved from the data analysis ($k_a=0.043 \text{ sr}^{-1}$) has been used. The multiple scattering factor has been taken equal to 0.4, assuming the occurrence of large crystals (compact) as observed from C130 in situ measurements (see Francis et al., this report).

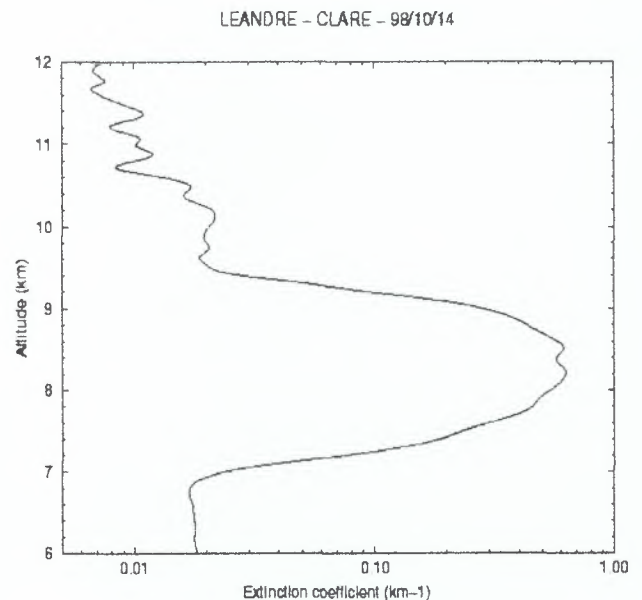


Figure 3 : Vertical profile of the extinction coefficient obtained after lidar signal inversion on 14 October.

CONCLUSION

Lidar measurements in stratocumulus can be analysed using a correction method to retrieve optical and microphysical cloud properties. Due to the high spatial resolution of lidar measurements, convective cells within the stratocumulus deck can be clearly evidenced. In such cells, values of the extinction coefficient larger than 10 km^{-1} at cloud top (corresponding to liquid water contents of several tenths of g/m^3) can be retrieved.

In semi-transparent cold clouds, the apparent optical thickness and the apparent backscatter-to-extinction ratio can be derived from lidar measurements.

In both cases the multiple scattering factor can be estimated to retrieve cloud optical parameters. It is a

limitating factor in the accuracy of the retrievals, and a poor knowledge of the multiple photon path length in dense clouds or crystal shape in cold cloud may lead to errors of the order of 30 %.

ACKNOWLEDGMENTS

ARAT data were acquired and processed with the support of the LEANDRE and INSU/DT aircraft teams which the authors want to particularly thank.

REFERENCES

- Chepfer H., G. Brogniez, L. Sauvage, P. H. Flamant, V. Trouillet, J. Pelon, 1998 : Remote sensing of cirrus radiative properties during EUCREX'94. Case study of 17 april 1994. Part 2 : Microphysical modelling, *Mon. Wea. Rev.*, 127, 504-518.
- Klett J. D., 1985 : Lidar inversion with variable bacscatter to extinction ratios, *Appl. Opt.*, 1638-1643.
- Pelon J, 1996 : French contribution to E-LITE'94 : Comparative measurements with the airborne backscatter lidar LEANDRE-1 Proceeding of the final E-LITE workshop, esa WPP-107.
- Pinnick R. G., S. G Jennings., P. Chyleck, C. Ham, W. T. Grandy, 1983 : Backscatter and extinction in water clouds, *J. Geophys. Res.*, 88, 6787-6796.
- Platt C. M. R, 1973 : Lidar and radiometric observations of cirrus clouds, *J. Atmos. Sci.*, 30, 1191-1294.
- Spinhirne J., D., R. Boers, and W. Hart, 1989 : Cloud top liquid water from lidar observations of marine stratocumulus, *J. Appl. Meteor.*, 28, 81-90.
- Sauvage L., H. Chepfer, V. Trouillet, P. H. Flamant, G. Brogniez, J. Pelon, F. Albers, 1998 : Remote sensing of cirrus radiative properties during EUCREX'94. Case study of 17 April 1994. Part 1 : Observations, *Mon. Wea. Rev.*, 127, 486-503.
- Trouillet V., 1997 : Etude de l'apport d'un lidar rétrodiffusion spatial pour la reposition des paramètre nuageux et de flux à la surface, Thèse de l'Université Pierre et Marie Curie, 289pp.

Observations of warm and cold clouds using the airborne backscattering lidar LEANDRE 1 during CLARE, part 2 : synergism with radar measurements

J. Pelon¹, J. Testud², M. Quante³, P. Francis⁴, A. Guyot², O. Danne³, V. Trouillet¹,
H. Chepfer⁵, V. Noel⁵, P. Flamant⁵, D. Leon⁶, S. Aimov⁶, G. Vali⁶

1-IPSL-Service d'Aéronomie du CNRS, 4 Place Jussieu, B 104, F-75252 Paris, France

2-IPSL-Centre d'Etude des Environnements Terrestres et Planétaires, 78 Vélizy, France

3-GKSS Research Centre, Institute for Atmospheric Physics, D-21502 Geetacht, Germany

4-UK Meteorological Office, Farnborough, Hampshire, GU14 6TD, UK

5-IPSL-Laboratoire de Météorologie Dynamique, Ecole Polytechnique, 91128 Palaiseau, France

6-University of Wyoming, USA

Phone : 33.1.44.27.37.79, Fax : 33.1.44.27.37.76, Email : Jacques.Pelon@aero.jussieu.fr

INTRODUCTION

Cloud parameters such as the extinction coefficient, the backscatter-to-extinction ratio or the depolarization factor can be retrieved from lidar measurements in dense or semi-transparent clouds as presented in the previous papers. Some microphysical parameters can be retrieved in dense clouds using physical hypotheses as described in part 1. However, it is expected that the synergism between lidar and radar measurements would help retrieving more accurately such parameters. Such a synergism is discussed in this paper in the frame of an approach similar to the one previously used to combine radar and lidar measurements (Intieri et al., 1993), although the formalism is slightly different.

ANALYSIS OF CLOUD PARAMETERS FROM LIDAR MEASUREMENTS

The cloud extinction coefficient α is defined as the extinction cross-section averaged over the whole particle size distribution. It can be written as a function of the extinction efficiency Q_e so that

$$\alpha(z, \lambda) = \pi \int_0^{\infty} Q_e(r, \lambda) r^2 N(r) dr \quad (1)$$

Q_e depends on the particle radius r and wavelength λ . The size parameter $x = 2\pi r/\lambda$ defines the scattering regime. For spheres, Mie theory shows that for cloud droplets Q_e is maximal for $x \approx 6$ or $r/\lambda \approx 1$ at visible wavelengths. At the measurement wavelength ($\lambda = 532$ nm), this corresponds to $r = 0.5 \mu\text{m}$. If we consider its average value over the droplet size distribution, Q_e differs from 2.1 by less than 5 % as the mean droplet radius varies between 2 and 100 μm (Pinnick et al., 1983). This range encompasses the droplet distributions in the observed clouds (Francis et al., this report). Assuming such a constant value of Q_e , the extinction coefficient α is proportional to the second order moment of the droplet size distribution. This approximation (known as the geometrical approximation) is also valid for crystals.

The liquid water content W is defined as the third order moment of the size distribution, whereas the effective diameter is defined as the ratio of the third to the second order moments. The extinction coefficient obtained from lidar measurements after multiple scattering correction (see part 1) can thus be written as the ratio of the liquid (or ice) water content (W) and the effective radius (r_e) of the cloud particle distribution

$$\alpha = 3 Q_e / 4 \rho W / r_e \quad (2)$$

where ρ is the water (ice) density. When the size distribution includes two independent modes (precipitating cloud for example) the extinction coefficient can be written as the sum of two contributions such as given by Eq. (2) for each mode.

ANALYSIS OF CLOUD PARAMETERS FROM RADAR MEASUREMENTS

Cloud droplets and small ice crystals have sizes much smaller than the 3mm wavelength of Kestrel or Miracle radar used during CLARE, so that Rayleigh scattering applies to radar measurements in most clouds. For an operation at a frequency of 95 GHz, the Rayleigh scattering hypothesis is verified for a typical maximal diameter of 200 μm . It can thus be used without restriction for non-precipitating clouds. Other theories need to be used when drizzle is occurring in warm clouds and in presence of large crystals in mixed phased and cold clouds.

In this preliminary analysis, we will use the Rayleigh approximation as a first hypothesis. The limitations of this approximation will be discussed in the last section.

As for the lidar signal, integrated parameters such as reflectivity Z can be deduced from the backscattering efficiency Q_b , in an equation similar to Eq. (1). However in the Rayleigh theory the scattering efficiency varies as r^4 so that the radar reflectivity is proportional to the 6th order moment of the droplet distribution.

We will also assume particles to follow a gamma size distribution as given by

$$N(D) = N_0 D^\mu \exp(-\Lambda D) \quad (3)$$

It is further possible using μ and Λ parameters to make sensitivity tests.

Assuming μ is an integer, the equivalent radar reflectivity Z_e (Z_e is used as both water or ice clouds are considered) can be written as a function of W (representing both water and ice contents) and r_e and of the parameter μ of the distribution

$$Z_e = K^2 \left(\frac{6Wr_e^3}{\pi\rho} \right) \frac{(\mu+6)!}{(\mu+3)!(\mu+3)^3} \quad (4)$$

where K is depending on the dielectric constants of water or ice. It is to be noted that in this expression the dependence with μ is weak (about 10 % for μ varying between 1 and 3), which reduces the impact of errors in the size distribution. K^2 is equal to 1 for water but only 0.19 for ice at 20 °C (Lhermitte, 1988).

This expression is close to the one derived by Atlas et al. (1995), although we are referring here to the effective radius and not to the average diameter of the size distribution.

POTENTIAL OF COMBINED RADAR AND LIDAR MEASUREMENTS

Simultaneous measurements by lidar and radar are thus representative of both parameters W and r_e . Their combination allows the representativeness of droplet distribution with gamma functions to be tested. The measurements conducted in the frame of CLARE can be analysed in terms of cloud microphysics combining both radar and lidar signals. Expressions for the total number of droplets N_T , the liquid water concentration W and the effective radius r_e can be derived from Eq. (2) and (4) so that

$$N_T = \frac{(\alpha/2\pi)^{3/2} \mu! [(\mu+6)!]^{1/2}}{Z_e^{1/2} [(\mu+2)!]^{3/2}}$$

$$W = \frac{\pi}{6} \rho_w \left(\frac{\alpha}{2\pi} \right)^{3/4} Z_e^{1/4} \frac{[(\mu+3)!]}{[(\mu+6)!]^{1/4} [(\mu+2)!]^{3/4}} \quad (5)$$

$$r_e = \frac{Z_e^{3/4}}{(\alpha/2\pi)^{1/4} [(\mu+6)!]^{1/4} [(\mu+2)!]^{3/4}}$$

The retrieval of W and r_e is less sensitive to errors in measurements than N_T , as the exponent of the extinction or reflectivity is smaller than 1. A low sensitivity to μ is observed as previously shown (Intieri et al. 1993). Accurate values of Z and α however need to be used.

These relationships also hold for ice accounting for the index change. The decrease in ice density with diameter

must be also considered at large diameter as derived from in situ measurements (Brown and Francis, 1994).

RESULTS

Equations (5) can be used to derive cloud parameters such as liquid (ice) water content and effective radius. A diagram allowing to directly derive these parameters can be also constructed from the same equations. A value of μ equal to 2 has been considered in this analysis.

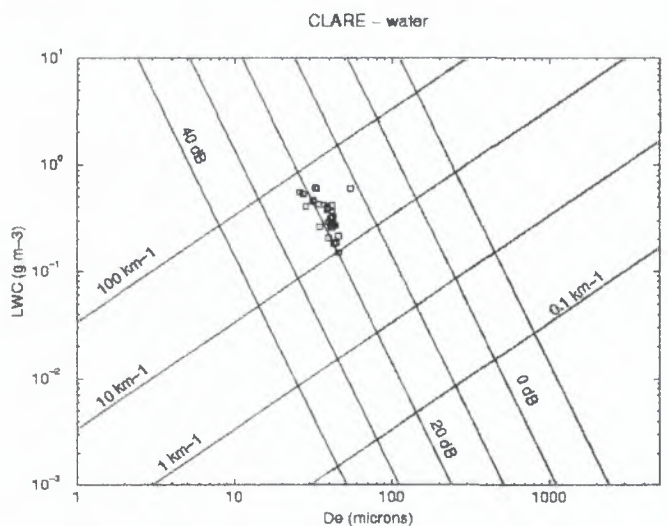


Figure 1 : M2 (13 October) observation results on stratocumulus plotted in Z - α diagram as a function of water content and effective diameter.

Lidar extinction coefficient and radar reflectivity have been obtained from LEANDRE 1 and Kestrel onboard the ARAT for the stratocumulus case of mission M2 (13 October). Results are plotted in Figure 1 in the Z - α diagram. Kestrel radar reflectivity has been re-calibrated by subtracting 11 dBZ according to post-campaign analysis (Guyot et al., this report). Maximum values are about -18 dBZ, whereas those of the extinction coefficient are within 75 km^{-1} . This corresponds to liquid water content at cloud top close to 0.3 g/m^3 in agreement with lidar data analysis presented in part 1. The effective radii are much larger than expected from lidar and in situ measurements (see Francis et al., this report). It is to be noted that the reflectivity obtained for the stratocumulus is still high and may correspond to the formation of drizzle droplets (Fox and Illingworth, 1997).

Data obtained on cirrus clouds observed on 14 October with the ground-based MIRACLE radar and the airborne lidar LEANDRE1 over Chilbolton are plotted in Figure 2. Measured radar reflectivity Z is -12 dBZ on average, after correction of attenuation (+1 dB) and recalibration (+2 dB). As the measured reflectivity is given with respect to water, the equivalent reflectivity corresponding to ice is about 7 dB smaller than Z , e.g. $Z_e = -19$ dBZ. Values of the corrected reflectivities are plotted with respect to the lidar ones (the average lidar extinction is about 0.8 km^{-1}) in Figure 2. The retrieved ice water contents are about 0.02 g/m^3 for an effective diameter close to 130 μm .

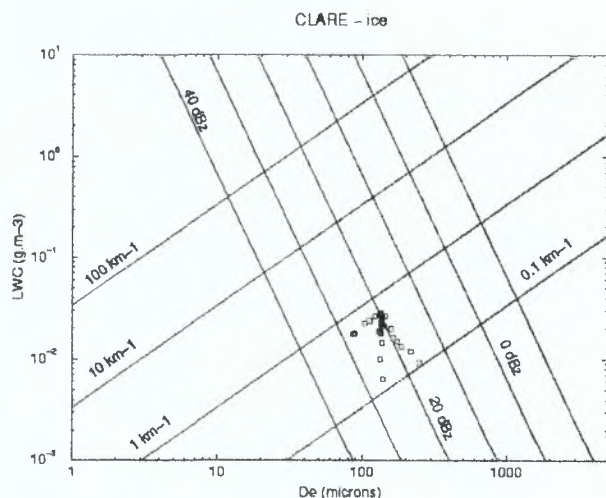


Figure 2 : M3 (14 October) observation results on cirrus plotted in Z- α diagram as a function of water (ice) content and effective diameter.

These values are comparable to average in situ measurements measured by the C130 during this mission (in situ IWC values are ranging from 0 to 0.04 g m^{-3} and effective radius of 50 μm at a 7.6 km altitude, see Francis et al., this report for more details).

DISCUSSION

Gamma distributions such as given by Eq. (3) have been observed to fit the size distribution of FSSP (small size droplets) in situ measurements in warm clouds. However, large size droplets have been measured during CLARE (Francis et al., this report), which do not allow the gamma distribution to be fully representative of the size distribution. The size distribution would be then better fitted by the sum of two gamma distributions (gamma and exponential distributions in fact). In such a case, lidar extinction becomes directly proportional to the sum of the two ratios LWC/r_e , related to the distribution sizes of both droplet distributions in cloud as their modal diameters ranges are different. It is the same for radar reflectivity as expressed in terms of the product $\text{LWC} \cdot r_e^3$. As the liquid water content in the larger size mode is smaller than the liquid water content in the smaller size mode, and as its effective radius is much larger (50 μm and above), extinction due to drizzle can be neglected for the in-cloud lidar signal analysis. However the contribution to the radar reflectivity is expected not to be negligible as the dependence in r_e may partly compensate the decrease in LWC. This contribution may be estimated to several dBZ.

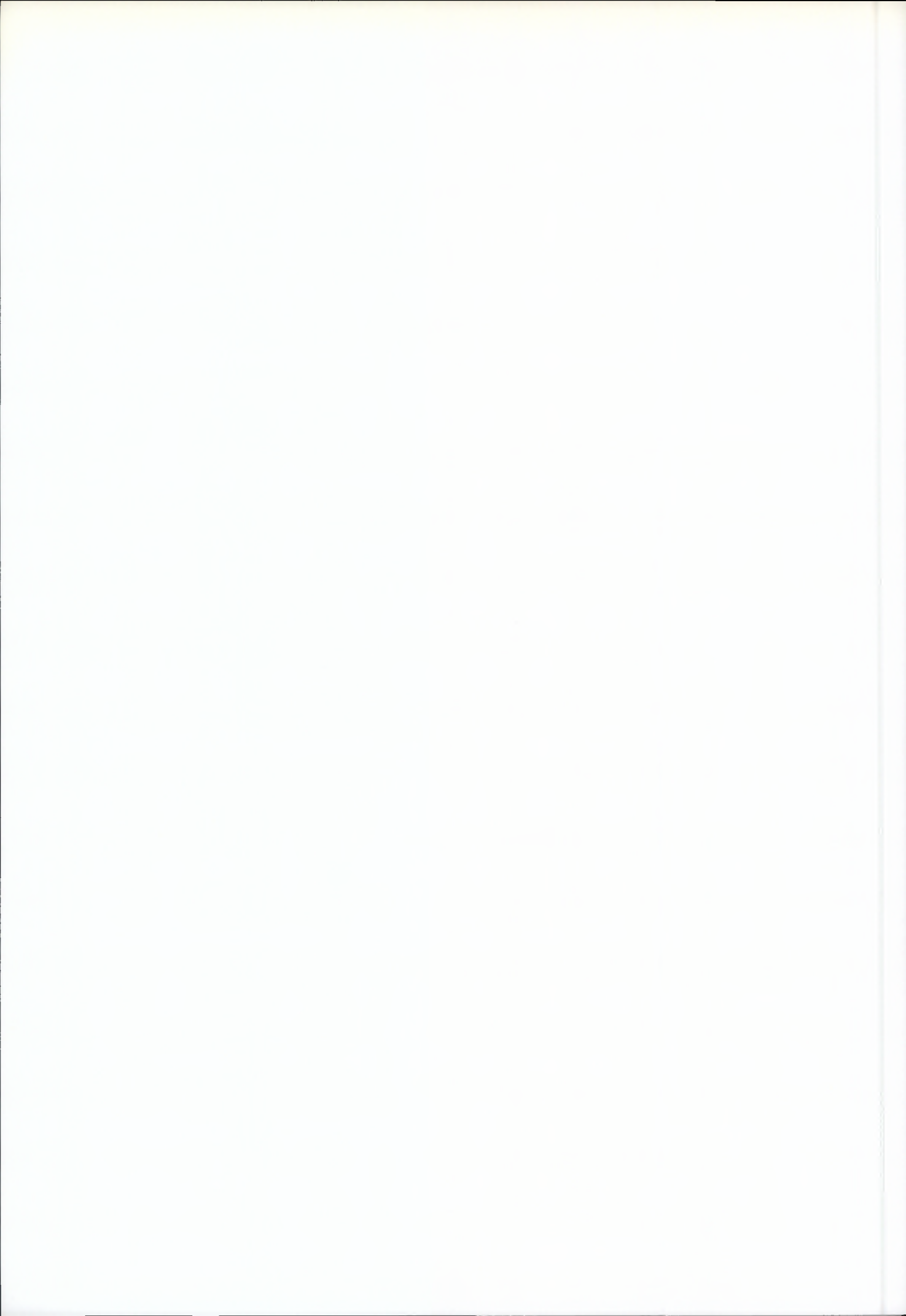
For precipitating clouds the effective radius of the drizzle size distribution is larger. This dependence shows that reflectivities will be about 10 to 20 dBZ higher if drizzle is occurring into the cloud. The occurrence of large droplets may thus explain the difference between remote sensing and in situ observations. The relationships used in the previous sections are no longer

valid. Doppler information may be used to filter out precipitation contribution and use the same procedure.

For cirrus clouds, the problem is more complex as falling velocities are small and non-spherical shapes precludes Mie type calculations. In the present approach ice density has been kept constant and Rayleigh scattering, applicable up to diameters of a few hundred microns, has been used as a first approximation. Despite these limitations a rather good agreement has been obtained. Dispersion may be attributed to the time and space difference. More coincident measurements are to be made to better compare results from remote sensing and in situ techniques.

REFERENCES

- Atlas D., S. Y. Matrosov, A. Heymsfield, M-D. Chou, D. Wolf, 1995 : Radar and radiation properties of ice clouds, *J. Appl. Meteor.*, 34, 2329-2344.
- Brown P. R. A. and P. Francis, 1995 : Improved measurements of the ice water content in cirrus using a total-water probe, *J. Atm. Ocean Tech.*, 12, 410-414.
- Fox N. I. and A. J. Illingworth, 1997 : The retrieval of stratocumulus cloud properties by ground-based cloud radar, *J. Appl. Meteor.*, 36, 485-491.
- Intieri J., G. L. Stephens, W. L. Eberhard and T. Uttal, 1993 : A method for determining cirrus cloud particle sizes using lidar and radar backscatter technique, *J. Appl. Meteor.*, 32, 1074-1082.
- Lhermitte R. M., 1988 : Cloud and precipitation remote sensing at 94 GHz, *IEEE Trans. Geosci. Rem. Sens.*, 26, 207-216.



Stratocumulus Liquid Water Content from Dual Wavelength Radar

Robin J. Hogan*, Anthony J. Illingworth, John W. F. Goddard†, Suzanne C. H. M. Jongen‡ and Henri Sauvageot††

Department of Meteorology, University of Reading, UK

†Radiocommunications Research Unit, Rutherford Appleton Laboratory, Chilton, UK

‡Technische Universiteit Eindhoven, The Netherlands

††Laboratoire d'Aérodynamique, Université Paul Sabatier, Toulouse, France

*Email: R.J.Hogan@reading.ac.uk.

INTRODUCTION

Of all clouds, low-level stratus and stratocumulus have the most profound impact on the earth's radiation budget because of their high optical depth and large global coverage. Microwave radiometry has the capability of measuring the path-integrated liquid water content (LWC) of such clouds, but active measurements are required in order to obtain information on the vertical distribution of liquid water in the cloud. One of the main problems in developing radar algorithms for measuring LWC is the ubiquitous presence of occasional drizzle drops, which contribute negligibly to LWC but dominate radar reflectivity such that the absolute value of reflectivity is essentially unrelated to LWC (Fox and Illingworth 1997).

In this paper we use the difference in attenuation between vertically-pointing 35 and 94 GHz radars to measure this parameter. In the Rayleigh regime the attenuation is proportional to LWC and increases with frequency, so there is no need to resort to any empirical relationships and, furthermore, the absolute calibration of the radars is unimportant. The differential-attenuation principle was first proposed for use in rain, although the problems of large drops attenuating in the Mie regime and Mie scattering by hail were difficult to overcome. More recently the concept was applied to clouds when Martner et al. (1993) measured LWC from horizontal scans of a dual-wavelength radar at 10 and 35 GHz, although the two-way differential attenuation per g m^{-3} of liquid water at 10°C is only 1.5 dB km^{-1} at these frequencies, and was only measurable at a resolution of 4 km or worse. At the higher frequencies we are using this figure becomes 7.1 dB km^{-1} , which is clearly measurable even for vertically-pointing radars. The differential attenuation due to atmospheric gases needs to be subtracted before the retrieval can be performed; this is calculated using the temperature and pressure diagnosed by the UK Met. Office (UKMO) Unified Model. For example, at 10°C and mean-sea-level pressure it has a (two-way) value of 1.0 dB km^{-1} if the air is saturated.

Measurements of liquid water path (LWP) and LWC taken during the 1998 Cloud Radar and Lidar Experiment (CLARE'98) at Chilbolton, England are presented. Good agreement is found with the LWP measured by microwave radiometers, giving us some confidence in the derived profiles of LWC.

THEORY

In conventional logarithmic units the reflectivity at frequency f and height z can be written as

$$Z_f = Z + 10 \log_{10} \left(\frac{|K_f|^2}{0.93} \right) - 2 \int_0^z \alpha_f + \kappa_f \text{LWC} dz \text{ dBZ},$$

where Z is the unattenuated reflectivity factor at centimeter wavelengths (for which $|K|^2 = 0.93$), α_f is the one-way specific attenuation coefficient due to atmospheric gases (predominantly molecular oxygen and water vapor) in dB km^{-1} , and κ_f is the specific attenuation coefficient of liquid water and has the units $\text{dB km}^{-1} (\text{g m}^{-3})^{-1}$. We calculate K and κ_f as functions of temperature using the formulation for dielectric constant of Liebe et al. (1989). The line-by-line model of Liebe (1985) is used to compute α_f as a function of temperature, pressure and humidity. Defining the dual-wavelength ratio as $\text{DWR} = Z_{35} - Z_{94}$, we can then determine the mean LWC in a layer using the DWR measured at the top and bottom (indicated by the subscripts 2 and 1 respectively):

$$\overline{\text{LWC}} = \frac{\text{DWR}_2 - \text{DWR}_1 - \beta - 2 \int_{z_1}^{z_2} \alpha_{94} - \alpha_{35} dz}{2 \int_{z_1}^{z_2} \kappa_{94} - \kappa_{35} dz} \text{ g m}^{-3},$$

where

$$\beta = 10 \log_{10} \left(\frac{|K_{35}(T_2)|^2 |K_{94}(T_1)|^2}{|K_{35}(T_1)|^2 |K_{94}(T_2)|^2} \right) \text{ dB}.$$

The temperature and pressure are taken from the UKMO model, and the air is assumed to have a relative humidity of 100% wherever the radar sees cloud. The sensitivity of the retrievals to errors in temperature and reflectivity factor was examined theoretically by Hogan (1998), who found that a dwell time of at least one minute is required to measure Z accurately enough that LWC can be retrieved with a vertical resolution of 150 metres.

INSTRUMENTATION

During the CLARE'98 campaign three ground-based cloud radars were in operation: the 35 GHz 'Rabelais' on loan from the University of Toulouse, the 94 GHz 'Galileo' funded by ESTEC, and the 95 GHz 'Miracle' owned by the GKSS institute near Hamburg. For logistical reasons the radars could not be installed right next to each other; the Rabelais and the Miracle were around 30 m apart and the Rabelais and the Galileo

were 100 m apart. Stratocumulus can often be very inhomogeneous for radar, especially when drizzle is present (which is nearly always the case when the cloud is sufficiently deep to allow measurement of differential attenuation). This meant that rather more temporal averaging was needed to overcome the differences in sampled cloud than would have been the case if the radars were next to each other. This was particularly true for the Rabelais and Galileo.

Another important consideration is the near-field effect; the antenna diameters of the Rabelais, Miracle and Galileo radars are respectively 1.4, 1.2 and 0.6 m. Conventionally the far-field approximation is taken to be valid beyond a range of $2D^2/\lambda$, where D is the antenna diameter and λ is the wavelength. The corresponding ranges for these radars are therefore 450, 900 and 225 m. Because the technique relies on measuring small differences in reflectivity, it cannot be used for clouds which lie in the near field of either radar of the dual-wavelength pair, and may even fail beyond this range if the errors associated with the far-field approximation are of the same

order as the accuracy required. At a range of $2D^2/\lambda$, reflectivity is underestimated by approximately 10% (0.4 dB), although this figure varies from antenna to antenna.

The other instruments used were a Vaisala CT75K lidar ceilometer, which was found to be useful for locating cloud base when the cloud was precipitating, and three microwave radiometers at 21.3, 23.8 and 31.7 GHz belonging to the Technical University of Eindhoven in The Netherlands, which provided an estimate of LWP.

RESULTS

There is an obvious trade-off between the accuracy of the retrieved $\overline{\text{LWC}}$ and the vertical resolution, and the most accurate measurement that can be made is of LWP through the whole depth of the cloud. We first present a comparison between LWP measured by dual-wavelength radar and by the three microwave radiometers during the CLARE'98 campaign. The radars used were the 35 GHz Rabelais and the 95 GHz Miracle. The first two panels of Fig. 1 show the reflectivity fields measured by the two radars, each with temporal resolution of 10 seconds. The vertical resolution of the 35 GHz radar was 75 m and that of the 95 GHz radar was 82.5 m. The two reflectivity fields were averaged in time into 100 s bins, and interpolated on to a common 40 m height grid. DWR was then calculated and is shown in the third panel of Fig. 1. It can be seen that through most its depth it fluctuates and so taking the vertical derivative to determine LWC would seem impossible. However, when the backscattered signal from the lidar ceilometer at Chilbolton is examined we see that most of the depth of the radar echo is in fact drizzle falling out of the base of the cloud (which is indicated by the dashed line overlaid on DWR), and the cloud itself only occupies the top 200 to 500 m of the signal. The fluctuating DWR in the drizzle is probably due to Mie scattering at 94 GHz by drops up to 1 mm in diameter, whereas in the cloud above, DWR appears to increase monotonically with height due to attenuation. The LWP of the cloud derived using the method described previously is shown in the last panel, together with that from the three microwave radiometers. The agreement is very good for most of the period although there are two points which show differences of a factor of two between the two measurements. There were no other liquid water clouds above 2.5 km during this period that could have contributed to the radiometer LWP.

The agreement between vertically-integrated LWC is encouraging, so the next step is to measure the vertical profile of LWC through a thicker cloud. Figure 2 shows profiles of Z , DWR and LWC measured by the Rabelais and Galileo radars on 22 October. Because these radars were 100 m apart, 6-minute averaging was required to overcome differences due to the inhomogeneous nature of stratocumulus. It was also necessary to fit a 5th-order polynomial through the measured DWR profile to reduce the noise caused by this separation. The ceilometer measured the base of the cloud to be at 500 m, so the Miracle radar could not be used reliably because its near-field zone extends up to 900 m. The derived profile of LWC looks reasonable, and is comparable to what one would expect for an adiabatic profile, although simultaneous aircraft measurements are

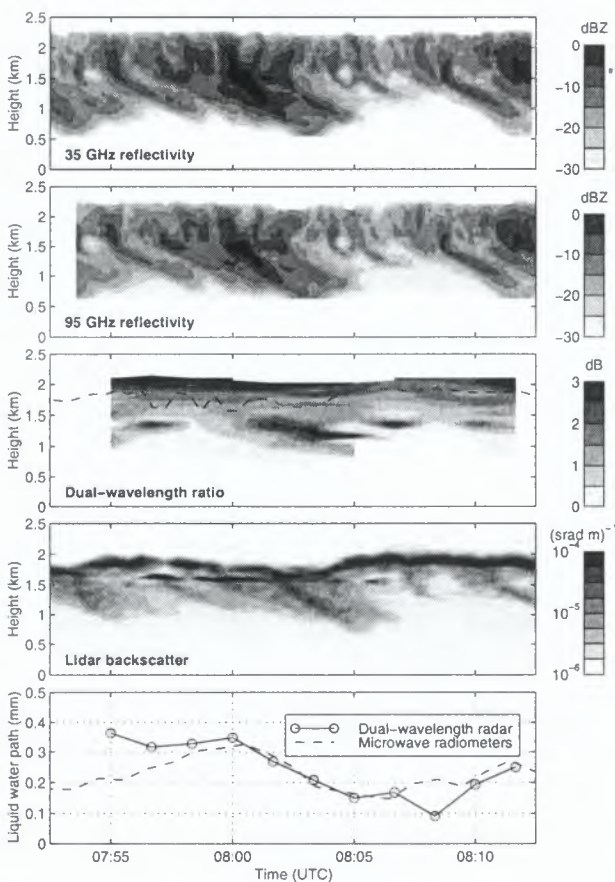


Fig. 1: Dual-wavelength radar measurements taken on 20 October 1998. The first two panels depict reflectivity at 35 and 95 GHz. The third shows the dual-wavelength ratio (DWR) calculated after averaging the two reflectivity fields over 100 seconds and interpolating onto a common height grid. The dashed line shows cloud base derived from lidar backscatter coefficient, which is shown in the fourth panel. The fifth panel shows LWP derived from DWR above cloud base, together with that measured by the microwave radiometers.

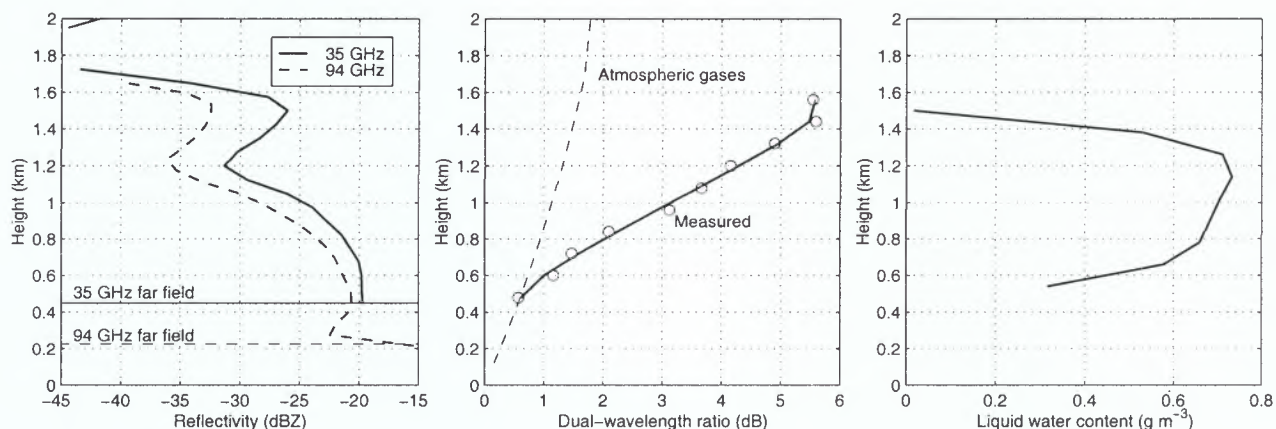


Fig. 2: Dual-wavelength radar measurements taken on 22 October 1998. The first panel depicts a 6-minute average of reflectivity at 35 and 94 GHz, starting at 15:00 UTC. The circles in the second panel show the corresponding dual-wavelength ratio (DWR), and the solid line is a 5th-order polynomial through these points. Also shown by the dashed line is the contribution to DWR from atmospheric gases, calculated from UKMO-analysed thermodynamic fields. The third panel shows the retrieved profile of LWC.

required for validation.

The importance of a good range calibration has become apparent in the course of this study, and it has been found that small changes in the relative range calibration of the two radars can have a surprisingly large effect on DWR, particularly in the vicinity of sharp gradients in reflectivity, such as at cloud top.

CONCLUSIONS AND FUTURE WORK

There is clearly promise in the use of dual-wavelength radars to make vertically-resolved measurements of LWC in stratocumulus, although a limitation of the current study was that the radars were not mounted next to each other and so rather a lot of temporal averaging was required to obtain believable profiles. Since this work was carried out, the Rabelais and Galileo radars have been mounted next to each other, so the next step is to try the technique with much less spatial averaging on recent data. We also intend to make simultaneous measurements of the Doppler spectrum in order to

- Estimate the number of independent pulses from the spectral width, and from this the magnitude of the error in derived LWC;
- Identify when drizzle drops larger than $600\ \mu\text{m}$ are present as these Mie scatter and therefore can bias the retrievals;
- Compare derived LWC with the reflectivity of the cloud-droplet component of the spectrum (as opposed to the drizzle component), as analysis of aircraft-measured size spectra suggest they should be well correlated (Hogan 1998).

Comparison of retrieved liquid water contents with aircraft measurements is seen as essential to validate the technique.

ACKNOWLEDGEMENTS

The Galileo radar was developed for the European Space Agency by Officine Galileo, the Rutherford Appleton Laboratory and the University of Reading, under ESTEC Contract No.

10568/NL/NB. Thanks to Olaf Danne for providing the data from the GKSS 95 GHz radar and to Peter Panagi and Ed Dicks for the UKMO model fields. Thanks also to Jon Eastment for some useful discussions. The CLARE'98 campaign was funded by ESTEC grant 12957/98, and this research also benefited from NERC grant GR3/8765.

REFERENCES

- Fox, N. I., and A. J. Illingworth, 1997: The potential of a spaceborne radar for the detection of stratocumulus clouds. *J. Appl. Met.*, **36**(6), 676–687.
- Hogan, R. J., 1998: *Dual-wavelength radar studies of clouds*. PhD Thesis, University of Reading, UK.
- Liebe, H. J., 1985: An updated model for millimeter-wave propagation in moist air. *Radio Science*, **20**(5), 1069–1089.
- Liebe, H. J., T. Manabe and G. A. Hufford, 1989: Millimeter-wave attenuation and delay rates due to fog/cloud conditions. *IEEE AP*, **37**, 1617–1623.
- Martner, B. E., R. A. Kropfli, L. E. Ash and J. B. Snider, 1993: Dual-wavelength differential attenuation radar measurements of cloud liquid water content. *Proc. 26th AMS Conference on Radar Meteorology*, Norman, Oklahoma.



Study of micro-physical and macro-physical measurements of water clouds during CLARE '98

R.J.P. Baedi, J.J.M. de Wit, H.W.J. Russchenberg and J.P.V. Poyares Baptista¹

IRCTR, International Research Centre on Telecommunications-transmission and Radar,

Department of Information Technology and Systems, Delft University of Technology,

Mekelweg 4, 2628 CD Delft, The Netherlands, <http://irctr.et.tudelft.nl/>

Phone: +31-(0)15-2786292 Fax: +31-(0)15-2784046 Email: H.W.J.Russchenberg@ITS.TUdelft.nl

¹European Space Research and Technology Centre

ABSTRACT

During the CLARE '98 campaign an extensive study of cloud microphysical and macrophysical properties has been made. The off line processing of the microphysical in-situ data is described and an alternative way of processing is proposed. Finally some case studies are presented using the alternative processing.

INTRODUCTION

Clouds play an important role in climate modelling. To quantify their effect on climate, parameterisation of clouds and cloud-related processes is required. Parameterisation of clouds in its turn requires a good understanding of cloud microstructure. The micro-structure of clouds is described in terms of spatial profiles of temperature, water vapour content, ice/liquid water content, reflectivity, water phase and cloud particle size distributions. There are several remote sensing techniques available for measuring these characteristics. However in-situ observations are still needed to validate the remote sensing techniques.

The aircraft involved in the Cloud Lidar and Radar Experiment, CLARE '98, provided among others in-situ measurements of temperature, water vapour content, ice/liquid water content and cloud particle size spectra. The particle size spectra are measured by a Forward Scattering Spectrometer Probe (FSSP) and a Two-Dimensional Cloud probe (2DC).

The FSSP measures cloud particles in the size range of 1 to 23.5 μm radius. The particles are sized in 15 radius bins of 1.5 μm each. The 2DC measures larger droplets in the range of 6.25 to 406.25 μm radius. The droplets are sized in 32 radius bins of 12.5 μm each. A more detailed description of the FSSP and the 2DC can be found in [1].

The cloud liquid water content (LWC) is measured by a Johnson-Williams LWC sensor (JW). This sensor is extensively described in [2].

First the standard off line processing is described. Especially the merging of the particle probes and the correction of the FSSP data are critically reviewed. Then an alternative an alternative merging technique is proposed. Finally some case studies using the alternative merging technique are presented.

STANDARD OFF LINE PROCESSING

During CLARE the measurements of the FSSP and the 2DC were integrated over a 5-second period. During this period the aircraft flew about 500 m. The volumes sampled in 5 seconds

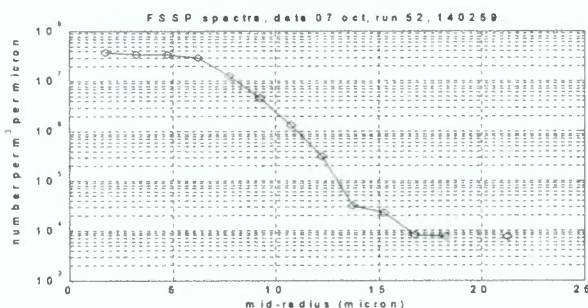


Fig. 1a

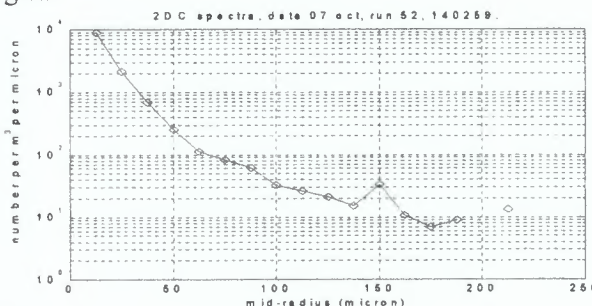


Fig. 1b

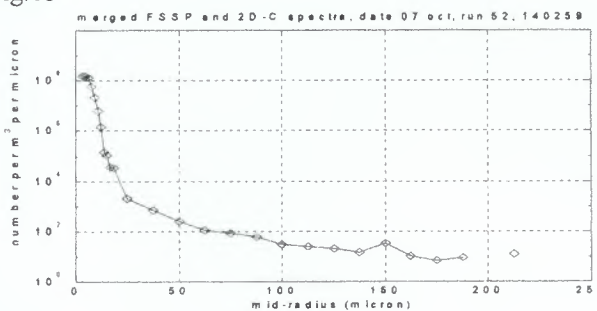


Fig. 1c

Fig.1 Typical examples of particle size spectra; the FSSP spectrum (a), the 2DC spectrum (b) and the merged spectrum (c). The merge is done using the new technique described in the text. October 7th, run 52.

are in the order of $25 \cdot 10^{-3} \text{ m}^3$ for the 2DC and 10^{-4} m^3 for the FSSP. These volumes are extremely small when compared to the volume sampled by a single radar pulse.

In order to obtain a complete size spectrum the measurements of the FSSP and the 2DC have to be merged. This merging is done following a two step procedure. In the first step the measurements at different size resolutions are fitted to the size resolution of the FSSP. To transform the data of the 2DC to the resolution of the FSSP a linear interpolation based on the 2DC data is used. This resolution transformation is performed

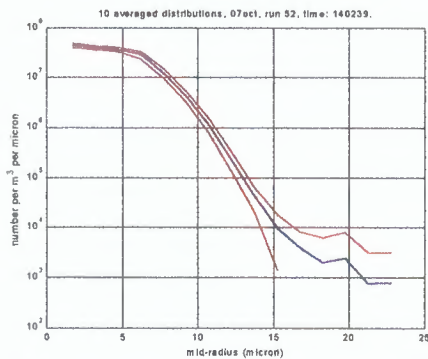


Fig.2a

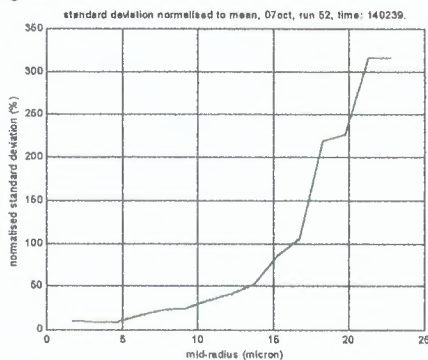


Fig.2b

Fig.2 Example of 50-second average of a FSSP spectrum (a). Figure (b) shows the standard deviation normalised to the mean. October 7th, run 52.

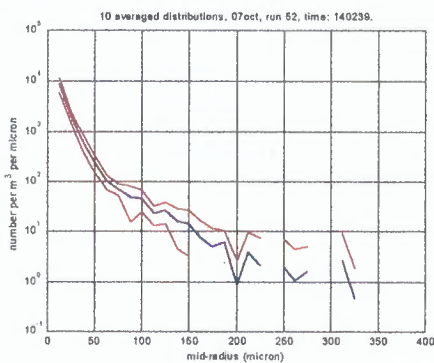


Fig.3a

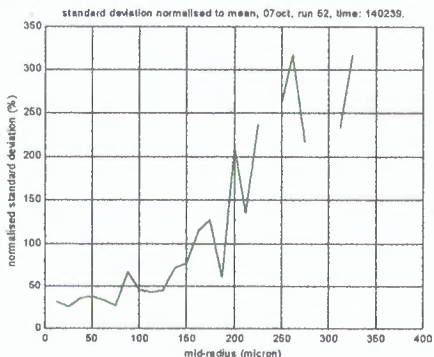


Fig.3b

Fig.3 Example of 50-second average of a 2DC spectrum (a). Figure (b) shows the standard deviation normalised to the mean. October 7th, run 52.

only in the size range where both instruments overlap. In the next step the overlapping size bins are averaged. If one of the probes did not measure any particles in a particular size bin the number of particles measured by the other is used in the merged spectrum. Fig.1 shows typical spectra measured by the FSSP and the 2DC and the merged spectrum.

After the merging the LWC from the spectra is calculated. Then the raw FSSP data are corrected so that the LWC from the merged spectra is equal to that measured by the Johnson-Williams. This correction is applied because the FSSP is known to under-estimate in cases where the size spectra are heavily weighted towards the smaller drop sizes [3]. In order to equalise the LWC from the FSSP and the Johnson-Williams the raw FSSP data are multiplied by a constant correction factor CF:

$$CF = \frac{LWC_{JW} - LWC_{2DC}}{LWC_{FSSP}} \quad (1)$$

The noise level of the Johnson-Williams is 0.01 gm^{-3} . Therefore the correction is not applied if the LWC measured by the Johnson-Williams is smaller than 0.01 gm^{-3} . Finally the corrected FSSP data are again merged with the 2DC data.

CRITICAL REVIEW; ALTERNATIVE PROCESSING

As mentioned the sample volumes of both the FSSP and the 2DC are very small. So it is questionable if the integration period is long enough to obtain statistically reliable measurements. Fig.2 and fig.3 show size spectra averaged over a 50-second period. The standard deviation normalised to the mean is also plotted in these figures. From these figures it is seen that the last bins of both the FSSP and the 2DC have very large relative standard deviations. Further increasing the integration times does not improve the results. If longer averaging times are used the normalised standard deviation increases again.

ALTERNATIVE MERGING TECHNIQUE

According to fig.2 and fig.3 the last three bins of the FSSP have larger standard deviations than the first bins of the 2DC. That is the concentrations measured in the first bins of the 2DC are statistically more reliable. Thus instead of merging the overlapping FSSP and 2DC bins, the 2DC bins should be used. For different reasons [4] also states that the last three bins of the FSSP should not be used.

In [4] it is also suggested that the first bin of each probe should not be used. The first size bin of both the FSSP and the 2DC are known to produce unreliable data. If all this is taken into account the merged spectrum will consist of bins two to twelve of the FSSP and bins two to thirty-two of the 2DC. The merged spectrum will then have a slight overlap of $0.25 \text{ }\mu\text{m}$. This new merging technique is used in this study.

ALTERNATIVE CORRECTION

The procedure to correct the FSSP data raises some doubts too. According to [1] the first bin of the 2DC is known to under-estimate. This under-estimation is however not

corrected. During the standard merging the last corrected bins of the FSSP are averaged with the first, under-estimated 2DC bin. With the new merging technique this is no longer the case.

In [2] it is reported that the Johnson-Williams under-estimates the amount of water in the larger droplets because these droplets splash off the instrument. This effect is noticeable for droplets with radii larger than 15 μm . Thus if the LWC from the 2DC spectra is very large, the correction factor may become less than unity. During the standard processing the FSSP data are nevertheless corrected, even though this correction is applied because the FSSP is known to under-estimate. However if the FSSP data are not corrected then effectively the Johnson-Williams is assumed to be wrong [3]. In this study the FSSP data are not corrected if the correction factor is less than unity. In practice a factor less than unity was only encountered twice, during run 11 of October 22nd.

If a constant-factor correction is applied, the measurements of each bin are multiplied by the same factor. In [5] it is suggested however that the sample volume of the FSSP probe is size dependent. That is some bins will under-estimate the concentration more than other bins. A size dependent correction algorithm is therefore developed. This alternative correction is described in [6].

In this study the new merging technique and the constant-factor correction for the FSSP data are applied. The correction factor is however calculated using only bins two to twelve of the FSSP and bins two to thirty-two of the 2DC. Typical values for the correction factor vary between 3 and 5.

MODELLING THE SIZE SPECTRA

In general cloud size spectra can be described well with a gamma distribution [7]:

$$N(r)dr = N_0 \cdot r^m \cdot \exp\{-\lambda r\}dr \quad (2)$$

where r is the drop radius and $N(r)dr$ is the number of droplets per m^3 in the radius range $(r, r+dr)$. The parameters N_0 and m are the scaling factor and the dispersion factor respectively; λ is usually taken as a function of m .

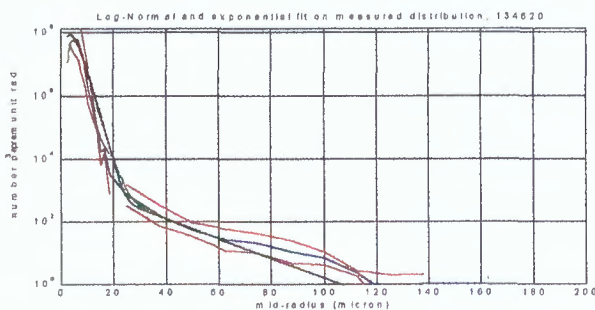


Fig.4 Example of 50-second moving average of a merged spectrum (blue dashed line). The merged spectrum is approximated by a sum of a gamma and an exponential distribution function (black solid line). The two grey outer lines represent the standard deviation of the measured size spectra. October 7th, run 51.

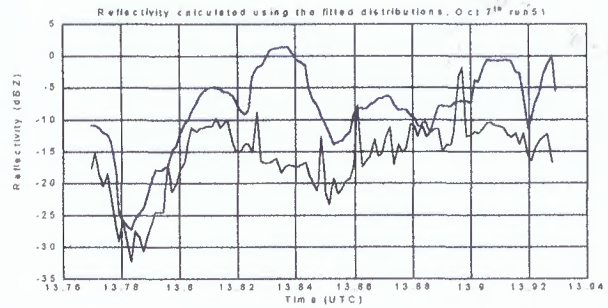


Fig.5a

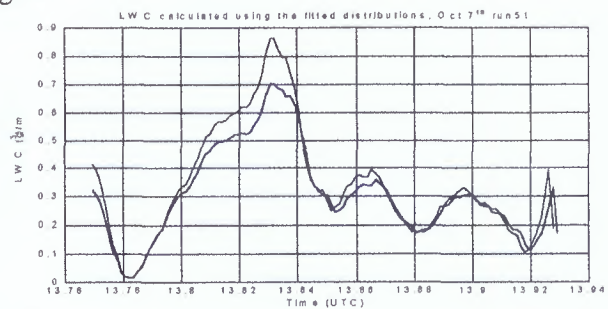


Fig.5b

Fig.5 Figure (a) shows the reflectivity from the spectra (blue line) using a 50-second moving average and the reflectivity from the gamma-exponential model (black line). Figure (b) shows the LWC from the spectra (blue line) using a 50-second moving average and the LWC from the gamma-exponential model (black line). October 7th, run 51, time axis is in decimal hours.

The gamma function is however not capable of fitting the tail of the measured distributions. Therefore an exponential distribution function is used to fit the 2DC data. The exponential function has the same form as the gamma function with $m = 0$. The complete size spectrum is then approximated by the sum of a gamma and an exponential distribution function.

Fig.4 shows an example of a size spectrum and its approximation. From this figure it is seen that the gamma function fits the FSSP data very well. The fit on the tail is however not very good. The fit under-estimates the number of large droplets. That this is generally true is confirmed by fig.5.

From fig.5a it can be seen that the reflectivity from the fitted spectra is 5 to 10 dBZ lower than the reflectivity from the actual measured spectra. This can be explained with the aid of fig.4. Due to the r^6 dependence the reflectivity is very sensitive to large droplets; that is the tail of the size spectrum. From fig.3 it can be seen that the large drops are under-estimated by the fit and thus the reflectivity from the fits will also be an under-estimate.

The LWC on the other hand is dominated by the small, FSSP-sized, particles. Since the gamma function fits the FSSP data very well, the LWC from the fits will approximate the LWC from the measured spectra very well too. That this is indeed the case can be seen from fig.5b.

The clearly two-sloped behaviour of the measured spectra is remarkable. And what is even more remarkable is the fact that all size spectra measured during CLARE show this behaviour.

Normally this type of behaviour is only seen near cloud edges [8]. Worth noticing is also that the transition of the two slopes is always in the area where the data of the different probes are merged. It is uncertain at this point whether this behaviour is due to a physical reason or a measurement issue.

CLARE '98 EXPERIMENTAL PLAN

The Cloud Lidar and Radar Experiment (CLARE) was carried out in October 1998 near Chilbolton in the United Kingdom. During the experiment simultaneous in-situ aircraft observations and co-located ground-based measurements were performed.

The C-130 Hercules aircraft carried particle size probes and a Johnson-Williams LWC sensor. The Fokker 27 Arat carried the 94 GHz Kestrel radar and the 532 nm Leandre lidar. And finally the Falcon E-20 jet carried among others the 532 nm Alex lidar. The ground-based observations included, among others, radar, lidar and radiometer measurements.

The three aircraft flew legs to the west of Chilbolton to and from the radar site. The Hercules flew through the clouds at 2 km to obtain in-situ microphysical measurements. The Arat flew above most of the cloud between 3 and 5 km to observe the cloud top. Finally the Falcon flew above all clouds at about 12 km. Although their speeds are different the aircraft arrived overhead Chilbolton simultaneously. A detailed description of CLARE '98 can be found in [9].

In this study only water clouds are analysed. At this point the data set is therefore limited to runs 11, 12, 51 and 52 of October 7th, run 51 and 52 of October 13th and run 11 of October 22nd. However on October 7th the Falcon aircraft was not yet operational so there are no data from the Alex lidar. Unfortunately for the runs made in the morning on October 7th (run 11 and 12) there are also no data from the Kestrel radar and the Leandre Lidar. On October 22nd only the Hercules was operational.

CASE STUDY OCTOBER 7th, RUN 12

During this run the Hercules flew at some distance from a rain shower. The LWC measured by the Johnson-Williams is indeed very low: below the noise level of the Johnson-Williams sensor.

The reflectivity from the spectra is around -70 dBZ, which is well below ordinary radar thresholds (see fig.6). The high

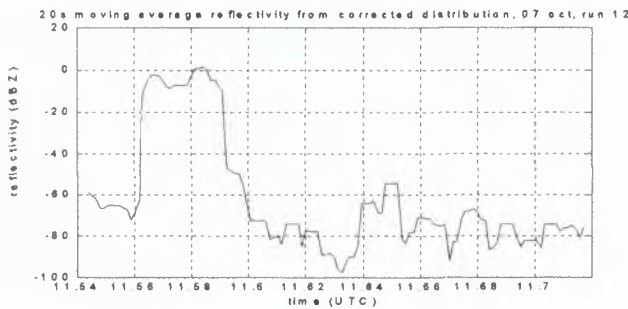


Fig.6 The reflectivity from the particle size spectra using a 20-second moving average. October 7th, run 12, time axis is in decimal hours.

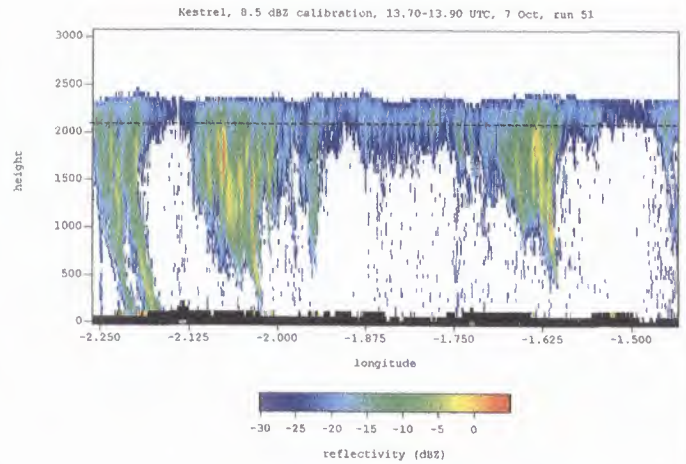


Fig.7 The reflectivity measured by the 94 GHz Kestrel radar. October 7th, run 51.

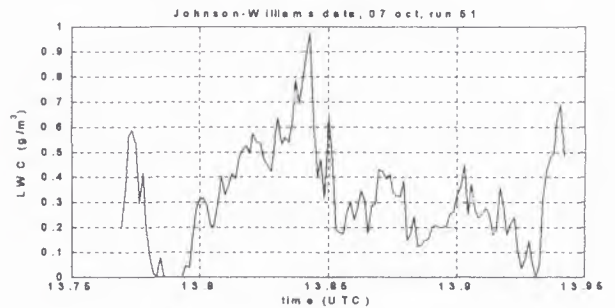


Fig.8 The liquid water content measured by the Johnson-Williams. October 7th, run 51, time axis is in decimal hours.

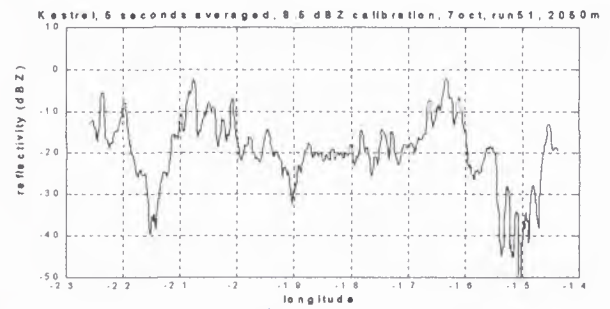


Fig.9a

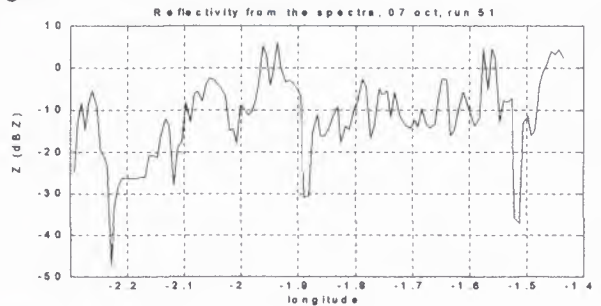


Fig.9b

Fig.9 The reflectivity measured by the Kestrel radar at 2.05 km (a) and the reflectivity from the spectra (b). During this run the Hercules flew between 2.032 and 2.074 km. October 7th, run 51.

values between 11.56 UTC_{dec} and 11.60 UTC_{dec} are due to measurement issues. The 2DC acquires its data in blocks; partially filled blocks can not be analysed. Usually this is not a problem, but if the number of particles sampled is very small, it will take a long time to fill up a data block. In that case the data have to be interpolated to get a size spectrum every 5 s. Within this interpolation period the size spectra are assumed to be identical [3]. Issues regarding the measurement accuracy of the in-situ data lead this run to be disregarded.

CASE STUDY OCTOBER 7th, RUN 51

During this run the Hercules flew through a precipitating stratocumulus cloud at 2 km. Fig.7 shows the image from the Kestrel radar. The dashed line shows the track of the Hercules.

The LWC measured by the Johnson-Williams is quite high. This is not surprising considering that the cloud is precipitating. Fig 8 shows the liquid water content measured by the Johnson-Williams.

The reflectivity from the spectra is about 7 dBZ higher than the reflectivity from the Kestrel, see fig.9. A calibration constant of 8.5 dBZ is subtracted from the Kestrel data. This is however not yet the definitive calibration constant [10]. Furthermore comparing the reflectivities one has to keep in mind that the velocities of the aircraft were not the same; the Arat flew slightly faster than the Hercules. Thus the reflectivity from the Kestrel and the reflectivity from the spectra agree reasonably well. The reflectivity from the spectra is calculated using the Rayleigh approximation.

In order to obtain the LWC with radar measurements alone, some relationship between the radar reflectivity and the LWC must exist. Several empirical Z-LWC relationships have been proposed [4]. Ignoring drizzle sized droplets for stratocumulus a relationship of the form:

$$z = 0.03 LWC^{1.31} \tag{3}$$

has been found [11]. For run 51 the relationship for only FSSP data is:

$$z_{FSSP} = 0.0068 LWC_{FSSP}^{1.06} \tag{4}$$

If the 2DC data are also taken into account the relation becomes:

$$z_{2DC+FSSP} = 0.72 LWC_{2DC+FSSP}^{1.63} \tag{5}$$

The 2DC data mainly cause a shift to higher reflectivities since the LWC is barely dependent upon the 2DC data. The scatter plots are shown in fig.10. The scatter in the Z_{2DC+FSSP} versus LWC_{2DC+FSSP} is much larger. That is not surprising since the last bins of the 2DC have large standard deviations, see figure 2 and 3.

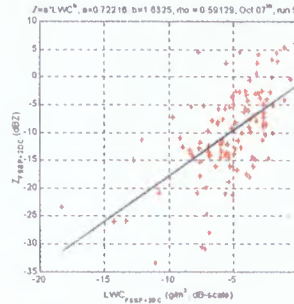


Fig.10a

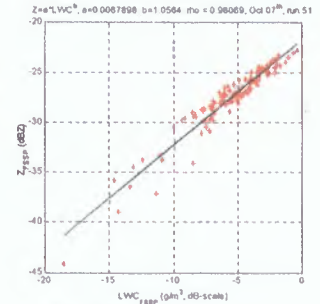


Fig.10b

Fig.10 The scatter plots of Z_{2DC+FSSP} versus LWC_{2DC+FSSP} (a) and Z_{FSSP} versus LWC_{FSSP} (b). October 7th, run 51.

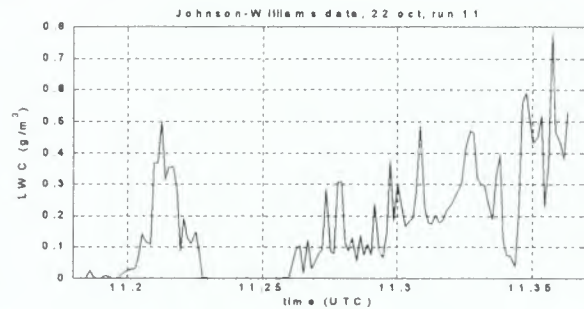


Fig.11 The liquid water content measured by the Johnson-Williams. October 22nd, run 11, time axis is in decimal hours.

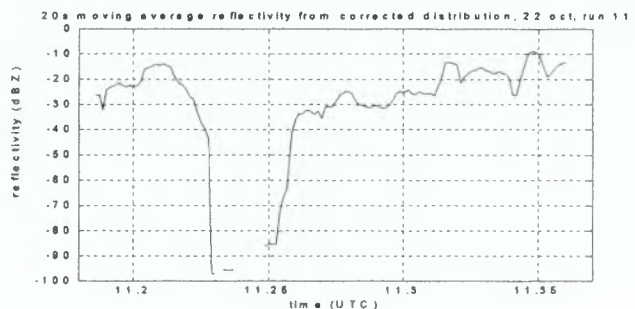


Fig.12 The reflectivity from the particle size spectra using a 20-second moving average. October 22nd, run 11, time axis is in decimal hours.

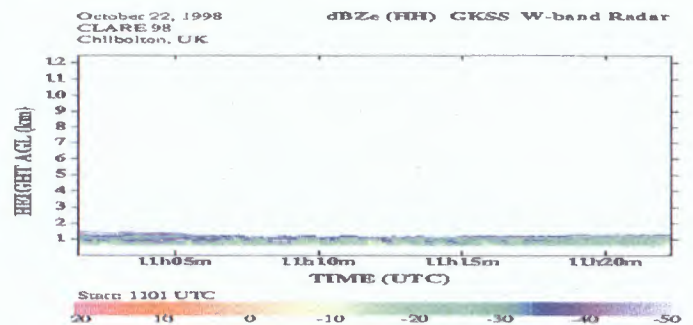


Fig.13 The reflectivity measured by the ground-based 94 GHz vertically pointing Miracle radar. October 22nd, run 11.

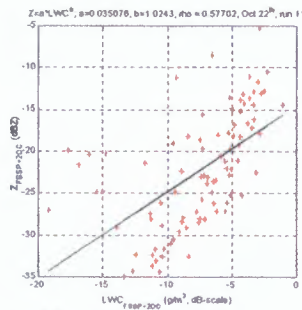


Fig.14a

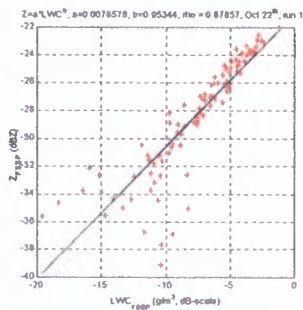


Fig.14b

Fig.14 The scatter plots of $Z_{2DC+FSSP}$ versus $LWC_{2DC+FSSP}$ (a) and Z_{FSSP} versus LWC_{FSSP} (b). October 22nd, run 11.

CASE STUDY OCTOBER 22nd, RUN 11

The Hercules flew around 1 km through a stratocumulus cloud. Unfortunately there are no images from the Kestrel radar for this run.

The liquid water content measured by the Johnson-Williams reaches values up to 0.7 gm^{-3} (fig.11). On average it is below 0.5 gm^{-3} .

The reflectivity from the spectra (fig. 12) is however very low; always below -10 dBZ . This is in agreement with the measurements of the 94 GHz Miracle radar (fig.13). The reflectivity measured by the Miracle is on average -20 dBZ . However one has to bear in mind that the Miracle is a vertically pointing radar. Hence the comparison is only really valid if the aircraft is overhead Chilbolton.

The fact that the reflectivity from the spectra is very low suggests that the 2DC did not measure a lot of particles. The scatter plots confirm this idea. Fig.14 shows the scatter plots of run 11. The relationship for only the FSSP data is:

$$z_{FSSP} = 0.0079 LWC_{FSSP}^{0.95} \quad (6)$$

And if the 2DC data are taken into account:

$$z_{2DC+FSSP} = 0.035 LWC_{2DC+FSSP}^{1.02} \quad (7)$$

Relationship (7) is very close to relation (3). Relation (3) was however found ignoring larger particles, thus during run 11 there were probably little large particles present.

CONCLUSIONS

In this study a slightly improved merging method is proposed. The first bin of both the FSSP and the 2DC are known to produce unreliable data. In the new merging method these bins are not used. Furthermore the last three bins of the FSSP are statistically unreliable. Therefore the second bin of the 2DC should be used instead of an average of the last FSSP bins and the second bin of the 2DC.

The FSSP spectra can be well approximated by a gamma distribution function. The gamma function is however not capable of fitting the tails of the spectra. The merged spectra can be approximated by the sum of a gamma and an exponential distribution function. The number of large droplets will then be under-estimated. Hence another

distribution function has to be found to model the tails of the size spectra.

All liquid cloud droplet spectra measured during CLARE show a two-sloped behaviour. Normally this type of behaviour is only observed near cloud edges. The transition of the slopes is always in the area where the FSSP and the 2DC data are merged. So it is questionable if this behaviour has a physical background. Further research is needed.

After applying the correction, the LWC from the spectra is equal to the LWC measured by the Johnson-Williams. For run 12 of October 7th the calculated and the measured LWC differ. During this run the measured LWC is below the noise level of the Johnson-Williams sensor. The measurements made during run 12 will thus not be very meaningful.

The agreement between the calculated reflectivity and the radar measurements is less obvious. For the runs studied in this text a good comparison is only possible for run 51 of October 7th. During the other runs the Kestrel was not operational. For run 51 the reflectivity from the Kestrel and the reflectivity from the spectra agree reasonably well.

REFERENCES

- [1] S.J. Moss, P.R.A. Brown, D.W. Johnson, D.R. Lauchlan, G.M. Martin, M.A. Pickering, A. Spice, "Cloud microphysics measurements on the MRF C-130: Working Group Report", Meteorological Research Flight, MRF Technical note no. 12, 1993
- [2] D.A. Johnson, "A study of the Johnson-Williams liquid water content meter as fitted to the MRF Hercules", Meteorological Office, Met. O. 15 Internal report no. 22, 1979
- [3] P.N. Francis, personal communication
- [4] A.J. Illingworth, C-L. Liu, I. Astin, B. Richards, "Study of the critical requirements for a cloud radar", Internal report ESTEC-European Space Agency, 1997
- [5] J.E. Dye, D. Baumgardner, "Evaluation of the Forward Scattering Spectrometer probe. Part I: electronic and optical studies", J. atmospheric and Oceanic Technology, Vol. 1, 329-344, 1984
- [6] R.J.P. Baedi, J.J.M. de Wit, H.W.J. Russchenberg, J.P.V. Poiars Baptista, "Alternative algorithm for correcting the FSSP measurements", Proc. CLARE '98 workshop, September 1999
- [7] H.R. Pruppacher, J.D. Klett, "Microphysics of clouds and precipitation", Kluwer Academic Publishers, 1997
- [8] J.P.V. Poiars Baptista, personal communication
- [9] R.J.P. Baedi, J.J.M. de Wit, J.P.V. Poiars Baptista, J.P.V., "Comparison of micro-physical and macro-physical measurements of clouds during the Cloud Lidar and Radar Experiment", Internal report ESTEC-European Space Agency, 1999
- [10] A. Guyot, personal communication
- [11] H. Sauvegeot, J. Omar, "Radar reflectivity of cumulus clouds", J. Atmospheric and Oceanic Technology, Vol. 4, 246-272, 1987

Development of retrieval algorithms of cloud parameters from radar and lidar based on the CLARE data set

J.J.M. de Wit, R.J.P. Baedi, J.S. Erkelens, J.P.V. Poiarés Baptista¹ and H.W.J. Russchenberg
IRCTR, International Research Centre on Telecommunications-transmission and Radar,
Department of Informational Technology and Systems, Delft University of Technology,
Mekelweg 4, 2628 CD Delft, The Netherlands, <http://irctr.et.tudelft.nl/>
Fax: +31 15 2784046 Email: H.W.J.Russchenberg@ITS.TUdelft.nl
¹**European Space Research and Technology Centre**

ABSTRACT

To measure the cloud liquid water content, time consuming in-situ aircraft measurements are needed. Radars on the other hand are capable of monitoring large volumes thus radar measurements are faster and cheaper than in-situ observations. Several Z-LWC relations have been proposed. However these relationships do not hold throughout a whole cloud because they ignore larger droplets. The effective radius is used to identify the parts of the cloud where the Z-LWC relations are not valid. Finally a procedure to obtain the effective radius with radar and lidar measurements is outlined.

INTRODUCTION

Clouds have a significant influence on the earth-atmosphere radiation budget. This influence is determined by their physical properties, e.g. the cloud liquid water content (LWC).

The LWC can be measured in-situ with a Johnson-Williams liquid water content sensor mounted on an aircraft [1]. The sample volume of the Johnson-Williams sensor is however very small. Hence to measure the LWC profile throughout a whole cloud a lot of flights have to be made. During the time needed to cover the whole cloud the cloud properties will alter. Next to that in-situ aircraft measurements are very expensive.

It would be less cumbersome if the LWC could be obtained with (ground-based) radars. The sample volume of ordinary radars is about 10^5 times as large as the sample volume of the Johnson-Williams sensor. In order to obtain the LWC with a radar some relation between the radar reflectivity and the LWC must be found. Therefore radar and in-situ measurements have to be correlated.

A comprehensive measurement campaign of cloud parameters using several remote sensing techniques and in-situ aircraft measurements was carried out during the Cloud Lidar and Radar experiment (Clare). The Clare campaign took place in October 1998 near Chilbolton in the United Kingdom. During the campaign simultaneous in-situ aircraft measurements and co-located ground-based measurements were performed. The ground-based

equipment consisted of radiometers, radars and lidars. The aircraft provided in-situ measurements of cloud droplet spectra, ice/liquid water content and radar and lidar measurements. The aircraft flew runs from and to the radar site. Although the aircraft had slightly different velocities they arrived at Chilbolton simultaneously. Each run is about 10 minutes long, that is 60 km. A more detailed description of the Clare '98 campaign can be found in [2].

PARTICLE SIZE SPECTRA

The particle size spectra are measured by the Forward Scattering Spectrometer probe (FSSP) and the Two-Dimensional Cloud probe (2DC). The FSSP measures water droplets in the size range of 1.75 μm to 22.75 μm radius. The particles are sized in 15 radius bins of 1.5 μm each. The raw FSSP data are corrected so that the LWC from the particle size spectra is the same as that measured by the Johnson-Williams LWC-sensor. This correction is performed because the Johnson-Williams sensor is much more accurate than the FSSP [3].

The 2DC measures the larger drop sizes in the range of 12.5 μm to 400 μm radius. The measured particles are sized in 32 radius bins of 12.5 μm each. The 2DC data are not tuned to the Johnson-Williams measurements.

The particle probes produce a spectrum every 5 seconds. In order to obtain the complete particle size spectrum the spectra measured by the FSSP and the 2DC are merged. Detailed information on the particle probes and the merging technique can be found in [4] and [2] respectively.

The liquid water content from the particle size spectra is computed as:

$$LWC = \frac{4}{3} \pi \cdot \rho_w \cdot 10^{-6} \sum N_i r_i^3 \quad [\text{g/m}^3] \quad (1)$$

Where ρ_w is density of water [kg/m^3], r_i is the mid-radius of bin i [mm] and N_i is the number of particles measured in bin i [m^{-3}]. The LWC is dominated by the smaller cloud particles, that is the FSSP-sized particles. The large

cloud droplets do not contribute much to the LWC because their concentrations are too low. Generally the contribution of the 2DC-sized droplets is 5% or less.

The radar reflectivity on the other hand is dominated by the 2DC-sized droplets. This is due to the r^6 dependence if the Rayleigh approximation is valid:

$$z = 64 \sum_i N_i r_i^6 \quad [\text{mm}^6/\text{m}^3] \quad (2)$$

Where z is the radar reflectivity.

Z-LWC RELATIONSHIPS

To be able to determine the LWC with radar measurements some relationship between the reflectivity and the LWC must exist. Several empirical Z-LWC relations have been proposed. However most of these relations ignore the 2DC-sized droplets [5].

Figure 1 shows the Z-LWC relation for a run made on October 7th in a precipitating stratocumulus cloud at 2.0 km height. Figure 2 shows the Z-LWC relation for six consecutive runs of October 7th.

These runs were all made in precipitating stratocumulus. The Z-LWC relations are found using a least-squares fit.

From figure 2b can be seen that the scatter is very small, if only FSSP data are taken into account. The scatter is much larger if the 2DC data are also taken into account, see figure 2a. The Z-LWC relation fitted on the FSSP data will therefore give a better estimate of the LWC. However radars do not discriminate between reflectivity due to FSSP-sized particles and reflectivity due to 2DC-sized particles.

If the 2DC data are taken into account the fit is not very good. In order to get a better fit the scatter has to be decreased. From figure 2a it is seen that most deviating data are data with high reflectivity and rather low LWC. That is, these spectra are heavily weighted towards the larger drop sizes.

The effective radius can be seen as a parameter that shows how many large, 2DC-sized drops occur relative to the smaller FSSP-sized droplets. Spectra that are heavily weighted towards the larger droplets have a large effective radius. The effective radius is defined as:

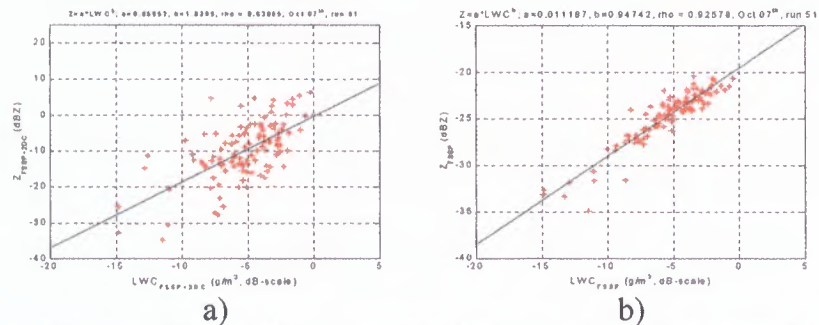


Figure 1. Scatter plot of $Z_{2DC+FSSP}$ versus $LWC_{2DC+FSSP}$ (a) and the scatter plot of Z_{FSSP} versus LWC_{FSSP} (b) for run 51 made on October 7th. The relationship for only the FSSP data is $Z_{FSSP} = 0.01 \cdot LWC^{0.95}$. The correlation between Z_{FSSP} and LWC_{FSSP} is 0.93. If the 2DC data are also taken into account the relationship is $Z_{2DC+FSSP} = 0.96 \cdot LWC^{1.83}$ and the correlation coefficient is 0.63.

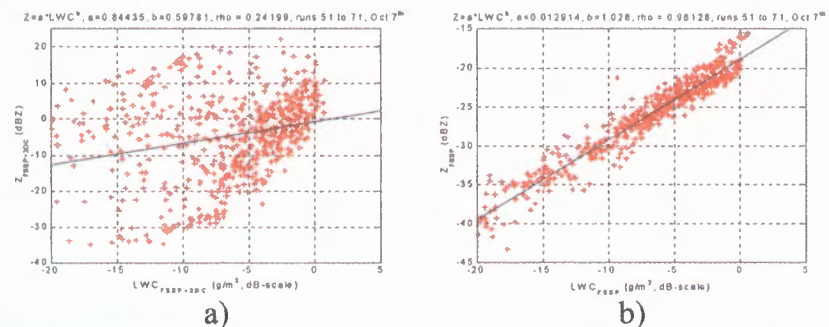


Figure 2. Scatter plot of $Z_{2DC+FSSP}$ versus $LWC_{2DC+FSSP}$ (a) and the scatter plot of Z_{FSSP} versus LWC_{FSSP} (b) for six succeeding runs made on October 7th. The Z-LWC relations are $Z_{2DC+FSSP} = 0.84 \cdot LWC^{0.60}$ and $Z_{FSSP} = 0.01 \cdot LWC^{1.03}$ respectively. If the 2DC data are taken into account the correlation coefficient is only 0.24.

$$r_e = \frac{\langle r^3 \rangle}{\langle r^2 \rangle} = \frac{\sum_i N_i r_i^3}{\sum_i N_i r_i^2} \quad [\mu\text{m}] \quad (3)$$

Indeed the spectra with high reflectivities and modest LWC have very large effective radii. See for example figure 3. This figure shows the reflectivity, the LWC and the effective radius from the spectra for a run also made in a precipitating stratocumulus cloud on October 7th. At the end of this run the LWC is very low while the reflectivity reaches values up to 20 dBZ. From the bottom figure it is seen that the effective radius is very large for those cases.

For the runs made on October 7th the limit for the effective radius is set to 10 μm . Figure 4 shows the Z-LWC scatter plot for the run shown in figure 3. The diamonds represent the spectra with $r_e > 10 \mu\text{m}$. It is easily seen that most deviating spectra have effective radii larger than 10 μm . If these spectra are filtered out the scatter will decrease significantly. Figure 5 shows the scatter plot if the spectra with $r_e > 10 \mu\text{m}$ are filtered out. The correlation coefficient is 0.61 compared to 0.24 if no

filtering is applied (see figure 2a). A lower limit of r_e does not improve the results significantly.

This method to decrease the scatter is however only useful if the effective radius can be derived with radar and other remote sensing data. Otherwise the probe measurements would still be necessary.

Z/α - R_E RELATIONSHIPS

The effective radius may be obtained by combining a radar and lidar operating in the Rayleigh and Mie region respectively. As mentioned earlier, the 2DC-sized drops dominate the radar reflectivity when the Rayleigh approximation is valid (i.e. when the particles are small compared to the wavelength). The smaller FSSP-sized droplets on the other hand dominate the extinction of the lidar signal that is computed from the spectra as:

$$\alpha = 2\pi \sum_i N_i r_i^2 \quad [\text{m}^{-1}] \quad (4)$$

Where the optical approximation of 2 for the extinction efficiency is used; i is the bin number.

In order to show that a relation exists between the effective radius, the radar reflectivity and the lidar extinction, let's first define the radar/lidar ratio as:

$$\frac{z}{\alpha} = \frac{64 \int N(r) r^6 dr}{2\pi \int N(r) r^2 dr} \quad (5)$$

Let's also assume that the merged FSSP and 2DC spectrum can be approximated by the summation of two exponential functions:

$$N(r) = N_{0,1} e^{-\lambda_1 r} + N_{0,2} e^{-\lambda_2 r} \quad (6)$$

Where λ_1 and λ_2 are the slopes of the FSSP and 2DC distributions respectively, and N_0 is a scaling factor. If it is further assumed that

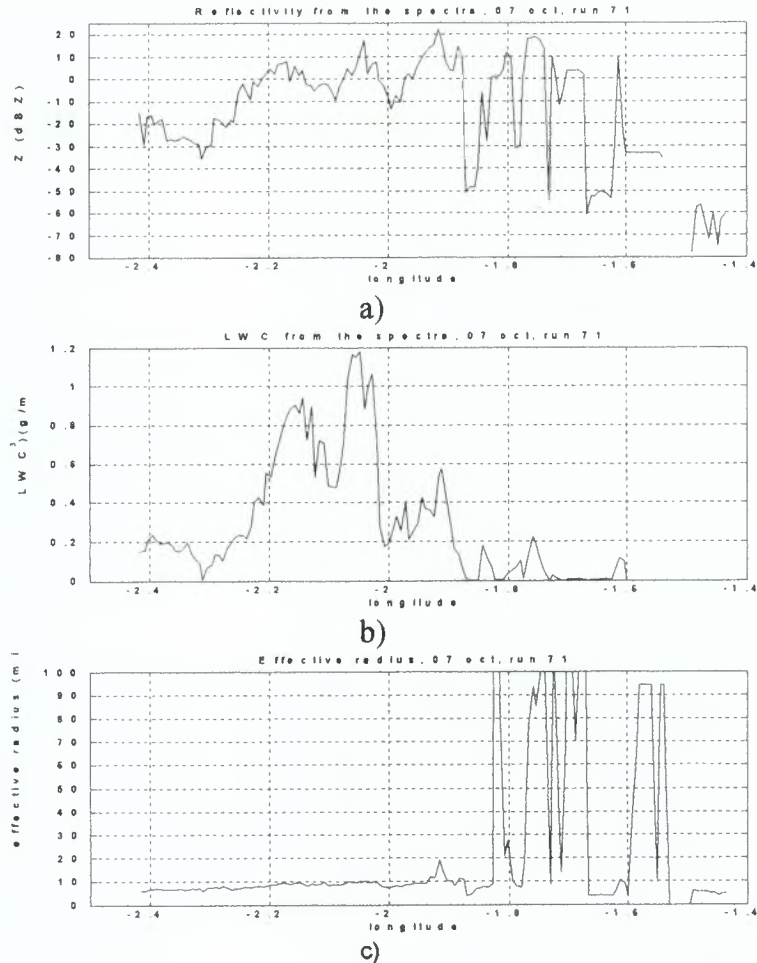


Figure 3. The reflectivity (a), liquid water content (b) and the effective radius (c) from the spectra for run 71 made on October 7th.

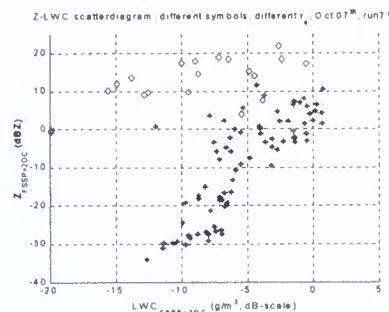


Figure 4. The scatter plot of $Z_{2DC+FSSP}$ versus the $LWC_{2DC+FSSP}$ for run 71 of October 7th. The asterisks represent spectra with $r_e \leq 10 \mu\text{m}$ and the diamonds represent spectra with $r_e > 10 \mu\text{m}$.

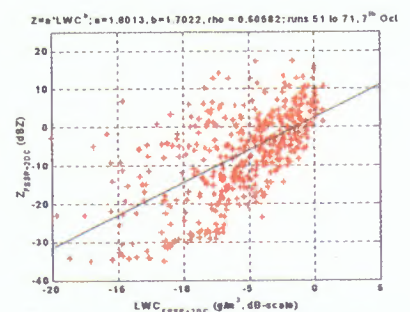


Figure 5. The scatter plot of $Z_{2DC+FSSP}$ versus $LWC_{2DC+FSSP}$ for six succeeding runs of October 7th. The spectra with $r_e > 10 \mu\text{m}$ are filtered out. The relation is $Z_{2DC+FSSP} = 1.80 \cdot LWC^{1.70}$ and the correlation coefficient is 0.61. The relation is found using a least-squares fit.

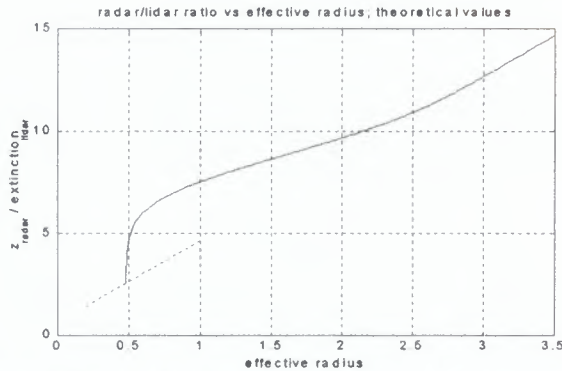


Figure 6. Plot of the radar/lidar ratio vs effective radius. Note that the values are logarithmic. These values are computed with the assumption that the size spectra measured by the probes can be approximated with a summation of two exponential functions. The solid line shows the case where λ_2 varies as λ_1 is held constant (see eq. (6) and (7)). The dashed line is the case where λ_1 varies as λ_2 is set to zero.

the integrals in equation (5) are infinite, which is reasonable since they are usually zero for large radii, the k^{th} moment can be written as:

$$\langle r^k \rangle = N_{0,1} (\lambda_1^{-1})^{k+1} k! + N_{0,2} (\lambda_2^{-1})^{k+1} k! \quad (7)$$

Then the radar/lidar ratio can be written as (ignoring the constants):

$$\frac{z}{\alpha} = \frac{N_{0,1} \lambda_1^{-7} 6! + N_{0,2} \lambda_2^{-7} 6!}{N_{0,1} \lambda_1^{-3} 2! + N_{0,2} \lambda_2^{-3} 2!} \quad (8)$$

and the effective radius can be written as:

$$r_e = \frac{N_{0,1} \lambda_1^{-4} 3! + N_{0,2} \lambda_2^{-4} 3!}{N_{0,1} \lambda_1^{-3} 2! + N_{0,2} \lambda_2^{-3} 2!} \quad (9)$$

Figure 6 shows the plot of the ratio vs r_e . The solid line shows the case where λ_1 and N_0 are held constant ($\lambda_1 = 1$) and λ_2 is varied between 0 and 1. It can be seen that when a lot of 2DC-sized drops are present (λ_2 is small), i.e. when the effective radius is relatively large, the curve converges to a r_e^4 dependency. This can also be seen from equations (8) and (9). The dashed line shows the situation where λ_2 is set zero while varying λ_1 . Again, the r_e^4 dependency is clearly seen.

In figure 7 a scatter diagram of the radar/lidar ratio versus the effective radius is shown. These data are computed from the measured size spectra, moving averaged on a 4 sample basis (20 seconds), of eight runs

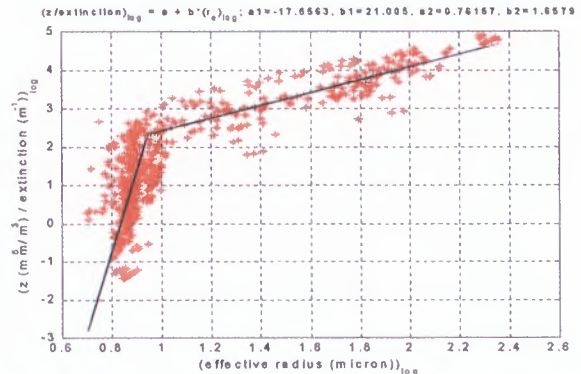


Figure 7. Scatter plot of the radar/lidar ratio vs effective radius. Note that the values are logarithmic. The solid line is the least-squares-fit on the data which are computed using eq. (2), (3) and (4). The data are moving averaged on a 4 sample basis (20 seconds). The dashed line in figure 6 does not appear here, since this line represents a situation where FSSP-sized droplets dominate the distribution; these data have a very low radar reflectivity and are filtered out by the threshold set at $Z = -35$ dBZ.

made on October 7th 1998 and two runs made on October 13th 1998.

In calculating the scatter plot, a threshold of -35 dBZ has been set on the radar reflectivity since this is the sensitivity of a typical radar system. As a consequence, the dashed line in figure 6 does not appear in the scatter plot, since that line represents the situation where FSSP-sized droplets dominate the distribution, implying a very low radar reflectivity (generally lower than -35 dBZ). The solid line is the least-squares-fit on the data. The line shows the following relation between the ratio and the effective radius:

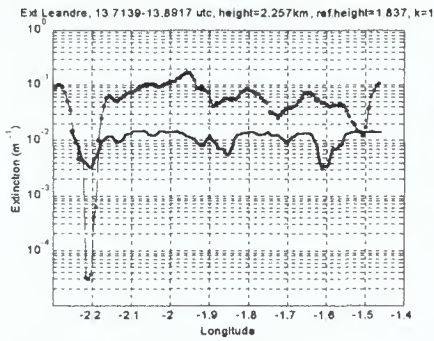
$$\left(\frac{z}{\alpha}\right)_{\log} = -17.56 + 21.01(r_e)_{\log} \quad \left(\frac{z}{\alpha}\right)_{\log} < 2.33 \quad (10)$$

$$\left(\frac{z}{\alpha}\right)_{\log} = 0.76 + 1.66(r_e)_{\log} \quad \left(\frac{z}{\alpha}\right)_{\log} \geq 2.33 \quad (11)$$

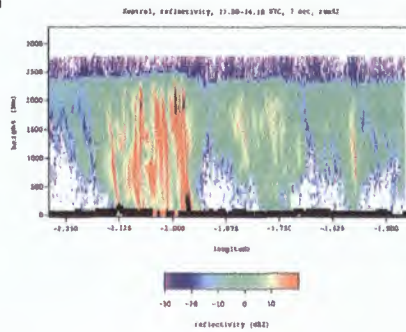
In order to give an indication of the reliability of these fits, the standard deviation of the retrieved effective radius is computed. For $(z/\alpha)_{\log}$ smaller than 2.33 ($r_e < 8.85\mu\text{m}$) the standard deviation is 0.894, whereas for $(z/\alpha)_{\log}$ greater than 2.33 ($r_e \geq 8.85\mu\text{m}$) the standard deviation is 29.13.

OBTAINING R_E FROM RADAR/LIDAR DATA

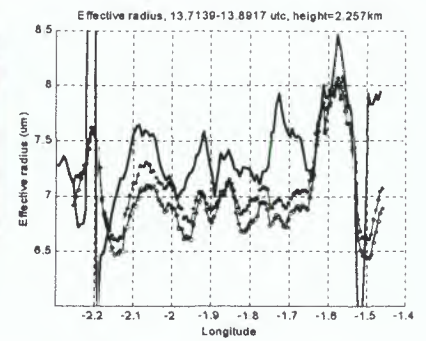
During Clare'98 a Fokker 27 'Arat' carried the Kestrel radar operating at 94 GHz (wavelength=3.19mm), and the Leandre lidar with a wavelength of 532 nm to observe the cloud top. In this paper, only water clouds are considered,



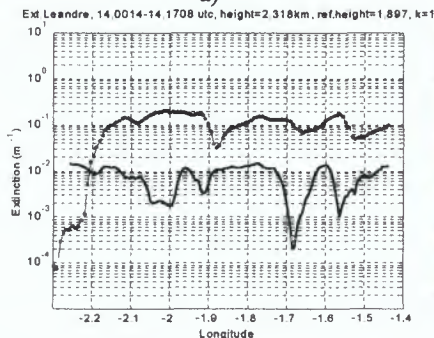
a)



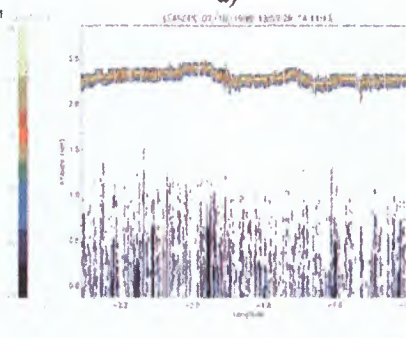
a)



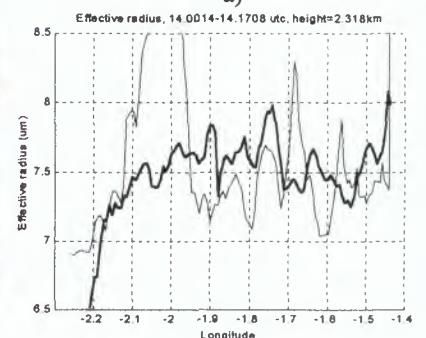
a)



b)



b)



b)

Figure 8. Plot of extinction vs longitude using a moving average on a 4 sample basis. The solid line shows the extinction extracted from the lidar signal. The dashed-dotted line shows the extinction calculated from the size spectra. Note that the extinction from the Leandre is taken at an altitude that is about 200 metres higher than the height the C130 was flying. Figure a) displays data taken from October 7th run 51, and figure b) shows data from October 7th run 52.

Figure 9. The top figure displays the radar reflectivity measured by the 94 GHz Kestrel. Figure b) shows the lidar backscatter measured by the Leandre at a wavelength of 532 nm. The measurements were taken on October 7th run 52.

Figure 10. Plot of effective radius vs longitude using a moving average on a 4 sample basis. The thin solid line shows r_e computed from relations (10) and (11), where the ratio is obtained from measurements of the Kestrel and the extracted extinction of the Leandre. The thick solid line shows r_e calculated from the size spectra. Figure a) also shows the r_e using $k=0.5$ and $k=1.5$. These are the dot-line and the circle-line respectively. Figure a) and b) show data from October 7th run 51 and 52 respectively.

and thus most particles encountered are very small compared to the radar wavelength, and very large relative to the lidar wavelength. Therefore, it may be assumed that in the radar and lidar point of view, the (spherical) particles encountered act as Rayleigh and Mie scatterers respectively.

The lidar extinction at a certain range R can be extracted from the lidar signal by using the inversion technique commonly known as the Klett algorithm [6]. This method assumes a power law relation between the backscatter β and the extinction of the form:

$$\beta = \text{const} \cdot \alpha^k \quad (12)$$

In this article, $k=1$ is used. An input boundary value α_m at some reference height R_m is also required. This

reference height should be taken further away from the receiver than the height at which the extinction is to be calculated, yet at an altitude where the range corrected lidar signal is still above the noise level. The performance of the Klett-algorithm is dependent on several factors, two of which are the selection of the reference extinction value, and the value of k that is used in relation (12). In [7] some analysis is done on how sensitive the retrieved extinction is to the boundary value. It appears that estimations with an α_m that is 100% above and 50% below the correct value still converge to the correct profile if the distance between R and R_m is large enough. In this paper, only the effect of the choice of k on the effective radius is presented.

It is difficult to choose the correct height at which the extinction is to be calculated, since the Hercules C130, the

aircraft carrying the particle probes, usually flew at a height where the lidar signal is completely attenuated. Therefore, the extinction is calculated about 200-300 metres above the height at which the Hercules had flown.

Two examples of the extracted lidar extinction and the extinction computed from the size spectra are shown in figure 8. From these figures it is seen that the extinction of the Leandre follows a similar pattern as the extinction that is calculated from the size distributions. However, the order of magnitude of the Leandre extinction lies roughly a factor 10 lower than the extinction from the spectra. The large difference seen in figure 8b) between about -2.05° and -1.95° longitude is a direct effect of the height difference. The lidar extinction is calculated at a height of 2.318 km, which is near the cloud top, whereas the Hercules flew near the cloud base, around 2.0 km. From figure 9 it is seen that during this interval of precipitation, both radar and lidar detect a slightly higher cloud top. Consequently there is no lidar signal at the height at which the extinction is calculated.

Figure 10 shows diagrams of the effective radius that is computed from relation (10) for $(z/\alpha)_{\log} < 2.33$ and from relation (11) for $(z/\alpha)_{\log} \geq 2.33$. The reflectivity and the extinction are then the measurements of the Kestrel and the extracted extinction of the Leandre respectively (thin solid line). In figure 10a the effect of k on r_e is also seen; the dot-line results from using $k=0.5$ and the circle-line is the result for $k=1.5$. It shows that the value for k does not have a very large impact on the effective radius. In this figure, the results for $k=1.5$ are almost identical to the results for $k=1$. The thick solid line is the effective radius calculated from the size spectra. In overall, the thin solid line comes in good approximation with the thick solid line; the difference between the two lines is generally less than 1 micron. In figure 10b) the effective radius is very large around -2.0° , which is a direct consequence of the difference in altitude mentioned earlier.

NOTES

In the examples discussed in this paper, the height difference of the two aircraft does not have a disastrous consequence. However, these runs are not useful in showing the operation of the r_e -filter, since the effective radius does not exceed the threshold value of 10 μm discussed before. Next to the difference in altitude, the calibration of the Kestrel radar has to be taken into account in calculating the radar/lidar ratio. At this point, it is not certain exactly how much the radar has to be calibrated. For the results in this paper, a calibration of 8.5 dBZ had been used [8]. This calibration factor has a great influence on whether relation (10) or (11) is used

in computing the effective radius. Another issue is that the data files of the Kestrel and the Leandre show different longitudes at the same time instances. Strangely enough, these instruments were on board the same aircraft.

These obstructing issues have to be resolved before other data can be analysed. Finally, the method described in this paper to derive the effective radius from radar and lidar data can only be reliably validated if data from the particle probes, the radar reflectivity, as well as the lidar extinction are available at the same location and altitude.

REFERENCES

- [1] Johnson, D.A., *A study of the Johnson-Williams liquid water content meter as fitted to the MRF Hercules*, Meteorological Office, Met. O. 15 Internal report no.22, 1979
- [2] Baedi, R.J.P., Wit, J.J.M. de, Poiars Baptista, J.P.V., *Comparison of micro-physical and macro-physical measurements of clouds during the Cloud Lidar and Radar Experiment*, Internal report ESTEC-European Space Agency, 1999
- [3] Francis, P.N., *Personal communication*
- [4] Moss, S.J., Brown, P.R.A., Johnson, D.W., Lauchlan, D.R., Martin, G.M., Pickering, M.A., Spice, A., *Cloud microphysics measurements on the MRF C-130: Working Group Report*, Meteorological Research Flight, MRF Technical note no.12, 1993
- [5] Illingworth, A.J., Liu, C-L., Astin, I., Richards, B., *Study of the critical requirements for a cloud radar*, Internal report ESTEC-European Space Agency, 1997
- [6] Klett, J.D., *Stable analytical inversion solution for processing lidar returns*, J. Applied Optics, Vol. 20, no.2, 211-220, 1981
- [7] Fong, A.Y., Lammeren, A.C.A.P. van, *Cloud Lidar research at the RNMI and KNMI2B2 version 2 Cloud Lidar analysis software documentation*, Technical report TR-172 KNMI, 1994
- [8] Guyot, A, *Personal communication*

Alternative algorithm for correcting FSSP measurements

R.J.P. Baedi, J.J.M. de Wit, H.W.J. Russchenberg and J.P.V. Poiarés Baptista¹
 IRCTR, International Research Centre on Telecommunications-transmission and Radar,
 Department of Informational Technology and Systems, Delft University of Technology,
 Mekelweg 4, 2628 CD Delft, The Netherlands, <http://irctr.et.tudelft.nl/>
 Phone: +31 15 2786292 Fax: +31 15 2784046 Email: H.W.J.Russchenberg@ITS.TUDELFT.nl
¹European Space Research and Technology Centre

INTRODUCTION

During Clare'98 several instruments were mounted on a Hercules C130 aircraft to measure cloud properties. Among the instruments were a Forward Scattering Spectrometer Probe (FSSP) and a Two-Dimensional Cloud probe (2DC) to measure cloud size distributions and a Johnson-Williams probe to measure liquid water content. The FSSP measures water droplets in the size range of 1 μm to 23.5 μm radius. The particles are sized in 15 radius bins of 1.5 μm each. The 2DC-probe images cloud particles in the size range of 6.25 μm to 406.25 μm radius, which are sized in 32 radius bins of 12.5 μm each. A detailed description of the particle probes can be found in [1]. More information on the Johnson-Williams sensor can be found in [2].

In order to obtain a complete size spectrum, the distributions measured by the two particle probes have to be merged. This paper assumes the merging technique as proposed in [3], which also discusses the standard off line processing of the measured size spectra. One of the standard procedures is to correct the FSSP-distributions such that the total liquid water content of the merged spectrum equals the liquid water content measured by the Johnson-Williams sensor (LWC_{JW}). This is done since the FSSP is known to under-read when the spectra are heavily weighted towards small drops [4]. The procedure corrects the FSSP-data by multiplying the entire FSSP-distribution by a constant correction factor, which is computed from:

$$CF_{const} = \frac{LWC_{JW} - LWC_{2DC}}{LWC_{FSSP}} \quad (1),$$

where LWC_{FSSP} and LWC_{2DC} are the liquid water content coming from the particles measured by the FSSP and 2DC probe respectively.

This correction method does not depend on the particle size. However, [5] suggest that the sample volume of the FSSP instrument is particle size dependent. Consequently, some bins will under-estimate the concentration more than other bins. In that case a size dependent correction factor is more appropriate.

DESCRIPTION OF THE ALGORITHM

An alternative, size dependent correction algorithm will be presented in this paper. This method assumes that the cloud

size distribution for FSSP-sized droplets is described by a gamma function, which is defined as:

$$N(r) = N_0 r^m \exp\{-\lambda r\} \quad (2),$$

where r is the drop radius and $N(r)$ is the number of drops per m^3 . The parameters N_0 and m are the scaling factor and the dispersion factor respectively; λ is usually taken as a function of m . The liquid water content (g/m^3) then follows as:

$$\begin{aligned} LWC &= \frac{4}{3} \pi \rho_w \int_{r_{\min}}^{r_{\max}} N(r) r^3 dr \\ &= \frac{4}{3} \pi \rho_w N_0 \int_{r_{\min}}^{r_{\max}} r^{m+3} \exp\{-\lambda r\} dr \end{aligned} \quad (3),$$

where r_{\min} and r_{\max} are the minimum and maximum radii of the droplets measured by the FSSP, and ρ_w is the density of water. Using the integral identity:

$$\int x^n \exp(ax) dx = \frac{1}{a} x^n \exp(ax) - \frac{n}{a} \int x^{n-1} \exp(ax) dx \quad (4),$$

equation (3) can be rewritten as:

$$LWC(\lambda) = \frac{4}{3} \pi \rho_w N_0 \left[-\exp(-\lambda r) (m+3)! \sum_{i=0}^{m+3} \frac{1}{(m+3-i)!} \frac{r^{m+3-i}}{\lambda^{i+1}} \right]_{r_{\min}}^{r_{\max}} \quad (5)$$

It is seen that if N_0 is assumed to be a constant, the LWC is a function of lambda only.

In principle, the method reconstructs the gamma function that produces LWC_{JW} (subtracted with LWC_{2DC}). The FSSP concentrations are then corrected by adjusting the slope of the FSSP-spectrum, λ_{FSSP} , such that it equals the slope of the 'true' spectrum, λ_{JW} . Thus, whereas the standard procedure corrects the data by adjusting the N_0 's, the correction method discussed in this paper corrects the FSSP-spectra by adjusting the lambda's of the original distributions. To achieve this, several assumptions have to be made. First, a value for m has to be chosen. Throughout this paper, $m=4$ is used, which is a typical value for precipitating clouds, such as the ones discussed in this paper [6]. Furthermore, the FSSP-concentrations have to be corrected in such a manner that relation (1) still holds. This is done to assure that in the end the liquid water content of the merged spectrum is equal to

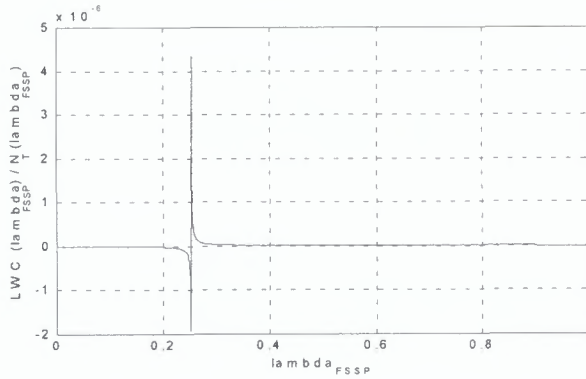


Fig. 1a

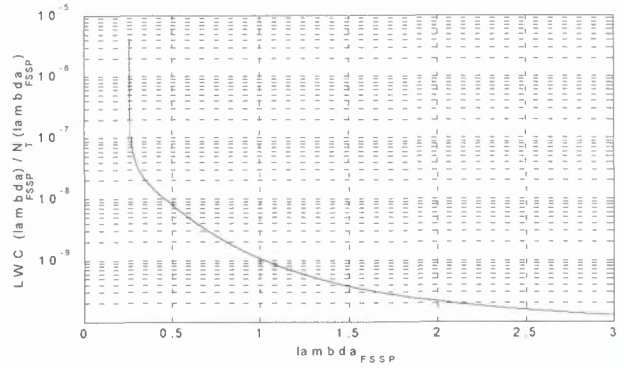
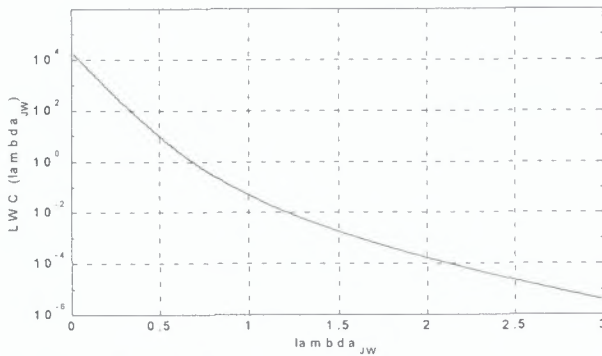


Fig. 1b

Fig. 1 Plot of $LWC(\lambda_{FSSP})/N_T(\lambda_{FSSP})$. Fig. 1b shows a close-up with the y-axis in log-scale.Fig. 2 Plot of $LWC(\lambda_{JW})$.

LWC_{JW} . Finally, in order to find a solution for λ_{JW} , it has to be either assumed that $N_{0,FSSP}=N_{0,JW}$, or it is assumed that the total number of droplets counted by both instruments are equal; $N_{T,FSSP}=N_{T,JW}$. It is doubtful that the latter assumption is correct, since it is known that the FSSP under-estimates the droplet concentrations. Therefore, the first assumption is used. The correction will not be applied if the Johnson-Williams measured an LWC smaller than 0.01 g/m^3 since this is the sensitivity threshold of the instrument. The total concentration N_T can be written as:

$$N_T(\lambda) = N_0 \int_{r_{min}}^{r_{max}} r^m \exp\{-\lambda r\} dr$$

$$= N_0 \left[-\exp(-\lambda r) (m)! \left\{ \sum_{i=0}^m \frac{1}{(m-i)! \lambda^{i+1}} \right\} \right]_{r_{min}}^{r_{max}} \quad (6)$$

Next, λ_{FSSP} is found by solving the following equality:

$$\frac{LWC_{FSSP}}{N_{T,FSSP}} - \frac{LWC(\lambda_{FSSP})}{N_T(\lambda_{FSSP})} = 0 \quad (7),$$

where LWC_{FSSP} and $N_{T,FSSP}$ are computed from the actually measured FSSP-data.

From fig. 1, which shows $LWC(\lambda_{FSSP})/N_T(\lambda_{FSSP})$, it is seen that, for positive values of $LWC(\lambda_{FSSP})/N_T(\lambda_{FSSP})$, equation (7) has a single solution. The figures imply that only solutions

exist for λ_{FSSP} greater than 0.25. However, [6] states that typical values of lambda lie around 1.

The merging technique that is used here neglects the first bin of the FSSP, since it is known to produce unreliable data [3]. If this is taken into account and it is assumed that $N_{0,FSSP} = N_{0,JW}$, the constant correction factor then follows as:

$$CF_{const} = \frac{LWC_{JW} - LWC_{2DC} - LWC_{neglect}}{LWC_{FSSP}}$$

$$= \frac{\int_{r_{min}}^{r_{max}} r^{m+3} \exp(-\lambda_{JW} r) dr}{\int_{r_{min}}^{r_{max}} r^{m+3} \exp(-\lambda_{FSSP} r) dr} \quad (8)$$

λ_{JW} can now be found by solving the following equality, which results from rewriting (8):

$$CF_{const} LWC(\lambda_{FSSP}) - LWC(\lambda_{JW}) = 0 \quad (9)$$

Fig. 2, which displays $LWC(\lambda_{JW})$, confirms that this equality has a single solution.

Finally, the size dependent correction factor is computed from:

$$CF_i = \frac{\exp(-\lambda_{JW} r_i)}{\exp(-\lambda_{FSSP} r_i)} \quad (10),$$

where i is the bin number.

RESULTS

Fig. 3 shows the results for October 7th run 51. During this run, a stratocumulus with little precipitation was present at a height of around 2.2 km. The Hercules flew at an altitude of about 2 km, which was near the cloud bottom. In fig. 3a the liquid water content from the alternative corrected spectra is displayed as the solid line, whereas the dashed line represents the LWC from the distributions corrected with the constant factor (which during this run is the same as LWC_{JW}). It shows that the LWC obtained using the corrected FSSP data matches

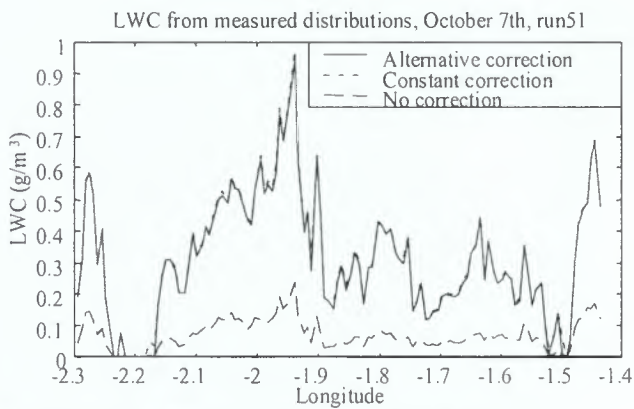


Fig.3a Plot of LWC from measured distributions.

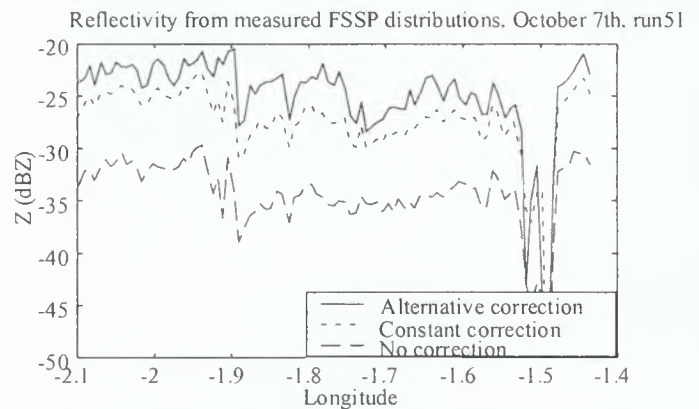


Fig.3c Plot of reflectivity from measured FSSP-distributions.

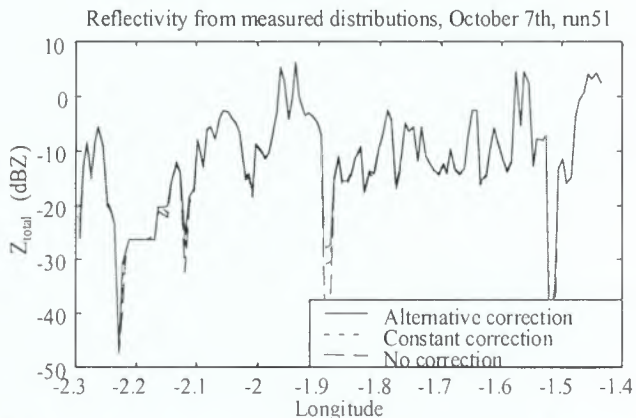


Fig.3b Plot of total reflectivity from measured distributions.

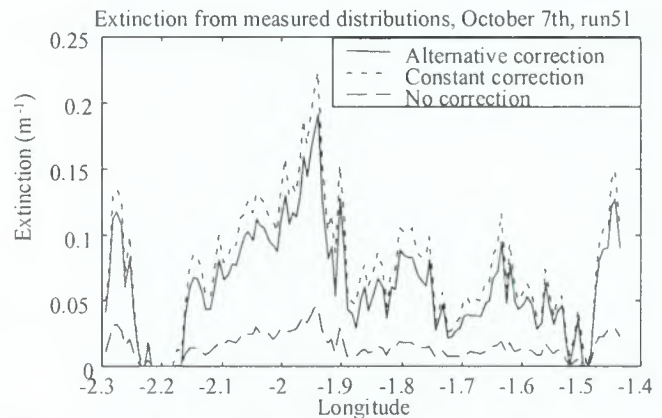


Fig.3d Plot of extinction from measured distributions.

Fig.3. Consequences of the size dependent correction factor for October 7th run 51. The solid lines in the graphs result from applying the alternative correction, the dotted lines represent the data from the constant correction, and the dashed lines are the uncorrected data. Fig.3a displays the LWC from the measured size spectra. The mean error is 0.0079. Fig.3b is a plot of the reflectivity from the merged FSSP and 2DC-spectra. Fig.3c shows the reflectivity computed from FSSP-distributions only, and fig.3d shows the effect of the corrections on the extinction (using the optical approximation).

the LWC of the Johnson-Williams generally well. The mean error between the two LWCs is 0.0079.

Fig.3b and fig.3c show the reflectivity of the merged and FSSP-spectra respectively. The size dependent correction factor does not have any impact on the reflectivity of the merged spectra, since the reflectivity is dominated by 2DC-sized drops; the FSSP-data contribute very little to the total reflectivity. If only FSSP-data are taken into consideration, however, a difference of about 4 dBZ exists between the reflectivity of the alternative correction, and the reflectivity using the constant correction. From fig.3d, which shows the extinction using the optical approximation, it is seen that when using the alternative method, the values for the extinction are slightly lower than when using the constant correction.

In fig.4 several size distributions are given to show the operation of the alternative algorithm. The figures on the right hand side show close-ups of the FSSP-distributions. Fig.4a and fig.4d show typical spectra from October 7th run 51. During this run, the spectra were heavily weighted towards the small drops. Consequently, the FSSP was underestimating the concentrations. The correction factors will therefore be relatively large. These graphs clearly show a

slope change in the spectrum of the alternative corrected data. Now, the slope of the FSSP-distribution better matches the slope of the 2DC-distribution.

Fig.4e shows a typical spectrum from October 7th run 72, at a time instance during which the cloud was precipitating. This run was flown at around 2.2 km, which was near the bottom of the cloud. The spectrum in this diagram is less weighted towards the small drops, compared to the ones in fig.4a and fig.4d. Therefore, the correction will be less severe as can be seen from fig.4f. The distribution displayed in fig.4g is taken from data measured off the Namibian coast. During this run a non-precipitating stratocumulus cloud was present with a base at around 0.95 km. The aircraft was flying at an altitude of 1.07 km. This is a typical example where the size-spectra are not weighted towards the smaller droplets. Therefore, very small correction factors are expected. This is indeed the case, as can be seen from fig.4h.

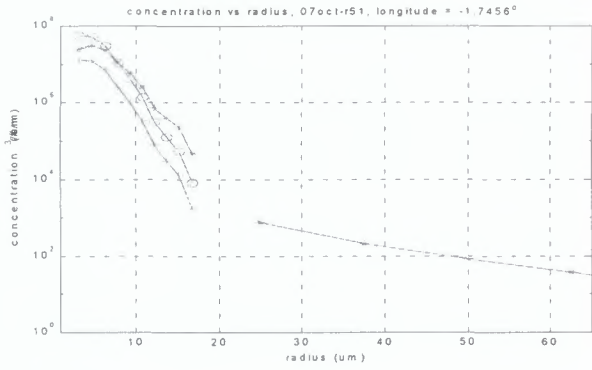


Fig.4a

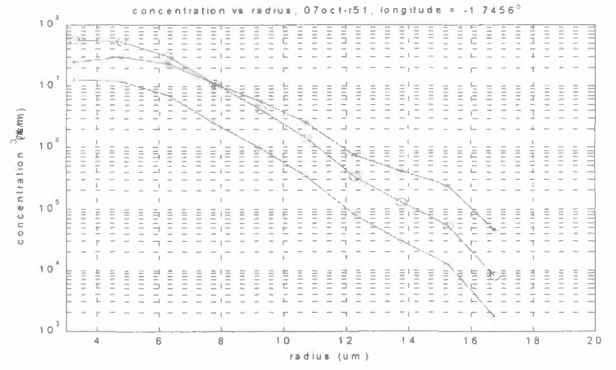


Fig.4b

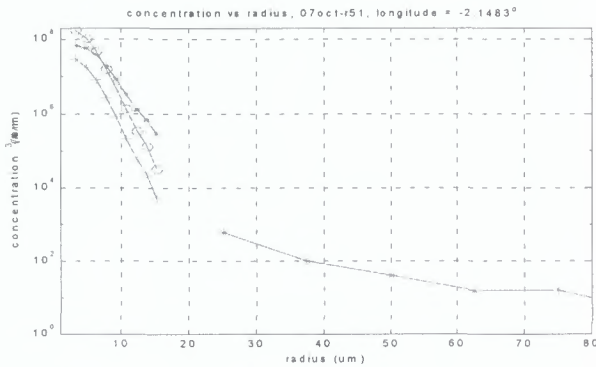


Fig.4c

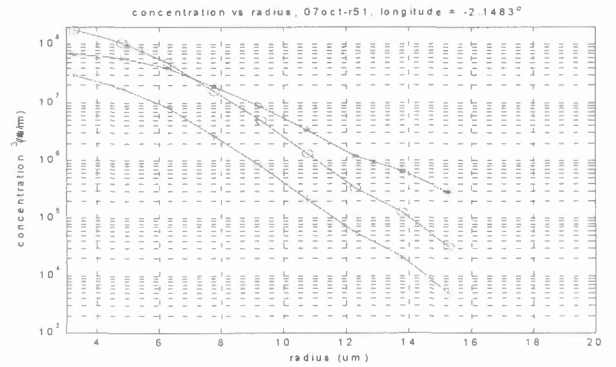


Fig.4d

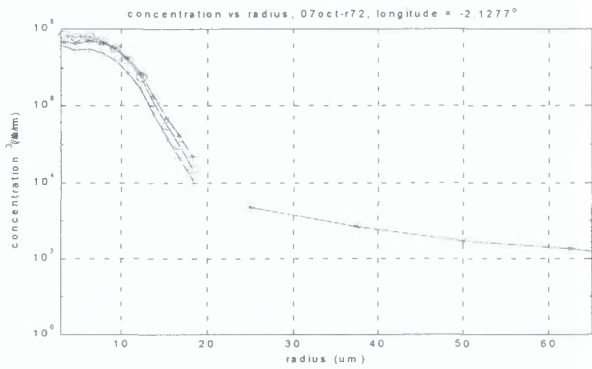


Fig.4e

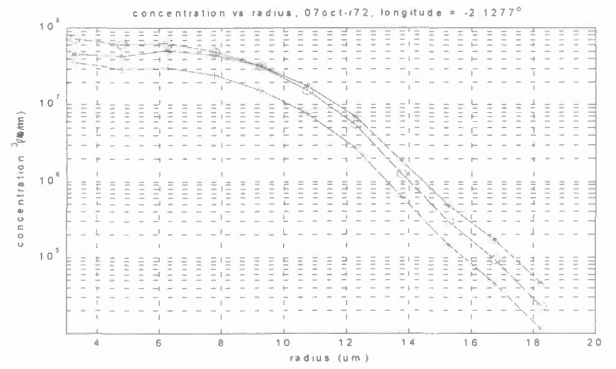


Fig.4f

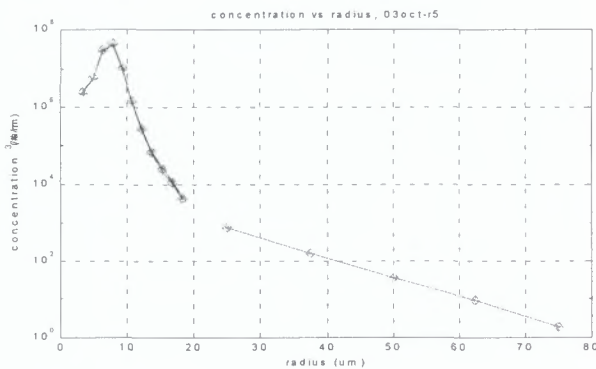


Fig.4g

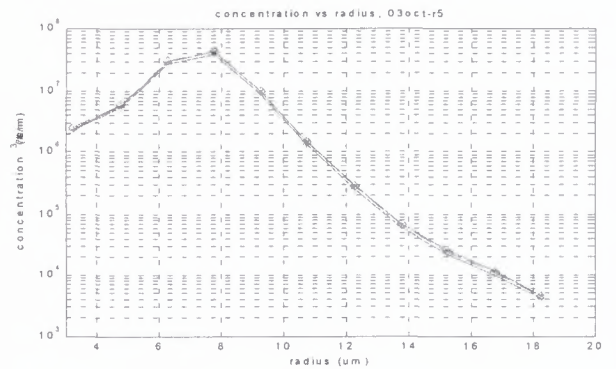


Fig.4h

Fig.4 Typical size distributions (number per m^3 per μm). The diagrams on the right show close-ups of the FSSP-spectra. The figures show data from October 7th 1998, run 51 (a - d), October 7th 1998, run 72 (e and f), and October 3rd 1995, run 5 (g and h). ** = alternative correction, ^{oo} = constant correction, ++ = no correction.

REFERENCES

- [1] S.J. Moss, P.R.A. Brown, D.W. Johnson, D.R. Lauchlan, G.M. Martin, M.A. Pickering, A. Spice, "Cloud microphysics measurements on the MRF C-130: Working Group Report", Meteorological Research Flight, MRF Technical note no. 12, 1993.
- [2] M. Oulbridge, "An introduction and guide to the Johnson-Williams liquid water content meter", Meteorological Office, Met. O. 15 internal report no. 41, 1982.
- [3] J.J.M. de Wit, R.J.P. Baedi, H.W.J. Russchenberg, J.P.V. Poiars Baptista, "Study of micro-physical and macro-physical measurements of water clouds during CLARE'98", Proc. CLARE'98 workshop, September 1999.
- [4] P.N. Francis, *Personal communication*.
- [5] J.E. Dye, D. Baumgardner, "Evaluation of the forward scattering spectrometer probe. Part I: electronic and optical studies", *J. Atmospheric and Oceanic Technology*, Vol. 1, 329-344, 1984.
- [6] R.J.P Baedi, J.J.M. de Wit, J.P.V. Poiars Baptista, "Comparison of micro-physical and macro-physical measurements of clouds during the Cloud Lidar and Radar Experiment", Internal report ESTEC-European Space Agency, 1999.



Estimation of cloud microphysical parameters from radar, lidar and microwave radiometer during CLARE'98

J. Erkelens¹, S. Jongen², H. Russchenberg¹, M. Herben², P. Francis³, and M. Quante⁴

¹IRCTR, Delft University of Technology, The Netherlands. Email: j.s.erkelens@its.tudelft.nl

²Eindhoven University of Technology, The Netherlands

³United Kingdom Meteorological Office, Farnborough

⁴GKSS Institut für Atmosphärenphysik, Geesthacht, Germany

ABSTRACT

In October 1998, the CLARE measurement campaign took place in Chilbolton, England. A variety of collocated instruments performed measurements on the clouds. Among the instruments were a microwave radiometer, lidars and radars. Also, particle size measuring probes were operated during flights through the clouds. Estimates of the cloud microphysical properties may be made by combining the measurements from the different remote sensing instruments. In this paper, two methods to estimate cloud microphysical properties are applied to the CLARE'98 data. Comparison of the results of one of the methods with in-situ data from the size measuring probes for 22 October shows reasonable agreement.

1. INTRODUCTION

The radiative properties of clouds depend on the concentrations and sizes of the droplets. By combining different remote sensing instruments, estimates of these microphysical cloud properties can be made. For example, Frisch *et al.* [1] combine a K_{α} -radar and a microwave radiometer to estimate liquid-water content, modal radius and droplet concentration in stratus clouds. Boers *et al.* [2] combine a lidar, an S-band radar and a microwave radiometer to estimate the concentration of cloud droplets. Hogan *et al.* [3] use the difference in attenuation between ground-based 35 and 94 GHz radars to estimate the liquid water content. Guyot *et al.* [4] use a dual-beam 95 GHz airborne radar to estimate cloud microphysical properties. Donovan *et al.* [5] combine radar and lidar to estimate effective radius in water and ice clouds.

Erkelens *et al.* [6] have applied the methods of Frisch *et al.* [1] and Boers *et al.* [2] to two cases of the CLARE data and compared the retrievals of droplet concentration. They showed that the Frisch-method is very sensitive to the value of the width parameter in the assumed lognormal distribution of cloud droplet sizes. This method will not work properly when drizzle is present. The Boers-method is less sensitive to drizzle, but needs an accurate estimation of cloud thickness.

In this paper, the methods of Frisch *et al.* and Boers *et al.* will be applied to more cases and for one case the results of the Boers-method are compared to measurements performed with airborne particle sizing probes. The instruments that have been used in this

study are the following: the microwave (21.3/31.7 GHz) radiometer of Eindhoven University of Technology, the Netherlands (on loan from ESA/ESTEC), the Vaisala CT75 ceilometer and the 35 GHz 'RABELAIS' radar of the Rutherford Appleton Laboratory, England (on loan from the Université Paul Sabatier, France), the 95 GHz 'MIRACLE' radar of GKSS, Germany [7], and the Forward Scattering Spectrometer Probe, the 2D-C probe and the Johnson-Williams liquid water content meter of the UK Meteorological Office.

The outline of the paper is as follows. In the next section the methods of Frisch *et al.* and of Boers *et al.* will be described. In section 3 examples of retrievals are shown and a comparison with in-situ data is made. A discussion of error sources is presented in section 4 and the paper finishes with some concluding remarks.

2. RETRIEVAL ALGORITHMS

Lognormal distribution

For both retrieval methods used in this paper the assumption is made that the cloud-droplet size distribution can be modeled by a lognormal distribution. The expression for the distribution and its moments, and the relationships between the moments and the remote-sensing measurements are given immediately below. After that, the retrieval methods are described.

The expression for a lognormal distribution is:

$$n(r) = \frac{N}{\beta\sqrt{2\pi}r} \exp[-(\ln r - \ln r_0)^2 / 2\beta^2] \quad (1)$$

where N is the droplet concentration (number of droplets per unit volume), β is the logarithmic width of the distribution and r_0 is the modal radius. The number of droplets per unit volume with radii between r and $r+dr$ is given by $n(r)dr$. Eq. (1) expresses that the logarithm of the droplet radii are distributed with a normal distribution. In general, the distribution may change with height in a cloud.

The k -th order moments M_k of this distribution are defined by:

$$M_k = \int_0^{\infty} r^k n(r) dr = N r_0^k \exp(k^2 \beta^2 / 2) \quad (2)$$

According to this definition, the zeroth order moment M_0 is the total concentration N . The measurements of different remote sensing instruments depend on the

moments of the droplet size distribution. For a lognormal distribution the expressions for the radar reflectivity factor Z , the liquid water content L and the lidar extinction σ are:

$$\begin{aligned} Z &= 2^6 M_6 = 64 N r_0^6 \exp(18\beta^2) \\ L &= (4\pi/3)\rho_w M_3 = (4\pi/3)\rho_w N r_0^3 \exp(4.5\beta^2) \quad (3) \\ \sigma &= \pi Q M_2 = \pi Q N r_0^2 \exp(2\beta^2) \end{aligned}$$

where ρ_w is the mass density of water, Q is the droplet extinction efficiency, which is about 2 for droplets much larger than the wavelength. One of the important cloud microphysical parameters is the effective radius, which is defined as the ratio of the third and second order moments, so for a lognormal distribution:

$$r_{\text{eff}} = M_3 / M_2 = r_0 \exp(2.5\beta^2) \quad (4)$$

Combining radar and radiometer – The Frisch-method

The radar delivers a height profile of the radar reflectivity factor, while the radiometer provides the liquid water path. Eq. (1) shows that three parameters (N , r_0 and β) are used to describe the cloud-droplet size distributions. Moreover, these parameters may have a height dependence. Therefore, a radiometer and radar do not provide enough information to estimate the detailed cloud microphysical properties. If one wants to say something about the droplet concentration, for example, assumptions have to be made about the other parameters and the height dependencies. Aircraft measurements performed in stratocumulus clouds suggest that the droplet concentration N and the width parameter β are approximately constant with height in the cloud [8],[9]. Frisch *et al.* [1] use these results in an algorithm that combines a K_α -radar and a microwave radiometer to estimate droplet concentrations and liquid water profiles. They assume a value of 0.35 for the width parameter. Eq. (3) shows that the liquid water content L is proportional to the square root of the radar reflectivity factor:

$$L = 0.52 \rho_w \sqrt{N} \sqrt{Z} \exp(-4.5\beta^2) \quad (5)$$

Integrating eq. (5) over the vertical and equating the result to the Liquid Water Path (LWP) provided by a microwave radiometer gives an estimate of the droplet concentration. Eq. (5) then provides an estimate of the vertical liquid water profile. Using the estimated concentration and the assumed value for the width parameter, a profile of effective diameter can also be computed. Note that the liquid water retrievals are influenced neither by radar calibration errors nor by a wrong assumption about the width parameter, but the concentration and effective diameters will be affected.

Combining radar, radiometer and lidar – The Boers-method

Boers *et al.* [2] developed a method to combine three remote sensing instruments to estimate the droplet concentration N . Eq. (3) shows the lidar extinction for a lognormal distribution. The extinction and the liquid water content are related according to:

$$L = 0.27 \rho_w N^{-1/2} \sigma^{3/2} \exp(3\beta^2/2) \quad (6)$$

However, it is often not possible to apply a technique similar to the one of Frisch *et al.*, because the lidar signal may not penetrate the entire cloud. Therefore, vertically integrating eq. (6) and adjusting N such that the result equals the liquid water path will not work in many cases. Boers *et al.* applied a different technique. Firstly, part of the extinction profile is estimated with the Klett-algorithm [10]. The additional assumption is made that the liquid water content increases linearly with height. The slope of the liquid water profile is found from the liquid water path and the thickness of the cloud. Boers *et al.* used an S-band radar with a vertical resolution of 30 m to find the cloud-top height, while the cloud bottom was defined as the height level immediately below the level where the lidar extinction curve exceeds 2 per km. It is necessary to use both instruments to determine the cloud boundaries, because each of the instruments alone does not suffice [11], [12]. Sassen [13] has calculated for water clouds that the cloud base obtained with lidar and radar will be about the same when the sensitivity of the radar is about -40 dBZ.

The extinction profile is now modeled by:

$$\sigma(h) = 3.84 \rho_w^{-2/3} N^{1/3} \left(\frac{LWP}{H^2} \right)^{2/3} h^{2/3} \exp(-\beta^2) \quad (7)$$

where LWP is the liquid water path, H is the cloud thickness and h is the height with respect to the bottom of the cloud. A least-squares fit of eq. (7) to the available points of the measured extinction profile provides an estimate for N .

3. RETRIEVALS

The two methods described above will be applied to five cases from the Clare'98 campaign at Chilbolton, in the United Kingdom. Figure 1 shows the results for 15 October 1998. The top panel shows the radar reflectivity factor of a thin stratocumulus cloud obtained with the 35 GHz radar 'RABELAIS'. The vertical resolution is 75 m and the time resolution of the picture is 1 minute. The middle panel shows a 5 minute average of the liquid water path (LWP) obtained from a microwave radiometer. The bottom panel shows retrievals of droplet concentration with

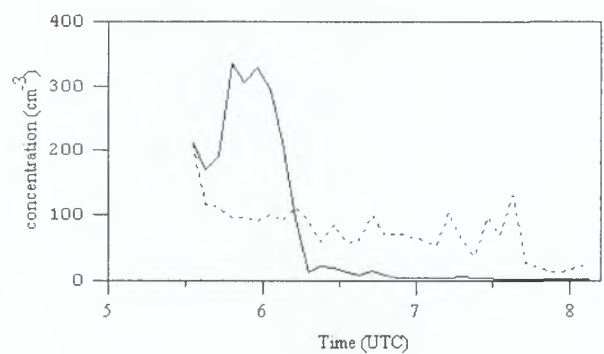
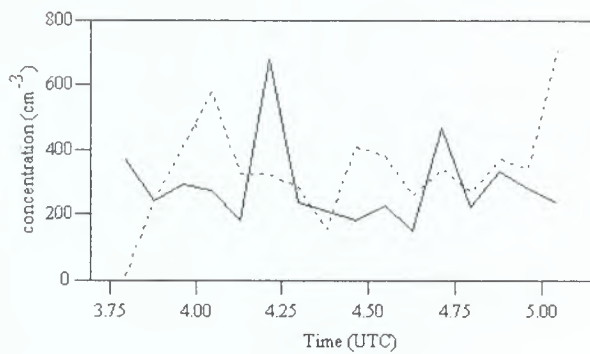
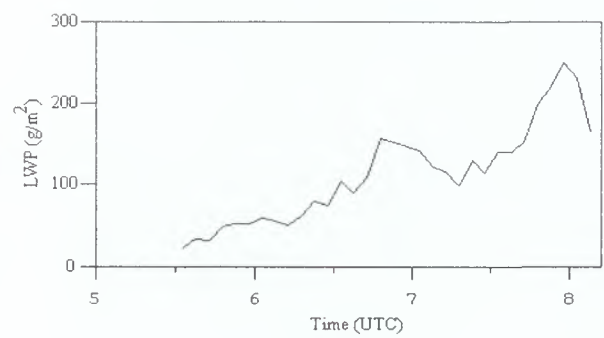
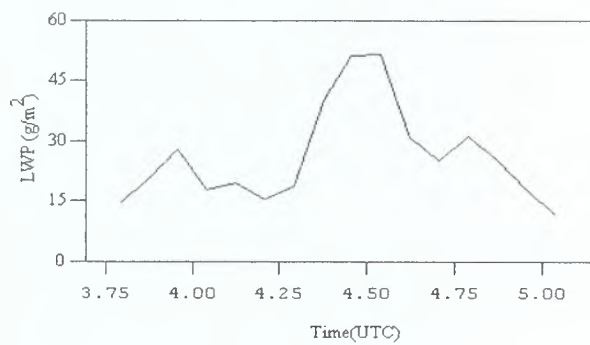
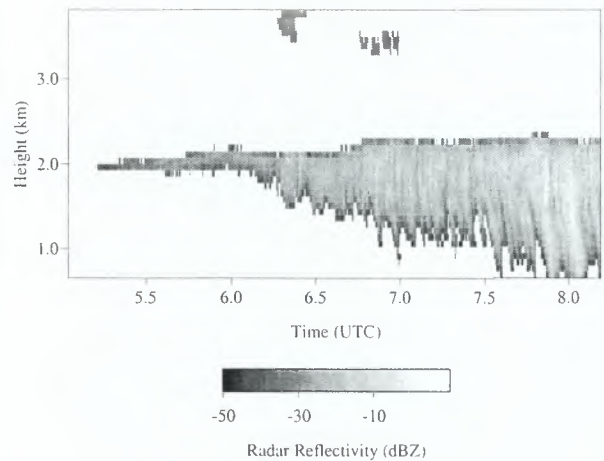
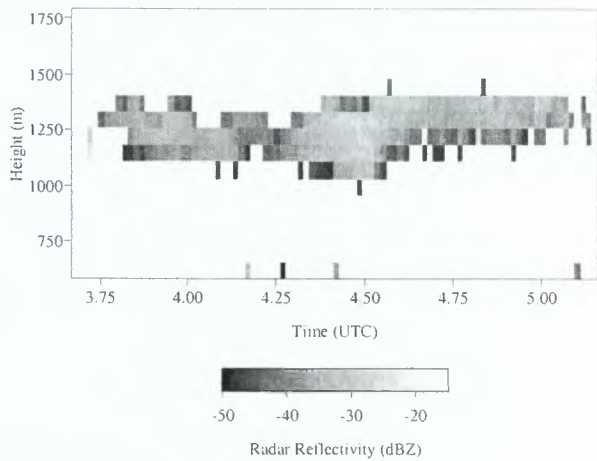


Figure 1. (a) Radar measurement of a stratocumulus cloud performed during the Clare'98 campaign (15 October 1998), with the 35 GHz radar 'RABELAIS'. (b) Liquid water path obtained from a microwave radiometer. (c) Retrievals of droplet concentration from the Frisch-method (solid line) and the Boers-method (dashed line).

Figure 2. (a) Radar measurement of a drizzling cloud performed during the Clare'98 campaign (20 October 1998), with the 35 GHz radar 'RABELAIS'. (b) Liquid water path obtained from a microwave radiometer. (c) Retrievals of droplet concentration from the Frisch-method (solid line) and the Boers-method (dashed line).

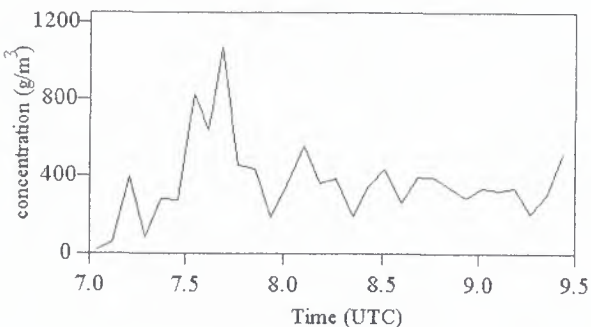
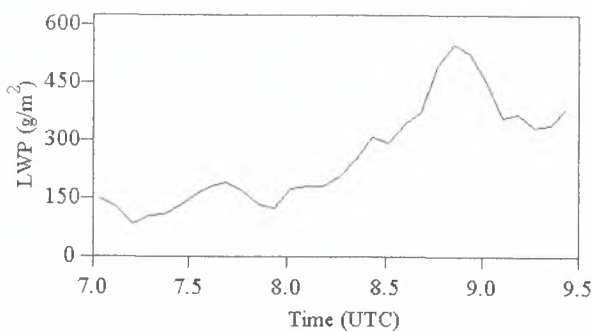
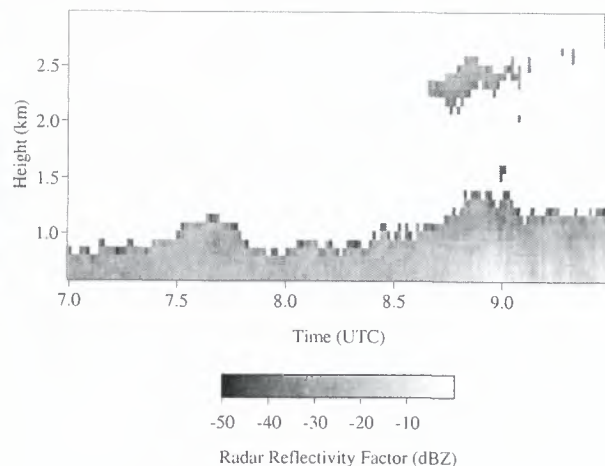
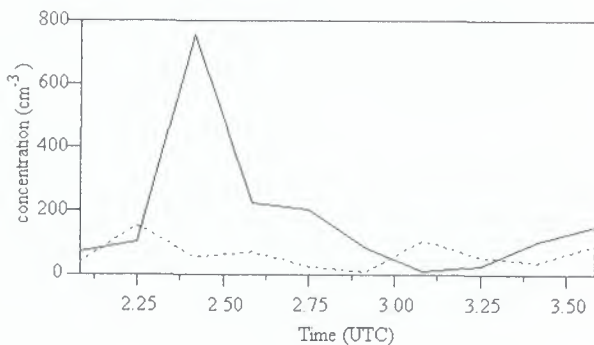
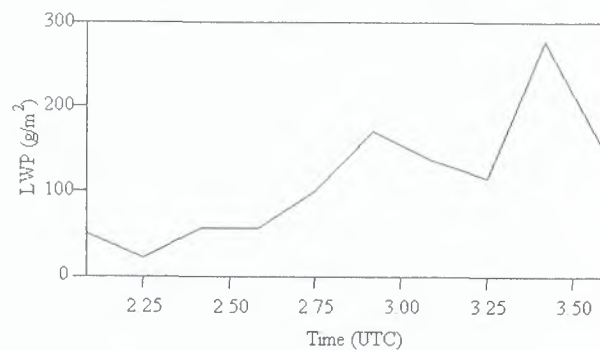
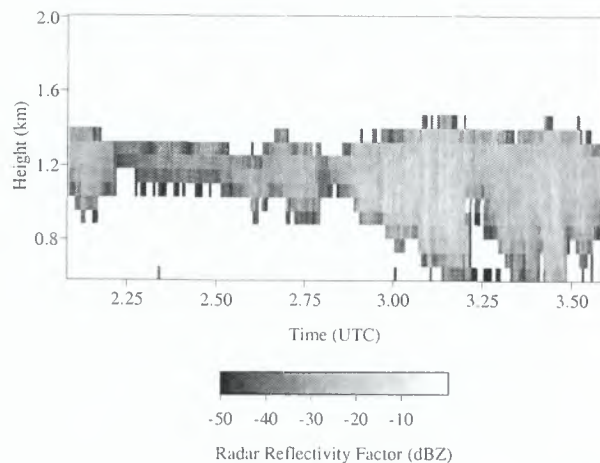


Figure 3. The top panel shows the 35 GHz radar measurement of a stratocumulus cloud performed on 13 October 1998. The middle panel shows the liquid water path for the same period and the bottom panel the concentrations estimated with the Frisch-method (solid line) and the Boers-method (dashed line).

Figure 4. The top panel shows the 35 GHz radar measurement of a stratocumulus cloud performed on 22 October 1998. The middle panel shows the liquid water path for the same period and the bottom panel the concentrations estimated with the Boers-method.

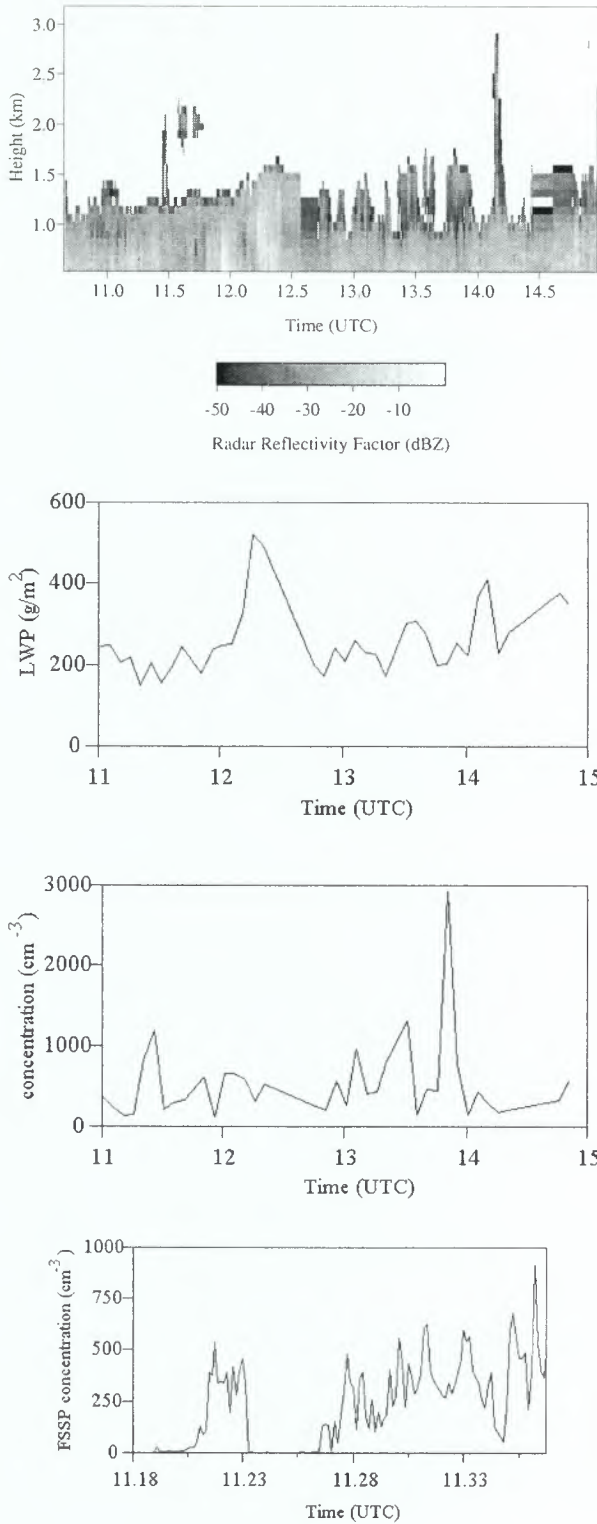


Figure 5. (a) About 4 hours of 95 GHz 'MIRACLE' radar data on 22 October 1998. (b) Liquid water path. (c) Droplet concentrations obtained with the Boers-method. (d) Concentrations from corrected FSSP-data, collected when the aircraft was close to the ground-based measurement location.

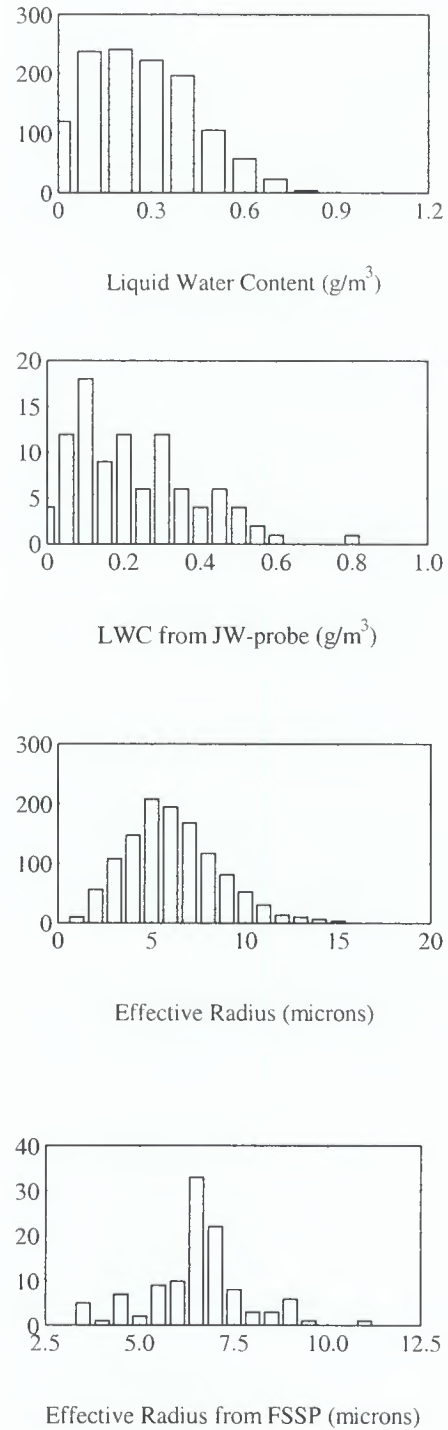


Figure 6. Histograms of liquid water content and effective radius obtained from the Boers-method and FSSP+JW-probe, respectively.

the two retrieval methods described above. The continuous line shows the concentration estimated with the Frisch-method, the dotted line the concentration given by the Boers-method. For both methods it has been assumed that the value of the logarithmic width β is equal to 0.35. The values that are obtained are reasonable. Unfortunately, no *in-situ* measurements are available for this case to validate the results, but a comparison with *in-situ* data could be made for 22 October, see figures 5 and 6. The average value of the droplet concentration found with the Boers-method is 338 per cm^3 , and the mean is 287 per cm^3 for the Frisch-method. An error in the assumed logarithmic width has a different influence on the concentrations found with each method. This can be seen from eqs. (5) and (6). If a value is used for β that is too low (high), then the estimates of droplet concentration from the Frisch-method will tend to be lower (higher) than those obtained with the Boers-method. The average values of the concentrations would become equal when $\beta=0.39$ is taken. Of course, the differences in the concentrations found could also originate from other error sources. Some of these will be discussed briefly in the next section.

The top panel in figure 2 shows a measurement of a cloud which starts to precipitate. This measurement was performed on 20 October 1998 with the 35 GHz radar as well. The middle panel shows the liquid water path. The retrievals of droplet concentration from the Frisch- and Boers-methods are the solid line and dashed lines shown in the bottom panel, respectively.

The Frisch-method is much more affected by the presence of drizzle, because the radar reflectivity is dominated by the largest drizzle droplets, while the liquid water content is determined by the smaller cloud droplets. In that case, the radar reflectivity and the liquid water content will almost be unrelated [14], [15]. It may be possible to distinguish between cases with and without drizzle by setting a threshold on the reflectivity or velocity [1]. Another method uses the effective radius estimated from radar and lidar [15].

Figures 3 and 4 show the results for two other cases on 13 October and 22 October. The Frisch-method could not be applied for the latter case, because the radar measured only part of the reflectivity profile.

Figure 5 shows the results of the Boers-method for a different period on 22 October. The top panel shows the radar reflectivity measured by the 95 GHz 'Miracle' radar. It is a concatenation of 11 periods of about 20 minutes each, with some gaps in between. The second and third panel show liquid water path and retrieved concentration, respectively. *In-situ* data has been collected during this period. The bottom panel shows the concentrations derived from the probes carried by the 'Hercules' aircraft, during run 11, when the aircraft was flying at an altitude of about 1 km. (The concentrations shown are from the FSSP, corrected such that the total liquid water content equals that of the Johnson-Williams probe.) The average value of the logarithmic width parameter for this data was 0.37.

The average concentration obtained with the Boers-method is 495 cm^{-3} . The average concentration for the *in-situ* data, when only values are taken into account for which the liquid water content as measured by the Johnson-Williams probe exceeds 0.01 g/m^3 , is 267 per cm^3 . The difference may be partly caused by the fact that the aircraft was flying near the base of the cloud layer, and did not stay in the clouds all the time, so the lower values found at the cloud edges may decrease the average concentration in the FSSP spectra.

The Boers-method models the liquid water profile as a straight line, the slope of which is calculated from cloud thickness and liquid water path. A profile of effective radius can be calculated from the retrieved concentration and this liquid water profile. Figure 6 shows histograms of liquid water contents and effective radii obtained this way, and also histograms of those quantities calculated from the corrected FSSP spectra. The ranges of values agree quite well with each other. Similar values of liquid water content have been found from the difference in attenuation between ground-based 35 and 94 GHz radars [3].

4. DISCUSSION

In this section, the most important sources of error in the retrieval methods will be discussed. In eq. (8) the dependency of concentration, effective radius and liquid water content on β and the measured quantities is shown for the Frisch-method:

$$\begin{aligned} N &\sim \frac{LWP^2}{Z_I} \exp(9\beta^2) \\ r_{\text{eff}} &\sim \sqrt[6]{\frac{Z \cdot Z_I}{LWP^2} \exp(-2\beta^2)} \\ L &\sim LWP \sqrt{\frac{Z}{Z_I}} \end{aligned} \quad (8)$$

where Z_I is the square of the height integral of the square root of the radar reflectivity factor:

$$Z_I = \left(\int \sqrt{Z} dz \right)^2 \quad (9)$$

The corresponding expressions for the Boers-method are:

$$\begin{aligned} N &\sim \frac{\sigma^3 H^4}{LWP^2} \exp(3\beta^2) \\ r_{\text{eff}} &\sim \frac{LWP}{\sigma H^2} \exp(2\beta^2) \\ L &\sim \frac{LWP}{H^2} \end{aligned} \quad (10)$$

The expressions show that radar calibration does not influence the estimate of liquid water content for the Frisch-method, and that β has no influence on liquid water content for both methods. It is also clear that errors in the measured quantities have the largest

impact on the concentration, and less on effective radius and liquid water content.

Both the Frisch- and the Boers-method make the assumption that the width parameter is constant with height and known (the value of 0.35 has been assumed here). The assumption of a constant value is questionable. For example, Gerber [16] finds values of β between 0.10 and 0.41 in marine stratocumulus clouds during ASTEX, and also a decrease with cloud height. FSSP measurements during the CLARA campaigns in 1996, in the Netherlands, show values between 0.19 and 0.44. This latter range of values would imply errors up to $\pm 60\%$ for the concentration obtained with the Frisch-method (if $\beta=0.37$ is used) and up to $\pm 23\%$ for the Boers-method (for $\beta=0.35$). The resulting errors in the effective radius are smaller (about 16% for both methods).

Both methods depend on the square of the Liquid Water Path (LWP). The LWP's are obtained with a non-linear algorithm called Matched Atmosphere Algorithm, developed at Eindhoven University of Technology [17]. The algorithm is a so-called profile algorithm: profiles of temperature, pressure, humidity and liquid water content are modeled. The humidity and liquid water profiles are changed until the brightness temperatures predicted by radiative transfer calculations match the measured ones. The tuning parameters are the cloud thickness and the slope of the liquid water profile. For this type of algorithm, the rms errors in derived LWP are of the order 10% - 20% [18] (but the errors are not less than about 10 g/m² for small amounts of liquid water). An error of 10% in LWP will cause errors of about 20% in concentration and 10% in liquid water content. The errors in effective radius will be about 10% for the Boers-method and 3% for the Frisch-method.

A calibration error in the radar reflectivity would influence the retrievals of concentration and effective radius for the Frisch-method, but not the estimates of liquid water content. A calibration error of 1 dB leads to an error of about 25% in the concentration and about 4% in effective radius.

For the Boers-method, it is very important to make an accurate estimation of the cloud thickness since the retrieval of the concentration depends on H^2 . Some of the clouds in the examples presented were not very thick (thickness about 300 m) and the resolution of the radars used was rather coarse (about 75 m), so an error of half a radar resolution cell would lead to errors in the order of 50%.

Errors in the derived lidar extinction will also contribute significantly to errors in the concentration. The Klett-algorithm [10] was used to infer the extinction profiles, which convergence increases with the optical thickness of the cloud. For the clouds studied here, convergence is probably not a problem. An error of 10% in extinction would cause an error of about 30% in concentration.

There are also a number of errors that are harder to quantify. Drizzle could seriously affect the performance of the Frisch-method, for example. If the

drizzle contains a significant amount of liquid water, then the Boers-method will also be affected. Also, the accuracy of the assumptions of a concentration constant with height and a linearly increasing liquid water content profile is unknown at present. Such assumptions should be validated with *in-situ* measurements. The cloud thickness is calculated from the radar cloud top and the lidar cloud base. Even if cloud thickness is estimated accurately, an error in cloud height would still influence the retrievals, because eq. (7) does not include an offset in the liquid water profile. It is possible to fit cloud base as well, if there are a sufficient number of points on the extinction profile [2], but that has not been done in this paper.

For very thin clouds, the mentioned errors and uncertainties may be so large that the retrievals become too unreliable to be of much practical value.

5. CONCLUDING REMARKS

Two methods to retrieve droplet concentration have been compared, the method of Frisch *et al.* [1] and the method of Boers *et al.* [2]. The concentrations obtained with the Frisch-method are more sensitive to errors in the assumed value of the width parameter than those from the Boers-method. For the latter method to work properly, however, an accurate determination of the cloud thickness and part of the extinction profile is necessary. The Frisch-method will not work when a cloud is drizzling, because the radar reflectivity will then be dominated by the drizzle drops while the liquid water path may still be dominated by the small cloud droplets. The Boers-method is less affected by drizzle.

More accurate results could be obtained, for example, by improving the retrievals of liquid water path. This may be done by providing the used profile algorithm with more information on atmospheric profiles and cloud height and temperature [19]. Using a radar with a finer height resolution can improve the accuracy of the measurements of cloud thickness.

ACKNOWLEDGMENTS

We thank John Goddard and Charles Wrench of the Radiocommunications Research Unit, Rutherford Appleton Laboratories, Chilton, United Kingdom for the ceilometer data, we are grateful to Henri Sauvageot and Nicolas Gaussiat of the "Laboratoire d'Aérodynamique, Université Paul Sabatier", Toulouse, France for providing the 35 GHz 'Rabelais' radar data, Olof Danne of GKSS, Germany kindly provided us with the 95 GHz 'Miracle' data, and we owe Robin Hogan of the Department of Meteorology, University of Reading, United Kingdom for doing the processing of the CLARE'98 data.

REFERENCES

- [1] Frisch, A.S., C.W. Fairall, and J.B. Snider, "Measurement of stratus cloud and drizzle parameters in ASTEX with a K_a -band radar and a microwave radiometer," *J. Atmos. Sci.*, Vol. 52, pp. 2788-2799, 1995.
- [2] Boers, R., H. Russchenberg, J. Erkelens, V. Venema, A. van Lammeren, A. Apituley, and S. Jongen, "Ground-based remote sensing of stratocumulus properties during CLARA-1996," *Accepted for J. Appl. Met.*, 1999.
- [3] Hogan, R.J., A.J. Illingworth, and H. Sauvageot, "Cloud characteristics from dual wavelength millimetre-wave radar," *Proc. 29th Conf. Radar Met.*, Montreal, Canada, pp. 457-459, 1999.
- [4] Guyot, A., F. Baudin, S. Haimov, P. Laborie, D. Leon, A. Pazmany, J. Pelon, J. Testud, V. Trouillet, and G. Vali, "Dual beam cloud radar and backscattering lidar on the same airborne platform: first results," *Proc. 29th Conf. Radar Met.*, Montreal, Canada, pp. 469-471, 1999.
- [5] Donovan, D., A. van Lammeren, and H. Russchenberg, "Cloud effective radius and water contents inferred from combined lidar and radar observations during CLARA," *Proc. symp. Remote Sensing of Cloud Parameters*, Delft, The Netherlands, October 1999.
- [6] Erkelens, J.S., S. Jongen, H. Russchenberg, and M. Herben, "Estimation of cloud droplet concentration from radar, lidar and microwave radiometer measurements," *Proc. symp. Remote Sensing of Cloud Parameters*, Delft, The Netherlands, 21-22 October 1999.
- [7] Quante, M., O. Danne, E. Raschke, and M. Chandra, "The GKSS 95 GHz cloud radar: system description, measurement examples, and calibration concepts," *European Trans. Telecom.*, in press.
- [8] Slingo, A., S. Nicholls, and J. Schmetz, "Aircraft observations of marine stratocumulus during JASIN," *Quart. J. R. Met. Soc.*, Vol. 108, pp. 833-838, 1982.
- [9] Martin, G.M., D.W. Johnson, and A. Spice, "The measurement and parameterization of effective radius of droplets in warm stratocumulus clouds," *J. Atmos. Sci.*, Vol. 51, No. 13, pp. 1823-1842, 1994.
- [10] Klett, J.D., "Stable analytical inversion solution for processing lidar returns," *Appl. Optics*, Vol. 20, No. 2, pp. 211-220, 1981.
- [11] Venema, V., H. Russchenberg, A. Apituley, A. van Lammeren, and L. Ligthart, "Cloud boundary height measurements using lidar and radar," *accepted for Phys. Chem. Earth*, 1999.
- [12] Clothiaux, E.E., T.P. Ackerman, G.G. Mace, K.P. Moran, R.T. Marchand, M.A. Miller, and B.E. Martner, "Objective determination of cloud heights and radar reflectivities using a combination of active remote sensing sensors at the ARM CART sites," *accepted for J. Appl. Met.*, 1999.
- [13] Sassen, K., G.G. Mace, Z. Wang, M.R. Poellot, S.M. Sekelsky, and R.E. McIntosh, "Continental stratus clouds: a case study using coordinated remote sensing and aircraft measurements," *J. Atmos. Sci.*, pp. 2345-2358, 1999.
- [14] Fox, N.I., and A.J. Illingworth, "The potential of a spaceborne radar for the detection of stratocumulus clouds," *J. Appl. Met.*, Vol. 36, No. 6, pp. 676-687, 1997.
- [15] de Wit, J.J.M., R.J.P. Baedi, J.S. Erkelens, H.W.J. Russchenberg, and J.P.V. Poyares Baptista, "Development of retrieval algorithms of cloud parameters from radar and lidar based on the CLARE data set," *Proc. symp. Remote Sensing of Cloud Parameters*, Delft, The Netherlands, 21-22 October 1999.
- [16] Gerber, H. "Microphysics of marine stratocumulus clouds with two drizzle modes," *J. Atmos. Sci.*, Vol. 53, No. 12, pp. 1649-1662, 1996.
- [17] Jongen, S., M. Herben, H. Russchenberg, and A. van Lammeren, "On the accuracy of water vapor and liquid water retrieval with the Matched Atmosphere Algorithm," *Proc. USNC/URSI National Science Meeting, Boulder, USA*, p. 71, January 1998.
- [18] Peter, R. and H. Kämpfer, "Radiometric determination of water vapor and liquid water and its validation with other techniques," *J. Geophys. Res.*, Vol. 97, No. D16, pp. 18,173-18,183, November 1992.
- [19] Erkelens, J.S., H.W.J. Russchenberg, S.C.H.M. Jongen, and M.H.A.J. Herben, "Cloud liquid water profile estimation combining radar and radiometer," *Proc. 8th URSI-F Symposium on Wave Prop. & Remote Sensing*, Aveiro, Portugal, pp. 167-170, 1998.

Photon Pathlengths Distributions and Cloud Optical Depth Derived from High Resolution Oxygen A-band Absorption Spectroscopy

O. Funk, C. v. Savigny, U. Platt, and K. Pfeilsticker
Institut für Umweltphysik, Universität Heidelberg
INF 229, 69120 Heidelberg, Germany

Phone: +49 6221 546313 Fax: +49 6221 546405 Email: ofunk@iup.uni-heidelberg.de

INTRODUCTION

High resolution spectroscopy of the oxygen A-band has emerged to a strong tool for the investigation of atmospheric radiative transfer especially for cloudy skies (Pfeilsticker *et al.*, 1998/99 [1,2]). Comparison with radiative transfer models however is ambitious because of the lack of initialization parameters for a usually largely under determined system. During the CLARE'98 campaign first simultaneous measurements of the detailed cloud structure and photon pathlengths distributions were carried out, allowing more detailed studies on the statistics of the radiative transfer. Together with radiative transfer modeling, the A-band measurements allow the deduction of an effective cloud optical depth for optically thick clouds.

MEASURING PATHLENGTH DISTRIBUTIONS

The method is based on absorption spectroscopy of oxygen. For a PDF $p(l)$ the transmission is given by eqn. (1) which can be interpreted as the Laplace transformation of $p(l)$ to $\tilde{p}(\alpha)$. $\tilde{p}(\alpha)$ can be measured at different absorption coefficients $\alpha(\lambda_i)$ of a set of oxygen absorption lines [i].

$$\frac{I(\lambda_i)}{I_0(\lambda_i)} = \int_0^{\infty} p(l) e^{-\alpha(\lambda_i)l} dl = \tilde{p}(\alpha(\lambda_i)) \quad (1)$$

The back transformation is ambiguous but can be solved by constraining $p(l)$ to gamma distributions, eqn. (2). Their Laplace transform is known and NLLS fitted to the measured transmissions.

$$p(l) = \frac{1}{\Gamma(\kappa) \left(\frac{l}{\kappa}\right)^\kappa} l^{\kappa-1} \exp\left(-\frac{\kappa l}{l}\right) \quad (2)$$

If vertical optical densities are used instead of the absorption coefficients, the pathlengths are in the more convenient units of vertical paths. Furthermore the gamma distribution is shifted by one vertical path, since shorter pathlengths can not occur for transmission measurements.

INSTRUMENTATION

The set-up consists of a zenith viewing telescope with a narrow field of view and the grating spectrometer with PDA detector, Fig. 1a. The spectral resolution is 20 pm. Due to the low spectral brightness of the sky, the spectrum has to be integrated for 15 min, in order to obtain sufficient S/N for this high resolution. The averaged

sky area depends on the cloud base height and the wind speed, Fig. 1b.

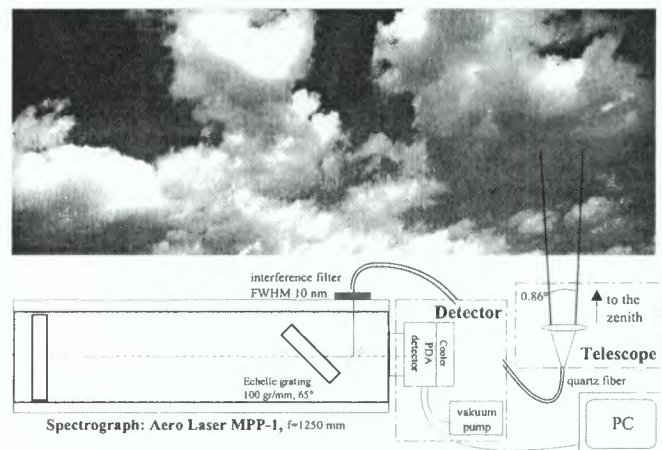


Figure 1a. Set-up of the A-band spectrometer

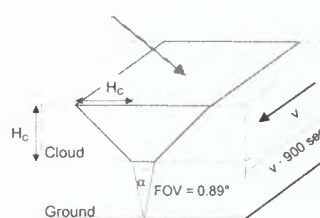


Figure 1b. Geometry of the observation. The probed cloud section depends also on the lateral photon transport (corresponds to the vertical cloud extension for homogeneous clouds)

The main problem in the spectrum evaluation is the insufficient spectral resolution of the spectrometer. This deficit is solved by modeling at high resolution (0.5e-4 nm). The spectroscopic model uses absorption line data from the HITRAN96 database, [4], and radio sonde atmospheric pressure and temperature profiles (40 layer atmospheric model, Voigt line profiles) to calculate vertical optical depth (VOD) references for the individual

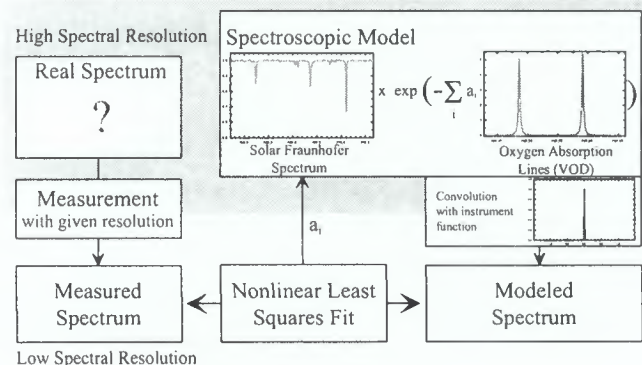


Figure 2. Scheme of the evaluation process

rotational absorption lines of the oxygen A-band ($^1\Sigma_g^+ \leftarrow ^3\Sigma_g^-, (\nu', \nu'')=(0,0)$ and $(1,1)$). The measured optical depth of the line i then is fit coefficient $a_i \cdot VOD_i$. Furthermore a 'zero air mass' called Fraunhofer reference has to be included. It is obtained by removing oxygen absorption from a sufficiently highly resolved (0.8e-3 nm) solar spectrum, (Kurucz *et al.*, 1984 [5]). The spectroscopic model is calibrated by direct sun light measurements.

In addition a fast sampling (2 Hz), narrow band photometer (centered at 753 nm, 10 nm wide, no oxygen absorption) with the same viewing geometry as the spectrometer was used to capture the temporal variation of the sky brightness. This data proved to be useful for understanding the composition of the integrated spectrum. The skylight intensity in the NIR spectral region is minimal for clear sky (with Rayleigh scattering only). It increases very sensitively with the appearance of optically relevant clouds and decreases again for optically very thick clouds, due to increasing reflection, Fig. 3. A detailed analysis of this signal, together with meteorological data, results in some basic properties of the investigated clouds. Spectral analysis reveals a characteristic scale break in the radiative field, at scales related to the vertical cloud extension (for details see Savigny *et al.*, 1999 [3]). Furthermore multifractal analysis techniques like structure functions and singular measures can be used to characterize the degree of stationarity and intermittency of data set, [3b].

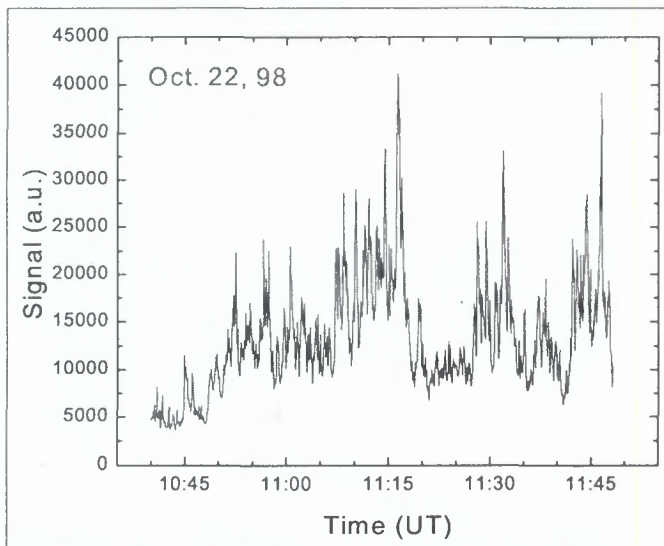


Figure 3. Photometer data set for Oct. 22nd, 98. Increased intensity marks episodes with clouds over the site

TWO CLOUD CASES

As an example, the evaluation process is shown for two spectra taken on Oct. 22nd. in Fig. 4. The top row shows the measured A-band spectra with the characteristic line pairs. Also included is the result of the fit. The transmissions in the resolution corrected (real) spectrum can be calculated from the fit coefficients a_i of the individual lines by $\exp(-a_i \cdot VOD)$. In the second row the transmission is plotted against the vertical

optical depth, which represents the Laplace transform of the pathlengths distribution. A fit with the Laplace transform of the gamma distribution yields the parameters of the distribution i.e., the first and second moment (Fig. 4, third row). The mean pathlength is about the same for both cases, but in the first case the distribution is much broader and skewed, while the second one is nearly gaussian. This can be explained by the vertical inhomogeneity of the clouds. The bottom row shows the cloud structure as measured by the colocated zenith looking 95 GHz Radar of the GKSS. Though cloud base height (taken from lidar) and cloud top height are the same for both cases, the vertical structure is different in both cases. During the first measurement two cloud layers with a gap of 4.5 km were present, while this gap closes till the start of the second measurement. Case 2 is more homogeneous, despite internal variability, leading to a narrow pathlengths distribution.

RADIATIVE TRANSFER MODELING AND CLOUD OPTICAL DEPTH

A plane parallel model (DISORT, Stamnes *et al.*, 1988 [6]) is used to calculate the transmissions for the observed lines. The cloud structure, i.e. the vertical extend of the layers is take from the cloud radar measurements. The optical depths $\tau_{c,j}$ of the cloud layers are free parameters in the RT-model and altered until measured and modeled transmissions converge (NLSF) for all absorption lines. The results are shown in Tab. 1. Derived total optical depths are 140 for the first case and 178 for the second. The only restriction of this retrieval algorithm is the usage of a plane parallel RT-model resulting in the optical depth of an equivalent homogeneous cloud. Furthermore this method only works in the regime of photon diffusion, i.e. for optically thick clouds.

Case	Cloud layers	g	τ_c
1	300 m - 900 m	0.85	18
	6000 m - 9300 m	0.7	122
2	300 m - 10000 m	0.85	178

Table 1. Results for τ_c of the RT-model. 40 atmospheric and 80 computational layers are used. The cloud extent is taken from Cloud Radar and Lidar measurements. g is the asymmetry factor of the Mie scattering phase function.

This effective cloud optical depth for the visible range can be compared with other cloud optical depth measurement. Within the CLARE98 data set the cloud optical depth can also be calculated from microwave radiometer liquid water path measurements, LWP, together with microphysical data from the particle probes on board of the C130 aircraft, r_e , by

$$\tau_c = \frac{3}{2Q_w} \cdot \frac{LWP}{r_e} \quad (3)$$

For days without in situ measurements a mean effective cloud droplet radius for the observed cloud type can be taken from look-up tables (e.g., Stephens, 1979 [7]).

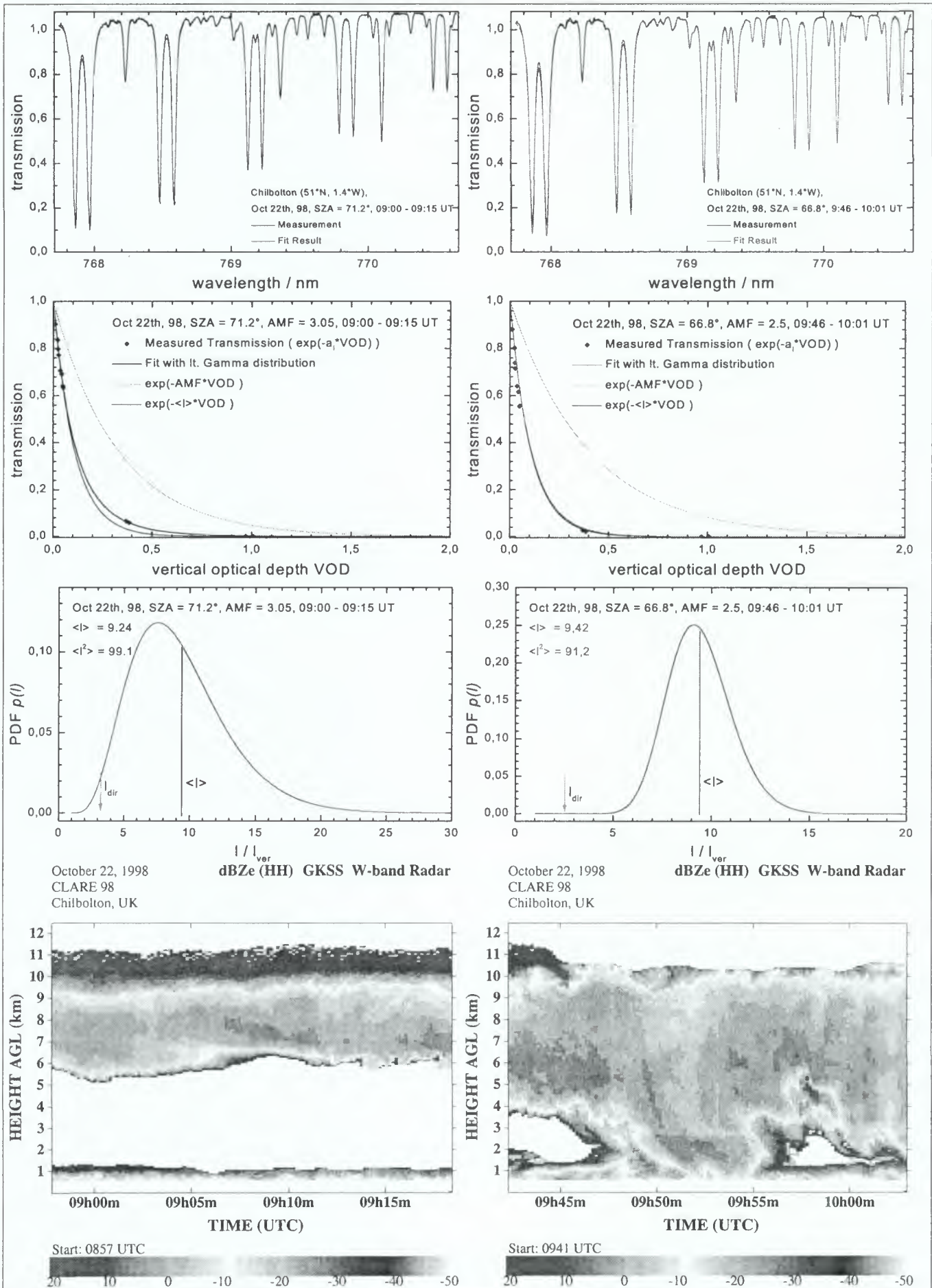


Figure 4. Evaluation for two cloud cases. Measured spectra and fit result (top row), result of the evaluation (2. row), derived pathlength distribution (3. row) and cloud structure (backscattering ratio) from the 95 GHz Cloud Radar of the GKSS (bottom row)

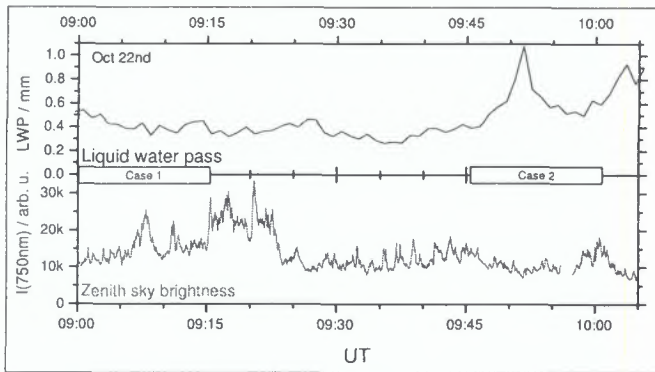


Figure 5. Liquid water pass from microwave radiometer measurements (TUE) (top panel) and zenith sky brightness variation from 750 nm narrow band photometer (bottom panel) for the two cloud cases on Oct. 22nd.

For accurate cloud optical depth calculation the LWC and r_e profiles are required. Another difficulty is the variation during the measurement. Tab. 2 summarizes the results for the two cloud cases. There is quite an uncertainty in the chosen r_e . The resulting cloud optical depths however, compare quite well.

Case	$\langle \text{LWP} \rangle / \text{mm}$	$r_e / \mu\text{m}$	τ'_c	τ_c^{RT}
1	0.45			
	0.08	5.4 (Sc1)	23	18
	0.35	6.2 (As)	85	122
2	0.65	6.2 (As)	157	178

Table 2. Calculated cloud optical depth from LWP. Effective radii for cloud types Sc1 and As are taken from Stephens, 1979 [7]. (Sc1: $\text{LWC}=0.14 \text{ gm}^{-3}$, $r_e=5.4 \mu\text{m}$; Ac: $\text{LWC}=0.28 \text{ gm}^{-3}$, $r_e=6.2 \mu\text{m}$). τ_c^{RT} are the results from the A-band measurements and the RT model. The resulting vertical cloud layer extends, calculated from observed LWP and typical LWC for the chosen cloud types (Case1: Sc 571 m, As 1250 m, Case2: 2710 m) are reasonable, considering all given uncertainties.

CONCLUSIONS

The interpretation of oxygen A-band measurements gains considerably from simultaneous cloud structure measurements supplied by cloud radar and lidar. The effect of cloud inhomogeneities on the form of the distribution can be measured. The cloud optical depth can be retrieved in a new independent way. These results should be compared to other cloud optical depth measurements like microwave radiometers. The CLARE data set can serve as input for detailed RT modeling and the study of the effect of cloud inhomogeneities on the photon pathlengths distribution.

ACKNOWLEDGMENTS This work was supported by the DFG (Deutsche Forschungsgemeinschaft) under the grant PF 384/1-1. We are grateful to M. Quante and O. Danne at GKSS for providing the cloud-radar images and Suzanne Jongen at TUE for the LWP data.

REFERENCES

- [1] Pfeilsticker, K., F. Erle, O. Funk, H. Veitel, and U. Platt, *First geometrical path lengths probability density function derivation of the skylight from spectroscopically highly resolving oxygen A-band observations. 1. Measurement technique, atmospheric observations, and model calculations*, J. Geophys. Res., Vol. 103, No. D10, 11,483-11,504, 1998, and 2. *Derivation of the Lévyindex for the sky light transmitted by midlatitude clouds*, J. Geophys. Res., Vol. 104, No. D4, 4101-4116, 1999
- [2] Veitel, H., O. Funk, C. Kurz, U. Platt, and K. Pfeilsticker, *Geometrical pathlength probability density functions of the skylight transmitted by midlatitude cloudy skies: Some case studies*, Geophys. Res. Lett., 25, 3355-3358, 1998.
- [3] von Savigny, C., O. Funk, U. Platt, and K. Pfeilsticker, *Radiative Smoothing in Zenith-Scattered Skylight Transmitted Through Optically Thick Clouds to the Ground*, Geophys. Res. Lett, Vol. 26, No. 19, p. 2949, 1999 and [3b] *Multifractal Characteristics of zenith-scattered Skylight transmitted through optically thick Clouds to the Ground*, in preparation
- [4] Gamache, R. R., Goldman, A., Rothman, L. S., *Improved Spectral Parameters for the Three Most Abundant Isotopomers of the Oxygen Molecule*, J. Quant. Spectr. Rad. Trans., Vol. 59, No 3-5, pp. 495-509, 1998
- [5] Kurucz, Furenlid, Brault, and Testerman, *Solar Flux Atlas from 296 to 1300 nm*, 1984
- [6] Stamnes et al., *Numerically stable algorithm for discrete-ordinate-method radiative transfer in multiple scattering and emitting layered media*, Appl. Op., 27, 2502-2509, 1988
- [7] Stephens, G. L., *Optical Properties of Eight Water Cloud Types*, Tech. Paper, no. 36, CSIRO, 1979

Comparison of cloud liquid water path estimates during CLARE'98

C.L. Wrench¹, S.C.H.M. Jongen², O.T. Davies³, P.A. Watson³

¹Radio Communications Research Unit, Rutherford Appleton Laboratory, Chilton, UK

²Eindhoven University of Technology, The Netherlands

³Dept. of Electronic and Electrical Engineering, University of Bath, Bath, UK

¹[Email: c.l.wrench@rl.ac.uk]

INTRODUCTION

Measurements of microwave emissions from atmospheric constituents can be used to estimate the column integrated liquid water along a selected path (LWP). The CLARE'98 campaign provided an opportunity to compare procedures for extracting estimates of LWP from measurements made with microwave radiometers. Measurements from two of the radiometer systems operated at Chilbolton in Southern England on 13th October 1998 have been analysed for the period of time when intensive measurements were being made using radars and lidars carried on aircraft above the site, as well as those situated on the ground.

A multi-frequency radiometer system belonging to ESTEC, and operated by the Technical University of Eindhoven (EUT), was making zenith brightness temperature measurements of the atmosphere at 21.3, 23.8 & 31.65 GHz for the whole of the CLARE'98 campaign period. Unfortunately, the 23.8 GHz channel was unstable during this period so that LWP has been estimated from measurements made at 21.3 & 31.65 GHz.

A 93 GHz radiometer belonging to the University of Bath operated until the 14th October 1998 when it suffered a component failure. LWP has been estimated from measurements at the radiometer frequency and coincident measurements of water vapour density above the Chilbolton site.

This paper describes the LWP estimation procedures and compares values collected on 13th October 1998 by the two radiometer systems.

RADIOMETER CHARACTERISTICS

(a) ESTEC Radiometer

- Frequency: 21.3, 23.8, 31.65 GHz +/- (10 MHz)
- Beamwidth:
 - 3dB: 1.9° + 0.1
 - 15 dB: 4.1° + 0.1
- Integration time: 1 second
- Resolution: 0.5K min
- Calibration by tip-curve technique.

(b) University of Bath Radiometer

- Frequency: 93.0 GHz +/- (20-250 MHz)
- Beamwidth: 1.3°(E-plane)*1.4°(H-plane)
- Integration time: 4 seconds
- Resolution: ~0.5K
- Lens corrected horn antenna pointing at zenith.
- Calibration by tip-curve technique.

ESTIMATION of LIQUID WATER PATH

ESTEC Radiometers:

EUT derived integrated amounts of water vapour (V) and liquid water (L) with the 21.3-31.65 GHz ESTEC radiometer. For retrieval both a linear (CCIR) and a non-linear algorithm, called Matched Atmosphere Algorithm (MAA), were implemented.

Linear retrieval (CCIR)

The CCIR model [1] is based on the CCIR report 719[2]. It assumes a linear relationship between the total attenuation $A(f)$ and the V , L and oxygen content. Therefore:

$$A(f) = a(f) \cdot V + b(f) \cdot L + c(f, h_0)$$

where:

a is the specific attenuation due to water vapour

b is the specific attenuation due to liquid water

c is the total attenuation due to dry-air (mainly oxygen)

h_0 is the height of the test site above sea level

Coefficients are determined from equations on specific attenuation as found in CCIR reports. $A(f)$ is calculated from brightness temperatures using:

$$A(f) = 10 \log \left[\frac{(T_{eff} - T_c)}{T_{eff} - T_b(f)} \right]$$

where:

T_{eff} = effective medium temperature [K]

T_b = brightness temperature [K]

T_c = cosmic background brightness temperature (~2.73 K) [K]

Because brightness temperatures are measured at two frequencies there are two equations, from which V and L are solved.

MAA retrieval

The MAA method is based on the 'profile algorithm' developed by Peter and Kämpfer [3]. It uses standard profiles, which are determined by real time data such as ground temperature, humidity and pressure. In our MAA implementation the CCIR temperature- and pressure profile [2], a relative humidity profile as proposed by Peter and Kämpfer and a liquid water (cloud) model as proposed by Slobin were taken as standard profiles. Next to ground data, the relative humidity- and liquid water profiles are determined by the following parameters:

- *RHref*: the relative humidity from 1.5 km above groundlevel to 1.5 km above the top of the assumed cloud,
- *Hbase*: the base of the cloud
- *Htop*: the top of the cloud
- *C*: a parameter that characterises the cloud and thereby the amount of L inside the cloud. It varies typically between 0.1 and 0.75.

The parameters *RHref* and *Hbase* are used to generate a set of atmospheres and accompanying brightness temperatures (calculated using MPM, Liebe [4]). The set of brightness temperatures, called lookup table or convergence area, is used to look up measured brightness temperatures and to determine V- and L values. The advantage of MAA with respect to linear retrieval (CCIR) is that it uses real time data. Next to that data of additional instruments, such as radar *Htop* values, can be used as input. Results obtained with these algorithms have been published earlier [5].

University of Bath Radiometer:

The procedure adopted for estimating LWP from 93 GHz brightness temperature T_b measurements required that we establish the level of total path zenith attenuation τ (dB) using the so-called 'brightness temperature equation':

$$\tau = 10 \log_{10} [(T_M - T_c) / (T_M - T_b)]$$

where:

T_M is the mean radiating temperature of the atmosphere;
 T_c is the cosmic background signal equal to 2.75 K.

Uncertainty in the value of T_M to be used when calculating τ was addressed by using the two possible extremes values, i.e. that associated with a clear sky (i.e. no cloud) situation T_{M1} , and that corresponding to the air temperature at the altitude of the liquid water cloud T_{M2} . T_{M1} was estimated by predicting clear sky attenuation using the Liebe model [4] together with air temperature and water vapour density profiles taken from ECMWF (The European Centre for Medium Range Weather Forecasting) analyses/forecasts for Chilbolton. These values of attenuation were confirmed by coincident measurements of

water vapour path using GPS (Global Positioning System). T_{M2} was estimated by establishing the cloud base height with measurements from an IR ceilometer that operated alongside the radiometers. In practice it can be shown that the values of τ are relatively insensitive to the value of T_M used.

Attenuation by the atmosphere when it is free of rain, τ , is an accumulation of loss caused by oxygen, water vapour and cloud liquid:

$$\tau = \tau_{oxy} + \tau_{vap} + \tau_{liq}$$

By estimating τ_{oxy} & τ_{vap} independently it was possible to arrive at a value for the loss due to liquid water cloud alone:

$$\tau_{liq} = \tau - \tau_{oxy} - \tau_{vap}$$

Then:

$$L = \tau_{liq} / K_L$$

where:

L is the total columnar liquid water path (LWP), and K_L is the liquid water absorption coefficient at the temperature of the cloud.

ECMWF Model data

Analyses/forecasts for the region above Chilbolton during the CLARE'98 campaign were performed every hour. Model variables, including pressure, temperature, and relative humidity were available at 31 model levels up to an altitude of ~25 km above sea level.

Gaseous attenuation, (τ_{oxy} & τ_{vap})

Using ECMWF profiles of pressure, temperature and water vapour density as inputs to the Liebe attenuation prediction model [4], it was possible to calculate estimates of atmospheric losses due to the presence of oxygen and water vapour at given times.

GPS estimates of water vapour path

Values of water vapour path derived from the ECMWF model data were confirmed by coincident measurements using the GPS (Global Positioning System).

Located near to the 93 GHz radiometer was a GPS receiver with a choke ring antenna. The receiver was able to simultaneously measure the change in phase of both the L1 and L2 carrier signals from up to 12 GPS satellites. The techniques used for obtaining zenith water vapour attenuation from GPS phase delay measurements are described by Davies et al [6] and have also been summarised below. Using the GIPSY GPS processing software from JPL and the precise positioning strategy, it is possible to produce estimates of the tropospheric zenith total delay at a time resolution of 5 minutes. Delays introduced in the ionosphere are removed by combination of the L1 and L2 phase measurements. The

zenith total delay is the sum of the zenith hydrostatic delay due to the dry constituents in the atmosphere and the zenith wet delay due to water vapour. The zenith hydrostatic delay can be estimated with some accuracy if the atmospheric pressure at the height of the choke ring antenna is known. The zenith wet delay can be found by simple subtraction of the zenith hydrostatic delay from the zenith total delay. Water vapour content is related to the zenith wet delay by a function which contains the medium temperature of water vapour in the atmosphere. The medium temperature of water vapour can be inferred using a temperature measurement at ground level. Zenith attenuation at 93 GHz is found by multiplying the water vapour content by the mass absorption coefficient for this frequency (0.05 dB/mm). Figure (1) shows the variation of zenith water vapour + oxygen attenuation at 93 GHz from 12 noon to 18-00 hrs. The GPS phase delay technique for the measurement of water vapour has the advantage of working in nearly all weather conditions.

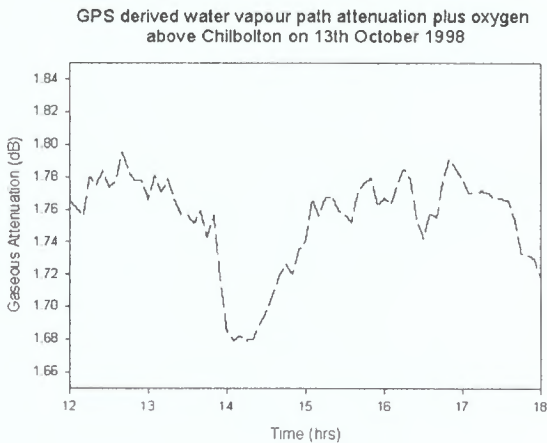


Figure 1

For 13th October 1998, using methods described, the following values were established for use in the estimation of LWP:

$$T_{M1} = 279.8 \text{ K}$$

$$T_{M2} = 287.0 \text{ K}$$

$$K_L = 0.0042 \text{ dB}/(\text{g}\cdot\text{m}^{-2})$$

$$[\tau_{\text{oxy}} + \tau_{\text{vap}}] = 1.68 \text{ dB}$$

RESULTS

The three radiometers described in this paper were calibrated using the so-called 'tipcurve' technique. The 93 GHz radiometer can also be calibrated using a cold load held at the temperature of liquid nitrogen. Figure (2) shows estimates of liquid water made using 93 GHz radiometer, and 21.3/31.65 GHz radiometer, brightness temperature measurements.

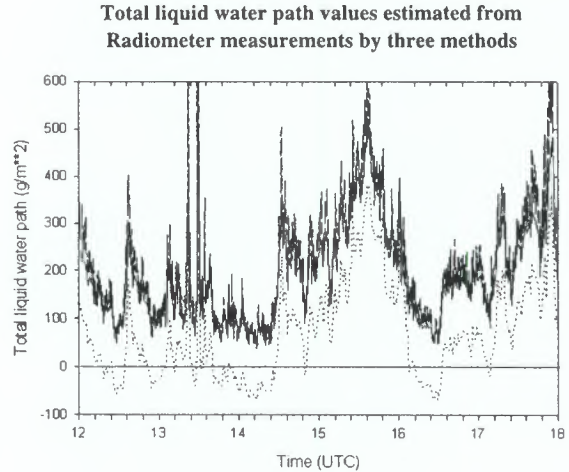


Figure 2

Solid line = 21.3/31.65 GHz MAA retrieval
 Dotted line = 21.3/31.65 GHz linear retrieval
 Dashed line = 93 GHz retrieval

In figure (3), the difference between liquid water path values retrieved from 21.3/31.65 GHz and 93 GHz measurements is plotted.

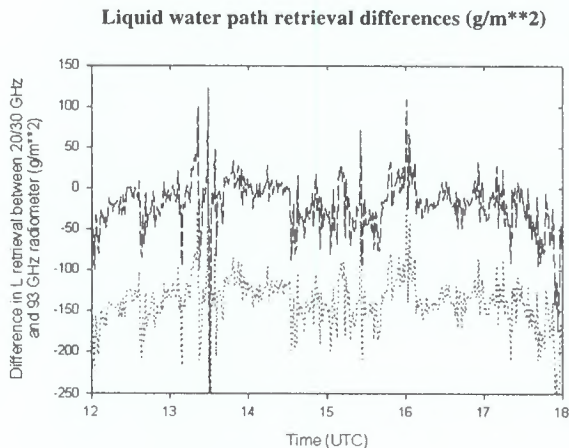


Figure 3

Dotted line = [21.3/31.65 GHz linear - 93 GHz] retrieval
 Dashed line = [21.3/31.65 GHz MAA - 93 GHz] retrieval

The results show very clearly that 21.3/31.65 GHz MAA liquid water path retrievals match best with the 93 GHz retrievals. It is observed that values of liquid water path based on 93 GHz data retrievals are marginally higher.

CONCLUSIONS

Analysis to estimate liquid water path has shown that, for correctly calibrated radiometers, 93 GHz and 21.3/31.65 GHz liquid water retrievals correspond quite well. Liquid water path values retrieved from 93 GHz data are marginally higher. This may be explained by the use of a value for liquid water temperature, T_{M2} , which is calculated from the air temperature at the base of the cloud. As a consequence there would be a slight underestimation of the applicable liquid water attenuation coefficient.

Negative values of liquid water path produced by the linear retrieval technique suggest that this method can lead to significant underestimation of liquid water path. Particularly as, on this day, coincident ceilometer measurements indicate that low level cloud persisted above the Chilbolton site throughout the period analysed.

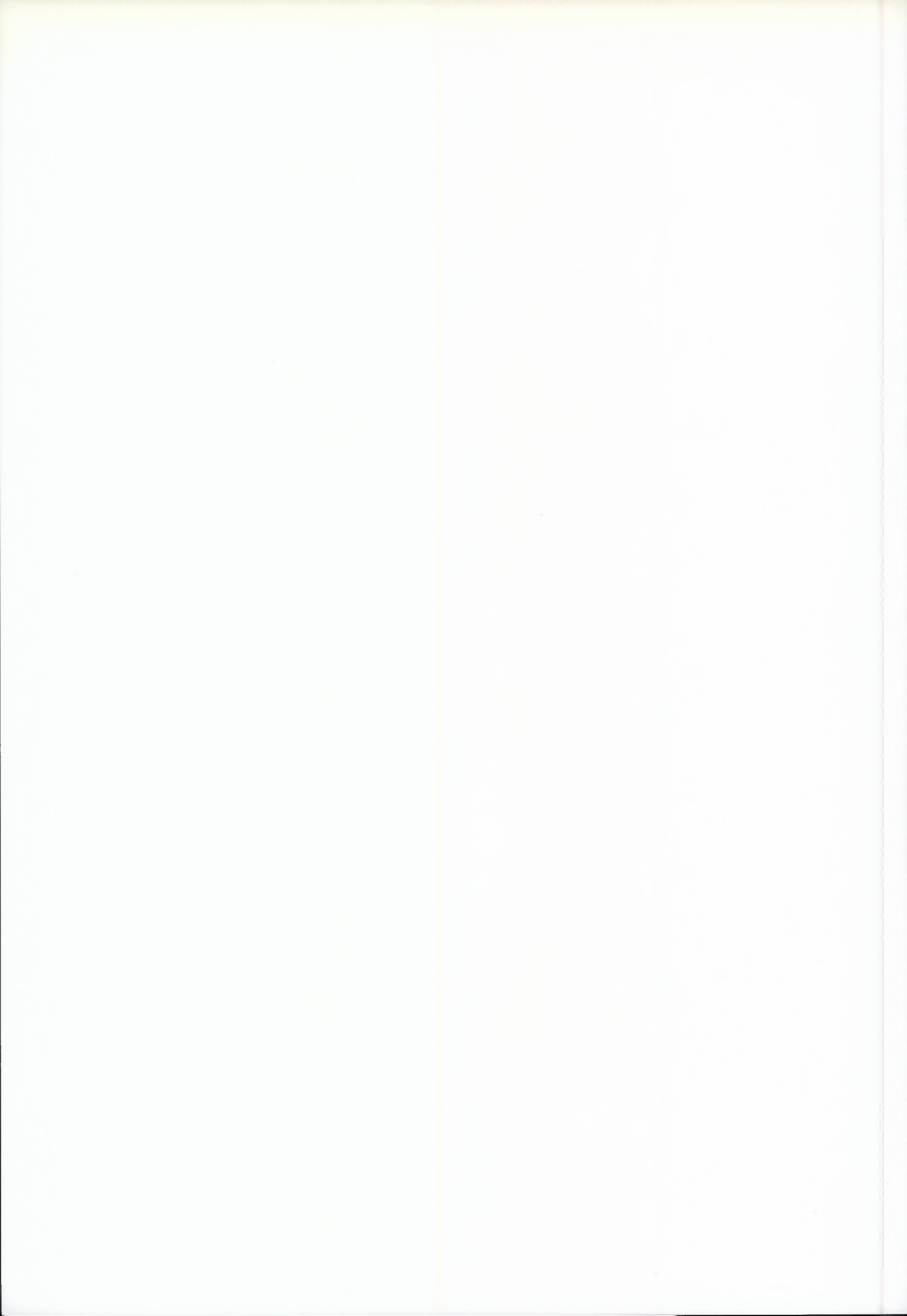
The MAA retrieval method is expected to give better results than the linear retrieval method as it is time and site dependent. This is not the case for the, more general, linear method.

Spikes in the retrieved data at ~13-20, ~13-30 and ~15-25 are occurring at times when there was evidence of very light rain detected on the ground at Chilbolton. This rain dramatically enhances the brightness temperature recorded by the radiometers and significantly reduces the validity of the retrieval algorithms employed. These spikes do not necessarily represent valid retrievals of liquid water path.

REFERENCES

- [1] 20/30 GHz Rescom radiometer manual
- [2] Recommendation ITU-R P.835-2. Reference standard atmospheres', ITU-R Recommendations, Geneva 1997, pp223-227
- [3] R. Peter and N. Kämpfer, 'Radiometric determination of water vapor and liquid water and its validation with other techniques', *J. Geophys. Res.*, Vol.97, No. D16, pp. 18,173-18,183, November 1992.
- [4] H.J.Liebe, 'MPM- An Atmospheric Millimeter -Wave Propagation Model', *Int. J. Infrared Millimeter Waves*, Vol.10, No. 6, pp.631-650,1989
- [5] S. Jongen, M. Herben, H. Russchenberg, A. van Lammeren, 'On the accuracy of water vapor and liquid water retrieval with the Matched Atmosphere Algorithm', *Proceedings of the 1998 USNC/ URSI National Science Meeting, Boulder, USA, 5-9 January 1998*, pp.71.
- [6] O.T. Davies and P.A.Watson, 'GPS phase-delay measurements - A new technique for the calibration and analysis in millimetre-wave radio propagation studies', *IEE Proc. Microwaves, Antennas and Propagation*, accepted for publication.

**Ice Water Retrieval
by Radar / Lidar Synergy**



Cloud effective radius and water contents inferred from combined lidar and radar observations during CLARE'98.

David P. Donovan and A.C.A.P. Van Lammeren

Royal Netherlands Meteorological Institution (KNMI), Postbus, 201, DeBilt, 3730 AE,
The Netherlands, e-mail: donovan@knmi.nl

J. Goddard, Rutherford Appleton Laboratory, UK

Henri Sauvageot, Laboratoire d'Aerologie, Universite Paul Sabatier, Toulouse, France

R.J Hogan, Department of Meteorology, University of Reading, UK

Abstract

In principle, combined lidar and radar cloud soundings are capable of providing detailed height resolved information of the effective sizes of cloud particles. However, accounting for extinction at the lidar wavelength in an appropriate manner can be problematic. In this paper a recently developed procedure for estimating cloud effective particle radius and water content profiles is described. The procedure accounts for extinction in a self-consistent manner and has many advantages over conventional lidar or radar only procedures. The technique has been applied to a number of CLARE cases and some examples will be presented here.

INTRODUCTION

Cloud lidar and radar share many similarities. Both are active systems which acquire information about their targets (clouds) by launching pulses of electromagnetic radiation and then detecting the returned radiation as a function of time after each given pulse was emitted. Both types of systems are capable of providing height-resolved information with a high temporal and spatial resolution. The key difference between lidar and radar systems is, of course, the large difference in their associated wavelengths. Cloud lidars typically employ wavelengths in the range of 0.5-1.0 microns while radar systems employ wavelengths in the millimeter to centimeter range. This large difference in wavelength leads to a large difference in the response to a cloudy volume with a given effective particle size.

The relative strengths of the lidar and radar backscatters as a function of effective radius for three different gamma-type cloud particle distributions is shown in Fig.1. The calculations were performed using Mie theory and assuming gamma type distributions where γ was set to 3, 5, and 7 respectively. i.e.

$$\frac{dn}{dr} = \frac{N_o}{R_m} \frac{1}{\Gamma(\gamma)} \left(\frac{r}{R_m} \right)^{\gamma-1} \exp \left[-r/R_m \right] \quad (1)$$

where dn/dr is the number of cloud droplets with radii between r and $r+dr$, R_m is the mode parameter and N_o is the total number of particles.

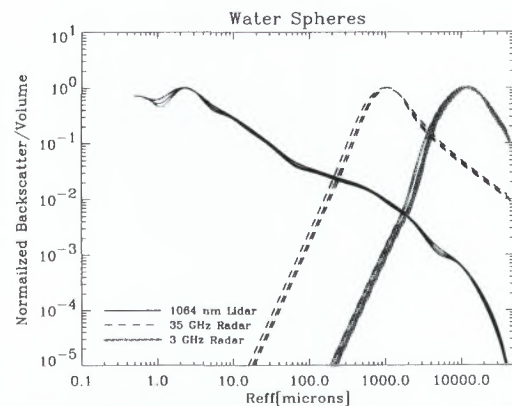


Figure 1. Normalized backscatter per unit volume as a function of R_{eff}

R_{eff} in Fig 1. Is defined in the normal fashion, i.e.

$$R_{eff} = \langle r^3 \rangle / \langle r^2 \rangle \quad (2)$$

where the braces denote averaging over the size distribution. It can be seen that, broadly speaking, the lidar will be sensitive to the presence of small particles while the radar will be most sensitive to the presence of larger droplets.

LIDAR/RADAR RATIO

Considering spherical scatters for the moment. Since cloud particles tend to be large compared to the lidar wavelength, the extinction and backscatter coefficients for a single particle will be approximately proportional to r^2 . Since the same particles will be small compared to the radar wavelength, they will act approximately as a Rayleigh scatterers and the radar backscatter will for a single particle scale with r^6 . Accordingly, the ratio of the radar backscatter to the lidar extinction is more usefully thought of as a function of

$$R'_{eff} = [\langle r^6 \rangle / \langle r^2 \rangle]^{1/4} \quad (3)$$

instead of R_{eff} . For a gamma type size distribution

$$R'_{eff} = \left[\frac{(\gamma + 5)(\gamma + 4)(\gamma + 3)}{(\gamma + 2)^3} \right]^{1/4} R_{eff} \quad (4)$$

The utility of using R'_{eff} is illustrated in Fig 2, where the ratio of the radar reflectivity to lidar extinction computed using different values of gamma are shown both as functions of R'_{eff} and R_{eff} . The radar reflectivity is related to the radar backscatter coefficient as

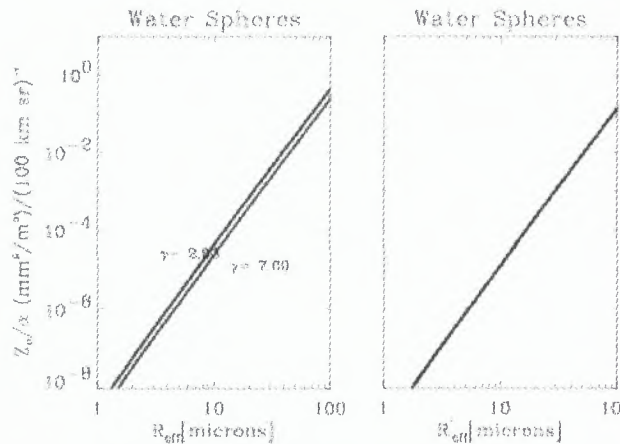


Figure 2. Reflectivity to extinction ratios for two values of gamma as a function of R_{eff} (left) and R'_{eff} (right).

$$Z_c = \frac{\lambda_{rad}^4}{\pi^5} \frac{1}{K_w} \beta_{rad} \quad (5)$$

It can be seen that plotting the ratios in terms of R'_{eff} removes the variations with gamma. The same results could have been obtained using different types of size distributions. R'_{eff} is the invariant size that will be measured using the lidar and radar signals. To infer other size measurements such as R_{eff} or to estimate water content then assumptions about the cloud size distribution have to be invoked (such as fixing the value of gamma in Eqn.(1).)

Ice Clouds

The previous considerations may be approximately extended to the case of randomly orientated ice crystals. Since the lidar extinction will mainly depend on the cross-sectional area of the particles and the radar reflectivity will mainly depend on the square of the mass of the particles we will model ice clouds using distributions of equivalent R'_{eff} spheres. However, the definition of R'_{eff} must be altered so that

$$R'_{eff} = \left[\frac{9 \langle (M(D)/\rho_i)^2 \rangle}{16\pi \langle Ac(D) \rangle} \right]^{1/4} \quad (6)$$

where, D is the maximum ice crystal dimension, M is the ice crystal mass, ρ_i is the density of solid ice and Ac is the cross-sectional area of the particles. For spherical particles Eqn.(6) will reduce to Eqn.(3).

In order to interpret a measurement of R'_{eff} in an ice cloud and to estimate its IWC it is necessary to know or assume both the form of the ice crystal particle size distribution (e.g. an appropriate value of gamma) and the crystal habit. The relationship between R'_{eff} and $D_v = \langle 6/\pi \cdot Vol(D) \rangle^{1/3}$ is shown in Fig.3 for several types of crystal habits assuming a gamma-type particle size distribution in D . The area-vs- D and mass-vs- D relationships used here were taken from Mitchell et al. [1996] and Mitchell and Arnott [1994]. In Mitchell's parameterization the volume and area vs D relationships change for D greater than around 50 microns this produces the shift seen in the non-spherical curves.

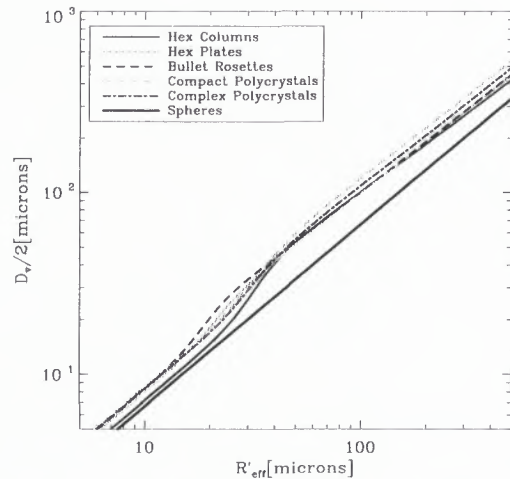


Figure 3. Relationship between R'_{eff} and D_v for different crystal habits.

INVERSION PROCEDURE

Referring back to Fig. 2 it can be seen that there is a well-defined power law relationship between the lidar extinction and the radar reflectivity. So, in principle, if the lidar extinction profile and the radar reflectivity profile were known then R'_{eff} could be estimated. However, in most circumstances the lidar extinction must be extracted from the lidar signal. The lidar signal is a function of both the lidar backscatter and extinction i.e.

$$P(z)z^{-2} = C_{lid} \beta_{lid}(z) \exp[-2 \int_0^z \alpha_{lid}(z') dz'] \quad (7)$$

where z is altitude, $P(z)$ is the power detected by the lidar originating from range z , C_{lid} is an effective calibration constant, and β_{lid} is the backscatter coefficient.

In order to invert Eqn.(7) some relationship between the lidar backscatter coefficient and the lidar extinction coefficient must be imposed. Instead of assuming a direct relationship between the extinction and backscatter coefficients (i.e. $\beta_{lid}(z) = C\alpha_{lid}^k(z)$ [Klett, 1981]), it is possible to parameterize the extinction and backscatter coefficients in terms of the radar reflectivity and their effective size. In particular, if we assume that

$$\alpha_{lid}(z) = B_\alpha(z) Z_e(z) R_{eff}^{A_\alpha}(z) \quad (8)$$

and that

$$\beta_{lid}(z) = B_\beta(z) Z_e(z) R_{eff}^{A_\beta}(z) \quad (9)$$

then Eqn.(7) can be written as

$$P(z)z^{-2} \frac{(B_\alpha(z) Z_e(z))^A}{B_\beta(z) Z_e(z)} = C_{lid} \alpha_{lid}^A(z) \times \exp[-2 \int_0^z \alpha_{lid}(z') dz'] \quad (10)$$

where $A \equiv A_\beta / A_\alpha$ and the A 's and B 's are the results of fits to Mie calculations like those shown in Fig 2. In general the A 's are nearly the same for ice or water particles. However, the B 's change a fair bit between water and ice mainly due to the large difference in refractive index between water and ice at radar wavelengths.

If A can be considered to be constant with range then the solution to Eqn.(10) is

$$\alpha_{lid}(z) = \frac{(S'(z)/S'(z_m))^{1/A}}{\frac{1}{\alpha_{lid}(z_m)} + \frac{2}{A} \int_z^{z_m} (S(z')/S'(z_m))^{1/A} dz'} \quad (11)$$

where z_m is some normalization range and

$$S'(z) = P(z)z^{-2} \frac{(B_\beta(z) Z_e(z))^A}{B_\alpha(z) Z_e(z)}$$

The treatment shown here is strictly applicable to the case where attenuation due to the cloud particles themselves at the radar wavelength can be neglected. However, attenuation at the radar wavelength could be taken into account using an iterative solution scheme.

Once the extinction profile is determined the R_{eff} profile can be determined using Eqn.(8). The effective particle

size profile thus determined will be consistent with the assumptions and procedure used in accounting for the lidar extinction.

Eqn.(11) is similar in form to the well-known so-called Klett solution for the lidar equation, except here the effective relationship between the lidar backscatter and extinction is a function of the cloud particles effective radius. Another difference is that, in Eqn.(11) the extinction boundary value can be estimated by estimating R_{eff} since

$$\alpha_{lid}(z_m) = B_\alpha(z_m) Z_e(z_m) R_{eff}^{A_\alpha}(z_m) \quad (12).$$

The solution of Eqn.(11) and the resulting R_{eff} profile depends on the choice of z_m and $R_{eff}(z_m)$. Without the radar signal as a guide it is often difficult to choose an appropriate boundary value for use in a conventional Klett type inversion. In simple terms, supplying a useful extinction boundary value implies estimating both R_{eff} and the cloud particle number density at a given point while the scheme described here only requires an estimate of R_{eff} .

Choosing a value for $R_{eff}(z_m)$ implies a certain value of C_{lid} in Eqn.(10). As described in more detail in Donovan et al.[1999], an automated procedure for determining an appropriate value of $R_{eff}(z_m)$ near the cloud top was developed. This procedure insures that a value of $R_{eff}(z_m)$ is chosen such that the inferred value of C_{lid} is within a certain range and also that the gradient in R_{eff} around the normalization range is a minimum. Simulations have indicated that under a wide range of circumstances that this procedure finds a value of $R_{eff}(z_m)$ which is within 10-20% of the true value.

APPLICATION TO CLARE-98 DATA

During CLARE-98 a large number of simultaneous lidar and radar cloud observations were made. Here we will present some examples of effective size and water content retrievals using data from the 35GHz 'Rabelais' radar from the university of Toulouse together with the Vaisala CT-75K 905 nm lidar-celiometer operated by RAL.

35GHz Radar

The calibration of the 35GHz Radar has been described by Hogan and Goddard. [1999] The gaseous attenuation at 35 GHz was calculated from the UKMO model parameters using the line-by-line model of Liebe et

al.[1985] while the temperature dependence of K_w was calculated using the approach of Liebe et al. [1989].

Attenuation of the radar beam due to scattering and absorption by the cloud particles themselves was ignored. In principle, this could be accounted for using an iterative approach. However, it is not too large an effect at 35GHz and, in general, the lidar attenuation is much more severe than the radar attenuation so that the lidar signal is usually completely extinguished long before the radar attenuation becomes significant.

Vaisala Lidars

During CLARA (in addition to other lidars) an automated Vaisala CT75K lidar was operated close to the Delft radar. The CT75K operates at a wavelength of 905nm and has a range resolution of 15meters and a temporal resolution of 30 seconds. The field-of-view is small (around 0.5 mrad) so that multiple scattering is not a great concern.

An example retrieval taken from data obtained on October 14th, 1998 is shown in Fig.4. Here the normalization altitude was about 7.25 km and the errors shown were determined using a combination of the estimated uncertainties in the lidar and radar signals as well as assuming a 25% error in the value of $R'_{eff}(z_m)$.

Here the temperatures were below $-15^{\circ}C$ at the cloud altitudes so it was assumed that the cloud was comprised of ice particles. The derived particles sizes (between 25-30 microns) are also consistent with ice particles. The ice water content was estimated using a complex-poly-crystal habit for the ice particles [Mitchell, 1996].

November 14th, 1998. Here the estimated effective sizes are largely in the range of 25-30 microns. Although a region of smaller particles seems to be present near the cloud top from 23-24 Hrs.

In contrast to the previous case where only high ice clouds were present. Figures 9-12 show a case where both high level ice clouds along with low level water clouds were present. Here the large contrast in particle size between the lower level clouds and the high cloud present overhead between around 12.0-12.5 Hrs is clearly visible.

The contrast between the ice and water clouds can be seen in more detail in Figures 14-and 15. Similar to Figure 4, Fig. 14 shows the results of the retrieval at 12.29 Hrs UTC where the particle sizes are in the range of 50-70 microns while the particle sizes shown in figure 14 are much smaller (5-20 microns).

It is interesting to note that in Fig. 14, it appears that a "drizzling" cloud is present. The main cloud deck appears to have a small effective radius (5-8 microns) which produces a large lidar signal. Below this main layer the lidar return is reduced and a "somewhat strong" radar return is present. The retrieval estimates that the drizzle drops have an effective of around 2-30 microns.

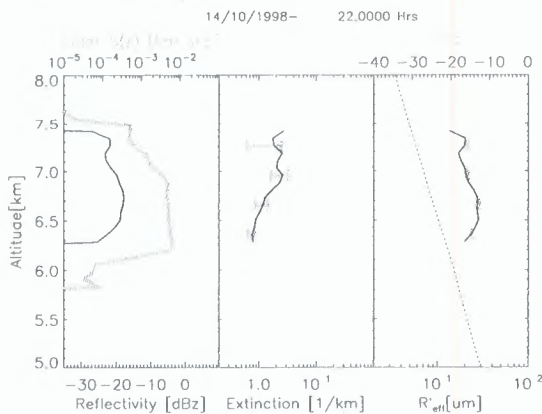


Figure 4 Lidar (Grey) and radar (thin Black) signal profiles for October 14, 1996 at 22.0 UTC (left). The middle panel shows the retrieved 905 nm extinction while the right panel shows the retrieved R'_{eff} profile and the UKMO temperature profile (upper -axis).

Figures 5-8 show, respectively, the radar reflectivity, the lidar signal, the estimated effective radius field and the estimated ice water content fields for 20-24 Hrs UTC for

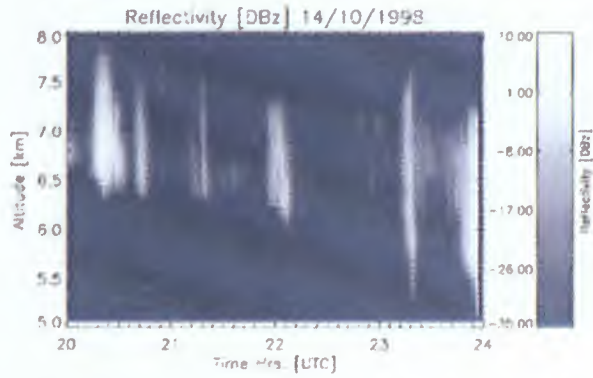


Figure 5. Effective reflectivity for October 14th, 1998.

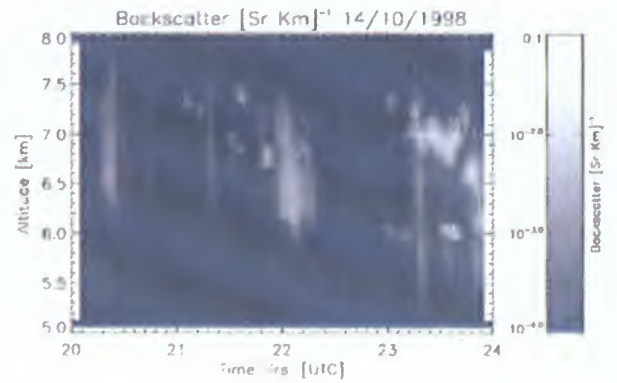


Figure 6. Uncorrected lidar backscatter for Oct. 14th.

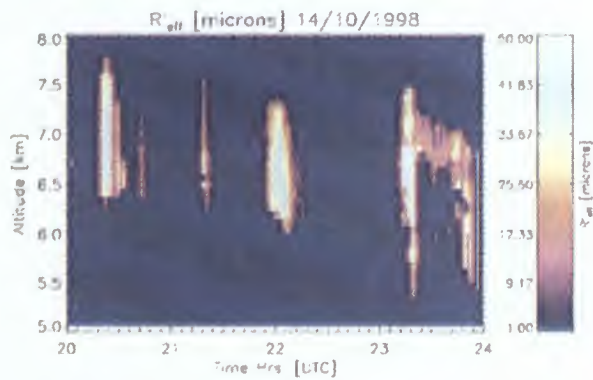


Figure 7. Effective radius field for October 14th, 1998.

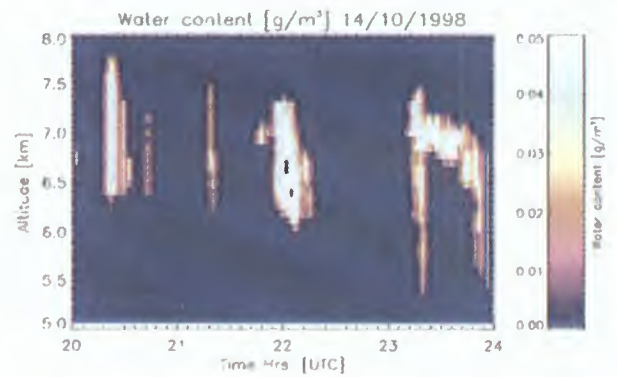


Figure 8. Water content for October 14th, 1998.

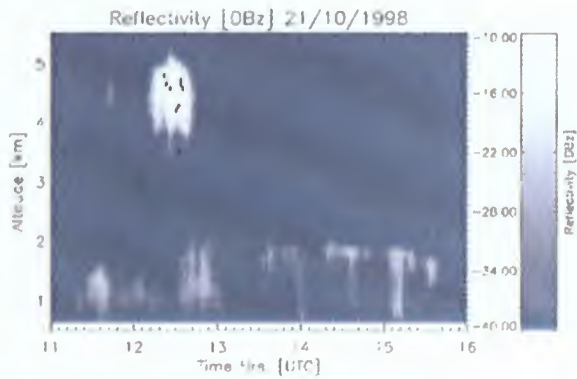


Figure 9. Effective reflectivity for October 21th.

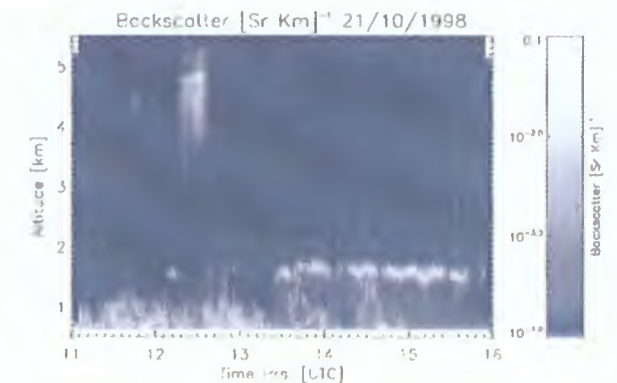


Figure 10. Uncorrected lidar backscatter for Oct. 21th.

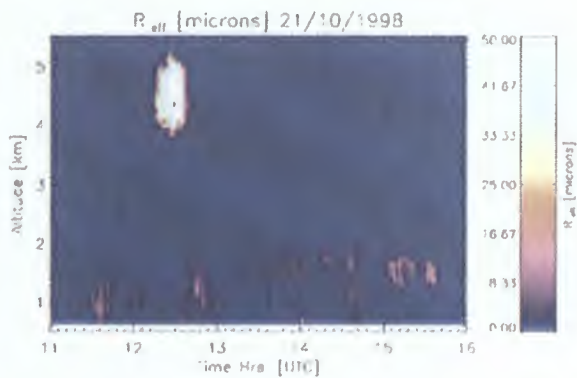


Figure 11. Effective radius field October 21th.

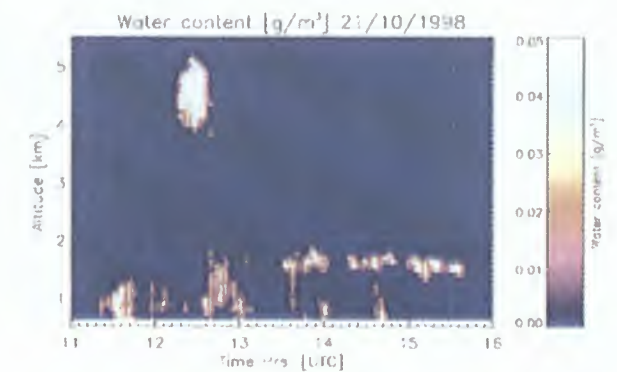


Figure 12. Water content for October 21th.

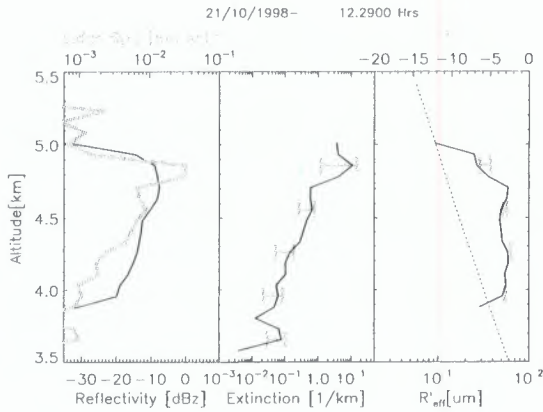


Figure 13 Lidar (Grey) and radar (thin Black) signal profiles for October 21, 1996 at 12.29 UTC (left). The middle panel shows the retrieved 905 nm extinction while the right panel shows the retrieved R'_{eff} profile and the UKMO temperature profile (upper -axis).

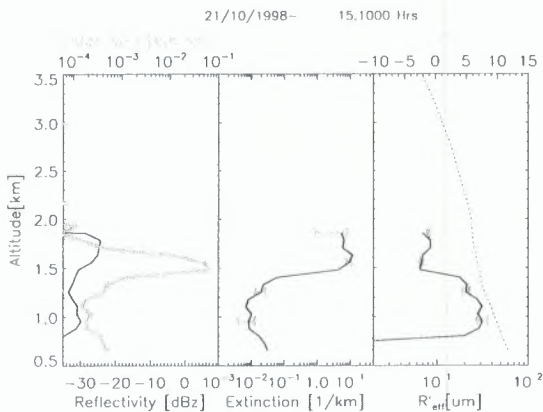


Figure 14 Lidar (Grey) and radar (thin Black) signal profiles for October 14, 1996 at 15.1 UTC (left). The middle panel shows the retrieved 905 nm extinction while the right panel shows the retrieved R'_{eff} profile and the UKMO temperature profile (upper -axis).

SUMMARY

Using lidar and radar systems in a synergetic fashion has definite advantages when applied to cloud studies. In particular, it is possible to construct a synergetic inversion scheme, which overcomes many of the traditional difficulties of inverting the lidar signal in clouds while simultaneously estimating an effective cloud particle size.

As well as effective particle size estimates, height and time resolved estimates of cloud water contents are also possible. However, the method only works up to the point where the cloud optical depth is such that the lidar still detects usable signal levels. Also, especially when dealing with ice clouds, it is still necessary to know (or

assume) the type of ice-crystals present and estimate the form of the particle size distribution.

Applied to real data, the algorithm appears to generate realistic values of particle sizes for both water and ice clouds. As of this time, no comparison of the results of this procedure with In-situ measurements has been preformed. However, it is hoped that this procedure will be soon validated using the results of aircraft-based measurements made during CLARE98.

REFERENCES

- Donovan D.P. and A.C.A.P. van Lammeren, Combined lidar and radar cloud particle effective size retrievals made during CLARA, submitted to *Physics and Chemistry of the Earth*, (1999).
- Hogan. R.J. and J.W.F Goddard, Calibration of the ground-based radars during CLARE'98, *This issue*.
- Liebe, H.J., An updated model for millimeter wave propagation in moist air, *Radio Sci.*, **20**, 1069-1089, (1985)
- Liebe, H.J. T. Manabe, and G. Hufford, Millimeter-Wave Attenuation and Delay Rates Due to Fog/Cloud Conditions, *IEEE Trans. Ant. Prop.*, **37**, 1617-1623, (1989).
- Mitchell, D.L., A. Macke, and Y. Liu, Modeling Cirrus Clouds. Part II: Treatment of Radiative Properties, *J. Atmos. Sci.*, **53**, 2967-2988 (1996)
- Mitchell, D.L., W.P. Arnott, A Model Prediction the Evolution of Ice Particle Size Spectra and Radiative Properties of Cirrus Clouds. PartII: Dependence of Absorption and Extinction on Ice Morphology, *J. Atmos. Sci.*, **51**, 817-832, (1994)
- Klett, J.D., Stable analytical inversion solution for processing lidar returns, *Appl. Opt.*, **20**, 211-220, (1981)
- Intrieri J.M., Stephens, G.L., Eberhard, W.L., and Uttal, T., A method for Determining Cirrus Cloud Particle Sizes Using Lidar and Radar Backscatter Technique *J. Appl. Met.*, **32**, 1074-1082, (1993)

Synergy in ice clouds between airborne nadir pointing radar and lidar during CLARE'98

Anne GUYOT, Jacques TESTUD,
IPSL - Centre d'étude des Environnements Terrestre et Planétaires, Vélizy, France

Jacques PELON and Vincent TROUILLET
IPSL - Service d'Aéronomie, Paris, France

Peter FRANCIS
UK Meteorological Office, Met. Research flights, Farnborough, U.K.

INTRODUCTION

A prototype airborne Radar-Lidar (RALI) system was flown during the CLARE field project (in October 1998, near Chilbolton, UK). The RALI system currently under development at IPSL will consist of a 95 GHz cloud radar and a dual wavelength (0.5 and 10 μm) backscattering lidar on the same airborne platform. The test version consisted of the Service d'Aéronomie LEANDRE-1 lidar and the University of Wyoming cloud radar (Kestrel). These instruments were mounted on the IGN Fokker-27 aircraft (ARAT). The LEANDRE lidar had a fixed nadir looking beam, while Kestrel had a nadir beam and a beam 40 degrees forward of nadir.

The LEANDRE lidar is a 0.5 micron backscattering lidar with a 0.2 degree beamwidth, 10 ns pulse, 15 m range resolution (direct detection), and a 10 Hz repetition cycle. The Wyoming cloud radar is a 95 GHz Doppler radar. Kestrel beams both had a 0.7 degree beamwidth and 30 or 60 m range resolution. A 50 ns transmit/receiver switch network allowed pairs of pulses to be sent alternately to each antenna. Reflectivity and Doppler velocity were recorded for each beam.

During the CLARE campaign the U.K. Meteorological Office C-130 made some in-situ measurements. It flew simultaneously along the same legs as the ARAT, in clouds sampled by RALI. These measurements are since they allow to check the validity of our results for the analyzed CLARE data.

First, a method which combines radar reflectivity and lidar backscatter coefficient to infer properties of the particle size distribution is described. In this paper we focus on ice clouds. Then, the first results of the analysis applied to CLARE data are given.

SYNERGETIC ALGORITHM FOR RADAR AND LIDAR

In this section we present the mathematical formulation of a synergetic algorithm for radar and lidar. In a set of data, zones where both measurements of radar and lidar are available, and where there is only one type of particles will be selected for the analysis. The method is formulated for ice

clouds.

In order to characterize the radiative and microphysical properties of a cloud, important parameters to determine are ice water content IWC and effective radius r_e defined as:

$$\text{IWC} = \frac{\pi}{6} \rho_i \int N(D) D^3 dD \quad (1)$$

$$r_e = \frac{3}{4\rho_i} \frac{\text{IWC}}{\alpha} \quad (2)$$

where $N(D)$ is the droplet size distribution, α is the extinction coefficient, and ρ_i the density of solid ice ($0.917 \cdot 10^6 \text{ g/m}^3$).

Considering LEANDRE wavelength (0.5 μm) and cloud particle sizes it can be assumed that $\pi D/\lambda \gg 1$. This corresponds to the condition of the geometric approximation, where α is expressed as:

$$\alpha = \frac{\pi}{4} \int N(D) D^2 dD \quad (3)$$

At an attenuated frequency as 95 GHz, the radar does not measure the true reflectivity Z , but an apparent reflectivity Z_a subject to the two-way path attenuation. Z_a is related to Z through $Z_a = Z - 2[Kdr]$ [dBZ] (4) where K (dB/km) is the specific attenuation.

For the formulation of the algorithm the assumption that a single type of particle is sampled is made. Then K and Z can be related with a powerlaw $K = aZ^b$. Under this assumption Hitschfeld and Bordan (1954) gave a solution of equation (4). By inverting the boundaries of the integral at the denominator, it can be expressed as:

$$Z(r) = \frac{Z_a(r)}{(1 + aI(r, r_0))^{1/b}} \quad (5)$$

where $I(r, r_0) = 0.46b \int_r^{r_0} Z_a^b(s) ds$

Similarly, the assumption of a relation $\alpha = f\beta$ is made (where β is the backscattering coefficient). It makes the constraining hypothesis that there is no molecular scattering. From Klett (1981) the attenuated backscattering coefficient can be expressed as a function of the extinction α and true

backscattering coefficients:

$$\beta(r) = \frac{\beta_a(r)}{1 + 2f \int_r^{r_0} \beta_a(s) ds} \quad (6)$$

From equations (5) and (6), specific attenuation K and extinction coefficient α profiles can be deduced:

$$K(r) = \frac{K(r_0) Z_a^b(r)}{Z_a^b(r_0) + 0.46bK(r_0) \int_r^{r_0} Z_a^b(s) ds} \quad (7)$$

$$\alpha(r) = \frac{\alpha(r_0) \beta_a(r)}{\beta_a(r_0) + 2\alpha(r_0) \int_r^{r_0} \beta_a(s) ds} \quad (8)$$

We set a relation between α and K ($\alpha = cK^d$), computed, as the K-Z relation, using a some Mie scattering calculations.

A constraint in the whole common zone of measurements: is chosen instead of a point by point constraint which would be too strong: $\int_{r_1}^{r_0} \alpha(s) ds = c \int_{r_1}^{r_0} K(s)^d ds$ (9)

where r_0 and r_1 are respectively the lower and upper range of the common zone sampled by the two instruments.

Replacing α (7) and K (8) in (9), a relation $\alpha(r_0) = f(\alpha(r_0))$ is obtained, where $f(\alpha(r_0))$ is:

$$f(\alpha(r_0)) = \frac{\beta_a(r_0)}{2 \int_{r_1}^{r_0} \beta_a(s) ds} [\exp(2\alpha(r_0) J(r_1, r_0)) - 1] \quad (10)$$

$$J(r_1, r_0) = \int_{r_1}^{r_0} \left(\frac{Z_a(r)^b}{Z_a(r_0)^b + \left(\frac{\alpha(r_0)}{c}\right)^{1/d} I(r, r_0)} \right)^d dr$$

$\alpha(r_0)$ can be determined by resolving equation (10). This value is then replaced in (8) to obtain the $\alpha(r)$ profile. The same procedure is used for K(r) once K(r₀) is estimated, using the $\alpha = cK^d$ relation.

It is important to note the calibration of both instruments does not appear in the result of the algorithm since apparent reflectivities and backscattering coefficients are at numerator and denominator in each equation.

The last step is to determine the ice water content and effective radius profiles. For the first version of this method, relations between these parameters and K will be used to estimate the profiles. We use the specific attenuation instead of the true reflectivity in order to eliminate calibration problems.

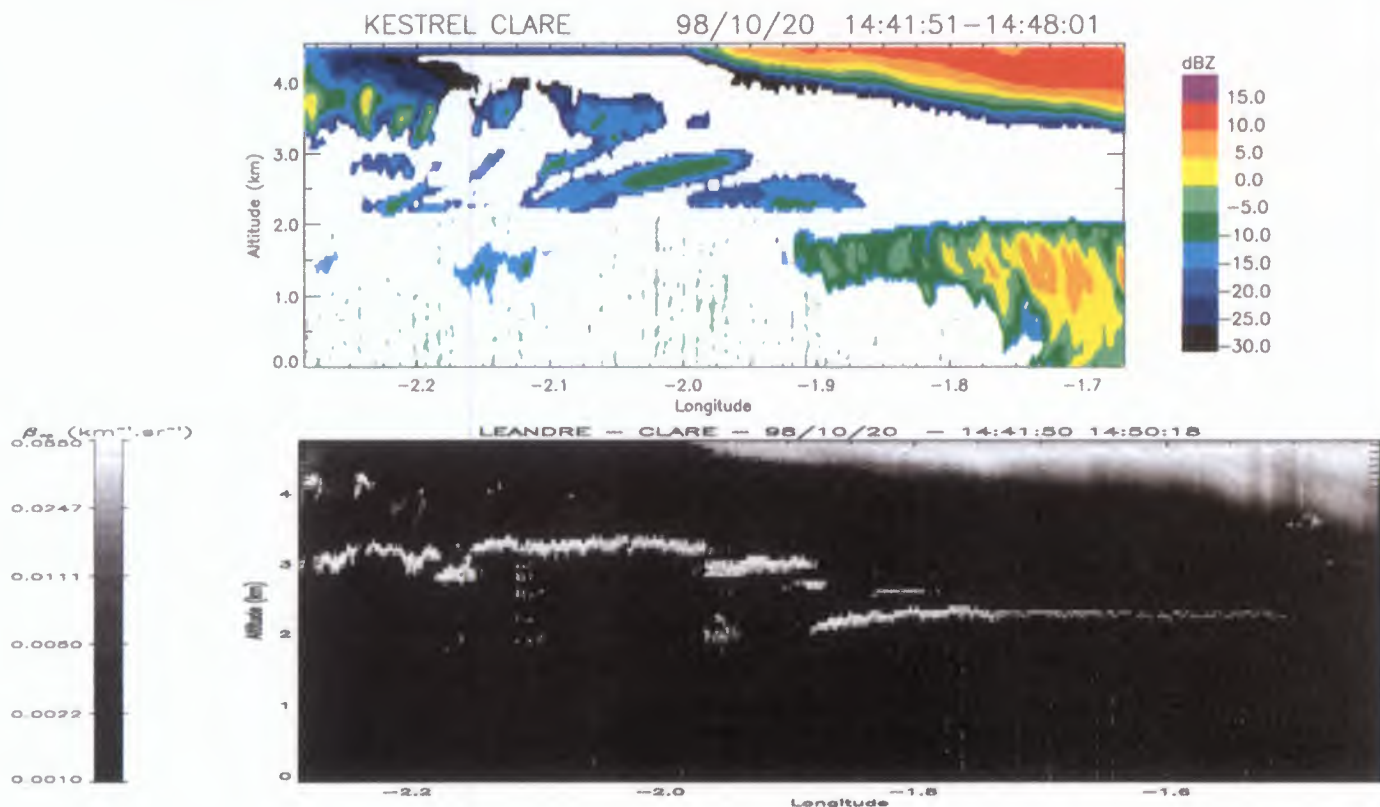


Fig.1: 20th of October 14:41:51-14:48:01, upper part: Kestrel reflectivities along the leg, lower part LEANDRE attenuated backscattering

coefficient.

ANALYSIS OF CLARE DATA

The only case of iced cloud measured by both instruments (below the ARAT) was sampled the 20th of October between 14:41:51 and 14:48:01, at the East side of the leg. Fig.1a and 1b display respectively reflectivity and attenuated backscatter coefficient measured along this leg. It is interesting to compare the two figures and see how the lidar penetrates in the ice cloud at 4 km altitude, while the signal is extinguished rapidly in all the other clouds sampled along the leg. In this study we focus on the part between -1.95° longitude and Chilbolton (14:45-14:48).

The first step is to determine the b coefficient of the K-Z relation, and the $\alpha = cK^d$ relation. In order to do this, we make the hypothesis that the particle size distribution is a normalized gamma function:

$$N(D) = N_0 * \frac{(3.67 + \mu)^4}{3.67^4} \frac{\Gamma(4)}{\Gamma(\mu + 4)} (\Delta D)^\mu \exp(-\Delta D)$$

The C-130 in-situ measurements were used to determine N_0^* . Fig.2 displays N_0^* in the selected cloud. It appears that this parameter does not vary to much. It is chosen to be invariant in the relations we determine.

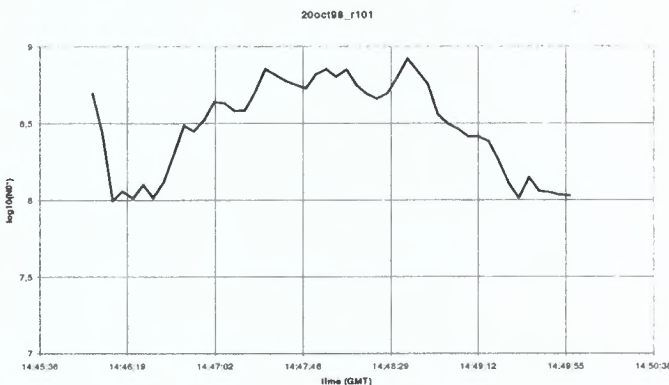


Fig.2: 20th Oct. 14:45-14:50, N_0^* computed from the C-130 2DC-2DP merged data

The K-Z relation b coefficient is computed from Mie scattering calculations, using a value of N_0^* of about $10^8.5$. Whereas the K- r_e and K-IWC relations are directly computed from the in-situ measurements performed by the C-130.

Various profiles of effective radius and ice water content in the selected cloud are plotted in Fig.3. They were chosen to be representative of all the results we obtain.

These results can be compared to the horizontal profiles of ice water content and effective radius calculated from the C-130 microphysical data. The horizontal profiles (fig. 4) are at about 4.6 km, just above what was sampled by RALI, but they give a first guess of the values we should retrieve with our method.

In most of the cases, especially when there are at least 500 m of common measurements (longitude $> -1.9^\circ$), IWC and r_e profiles are very similar from one profile to another. Ice water content increases from cloud base to the top of the measurements, where it reaches values close to 0.05 g/m^3 . These values seem to be underestimated when compared to the horizontal profile in fig. 4, IWC are about 2 or 4 times weaker than the estimation from in-situ measurements. Effective radius values at the top of the common zone are inconsistent with the estimation from 2DC-2DP data.

The profile at -1.911° is representative of all the profiles retrieved around and at the West of this longitude. It appears that IWC is overestimated and effective radius are too weak compared to the C-130 measurements computation. This problem in the retrieval is certainly due to the small thickness of the common zone of radar-lidar measurements.

CONCLUSION

During CLARE, the RALI instrument combination collected simultaneous measurements in clouds of a lidar nadir pointing and a radar nadir and 40° fore pointing.

When clouds are optically thin the lidar penetrates and makes simultaneous measurements with the radar. Then the synergetic algorithm formulated in this paper may be used. It allows to determine the parameters characterizing the cloud when there is only one type of particle sampled in the cloud.

Results obtained for the selected cloud during CLARE underestimate ice water content and effective radius, when referring to the C-130 in-situ measurements. It also clearly appears that when the common zone of radar and lidar measurements is thin, the retrieved profiles are not correct.

The method presented in this paper is a very first version which must be improved. A careful critical analysis of the analysis will be done in order to determine the origin of the error of estimation observed in the retrieval of IWC and r_e .

ACKNOWLEDGMENTS

The authors express their appreciation to K. Caillault (CTEP) for providing her analysis of the microphysical data.

REFERENCES

- Hitschfeld, W., and J. Bordan, 1954: Errors inherent in the radar measurement of rainfall at attenuating wavelengths. *J. Meteor.*, **11**, 58-67.
- Klett, J. D., 1981: Stable analytical solution for processing lidar returns. *Applied Optics*, **20**, 211-220.

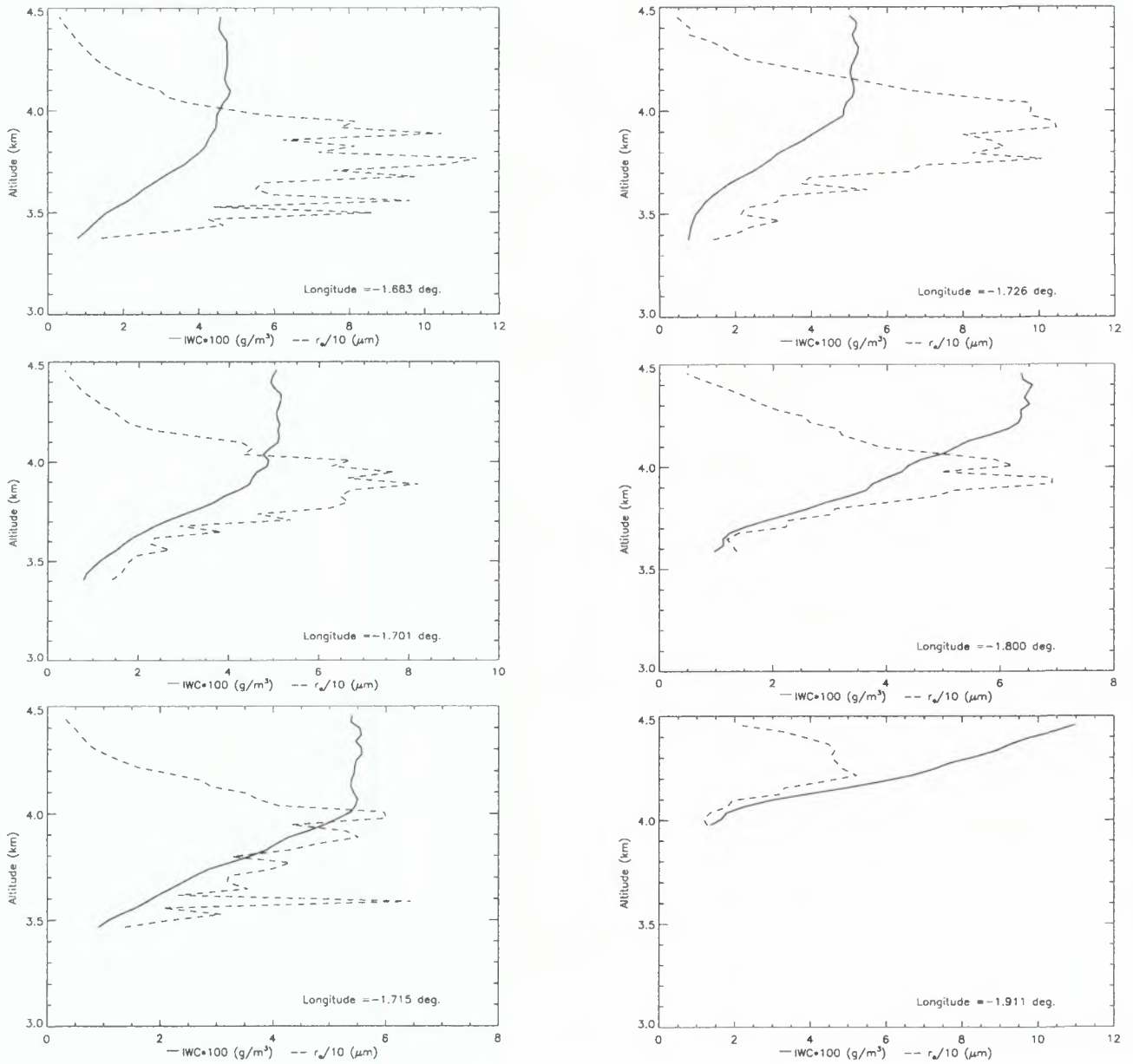


Fig.3: 20th Oct. (14:45-14:49) Retrieved ice water content IWC and effective radius r_e profiles for different longitudes using the synergetic radar-lidar algorithm, in the common zone of measurements.

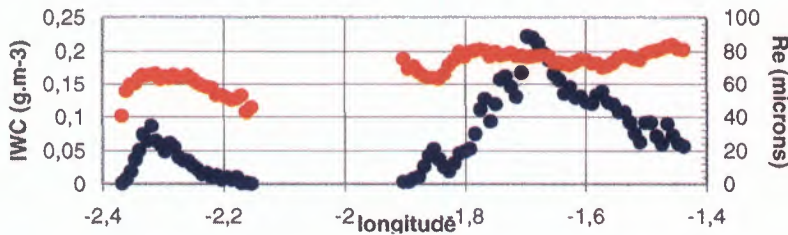


Fig.4: 20th Oct. (14:41-14:49) IWC and r_e profiles along the leg computed from the C-130 in-situ measurements

Non-Rayleigh scattering effects in mixed phase cloud observations

Nicolas Gaussiat* and Henri Sauvageot
 Laboratoire d'Aérodologie, Observatoire Midi-Pyrénées, Toulouse, France
 *email: gaun@aero.obs-mip.fr

1. INTRODUCTION

In most parts of the troposphere, temperature is negative. That is why, for a large fraction, the tropospheric clouds are mixed clouds. To correctly describe the radiation transfers in mixed clouds, the knowledge of both ice and liquid water profiles is required.

In mixed clouds, radar reflectivity is dominated by ice while liquid water is responsible for attenuation. Gosset and Sauvageot (1992) have proposed a dual-wavelength radar method for the remote sensing of cloud profiles. In this algorithm, liquid water cloud M_w is deduced from the differential attenuation between the two wavelength and ice water content M_i is computed from the radar reflectivity. This method assumes that the size of the hydrometeors satisfies the Rayleigh approximation for both scattering and attenuation, because, in the presence of non-Rayleigh effects, an ambiguity appears on M_w and M_i .

The object of this paper is to discuss the effect of non-Rayleigh scattering on the performances of the dual-wavelength radar algorithm.

2. THEORY

Let $Z_{m\alpha}$ be the radar reflectivity measured for the wavelength α , that is :

$$Z_{m\alpha} = Ze_{\alpha} \times 10^{-0.1 \int_0^r A_{\alpha}(r) dr} \quad (1-1),$$

where Ze is the unattenuated radar reflectivity factor, A is the total attenuation factor and r the radar target distance. A , in $dB \text{ km}^{-1}$, is the sum of A_g and A_h , the two-way attenuation factors for gas and hydrometeors respectively. A_g is computed from the standard profile of temperature.

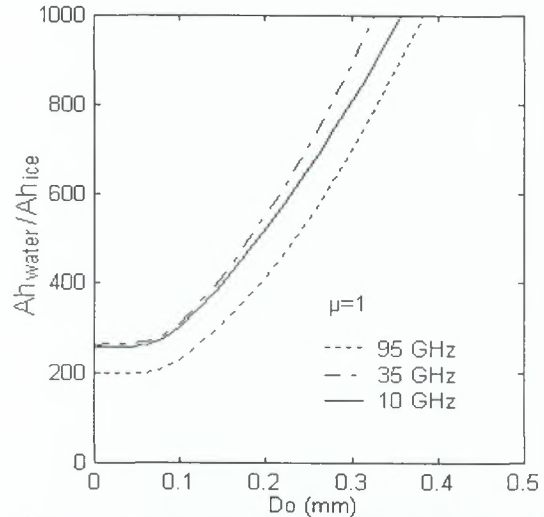
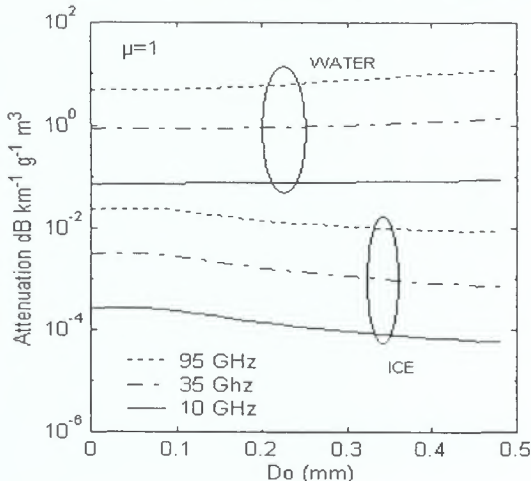


Fig.1 : Variation of the attenuation by ice and water clouds and ratio A_{h_w}/A_{h_i} as a function of D_o , for the frequency 95, 35 and 10 GHz.

A_h is computed by the summation of the Mie attenuation cross-section $Q_e(D)$, where D is the equivalent spherical diameter, over the hydrometers size distribution $N(D)$. The strong difference between ice and water cloud attenuation appears on figure 1, where A_h and A_{h_w}/A_{h_i} , as a function of D_o , the mean volume diameter, are presented.

In the Rayleigh approximation conditions the attenuation factor for liquid water cloud droplets, and for frequency α , is:

$$A_{\alpha}(r) = 2C_{\alpha}(r)M_w(r) \quad (1-2),$$

where M_w is in $g \text{ m}^{-3}$ and C_{α} is the water cloud attenuation coefficient in $dB \text{ km}^{-1} g^{-1} m^3$ for one way.

Thus, for two frequencies having significantly different attenuation properties we can write:

$$M_w = \frac{A_{\beta} - A_{\alpha}}{2(C_{\beta} - C_{\alpha})} = \frac{A_d}{2(C_{\beta} - C_{\alpha})} \quad (1-3),$$

where α and β stand for the lower and higher frequency respectively and A_d is the differential attenuation. The Dual wavelength ratio (DWR) is defined (Eccles and Muller, 1971) by:

$$Y_{\alpha,\beta} = 10 \log \left(\frac{Z_{m\alpha}}{Z_{m\beta}} \right) \quad (1-4),$$

where Z_m is in mm^6m^{-3} . Using (1-1) in (1-4) gives

$$Y_{\alpha,\beta} = 10 \log \left(\frac{Z_{e\alpha}}{Z_{e\beta}} \right) + \int_0^r A_d(r) dr \quad (1-5).$$

Taking the range derivative of (1-5), we found:

$$A_d = \frac{dY_{\alpha,\beta}}{dr} \quad (1-6).$$

Then, with (1-3), the liquid water content for Rayleigh conditions is obtained:

$$M_w = \frac{1}{2(C_\beta - C_\alpha)} \frac{dY_{\alpha,\beta}}{dr} \quad (1-7)$$

It is assumed that $N(D)$ can be represented by a modified gamma distribution :

$$N(D) = N_0 \times D^\mu \times \exp \left[- (3.67 + \mu) \frac{D}{D_0} \right] \quad (1-8),$$

where N_0 , μ , D_0 are the parameters and $N_T = \int N(D) dD$ is the total number of hydrometeors by cubic meter.

For Mie scattering, $Z_{e\alpha}$ has to be rewritten (Lhermitte 1988, Sekelsky et al. 1996) :

$$Z_{e\alpha} = \frac{10^{12} \lambda_\alpha^4 N_0}{4\pi^4 |K_w(\lambda_\alpha)|^2} \int_0^\infty \xi_{b,\alpha}(D, \lambda_\alpha, \rho) D^{2+\mu} \exp \left[- (3.67 + \mu) \frac{D}{D_0} \right] dD \quad (1-9),$$

where $Z_{e\alpha}$ is in mm^6m^{-3} , λ is the wavelength, $|K_w(\lambda_\alpha)|^2$ is the dielectric factor for λ_α , ρ is the hydrometeor density and $\xi_b(D)$ is the back-scattering efficiency as a function of D .

Using (1-9) in (1-5) gives :

$$Y_{\alpha,\beta} = 10 \log \left(\frac{|K_w(\lambda_\beta)|^2 \lambda_\alpha^4 \int_0^\infty \xi_{b,\alpha}(D) D^{2+\mu} \exp \left[- (3.67 + \mu) \frac{D}{D_0} \right] dD}{|K_w(\lambda_\alpha)|^2 \lambda_\beta^4 \int_0^\infty \xi_{b,\beta}(D) D^{2+\mu} \exp \left[- (3.67 + \mu) \frac{D}{D_0} \right] dD} \right) + \int_0^r A_d(r) dr \quad (1-10),$$

with λ_α in cm and $\rho = \rho(D)$.

Taking the derivative and inverting (1-10), we obtain :

$$A_d = \frac{dY_{\alpha,\beta}}{dr} = \frac{dD_0}{dr} \times Ec(D_0, \mu) \quad (1-11),$$

with

$$Ec(D_0, \mu) = \frac{10(3.67 + \mu)}{D_0^2 \text{Ln}10} \left\{ \frac{\int_0^\infty \xi_{b,\alpha}(D) D^3 N(D) dD}{\int_0^\infty \xi_{b,\alpha}(D) D^2 N(D) dD} \frac{\int_0^\infty \xi_{b,\beta}(D) D^3 N(D) dD}{\int_0^\infty \xi_{b,\beta}(D) D^2 N(D) dD} \right\} \quad (1-12).$$

Using (1-12), $Ec(D_0, \mu)$ was computed for water and ice, with μ as a parameter, for the pair 35-95 GHz and 10-35 GHz. The results are presented on Fig 2.

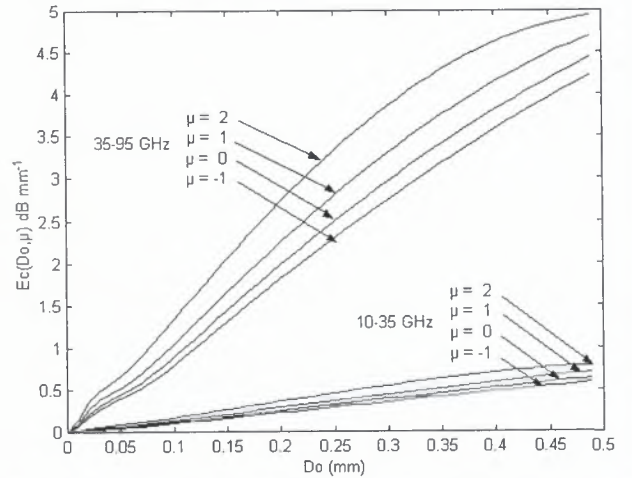


Fig 2 : Variation of $Ec(D_0, \mu)$ as a function of D_0 with μ as a parameter for ice hydrometeor distribution and for the 35-95 GHz and 10-35 GHz pairs.

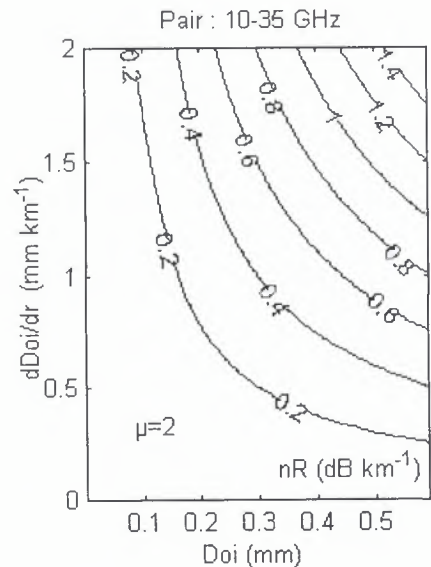
In non-Rayleigh conditions (1-7) becomes :

$$M_w = \frac{1}{2(C_\beta - C_\alpha)} \left\{ \frac{dY_{\alpha,\beta}}{dr} - nR(D_0, \mu) \right\} \quad (1-13),$$

with

$$nR(D_0, \mu) = \frac{dD_0}{dr} \times Ec(D_0, \mu) \quad (1-14),$$

where $nR(D_0, \mu)$ is in dB km^{-1} .



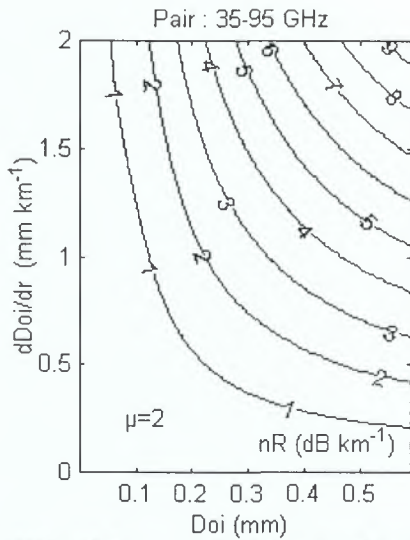


Fig 3 : Variation of $nR(D_o, \mu)$ and $dDoi/dr$ as function of Do_i for an ice hydrometeor distribution with μ as a parameter for the 35-95 GHz and the 10-35 GHz pairs.

Of course, neglecting the non-Rayleigh effects can lead to an error in the estimation of the liquid water content M_w .

3. MIXED-CLOUD MICROPHYSICS.

In situ observation shows that mixed-clouds are typically made up of 1) a supercooled water cloud with N_o very large and Do not larger than about $30 \mu m$ and 2) a bimodal distribution of ice particles with a large number of crystals smaller than about $50 \mu m$ and a small number of particles with size between 100 and $400 \mu m$ (Heymsfield et al. 1991; Sassen 1991; Mitchel and al. 1996). The large ice particles, because their low terminal fall velocities create slanted streamers with high reflectivity. Thus mixed-clouds can schematically be described as the addition of an attenuating, Rayleigh scattering water cloud and a non attenuating, non-

Rayleigh scattering bimodal ice cloud.

In the present work dedicated to the study of the radar propagation, for sake of simplicity, we choose to ignore the small mode of the ice particle distribution.

4. SIMULATION

Let $N_w(D, z)$ and $N_i(D, z)$ (eq. 1-9) be the water and ice cloud particle size distributions respectively. For all simulated cases, we used $N_{T,w} = 4 \times 10^7 m^{-3}$, $\mu_w = 1$ and $Do_w(z)$ varying from the bottom to the cloud top following the polynomial curve presented in Fig 4.

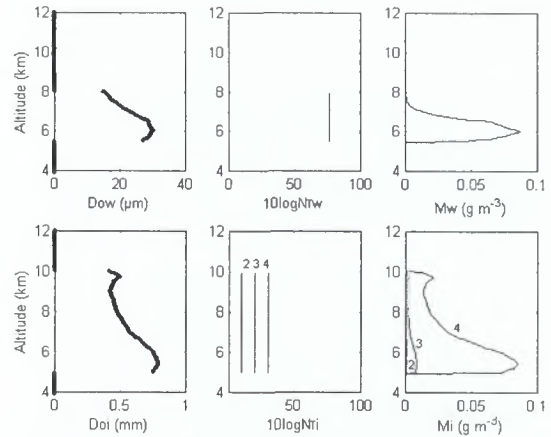


Fig 4 : Vertical profiles of $N_w(D)$ and $N_i(D)$ parameters and corresponding liquid water and ice water content.

For $N_i(D, z)$, the parameter $Do_i(z)$ has the same profile for the four simulated cases : a polynomial variation between the bottom and the top of the cloud (Fig. 4). $N_{T,i}$ takes the values $0, 10^1, 10^2$ and 10^3 for the four cases respectively, μ_i is constant and equal to 2

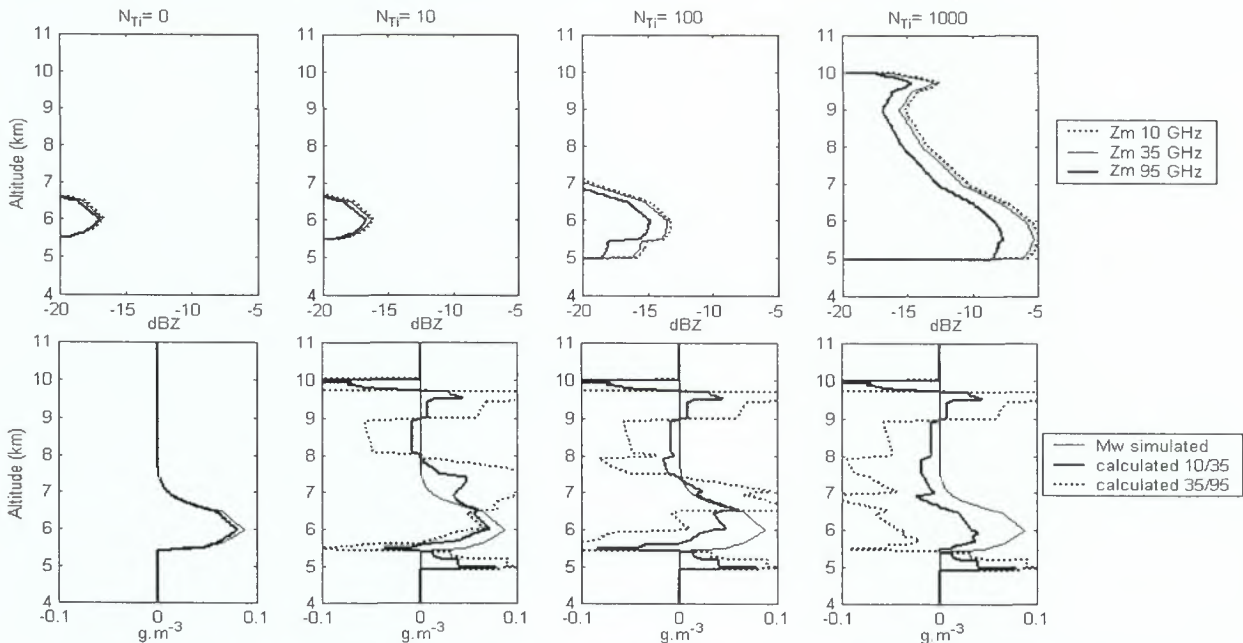


Fig 5 : Upper Row, reflectivities at 10, 35 and 95 GHz for a mixed cloud. $N_{T,i}$ is the number of large ice particles. Lower Row, liquid water content simulated and retrieved from the wavelength pairs 10-35 GHz and 35-95 GHz.

5. RESULTS

In the absence large ice particles ($N_{Ti}=0$), the dual wavelength method gives correct results for both wavelength pair (See Fig 5, the first column of the simulation).

As the number of large ice particles increases, incorrect values of liquid water content appear. The errors are related to the Doi gradients.

These errors are larger for the 35-95 pair than for the 10-35 one, but in both cases, retrieved liquid water profiles are jeopardized.

6. CONCLUSION

Simulations showed in the present work suggest that the dual wavelength radar method for liquid water content retrieval in the mixed cloud is very sensitive to the non-Rayleigh effect induced by large ice particles

7. REFERENCES

Eccles , P. J. and E. A. Mueller, 1971 : X-Band attenuation and liquid water content estimation by dual-wavelength radar. *J. Appl. Meteor* 10, 1252-1259.

Gosset, M. and H. Sauvageot, 1992 : A Dual-Wavelength Radar Method for Ice-Water Characterisation in Mixed-Phase Clouds. *J. Atmos. Oceanic. Technol.*, 14., 256-272

Heymsfield, A. J., L. M. Miloshevich, A. Slingo, K Sassen and D. O'C Starr, 1991/ An observational and theoretical study of highly supercooled altocumulus. *J. Atmos. Sci.*, 48, 923-945.

Lhermitte, R. M., 1988 : Cloud and precipitation remote sensing at 94 GHz *Trans. Geosci. Remote Sens* 26, 207-216.

Mitchell, D.L., S.K. Chai, Y.Liu, A.J. Heymsfield and Y. Dong, 1996 : Modeling cirrus clouds. Part I : Treatment of bimodal size spectra and case study analysis. *J. Atmos. Sci.*, 53, 2956-2966.

Sassen, K., 1991 : Aircraft-produced ice particles in a highly supercooled altocumulus cloud. *J. Applied Met.*, 30, 765-775.

A climatology of supercooled layer clouds from lidar ceilometer data

Robin J. Hogan*

Anthony J. Illingworth

Department of Meteorology, University of Reading, UK.

*Email: R.J.Hogan@reading.ac.uk

INTRODUCTION

It was demonstrated during the Cloud Lidar And Radar Experiment (CLARE'98) that supercooled water in the atmosphere can occur in the form of distinct layers several hundred metres thick that provide a strong signal for lidar, but because of the small droplet size are undetected by radar when ice is present (e.g. Hogan et al. 1999). The fact that these layers give such a strong echo at visible wavelengths implies that, when present, they are much more important in determining the radiative properties of the cloud than any ice that may be around. They will also be important in glaciation processes and therefore have an impact on cloud lifetime and precipitation formation. Currently, atmospheric forecast and climate models usually assume a simple ratio between ice and liquid water content that varies with temperature only; Fig. 1 shows this ratio for the ECMWF model. Clearly if such layers are common then there is a need to improve the representation of supercooled water in models.

Intensive observing periods, such as during CLARE'98, have served to demonstrate the existence of these layers and establish that supercooled liquid water is responsible. However, long-term measurements are required to determine their frequency and mean properties, ultimately what model climatologies would be tested against. In this paper a first attempt is made to characterise the frequency of supercooled layers using data taken from a 905 nm Vaisala CT75K lidar ceilometer, which has been operating almost continuously at Chilbolton, England since June 1996. Figure 2 shows a time-height section of lidar backscatter coefficient (β) from this instrument (resolution 30 metres and 30 seconds) through a typical layer with a temperature of around -20°C , on 15 October 1998 during

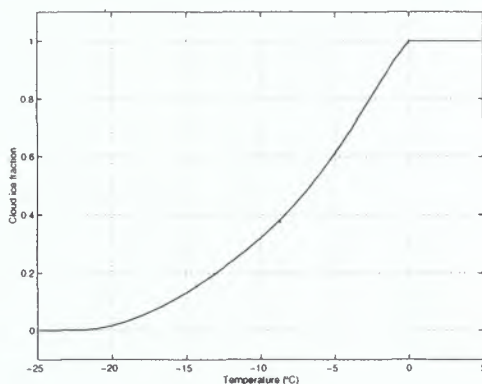


Fig. 1: The fraction of cloud water that is in the form of ice in the ECMWF model, as a function of temperature.

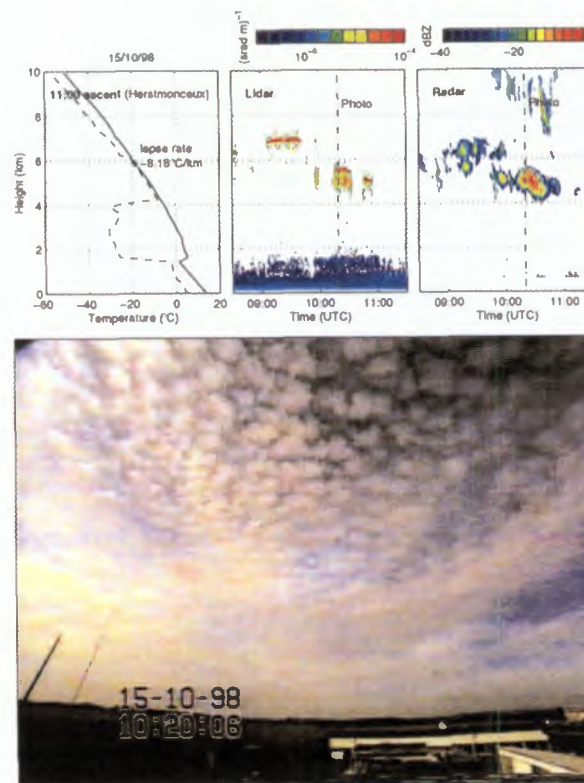


Fig. 2: Time-height section of lidar backscatter coefficient and 35 GHz radar reflectivity through a supercooled layer, with a simultaneous snap shot from the cloud camera. The radiosonde dry-bulb and dew-point temperature profile measured at Hersmonceux is also shown. The data were taken on 15 October 1998 at Chilbolton.

CLARE'98. Small cells characteristic of altocumulus are apparent in the accompanying snap shot from the cloud camera, indicating that these layers are convective in nature. No layer is visible in the accompanying observations by the 35 GHz Rabelais radar at Chilbolton (resolution 75 metres and 30 seconds), since the echos at this frequency are dominated by the contribution from the larger ice particles falling beneath the glaciating water cloud. Ice cloud is visible in the photograph as much fainter but more homogeneous wisps beneath the liquid water cells. The cells in this case were around 500 m across, too small to be resolved by the 30 s resolution of the lidar given the typical wind speeds at this altitude. The radiosonde ascent shows that the layer was saturated with respect to liquid water and convectively unstable. Heymsfield et al. (1991) presented aircraft measurements of liquid water in two altocumulus clouds

and demonstrated using a numerical model that the observations were consistent with radiatively-driven convective overturning.

There are of course a number of limitations in using a ground-based lidar ceilometer. Firstly, it measures only lidar backscatter coefficient (β), and strictly one requires depolarisation ratio as well in order to distinguish between liquid water and ice with confidence. However, one of the main reasons these layers are important is because of their high optical depth and the consequent effect on radiation, so it could be argued that the phase of a particular layer of high β is irrelevant. For glaciation the phase is obviously of primary importance. A second problem is that ground-based lidars suffer very strong attenuation by low-level liquid water clouds, so most of the time in mid-latitude maritime climates cannot even see up to the 0°C isotherm. Furthermore, the layers themselves attenuate the signal making it difficult to identify multiple supercooled layers.

On a more cautionary note, it should be recognised that there is a possibility that not all layers of high β correspond to the presence of liquid water; Thomas et al. (1990) reported observations of relatively high β in ice cloud, the magnitude of which was seen to fall rapidly as the lidar pointing angle was moved a little away from zenith. This was interpreted as being due to specular reflection from horizontally-aligned plate crystals. Throughout the period of ceilometer observation in this study the instrument was operating in a zenith-pointing configuration, so could be affected. It would seem fairly safe to assume that the layers observed on 20 October in CLARE'98 (see Hogan et al. 1999) were composed primarily of liquid water droplets because of the low lidar depolarisation and the in situ verification. The radiosonde profile in Fig. 2 strongly suggests that the layer in this example is composed of liquid water. One striking property of these layers is that they tend to completely extinguish the lidar signal (see Fig. 3 for an example), whereas specular reflection from plates is only an enhancement of the backscatter, and the extinction should remain largely unchanged. Certainly the clouds observed by Thomas et al. (1990) did not strongly attenuate the lidar signal. An apparent layer was observed on 21 October 1998 during CLARE'98 at a temperature of around -20°C that had a high depolarisation ratio (indicating ice crystals) and according to the in situ measurements did not contain significant liquid water. Clearly more work is required to establish whether layers composed only of ice are common, but for the remainder of this paper we shall assume that they are all supercooled liquid water.

METHOD

Layers can be identified easily by eye from time-height sections of β , so the first step is to automate the process of layer identification using a set of fixed rules. The data acquisition system from this commercial instrument outputs the height of the first cloud base (h) in addition to the β profile. It calculates h by performing a so-called Klett inversion of the β profile assuming a fixed extinction-to-backscatter ratio, and considers the slope, absolute value and historic observations at that height. Comparing h from this procedure with the β profile indicates that supercooled layers identified subjectively *always* coincide with the first cloud base, but that when no layer or sharp gradient in β is

present, the first cloud base tends to occur in the thickest part of any cirrus cloud that is present.

Hence we use h as the starting point for automatic layer identification, and do not attempt to identify more than one layer in each ray. Firstly, the height of the maximum β within 150 metres of h is found. Two tests are then applied that have been found to give best agreement with layers identified subjectively: a layer of supercooled water should have a value of β greater than 4×10^{-5} sterad $^{-1}$ m $^{-1}$ and this peak value should be at least 20 times greater than the value 300 m (10 range gates) above. An example of layer identification using this simple algorithm is shown in Fig. 3. An algorithm based on β alone was tried, but it was found that very cold layers could be missed while reflective clouds that were not layer-like in appearance, such as the lower parts of deep cirrus, tended to be included.

Radiosonde data was used to estimate the temperature at the altitude of the layer. The nearest operational upper-air station to Chilbolton is Herstmonceux, 125 km away, which carries out ascents every six hours. This station is used in preference to the so-called 'range' station at Larkhill, which is only 25 km away but does not perform regular ascents. Linear interpolation was performed in both time and height, but there is likely to be a residual error of several degrees in the derived temperature profile over Chilbolton.

RESULTS

The algorithm has been applied to all the ceilometer data taken at Chilbolton, from when the instrument was installed in the summer of 1996 until April 1999. Some data is missing, particularly in the first five months, but in total 2.47 million 30-second rays have been processed, equivalent to over 28 continuous months of observations.

We first consider the dataset as a whole to estimate the occurrence of supercooled layers as a function of temperature. The results are summarised in Fig. 4. Panel (a) shows the fraction of the dataset for which the instrument observed any cloud in each 5° temperature interval between -50°C and -5°C. Pixels were defined to be cloudy if the lidar backscatter coefficient was at least 2×10^{-7} sterad $^{-1}$ m $^{-1}$. At temperatures warmer than -5°C the data were often contaminated by aerosol so are not shown. A method was devised to 'clean-up' the clear-air noise occasionally produced by this instrument. It can be seen that the occurrence of cloud in each 5° bin was less than 10% and decreased with decreasing temperature. This will be appreciably less than the true cloud occurrence, because of the problem of obscuration by lower level clouds at lidar wavelengths.

Panel (b) shows the fraction of clouds that contain a layer satisfying the definition given earlier, in each 5° interval. As one might expect, the fraction of clouds containing a supercooled layer decreases with temperature; 18.5% of clouds between -10°C and -15°C contain a supercooled layer, whereas between -30°C and -35°C the value is only 5.5%. The lower two panels depict similar information but in a cumulative sense. Panel (d) shows the fraction of observations with clouds colder than a given temperature that contained a layer colder than this temperature. We see that around 30% of

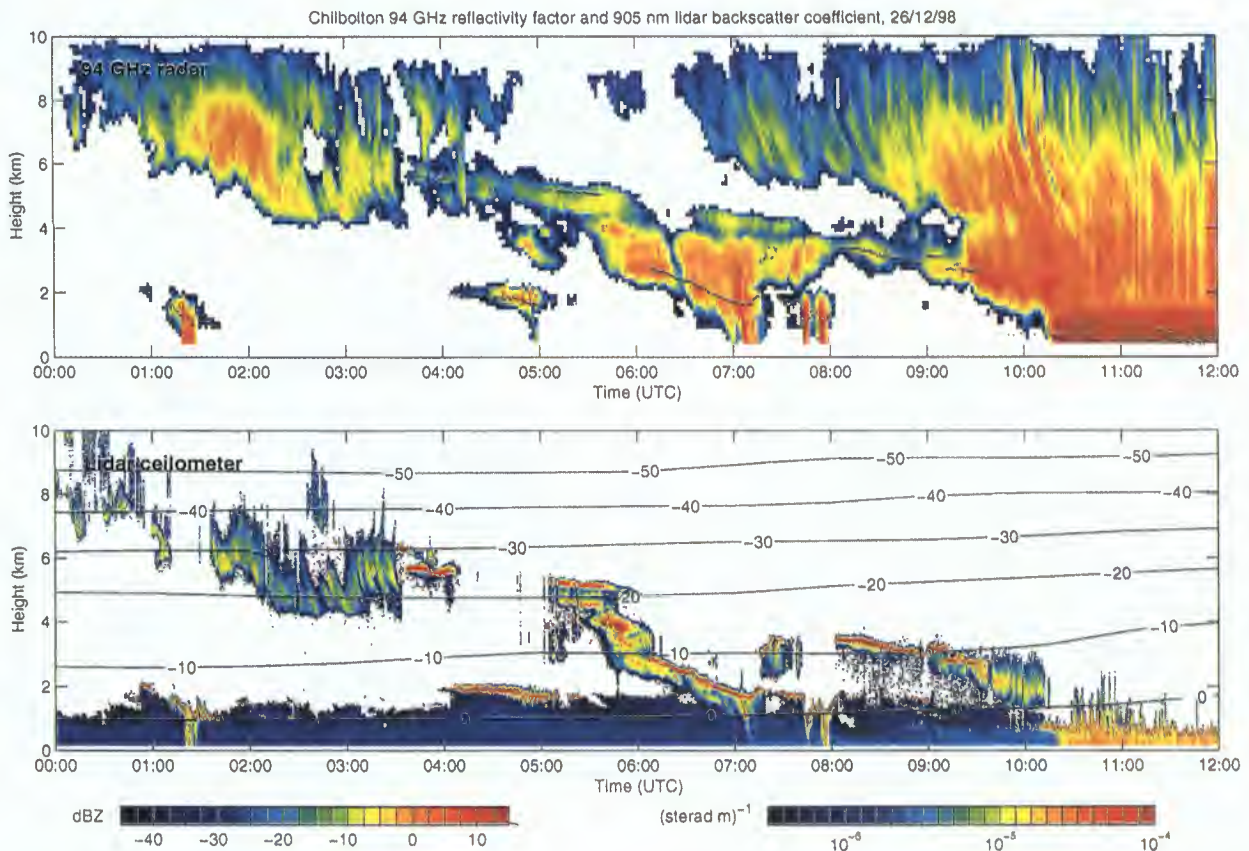


Fig. 3: Example of the objective layer-identification scheme. The top panel shows a time-height section of radar reflectivity from the 94 GHz Galileo radar at Chilbolton (resolution 2 minutes and 120 metres). Superimposed are black points indicating the presence of a layer, derived from the ceilometer data shown in the lower panel (resolution 30 seconds and 30 metres). Also shown is temperature according to the ECMWF model.

the time that cloud colder than -10°C was observed, a layer was observed in it, falling to 20% when considering only clouds colder than -20°C .

Figure 5 shows the mean layer duration and horizontal extent as a function of temperature. Horizontal extent was calculated from layer duration using the wind speed at that height as given by the interpolated radiosonde profile. Because of the frequent temporary obscuration of the layers by passing low level cumulus, layers were deemed continuous in this analysis if any gaps in them lasted no longer than 10 minutes. We see that at -5°C the average layer persisted for over half an hour, with the average duration falling steadily with decreasing temperature. Typical horizontal extents were between 20 and 30 km, although because of obscuration this is likely to be a considerable underestimate. In a few individual cases, layers associated with the tops of altocumulus were observed to persist for up to 9 hours.

It is apparent from Fig. 4b that the fraction of clouds containing a layer does not fall quite to zero at -40°C , where in theory no supercooled water should exist. There are a number of reasons for this; the most likely possibility is that the algorithm is wrongly identifying a very few high clouds as being supercooled layers when they are entirely composed of ice. Visual

examination of the ceilometer data on such occasions suggests these events are aircraft contrails, which due to the large numbers of aerosols present tend to consist of high concentrations of very small ice crystals, so can understandably be mistaken for layers of liquid water. Indeed, Fig. 5 indicates that clouds identified as supercooled layers that are colder than -40°C persist on average for only three minutes. It is also possible that the temperature calculated by interpolating radiosonde profiles could be in error by in excess of 5° . In any case, layers colder than -40°C were diagnosed for only 4.9 hours of the 28 months of observations, corresponding to only 0.024% of the dataset.

An attempt was made to estimate the optical depth of these layers by performing a simple Klett-type inversion on each profile to remove the effects of attenuation. An extinction-to-backscatter ratio suitable to liquid water of 15 sterad was employed. However, all gate-by-gate procedures for correcting attenuated backscatter profiles are potentially unstable and very sensitive to both instrument calibration and the chosen extinction-to-backscatter ratio, and indeed our retrieved optical depths calculated by this method were often impossibly large. The mean optical depth of those layers for which the procedure did not explode was around 0.2, but given the problems with this technique it is doubtful that this value is accurate.

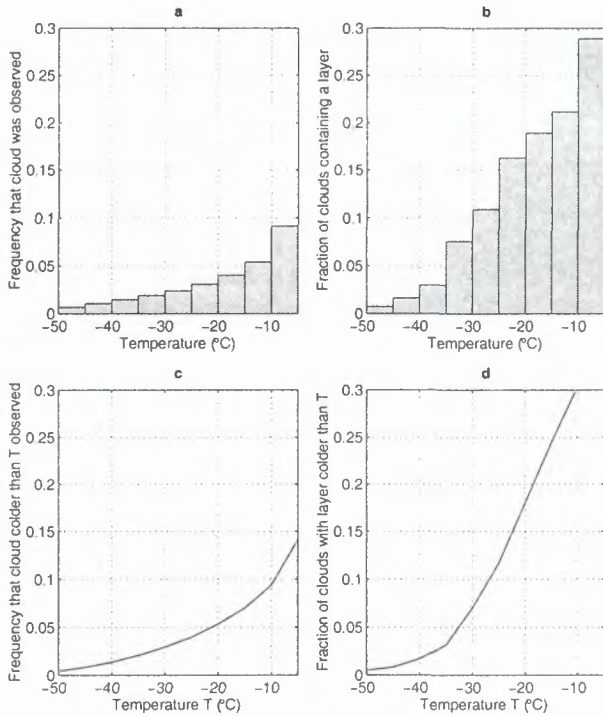


Fig. 4: Statistics from the full 31-month dataset: (a) Fraction of observations in which cloud was seen in each 5° temperature range; (b) Fraction of clouds that contain a layer in each 5° temperature range; (c) Fraction of observations in which a cloud colder than a given temperature is observed; (d) Fraction of clouds colder than a given temperature that contain a layer.

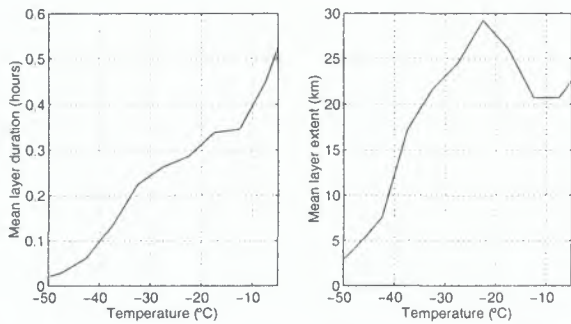


Fig. 5: Mean duration and horizontal extent of individual layers versus temperature.

The apparent physical thickness of the high β region was typically around 150 metres (5 range gates), but because of the strong attenuation the true thickness is likely to be greater.

We next divided the dataset into months to look for any seasonal or longer-term trend. A few months had too little time in which the ceilometer was operating to produce robust statistics, so have been rejected from this analysis. The remaining 31 months all have data equivalent to more than 15 continuous days of observations, and the average is equivalent to 27.7 continuous days. Figure 6 shows the fraction of clouds in three different 10° temperature intervals that contain a supercooled layer, as a function of time. We use 10° rather than 5° intervals in an attempt to reduce scatter. No robust seasonal or other

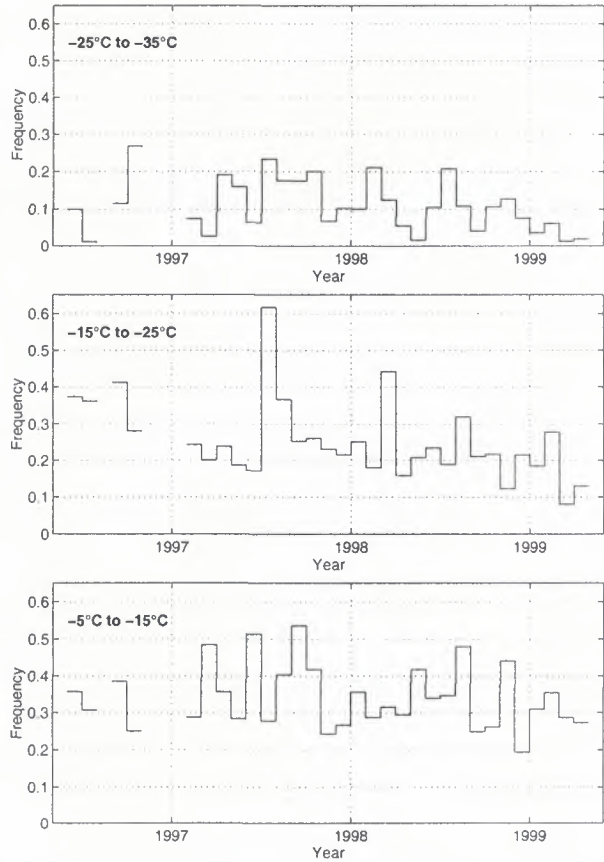


Fig. 6: Frequency of supercooled layers in three different temperature ranges, for individual months.

trend is obvious, but in any case the dataset can only really be considered continuous from February 1997, and it appears that 2 years is not sufficient to reveal any trend if one exists.

THE SUN-CLIMATE LINK

On a more speculative note, there is currently an ongoing controversy over the possible role of the sun in climate change, and a possible mechanism that has been suggested relates to the 11 year cycle in sunspots and solar-wind intensity moderating the flux of high-energy galactic cosmic rays at the top of the atmosphere. This much is well established, but the more speculative part is the suggestion that these cosmic rays can initiate glaciation, which in turn could be important in the development of weather systems. Observational support for this the sun-climate link has always rested on alleged correlations between sunspot activity and, for instance, rainfall over a particular location, but observational evidence to support particular mechanisms is conspicuously absent. Datasets such as in this paper could be used to support or refute the glaciation link because it is exactly the clouds that are claimed to be affected by cosmic rays that are being measured.

During the period of this dataset, solar activity was increasing, and therefore cosmic-ray flux decreasing. Hence if cosmic rays can cause supercooled water to glaciate and disperse, then their occurrence should increase through the data

set. Certainly from this relatively short time series no such trend is evident (if anything there seems to be a slight trend in the opposite direction). In the -25°C to -15°C region where one might expect any signal to be strongest (because it is colder than the ice multiplication region and warmer than the homogeneous nucleation region), the frequency of occurrence is around 0.2, and there are some obvious 'spikes' corresponding to September 1996, July 1997 and March 1998. In all probability these are no more than statistical noise.

CONCLUSIONS AND FUTURE WORK

A first attempt has been made to characterise the frequency of supercooled layer clouds as a function of temperature. More work is required to verify that the majority of these layers indeed consist of supercooled water, but it is found that they occur surprisingly frequently; 30% of the time that the lidar sees cloud colder than -10°C it also sees a layer colder than this. Given that they are much more radiatively important than any ice at the same altitude, and their role in glaciation and precipitation processes, it is important that some attempt is made to represent them properly in forecast and climate models. It would appear that a simple fixed ratio between ice and liquid water as a function of temperature is too crude to simulate the radiative properties of sub-freezing clouds. It would be useful to investigate with existing ceilometer data whether the occurrence of supercooled layers can be correlated with any large scale model field that could be used as the basis for a parameterisation. Much would also be learned by combining β with simultaneous measurements of radar reflectivity and lidar depolarisation.

The dataset was clearly not long enough for any seasonal or interannual trends to be evident, so it would be interesting to repeat the procedure for a longer period and at different sites.

ACKNOWLEDGEMENTS

We are indebted to RCRU at the Rutherford Appleton Laboratory for providing access to their lidar ceilometer archive, particularly to Charles Wrench, John Goddard and Mark Blackman. The radiosonde data were provided by the UK Meteorological Office, the ECMWF fields by Christian Jakob, and the cloud-camera video by André van Lammeren. The 94 GHz Galileo radar was developed for the European Space Agency under ESTEC Contract No. 10568/NL/NB. Thanks also to Giles Harrison for a number of interesting discussions regarding the sun-climate link.

REFERENCES

- Heymsfield, A. J., L. M. Miloshevich, A. Slingo, K. Sassen and D. O'C. Starr, 1991: An observational and theoretical study of highly supercooled altocumulus. *J. Atmos. Sci.*, **48**(7), 923–945.
- Hogan, R. J., A. J. Illingworth and P. R. Field, 1999: Polarimetric radar observations of the growth of highly-aligned ice crystals in the presence of supercooled water. *CLARE'98 Final workshop, 13–14 September 1999, ESA/ESTEC, Noordwijk, The Netherlands.*

Thomas, L., J. C. Cartwright and D. P. Wareing, 1990: Lidar observations of the horizontal orientation of ice crystals in cirrus clouds. *Tellus*, **42B**, 211–216.



Polarimetric radar observations of the growth of highly-aligned ice crystals in the presence of supercooled water

Robin J. Hogan*, Anthony J. Illingworth and Paul R. Field†

Department of Meteorology, University of Reading, UK

†Meteorological Research Flight, DERA, Farnborough, UK

*Email: R.J.Hogan@reading.ac.uk

ABSTRACT

In this paper, observations by a Rayleigh-scattering S-Band radar are presented of high values of differential reflectivity (up to 6 dB) in stratiform ice clouds, and are shown to coincide with the presence of supercooled liquid water. By contrast differential reflectivity tends to be much lower (less than 0.5 dB) when no liquid water is present. Because liquid droplets are too small to contribute significantly to the radar signal themselves, the indication is that ice crystals in a highly supersaturated environment tend to grow very aspherical (aspect ratios in excess of 10:1), whereas under the more usual low-supersaturation growth conditions they tend to remain more spherical (aspect ratios generally less than 2:1). Aircraft 2D-probe observations indicate that under usual conditions ice crystals tend to be irregular although not highly aligned, which suggests that the normal growth mechanism (for the larger crystals at least) is aggregation and it is only when liquid water is present that vapour deposition can dominate.

THEORY

Differential reflectivity (Z_{DR}) is defined as the ratio of radar reflectivity factor measured at horizontal and vertical polarisations, and is usually expressed in logarithmic units:

$$Z_{DR} = 10 \log_{10} \left(\frac{Z_H}{Z_V} \right) \text{ dB.}$$

It is a measure of hydrometeor alignment in the pulse volume, and in rain can be directly related to mean size because of the unique relationship between raindrop size and shape. In ice its interpretation is much more ambiguous because ice crystals occur in a multitude of different shapes and sizes. It also varies with density, and at sizes greater than around 100 μm inclusions of air mean that ice crystals can no longer be regarded as being composed of solid ice. Furthermore, it is known that the longest axes of free-falling crystals usually tend to be aligned in the horizontal (e.g. Liou 1986), but any deviation from this behaviour will result in a lower Z_{DR} for a given aspect ratio and density.

Figure 1 shows Z_{DR} as a function of ice-air ratio for homogeneous oblate spheroids with a variety of different aspect ratios, calculated using an extension to Rayleigh theory developed by Gans (1912). Note that Z_{DR} is not directly related to size, but size can have an indirect effect because larger crystals tend to be less spherical (Auer and Veal 1970) and have a lower density (Brown and Francis 1995).

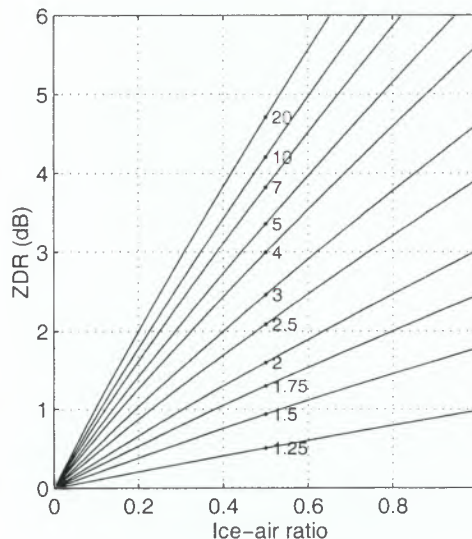


Fig. 1: Z_{DR} as a function of ice-air ratio for single horizontally-aligned oblate spheroidal crystals with various aspect ratios.

Mostly the Z_{DR} of cirrus and mid-level cloud at Rayleigh-scattering frequencies ranges between 0 and 0.5 dB, indicating that the crystals are not highly aligned. Simultaneous aircraft 2D probe and radar observations by Hogan (1998) in cirrus confirmed that in such situations the particles are irregular polycrystals that fall with their longest axes in the horizontal, resulting in positive but small Z_{DR} .

Observations of high values of Z_{DR} at temperatures down to -10°C have been presented in the literature, although all are in strongly convective systems (associated with values of Z often well in excess of 30 dBZ) and have been shown to be caused by small numbers of very large supercooled raindrops carried up in strong updraughts (Illingworth et al. 1987). However, high values of Z_{DR} are also observed in relatively quiescent stratiform clouds at temperatures lower than -10°C , for which another explanation is required.

To understand the observations presented in the following section, use will be made of Fig. 2, which shows the crystal habits that tend to grow as a function of temperature and supersaturation.

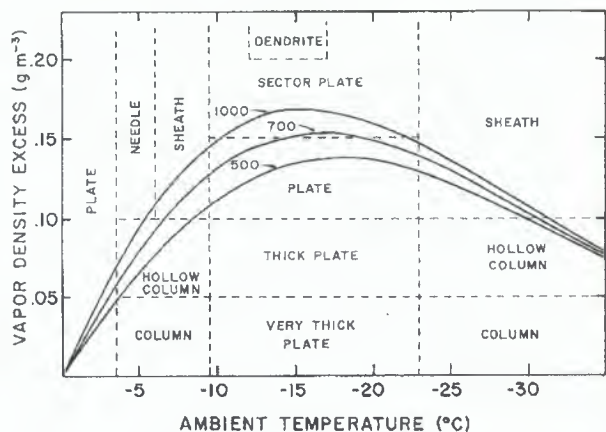


Fig. 2: The habits attained by large ice crystals growing by vapour deposition as a function of temperature and the vapour density excess between the environment and the crystal surface. The vapour density excesses corresponding to water at 100 mb, 700 mb and 500 mb are shown to indicate the types of crystal that will grow if there is supercooled water present. From Young (1993).

OBSERVATIONS

Results are presented from two case studies in which high Z_{DR} was observed by the Chilbolton radar while simultaneous aircraft measurements indicated the presence of supercooled liquid water in the same location.

CLARE'98 case study on 20 October 1998

The first event took place on 20 October 1998 during the Cloud Lidar And Radar Experiment (CLARE'98), and is summarised in Fig. 3. The first panel depicts backscatter coefficient (β) as measured by the nadir-pointing ALEX lidar on board the DLR Falcon aircraft. Thin layers of high β can be seen embedded in the mid-level cloud, and the low depolarisation of these layers as shown in the second panel indicates that they are supercooled water. The temperature of the highest layer is around -15°C . The third panel shows Z as measured by the scanning 3 GHz radar at Chilbolton, and the fourth shows the corresponding Z_{DR} . The cirrus above 9 km is largely below the sensitivity limit of the radar. There is no sign of the supercooled layers in the reflectivity field because the radar signal is dominated by the contribution from the much-larger ice crystals. However Z_{DR} is observed to rise to 6 dB in the vicinity of the layers, indicating a distinct change in ice growth behaviour. The UK Meteorological Office C-130 aircraft was making in situ microphysical measurements at an altitude of 4 km, where the temperature was -7°C , and the last panel shows liquid water content (LWC) measured by the Johnson-Williams probe and ice water content (IWC) measured by the 2D cloud and precipitation probes.

LWC is seen to rise to 0.2 g m^{-3} directly beneath the region of highest Z_{DR} . There is a suggestion of layers in the lidar echo at the altitude of the C-130 that coincide with the measurements of liquid water, although strong attenuation by the layers above mean that the signal is very weak. After this run the C-130 performed two further inbound and outbound runs, at 4.6 km (-10°C) and 5.5 km (-15°C), but by the time it had as-

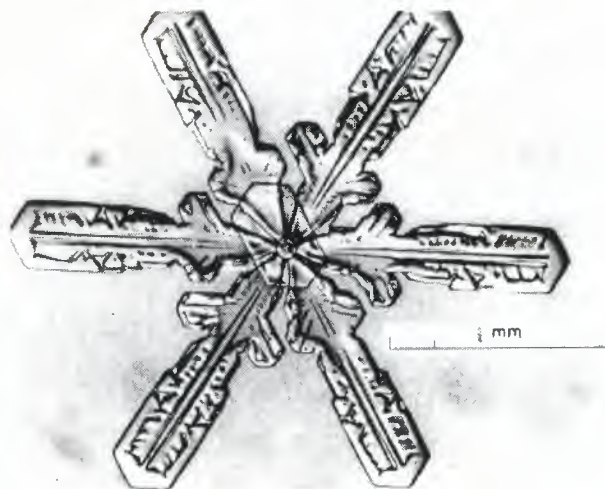


Fig. 4: Photograph of a sector plate. From Young (1993).

2DC IMAGE DISPLAY
A632 142411.97

2DP IMAGE DISPLAY
A632 142413.53

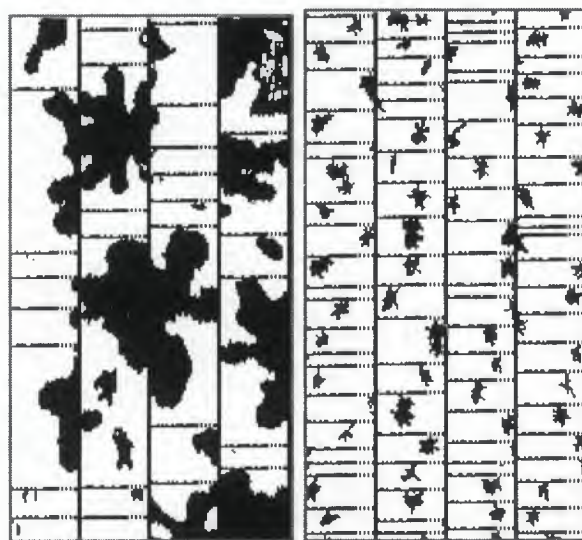


Fig. 5: Crystal images from the 2D cloud and 2D precipitation probes beneath the high Z_{DR} region shown in Fig. 3, but from the outbound leg a few minutes later. The array width of the 2D cloud probe is 0.8 mm and that of the 2D precipitation probe is 6.4 mm.

cended to these altitudes layers were no longer visible by the lidar, Z_{DR} had fallen back to its more usual range of 0 to 0.5 dB, and no significant liquid water was detected. This strongly suggests that high Z_{DR} is intimately associated with the presence of liquid water.

The C-130 did not fly directly through the very high Z_{DR} region on this occasion, but the crystals sampled beneath it will have fallen through the liquid water layers and be strongly affected by them. At -15°C , the temperature of the highest layer, growth is mainly in the prism faces of the crystals and thus plates tend to be the predominant crystal type. From Fig. 2 we see that at high water vapour excesses (caused by evaporating liquid water droplets), sector plates in particular should form. Sector plates are characterised by distinctive broad branches, as

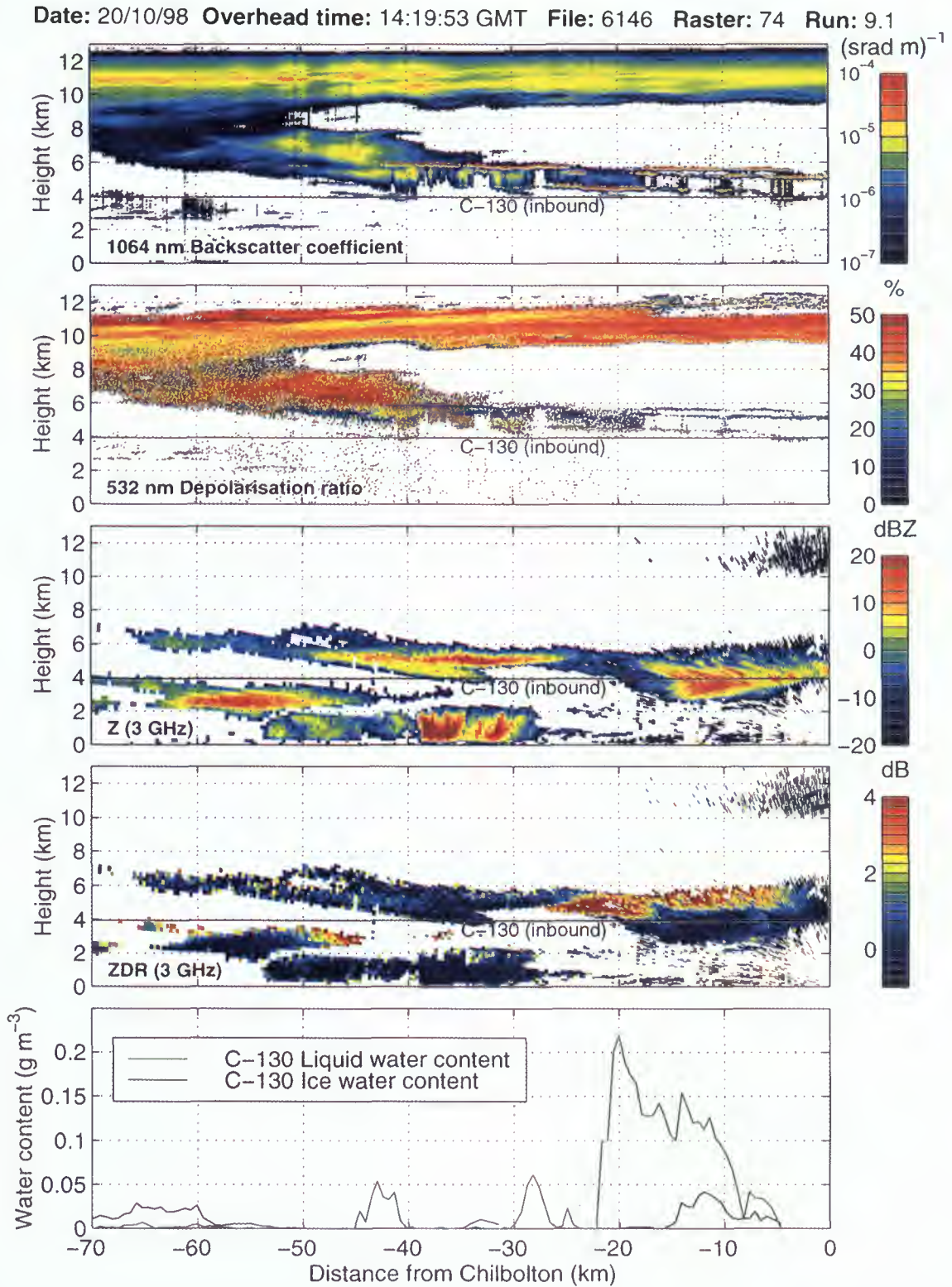


Fig. 3: Composite of observations flying from 20 October 1998 during CLARE'98. The first two panels show measurements by the nadir-pointing lidar on board the Falcon aircraft flying at an altitude of 13 km. Simultaneous measurements of Z and Z_{DR} by the ground based 3 GHz radar at Chilbolton are shown in the next two panels, and the last shows liquid and ice water content measured by the C-130 aircraft at an altitude of 4 km.

shown by the photograph in Fig. 4, and indeed the crystal images from the 2D probes on the C-130 as it flew beneath the high Z_{DR} regions exhibited precisely the same broad branches (Fig. 5).

It is easy to see why sector plates should have such a high Z_{DR} . It is known that free-falling ice crystals tend to be aligned with their longest axis in the horizontal (e.g. Liou 1986), although this is not apparent from 2D probe images because turbulence generated as crystals are drawn into the sample volume of the instrument sets them tumbling. Hence we cannot measure extreme aspect ratios from the 2D probes. However, the crystals measured by the C-130 were around 1 mm across, corresponding to an aspect ratio in excess of 10:1 according to the typical diameter-width relationships of Ono (1970). Young (1993) estimates the bulk density of sector plates to be 0.5 g m^{-3} , so from Fig. 1 we see that this corresponds to a Z_{DR} of around 4.5 dB, in agreement with what was observed.

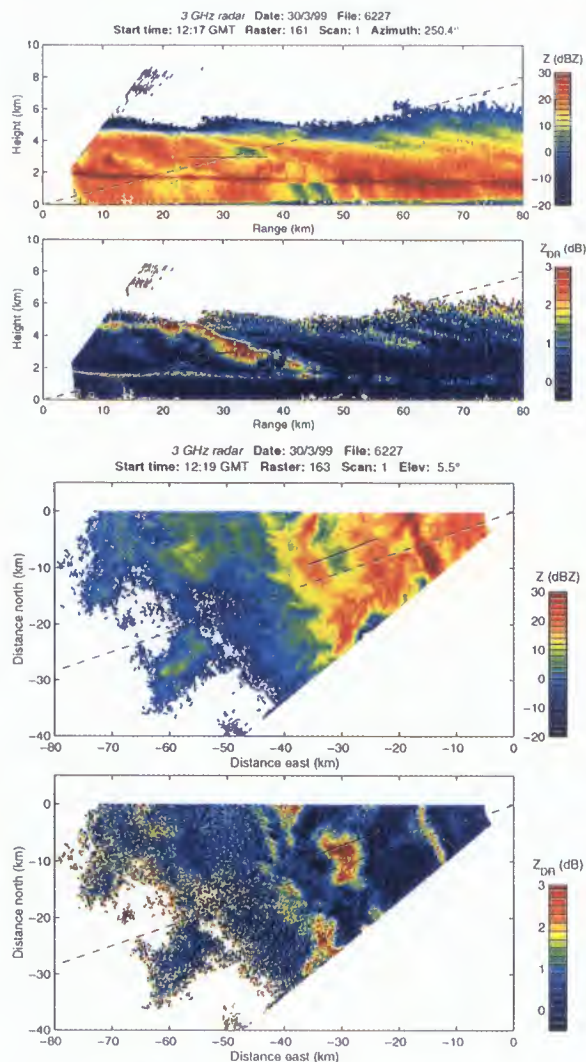


Fig. 6: Horizontal and vertical scans through a region of high Z_{DR} during the CWVC flight on 30 March 1999. The solid lines show the path of the C-130 aircraft during run 19.

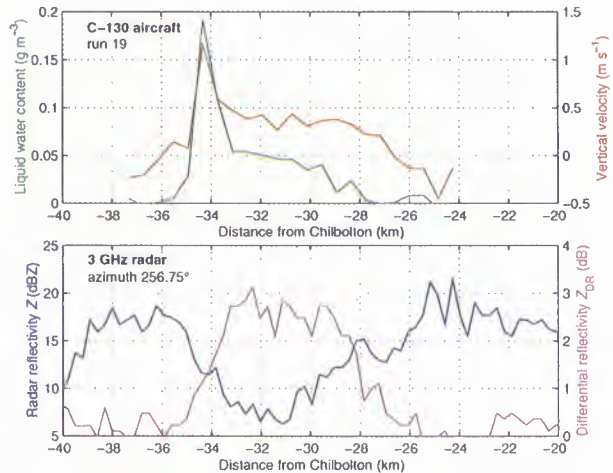


Fig. 7: Comparison of simultaneous aircraft and radar parameters for aircraft run 19. The top panel shows LWC and vertical velocity measured by the aircraft, and the bottom panel shows the corresponding Z and Z_{DR} measured by the radar during the horizontal scan shown in Fig. 6.

CWVC case study on 30 March 1999

The second case study was a C-130 flight over Chilbolton on 30 March 1999, part of the NERC-funded Clouds, Water Vapour and Climate (CWVC) program. The main interest was in supercooled water associated with weak 'embedded convection' within stratiform precipitation, and it was only afterwards that it was realised that the high liquid water contents coincided with high Z_{DR} . The flight strategy was for the aircraft to fly towards and away from Chilbolton at around -5°C until a localised region of supercooled water was encountered in coincidence with an updraught, and then to switch to a Lagrangian flight pattern, consisting of a sequence of short 2-minute runs while slowly drifting and ascending with the air.

Figure 6 shows two scans through a region of supercooled water that was sampled by the C-130 during one of these ascents. The first two panels show Z and Z_{DR} from a vertical scan, and the convective plume is indicated clearly by a region of high Z_{DR} . The solid line shows the path of the C-130 during a short run, and the dashed line indicates the elevation of a horizontal scan taken 2 minutes later and shown in the following two panels.

The top panel of Fig. 7 shows LWC measured by the Johnson-Williams probe and vertical velocity as the aircraft flew through the plume, and the bottom panel shows Z and Z_{DR} measured simultaneously by the radar. LWC peaks at 0.19 g m^{-3} at the same time that the maximum updraught of 1.2 m s^{-1} . As well as Z_{DR} rising to 3 dB in the plume, we see that Z falls by 10 dB. Crystal images taken by the 2D cloud probe (not shown) indicate the presence of columns in the regions of liquid water and larger aggregates (with the suggestion of sector-plate-like broad branches) to each side. Hence it appears that the updraught prevents the large aggregates from falling into this region, leaving only aligned columns, which grow in situ. The temperature at the altitude of the aircraft was -5.9°C , corresponding to around the middle of the column growth region (Fig. 2).

There appears to be an extensive region of Z_{DR} greater than 1 dB at the top of the cloud. This can be explained by the fact that when crystals first grow it is by vapour deposition, and it is only when they have an appreciable fall speed that aggregation becomes important and Z_{DR} falls to around 0 dB.

DISCUSSION

The picture that emerges from the aircraft observations in the CWVC case is of localised patches of supercooled water being carried up in updraughts, and this is backed up to some extent by the radar scans showing a plume of high Z_{DR} around 5 km across. The lidar observations from CLARE'98 showed a number of very distinct layers rather than a plume, so the question is whether the two cases, which are in the same temperature range, can be reconciled. It is not easy to speculate on what an airborne lidar would have seen in the CWVC case. Certainly in the absence of the lidar observations in CLARE'98 the two cases do not look dissimilar, with both seeing a localised region of high Z_{DR} around 5 km across, which coincides with supercooled water with an LWC peaking at 0.2 g m^{-3} . The layers observed in CLARE'98 were far from horizontally homogeneous, and it is possible that the aircraft observations of liquid water in CWVC were from passes through a number of layers at different levels.

Long-term observations by lidar ceilometer suggest that supercooled layers at the top of altocumulus can be very long lived (12 hours in some cases), but as one would expect, when ice is falling through them they tend to be eroded more rapidly and usually last no longer than one hour.

We have seen how the types of crystals that are produced in highly supersaturated environments such as sector plates can give very high values of Z_{DR} . From Fig. 2 it is clear that between -9.5°C and -23°C , Z_{DR} should depend strongly on whether liquid water is present, since at lower supersaturations much thicker plates (aspect ratios of around 2:1) will tend to grow. Outside this temperature range, columns and needles are the dominant crystal types and from this one might expect to see high Z_{DR} in all clouds regardless of supersaturation, rather than the usual range of 0 to 0.5 dB. However, 2D probe images at temperatures colder than -23°C show needles relatively rarely; by far the most common are irregular 'polycrystals', although bullet rosettes occur fairly frequently also. One should remember that radar parameters such as Z_{DR} are weighted by the square of the mass of the particles, and it is therefore the larger particles that are most important. From this it would seem likely that aggregation is the dominant growth mechanism at the larger sizes in most ice clouds, resulting in the observed irregular, low-density crystals, and it is only when liquid water is present that vapour deposition becomes important at all sizes producing the highly-aligned high-density crystals that were observed in these two cases.

CONCLUSIONS AND FUTURE WORK

For the first time high Z_{DR} in ice cloud has been shown to coincide with the presence of liquid water, explained by the rapid growth of either columns or thin sector plates. Given the importance of supercooled water for radiation and the development of precipitation, there is a clear need for more aircraft

flights over Chilbolton to further investigate the spatial and microphysical properties of liquid water within ice clouds. The finding that Z_{DR} is linked to the presence of liquid water means that the radar could be much more useful in directing the aircraft towards the most promising areas. It also means that Z_{DR} could be used near airports for to warn about the possibility of aircraft icing.

ACKNOWLEDGEMENTS

Many thanks to RCRU at the Rutherford Appleton Laboratory for the Chilbolton radar data, to Peter Francis at the UK Meteorological Office for providing the C-130 aircraft data from CLARE'98, and to Harald Flentje and Wolfgang Renger of DLR for the Falcon lidar data. The CLARE'98 campaign was funded by ESTEC and the CWVC experiment by NERC.

REFERENCES

- Auer, A. H., and D. L. Veal, 1970: The dimension of ice crystals in natural clouds. *J. Atmos. Sci.*, **27**, 919–926.
- Brown, P. R. A., and P. N. Francis, 1995: Improved measurements of the ice water content in cirrus using a total-water probe. *J. Atmos. Oceanic Tech.*, **12**(2), 410–414.
- Gans, R., 1912: Über die form ultramikroskopischer goldteilchen (On the shape of ultra-microscopic gold particles). *Ann. Phys.*, **37**, 881–900.
- Hogan, R. J., 1998: *Dual-wavelength radar studies of clouds*. PhD Thesis, University of Reading, UK.
- Illingworth, A. J., J. W. F. Goddard and S. M. Cherry, 1987: Polarization radar studies of precipitation development in convective storms. *Quart. J. Roy. Met. Soc.*, **113**, 469–489.
- Liou, K.-N., 1986: Influence of cirrus clouds on weather and climate processes: A global perspective. *Monthly Weather Rev.*, **114**, 1167–1199.
- Ono, A., 1970: Growth mode of ice crystals in natural clouds. *J. Atmos. Sci.*, **27**, 649–658.
- Young, K. C., 1993: *Microphysical processes in clouds*. Oxford Univ. Press.



Comparison of Lidar/Radar Ice cloud parameter retrievals with in-Situ Measurements.

D.P. Donovan and A.C.A.P. Van Lammeren, KNMI, De Bilt, the Netherlands (donovan@knmi.nl)

R. Hogan, Dept. of Meteorology, University of Reading, UK.

P. Francis, UK meteorological Office, Met. Research flights, Farnborough, U.K.

J. Testud, IPSL Centre d'étude des Environnements Terrestre et Planétaires, Vélizy, France

J. Pelon, IPSL-Service d'Aéronomie, Paris, France.

M. Quante, GKSS, Institute for Atmospheric Physics, Geesthach, Germany

J. Goddard, Rutherford Appleton Laboratory, UK

Abstract

The results of a newly developed lidar/radar cloud sounding technique are compared with in-situ measurements made using aircraft mounted 2d probe particle-sizing measurements. Comparisons are presented for two days during the CLARE98 multi-sensor cloud measurement campaign when ice-clouds were sampled. For both days, the remotely derived cloud properties are in good qualitative and quantitative agreement with the in-situ results.

Introduction

During CLARE98, several flights of the UK meteorological office C-130 aircraft were conducted [Francis, 1999]. The C-130 mounted several in-situ particle sizing instruments including 2D-C and 2D-P probes. These instruments are, in principle, capable of measuring the effective size of ice-crystals and to infer the ice-water content of the sampled cloudy volume. Recently, a new procedure for estimating cloud particle effective size and water content profiles using combined lidar and radar data was proposed and has been applied to CARE98 data.

In this paper, comparisons between the C-130 2D probe measurements and the results of both ground and aircraft based lidar/radar cloud soundings are presented for two days during the CLARE98 campaign. For two overflights of the UKMO C-130 on October 21st, results are shown which use the combination of the ground-based GKSS 94GHz radar and the Viasala CT-75K 905 nm lidar ceilometer. For October 20th, comparisons between the lidar/radar inversion results using the airborne

KESTREL 94 GHz radar together with the LEANDRE 532nm (both mounted on the ARAT aircraft) and in-situ measurements made during a near coincident C-130 flight are presented.

Algorithm

The lidar/radar algorithm that is employed here is the same as that described in Donovan et al. (1999) except that multiple scattering has been accounted for in an approximate fashion using the formalism described in Eloranta (1998). To a large degree, the contribution of multiply scattered light to the observed lidar signal depends on the angular width of the forward scattering lobe of the cloud particle's phase function compared with the field-of-view of the lidar receiver. The width of the forward scattering lobe is, in turn, related to the cross-sectional area of the cloud particles. In general, the larger the particles are the narrower the forward scattering lobe is.

If multiple scattering is ignored, then the retrieved extinction will be lower than the true extinction. Simulations made using both a Monte-Carlo model and the approximate model of Eloranta have shown that for the measurements of ice-clouds made using the CT-75K lidar this effect is generally expected to be below 10-20 % since the field of this instrument is less than 0.6 mrad. For the airborne LEANDRE lidar, with a 3.5 mrad fov, the measured extinction will be only about half the true extinction.

To account for multiple scattering effects, first an inversion is performed assuming no multiple scattering, then the retrieved extinction profile and particle sizes are used to estimate the multiple scattering contribu-

October 21st

tion (to 3rd or 4th order). To do this, the angular width of the forward scattering peak is estimated using the derived *lidar/radar effective radius* (R'_{eff}) [Donovan et al. (1999)] profile together with diffraction theory. Once the multiple scattering contribution has been estimated as a function of range from the lidar the single scattered power can be estimated. When this is done, an inversion is performed on the estimated single-scatter only signal. The multiple scattering contribution is then re-estimated as before and another inversion is then performed. The process is then repeated until the estimated single-scatter power only profile has converged.

A schematic view of the inversion procedure (including multiple scattering effects) is outlined in Fig. 1. The basic method used to determine the inversion far-end boundary value (in R'_{eff}) is the same as that previously described [Donovan and Lammeren, (1999)]. In brief, once $R'_{eff}(z_m)$ is specified and a Klett-type inversion performed, it is possible to calculate what the effective value of C_{lid} must have been (assuming that the radar calibration is reasonable well known). In effect, the inversion procedure performs a number of different Klett-type inversions each with a different boundary value and then chooses the boundary value which gives the smoothest retrieved R'_{eff} profile which corresponding to a feasible value of C_{lid} .

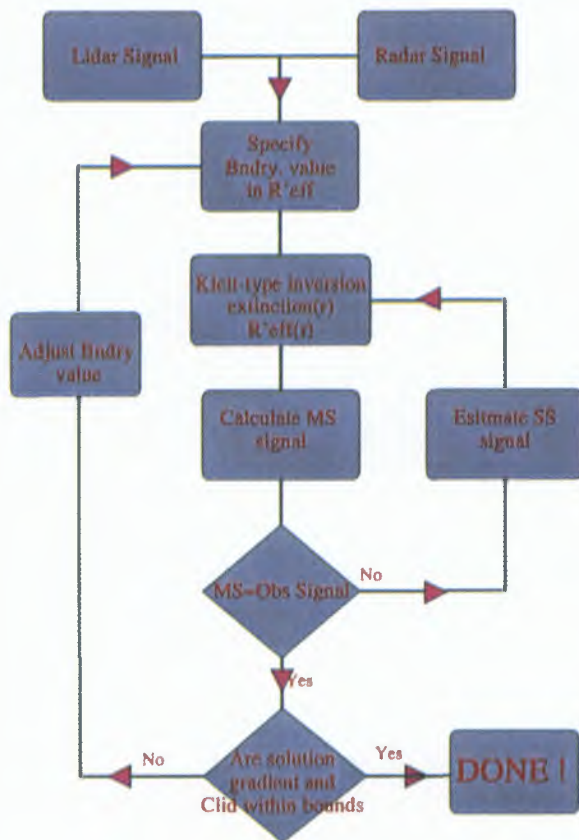


Figure 1: Schematic representation of the lidar/radar inversion procedure including multiple scattering effects.

On this day the UKMO C-130 passed over the Chilbolton site four times at an altitude of around 5.8 km. Two of the overpasses occurred around 10:20 Hrs. UTC and two around 10:50 Hrs. UTC. Throughout the campaign a ground-based Viasala CT-75K 905nm lidar was in continuous operation [Goddard (1999)]. During the aircraft flight times, the GKSS 94 GHz radar and the Rablies 35GHz radar were mainly operating in a scanning mode, but they also obtained vertically pointing 'snap-shots' around the direct overpass times. Here the GKSS radar data was chosen for comparison with the lidar due to the higher spatial resolution of the snapshot data. Details of the GKSS radar are described in Danne and Quante (1999).

The Viasala CT-75K lidar signal along with the effective reflectivity observed by the GKSS radar are shown in Fig. 2. The radar signal here is a snap-shot of around 10 seconds while the lidar signal is an average of about 1.5 minutes. The raw CT-75K measurements have a temporal resolution of 30 seconds and averaging beyond this was found to be necessary. This was due to the relatively low signal-to-noise ratio of the lidar signal and the sporadic detection of the cloud layer between 5.5 and 7km by the lidar ceilometer. Figure 2 also shows the ice-water content (IWC) and R'_{eff} profiles derived for the lidar and radar signals together with the values estimated for the IWC and *normal effective radius* ($R_{eff} = 3/4 < mass/\rho_s > / < area >$) from the 2D probe data at around 5.8 km during the overpass.

The lidar/radar derived masses were estimated assuming the complex-polycrystal model relationship between particle mass and cross-sectional area of Mitchell et al. (1996), while the 2D probe estimates were made using two different methods. One method uses an empirical relationship between the particle mass and its cross-sectional area as determined by the probe. The other method uses a relationship between the mass and average mean dimension of the particles. These two methods tend to agree for smaller particles but diverge for larger particle sizes. It can be seen that the values for the ice-water content estimated using the lidar/radar inversion are consistent with the 2D probe estimates. Though R'_{eff} and R_{eff} are not directly comparable, they are expected not to differ by more than 15% for common size distributions. In this figure it can be seen that the effective radii estimates at 5.8 km seem consistent within their respective uncertainties. For both the IWC estimate and the effective size estimate the lidar/radar results tend to agree better with the area-derived 2D probe estimates.

The results for a later overpass are shown in Figure 3. Here, it appears that the aircraft sampled near the top of the cloud. The agreement here is seen not to be as good as for the earlier overpass, particularly with regards to the effective size estimates. However, given

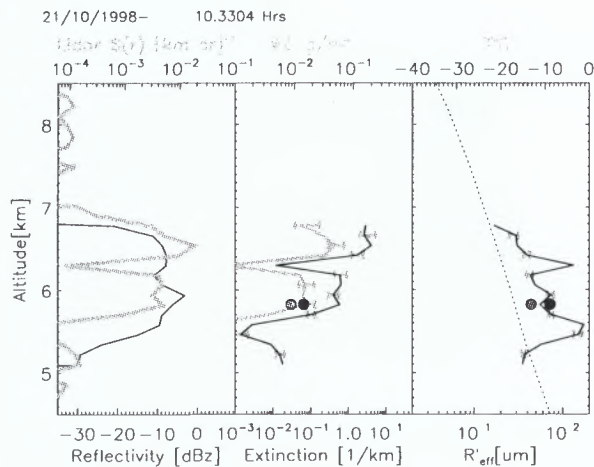


Figure 2: Lidar (Grey) and radar (thin Black) signal profiles for October 21, 1996 at 10.33 Hrs UTC (left). The middle panel shows the retrieved 905 nm extinction profile and estimated IWC profile (Grey) while the right panel shows the retrieved R_{eff}^l profile and the UKMO temperature profile (upper-axis). The black circles denote the values inferred from the C-130 mounted 2D probes using the mass-vs-area relationship while the Grey dots show the respective estimated made using the mass-vs-maximum average dimension relationship.

the variability of the clouds at this time and the somewhat miss-matched temporal resolutions of the lidar and radar data used here it is hard to attach too much significance to the disagreement (or even agreement) between the lidar/radar and in-situ results in this and the previous case.

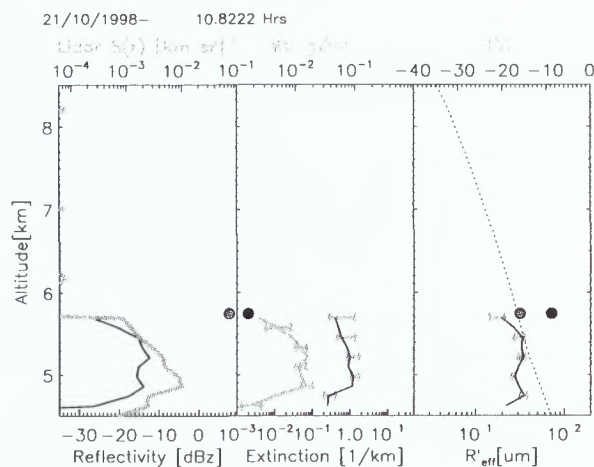


Figure 3: As Fig. (2) except for 10.83 Hrs UTC.

October 20th

On October 20th a near coincident flight path was flown by the French ARAT aircraft and the UKMO C-

130. The ARAT carried the LEANDRE 532nm lidar along with the KESTREL 94 GHz Radar. Details of the two instruments can be found in Guyot et al., (1999a) and Guyot et al., (1999b). The observed lidar reflectivities and backscatter signals for this flight are shown in the upper panels of Fig. (4). Here a large cloud is visible in the top right portion of both panels while the lidar image shows several strong backscattering layers not prominent in the radar reflectivities. These layers also appear to largely attenuate the lidar returns so that in general no useful lidar signal is present below about 2.0 km.

The lower panels of Fig. (4) show the estimated lidar/radar effective particle size and the estimated water contents. The C-130 flights at conducted on this day show that layers of liquid water were often present over and around Chilbolton. However, little water was encountered during the coincident C-130 flight at 4.6 km. The inversion results shown here were conducted assuming that the strong backscattering layers below about 3.25 km ($T=-4$ Degrees Celsius) were comprised mainly of liquid water while elsewhere it was assumed that the clouds were ice. If an inversion is conducted assuming ice everywhere then the inferred particle sizes in these layers are still quite small (less than 2-4 microns). Since the far-end boundary values used in the inversions were set at the altitudes of these layers, assuming they are mainly ice instead of water alters the particle sizes and IWCs inferred for altitudes closer to the aircraft are changed by 10-20%.

The separation in space and time as a function of latitude between the ARAT and the UKMO C-130 are shown in Fig. (5). It can be seen that within about 10km of Chilbolton the horizontal separation of the two aircraft was within 300 meters and the time difference within half a minute. Such separations are not ideal but given the large extent and high apparent stability of large ice cloud sampled here together with the horizontal resolution of the aircraft measurements (about 500-600 meters for the C-130 measurements) they may be considered adequate for useful comparison in this case.

A comparison between various cloud properties inferred from the 2D probe measurements and the lidar/radar inversion results is shown in Fig. (6). The lidar/radar results shown are for an altitude of 4.55 km which was the maximum height at which reliable data was obtained. The C-130 flew at an altitude of around 4.6 Km which is just slightly higher than the maximum height of the lidar/radar data but is within one range bin (the resolution of the lidar data was 60 meters) of the top of the lidar/radar data. As before, results for the two different ways of interpreting the 2D probe data are presented except for the case of the inferred extinction. Since the optical extinction inferred from the 2D probes is just twice the cross-sectional area of the particles, the area binned 2D probe results for extinction are considered to be more accurate than those

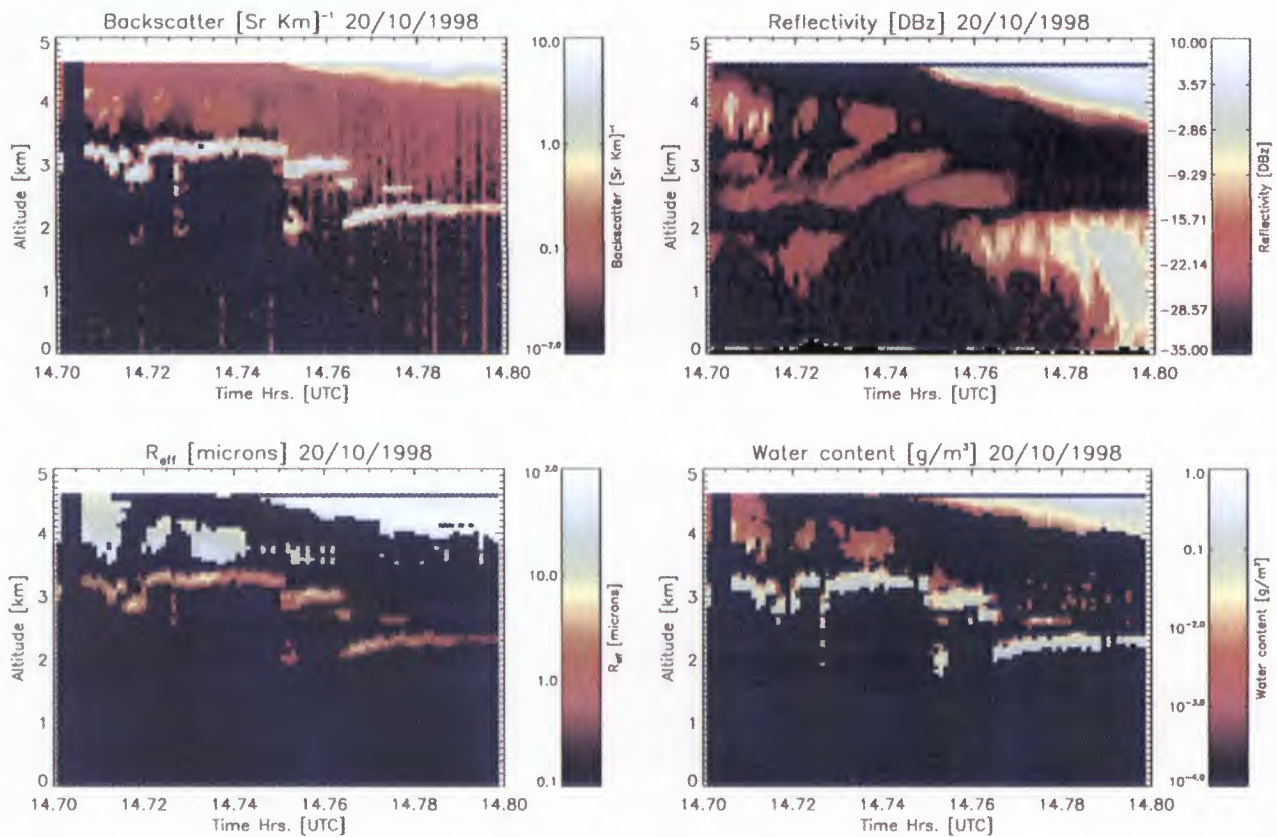


Figure 4: Observed radar reflectivity and lidar backscatter signal (top) together with the results of the lidar/radar inversion (bottom) for the ARAT flight path.

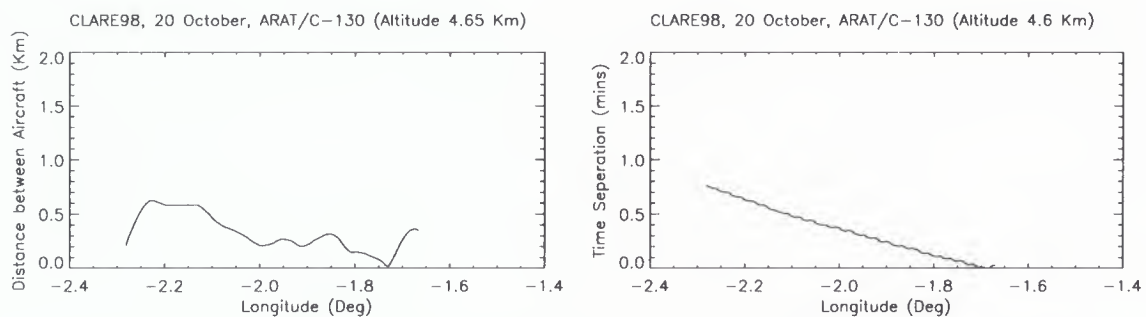


Figure 5: Separation in space and time between the ARAT and the UKMO C-130 as a function of latitude.

that may be inferred from the average dimension spectra. The lidar/radar IWC and R_{eff} estimates shown here were generated using the complex-polycrystal model of Mitchel et al. (1996). This model specifies a different mass-vs-area relationship than either of the two approaches used to interpret the 2D probe data.

The comparisons between the lidar/radar derived quantities and the 2D probe measurements are seen to be consistent within the uncertainty between the two methods for determining particle mass. In particular, the lidar/radar results for IWC appear to agree somewhat better for most of the flight path with the area derived 2D

probe estimates. However, past the peak of the IWC values the lidar/radar values appear to match the average dimension binned results better. The significance of this result is unclear at this point. A more rigorous comparison should be made which would incorporate the same mass-vs-area relationship in the lidar/radar retrievals as that used in the 2D probe estimates.

Conclusion

The agreement obtained between the remotely derived and in-situ derived cloud properties presented here

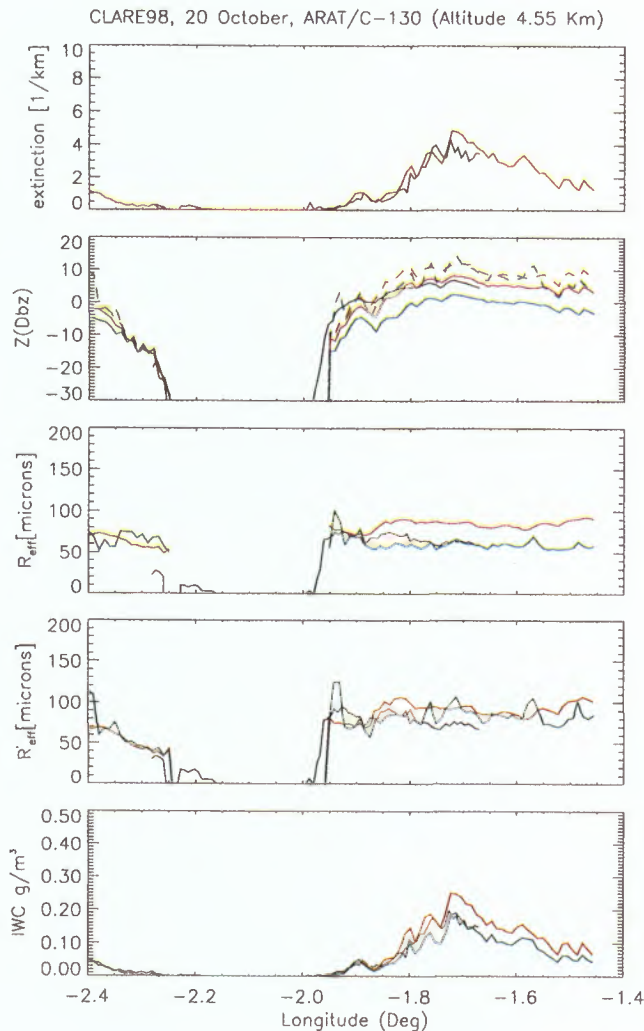


Figure 6: Comparison of lidar/radar results and 2D probe results for the ARAT/C-130 flight path. The black-solid lines show the respective results from the lidar/radar inversions at 4.55 km. The red lines show the respective results for the 2D probe data using the mass-vs-area relationship while the green lines show the respective results of the mass-vs-maximum average dimension relationship. In the panel showing the Z values, the dashed lines show the reflectivities calculated from the 2D probe data assuming Rayleigh scattering while the solid lines show the values calculated using Mie theory for spheres with the same cross-sectional area and mass as given by the 2D-probes.

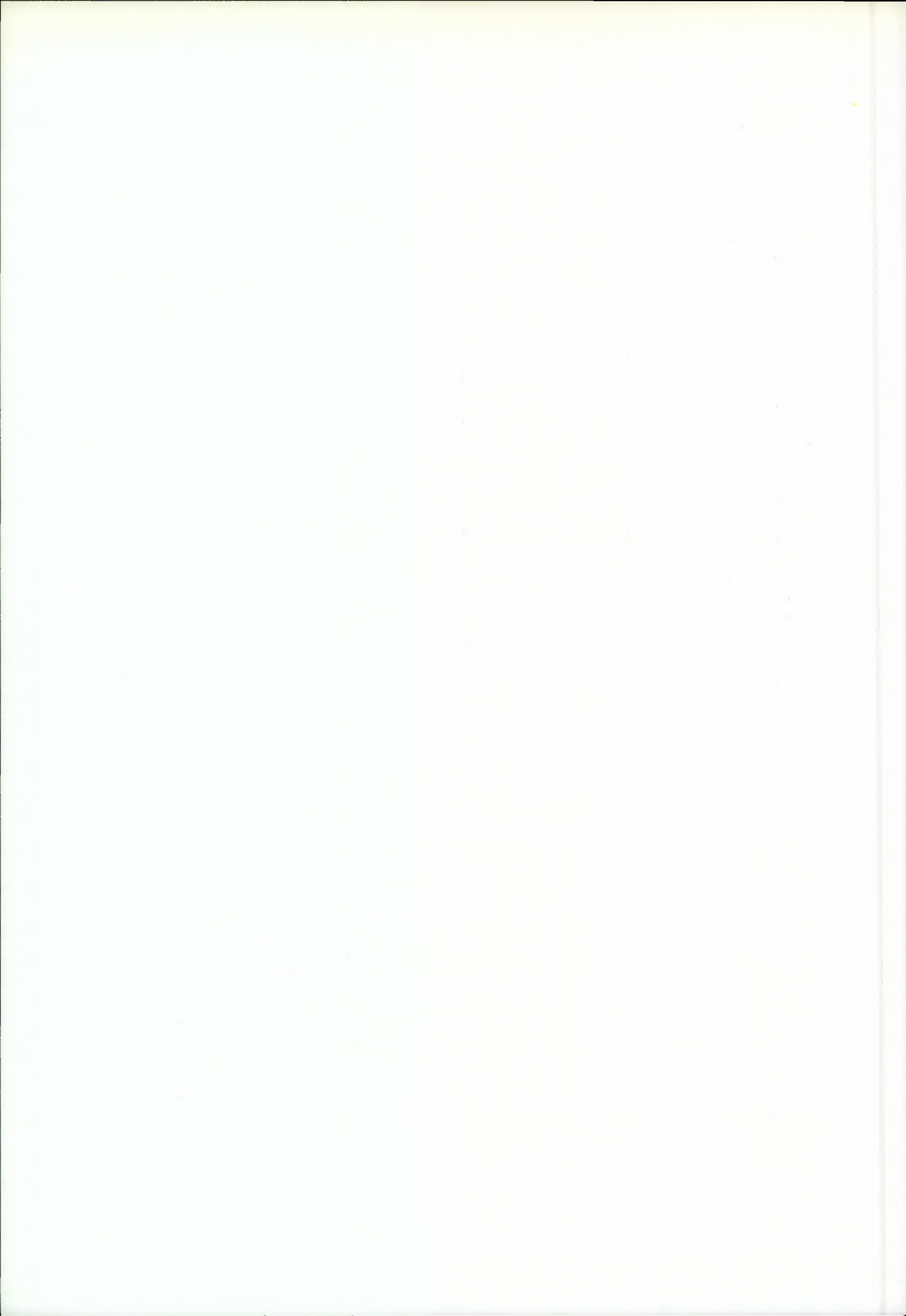
is impressive, especially considering the diversity of the two approaches and the many possible sources of uncertainty inherent in both the lidar/radar retrieval process and the interpretation of the 2D probe images. It remains to be seen whether such agreement is to be commonly expected or is limited to certain special circum-

stances.

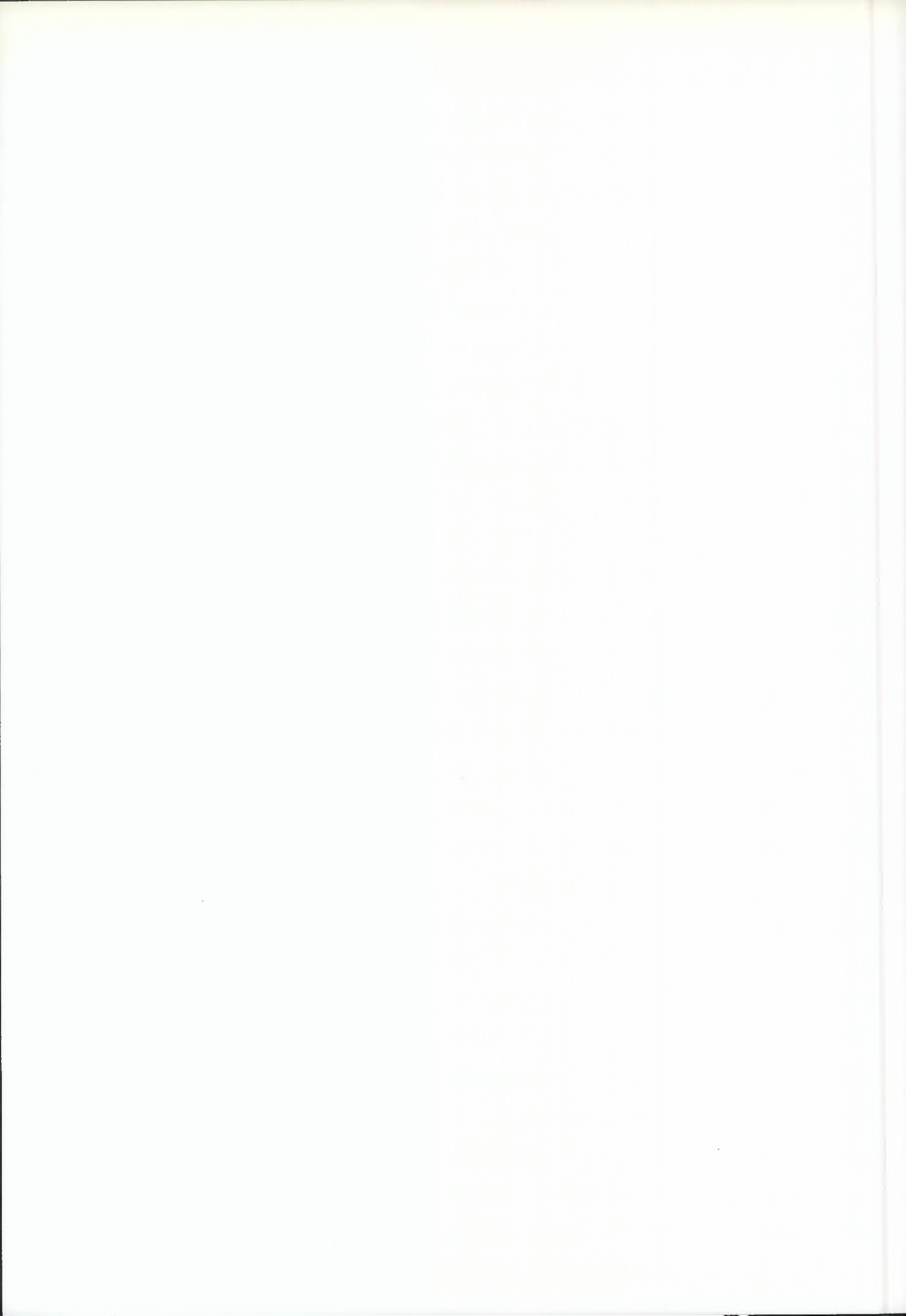
Further work should be performed to investigate the validity of the approximate treatment of non-spherical particle scattering implicitly used in the lidar/radar inversion process. As well, better characterization of the nature of proper mass-vs-area relationships for ice crystals would benefit both the interpretation of 2D probe data as well as aid in the accurate inversion of combined lidar and radar data.

References

- Donovan, D.P., J. Goddard, H. Savgeot and R.J. Hogan. Cloud effective radius and water contents inferred from combined lidar and radar observations during CLARE98, *this report*, (1999).
- Donovan, D.P, and A.C.A.P. Van Lammeren, Combined lidar and radar cloud particle effective size retrievals made during CLARA, to appear in, *Phys. and Chem. of the Earth* (1999).
- Eloranta, E.W., Practical model for the calculation of multiply scattered lidar returns, *Appl. Opt.*, **37**, 2464-2472 (1998).
- Francis, P.N., A summary of the cloud microphysics data collected during CLARE'98 by the UKMO C-130 Aircraft, *em this report* (1999).
- Goddard J.W.F., Performance of the Ground-based instruments at Chilbolton, *This Report*, (1999).
- Guyot, A., J. Testud, O. Danne, M. Quante, and P. Francis, Calibration of the University of Wyoming 95 GHz airborne radar during CLARE'98, *This Report*, (1999a).
- Guyot, A., J. Testud, J. Pelon, V. Trouillet, and P. Francis Synergy in ice clouds between airborne nadir pointing radar and lidar during CLARE'98 *This Report*, (1999b).
- Mitchell, D.L., A. Macke, and Y. Liu, Modeling Cirrus Clouds. Part II: Treatment of Radiative Properties, *J. Atmos. Sci.*, **53**, 2967-2988 (1996).
- Danne, O., and M. Quante, The GKSS 95 GHz cloud radar during CLARE 98: System performance and data products, *This Report*, (1999).



Satellite Implications and Comparisons



Multiple scattering in cirrus and mixed phase mid-level ice/water clouds during CLARE'98 and implications for space lidar

H. Flentje, Ch. Kiemle and W. Renger
 Arbeitsgruppe Lidar, DLR-Oberpfaffenhofen, D-82234 Wessling, Germany
 Phone : +49 8153 282525 Fax : +49 8153 281271
 Email: harald.flentje@dlr.de

INTRODUCTION

The resolution and parametrisation of (sub-visible) cirrus as well as mid-level clouds in global climate models is one of the major error sources in the attempt to predict future atmospheric changes. Especially the radiative transfer in these clouds related to multiple scattering of solar and terrestrial photons is yet poorly quantified. In fact the budget of net in- and outgoing radiation from a cloud layer is quite sensitive to its optical properties which have to be derived from or parameterised according to optical measurements.

The effects of multiple scattering on remote sensing e.g. by lidar are first an increased penetration depth of the pulses into the clouds which leads to a reduction of the observed extinction. Second the path length of multiply scattered photons is longer than the single scattered path which distorts the range determination and causes a washout of the cloud's far boundary [1, 2, 3]. Platt [1] showed that for a given wavelength multiple scattering increases with cloud optical depth, cloud range, range into the cloud, cloud particle size and with the receiver field of view. This implies that there is a large amount of information convoluted in the back-scattered lidar signal. The separation of and accounting for the single contributions determining the profiles thus requires some ad hoc or experience-based assumptions i.e. a simplified model to reduce the problem's degrees of freedom.

The CLARE'98 campaign from 5 to 23 October 1998 near Chilbolton, southern UK combined ground-based and airborne lidar and radar systems as well as a comprehensive set of airborne in-situ measurements to characterise the optical and micro-physical parameters of mid-level mixed-phase clouds.

DOUBLE SCATTERING INVERSION ALGORITHM

Though multiple scattering is less important in lidar applications than in natural atmospheric radiative transfer due to the small laser beam divergence and the narrow field of view, it nevertheless needs to be considered especially for high optical depths. An exact however very costly treatment of multiple scattering can be achieved by (stochastic) Monte Carlo techniques if they have been made feasible by variance reduction. But even so, these are not suitable for routine applications, instead numerically fast and sufficiently precise approximated models are required.

In the algorithm applied here, developed by Ruppersberg et al. [4], the multiple scattering is approximated by the double scattering term which holds if the phase function is largely dominated by forward scattering (e.g. realised in cirrus clouds consisting of large ice particles). Mathematically a double scattering term $Q_{ms}^{(2)}(r)$ is introduced into the lidar equation:

$$\Delta P(r) = P_i \Delta r A \frac{1}{r^2} \beta(r) \tau^2(r) (1 + Q_{ms}^{(2)}(r)), \quad (1)$$

$\Delta P(r)$ and P_i denote the number of photons received in the range interval $\Delta r = c\Delta t/2$ and at a reference distance r , A being the effective receiver area, $\beta(r)$ the backscatter coefficient and $\tau(r)$ the optical depth of the atmosphere between the lidar system and the sampling interval at the distance r . The double scattering correction

$$Q_{ms}^{(2)}(r) = \frac{\Delta P^{(2)}(r)}{\Delta P^{(1)}(r)} \quad (2)$$

is the ratio of singly to doubly scattered photons in a sampling interval. The analytical formulas for this inversion are derived by Ruppersberg et al. [1997].

The phase function of Cirrus ice crystals decreases by several orders of magnitude when going from 0 to some 10 mrad scattering angle and may be approximated by a simple exponential function. If, as the Babinet theorem (e.g. [5]) states, the diffraction lobe produces 50% of the extinction coefficient σ_c and its width is proportional to the wavelength λ , this allows for an analytical integration of an approximate $Q_{ms}^{(2)}(r)$:

$$Q_{ms}^{(2a)}(r) = \Delta r \sigma_e(r_i) + \quad (3)$$

$$\Delta r \sum_{j=1}^{i-1} \sigma_e(r_j) \left[1 - \left(1 + \frac{i-1/2}{i-j} \frac{\alpha}{\vartheta_w(\lambda, r_j)} \right) \exp \left(- \frac{i-1/2}{i-j} \frac{\alpha}{\vartheta_w(\lambda, r_j)} \right) \right]$$

for $i = 2, \dots, n$ and $Q_{ms}^{(2a)}(r_i) = 0$ at start, α being the receiver field of view (FOV). The $1/e$ -width of the phase function ϑ_w ,

is parameterised using Babinet's theorem by its forward scattering value at an angle of zero degrees β'_λ :

$$\vartheta_w(\lambda, r_p) \approx \frac{1}{2\sqrt{\pi}\beta'_\lambda(0, r_p)} \frac{\lambda}{\lambda_0} \quad (4)$$

As an alternative quantification of the multiple scattering contribution profiles of Platt's Eta parameter [1] are shown in the Figures which supply the seemingly reduction of the optical depth caused by multiple scattering.

In this article we always refer to the backscatter ratio γ as the measure of the particle scattering:

$$\gamma = \frac{\beta_p}{\beta_m} + 1$$

β_p and β_m being the particle and the molecular backscatter coefficient. β_m is calculated via the Rayleigh formula from standard profiles of temperature and pressure. Thus this quantity can easily be transformed to the particle backscatter coefficient $\beta_p(h) = (\gamma - 1)\alpha_m(h)/8.38$ with the Rayleigh extinction standard profile $\alpha_m(h, T, p, \lambda) = 8\pi/3 * \beta_m(h, T, p, \lambda)$ ($8\pi/3 =$ lidar ratio for Rayleigh scattering). In Figure 1 the Rayleigh backscatter standard profile $\beta(h, T, p, \lambda)$ applied for the calculations presented in this article is plotted for the three wavelengths as a function of height valid for a mid-latitude standard temperature and pressure profile [9].

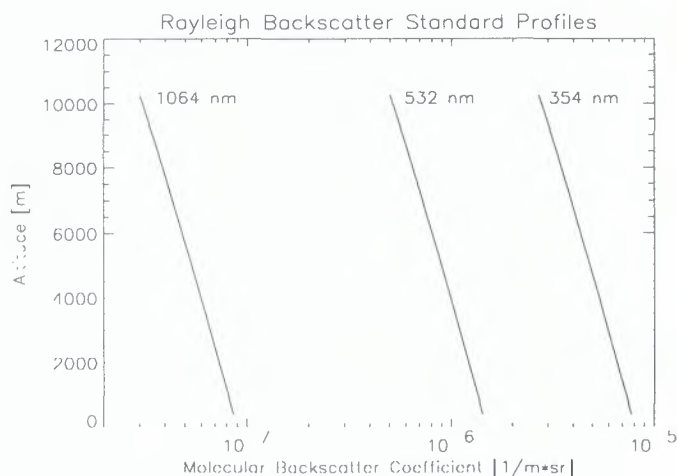


Figure 1: Standard profile of the Rayleigh (molecular) backscatter coefficient calculated from the analytical formula with standard temperature and pressure profiles

THE BACKSCATTER LIDAR

During the CLARE'98 campaign the 3 wavelength lidar of the DLR (ALEX - see Fig. 2) was operated in down-looking mode onboard a FALCON 20 aircraft. It makes use of a Nd:YAG laser emitting at 1064nm. Frequency doubling and tripling provides 532nm and 355nm channels. The received 532nm signal is split into two perpendicularly polarised

portions which allows to calculate the depolarisation of the light. With a repetition rate of 10Hz for typical aircraft speed of 150m/s the raw data resolution is about 15m horizontally.

Table 1: Aerosol Lidar EXperiment system parameters

Transmitter	Continuum Nd:YAG-laser NY61
Wavelengths, Energy per pulse, detector	1064 (150mJ) APD 532 (120mJ) PMT 355 (150mJ) PMT
Pulse lengths	6 ns
Beam divergence	0.7 mrad
Pulse repetition rate	10 Hz
Telescope	35 cm, Cassegrain
Field of view (full angle)	1 mrad
Focal length	5 m

Vertically the ADC sampling rate results in a resolution of 15m. However, to improve the S/N ratio the compromise between signal noise and resolution leads to a respectively processed data resolution of 1-3 km horizontally and 30m vertically. The receiver is a Cassegrain telescope ($r = 17.5\text{cm}$) with 1mrad field of view. Performance of the lidar system and data limitations are described by [6](this issue) and on principle also by [11].

ALEX Principle

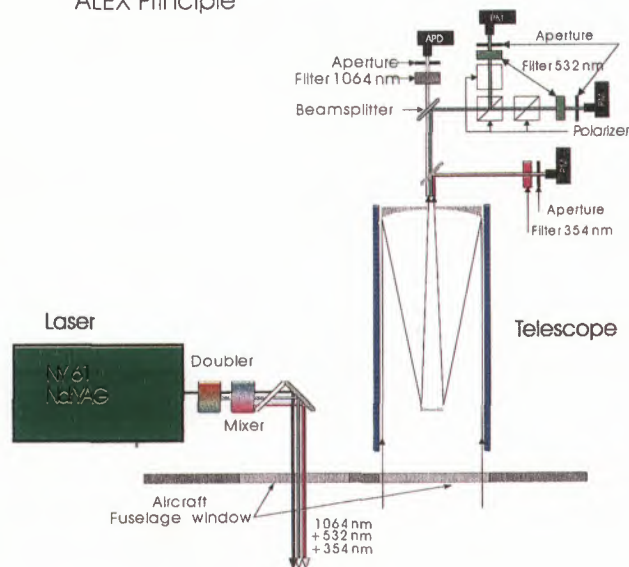


Figure 2: Bi-axial optical system and beam path of the ALEX lidar. Left side: transmitter, right: receiver. System parameters according to Table 1. The overlap of the laser beam and the receiver field-of-view is achieved after a distance of about 1-1.5 km.

The attenuated atmospheric backscatter directly measured by the lidar is either given absolutely as backscatter coefficient [$\text{m}^{-1}\text{sr}^{-1}$] or relative to Rayleigh scattering (calculated from air

density) as backscatter ratio $\gamma = (\beta_{\text{particle}} + \beta_{\text{molecule}})/\beta_{\text{molecule}}$, the relative contribution of particle scattering to the total signal (cf. Figure 1). The attenuation of the laser beam in the atmosphere is considered employing a numerical inversion of (1) whereby an extinction/backscatter ratio (lidar ratio) and a starting value at some distance from the receiver has to be assumed to iteratively derive the profiles. With the inferred lidar ratio the extinction coefficient and its integral, the optical depth, can be estimated from the backscatter signal. From (3) the double scattering term $Q_{m_s}^{(2)}(r)$ is calculated and fed into the inversion. The ratio of the orthogonal and parallel (to the incident beam) polarised 532nm signals $\beta_{\perp}/\beta_{\parallel}$ i.e. the depolarisation of the light by the scattering particles contains information about their sphericity. A volume depolarisation of 1.4% occurs if only the unsymmetrical air-molecules contribute to the depolarisation. If depolarising (non-spherical, solid) particles are within the measured volume the volume-depolarisation is between 0.014 and 1 depending on the concentration and shape of the scattering particles. Clouds with *only* spherical (liquid) particles may cause volume-depolarisation ratios below 1.4% since they increase only the intensity in the parallel channel.

DATA EVALUATION

The double scattering inversion algorithm of Ruppertsberg et al. [4] has been applied to clouds of different type and density observed during the CLARE'98 campaign to derive the approximate multiple scattering factor and the optical depth of the clouds simultaneously. However the extinction coefficient is not determined independently but calculated via the inferred backscatter/extinction ratio (lidar ratio). This quantity is changed incrementally during the inversion to approach a backscatter ratio beyond the clouds which is known or may be estimated (e.g. from a standard atmospheric profile). If the multiple scattering contribution is neglected or underestimated a wrong lidar ratio results from the inversion. Thus the inferred lidar ratio tends to get abnormally high if relevant scattering orders are neglected (this effect is especially strong in the classical single scattering inversion).

The total optical depth (one way) penetrated by the laser beam in practice is limited to a value of $\tau \approx 2-3$ depending on the adjustment and the energy distribution between the three wavelength channels. However the inversion of the signal remains stable only for optical depths $\tau < 1-1.5$. This limits our study to optically thin or shallow dense clouds.

As quoted above there are now several optical- and system-parameters known to determine whether and to what extent higher scattering orders are relevant for a given optical system. Namely the wavelength, the optical depth τ , the cloud type (i.e. the particle size distribution) and the range into the cloud varied (either naturally or operationally) during the flights. The dependence of $Q_{m_s}^{(2)}(r)$ on the cloud range is briefly discussed comparing airborne and satellite borne cloud observing systems [10].

We first will discuss the correlation between multiple scattering (approximated by double scattering) and the optical

depth of the clouds. The cloud density typically varied along the lidar sections allowing consecutive measurements in clouds of the same type. However in most cases the density soon exceeded the penetration depth of the laser beam. For the less dense clouds the relation between optical depth and the double scattering factor is compared for different cloud types.

Though the unknown phase function of the clouds is a general source of error the authors of [4] conclude that using phase functions of a wrong cloud type for optical depths $\tau < 1$ and a FOV of 1mrad has only a minor effect on the retrieved optical depth and the multiple scattering contribution. To check the sensitivity of the results, test inversions based on phase functions for different cloud size distributions were performed. The according phase functions have been taken from [4] and in order to check their range interval also derived from model distributions of major cloud classes established by Carrier et al. [7] based on an extensive literature survey. The model distributions were approximated by log-normal-functions for which Mie calculations provided the value at a scattering angle of zero. This is sufficient since in the applied algorithm the phase function is parameterised by its forward value $\beta'_{\lambda_s}(0, r_p)$ assuming an exponential decrease around 0° and that 50% of the attenuation is due to the diffraction lobe. If not otherwise noted, we apply forward values $\beta'_{\lambda_s} = 20000/\text{sr}$, $8550/\text{sr}$ and $2500/\text{sr}$ of the phase function at 355 nm, 532 nm and 1064 nm, respectively.

MEASUREMENTS AND RESULTS

Meteorological situation: Throughout the FALCON-campaign the synoptic situation in western Europe was dominated by a pronounced westerly current in which short wave disturbances in rapid succession affected South Britain. The associated fronts passed nearly daily and caused distinct air-mass transitions between the pre- and post frontal flows. Thus overcast and alternating conditions prevailed with multi-level clouds frequently occurring throughout the troposphere. On 12 October Chilbolton was lying inside a north-westerly flow of relatively instably stratified maritime sub-polar air (mP) which, getting into the warm sector of the Iceland cyclone SASKIA, on 13 Oct was replaced by humid maritime sub-tropical (mS) air-masses. In its cold sector again mP air interspersed (15 Oct), before after temporary mS advection on 16/17 Oct maritime arctic air (mA) reached Chilbolton in a high-reaching northerly flow on 18 Oct. Following it turned westwards and transformed into mP air by 20 Oct. On 21 Oct the warm sector of the North Atlantic low VALERIE II initiated another upsliding motion of mS air-masses.

From the 5 flight missions of the CLARE'98 campaign a number of clouds were investigated in terms of their multiple scattering contribution. Two representative measurements were selected for detailed cases studies, the 5th leg on 14 October (about 13:06 UT) and the 2nd leg on 20 October (about 09:46 UT), 1998. Then moderately dense clouds of different type were observed which varied in optical depth

along the flight path but were optically thin enough to be penetrated by the lidar beam. On 14 October 98 around 1300 UT the front associated with the cold sector of the cyclone SASKIA had just passed and extended cirrus were observed between 6.8 and 8.3km height with backscatter ratios larger than 1000 at 1064 and 120 and 532nm as shown in Figure 4. In its denser regions the volume depolarisation was about 20-50%. The top of the boundary layer is marked by low diminishing stratus/stratocumulus near 1000m above the ground.

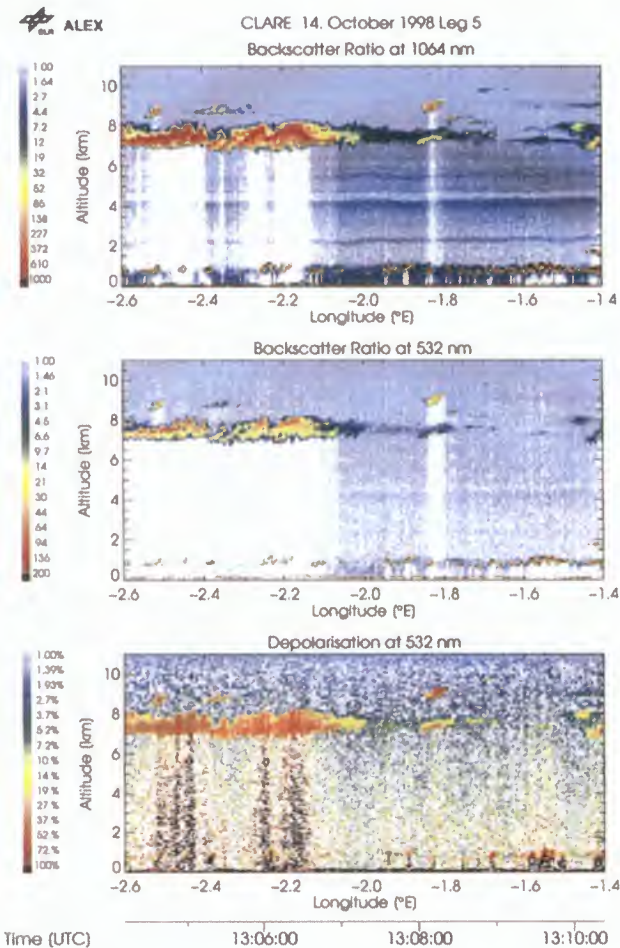


Figure 3: Sections of backscatter ratio at 1064 nm (upper panel) at 532nm (middle panel) and volume depolarisation (@532nm) along the FALCON flight path on 14 October 1998, 13:04 UT – 13:10 UT. Not corrected for extinction!

For three relatively homogenous regions of this cirrus, profiles of the (cumulative) optical depth and the double scattering factor resulting from the inversion at the three wavelengths 1064 nm, 532 nm and 355 nm are shown in Figures 3a, 3b and 3c. The profiles are each averaged over 10 - 20 s (each the same at the different wavelengths) which is about 2-4 km horizontally or 0.03-0.06° in longitude. The optical depth of the cloud between about 6.8 and 8.2 km is nearly the same at the three wavelengths ($\tau \approx 0.5$ at 13:04:29 (-2.54°E), $\tau \approx 0.7$ @13:06:18 (-2.2°E) and $\tau \approx 0.03$ @13:06:58 (-2.07°E)) as is expected for a cirrus cloud with

particles much larger than the wavelengths. Even at 13:06:58 UT where most of the attenuation at the short wavelengths occurs outside the cloud the optical depth is nearly wavelength independent.

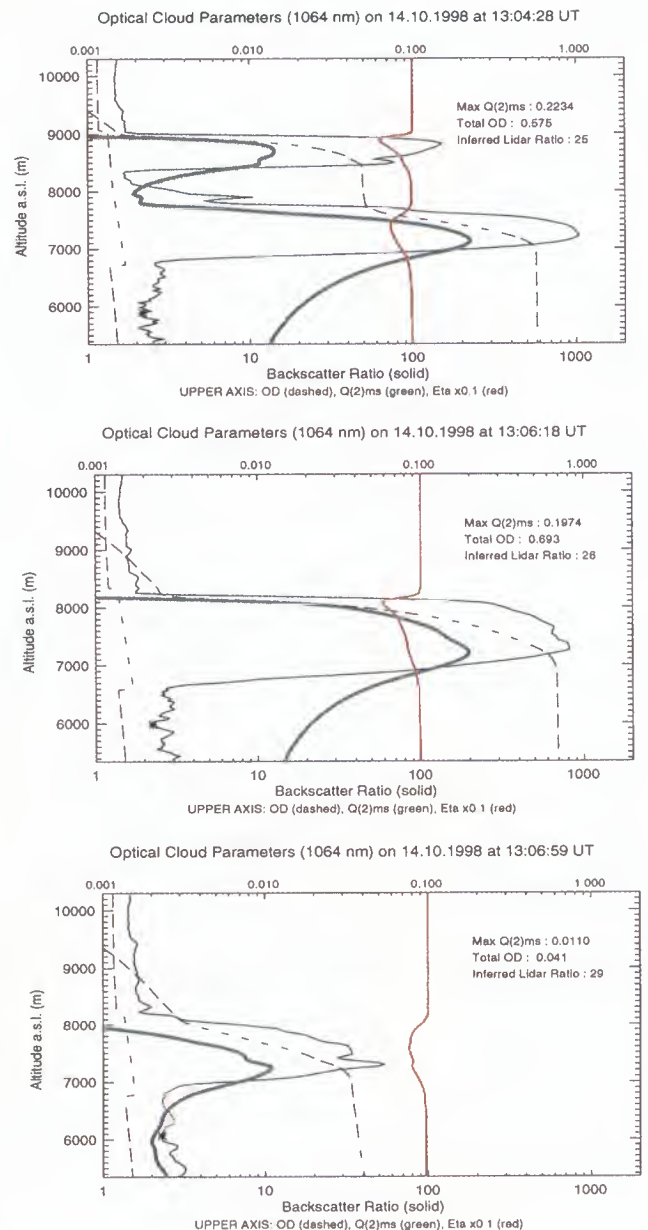
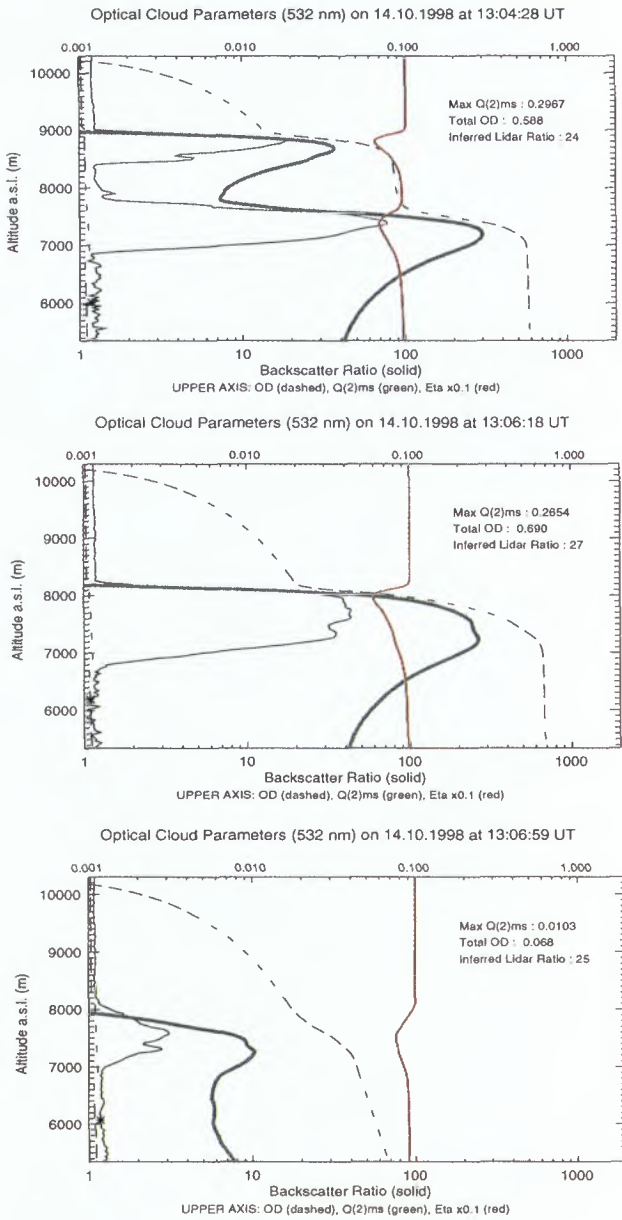


Figure 4a: Vertical profiles of backscatter ratio BSR (solid), optical depth (dashed), double scattering factor $Q_{ms}^{(2)}(r)$ (green) and Platt's Eta (red) at 1064 nm on 14 October 13:04:28, 13:06:18 and 13:06:59 (cf. Fig. 2). The corresponding longitudes are -2.54°E, -2.2°E and -2.07°E, respectively. The optical parameters (upper right corner) are inferred using a cirrus phase function. $Q_{ms}^{(2)}(r)$ is plotted only below the top of the investigated cloud. The most left (dashed) line shows the BSR of the standard profile whereby the interval, in which a special lidar ratio for the cloud is assumed, is enhanced by the ratio of in-cloud/out-of-cloud lidar ratio. The asterisk indicates the altitude where the reference value is prescribed.



lidar ratio. Otherwise, if too strong scattering occurs inside one layer the signal becomes saturated or multiple scattering of higher orders occurs both of which can be compensated by assuming an erroneous lidar ratio to supply a backscatter profile which matches the prescribed reference values in the cloud free regions. However, then the extinction coefficient or the optical depth of that layer can not be determined via the lidar ratio but at most from the jump of the signal across the cloud if the atmospheric conditions are accurately known. The rather high lidar ratios of about 25 inferred for the cirrus in the infrared and green channel may presumably be due to reflection at the horizontally oriented ice crystals.

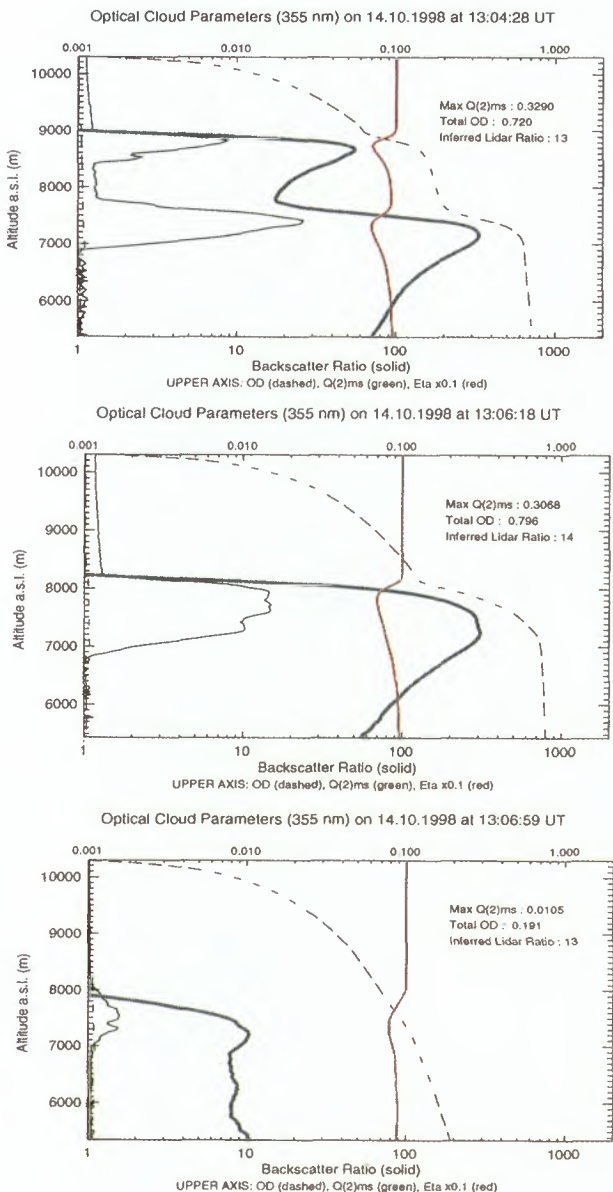


Figure 4b: Vertical profiles of backscatter ratio (solid), optical depth (dashed), double scattering factor $Q_{ms}^{(2)}(r)$ (green) and Platt's eta (red) at 532 nm on 14 October 13:04:28, 13:06:18 and 13:06:59 (Fig. 3) as in Figure 4a.

On the contrary the optical depth below the cloud is clearly negatively correlated to λ (from 5 – 6.8 km: $\tau \approx 0.006$ @1064 nm, $\tau \approx 0.025$ @532 nm, $\tau \approx 0.06$ @355 nm) due to much smaller (aerosol) particles which are apparent as stratified layers in the upper panels of Figure 3.

However the vagueness of the lidar ratio (i.e. the inferred backscatter / extinction ratio used to calculate τ from β) is a considerable source of uncertainty. If the extinction correction which feeds into the calculation of the backscatter profile is small in the case of optically very thin clouds than the inversion of such profiles supplies only a vague determination of the free parameters, which in our case is the

Figure 4c: Vertical profiles of backscatter ratio (solid), optical depth (dashed), double scattering factor $Q_{ms}^{(2)}(r)$ (green) and Platt's Eta (red) at 355 nm on 14 October 13:04:28, 13:06:18 and 13:06:59 (Fig. 3) as in Figure 4a.

Our inversion allows to choose two height intervals with different lidar ratios, one of which we always set to an average background tropospheric value of 48 ([4]). The other one is chosen within the cloud of interest and acts as free parameter for the inversion. To concentrate on the selected cloud layer the double scattering factor $Q_{ms}^{(2)}(r)$ is calculated and plotted starting at the top of this cloud.

$Q_{ms}^{(2)}(r)$ increases with decreasing wavelength λ . Its mean value increases with the optical depth of the cloud (see Table 2). It reaches its highest value near the cloud base and at 1064 nm decreases by about an order of magnitude 1 000 m below the cloud. This decrease is slower at smaller wavelengths. Though we sometimes refer to the maximum value of $Q_{ms}^{(2)}(r)$ its mean value over the cloud, given in Table 2, actually is the relevant quantity for the multiple scattering contribution. The apparent reduction of the optical depth caused by the multiple scattering in this cirrus as expressed by Platt's Eta parameter ([1]) is in the order of 20-40% and varies only slightly with wavelength (see Table 2) except its gradual increase below the cloud which is slower at the short wavelengths. It tends to have a minimum just below the cloud top.

Table 2: Optical cloud parameters for cirrus on 14 October 98 at 1306 UT: Optical depth τ , Mean value of Q inside the cloud and minimum value of Platt's Eta @ 1064, 532 and 355 nm

Time	Type- λ	τ	Mean $Q_{ms}^{(2)}$	Min η_{Platt}
13:04:33	Ci - 1064	0.53	0.088	0.72
13:06:18	Ci - 1064	0.69	0.102	0.58
13:06:58	Ci - 1064	0.03	0.005	0.76
13:07:30	Ci - 1064	0.01	0.001	0.93
13:04:33	Ci - 532	0.51	0.163	0.69
13:06:18	Ci - 532	0.67	0.17	0.60
13:06:58	Ci - 532	0.03	0.006	0.75
13:07:30	Ci - 532	0.02	0.002	0.92
13:04:33	Ci - 355	0.54	0.193	0.70
13:06:18	Ci - 355	0.70	0.205	0.69
13:06:58	Ci - 355	0.03	0.006	0.77

On 20 October 98 two FALCON missions took place in the morning and in the early afternoon. Starting before noon a rapid formation of cirrus was observed above 8 km height due to the approaching occluded cold front of low VALERIE II. In a strong westerly current (≈ 15 m/s) a narrow altostratus cloud layer in 3.8 – 4.2 km altitude appeared above a dense stratocumulus cloud cover at the top of the boundary layer near 2 km and persisted in the Chilbolton flight corridor until the afternoon (see Figure 3 in [8], this issue). At that time it was tilted vertically by nearly 2 km in height over the distance of one leg (1.5°). This altostratus layer blocked the lidar beam nearly completely such that a data evaluation below it is not possible except for parts of the first three flight legs where the cloud cover was still broken (near -1.8°E of

the selected leg 2 from 09:43 to 09:50 in Figure 5). This region where the cloud covers were broken moved eastward with little change during the consecutive legs. A thin cirrus above (7.8 – 8.7 km) only exhibits maximum optical depths of $\tau \approx 0.1$ and thus does not influence the inversion of cloud parameters below it.

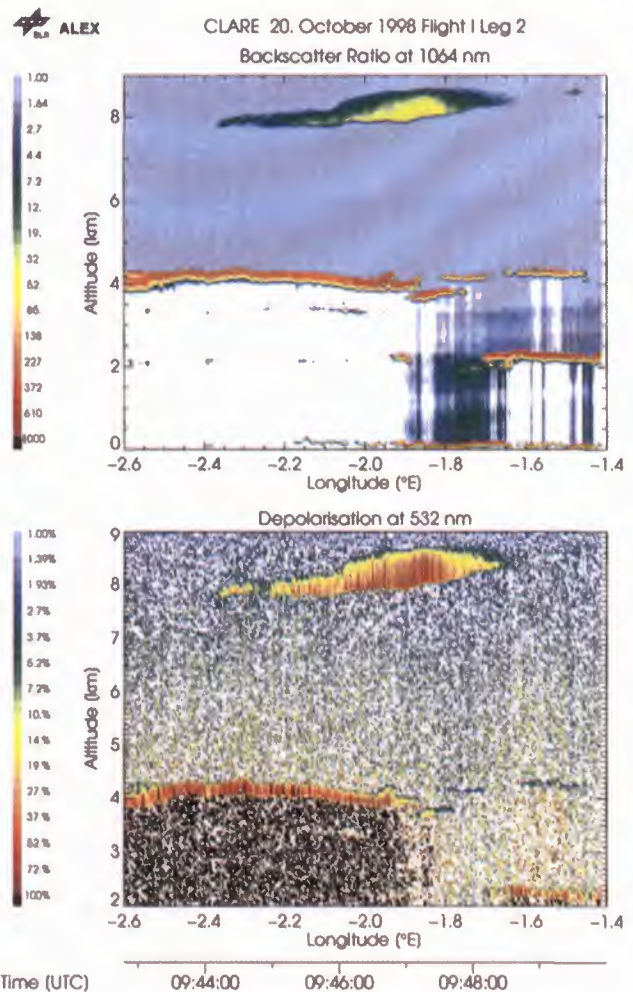


Figure 5: Sections of backscatter ratio at 1064 nm (upper panel) and at 532nm (middle panel) and volume depolarisation (@532nm) along the FALCON flight path on 20 October 1998, 09:43 UT – 09:50 UT. Not corrected for extinction!

The cloud situation at this time was already very similar to that several hours later which is one of the high priority cases defined by the CLARE community and which is referred to by several other studies in this issue. However, since at that time our lidar measurements suffered from strong attenuation in a thick cirrus cloud above 9 km altitude we concentrate on the previous flight. We expect that the micro-physical properties of this cloud moving at a constant altitude of about 4 km remained approximately unchanged between 09:48 and 14:20 suggesting that the early afternoon micro-physical measurements are also representative for the cloud stage in the morning. At 14:20 this altostratus cloud cover has been intensively investigated with different radars, lidars and airborne in situ probes installed onboard a Hercules C-130

aircraft. The layer dispersed and dissolved over Chilbolton around 14:40 UT when it has been embedded in a thick cirrus. In Figure 6 the change of the temperature profile between 10 UT and 14 UT is shown. It indicates the advection of a narrow layer of relatively warm (mP) air sliding up onto the colder (mA) air-mass (occlusion with warm front character). The associated drying of the 2 – 4 km level lead to the observed vanishing of the altostratus layer around 1440 UT. Simultaneously the overlying air-mass was lifted over the condensation level by the upsliding motion as indicated by rapid cirrus formation.

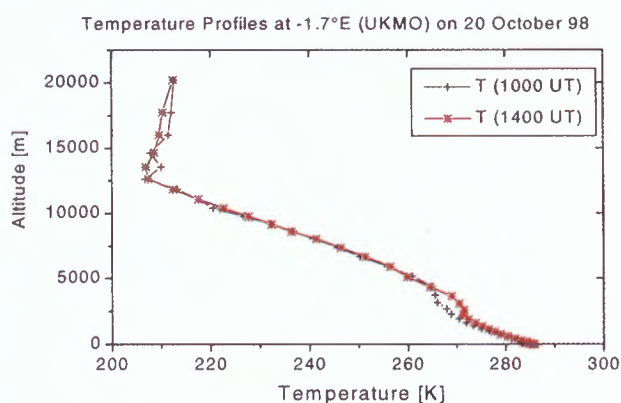


Figure 6: Temperature Profiles on 20 October 1998 from UKMO at 1000 UT and 1400 UT. Labile stratification dominates over most of the troposphere. Warm advection leads to development of an inversion in about 2 km altitude.

The low volume depolarisation ratio of the altostratus cloud of about 5% apparent in Figure 4 indicates that it contained a large fraction of spherical i.e. liquid particles (the high depolarisation west of -1.9°E is an artefact due to saturation of the parallel 532 nm signal and likely also to depolarising multiple scattering). The mixed-phase nature of this cloud is confirmed by in situ micro-physical measurements of the particle probes onboard the Hercules C-130. Accordingly at a temperature of -8.6°C in 4 km a mixture of ice crystals, graupel and water droplets was observed. A more detailed description of these measurements is given in [8].

The altostratus exhibits (extinction corrected) backscatter ratios of more than 1000 (in regions where the signal was saturated – not shown) in the infrared, up to 300 in the green and up to 70 in the blue wavelength region (Figures 7a-c). In the dense regions of the cloud the signal is saturated – especially in the IR (i.e. the capacity of the data acquisition is exceeded). Thus the double scattering contribution cannot be quantified there. The signal in the low wavelength channels was severely attenuated and are thus very noisy below the cloud. As with the cirrus discussed before, the optical depth does only slightly depend on the wavelength. In its denser regions (west of -1.9°E) the cloud cover reaches optical depths of $\tau > 1.5$ while e.g. the section near -1.7°E in 4.2 km exhibits $\tau \approx 0.1$ only.

Since this cloud contains a major fraction of liquid particles next to solid and crystal like ones, the inversion has been carried out with either an ice cloud - and a water cloud phase function, representing a cirrus and a Deirmendjian-C1 water cloud distribution with forward scattering values β'_{λ_0} ($\beta'_{\lambda_0} = 2650/\text{sr}$ @355 nm, $\beta'_{\lambda_0} = 210.2/\text{sr}$ @550 nm, $\beta'_{\lambda_0} = 60.5/\text{sr}$ @1064 nm) taken from [4] (extrapolated quadratically for 355 nm).

The cloud optical depth as well as the double scattering factor averaged over the cloud and the calculated reduction of τ as expressed by Platt's Eta parameter, are given in Table 3a for the Deirmendjian-C1 phase function and in Table 3b using the ice crystal phase function. Again, as for the cirrus discussed before, $Q_{ms}^{(2)}(r)$ increases in the cloud down to the cloud base. However it decreases more rapidly below the cloud. This drop below the cloud is even larger if we use the water cloud phase function ϕ_w (Figure 7a-c) rather than the ice phase function ϕ_{ci} . Applying ϕ_{ci} to the double cloud layer near -1.8°E , the double scattering contribution increases stepwise at the single layers due to the slow degradation of $Q_{ms}^{(2)}$ below each cloud while this effect misses if ϕ_w is used (second panel in Figures 6b and c). It reaches quite high values $Q_{ms}^{(2)} > 0.6$ with ϕ_{ci} ($Q_{ms}^{(2)} > 0.3$ with ϕ_w) and likely becomes even larger in the regions which are not accessible to our study.

The retrieved optical depth depends only weakly on the selected phase function. But the calculated double scattering factors varied for more than 100% when applying the described phase functions. For a comparable optical depth there is considerably more double scattering in the mixed-phase cloud than in the cirrus if ϕ_{ci} for ice crystals is used while from applying ϕ_w representing water clouds slightly smaller values result (see Tables 2 and 3a,b). This is plausible because for the broader function ϕ_w a larger part of the diffraction cone is out of the receiver FOV and thus does not contribute to the received doubly scattered signal.

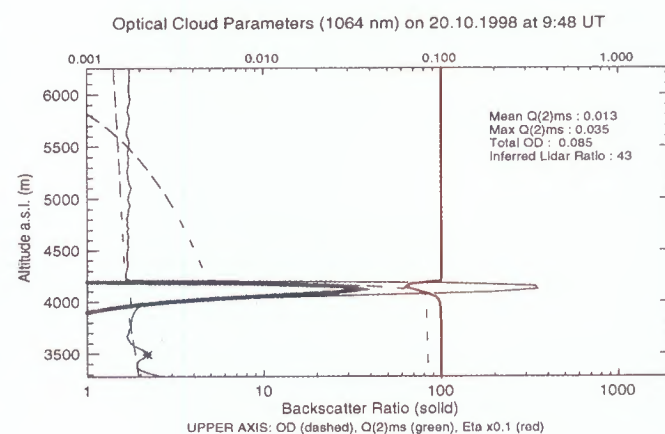


Figure 7a: Vertical profiles of backscatter ratio (solid), optical depth (dashed), double scattering factor $Q_{ms}^{(2)}(r)$ (green) and Platt's Eta (red) at 1064 nm on 20 October 09:48 UT at -1.73°E (Figure 4) as in Figure 4 but with water cloud phase function.

Since we are dealing with a mixed phase cloud it may be expected that a combination of both phase functions is the best approximation to the actual one. With this assumption the actual dependence of $Q_{ms}^{(2)}(r)$ on the optical depth does not differ significantly for the cirrus and the altocumulus cloud. However, it turns out to be quite important to choose an appropriate phase function whereby the ones selected here already cover a broad spectrum of ambient cloud types.

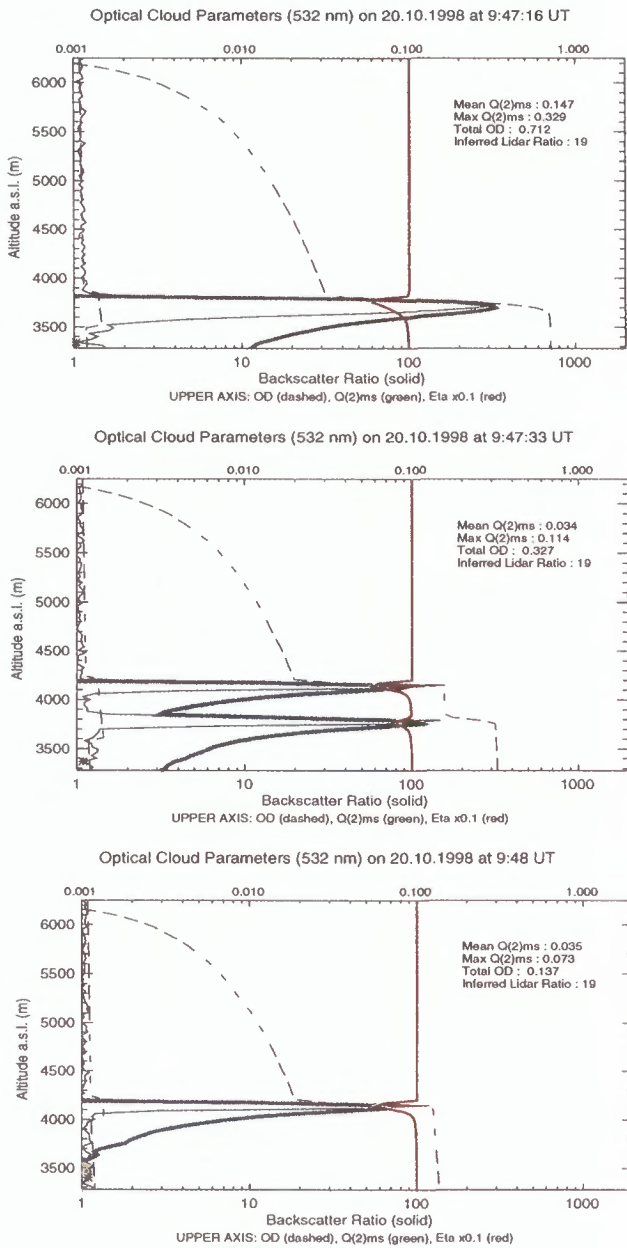


Figure 7b: Vertical profiles of backscatter ratio (solid), optical depth (dashed), double scattering factor $Q_{ms}^{(2)}(r)$ (green) and Platt's Eta (red) at 532 nm on 20 October 09:47:17, 09:47:33 and 09:48:00 UT as in Figure 4 but using a water cloud phase function. The corresponding longitudes are $-1.85^{\circ}E$, $-1.8^{\circ}E$ and $-1.73^{\circ}E$, respectively.

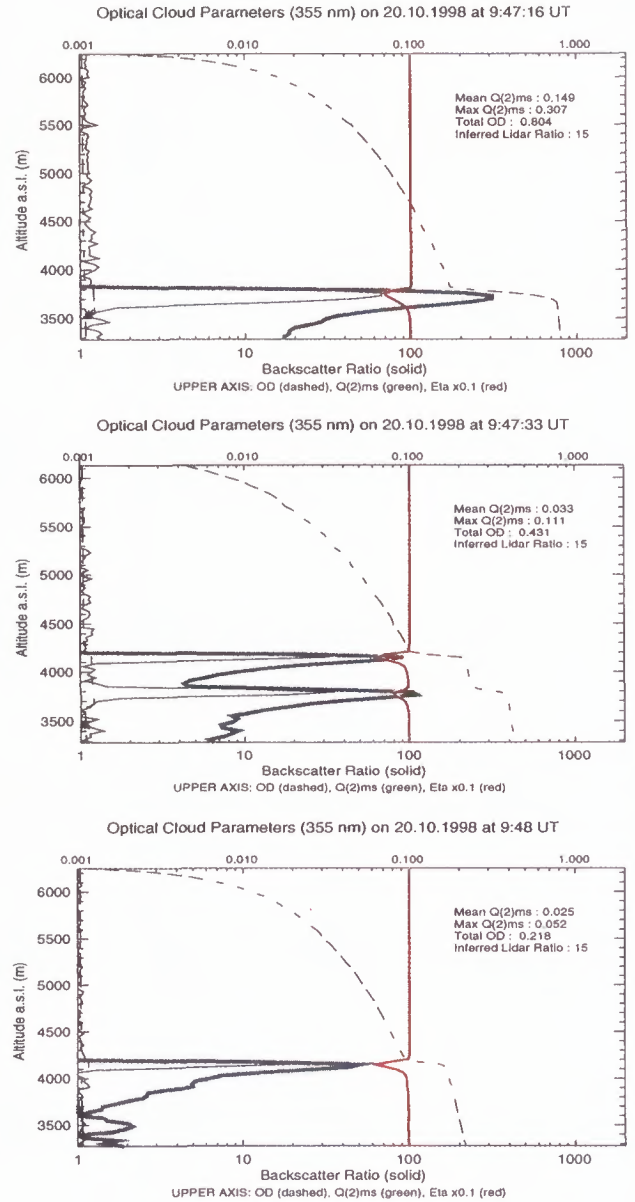


Figure 7c: Vertical profiles of backscatter ratio (solid), optical depth (dashed), double scattering factor $Q_{ms}^{(2)}(r)$ (green) and Platt's Eta (red) at 355 nm as in Figure 6b.

Table 3a: Optical parameters for altocumulus cloud cover on 20 October 98 at 0946 UT: Optical depth τ , Mean value of Q inside the cloud and minimum value of Platt's Eta @ 1064, 532 and 355 nm. A Deirmendjian-C1 water cloud phase function was used.

Time	Type- λ	τ	Mean $Q_{ms}^{(2)}$	Min η_{Platt}
09:48:00	Ac - 1064	0.09	0.013	0.61
09:47:16	Ac - 532	0.71	0.15	0.6
09:48:00	Ac - 532	0.14	0.06	0.53
09:47:16	Ac - 355	0.80	0.15	0.69
09:48:00	Ac - 355	0.22	0.025	0.51

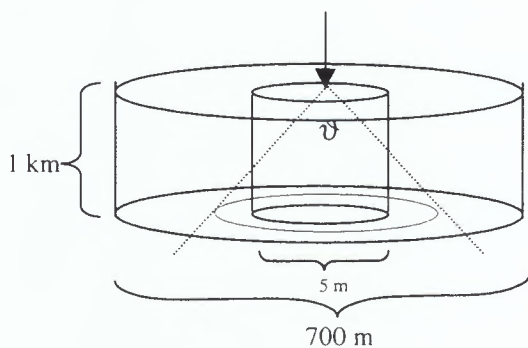
Table 3b: Optical parameters for altocumulus cloud cover on 20 October 98 at 0946 UT like in Table 3a but calculated using a cirrus cloud phase function.

Time	Type- λ	τ	Mean $Q_{ms}^{(2)}$	Min η_{platt}
09:48:00	Ac - 1064	0.08	0.034	0.66
09:47:17	Ac - 532	0.72	0.38	0.6
09:48:00	Ac - 532	0.09	0.06	0.56
09:47:17	Ac - 355	0.7	0.39	0.63
09:48:00	Ac - 355	0.09	0.06	0.62

EXTRAPOLATION TO A SATELLITE BORNE LIDAR SYSTEM:

On 14 October the flight level of the FALCON was 11570 m a.s.l. thus the cloud - receiver distance ranged from 3270 to 4770 m for the near and far cloud boundary. The flight level on 20 Oct 9:46 UT was about 10280 m a.s.l. resulting in a cloud - receiver distance of 6 - 6.3 km. With 1 mrad FOV this corresponds to a (approximately) cylindrical cloud region with a diameter of about 3-6 m contributing to the received signals. At space distances ($d \approx 700$ km) the cloud area visible by a 1 mrad FOV receiver has a diameter of approximately 700 m. Thus the FOV volume detected by the telescope is approximately proportional to the square of the cloud - receiver distance. However, the scattering phase function of particles much larger than the wavelength largely peaks in the forward direction. Thus the larger the particles the less the multiple scattering contribution depends on this target area. In the following we will derive a rough estimate of how much more a satellite borne instrument would suffer from multiple scattering than an aircraft borne system.

We assume a homogeneous cloud layer of 1 km depth containing no absorbing particles ($\sigma_a = \sigma_s$) in which for the given geometry the double scattering approximation of [4] is valid. Let this cloud be hit by a non-divergent laser beam from an airborne ($d = 6$ km) and a satellite borne ($d = 700$ km) lidar with a FOV of few mrad each. It may consist of either ice crystals or water droplets with a diffraction lobe 1/e-width of $\vartheta_i = 6$ mrad and $\vartheta_w = 36$ mrad (@ 1064 nm), respectively. To get an upper limit estimation of the distance effect let all scattering occur at the cloud top (near side) as illustrated (strongly jolted) below, where the FOV volumes of the two lidar systems are outlined as cylinders of different radii.



It is obvious that the deeper (in mean) inside the cloud the scattering events occur the smaller the difference in the multiple scattering contributions to the received signals will be. Geometrical considerations show that as long as the ϑ -cone (defined by the 50% decrease of φ) lies within the airborne lidar FOV (inner cylinder) there would be hardly more scattered photons detected by the satellite system because the forward-scattered photons once diverted from the incident beam are mostly lost after the following back-scattering. The same is true for the broader phase function as well as long as one confines to twice scattered photons.

If on the other hand the scattering medium is diffusive (i.e. its geometrical thickness is much larger than the mean free path of photons) it may as a first approximation be regarded as isotropic source of multiply scattered photons and $Q_{ms}(r)$ then becomes dominated by the viewed cloud area rather than by other parameters. The intermediate domain of moderate multiple scattering is not accessible to simple analytic considerations. Instead the estimation of the difference in the multiple scattering impact then needs numeric efforts like Monte-Carlo- or ray-tracing techniques.

SUMMARY

From 12 - 21 October 1998 the ALEX lidar onboard a FALCON 20 aircraft participated in the CLARE'98 campaign flown on a SW-NE orientated corridor near Chilbolton in South Britain. During the 5 flights of the campaign different types of multiply layered clouds were measured. In this article we discuss two different cloud types, a cirrus observed on 14 October and an altocumulus mixed-phase cloud from 20 October, in terms of the double scattering contributions (as approximation to multiple scattering) to the received signals. The optical depths of the investigated cloud regions ranged over about $0 \leq \tau \leq 0.8$. The double scattering factor $Q_{ms}^{(2)}(r)$ strongly depends on the cloud's optical depth and the wavelength. It reaches typical values of $0\% < Q_{ms}^{(2)}(r) < 60\%$ of the single scattered intensity and does not depend on the wavelength. It increases with the distance into the cloud, reaches its maximum near the cloud base and slowly decreases beyond the cloud. The decrease strongly depends on the applied phase function. If one deals with mixed phase or water clouds the selection of a scattering phase function for a wrong cloud type causes substantial errors in the double scattering contribution $Q_{ms}^{(2)}$. But though for the discussed altocumulus cloud an uncertainty of more than a factor of two in $Q_{ms}^{(2)}$ has been derived this causes only a small error in the retrieved backscatter profile since the factor $(1 + Q_{ms}^{(2)})$ feeds into the lidar equation.

REFERENCES

- [1] Platt, C.M.R., Lidar and Radiometric Observations of Cirrus Clouds, J. Atm. Sci., 30, 1191-1204, 1973.

- [2] Nicolas, F., L.R. Bisonette and P. H. Flamant, Lidar effective multiple scattering coefficients in cirrus clouds, *Appl. Optics*, 36, 15, 3458-3468, 1997.
- [3] Wandinger, U., Multiple scattering influence on extinction- and backscatter-coefficient measurements with Raman and high-spectral resolution lidars, *Appl. Optics*, 37, 3, 417-427, 1998.
- [4] Ruppertsberg, G.H., M. Kerscher, M. Noormohammadian, U.G. Ooppel and W. Renger, The Influence of Multiple Scattering on Lidar Returns by Cirrus Clouds and an Effective Inversion Algorithm for the Extinction Coefficient, *Contr. Atmos. Phys.*, 70, 2, p. 91-107, 1997.
- [5] v.d.Hulst, H.C., *Light scattering by small particles*, John Wiley & Sons, Inc., New York, 1957.
- [6] Mörl, P., M.E. Reinhardt, W. Renger and R. Schellhase, The use of the airborne LIDAR system "ALEX F1" for aerosol tracing in the lower troposphere, *Beitr. Phys. Atmos.*, 54, 401-410, 1981.
- [7] Carrier, L.W. et al., *Appl. Opt.*, 6, 1209-1216, 1967, in: E.J. McCartney, *Optics of the Atmosphere - Scattering by Molecules and Particles*, John Wiley & Sons, New York, 1976.
- [8] Quante, M., O. Danne, H. Flentje, W. Renger and P. Francis, Cloud boundaries and structure in mixed phase mid-level clouds as deduced from ground based 95-GHz radar and airborne lidar measurements during CLARE'98, this issue.
- [9] Jursa, A. S., *Handbook of Geophysics and the Space Environment*, United States Air Force, 1985, p. 18-7, p. 19-1
- [10] Wiegner, M., U. Ooppel, H. Krasting, W. Renger, C. Kiemle and M. Wirth, Cirrus measurements from a Spaceborne Lidar: Influence of Multiple Scattering, in A. Ansmann et al., *Advances in Atmospheric Remote Sensing with Lidar. selected papers of the 18th ILRC*, Springer, Berlin, 1996.
- [11] Flentje, H., C. Kiemle, V. Wiess, M. Wirth and W. Renger, The 3 wavelength lidar ALEX and other instrumentation onboard the FALCON during CLARE'98, this issue.

Cloud-Field Variability from Ground-Based Lidar and Radar Observations

D.P. Donovan and A.C.A.P. Van Lammeren, KNMI, Postbus 201,
3730 AE De Bilt, the Netherlands (donovan@knmi.nl)

H. Russchenberg, IRCTR, T.U. Delft, the Netherlands

A. Apituley, RIVM, Bilthoven, the Netherlands

Introduction

Cloud-variability has obvious implications with regards to synergetic cloud remote sensing. By combining measurements made with different instruments in principle it is possible to extract much more information than is the case by using each instrument in isolation. However the different instruments may have different footprints and sampling rates as well there may be some spatial and/or temporal separation between the measurements made by the different sensors. Hence, it is necessary to know to what extent two spatially and temporally separated soundings may be meaningfully compared. To further complicate matters, the degree of signal variability in space and time depends not only on the physical variability of the cloud field itself but also on what exactly a given instrument is measuring.

Such cloud-variability considerations play an important role with respect to the proposed Earth Radiation Mission (ERM) where flying different instruments on different co-orbiting platforms is being considered (see Fig. 1). It is important to quantify what errors may result from a given time and spatial separation between the passage of the different instruments over a given cloudy volume.

Ground-Based Measurements

Ground-based lidar and radar measurements, such as those made during the Netherlands CLOUD And Radiation experiment (CLARA) [Lammeren et al. 1996] and CLARE'98 can be used as a basis

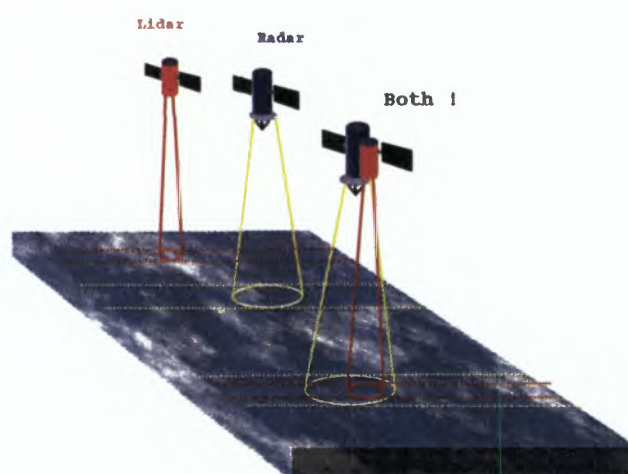


Figure 1: Split-mission vs. single platform scenarios for the ERM.

for investigating cloud-variability effects. During the third CLARA campaign two nearly identical lidars were operated within 4 km of each other on a continuous basis. The ESTEC-CT75 lidar was operated at the main CLARA site in Delft while the KNMI lidar of similar type was operated about 4 km away. So, in this study we are able to explore two avenues with regard to assessing the effects of cloud-field variability, namely:

- The effect of a known spatial separation
- The effect of a (simulated) temporal separation

We will first discuss the results of the comparison

between the separated KNMI and ESTEC lidars during CLARA. Then we will discuss the general temporal behavior of the signals using both lidar and radar signals acquired during CLARA as a whole. Finally, we will use the results of the investigations into the general behavior of the observed signals as the basis for conducting simulations aimed at predicting the effect of different sampling parameters (e.g. instrument footprint, spatial separation) with respect to a space-based lidar/radar instrument.

Spatial Separation

As an illustrative example we will present CLARA data from November 20 taken with the separated lidar systems. Fig. 2 shows the time-height lidar signals for both lidars on this day at full resolution (12.5 meters and 30 seconds). At the scale of the color images not much difference can be discerned between the two images. On this day, Delft was near the center of a low pressure system [Donovan et al, 1999] and the cloud cover was somewhat sporadic with most of the clouds being between 1 and 2 km.

Fig. 3 shows two constant altitude cross-sections through Fig. 2 for 0.5 km and 1.8 km. The slice at 0.5 km is below the bulk of the clouds and the backscatter is likely mainly due to boundary layer aerosols while the 1.8 km slice goes through the bulk of the clouds. Evidently the signals at 0.5 km are well correlated, however at 1.8 km the situation is less clear. At 1.8 km, the signals are both sporadic and not necessarily in good correspondence with each other.

A space-based lidar would not make measurements with such a high resolution as the data shown in Fig. 3, but instead it would perhaps have a measurement resolution of 100 meters in the vertical and about 5 km in the horizontal. So it is useful to compare the two separated lidar returns rebinned to a resolution comparable to that that may be envisioned for a space-based instrument. Degrading the vertical resolution is trivial. However, simulating a given horizontal resolution is impossible without making some assumptions first. First we must assume that the cloud field at some scale varies the same in time as it does in space and secondly we must choose some relationship between the time and space coordinates. Here we have chosen to sim-

ply use the mean wind speed to relate the time and space coordinates. Here the winds at 1 km were on the order of 25 km per hour so that a temporal resolution of about 0.2 hours should be comparable to a horizontal resolution of 5 km.

The same data as shown in Fig. 2 are shown in Fig. 4 but at low resolution. Fig. 5 shows an example low resolution signal profile for both the KNMI and ESTEC lidars at about 20 UTC. Here it is obvious that the high resolution profiles for each lidar are notably different from each other. It may be supposed that rebinning the data to degrade the resolution may remove the differences. However, it can be seen that the low resolution profiles still retain differences.

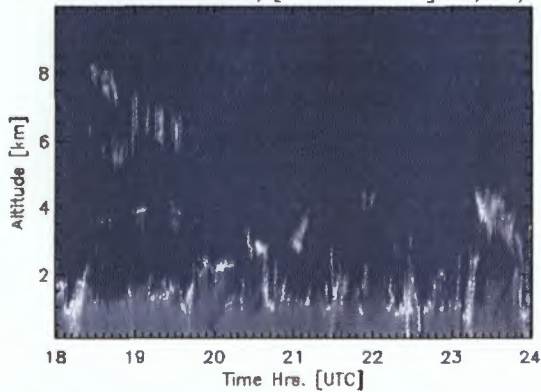
Low resolution signal cross-sections for 0.56 and 1.8 km along with the correlation coefficient between the low resolution KNMI and ESTEC signals are shown in Fig. 6. Here ρ refers to Pearson's correlation coefficient, which in general can be written (with respect to two random variables x and y) as:

$$\rho = \frac{\sum_i (x_i - \bar{x})(y_i - \bar{y})}{\sqrt{\sum_i (x_i - \bar{x})^2 \sum_i (y_i - \bar{y})^2}} \quad (1)$$

where the bars denote averages and the subscripts refer to the measurement index. As can be expected from Fig. 3 at 0.56 km the correspondence is good $\rho = 0.90$ while even at low resolution the correspondence at 1.8 km is fairly low with a correlation coefficient of about 0.77.

Fig. 7 shows the height dependent correlation coefficients derived in a manner similar to those presented in Fig. 6. The average signal profiles for the KNMI and ESTEC lidars along with the maximum and minimum signal envelopes are also shown in Fig. 7. It can be seen that at certain altitudes there is a very good correspondence between the measurements made by the separated lidars while at other altitudes the correspondence is quite low. In general, most of the correlation coefficients are above 0.7 but there is a wide range of scatter. The same analysis as presented here was performed on all the days in which data from both lidars was available (about 6 days). For all the cases considered, which spanned a variety of conditions, correlation coefficients around 0.8 were most common with a wide degree of scatter being usually present. Evidently then, 4 km appears to be a "medium" spatial separation compared to the mean correlation distance for the cases considered here.

VIS Lidar Backscatter 1/[100*srad*km] 20/11/1996



VIS Lidar Backscatter 1/[100*srad*km] 20/11/1996

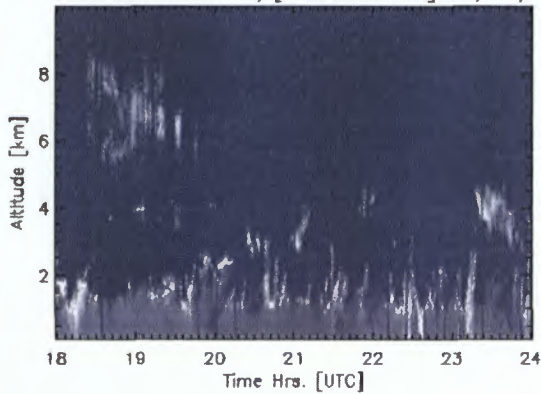


Figure 2: KNMI and ESTEC lidar signals for November 20th, 1996 (CLARA). Both lidars were of the same type (Vaisala CT-75K) but the KNMI lidar was located approximately 4 km from the main CLARA site. The upper image is for the ESTEC lidar while the lower image is for the KNMI lidar.

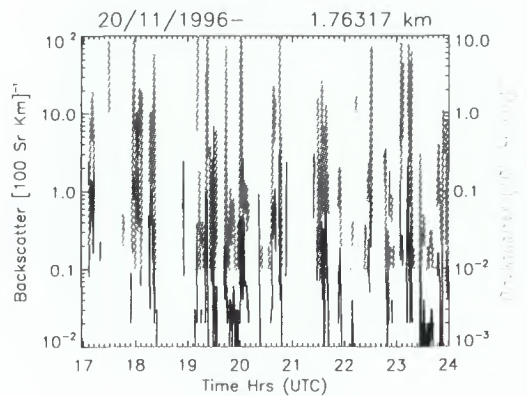
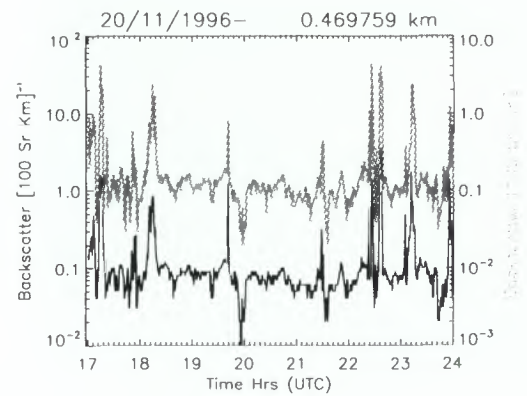
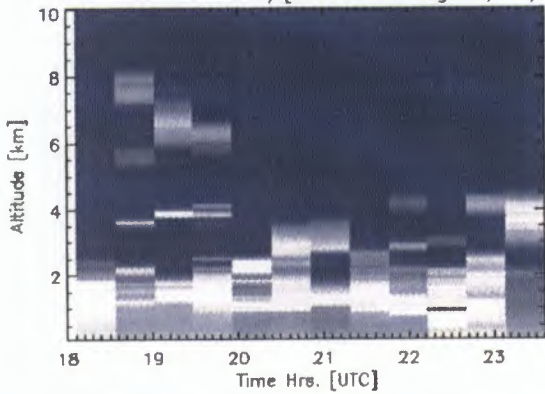


Figure 3: High resolution signal cross for the KNMI and ESTEC lidar signals for November 20, 1996 (CLARA) for 0.5 and 1.8 km respectively. The Grey line is for the KNMI lidar signals while the dark line shows the ESTEC lidar signals.

VIS Lidar Backscatter 1/[100*srad*km] 20/11/1996



VIS Lidar Backscatter 1/[100*srad*km] 20/11/1996

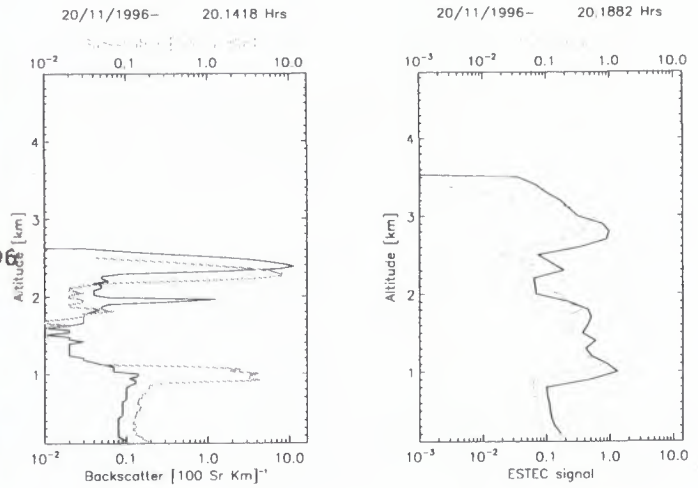
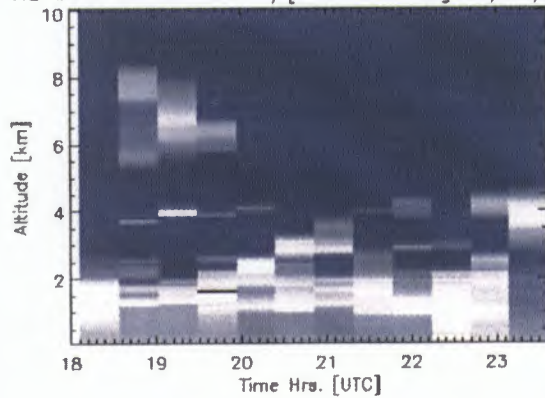


Figure 5: High resolution (Right) and low resolution (Left) signal profiles for 20.18 hours The Grey line shows the profile for the KNMI lidar while the darkline shows the signals for the ESTEC lidar.

Figure 4: The same lidar signals as shown in Fig. 2 but rebinned to a much lower resolution. Here the vertical resolution is 100 meters while the temporal resolution is 12 min. The upper image is for the ESTEC lidar while the lower image is for the KNMI lidar.

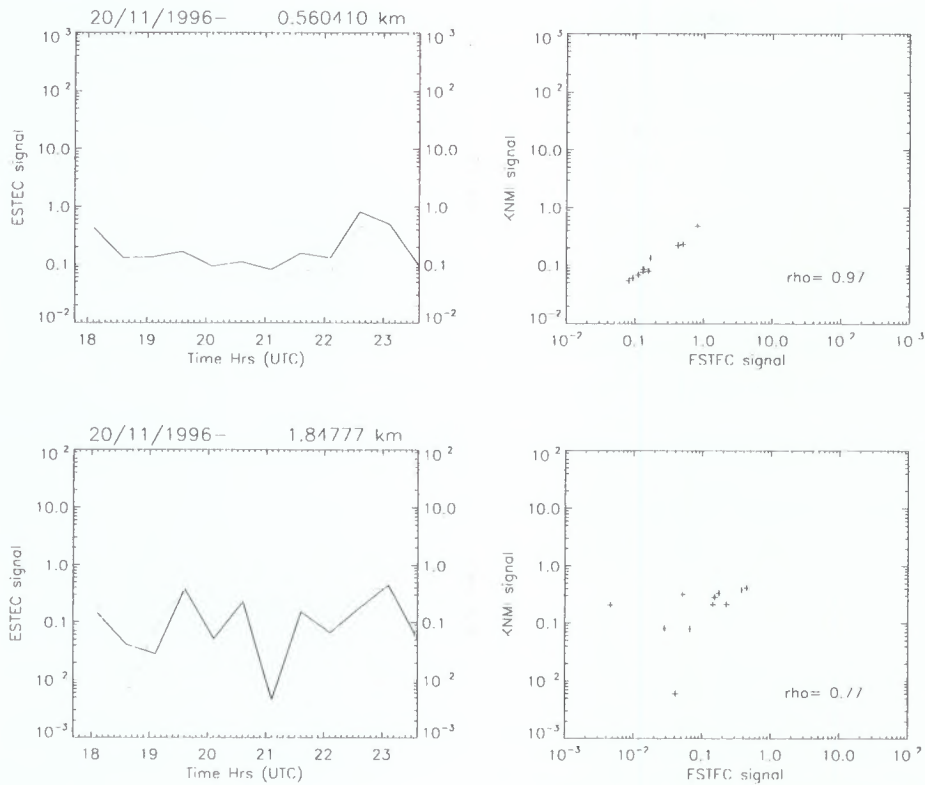


Figure 6: Low resolution time series of signals at 0.56 km (Top-Left) and (Top-Right) the signals plotted as a function of each other. The bottom panels are for 1.8 km. The Grey line corresponds to the the KNMI lidar while the darkline shows the signals for the ESTEC lidar.

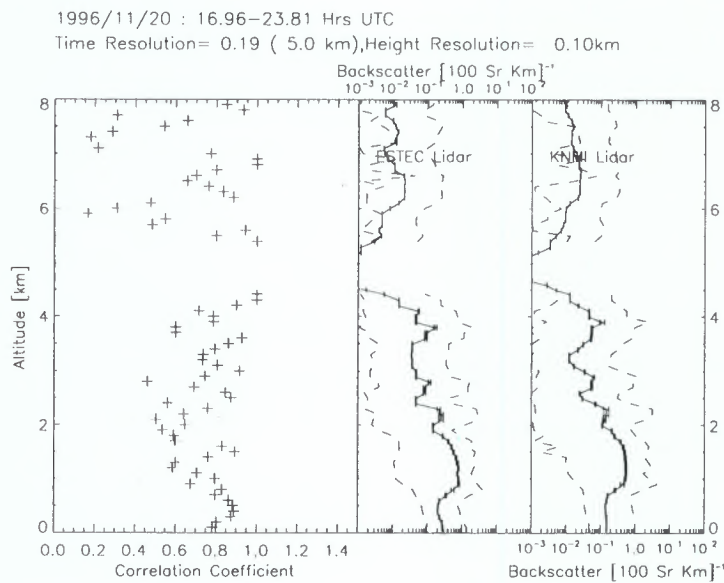


Figure 7: Average signals for the KNMI and ESTEC lidars (Middle and Left). The error bars give the standard deviation of the average while the dashed lines show the minimum and maximum signal envelopes respectively. The plus marks (Left) show the altitude dependent correlation coefficients.

Single Instrument Time Series

Here we will address the question of cloud variability using information that may be obtained by using single instrument signal time series. We are interested in using the ground-based single instrument time series to aid in characterizing the errors that could arise from comparing space-based measurements that have been obtained at different times and for slight different orbit tracks. Example time series for April 18th and November 29th, 1996 (CLARA) are shown in Figs. 8 and 9. An obvious first course of action is to examine the effect of applying a time shift to the same data time series. In principle this is easy to do; one just compares the relative differences between the unshifted time series and a series of identical but shifted (in time) series. i.e.

$$\langle \text{RelativeError}(k) \rangle = \frac{\left[\sum_0^N (S_i - S_{i+k})^2 \right]^{1/2}}{\text{sum}_0^N S_i} \quad (2)$$

where k is the number of shifted indices such that $\delta t = k * dt$. If we assume that the effect of a spatial offset (δx) may be approximated by a time shift of $\delta t = \delta x/v$, where v is some *scene velocity* we may also investigate the effects of spatial separations in an approximate manner.

Since the expected resolutions of the instruments on the ERM are much smaller than those of the ground based instruments used here the results must be extrapolated to the resolution we expect for the space-based observations. To do this, it is not advisable to smooth the signals to space-resolution and then find the relative differences between the shifted and unshifted signals. This is due to the fact that by smoothing the time series one will average over the same data between the shifted and unshifted signals. This will not occur in the situation we are trying to simulate (that of two co-orbiting platforms). However, we can employ an alternative approach to extrapolating the high resolution observed differences to lower resolutions by simply assuming that the observed relative error will decrease with increasing sample size. i.e.

$$\begin{aligned} \langle \text{RelativeError}_N \rangle &= \left[\frac{N1}{N} \right]^{1/2} \\ &\times \langle \text{RelativeError}_{N1} \rangle \end{aligned}$$

Fig. 10 shows the expected average relative error as a function of time delay for different resolutions for the data shown in Fig. 8. Given a mean scene velocity of about 10 meters per second (similar to the wind speed at this altitude measured by local radiosondes) the upper curve is appropriate for a space-based resolution of about 300 meters while the lowest curve is appropriate for a resolution of about 1.2 km. In Fig. 10 it can be seen that the error increases rapidly with temporal delay, reaching a maximum after about 0.5 hours. Fig. 11 is similar to Fig. 10 except that it corresponds to the data shown in Fig. 9 here the errors are generally much more than those shown in the previous example and the maximum errors are reached after only about 6 minutes or so.

The approach outlined so far is somewhat limited as there is no real way to incorporate the effects of instrument differences and combined spatial and temporal offsets in a logical fashion. Also, it would be difficult to assess issues such as instrument footprint size using this approach. To more beyond we need to examine the intrinsic characteristics of the signals themselves. Once we have amassed enough information on the inherent scales and variances of the lidar and radar signals we can use this information as the basis for conducting full 2-dimensions simulations in a more rational manner.

In the next section we will treat the lidar and radar signals as standard time series and derive such quantities as the correlation time and the exponent of the *power spectral density*. Since cloud fields self-similar to some degree, that is, at large scales they similar to the way they do at small scales, we will also employ some statistical methods that are useful when analyzing *fractal* signals.

VIS Lidar Backscatter $1/[100 \cdot \text{srad} \cdot \text{km}]$ 18/4/1996 VIS Lidar Backscatter $1/[100 \cdot \text{srad} \cdot \text{km}]$ 29/11/1996

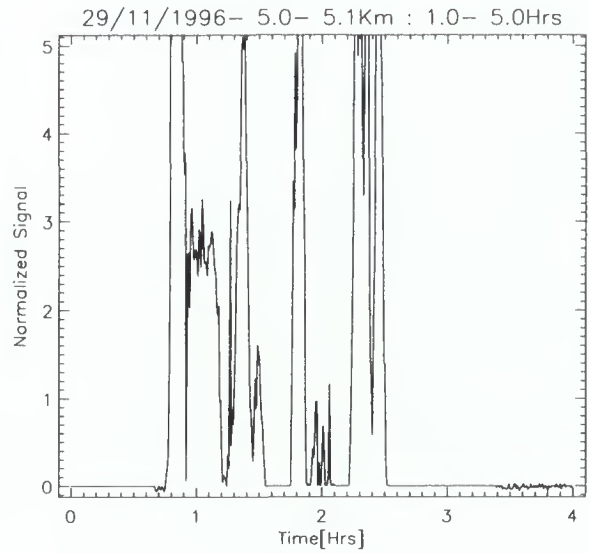
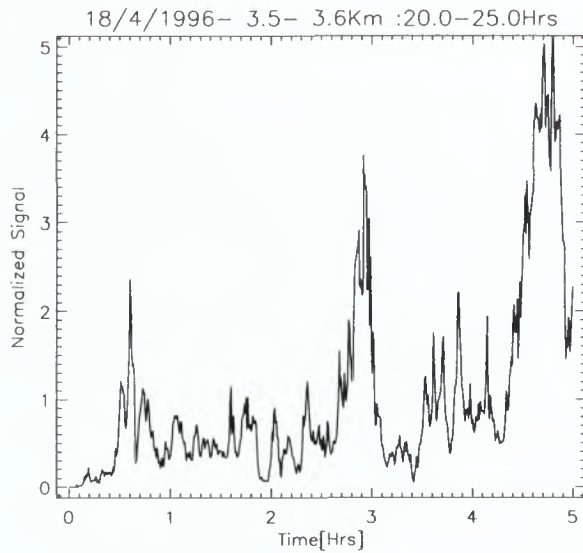
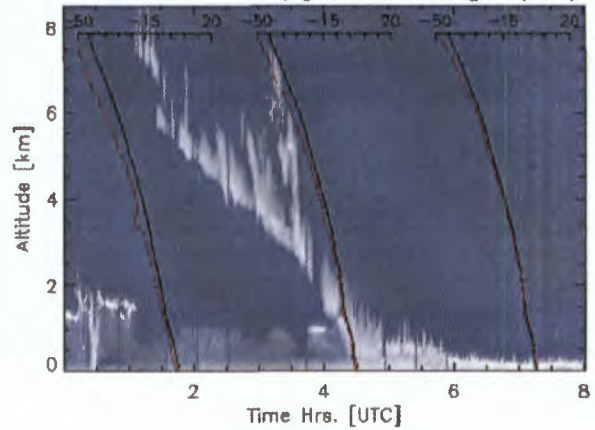
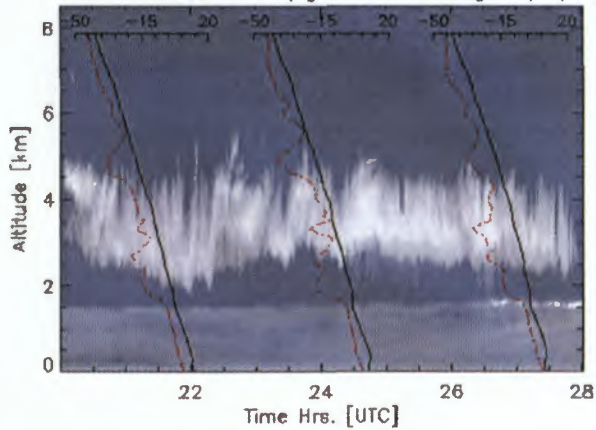


Figure 8: Lidar signals along with temperature (dark line) and dew point (red line) profiles extrapolated from sonde measurements (top panel). Sample signals time series take through the main cloud (bottom).

Figure 9: Lidar signals along with temperature (dark line) and dew point (red line) profiles extrapolated from sonde measurements (top panel). Sample signals time series take through the main cloud (bottom).

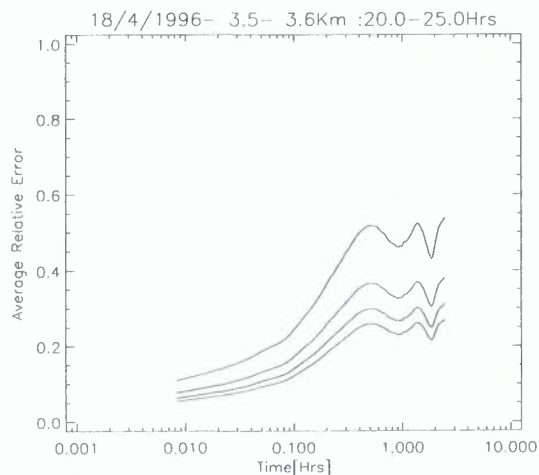


Figure 10: Relative error as a function of delay for different sampling resolutions for the time series shown in Fig. 8 (April 19th). From 300 meters (topcurve) to 1200 meters (lowest curve).

Spectral Analysis

In Fig. 12 the radar and lidar signals for April 19th are shown while in Fig. 13 an example normalized constant altitude signal cross-section is shown. The corresponding power spectral density (PSD), the autocorrelation, and a modified form of the so-called *second order structure function* [Davis et al. 1996] are shown are also shown in Fig. 13. The power spectral density is a measure of the power present in the time series as a function of frequency and is deduced using standard Fourier analysis techniques. The autocorrelation function is defined as:

$$ACorr(T_n) = \frac{\sum_{i=0}^{N-n-1} (X_i - \langle X \rangle)(X_{i+n} - \langle X \rangle)}{\sum_{i=0}^{N-1} (X_i - \langle X \rangle)^2} \quad (3)$$

where X_i denotes the i th point of the time series and the braces $\langle \rangle$ are used to denote averages. In Fig. 13 we also shown the square root of the structure function $D(T_n)$ here defined as

$$D(T_n) = \frac{\langle (X_{i+n} - X_i)^2 \rangle}{\langle X^2 \rangle} \quad (4)$$

The PSD, autocorrelation function, and the

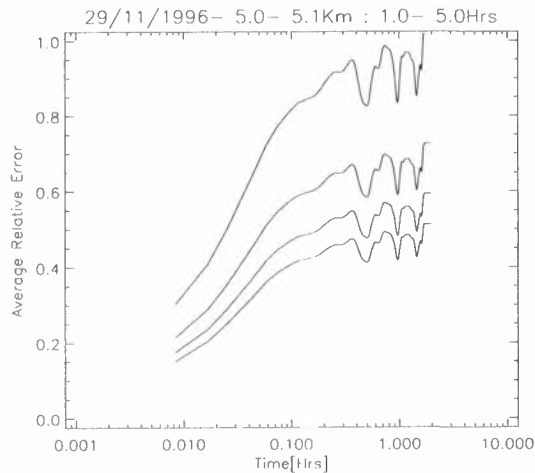


Figure 11: Relative error as a function of delay for different sampling resolutions for the time series shown in Fig. 9 (November 29th). From 300 meters (topcurve) to 1200 meters (lowest curve).

structure function are all related to each other and give complementary information. For fractal signals $D(T_n)$ often possesses a regime where it follows a power law, that is:

$$D(T_n) \propto T_n^H \quad (5)$$

It can be shown [Davis et al. 1996] that this implies that the PSD will also follow a power law with exponent $\beta = 2H + 1$. Generally H will be equal to 2 for processes resembling Brownian motion while H will equal 0 for white noise.

In Fig. 13 we see that that D indeed does obey a power law with $H = 0.5$ for T_n less than about 0.08 Hrs while for T_n greater than about 0.2 Hrs D is nearly flat ($H = 0$). By referring to the correlation coefficient it can also be seen that the point where D "becomes flat" corresponds roughly to the point where the autocorrelation becomes 0. This example clearly shows that for 2 points in this radar signal time series to be considered to be correlated ($ACorr > 0.9$) they must, in general be separated by no more than 0.01 Hrs (about 30 seconds). This small separation is still well above the sampling interval of the radar used here (5 seconds).

Fig. 14 shows the lidar signals time series analysis corresponding to Fig. 13. Here the spectral exponents are similar to those for the corresponding radar time series. The correlation length is slightly

larger though. Here D follows a power law until T_d equals 0.3 Hrs where it abruptly departs (a so-called 'scale-break'). In general, the lidar and radar respond to particles in fairly different size regimes. Roughly speaking, the lidar backscatter goes as the particle radius to the 2nd power while the radar backscatter scales as the particle radius to the 6th power. This difference in response can be expected, in general, to give rise to different exponents and correlation times for the lidar and radar signal time-series even though the lidar and radar measurements may be co-located. Although here the exponents between the lidar and radar are very similar. This may imply, that in the case shown in Fig. 14, that average size of the cloud particles was fairly constant with time.

The similarity between the radar and lidar signal statistics presented in Figs. 13 and 14 for April 18th is contrasted by the data shown in Figs. 15-17 for April 23rd. Here the radar signals are very weakly correlated with a scale-break occurring around 0.02 hours for the Radar signals. For the lidar signal time-series, the scale-break occurs near 0.2 Hrs with high values of **ACorr** being present out to 0.1 hours. In this example, there were clearly large cloud particles present and the average size of the cloud particles must have changed with time giving rise to the differences in behaviour between the lidar and radar signal time-series.

In Figs. 18-20 a final example is presented. Here the results of analyzing 2 radar time series both at the same times but for different altitudes are shown. Fig. 19 shows the results of the analysis of a time series taken above the peak return while 20 shows the results for a time-series taken at the peak return altitudes. The time series centered at 2.1 Km is dominated by the strong return at 1.8 Hrs while the time series at 0.6 km is not dominated by any single strong event. Here the scaling exponents are seen to be different and the correlation ranges are also seen to be different. The correlation coefficient curves for these two altitudes are also of different character. The upper altitude time series is highly correlated at short time scales but quickly becomes uncorrelated. The lower altitude time series is not as strongly correlated for small temporal separation but the correlation coefficient does not become 0 until nearly 1 hour.

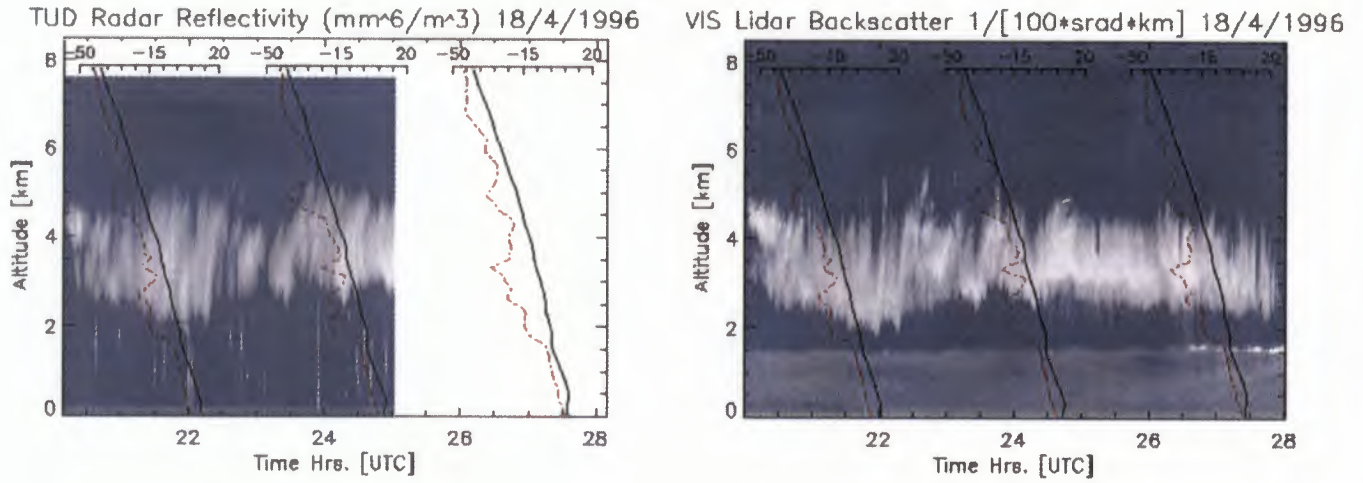


Figure 12: Radar (Left) and lidar (Right) signals for April 18, 1996 (CLARA).

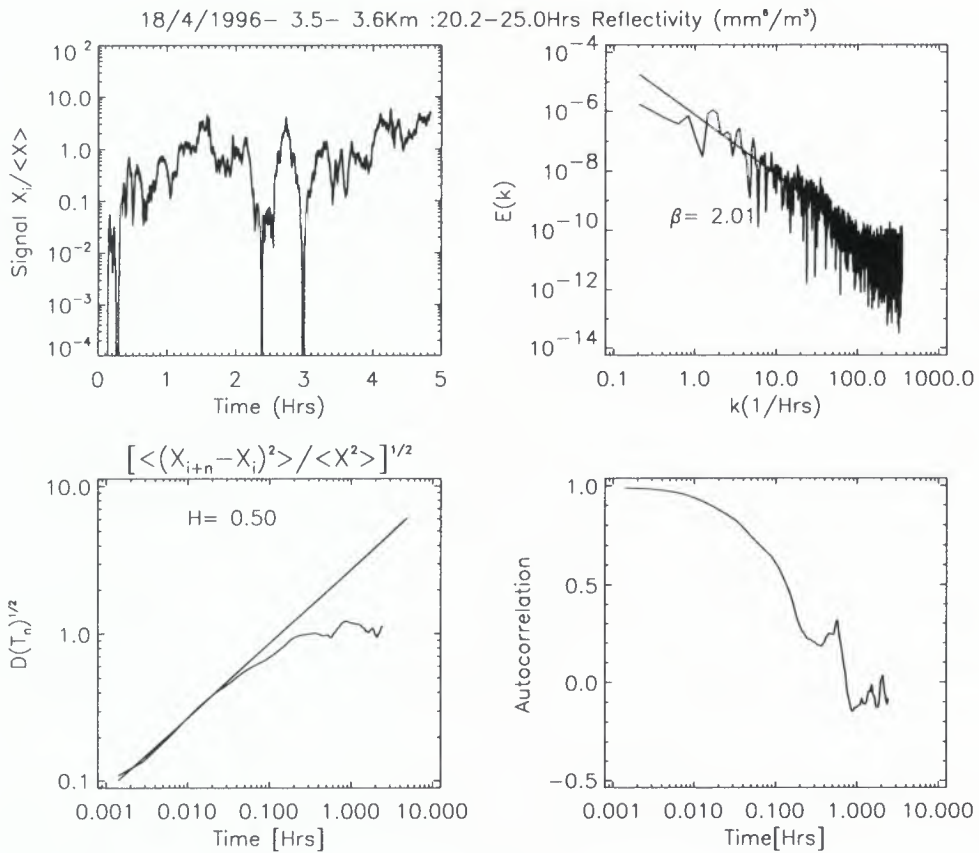


Figure 13: Spectral analysis results for radar signals for April 18th. The normalized signal ($X / \langle X \rangle$, Top left) the PSD (Top Right), the structure function (Bottom Left) and the autocorrelation (Bottom Right).

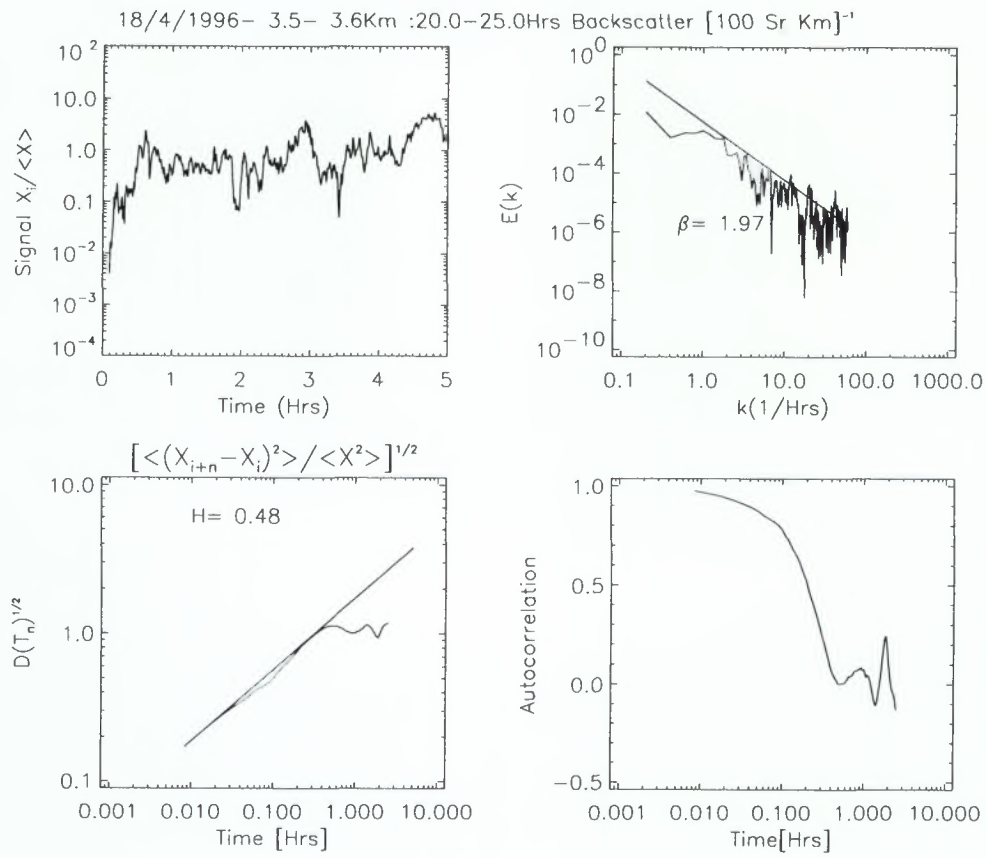


Figure 14: Spectral analysis results for lidar signals of April 18th.

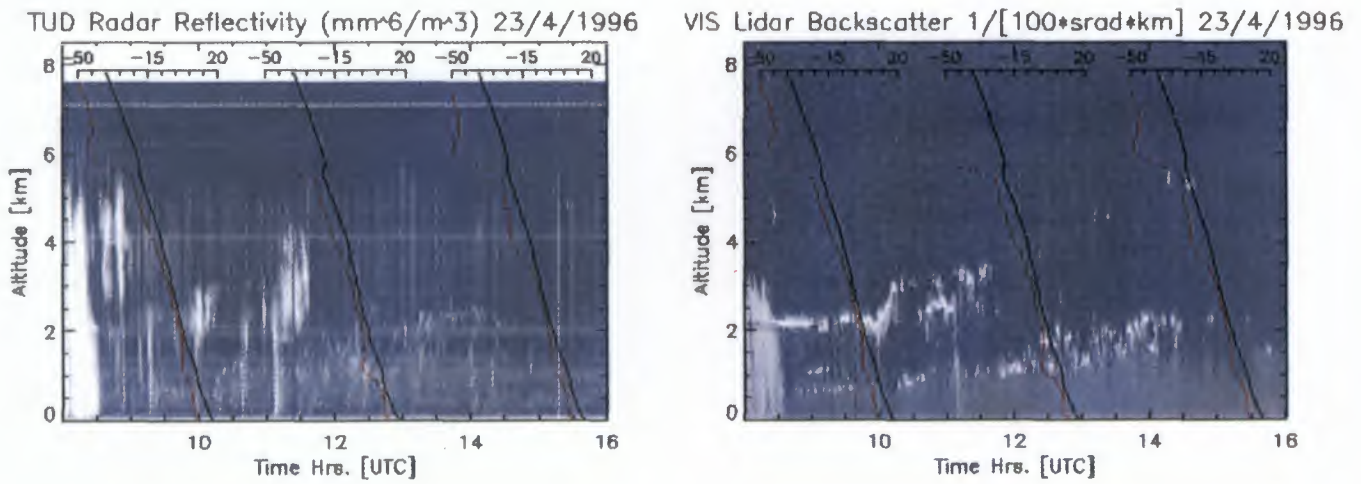


Figure 15: Radar (Left) and lidar (Right) signals for April 23, 1996 (CLARA)

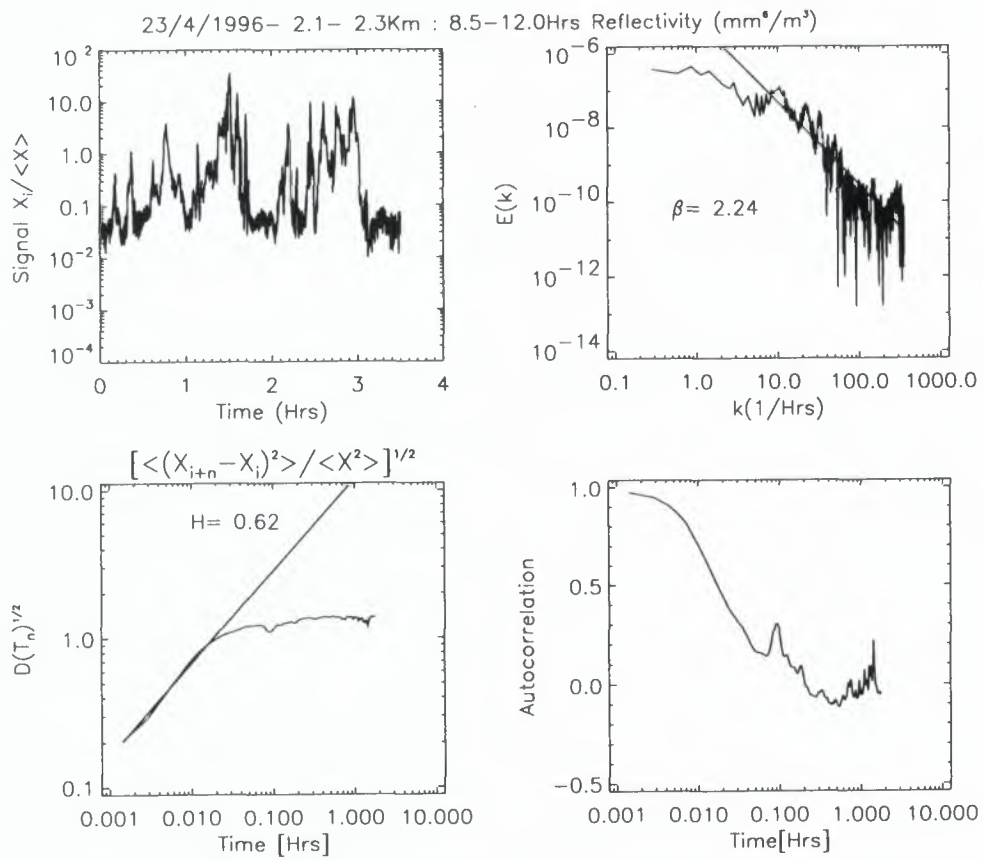


Figure 16: Spectral analysis results for radar signals of April 23, 1996 (CLARA).

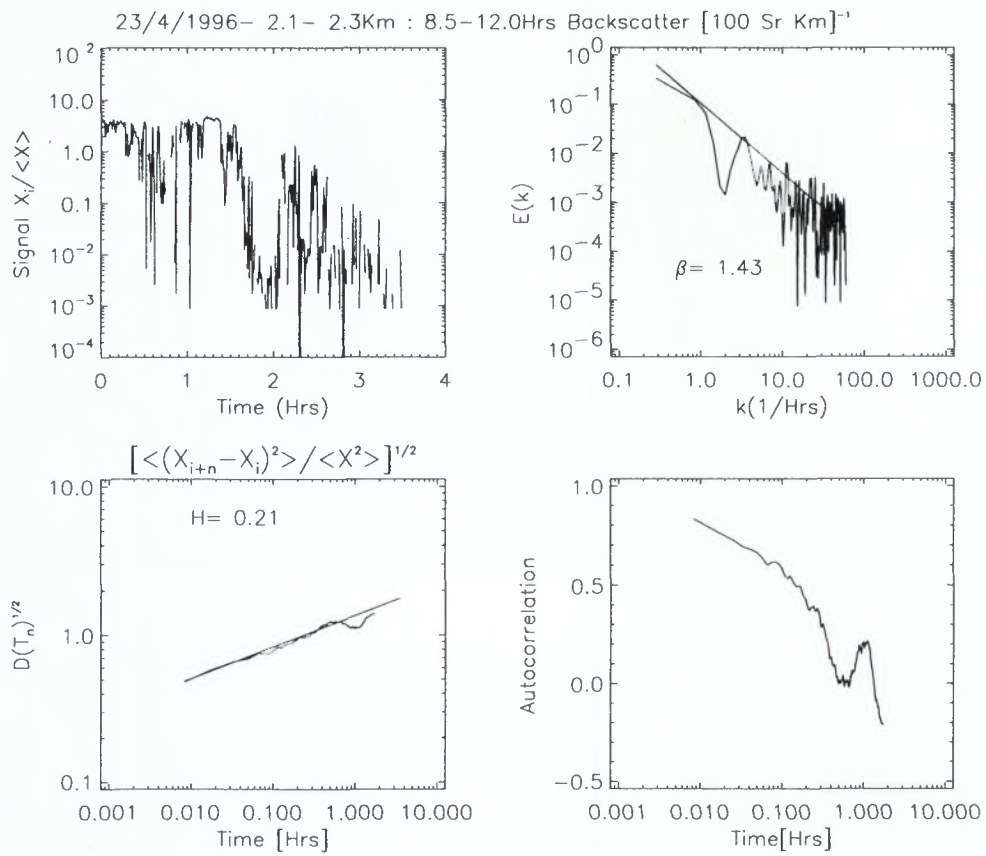


Figure 17: Spectral analysis results for lidar signals in April 23, 1996 (CLARA)

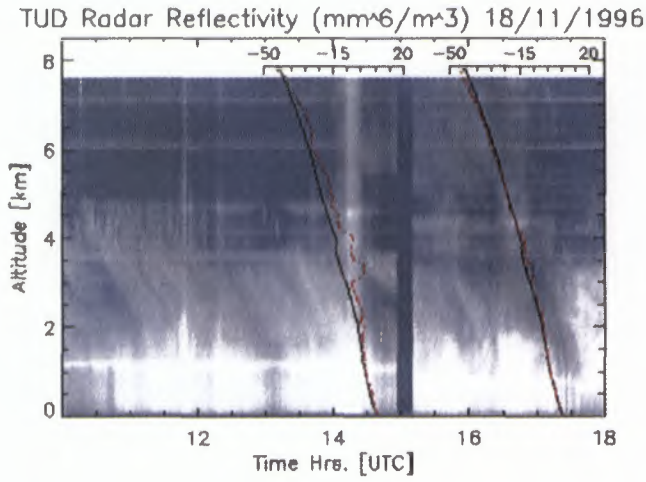


Figure 18: Radar signals for November 18th, 1996 (CLARA).

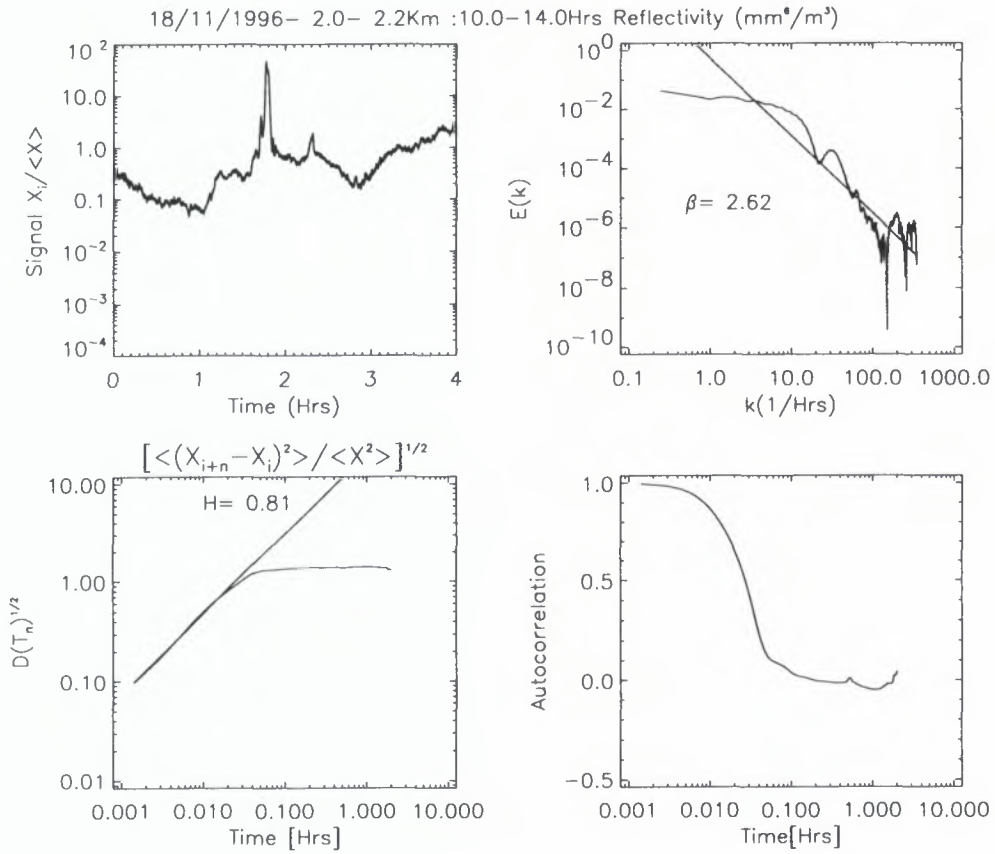


Figure 19: Spectral analysis results for radar signals in November 18th, 1996 (CLARA).

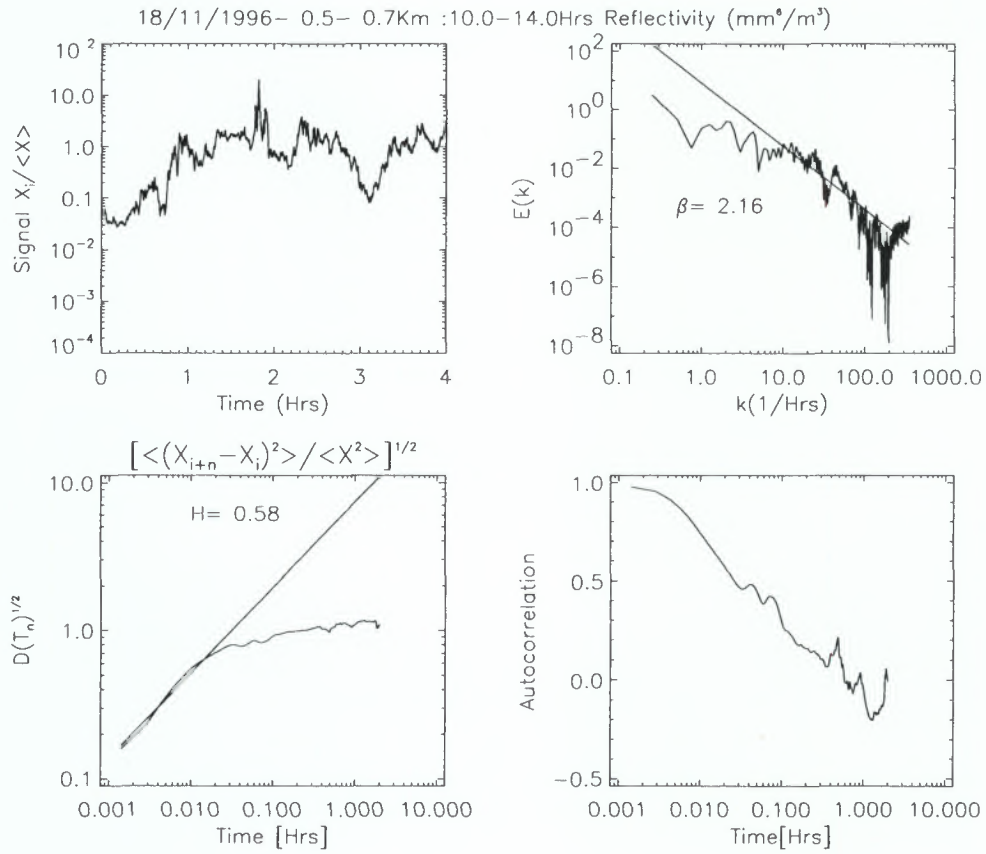


Figure 20: Spectral analysis results for lidar signals in November 18th, 1996 (CLARA)

Summary of Spectral Analysis Results

A summary of the results of the spectral analysis performed on the CLARA data to date is presented in Table 1. Here several key parameters have been listed, the point where the PSD (and D) depart from power law behavior, the H exponent, and the time at the correlation coefficient (A_{corr}) drops to 0.9. It can be seen at a glance that very small correlation times (less than 0.01 Hrs or 0.6 minutes) are much more common than larger ones (over 0.05 Hrs or 3 minutes).

Simulations

Now that we have examined the characteristics of the lidar and radar signals in some detail, we can extend our analysis. We can now proceed to generate 'realistic looking' two dimensional cloud signal fields. The results that will be shown in this section represent an attempt to generalize the inherently 1-d information in the time series data to 2 dimensions and are subject to some limitation, namely a time to space relationship must be assumed (mean-wind-speed) and it must be assumed that the statistical properties of the cloud field are isotropic.

The steps used to generate the signal fields are:

1. First a two dimensional field (of appropriate dimensions) of random numbers is generated.
2. The field is then convoluted with a specified correlation function. The properties of this function (together with a mean-scene wind velocity) determine the PSD and correlation properties of any slice through the resulting field. The resulting numerical field is used to represent the lidar-signal field.
3. A Radar signal field corresponding to the lidar signal field is then generated. This is done using the lidar signal field and specifying a simple model for the relationship between the lidar and radar signals and the underlying particle effective radius and number density.

In practice the random number field was generated using Gaussian random pseudo-random deviates but using uniform deviates changes the initial results little.

To generate the lidar fields correlation functions of the form

$$\left(\frac{1.0}{1.0 + c1 \cdot r} \right)^{cp} \quad (6)$$

where used. In Eqn.(6) r is the radius (distance from the peak of the 2-d correlation function) while $c1$ and cp are adjustable parameters. Generally speaking, $c1$ controls where T_b occurs (the correlation distance) while cp controls the value of H (how fast the correlation decays). An offset and a clipping value were then applied to the field to eliminate negative values. In Fig. 21 an example lidar signal field which mimics conditions roughly similar to those on April 18th, 1996 during CLARA is shown. A cross-section of the signals obtained by taking a horizontal cut through the center of Fig. 21 is shown in Fig. 22.

To generate a reasonable link between the lidar and radar fields a simple mode was used. The lidar signals was considered to be the product of a number density (N_o) and an effective radius (R'_{eff}) field such that

$$S_{lid} = N_o R'_{eff}{}^2 \quad (7)$$

while the Radar field was given by

$$S_{rad} = N_o R'_{eff}{}^6 \quad (8)$$

For simplicity, the effective radius field (N_o) was linked directly to the lidar signal field as:

$$R'_{eff} = AS_{lid} + B \quad (9)$$

Where A and B are adjustable parameters. If A is equal to zero then R'_{eff} is constant and the lidar and radar fields will be proportional to each other and will have identical spectral characteristics. For A not equal to zero the lidar and radar fields will have different spectral characteristics. If A is not equal to zero R'_{eff} and N_o will be related as:

$$R'_{eff} = \frac{1 - (1 - 4ABN_o)^{1/2}}{2AN_o} \quad (10)$$

An example scene is shown in Fig. 23 which was generated using the same parameters as those used in the data shown in Fig. 21 except that a coupled lidar and radar field are shown. Fig. 24 shows a lidar and radar signal cross-section taken from the same data used in Fig. 23. Fig. 24 also shows the

Case	Date	Time	Instrument	Alt.(Km)	$T_{break\ hours}$	H	T(0.9) Hrs
1.	17 Apr	13.5-15.5	Radar RIVM	6.0-6.1	0.03 0.03	0.4 0.37	0.01 0.002
2.	18 Apr	20.2-25.0	Radar Vis	3.5-3.6	0.2 0.4	0.5 0.48	0.02 0.04
3.	23 Apr	8.5-11.3	Radar Vis	2.1-2.3	0.01 0.5	0.6 0.27	< 0.001 < 0.01
4.	26 Apr	7.0-8.4	Vis	7.0-8.4	0.5	0.5	0.02
5.	25 Aug	12.5-19.0	Radar Vis	4.0-4.1	0.02 0.02	0.58 0.37	0.02 < 0.01
6.	02 Sep	8.0-16.0	Vis	1.8-2.0	0.04	0.28	< 0.01
7.	18 Nov	10.0-14.0	Radar Radar	0.5-0.7 2.0-2.2	0.01 0.05	0.60 0.79	0.004 0.01
8.	19 Nov	0.0-7.0 10.0-12.0 0.0-8.0 10.0-12.0	Radar Radar Vis Vis	0.6-0.7 2.5-2.6 0.6-0.7 2.5-2.6	0.04 0.02 0.02 0.02	0.12 0.55 0.52 0.51	< 0.001 0.01 < 0.01 < 0.01
9.	20 Nov	14.0-22.0 17.0-22.0	Radar Vis	6.0-6.1 1.0-1.1	0.07 0.03	0.25 0.43	0.001 < 0.01
10.	29 Nov	1.0-5.0	Radar Vis	5.0-5.1	0.02 0.05	0.61 0.65	0.01 0.02
11.	05 Dec	11.0-18.5	Radar Vis	5.0-5.1	0.02 1.0	0.2 0.15	< 0.001 < 0.01

Table 1: Summary of current spectral analysis results.

associated time-series analysis. The PSDs, structure functions, and the autocorrelations fall well within the range calculated from the CLARA data set. Here the N_o -vs- R'_{eff} coefficients were chosen so that the lidar and radar fields are similar but not identical to each other.

Once suitable artificial fields which mimic the relevant statistical features of the 1-D CLARA data sets have been created one is then able to fly lidars and radars with different sampling characterizes (footprint, shot separations, spatial and temporal offsets) over the generated scenes. Effective radius and volume retrievals are then carried out using the lidar and radar signals and the results compared with the true values.

Two examples are shown in Figs. 25 and 26. In Fig. 25 the left panel shows various signal time (distance) series that would have been measured by an instrument overflight with the specified sampling rate and beam footprint for different spatial offsets. The effective radii retrieved using the lidar and var-

ious radar signal pairs are also shown. The right panel shows the corresponding fraction of points whose error exceeds 100 %. In this case, even spatial offsets on the order of the radar footprint (here 0.5 km) can be seen to cause significant errors in the effective radius determination. Fig. 26 is similar to Fig. 25 except that the right panel shows the fraction of points in error in excess of 50 %.

Conclusion

Various simulations (though admittedly not exhaustive) have been conducted along the lines of those shown in the last section. It is hard to formulate any general rules. As even for cases in which the broad statistical parameters derived from the spectral analysis appear to be the same the errors turn out to depend in a strongly random fashion on the exact paths chosen for comparison. Very many systematic runs would have to be conducted for a given set of parameters before

any meaningful hard statistics could be generated. However, this in itself is a useful result. This observation implies that the error due to any spatial and/or temporal separation between the lidar and radar orbits would be very hard to quantify in practice. Even if the general 'cloud field type' being observed were known the errors encountered in practice may be 'all over the board' likely making any kind of correction unfeasible.

The investigation of 'cloud variability' is not yet complete, in the sense that we have not produced a definitive hard answer to the question "under general circumstances how much time and spatial difference may be allowed between two observations if we want to meaningfully compare them?". However, the question we have been trying to answer is somewhat ill-posed and trying to produce an exact answer to such a question may not be feasible. However putting all the evidence gathered in this study together the upper range of the answer is certainly "not much time (under a minute) and not much space (under a km)" with the lower range being still somewhat undefined.

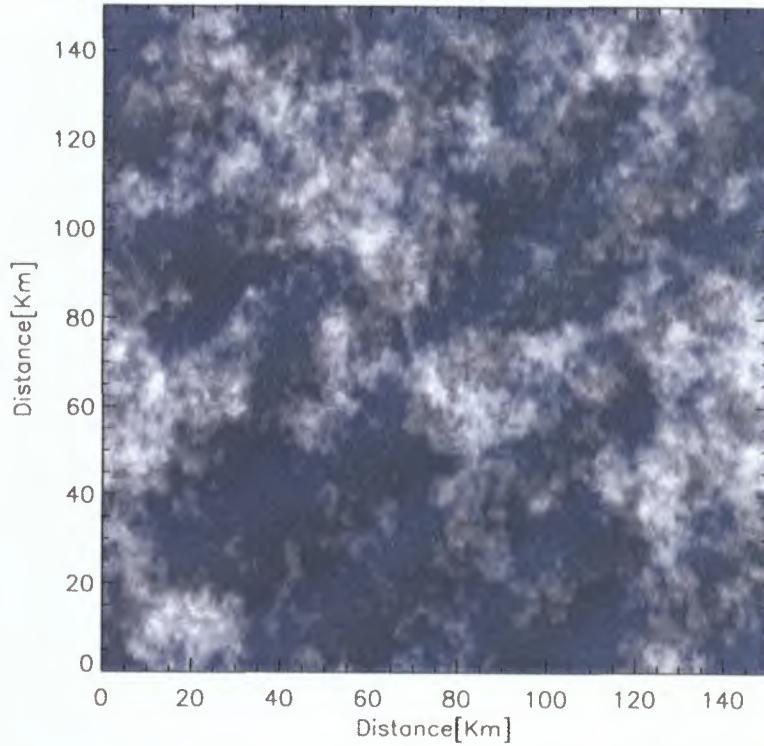


Figure 21: Synthetic 2-dimensional Lidar signals representative of a situation similar to April 18th, 1996 (CLARA)

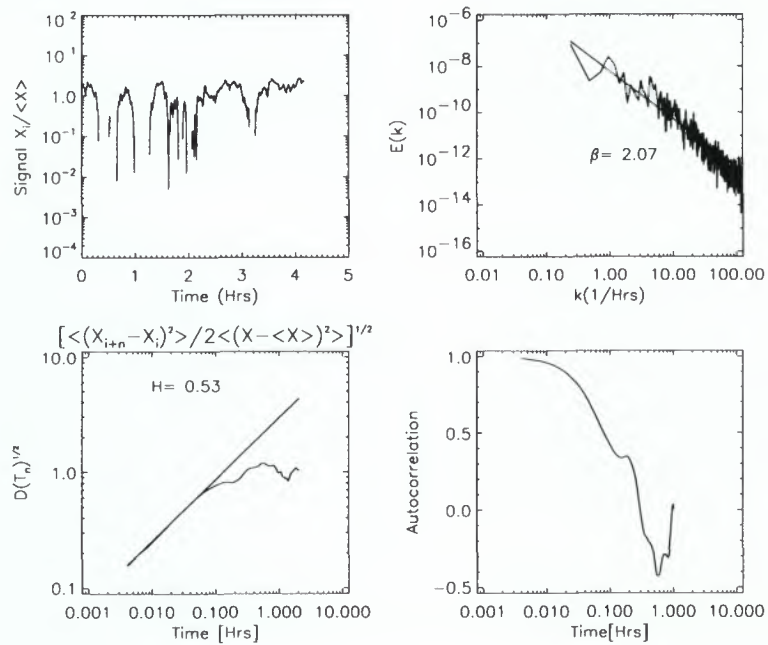


Figure 22: The top left panel shows lidar signals taken from a slice through the data shown in Fig. 22. The other panels show the PSD, structure function, and the autocorrelation coefficient of the signals respectively.

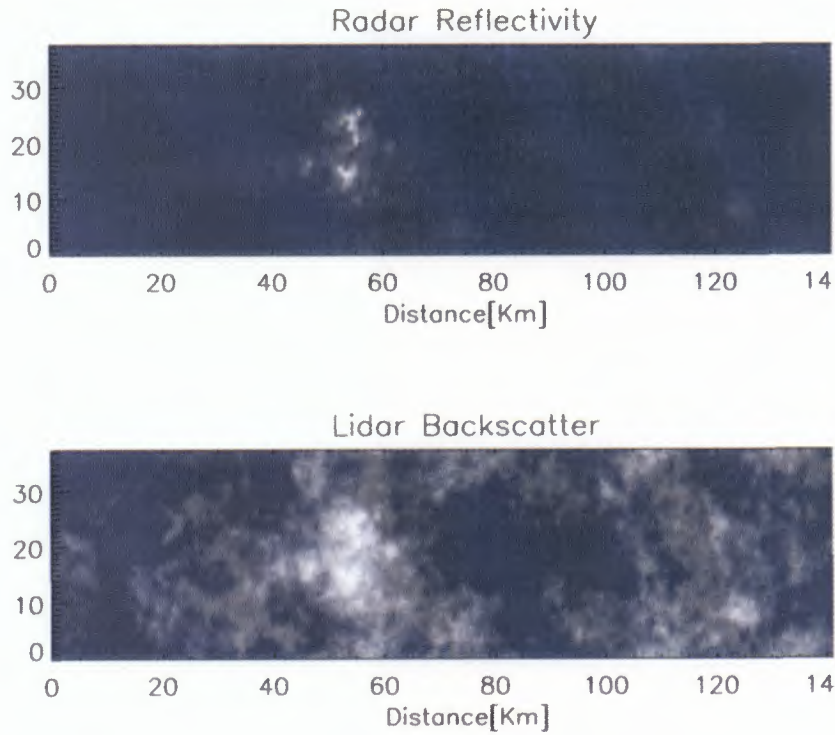


Figure 23: Synthetic 2-dimensional Lidar (Bottom) and Radar (Top) signals representative of a situation similar to April 18th, 1996 (CLARA)

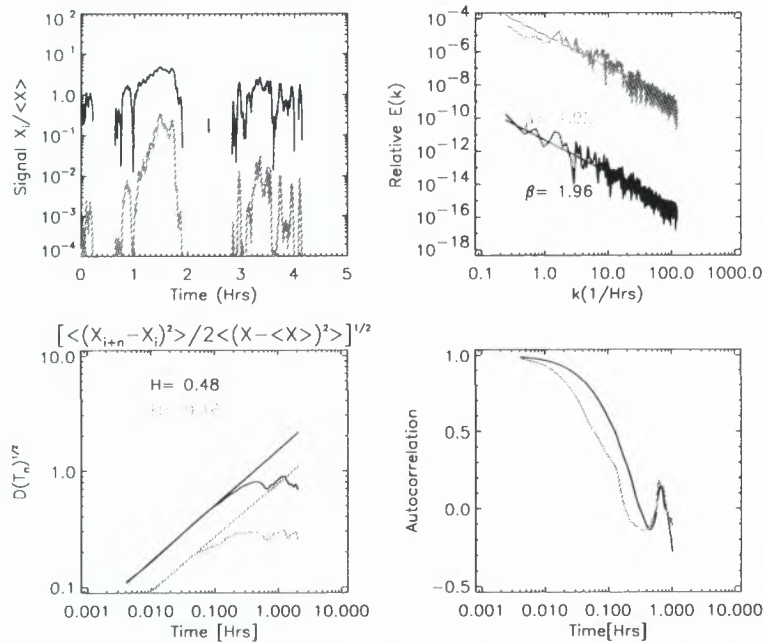


Figure 24: The top left panel shows lidar (dark thin line) and radar (thick Grey line) signals taken from a slice through the data shown in Fig. 23. The other panels show the PSD, structure function, and the autocorrelation coefficient of the signals respectively.

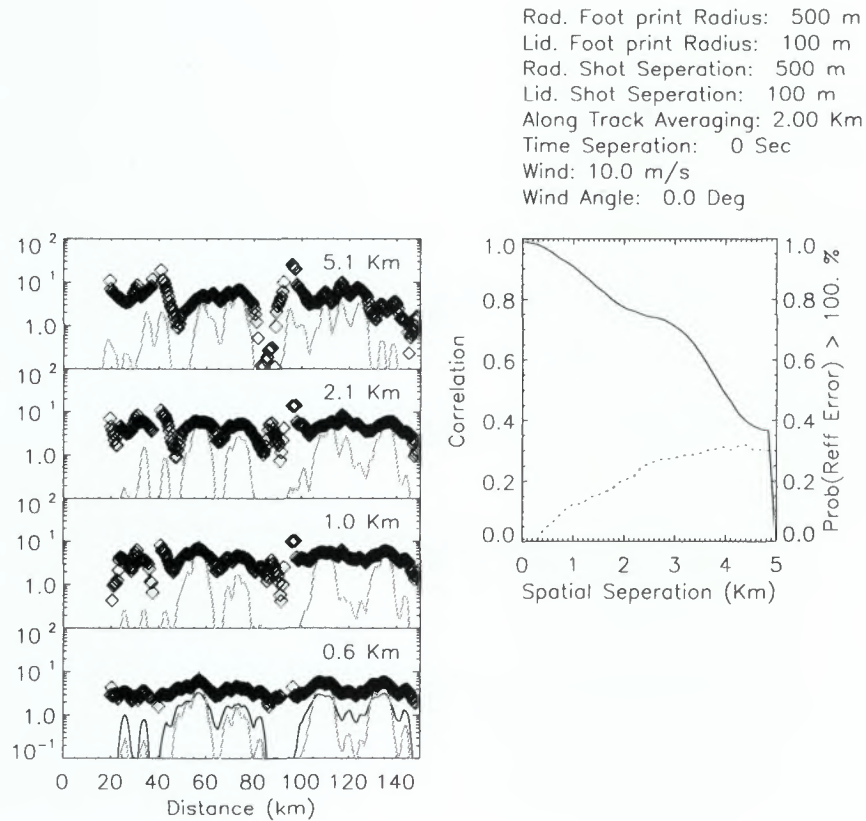


Figure 25: Left Panel: Lidar signals generated from an 'overflight' of the data shown in Fig. 24. Here the thin dark line shows the lidar signal while the Grey lines show radar signals for various tracks that are offset from the original lidar track. The numeric label gives the location of the overpass relative to the bottom of the image. The diamonds show the results of various effective radius retrievals using the various lidar and radar signal pairs. The right panel shows the fraction of measurements in error by more than 100 % compared to the true values of the effective radius along the lidar track.

Rad. Foot print Radius: 500 m
 Lid. Foot print Radius: 100 m
 Rad. Shot Separation: 500 m
 Lid. Shot Separation: 100 m
 Along Track Averaging: 2.00 Km
 Time Separation: 0 Sec
 Wind: 10.0 m/s
 Wind Angle: 0.0 Deg

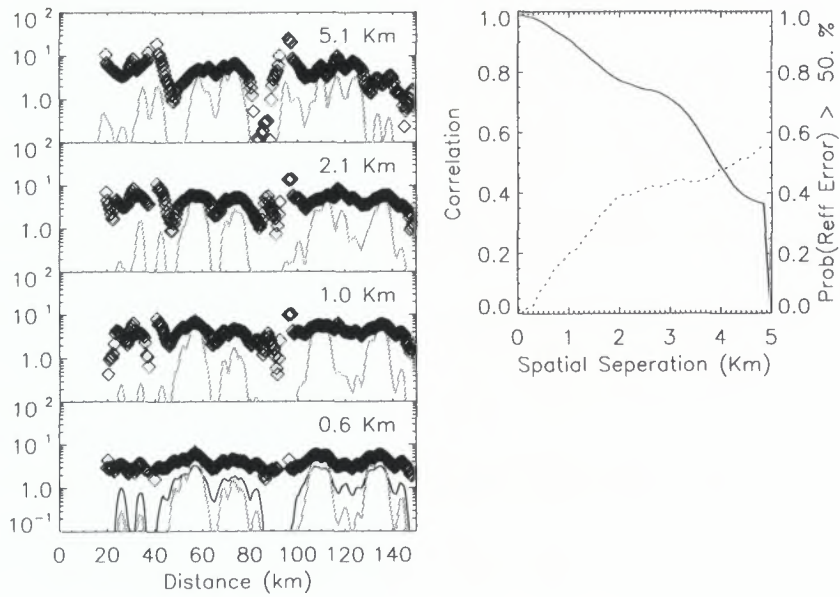
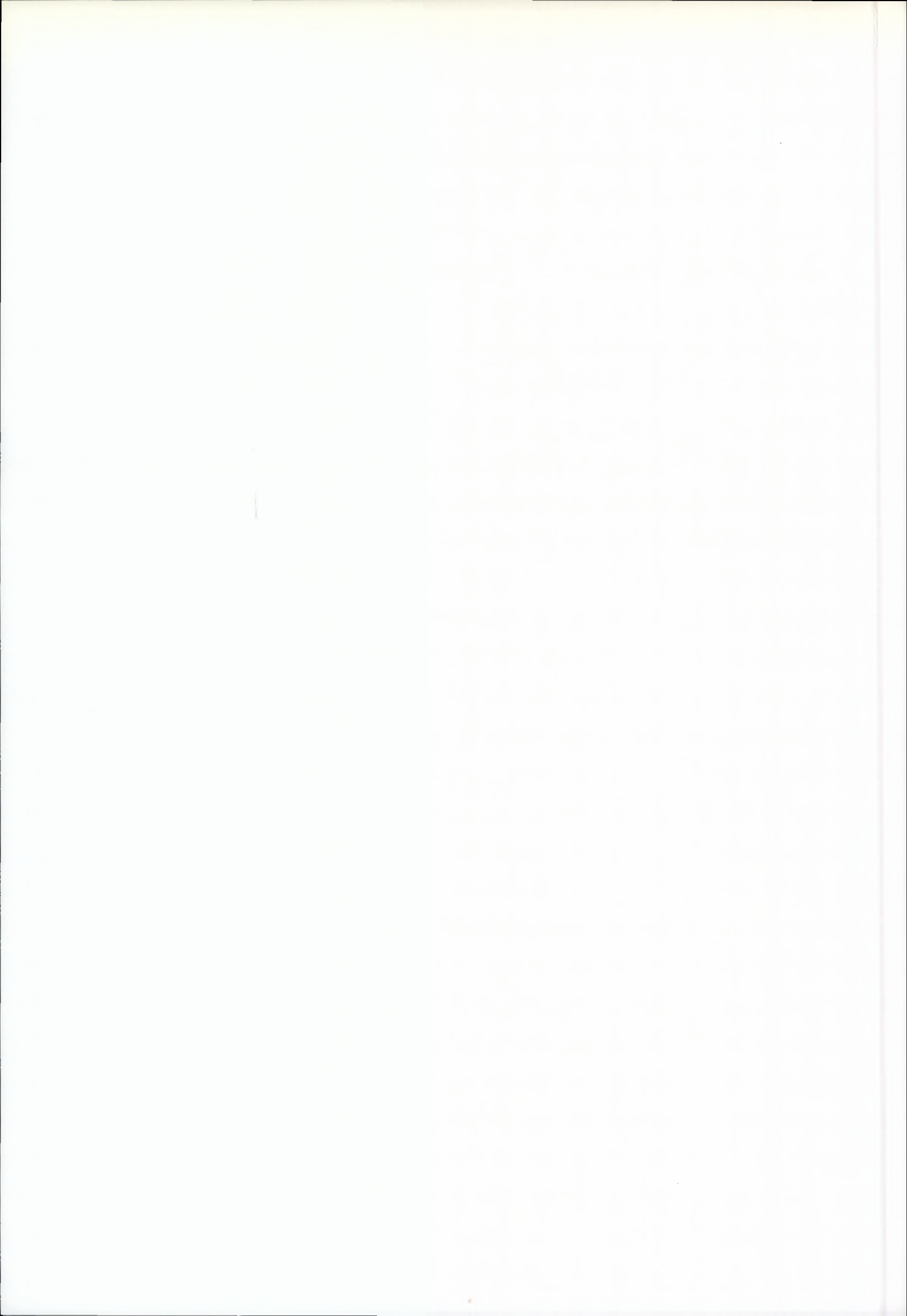


Figure 26: As Fig. 25 except that the threshold in the right panel has been lowered to 50 %

References

- Davis A., A. Marshak, W. Wiscombe, and R. Cahalan, Scale Invariance of Liquid Water distributions in Marine Stratocumulus Part 1: Spectral Properties and Stationarity Issues, *J. Atmos. Sci.*, **53**, 1538-1558, 1996.
- Donovan, D., A.C.A.P van Lammeren, A. Feijt, H. Bloemink, H. Russchenburg, A. Apituley, Analysis of ERM synergy by use of CLARA observations, Study note 1: Description of Selected Data Sets, KNMI, ESA contract No 12953/98/NL/6D , 1998.
- Lammeren, A.C.A.P, Russchenberg ,H., Apituley, A., Brink H.T., and Feijt A., CLARA: a Data Set to Study Sensor Synergy, in *Synergy of Active Instruments in the Earth Radiation Mission, 12-14 November 97, Geesthacht*, Quante W., Baptista, J.P.V., and Raschke E., Eds., ESA EWP-1968 - GKSS 98/E/10, 157-160, 1998.



Implications for the split mission scenario

Robin J. Hogan*

Anthony J. Illingworth

Department of Meteorology, University of Reading, UK.

*Email: R.J.Hogan@reading.ac.uk

INTRODUCTION

It has been suggested that financial constraints may exclude the possibility of a payload of two active instruments on a cloud profiling satellite, and that work should be carried out to determine whether or not dividing the instruments between two satellites in very close orbits would severely reduce the accuracy of size retrievals. It has been shown that a second satellite could trail the first with the footprints drifting towards and away from each other by as much as 5 km.

In this paper synthetic cloud fields are generated with the same spectral characteristics as those observed by ground based radars, the spaceborne radar and lidar are 'flown' across the field with varying footprint separation, and the changes in the measured radar/lidar backscatter ratio are simulated as a function of footprint separation. A mean ice particle size can be derived from the radar/lidar backscatter ratio in cirrus provided this ratio is not affected by footprint separation.

GENERATION OF SYNTHETIC CLOUD FIELDS

In order to estimate the magnitude of the errors arising from non co-located footprints we need to know the typical spatial structure of real cirrus clouds. This information has been obtained using vertically-pointing ground-based 35 and 94 GHz observations at Chilbolton, England. Ten second averages of reflectivity factor were recorded with a vertical resolution of 75 m. Averaging was performed to reduce the vertical resolution to 525 m, close to the 500 m proposed for a spaceborne radar. A number of 1024-point time-series of reflectivity factor (in dBZ) in cirrus were selected, and the temporal scale converted to a spatial scale using a simple Taylor transformation and the mean wind speed over Chilbolton at that time and altitude as diagnosed by the UK Meteorological Office Unified Model. Only time-series in which all points registered cloud were considered. Information on the horizontal structure was then obtained by fitting power laws of the form

$$E = E_0 k^\mu \quad (1)$$

to the Fourier spectra of these data, where k is wavenumber, E is power spectral density, and E_0 and μ are constants. The best fit lines were least squares fits in log-log space after 7-point averaging of the spectra to reduce scatter. The parameter μ was found to vary between -1.8 and -2.4 in cirrus, which compares with the range -1 to -2 found by Danne et al. (1996). A spectrum typical of those analysed is shown in Fig. 1. It had the form $E = 2.03 \times 10^{-5} k^{-2.16}$ dBZ² m (where k is in m^{-1}), and we will use this from now on.

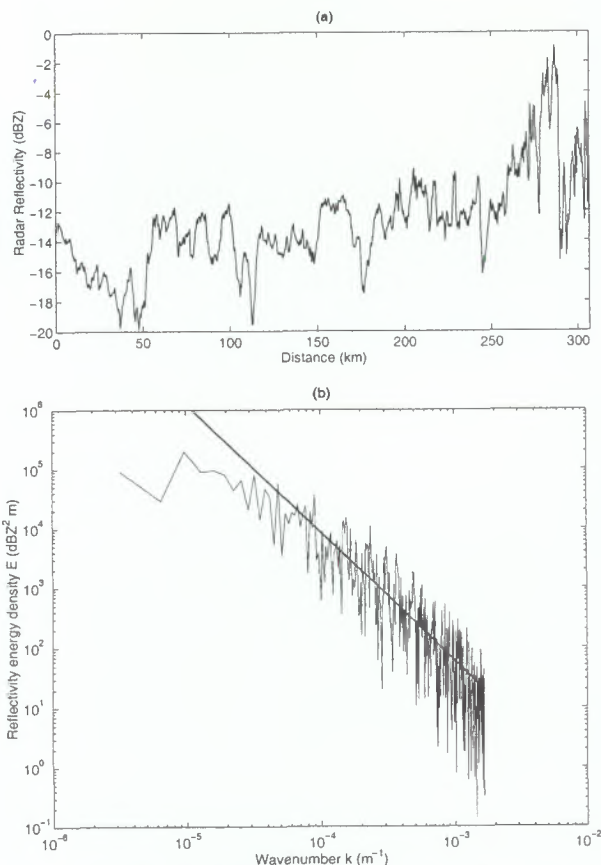


Fig. 1: (a) 35 GHz reflectivity factor at an altitude of 7 km. The abscissa has been converted from time to space using a mean wind at this altitude of 30 m s^{-1} . (b) The corresponding power spectrum. The best fit line is $E = 2.03 \times 10^{-5} k^{-2.16}$.

Cloud fields were generated by calculating the inverse two-dimensional Fourier transform of synthetic matrices containing wave amplitudes consistent with the energy at the various scales indicated by the one-dimensional spectrum. The phase of each wave component of the matrix was random, so that each cloud field was different. The domains were square and measured 25.6 km on a side with a resolution of 100 m. Fourier analysis of cross-sections through the domain confirmed that they had almost identical spectral properties as the original data. An example is shown in Fig. 2. Note that these cloud fields are spectrally isotropic, whereas real cirrus clouds with fallstreaks are not because the fallstreaks tend to be aligned parallel to the vertical wind-shear vector. On average this is not

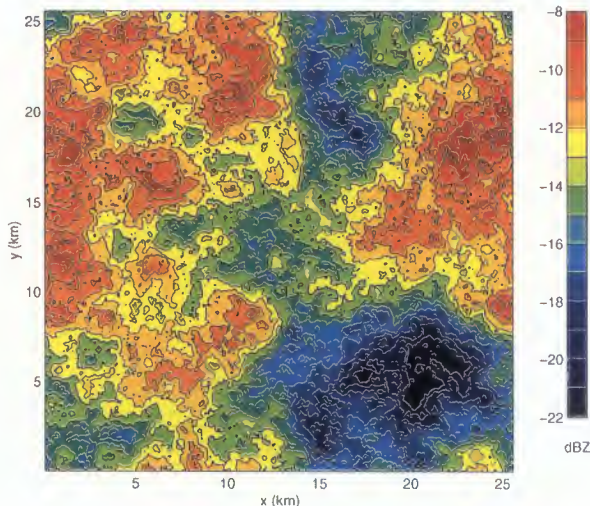


Fig. 2: Example of a simulated two-dimensional cloud field.

expected to significantly bias the results.

EFFECT OF BEAM SEPARATION ON THE LIDAR/RADAR BACKSCATTER RATIO

We shall consider a 1-second averaging time for the spaceborne radar and lidar to achieve sufficient sensitivity, which results in a pixel length of 7 km. The effect of footprint separation has been simulated using 64 synthetic cloud fields generated by the procedure described in the previous section. The footprint of the lidar was taken as 100 m and that of the radar to be 700 m with both instruments having a Gaussian beam pattern. Calculating the radar backscatter is relatively straightforward, but to calculate the lidar backscatter the radar reflectivity field was transformed to an optical extinction using an empirical relationship from Hogan and Illingworth (1999) and then a constant extinction to backscatter ratio was assumed for the ice cloud to calculate the lidar backscatter field. Because we are only interested in the change in the radar/lidar backscatter ratio with footprint separation the exact choice of the constant value of the extinction to backscatter ratio is immaterial.

The swaths of the spaceborne radar and lidar were offset by up to 10 km in the direction parallel to the satellite motion. The resultant mean fractional error in the backscatter ratio as a function of the separation distance is displayed in Fig. 3. Note that even when the centres of the footprints are both co-located there is an error in the backscatter ratio because the radar footprint is larger than that of the lidar, but the rms value of this error is only 0.2 dB, or less than 5%, so can be neglected. When the footprint separation distance reaches 5 km then the error approaches 3 dB, or a factor of two, and this is unacceptable.

CONCLUSIONS

A spaceborne cloud radar and lidar have been 'flown' over synthetic cloud fields having the same spatial characteristics and variability as those observed by ground based radars, and the change in the apparent radar/lidar backscatter ratio has been calculated. Even with perfectly co-located footprints there is a small error in the backscatter ratio because the lidar footprint

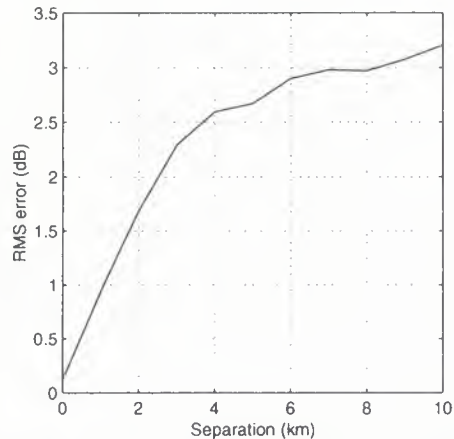


Fig. 3: RMS error in the lidar/radar backscatter ratio as a function of footprint separation.

is 100 m is less than the 700 m radar footprint, but this error is less than 5% and can be neglected. When the tracks of the footprints of the two instruments are 5 km apart then the mean error in the backscatter ratio approaches a factor of two, which is unacceptable. The simulations are idealised and in practice the degradation will be greater than calculated. Firstly, and most importantly, it has been assumed that the lidar backscatter signal is unattenuated, but in practice it will be heavily attenuated and a correction for such attenuation must be made. Gate-by-gate correction algorithms are notoriously unstable, and so the most reliable attenuation correction algorithms use the radar reflectivity profile as a first guess to constrain the extinction profile (see other CLARE papers). Clearly, if the first guess constraint is taken from a radar profile some distance from the lidar profile there is no guarantee that this correction procedure will converge to a stable solution. Further simulations would be needed to quantify this effect. A second effect is the time separation of the two platforms. If they are separated by (say) one minute, then cirrus clouds moving at (say) 30 m s^{-1} could lead to a further spatial separation of up to 2 km and of course their structure could also evolve.

The conclusion of this analysis is that flying the radar and lidar on separate platforms would lead to an unacceptable degradation in the derived radar/lidar backscatter signal.

ACKNOWLEDGEMENTS

The radar data were provided by the Radiocommunications Research Unit at the Rutherford Appleton Laboratory.

REFERENCES

- Danne, O., G. G. Mace, E. E. Clothiaux, X. Dong, T. P. Ackerman and M. Quante, 1996: Observing structures and vertical motions within stratiform clouds using a vertical pointing 94-GHz cloud radar. *Beitr. Phys. Atmosph.*, **69**(1), 229–237.
- Hogan, R. J., and A. J. Illingworth, 1999: The potential of spaceborne dual-wavelength radar to make global measurements of cirrus clouds. *J. Atmos. Oceanic Tech.*, **16**(5), 518–531.

Comparison of ECMWF Cloud Cover with Radar Derived Values

Robin J. Hogan*, Christian Jakob† and Anthony J. Illingworth

Department of Meteorology, University of Reading, UK

†European Centre for Medium-Range Weather Forecasts, Reading, UK

*Email: R.J.Hogan@reading.ac.uk.

INTRODUCTION

The limited spatial resolution available to global atmospheric models means that in addition to the usual prognostic variable of cloud water content, it is necessary for them to include some estimate of the sub-gridscale fluctuation in cloudiness. Most models diagnose cloud cover every timestep from prognostic model variables such as humidity and cloud water content, but in the current version of the European Centre for Medium-Range Weather Forecasts (ECMWF) model, cloud cover is itself formulated as a prognostic variable (Tiedtke 1993). The physical basis underlying the treatment of this parameter (as either diagnostic or prognostic) is somewhat uncertain, and consequently errors in model radiative fluxes are often blamed on poor model cloud cover. The fundamental role played by clouds in the earth's radiation budget means that it is important that this parameter can be predicted accurately for climate simulations to be reliable.

A previous attempt to validate the cloud cover in the ECMWF model used AVHRR data to estimate the total cloud cover for a model gridbox through the whole depth of the atmosphere (Karlsson 1996), but there is clearly a need for vertically-resolved observations of to be used to perform the validation at each model level. In this study, ECMWF cloud cover is compared with that derived by three active instruments located at Chilbolton, England, for a three-month period. Throughout most of the depth of the atmosphere one of two vertically-pointing cloud radars (the 'Rabelais' operating at 35 GHz and the 'Galileo' operating at 94 GHz) is used, but up to the freezing level we use the cloud base reported by a lidar ceilometer in preference, since this instrument is more effective at detecting liquid water clouds. However, it is rapidly attenuated so cannot be used above the base of the first cloud.

An earlier comparison by Mace et al. (1998) employed a much simpler technique; each model gridbox was determined to be either cloudy or cloud-free according to whether a 35 GHz radar observed any cloud in it during the model timestep, and this was compared with the same 'binary' information derived from the ECMWF cloud fields.

METHOD

The principle of the technique is quite straightforward; daily time-height sections of radar reflectivity are divided into boxes centred on the model height levels and timesteps, and cloud cover is then simply taken to be the fraction of radar pixels in each box that register the presence of cloud. The model has 31

levels in the vertical and a timestep of 20 minutes. The radar data have been averaged over 2 minutes and 150 metres, which increases the sensitivity by 7 dB over the raw 10 second/75 metre data, yet still provides several tens of pixels in each box from which cloud cover can be calculated. The horizontal resolution of the model is around 60 km, so there is a question as to whether measurements taken at a single site during a 20 minute period can be representative of all the clouds in an area this size; the wind speed would have to be 50 m s^{-1} for clouds to be sampled from both sides of the gridbox.

Care has been taken to ensure that only signals from clouds are included in the analysis. The main consequence is that the radar returns below around 500 m cannot be used because of leakage by the transmit pulse into the receiver and the presence

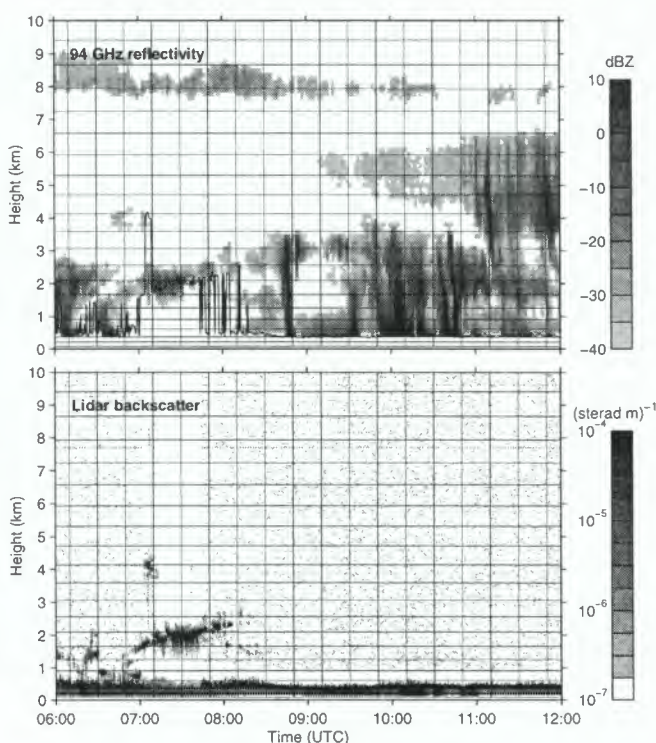


Fig. 1: An example of the data from which cloud cover can be derived, taken on Christmas Day 1998. The top panel shows radar reflectivity measured at 94 GHz, with lidar-derived cloud base indicated by the solid line. The bottom panel depicts lidar backscatter coefficient. Overlaid on each are the model gridboxes.

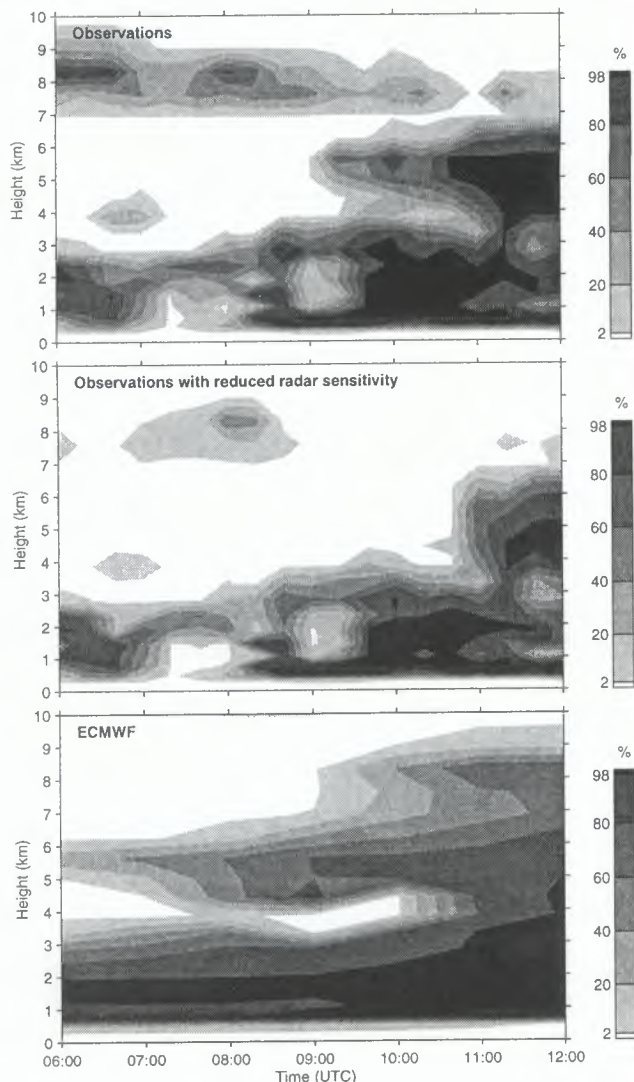


Fig. 2: The top panel shows cloud cover derived from the observations presented in Fig. 1, and the second lower panel shows cloud cover derived in the same way but after reducing the radar sensitivity by 10 dB. The lower panel depicts the corresponding values predicted by the ECMWF model.

of ground clutter. The common problem of insects in the boundary layer is non-existent at 51°N during winter, when the data for this study were taken. A further difficulty, however, is that in the presence of rain the radar is unable to detect cloud base. We therefore use cloud base measured by a Vaisala CT75K lidar ceilometer operating at 905 nm (30 second, 30 metre resolution) to estimate cloud cover at the base of clouds warmer than 0°C , where the temperature is taken from the model. It is found that even stratocumulus can have sufficient drizzle falling out of it that cloud base height according to the radar can be underestimated by several hundred metres. Invariably the signal from the lidar is rapidly extinguished in liquid water clouds and the radar must be used above.

To illustrate the retrieval process, Fig. 1 shows 6 hours of lidar and 94 GHz radar data taken on 25 December 1998. Ex-

cept for the period between 07:00 and 08:00 UTC, the lidar signal is completely blocked by low-level cloud, which has a base at 400 m. Note that the lidar also detects aerosols in the boundary layer, although they give a much lower return. The model gridboxes are shown superimposed. The cloud cover derived from these observations is shown in the top panel of Fig. 2. The 0°C isotherm was at around 2.3 km on this day.

It is naturally very important the instruments are able to detect the large majority of all clouds. Liquid water clouds tend to have very distinct boundaries in the short wave and there is therefore no difficulty in detecting them with the lidar. Cirrus clouds on the other hand do not have distinct boundaries and there is always some doubt as to whether the radar is detecting their full extent. The 94 GHz radar in this example had a minimum detectable reflectivity of -55 dBZ at 1 km and -35 dBZ at 10 km. It was shown by Brown et al. (1995) that virtually all 'radiatively significant' cirrus has a reflectivity at 94 GHz of greater than -30 dBZ. However we can illustrate the potential problem by reducing the sensitivity of the radar by 10 dB at all heights. The cloud cover derived after degrading the data in this way is shown in the second panel of Fig. 2. Clearly much less cirrus is observed but it is interesting to note that the retrieved cloud cover at low levels is virtually unchanged, although this is mainly because the radar is intrinsically much more sensitive to nearby clouds. It is worth mentioning that attenuation by rain can attenuate the (two-way) signal at 94 GHz by up to around 10 dB, and the light rain at 08:50 and between 10:00 and 11:00 UTC may have caused a certain amount of attenuation of the signal and reduced the amount of cirrus detected. This is much less of a problem at 35 GHz.

ECMWF cloud cover for this period is shown in the lower panel of Fig. 2; note that although the model timestep is 20 minutes, only the hourly fields are recorded routinely. The model predicted a similar amount of cloud between 0.5 and 3 km as was observed, although its cloud-cover field is much smoother. There are significant differences between the predicted and observed amounts of mid-level and high cloud.

RESULTS

Cloud cover has been calculated from the near-continuous observations taken between 24 October 1998 and 23 January 1999 at Chilbolton, and Fig. 3 shows a comparison of observed and modelled cloud cover during a six-week period in November/December 1998. It is apparent from the fluctuations in the observed cloud cover in Fig. 2 that 20 minutes is not really long enough for adequate sampling of the cloud in a model gridbox, so the observations have been averaged over an hour. The larger scale features appear to match up reasonably well, but an objective comparison is required to highlight where the model is deficient.

The first step in such an analysis is to compare the distribution of cloud cover for the entire three month period. The first panel of Fig. 4 shows mean cloud cover as a function of height from the model and the observations, and the following two show this information split up into 'frequency of occurrence' and 'amount when present', using a trigger level of 5%. Figure 4 also shows the frequency distribution of cloud

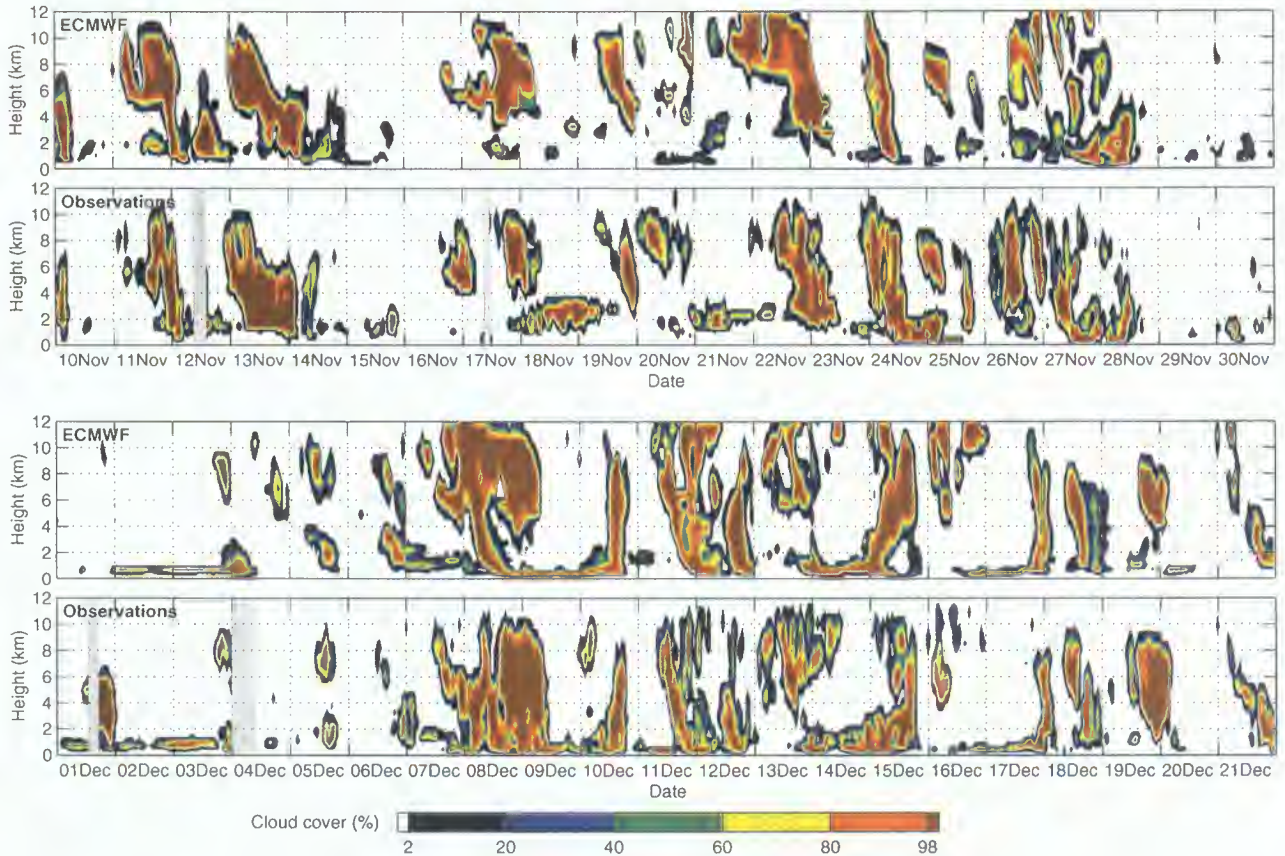


Fig. 3: Comparison of observed and ECMWF model cloud cover at Chilbolton for a six-week period. Only the 94 GHz radar was used during this time. The very light grey rectangles indicate when the radar was not operating vertically.

cover at the three different height levels. We see that on average the model tends to predict too little low and medium-level cloud but too much high cloud. However, it performs much better in simulating the frequency of cloud occurrence (analogous to the comparison performed by Mace et al. 1998). Hence the problem is not of clouds being produced when there are none (or vice versa) but of simulating the right cloud cover when clouds are present.

One problem with the comparison is that the observations cannot distinguish between ice cloud and ice precipitation (i.e. snow) whereas the model treats them separately such that snow does not contribute to cloud cover. In reality of course they are a continuum, but this ambiguity results in the tendency, apparent from Fig. 4, that a little more cloud is observed at altitudes of around 4 km than is modelled.

The difference between the model and the observations at high levels is much greater, with the model apparently overestimating cloud cover considerably. There is obviously the possibility that there are tenuous cirrus cloud tops not detected by the radar, and as already mentioned, attenuation by rain and low-level liquid water cloud can considerably reduce the sensitivity of the 94 GHz radar to cirrus.

The next step is to see how well the model agrees with the

observations on a pixel-by-pixel basis. The first panel of Fig. 5 shows the correlation coefficient of the two fields versus height and lag time. Throughout most of the troposphere the correlation is around 0.5 and there is no lag, but we find the surprising result that in the lowest 1 km the model tends to simulate cloud features up to 3 hours before they are observed.

The second panel of Fig. 5 shows the mean absolute difference in percentage cloud cover between the the model and the observations as a function of height. Throughout most of the depth of the atmosphere the difference is around 18% (expressed in percent because that is the unit of cloud cover, i.e. this figure does not mean that the mean absolute difference is 18% of the mean). From Fig. 4 we see that this is not much less than the typical mean cloud covers of between 15% and 30%, implying that the model is performing poorly. However, the requirement that the model should be accurate to one hour and one model level is perhaps overly stringent, and it is certainly not essential for radiation that the model is this accurate. It would be fairer to first average both fields onto a coarser grid that better reflects the spatial and temporal accuracy required.

Mean absolute difference is shown as a function of time of day in the third panel of Fig. 5, and we see that the error increases from 15% at the beginning of the day to around 18% at

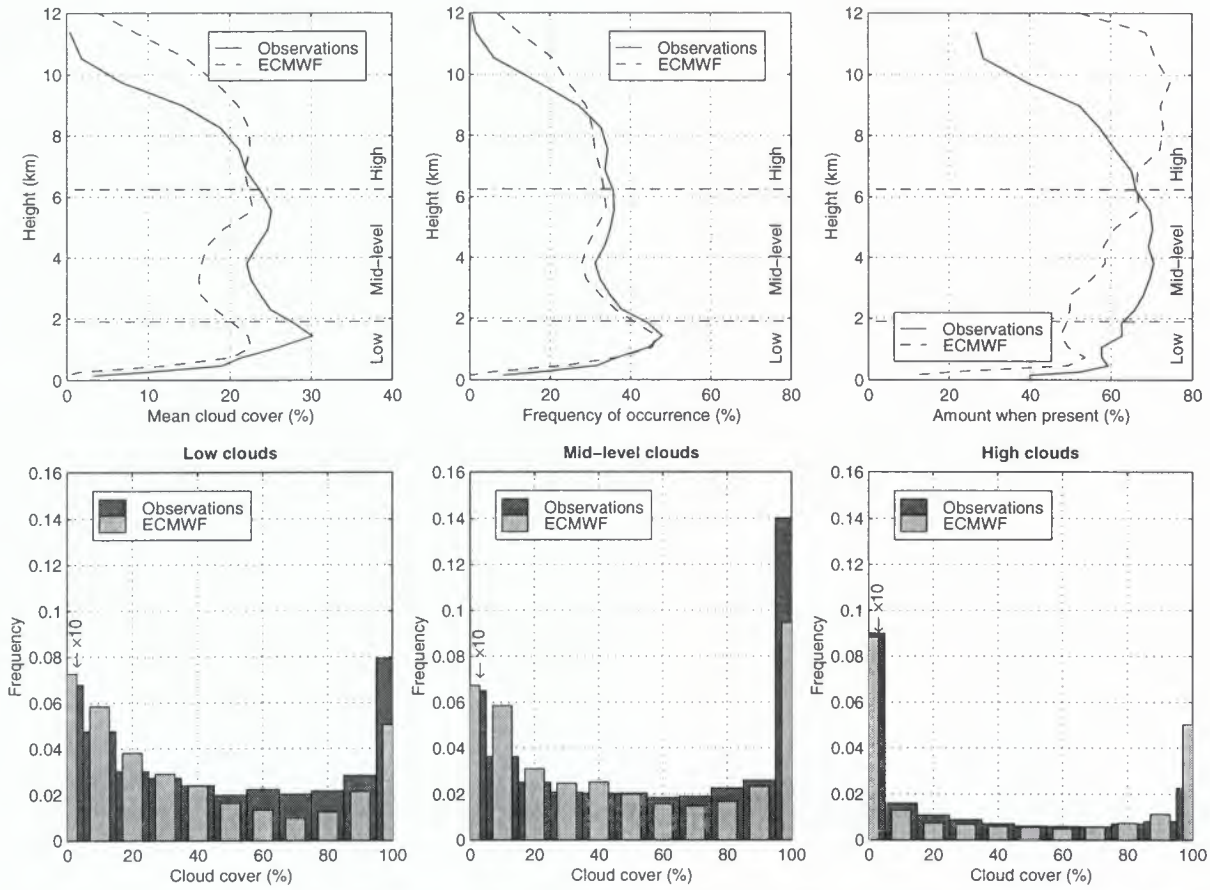


Fig. 4: Cloud cover statistics for the entire three-month period. The top row panels depict (as a function of height) mean cloud cover, frequency that cloud cover is over 5% and mean cloud cover when more than 5%. The bottom row shows the frequency distribution of cloud cover in the three height bands used by the model (bounded by the 800 mb and 450 mb surfaces). Note that the bars centred on 0% are shown at one tenth of their true value.

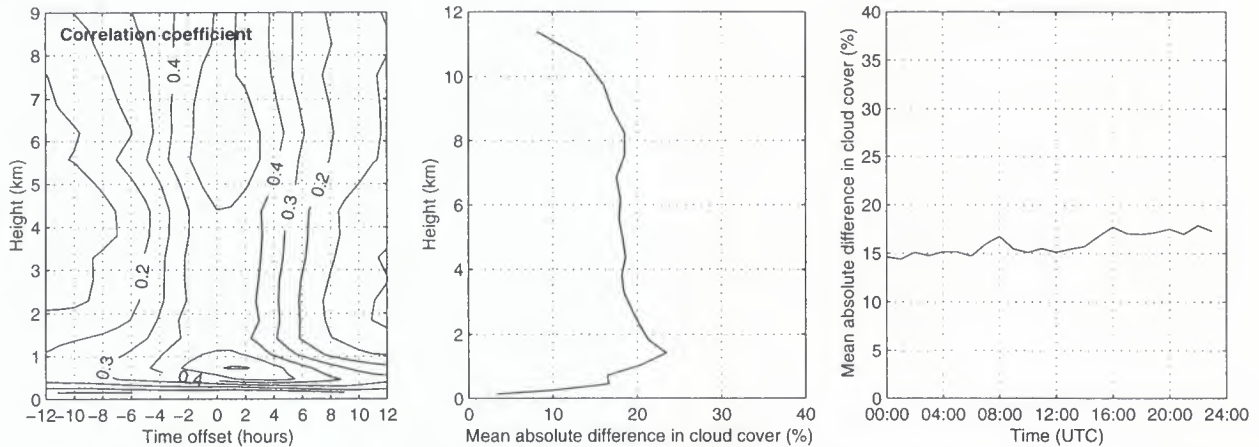


Fig. 5: The first panel shows the correlation of the observed and modelled cloud cover fields as a function of height and lag time. A positive lag corresponds to the model simulating features before they are observed. The second and third panels show the mean absolute difference between the two fields versus height and time of day respectively.

the end. This is simply because the model fields were produced on a daily basis from forecasts initialised at 12 UTC the previous day, and the accuracy of the model naturally decreases with time. This also explains the sharp changes often seen in model cloud cover between 23 UTC and 00 UTC the following day.

CONCLUSIONS AND FUTURE WORK

It has been shown that the very different but complimentary scattering properties of radar and lidar have the capability to perform a very valuable role in validating the representation of clouds in models. From a climatology point of view the model is found to be reasonably good at forecasting the frequency that cloud cover is more than 5%, but when cloud is present it performs poorly in predicting the actual cloud cover. On a pixel-by-pixel basis the model performance is also poor, but a fairer test needs to be devised involving appropriate filtering of the data.

A number of improvements could be made to the algorithm that derives cloud cover from the raw observations. The model consistently generates more high-level cloud than is measured, but the sensitivity of the radar at this altitude is a problem when there is attenuation. Throughout the three-month period a drop-counting rain gauge was deployed at Chilbolton, and visual inspection of the radar data suggests that extinction of the signal at 94 GHz is only a problem in moderate to heavy rain. A suitable rain-rate threshold could be chosen in order to reject from the comparison any cloud cover derived when attenuation is likely to be very strong.

The distinction between cloud and precipitation has been very successful in the case of rain, with the lidar ceilometer always able to locate cloud base when the radar signal is dominated by the contribution from the much-larger raindrops. In ice-phase precipitation such a distinction is not really possible and snow is therefore included in the observed cloud cover fields. Hence it would be appropriate to use the snow flux held in the model to estimate 'snow cover', which could be combined with model cloud cover before performing the comparison with observations.

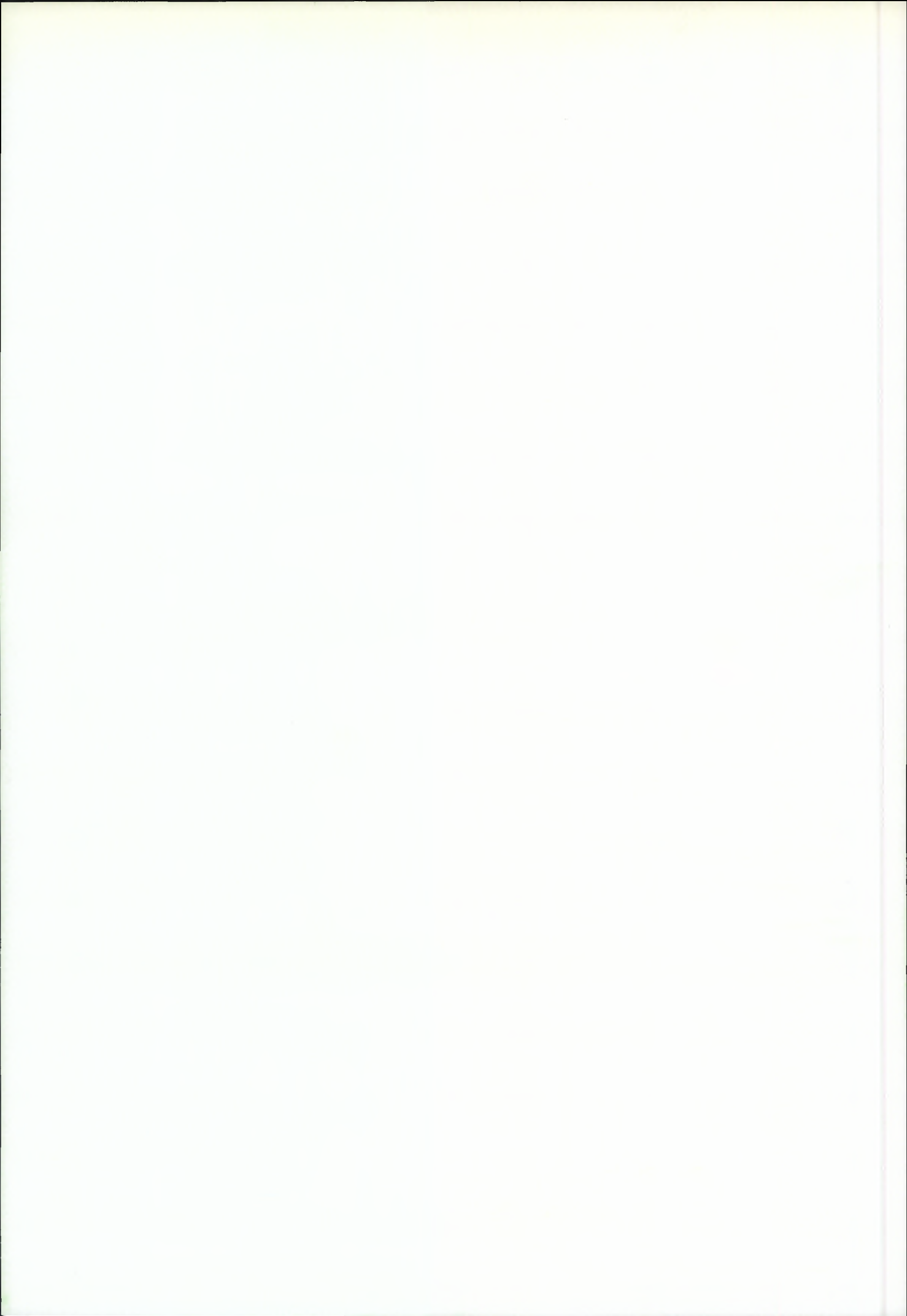
We also intend to compare ice water content derived from reflectivity and temperature (Liu and Illingworth 1997) or from dual-wavelength radar (Hogan et al. 1999) with the values held in the model. This study also highlights the possibility that active instruments could provide real-time information on clouds for assimilation into models; the proposed spaceborne cloud radar would be particularly suited to this task.

ACKNOWLEDGEMENTS

We wish to thank the Radiocommunications Research Agency at the Rutherford Appleton Laboratory for the use of the radars and lidar at Chilbolton. The Galileo radar was developed for the European Space Agency by Officine Galileo, the Rutherford Appleton Laboratory and the University of Reading, under ESTEC Contract No. 10568/NL/NB. The Rabelais radar is on loan from the University of Toulouse. This research received funding from NERC (grant GR3/8765).

REFERENCES

- Brown, P. R. A., A. J. Illingworth, A. J. Heymsfield, G. M. McFarquhar, K. A. Browning and M. Gosset, 1995: The role of spaceborne millimeter-wave radar in the global monitoring of ice-cloud. *J. Appl. Met.*, **34**(11), 2346–2366.
- Hogan, R. J., A. J. Illingworth and H. Sauvageot, 1999: Measuring crystal size in cirrus using 35 and 94 GHz radars. *J. Atmos. Oceanic Tech.*, in press.
- Karlsson, K. G., 1996: Validation of modelled cloudiness using satellite-estimated cloud climatologies. *Tellus A*, **48**(5), 767–785.
- Liu, C. and A. J. Illingworth, 1997: Cirrus cloud ice water content retrieval algorithms for a future spaceborne cloud radar. *Proc. 28th AMS Conference on Radar Meteorology*, Austin, Texas, 109–110.
- Mace, G. G., C. Jakob and K. P. Moran, 1998: Validation of hydrometeor occurrence predicted by the ECMWF using millimeter wave radar data. *Geophys. Res. Lett.*, **25**(10), 1645–1648.
- Tiedtke, M., 1993: Representation of clouds in large-scale models. *Mon. Weath. Rev.*, **121**, 3040–3061.



Radiation Calculations



An Analysis of the Airborne Broad-Band Radiometer Measurements Collected during CLARE'98

P.N. Francis

Meteorological Research Flight, UK Meteorological Office

Y46 Building, DERA Farnborough, Hampshire, GU14 0LX, United Kingdom

Phone : +44 (0)1252 395403 Fax : +44 (0)1252 376588 Email: pnfrancis@meto.gov.uk

H. Flentje, DLR, Oberpfaffenhofen, Germany

J. Pelon, IPSL - Service d'Aéronomie du CNRS, Paris, France

J. Testud, IPSL - Centre d'Etude des Environnements Terrestre et Planétaires, Vélizy, France

INTRODUCTION

This paper looks at the broad-band radiometer data collected from the ARAT and Falcon aircraft during the CLARE'98 field campaign. Data from four flights have been analysed, two from predominantly water cloud cases (7 October and 13 October) and two from ice cloud cases (14 October and 21 October). The mixed-phase flight has not yet been analysed.

Our approach has been to look at albedo data when flying above cloud layers or transmission data when flying below cloud layers, and by making use of a one-dimensional radiative transfer model, to investigate how much cloud needs to be added to the model profiles to match the observed irradiances. We have used the Edwards and Slingo (1996) code for this purpose.

7 OCTOBER 1998

Data from 3 legs have been analysed here, those for times 135927-141042, 142920-144011 and 145919-151142. Results from the first of these are shown in figure 1. We see that the broad-band albedo measured from the ARAT is high, typically around 0.8 or higher, which would seem to indicate a cloud of high optical thickness. The Kestrel cross-section shown in the second panel also indicates a thick cloud, with 2 or 3 pronounced precipitation episodes apparent during the course of the run. There is some indication of albedo increases associated with these regions. The Leandre cross-section (third panel) shows the cloud top clearly, but fails to penetrate to any depth in the cloud as expected.

The radiative transfer calculations were performed with the Edwards and Slingo (1996) code using a model cloud of effective radius $6\mu\text{m}$, consistent with the C-130 *in situ* observations, and the cloud was placed between the surface and 2.5 km, i.e. below the observed temperature inversion. The surface albedos used in the calculations for this case and throughout the paper were characterised from a pair of low-level runs flown on 20 October, under the required

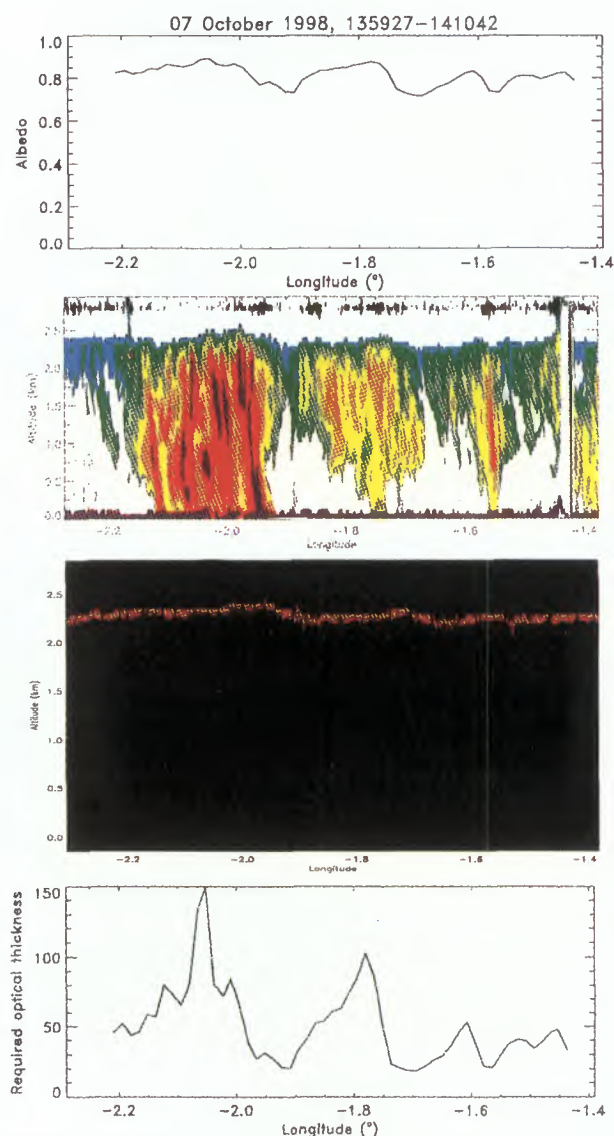


Figure 1. ARAT run above cloud, 7 October 1998, between times 135927 and 141042. The first panel shows the albedo measured from above the cloud, the second panel shows the Kestrel 94 GHz reflectivity, the third panel shows the Leandre lidar backscatter and the fourth panel shows the model optical thickness required to match the albedo measurements, assuming an effective radius of $6\mu\text{m}$.

conditions of diffuse illumination from above. The results for this are shown in figure 2.

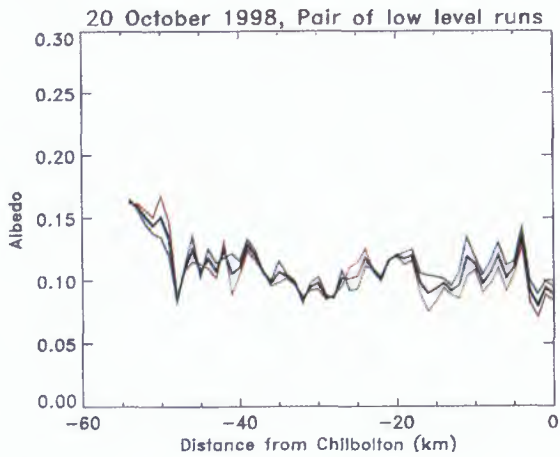


Figure 2. Albedo measured from two low-level runs flown below cloud on 20 October. The red and green lines correspond to data from the individual legs. The black line is the average, used to infer the surface albedo needed for the calculations.

The optical thickness required to match the calculations and the observed albedo is shown in the fourth panel of figure 1. The regions of high optical thickness associated with the precipitation episodes are clearly in evidence.

The results from the 142920-144011 leg are shown in figure 3, and are broadly similar to the first leg. There seem to be indications from the albedo measurements and the Kestrel data that the cloud is not quite as thick in this case, and the high optical thickness peaks associated with the precipitation events are not as marked.

The third leg results are shown in figure 4. Here there is clear evidence of the cloud thinning towards the Chilbolton end of the leg from the Kestrel data, and the albedo data support this. However, it is interesting to note that radar is essentially seeing no cloud between around -1.6° longitude and Chilbolton at -1.43° longitude, whereas the lidar is still seeing a clear signal from the cloud, and the albedo measurements are still indicating the presence of cloud, albeit with decreasing optical thickness.

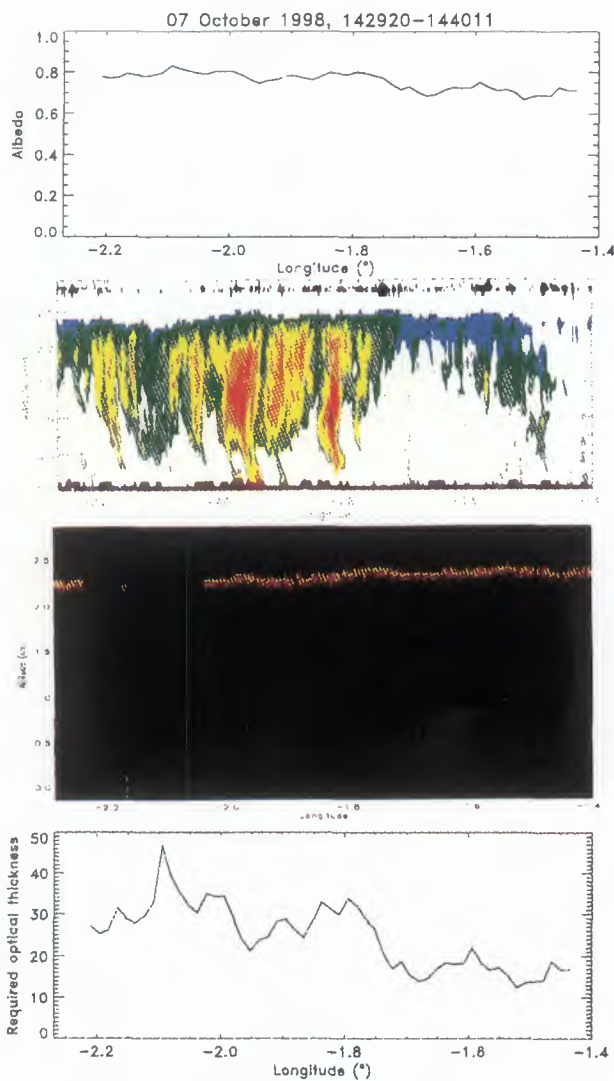


Figure 3. As for figure 1, but for the second ARAT run above cloud, between times 142920 and 144011.

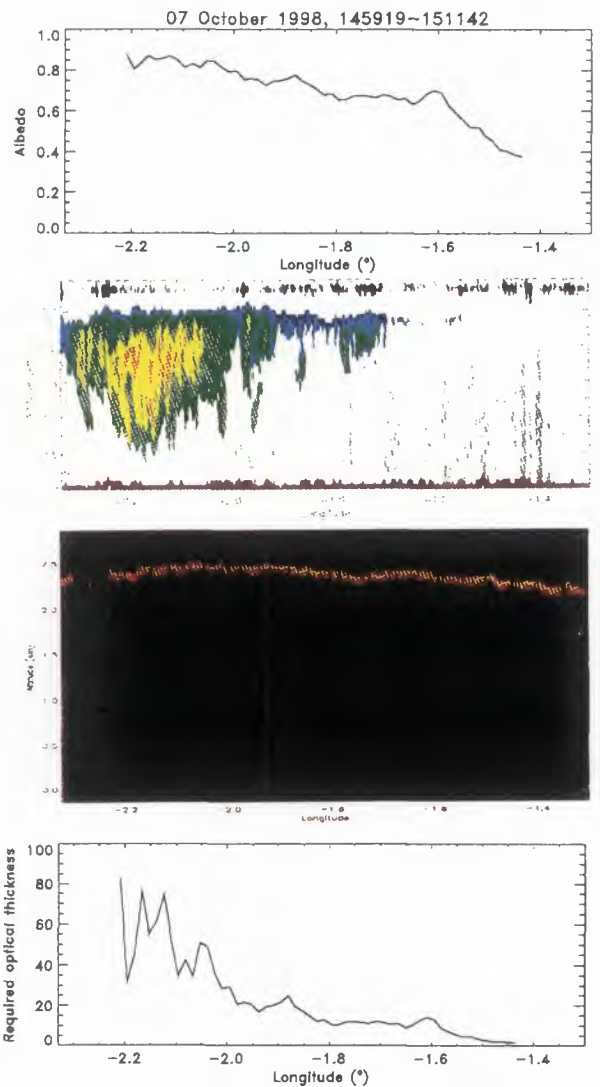


Figure 4. As for figure 1, but for the third ARAT run above cloud, between times 145919 and 151142.

13 OCTOBER 1998

Data from 4 legs have been analysed here, those for times 133300-134015, 134312-135727, 140049-140947 and 141427-142727. The analysis of these legs is more problematical than for the 7 October case, due to the presence of significant amounts of cloud above the flight level of the ARAT for much of the time. This cloud is apparent in the Falcon Alex lidar data and also in the ARAT upper broad-band radiometer data. Because of this, we have only analysed albedo data for limited sections of the runs, generally between -1.75° longitude and the Chilbolton end of the runs at -1.43° longitude.

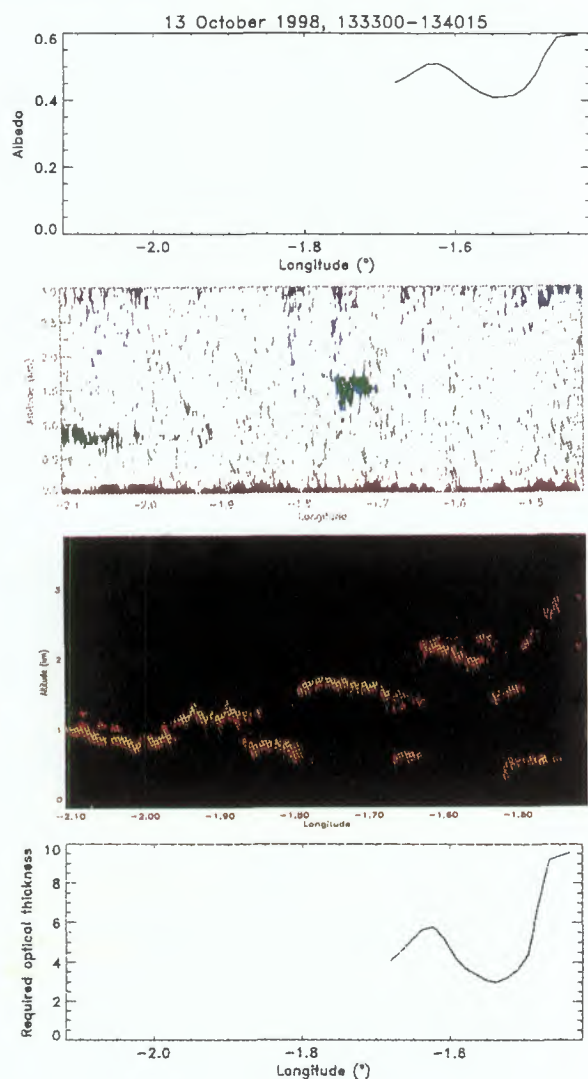


Figure 5. ARAT run above cloud, 13 October 1998, between times 133300 and 134015. The first panel shows the albedo measured from above the cloud, the second panel shows the Kestrel 94 GHz reflectivity, the third panel shows the Leandre lidar backscatter and the fourth panel shows the model optical thickness required to match the albedo measurements, assuming an effective radius of $6\mu\text{m}$.

Figure 5 shows the analysis for the first of the runs. The albedo of the region not contaminated by cloud above the

ARAT is seen to vary between around 0.4 and 0.6, significantly lower than for the 7 October case. This cloud does not appear to have been detected by the radar, whereas the lidar indicates 2 or 3 separate cloud layers in this region. If an effective radius of $6\mu\text{m}$ is again assumed, consistent with the C-130 *in situ* data, then the radiative transfer calculations suggest that water cloud with optical thickness between 3 and 10 is needed to reproduce the observed albedo variations.

Figure 6 shows the second run. This gives an almost identical situation, in that for the region not affected by cloud above the ARAT (i.e. between -1.75° and -1.43° longitude) the lidar is detecting cloud not sensed by the radar. The radiative transfer calculations suggest that cloud optical thicknesses of between 2 and 9 are required to match the measured irradiances.

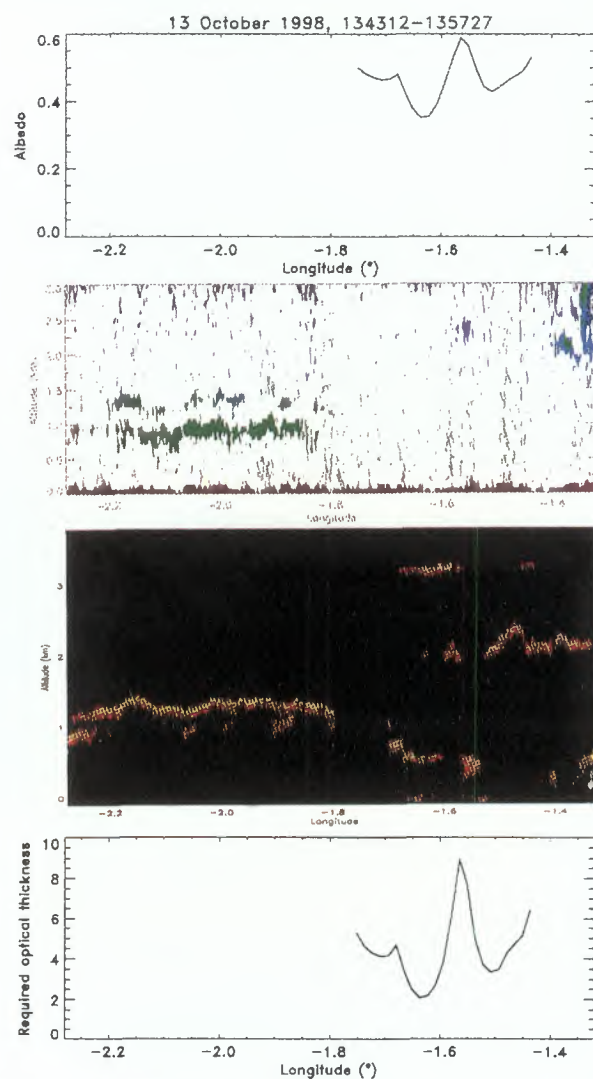


Figure 6. As for figure 5, but for the second ARAT run above cloud, between times 134312 and 135727.

It is also apparent from figure 6 that the radar is detecting cloud in the region between around -2.2° and -1.8° longitude. Unfortunately, the Falcon lidar indicates that in

this region there is significant cloud above the ARAT, which makes the analysis of the albedo data difficult.

In figures 7 and 8 we see that the layer of cloud seen by the radar is moving eastwards, extending to around -1.7° longitude in figure 7 and around -1.6° longitude in figure 8. This layer of cloud is seen by the Leandre lidar in both cases, but in both cases the lidar also sees the above-mentioned characteristic multi-layer cloud structure to the east of it, which the radar still misses. The albedo of the cloud layer seen by the radar goes up to around 0.65 in figure 7 and 0.7 in figure 8, corresponding to optical thicknesses of up to around 18.

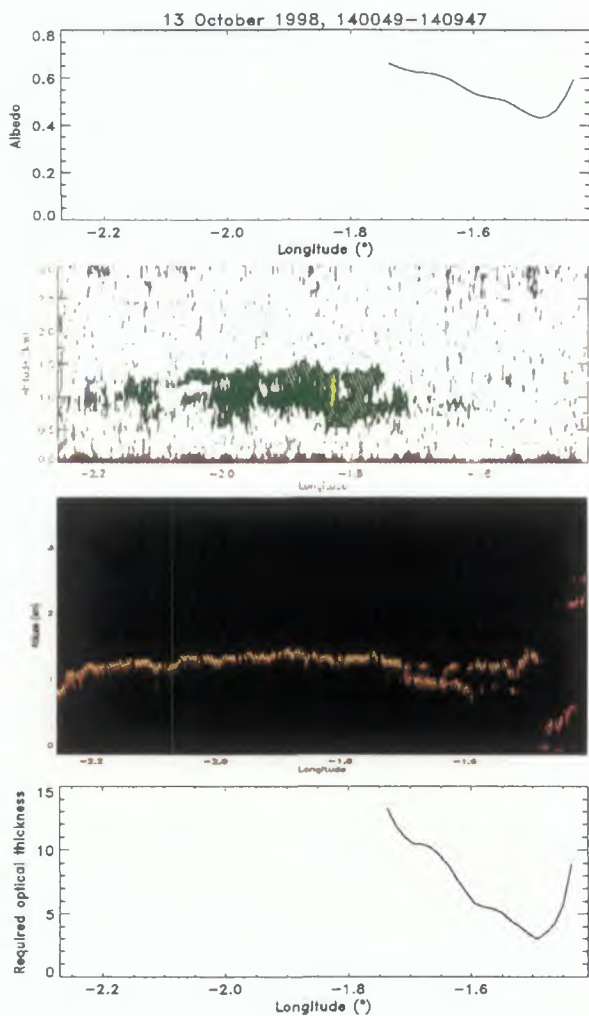


Figure 7. As for figure 5, but for the third ARAT run above cloud, between times 140049 and 140947.

14 OCTOBER 1998

Data from 2 legs have been analysed here, corresponding to the Falcon runs above cloud for times 131600-132500 and 133400-134000. Figure 9 shows data from the 131600-132500 leg. The albedo measured from above the cirrus is in the range 0.29-0.34, and the regions where the albedo

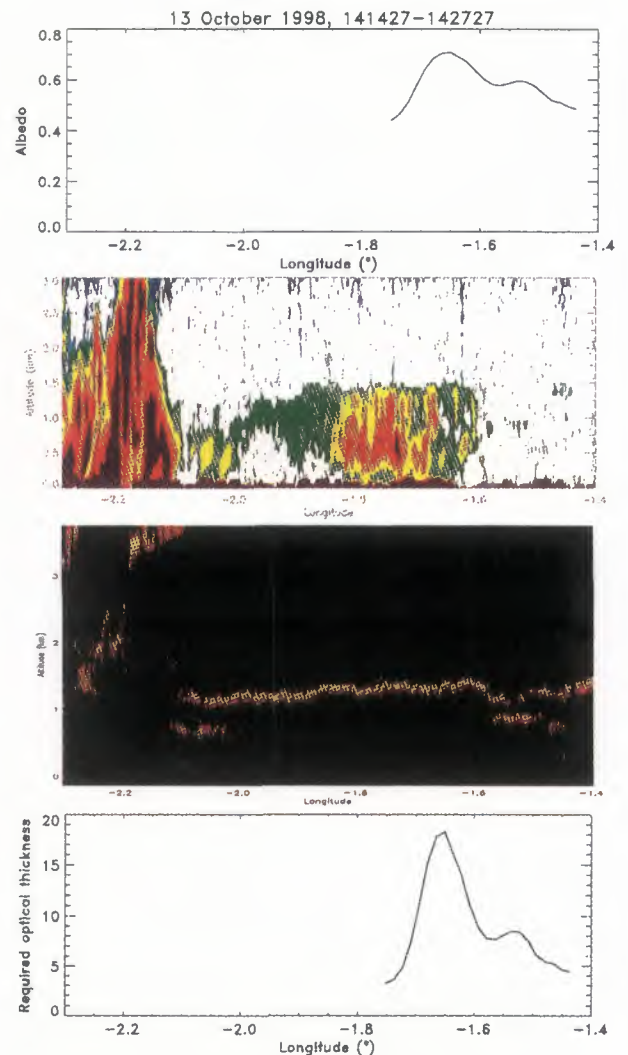


Figure 8. As for figure 5, but for the fourth ARAT run above cloud, between times 141427 and 142727.

increases are seen to correlate well to the structures observed in the lidar cross-section. However, also evident from the lidar data is the fact that boundary layer water cloud is present throughout the run. In addition, ground returns are noted at all times, so that the total optical thickness of the atmospheric column is not going to exceed a value of around 4.

We have performed radiative transfer equations assuming that the effective radius of the water droplet size distribution is $6\ \mu\text{m}$ and that of the ice crystal size distribution is $55\ \mu\text{m}$, consistent with the C-130 *in situ* data. The crystal shape has been assumed to be the bullet-rosette for the purpose of calculating typical ice crystal single scattering properties. The optical thickness of cirrus required to give agreement with the observed albedo is between 12 and 21 if we assume that it is only the cirrus layer beneath the Falcon. If we put only boundary layer liquid water cloud into the model, the required optical thickness is less than 4 throughout. Thus, we can only really conclude that it is the liquid water cloud that is having the major influence on the measured albedo in this case.

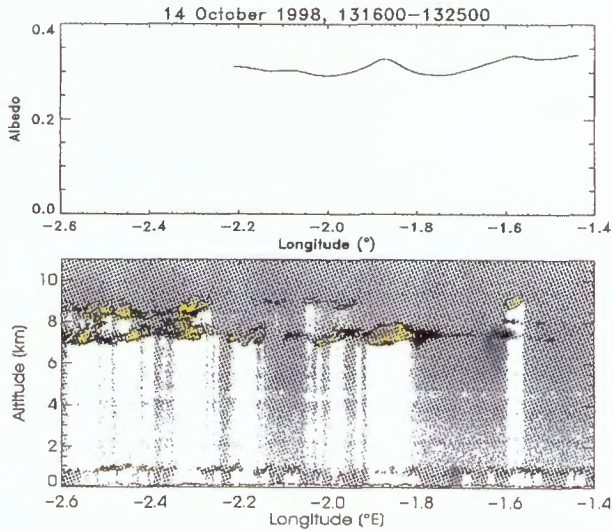


Figure 9. Falcon run above cloud, 14 October 1998, 131600 to 132500. The lower panel shows the Alex lidar 532 nm backscatter.

Figure 10 shows data from the other leg. The albedo varies between 0.28 and 0.36, similar to the preceding run, and similar arguments apply in this case, i.e. we conclude that it is the liquid water cloud that is having the major influence on the measured albedo.

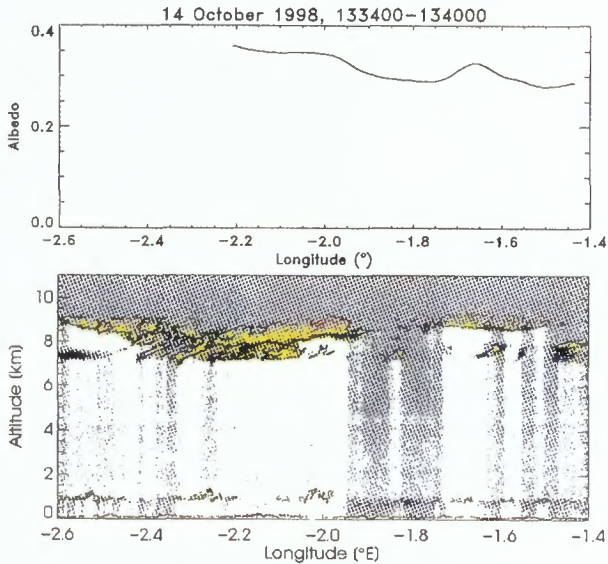


Figure 10. Falcon run above cloud, 14 October 1998, 133400-134000. The lower panel shows the Alex lidar 532 nm backscatter.

21 OCTOBER 1998

Data from one leg has been analysed here, from the Falcon for times 102500-103400. Figure 11 shows the data. The measured albedo is seen to be reasonably high, between around 0.4 and 0.6, although again it is unclear as to how

much of this signal is due to underlying boundary layer clouds. The peaks in the albedo at around -1.9° and -1.45° longitude seem to coincide with the regions where the lidar penetrates the least distance into the upper cloud layer.

Ground returns are only visible for part of this leg, indicating that the column optical thickness is in general larger than for the 14 October case outlined above. We restrict our calculations to two of the regions where obvious ground returns are present, those centred around -2.0° and -1.6° longitude, in order to provide at least some constraint. If we set the boundary layer liquid water cloud to have an optical thickness of 4, and assume that the upper cloud is ice, our calculations show that this upper layer would still need a significant optical thickness to give agreement with the measured albedo. By assuming that the upper layer is liquid water, the required optical thickness is reduced a great deal, such that the total column optical thickness is in the range 3 to 8, as shown in the lower panel of figure 11, and therefore much more consistent with the lidar measurements. This provides some evidence that the thin, bright layer present at the top of the upper cloud is liquid water rather than ice.

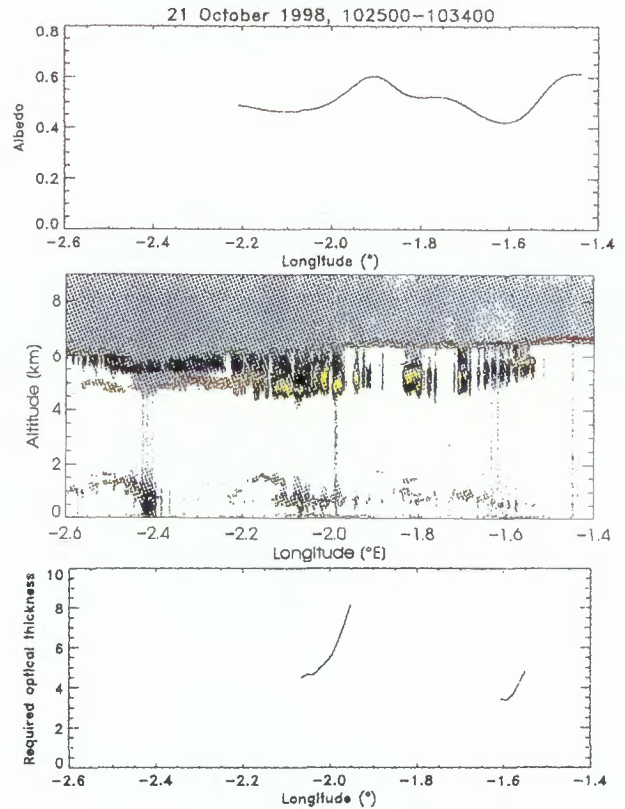
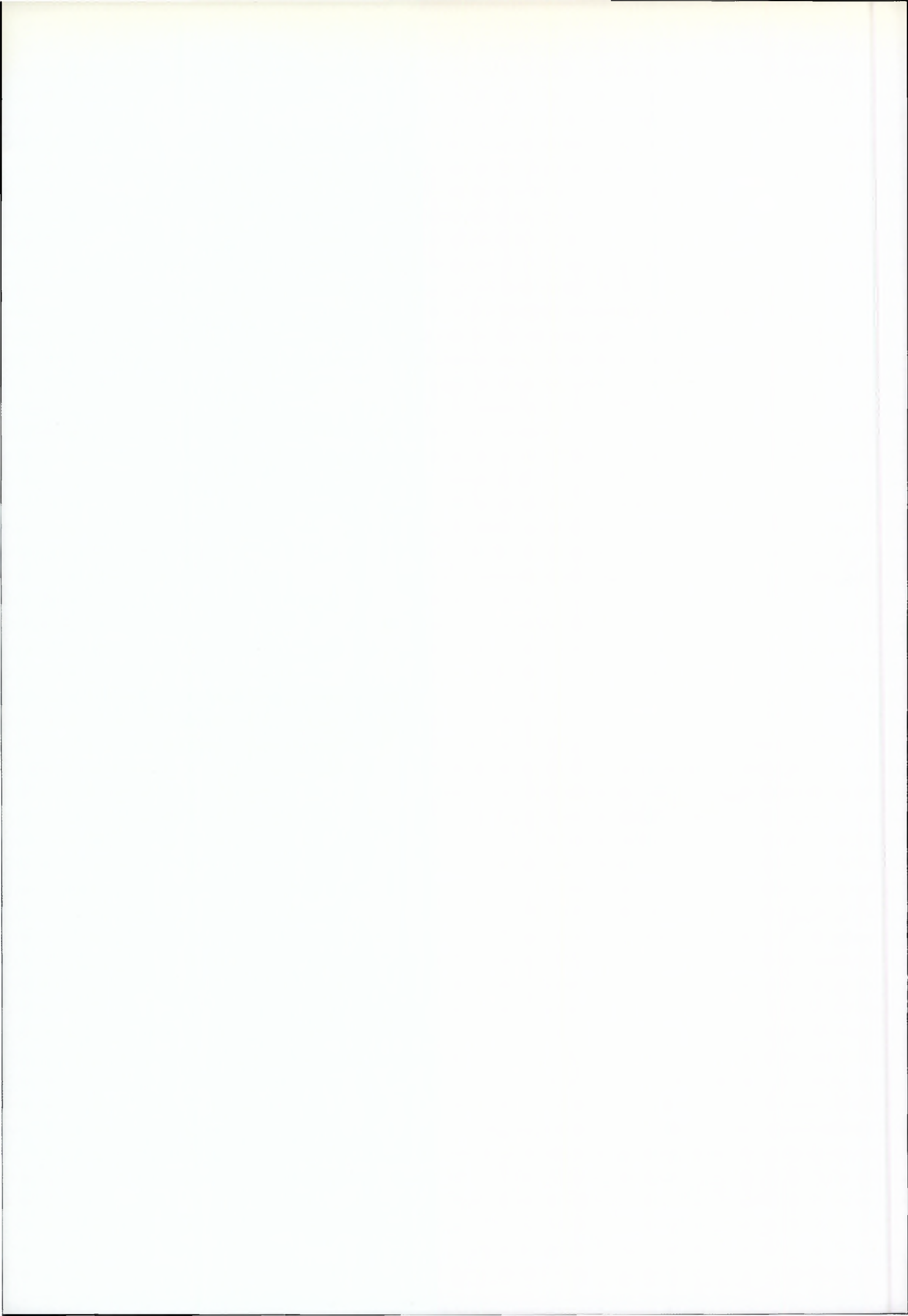


Figure 11. Falcon run above cloud, 21 October 1998, 102500 to 103400. The middle panel shows the Alex lidar 532 nm backscatter.

REFERENCES

- Edwards, J.M., and Slingo, A., 1996: Studies with a flexible new radiation code. I: Choosing a configuration for a large-scale model. *Quart. J. Roy. Meteorol. Soc.*, **122**, 689-720.



Active-passive sensor synergy for cloud observation; IR cloud properties and cloud liquid water

H.I. Bloemink [1], A.C.A.P. van Lammeren [1], A.J. Feijt [1] and S.C.H.M. Jongen [2]

[1] Royal Netherlands Meteorological Institute (KNMI), P.O. Box 201, 3730 AE De Bilt, The Netherlands

[2] Technical University Eindhoven, Faculty of Electrical Engineering, P.O. Box 513, 5600 MB Eindhoven, The Netherlands

INTRODUCTION

Sensor synergy of remote-sensing data enables retrieval of higher order cloud properties. Combining data from various instruments can yield information on *e.g.* cloud boundaries (combining radar and lidar [Uttal 95]), effective particle radius (again radar and lidar [Intrieri 93]) and IR emissivity. This study focuses on the latter, which is an example of active (lidar) and passive (IR radiometer) sensor synergy. Data from the ground-based instruments of the campaigns like CLARA and CLARE'98 can be used. IR Emissivity is a measure for the opacity of a cloud in the IR. The IR emissivity of a cloud is defined as the ratio of the radiation emitted by the cloud and the radiation emitted by a black body at the cloud base, and is an important parameter in the radiation balance. The radiation from the cloud can be determined from the IR radiometer data. The lidar can provide the cloud base altitude, and black body radiation from that altitude can be calculated by using the temperature profile measured by the radio sondes.

Cloud liquid water can be derived from microwave radiometer data. When this is compared with the IR emissivity, a clear relation between the two is found in the case of water clouds. This relation is different from the relation between the optical depth and cloud liquid water, because of the different scattering properties of cloud particles in the visible and the IR.

In this paper, we show results for two cases of the CLARA campaign [Lammeren 98]. Clearly, water and ice clouds can be distinguished, although we expect mixed-phase clouds to be harder to interpret. A clear relationship between cloud liquid water and the IR emissivity is present in these results for water clouds. Combined with a simple approximation for the extinction efficiency of water droplets in the wavelength region of the IR radiometer, these (and other) results suggest that only the LWP of a cloud determines its IR emissivity, and not the precise drop size distribution (*e.g.* the effective radius and the width of the distribution).

THEORY

The liquid water content of a cloud can be expressed as:

$$LWC = \frac{4}{3}\pi \int n(r)r^3\rho_w dr \quad (1)$$

with r the particle radius, $n(r)$ the drop size distribution and ρ_w the density of liquid water. The liquid water path LWP is then the LWC integrated over the vertical extend of the cloud.

In general form, the optical thickness of a cloud can be expressed as

$$\tau = \int_{cloudbase}^{cloudtop} \pi \int n(r)r^2 Q_{ext}(r) dr dz \quad (2)$$

with $Q_{ext}(r)$ the extinction efficiency and z the vertical direction. This extinction efficiency depends not only on the particle size, but also on the particle phase (ice/water) and shape and on the wavelength. Figure 1 shows $Q_{ext}(r)$, calculated from Mie theory [Rooij 84], for two wavelengths; the lidar wavelength (905 nm) and the wavelength used in the IR radiometer (10 μ m). In both cases, spherical water droplets were assumed.

In general, for visible wavelengths, the asymptotic value of 2 is used for Q_{ext} , leading to the well-known relation between LWP and τ :

$$\tau = \frac{3 LWP}{2 \rho_w r_{eff}} \quad (3)$$

where r_{eff} is the effective radius and defined as

$$r_{eff} = \frac{\int n(r)r^3 dr}{\int n(r)r^2 dr} \quad (4)$$

However, it is clear from Figure 1 that such an approximation cannot be applied to a water cloud in the IR. Instead, we propose a linear relation between Q_{ext} and r : $Q_{ext}(r) = C \cdot r$. Although such an assumption was mentioned in general in [Platt '76], to our knowledge it has not been applied directly to Q_{ext} for specific wavelengths. This will be a reasonable approximation for particles of up to about 10 μ m (see Figure 1). Note that this applies to the real particle radius r , and not to the effective particle radius r_{eff} .

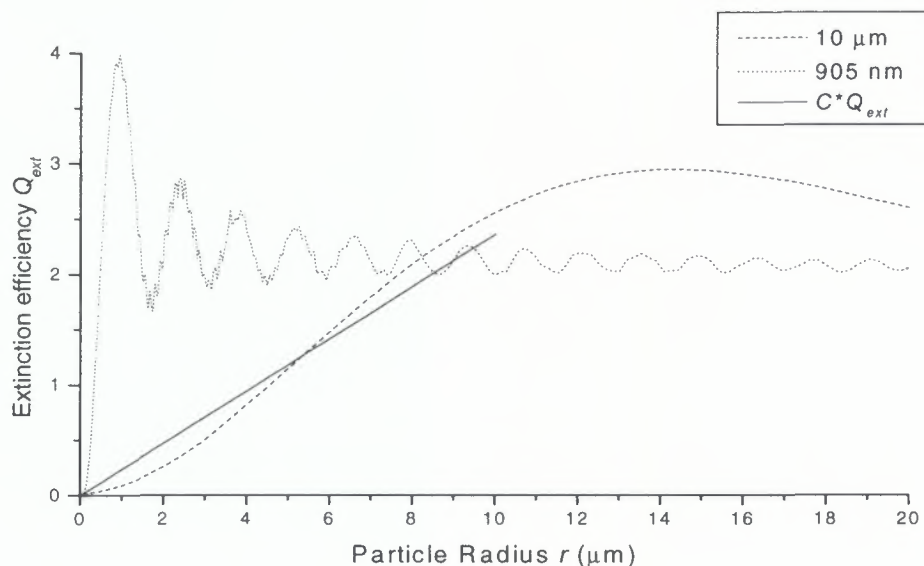


Figure 1: Extinction efficiencies Q_{ext} calculated as a function of particle radius r for the two wavelengths indicated. Also shown is the linear fit to the Q_{ex} for the

Using this approximation, Eq. (2) becomes:

$$\tau_{IR} = C\pi \int n(r)r^3 dr \quad (5)$$

and combining this with Eq. (1) results in

$$\tau_{IR} = C \frac{3}{4} LWP / \rho_w. \quad (6)$$

In other words, for water clouds, the optical depth in the IR depends solely on the cloud liquid water, and not on the particle sizes or the particle size distribution, as long as the cloud particles are smaller than about 10 μm .

The value for C can be found by performing a linear fit to $Q(r)$. This will depend on the cut-off radius that will be used for the fit. A reasonable value for the particle radius of strato cumulus clouds is 7 μm . This results in $C = 0.21 \mu\text{m}^{-1}$. Again, the radius used here is the real particle radius r and not the effective radius r_{eff} .

The IR emissivity ϵ of a cloud can be determined using the IR sky temperature, and the temperature at the cloud base, according to the LIRAD method [Platt 73]:

$$\epsilon = \frac{T_{IR}^4}{T_{cloudbase}^4}. \quad (7)$$

When T_{ir} is determined in a limited wavelength interval, as is the case here, the T dependence of ϵ changes somewhat. For the moment, this relatively small effect has not been taken into account.

The relation between the optical depth in the IR τ_{IR} and ϵ at nadir is:

$$\epsilon = 1 - e^{-\tau_{IR}}. \quad (8)$$

Here, it is assumed that scattering effects are small. This assumption is confirmed for low-level water clouds by various experiments (see e.g. the review paper [Fouquart 89]).

EXPERIMENT

In order to test the above theory, observational data from the CLouds And RAdiation (CLARA) campaign is used. CLARA is a project of which the cloud observation campaigns took place in The Netherlands in 1996. The objective of the campaigns was to observe strato cumulus clouds, and besides in situ measurements using FSSP and 2D probes, a large number of remote sensing instruments were co-located. We will restrict ourselves to describe only those instruments that are relevant to the current research. For more details on the CLARA campaigns the

reader is referred to [Lammeren 98] and other papers of the current workshop.

Three instruments are needed to determine the IR emissivity: an IR radiometer, a lidar and a radio sonde. The IR radiometer used during CLARA was a Heimann KT15.85A with a wavelength range of 9.6 – 11.5 μm . A measurement of the sky temperature is taken every 1.2 seconds, and averaged over 1 minute. The lidar that was used is a commercially available Vaisala CT75K ceilometer. Here data is averaged every 30 seconds, with a vertical resolution of 30 m. Radiosondes (Vaisala) were launched every 6 hours. A microwave radiometer was used to measure cloud liquid water with a 1 second time resolution.

The determination of the IR emissivity from the observations was done using Eq. (7) in the following way. The IR sky temperature T_{IR} is measured directly by the IR radiometer. Next, the cloud base altitude is determined using the lidar data. A cloud base detection algorithm triggered by a positive sign change of the derivative of the lidar signal as a function of height has been used [Pal 92]. Then this cloud base height is converted into a cloud base temperature $T_{cloudbase}$, using the radiosonde data, taking into account the atmospheric correction. (Modtran, [Kneizys 96]) Then, Eq. (7) is applied. Given the detection limits of the instruments, this method allows ϵ values between roughly 0.4 and 1.0 to be measured.

Cloud liquid water is extracted from the microwave radiometer data [Jongen 98].

Note that LWP and ϵ are obtained using only remote sensing instruments, and that they are measured completely independent. In case no radiosonde data is available, model output could be used instead.

RESULTS

Two cases from CLARA were selected for this work: 0-8 UTC on 19 April, 1996 and 6-14 UTC on 26 April, 1996. The 26 April case consists of a thin layer of strato cumulus at about 1.3 km altitude, which disappears after 8:30 UTC.

The 19 April case begins with an ice cloud at about 3.5 km altitude, which disappears after about 4 UTC, when a thin layer of strato cumulus forms at about 1.5 km altitude.

For more details on these cases, the reader is referred to the CLARA web site: <http://www.knmi.nl/CLARA>.

Figures 2 and 3 show the results of ϵ vs LWP for these two cases. In the case of 19 April, a distinction has been made for measurements before 4.3 UTC (the ice cloud) and after 4.3 UTC (the water cloud). In both figures, only points where ϵ can be determined are plotted.

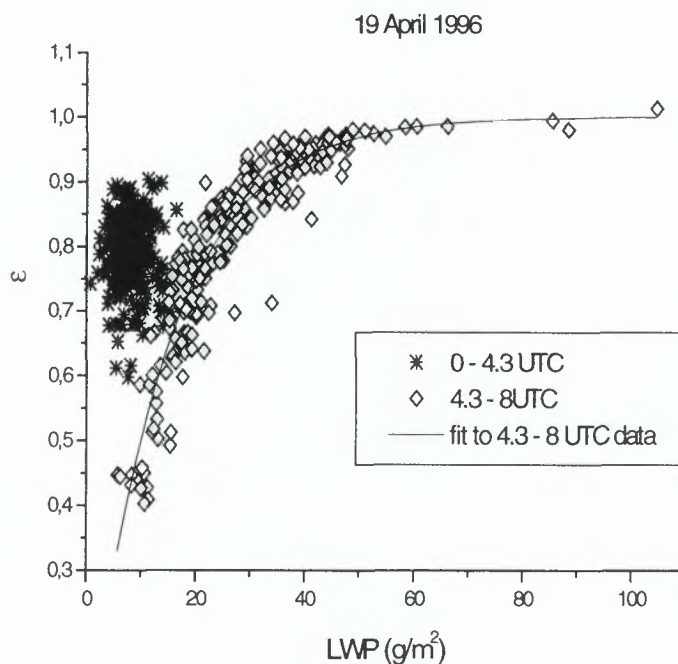


Figure 2: Experimental results for the case of 19 April. Also shown is the fit to the data according to Eq. (9) between 4.3 and 8.0 UTC. See text for further details.

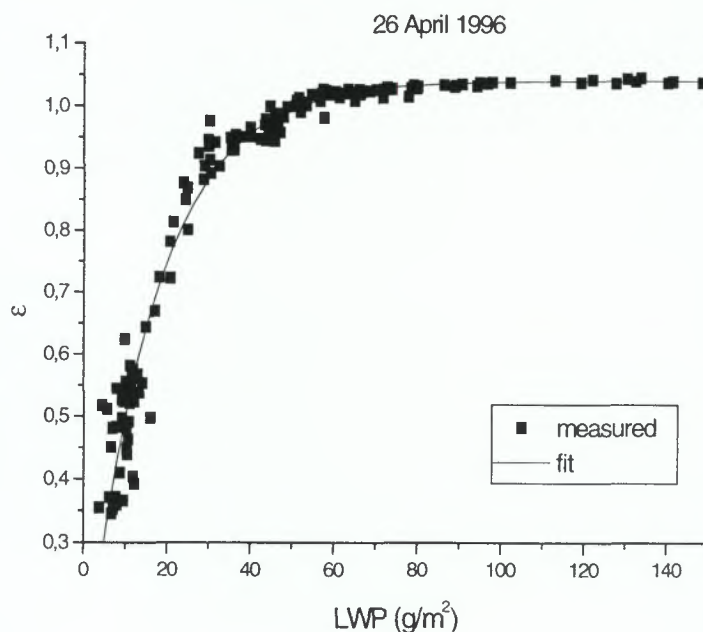


Figure 3: Experimental results for the case of 26 April. Also shown is the fit to the data according to Eq. (9). See text for further details.

DISCUSSION

The fits shown in Figures 2 and 3 are least-square fits to the equation:

$$\varepsilon = 1 - e^{-a_0 L W P} \quad (9)$$

In the 26 April case, all available data were fitted, and in case of 19 April, data after 4.3 UTC were fitted. The results of the fit are shown in Table 1.

	19 April	26 April	[Stephens78]
a_0	0.070	0.067	0.0698

Table 1: Results from the fits shown in Figures 2 and 3.

Clearly, the two fits are in agreement with each other. When these results are compared with ref. [Stephens 78], they are also in agreement. In fact, the results of 19 April are exactly the same as those of [Stephens 78]. Other measurements also agree with our results [Fouquart 89].

In Figure 4, the experimental results are compared with the theory, where the fitting range of the particle radii for Q_{ext} was chosen to be 0 – 7 μm . The theoretical a_0 is corrected by a factor of 1.66 for vertical radiation [Elsasser '42].

The Figure shows that the experimental data agrees better with one another than with the theory, although, when comparing with Figures 2 and 3, the theoretical curve falls just within the limits of the spread of the experimental data. The only parameter that can be somewhat tuned, is the range for which Q_{ext} is fitted. This will depend on the range of particle sizes present in the cloud. These results suggest that this range is chosen too large, since ranges smaller than particle radii of 0 – 7 μm give better agreement with the experimental values. Another way of looking at the difference between the theory and experiment is to consider the difference between Q_{ext} and the approximation we used for it (see Figure 1). For very small particles, the approximation overestimates Q_{ext} . If there are many small particles (compared to larger ones), this will lead to an overestimation of the IR optical depth (Eq. (2)), and thus of the IR emissivity.

From a remote sensing point of view, the relation between ε and LWP can be used to extract more cloud properties from the various instruments. For instance, if LWP is determined from μ -wave radiometer measurements, one can determine the IR emissivity using the relation of Eq. (9). One condition, however, is that the cloud that is observed does not contain ice. This is because

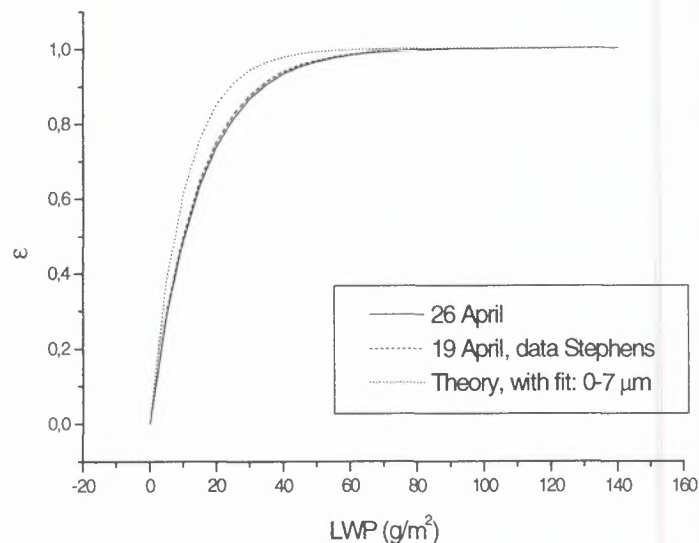


Figure 4: Comparison of the experimental results and the theory. See text for further details.

the micro wave radiometer can only observe cloud liquid water, and not cloud ice. Reversing this argument means that, if ε is determined (using the LIRAD method), LWP can be found for values of ε smaller than 1. Again, only liquid water clouds can be studied. When both properties are known, as is the case in this paper, fitting the data according to Eq. (9) can provide a calibration of the baseline of the μ -wave radiometer. This will only be possible if the range of ε (and LWP) values is suitably large.

CONCLUSIONS

Remote sensing, in combination with sensor synergy, is well suited to determine simultaneously cloud liquid water and the IR emissivity. This makes it possible to study the relationship between these two quantities for a much larger number and variety of clouds, compared to the in-situ measurements of the drop size distribution used so far.

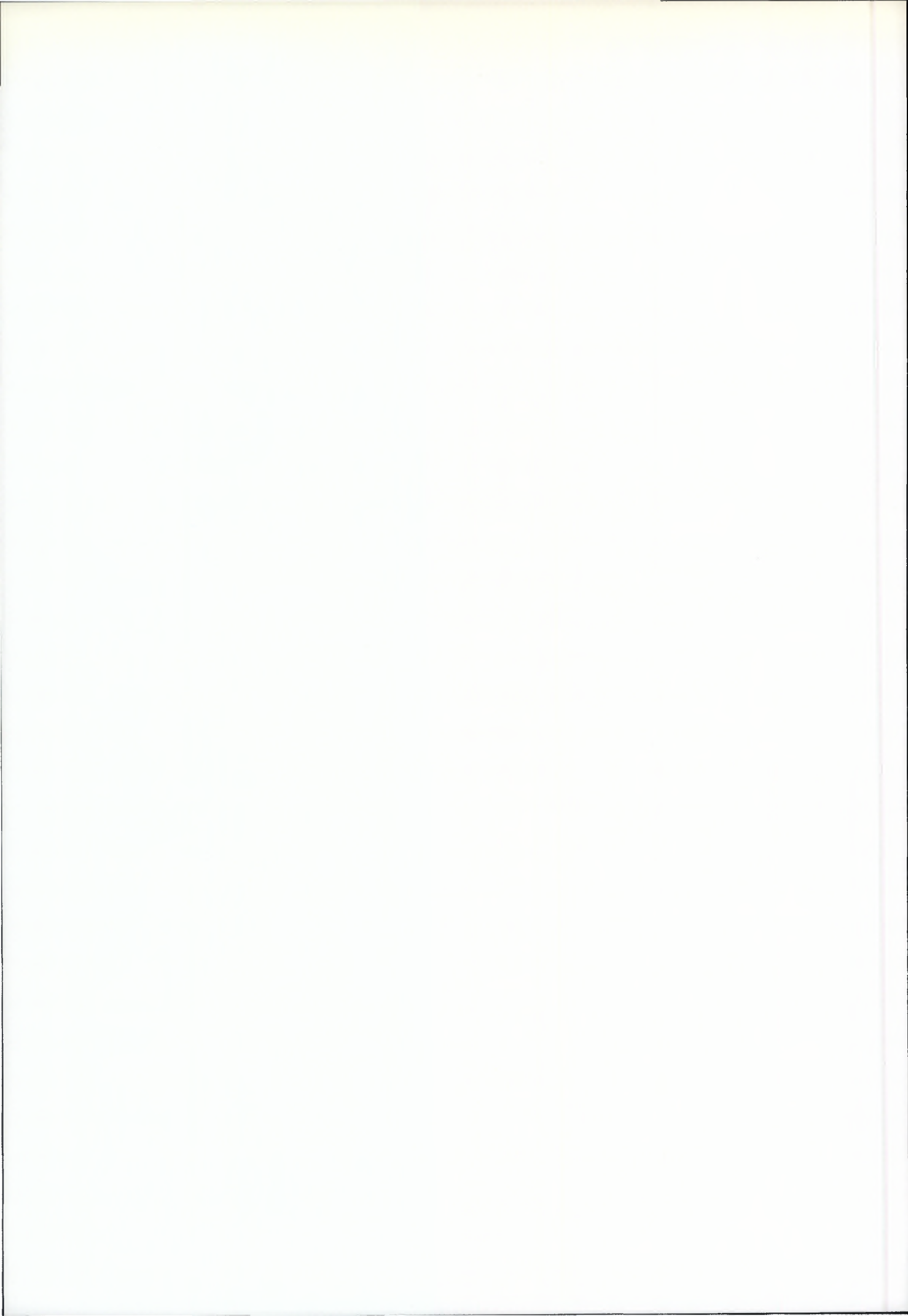
The simple approximation used for the extinction efficiency of water droplets in the 10 μm wavelength region is in agreement with our (and other) experimental results that the IR emissivity solely depends on cloud liquid water, and not on the details of the particle size distributions of the clouds.

For the liquid water clouds studied here, it was found that cloud liquid water can be determined from the IR emissivity of the cloud, provided that the IR emissivity is less than 1. Reversely, the IR emissivity can be found from the cloud liquid water.

In the near future the method described above will also be applied to data from other campaigns like CLARE'98 and CARL.

REFERENCES

- [Elsasser '42]: Elsasser, W.M., *Harvard Meteor. Stud.* **6**, Harvard University Press, 107 pp (1942).
- [Fouquart 89] Fouquart, Y., J.C. Buriez, and M. Herman, *Atmos. Res.* **23**, 203-228 (1989).
- [Intrieri 93] Intrieri, J.M., G.L. Stephens, W.L. Eberhard and T. Uttal, *J. Appl. Meteor.* **32**, 1074-1082 (1993).
- [Jongen 98] Jongen, S.C.H.M., M.H.A.J. Herben, H.W.J. Russchenberg and A.C.A.P. van Lammeren, *Proc. 1998 USNC/URSI National Radio Science Meeting*, Boulder, CO, 5-9 Jan. 1998, University of Boulder, CO, p. 71 (1998).
- [Kneizys 98] Kneizys, F.X., L.W. Abreu, G.P. Anderson, H.J. Chetwynd, E.P. Shettle, A. Berk, L. Bernstein, D.C. Robertson, P. Acharya, L.S. Rothman, J.E.A. Selby, W.O. Gallery and S.A. Clough, *MODTRAN Report 1/11/96*, Philips Laboratory, Geophysics Directorate, Hanscom AFB (1998).
- [Lammeren 98] Lammeren, A.C.A.P. van, H.W.J. Russchenberg, A. Apituley, H. ten Brink and A.J. Feijt, *Proceedings of the Workshop: Synergy of Active instruments of the Earth Radiation Mission*, 12-14 November 1998, GKSS research Center, Geesthacht, Germany.
- [Pal 92] Pal, S.R., W. Steinbrecht and A.I. Carswell, *Appl. Opt.* **31**, 1488-1494 (1992).
- [Platt 76] Platt, C.M.R., *Quart. J. R. Met. Soc.* **102**, 553-561 (1976).
- [Platt 73] Platt, C.M.R., *J. Atmos. Sci.* **30**, 1191-1294 (1973).
- [Stephens 78]: Stephens, G.L., G.W. Paltridge and C.M.R. Platt, *J. Atmos. Sci.* **35**, 2133-2141 (1978).
- [Rooij 84] Rooij, W.A. de, and C.C.A.H. van der Stap, *Astron. Astroph.* **131**, 237-248 (1984).
- [Uttal 95] See e.g. Uttal, T., E.E. Clothiaux, T.P. Ackerman, J.M. Intrieri, and W.L. Eberhard, *J. Atmos. Sci.* **52**, 4276-4284 (1995).



LIST OF PARTICIPANTS

J. Agnew
Rutherford Appleton Lab. (RAL)
Radio Communications Research Unit
Chilton, Didcot, Oxon OX11 0QX, UK
Tel: +44 1235 44 57 70
Fax: +44 1235 44 61 40
E-mail: J.L.Agnew@rl.ac.uk

R. Baedi
Delft University of Technology
Faculty of Information Technology and
Systems
P.O. Box 5031
2600 GA Delft, The Netherlands
Tel: +31 15 278 14 29
Fax: +31 15 278 40 46
E-mail: R.P.Baedi@its.tudelft.nl

A. Culoma
ESA/ESTEC APP/FPE
Keplerlaan 1
2200 AG Noordwijk, The Netherlands
Tel: +31 71 565-5666
Fax: +31 71 565-4696
E-mail: aculoma@estec.esa.nl

D. Donovan
KNMI
Postbus 201
3730 AE De Bilt, The Netherlands
Tel: +31 30 22 06 465
Fax: +31 30 22 10 407
E-mail: donovan@knmi.nl

H. Flentje
DLR
Lidar Group
PO Box 1116
82234 Wessling, Germany
Tel: +49 8153 28 25 25
Fax: +49 8153 28 12 71
E-mail: harald.flentje@dlr.de

E. Attema
ESA/ESTEC SCI/VRS
Keplerlaan 1
2200 AG Noordwijk, The Netherlands
Tel: +31 71 565-4461
Fax: +31 71 565-5675
E-mail: eattema@estec.esa.nl

J. Poiares Baptista
ESA/ESTEC TOS/EEP
Keplerlaan 1
2200 AG Noordwijk, The Netherlands
Tel: +31 71 565-4319
Fax: +31 71 565-4999
E-mail: pedro@xe.estec.esa.nl

O. Danne
GKSS
Institut for Atmospheric Physics
21502 Geesthacht, Germany
Tel: +49 4152 87 15 20
Fax: +49 4152 87 20 20
E-mail: danne@gkss.de

J. Erkelens
Delft University of Technology
Faculty of Information Technology and
Systems
P.O. Box 5031
2600 GA Delft, The Netherlands
Tel: +31 15 278 62 57
Fax: +31 15 278 40 46
E-mail: j.s.erkelens@its.tudelft.nl

P. Francis
UK Meteorological Office
Meteorological Research Flight
Y46 Building
DERA Farnborough, GU14 0LX, UK
Tel: +44 1252 39 54 03
Fax: +44 1252 37 65 88
E-mail: pnfrancis@meto.gov.uk

O. Funk
 Institut für Umweltphysik
 Universität Heidelberg
 Im Neuenheimer Feld 229
 69120 Heidelberg, Germany
 Tel: +49 6221 54 63 13
 Fax: +49 6221 54 64 05
 E-mail:
oliver.funk@iup.uni-heidelberg.de

J. Goddard
 Rutherford Appleton Lab. (RAL)
 Radio Communications Research Unit
 Chilton, Didcot, Oxon OX11 0QX, UK
 Tel: +44 1235 44 61 27
 Fax: +44 1235 44 61 40
 E-mail: j.w.f.goddard@rl.ac.uk

R. Hogan
 Dept. of meteorology
 Univ. of Reading
 Reading, RG6 6BB, UK
 Tel: +44 118 98 75 123, ext 7381
 Fax: +44 118 931 89 05
 E-mail: R.J.Hogan@reading.ac.uk

P. Ingmann
 ESA/ESTEC SCI/VRA
 Keplerlaan 1
 2200 AG Noordwijk, The Netherlands
 Tel: +31 71 565-4459
 Fax: +31 71 565-5675
 E-mail: pingsmann@estec.esa.nl

C-C. Lin
 ESA/ESTEC APP/FPE
 Keplerlaan 1
 2200 AG Noordwijk, The Netherlands
 Tel: +31 71 565-5813
 Fax: +31 71 565-4696
 E-mail: clin@estec.esa.nl

M. Quante
 GKSS
 Institut for Atmospheric Physics
 21502 Geesthacht, Germany
 Tel: +49 4152 87 15 01
 Fax: +49 4152 87 20 20
 E-mail: markus.quante@gkss.de

N. Gaussiat
 Université P. Sabatier
 Laboratoire d'Aerologie
 Observatoire Midi-Pyrénées
 31400 Toulouse, France
 Tel: +33 5 61 33 27 41
 Fax: +33 5 61 33 27 90
 E-mail: gaun@aero.obs-mip.fr

A. Guyot
 IPSL-CETP
 10-12, avenue de l'Europe
 78140 Vélizy, France
 Tel: +33 1 39 25 39 21
 Fax: +33 1 39 25 47 78
 E-mail: guyot@cetp.ipsl.fr

A. Illingworth
 Dept. of meteorology
 Univ. of Reading
 Reading, RG6 6BB, UK
 Tel: +44 118 931 65 08
 Fax: +44 118 931 89 05
 E-mail: a.j.illingworth@reading.ac.uk

A. van Lammeren
 KNMI
 Postbus 201
 3730 AE De Bilt, The Netherlands
 Tel: +31 30 22 06 385
 Fax: +31 30 22 10 407
 E-mail: lammeren@knmi.nl

J. Pelon
 Univ. Pierre et Marie Curie
 CNRS-IPSL
 Service d'Aéronomie
 Tour 15, couloir 15-14, B102
 4, place Jussieu
 75252 Paris Cedex 05, France
 Tel: +33 1 44 27 37 79
 Fax: +33 1 44 27 37 76
 E-mail: jacques.pelon@aero.jussieu.fr

C. J. Readings
 ESA/ESTEC SCI/VR
 Keplerlaan 1
 2200 AG Noordwijk, The Netherlands
 Tel: +31 71 565-5673
 Fax: +31 71 565-5675
 E-mail: creading@estec.esa.nl

H. Russchenberg
Delft University of Technology
Faculty of Information Technology and
Systems
P.O. Box 5031
2600 GA Delft, The Netherlands
Tel: +31 15 278 62 92
Fax: +31 15 278 40 46
E-mail: h.w.j.russchenberg@itr.tudelft.nl

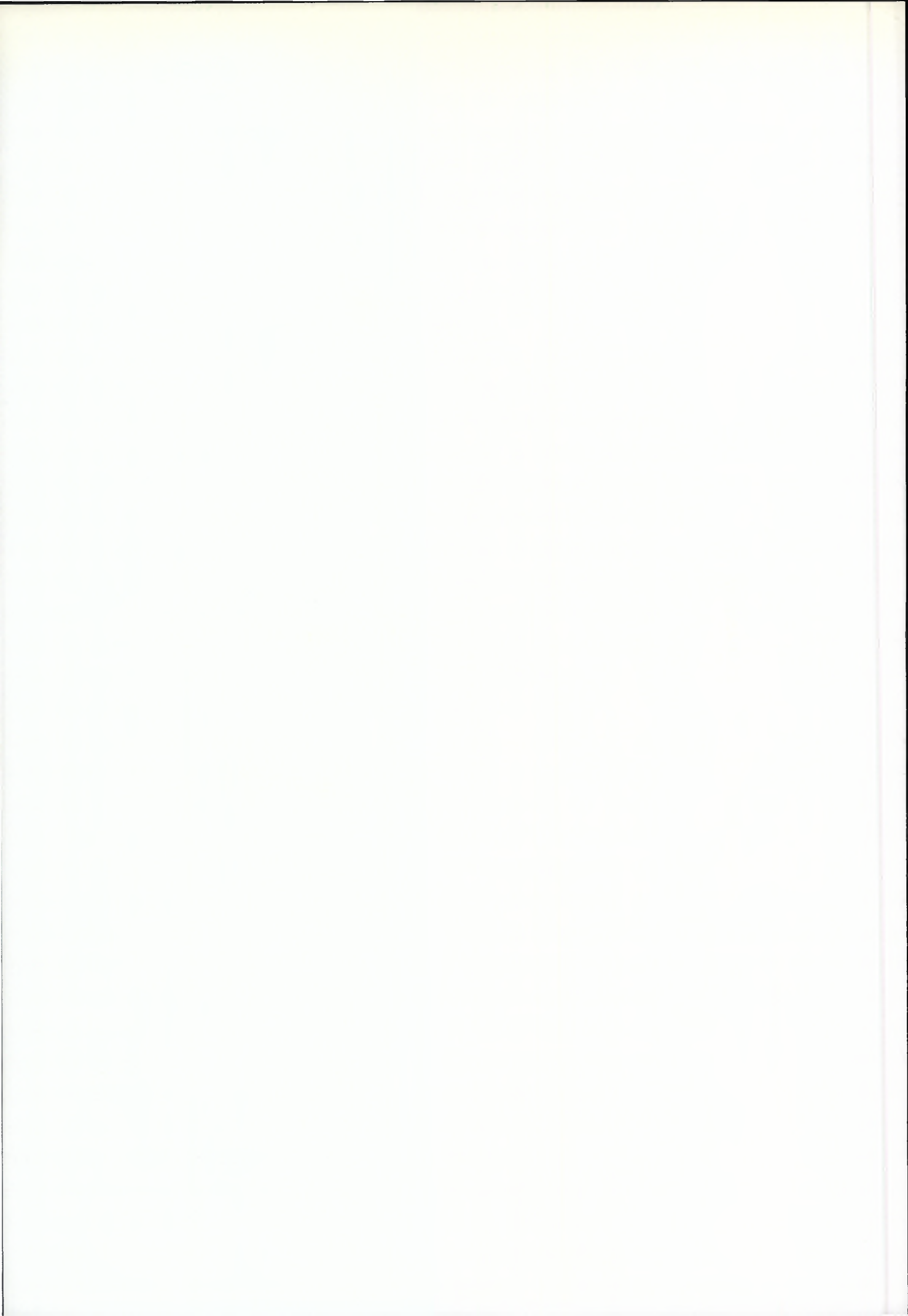
V. Venema
Delft University of Technology
Faculty of Information Technology and
Systems
P.O. Box 5031
2600 GA Delft, The Netherlands
Tel: +31 15 278 78 60
Fax: +31 15 278 40 46
E-mail: V.K.C.Venema@its.tudelft.nl

C. Wrench
Rutherford Appleton Lab. (RAL)
Radio Communications Research Unit
Chilton, Didcot, Oxon OX11 0QX, UK
Tel: +44 1235 44 64 27
Fax: +44 1235 44 61 40
E-mail: c.l.wrench@rl.ac.uk

J. Testud
IPSL-CETP
10-12, avenue de l'Europe
78140 Vélizy, France
Tel: +33 1 39 25 47 76
Fax: +33 1 39 25 49 22
E-mail: jacques.testud@cetp.ipsl.fr

J. de Wit
Delft University of Technology
Faculty of Information Technology and
Systems
P.O. Box 5031
2600 GA Delft, The Netherlands
Tel: +31 15 278 14 29
Fax: +31 15 278 40 46
E-mail: dewit@ircr.et.tudelft.nl

P. Wursteisen
ESA/ESTEC SCI/VRS
Keplerlaan 1
2200 AG Noordwijk, The Netherlands
Tel: +31 71 565-4818
Fax: +31 71 565-5675
E-mail: pwurstei@estec.esa.nl





European Space Agency
Agence spatiale européenne

Contact: *ESA Publications Division*
c/o ESTEC PO Box 299 2200 AG Noordwijk The Netherlands
Tel (31) 71 565 3400 Fax (31) 71 565 5433